WILEY-VCH

Cristiano Benelli and Dante Gatteschi

Introduction to Molecular Magnetism

From Transition Metals to Lanthanides

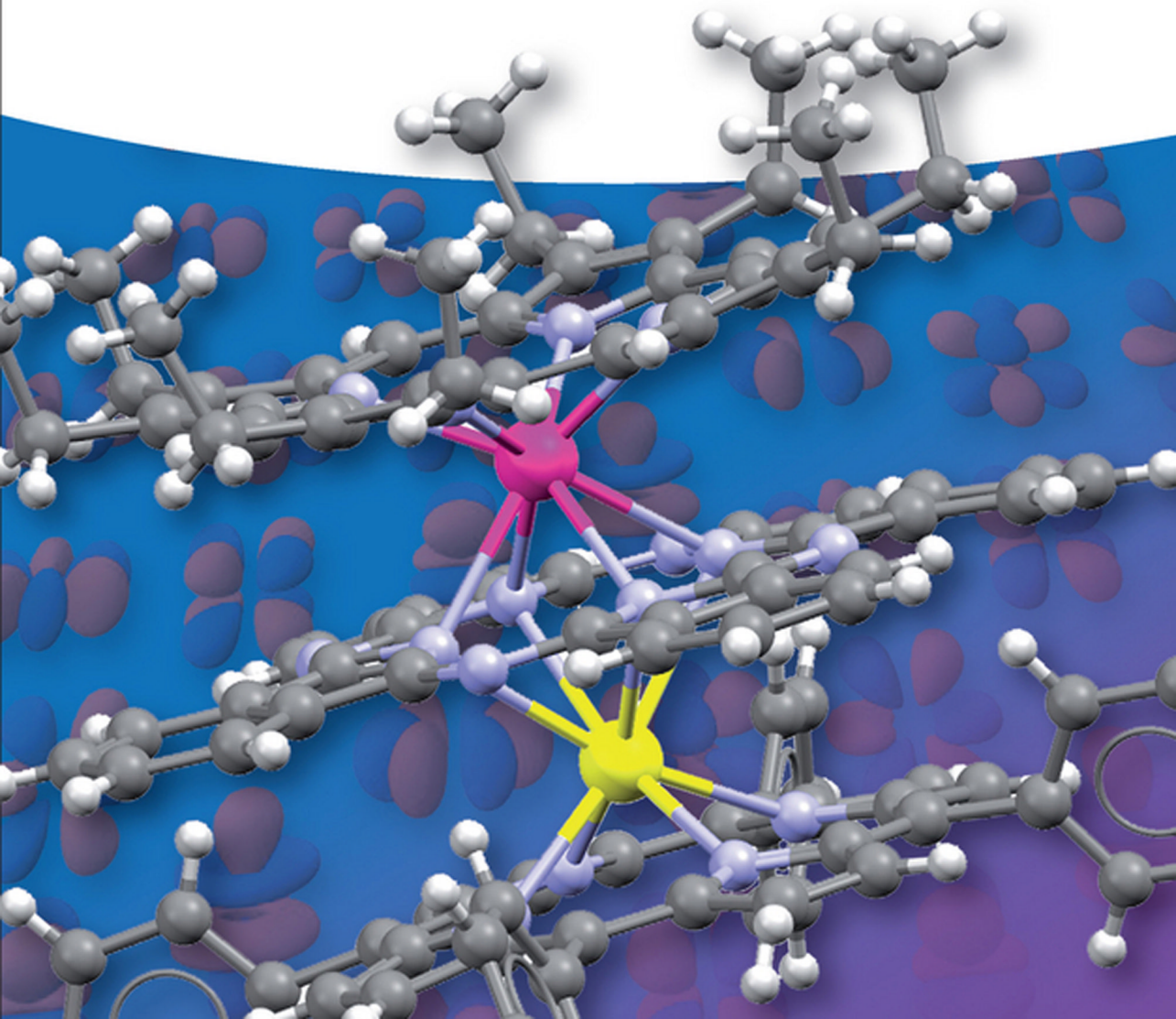

Cristiano Benelli and Dante Gatteschi

Introduction to Molecular Magnetism

Related Titles

Layfield, R.A., Murugesu, M. (eds.)

Lanthanides and Actinides in Molecular Magnetism

2015
Print ISBN: 978-3-527-33526-8
(Also available in a variety of electronic formats)

Hilzinger, R., Rodewald, W.

Magnetic Materials
Fundamentals, Products, Properties, Applications

2013
Print ISBN: 978-3-895-78352-4

Cullity, B.D., Graham, C.D.

Introduction to Magnetic Materials
2nd Edition

2009
Print ISBN: 978-0-470-38631-6

Bruce, D.W, O'Hare, D., Walton, R.I. (eds)

Molecular Materials

2010
Print ISBN: 978-0-470-98677-6
(Also available in a variety of electronic formats)

Cristiano Benelli and Dante Gatteschi

Introduction to Molecular Magnetism

From Transition Metals to Lanthanides

WILEY-VCH
Verlag GmbH & Co. KGaA

The Authors

Prof. Dr. Cristiano Benelli
University of Florence
Department of Industrial Engineering
Via di S. Marta 3
50139 Florence
Italy

Prof. Dr. Dante Gatteschi
University of Florence
Department of Chemistry
Via della Lastruccia 3
50019 Sesto Fiorentino
Italy

All books published by **Wiley-VCH** are carefully produced. Nevertheless, authors, editors, and publisher do not warrant the information contained in these books, including this book, to be free of errors. Readers are advised to keep in mind that statements, data, illustrations, procedural details or other items may inadvertently be inaccurate.

Library of Congress Card No.: applied for

British Library Cataloguing-in-Publication Data
A catalogue record for this book is available from the British Library.

Bibliographic information published by the Deutsche Nationalbibliothek
The Deutsche Nationalbibliothek lists this publication in the Deutsche Nationalbibliografie; detailed bibliographic data are available on the Internet at <http://dnb.d-nb.de>.

© 2015 Wiley-VCH Verlag GmbH & Co. KGaA, Boschstr. 12, 69469 Weinheim, Germany

All rights reserved (including those of translation into other languages). No part of this book may be reproduced in any form – by photoprinting, microfilm, or any other means – nor transmitted or translated into a machine language without written permission from the publishers. Registered names, trademarks, etc. used in this book, even when not specifically marked as such, are not to be considered unprotected by law.

Print ISBN: 978-3-527-33540-4
ePDF ISBN: 978-3-527-69056-5
ePub ISBN: 978-3-527-69055-8
Mobi ISBN: 978-3-527-69045-9
oBook ISBN: 978-3-527-69054-1

Typesetting Laserwords Private Limited, Chennai, India
Printing and Binding Markono Print Media Pte Ltd., Singapore

Printed on acid-free paper

Contents

Preface *XI*

1 Introduction *1*
1.1 A Nano History of Molecular Magnetism *1*
1.2 Molecules, Conductors, and Magnets *4*
1.3 Origin of Molecular Magnetism *5*
1.4 Playing with the Periodic Table *7*
1.5 p Magnetic Orbitals *7*
1.6 d Magnetic Orbitals *10*
1.7 f Magnetic Orbitals *13*
1.8 The Goals of Molecular Magnetism *14*
1.9 Why a Book *15*
1.10 Outlook *16*
1.11 The Applications of Ln *18*
1.12 Finally SI versus emu *21*
References *22*

2 Electronic Structures of Free Ions *25*
2.1 The Naked Ions *25*
2.2 Spin–Orbit Coupling *28*
2.3 Applying a Magnetic Field *31*
References *32*

3 Electronic Structure of Coordinated Ions *33*
3.1 Dressing Ions *33*
3.2 The Crystal Field *35*
3.3 The *aquo* Ions *38*
3.4 The Angular Overlap Model *40*
3.5 The Lantanum(III) with Phthalocyanine (Pc) and PolyOxoMetalates (POM) *42*
3.6 Introducing Magnetic Anisotropy *47*
References *49*

4 Coordination Chemistry and Molecular Magnetism *51*
4.1 Introduction *51*
4.2 Pyrazolylborates *52*
4.3 Phthalocyanines *53*
4.4 Cyclopentadiene and Cyclooctatetraene *54*
4.5 Polyoxometalates (POMs) *56*
4.6 Diketonates *58*
4.7 Nitronyl-nitroxides (NITs) *60*
4.8 Carboxylates *62*
4.9 Schiff Bases *62*
References *65*

5 Magnetism of Ions *69*
5.1 The Curie Law *69*
5.2 The Van Vleck Equation *72*
5.3 Anisotropy Steps in *75*
References *82*

6 Molecular Orbital of Isolated Magnetic Centers *83*
6.1 Moving to MO *83*
6.2 Correlation Effects *84*
6.3 DFT *87*
6.4 The Complexity of Simple *88*
6.5 DFT and Single Ions *90*
6.6 DOTA Complexes, Not Only Contrast *93*
References *96*

7 Toward the Molecular Ferromagnet *99*
7.1 Introduction *99*
7.2 A Road to Infinite *102*
7.3 Magnetic Interactions *104*
7.4 Introducing Interactions: Dipolar *110*
7.5 Spin Hamiltonians *113*
7.6 The Giant Spin *114*
7.7 Single Building Block *115*
7.8 Multicenter Interactions *115*
7.9 Noncollinearity *117*
7.10 Introducing Orbital Degeneracy *119*
References *124*

8 Molecular Orbital of Coupled Systems *127*
8.1 Exchange and Superexchange *127*
8.2 Structure and Magnetic Correlations: d Orbitals *129*
8.3 Quantum Chemical Calculations of SH Parameters *130*
8.4 Copper Acetate! *132*

8.5 Mixed Pairs: Degenerate–Nondegenerate *136*
8.6 f Orbitals and Orbital Degeneracy *138*
References *140*

9 Structure and Properties of *p* Magnetic Orbitals Systems *143*
9.1 Magnetic Coupling in Organics *143*
9.2 Magnetism in Nitroxides *145*
9.3 Thioradicals *147*
9.4 Metallorganic Magnets *149*
9.5 Semiquinone Radicals *152*
9.6 NITR Radicals with Metals *155*
9.7 Long Distance Interactions in Nitroxides *158*
References *160*

10 Structure and Properties of Coupled Systems: d, f *163*
10.1 d Orbitals *163*
10.2 3d *164*
10.3 4d and 5d *165*
10.4 Introducing Chirality *169*
10.5 f-d Interactions *171*
10.6 A Model DFT Calculation *172*
10.7 Magneto-Structural Correlations in Gd-Cu *173*
10.8 f Orbital Systems and Orbital Degeneracy *176*
References *177*

11 Dynamic Properties *179*
11.1 Introductory Remarks *179*
11.2 Spin–Lattice Relaxation and T_1 *181*
11.3 Phonons and Direct Mechanism *182*
11.4 Two Is Better than One *185*
11.5 Playing with Fields *187*
11.6 Something Real *189*
11.7 Spin–Spin Relaxation and T_2 *191*
References *193*

12 SMM Past and Present *195*
12.1 Mn_{12}, the Start *195*
12.2 Some Basic Magnetism *198*
12.3 Fe_4 Structure and Magnetic Properties *201*
12.4 Fe_4 Relaxation and Quantum Tunneling *205*
12.5 And τ_0? *207*
12.6 Deep in the Tunnel *207*
12.7 Magnetic Dilution Effects *210*
12.8 Single Molecule Magnetism *211*
References *213*

13 Single Ion Magnet (SIM) *217*
13.1 Why Single *217*
13.2 Slow Relaxation in Ho in Inorganic Lattice *218*
13.3 Quantum Tunneling of the Magnetization: the Role of Nuclei *219*
13.4 Back to Magnets *222*
13.5 The Phthalocyanine Family: Some More Chemistry *223*
13.6 The Anionic Double Decker *224*
13.7 CF Aspects *225*
13.8 The Breakthrough *226*
13.9 Multiple Deckers *229*
13.10 The Polyoxometalate Family *231*
13.11 More SIM *233*
13.12 Perspectives *235*
References *236*

14 SMM with Lanthanides *239*
14.1 SMM with Lanthanides *239*
14.2 More Details on SMM with Lanthanides *245*
14.3 New Opportunities *247*
References *249*

15 Single Chain Magnets (SCM) and More *251*
15.1 Why 1D *251*
15.2 The Glauber Model *253*
15.3 SCM: the d and p Way *257*
15.4 Spin Glass *259*
15.5 Noncollinear One-dimensional Systems *260*
15.6 f Orbitals in Chains: Gd *262*
15.7 f Orbitals in Chains: Dy *266*
15.8 Back to Family *271*
References *274*

16 Magic Dysprosium *277*
16.1 Exploring Single Crystals *277*
16.2 The Role of Excited States *282*
16.3 A Comparative Look *289*
16.4 Dy as a Perturbation *292*
References *293*

17 Molecular Spintronics *295*
17.1 What? *295*
17.2 Molecules and Mobile Electrons *297*
17.3 Of Molecules and Surfaces *302*
17.4 Choosing Molecules and Surfaces *305*
17.5 Is it Clean? *307*

17.6 X-Rays for Magnetism *308*
17.7 Measuring Magnetism on Surfaces *310*
17.8 Transport through Single Radicals *311*
17.9 Pc Family *314*
17.10 Mn_{12} Forever *317*
17.11 Hybrid Organic and f Orbitals *318*
17.12 Magnetically Active Substrates *319*
17.13 Using Nuclei *321*
17.14 Some Device at Last *324*
References *325*

18 Hunting for Quantum Effects *329*
18.1 From Classic to Quantum *329*
18.2 Basic QIP *331*
18.3 A Detour *334*
18.4 Endohedral Fullerenes *335*
18.5 Criteria for QIP *338*
18.6 Starting from Inorganic *340*
18.7 Molecular Rings *341*
18.8 V_{15} *346*
18.9 Qubit Manipulation *347*
18.10 Some Philosophy *347*
References *348*

19 Controlling the Growth *351*
19.1 Introduction *351*
19.2 Metal–Organic Frameworks MOFs *352*
19.3 From Nano to Giant *358*
19.4 Molybdates *358*
19.5 To the Limit *360*
19.6 Controlling Anisotropy *363*
19.7 Cluster with Few Lanthanides *365*
19.8 Analyzing the Magnetic Properties *366*
19.9 Two-Dimensional Structures *369*
References *371*

20 ESR *375*
20.1 A Bird's Eye View of ESR of Ln *375*
20.2 Gd in Detail *376*
20.3 Gd with Radicals *379*
20.4 Including Orbit *381*
20.5 Involving TM *384*
20.6 Ln Nicotinates *388*
20.7 Measuring Distances *391*
References *392*

21 **NMR** *395*
21.1 NMR of Rare Earth Nuclides *395*
21.2 NMR of Lanthanide Ions in Solution *395*
21.3 Lanthanide Shift Reagents (LSR) *404*
References *407*

22 **Magnetic Resonance Imaging** *409*
22.1 Chemical Exchange Saturation Transfer (CEST) *415*
References *419*

23 **Some Applications of MM** *421*
23.1 Magnetocaloric Effect *421*
23.2 Luminescence *424*
23.2.1 Electroluminescent Materials for OLED *429*
23.2.2 Biological Assays and Medical Imaging *432*
References *432*

Appendix A *435*

Appendix B *437*

Index *439*

Preface

The last years have seen an explosive increasing interest for the development of molecular magnetism, that is, for the magnetic properties of materials based on molecules. These materials have properties, which are related to those of the classic magnets, based on inorganic materials such as metals, just think about iron, or oxides such as magnetite but have interesting properties also for simple molecules. It was in the 1980s of last century that it was realized that magnetism developed with molecules could give rise to novel properties. In particular, it was discovered that beyond bulk magnetism mentioned earlier, it was possible to make new magnetic materials in which chemical engineering played a major role. The new field was called Molecular Magnetism (MM) and gave rise to new physics of which single molecule magnets (SMM) and single chain magnets (SCM) were understood by many researchers as a breakthrough to new materials.

The development of MM required a chemical background, which was not easily available to physicists, and a physical background, which was hard to understand for chemists. The field actually developed, thanks to the efforts of pioneers who explored the new field and translated the awkward local languages in something that could be understood by everybody. As will be discussed in the present book, it is tempting to identify the book *Magneto-Structural Correlations in Exchange Coupled Systems* edited by R. D. Willet, D. Gatteschi, and O. Kahn, with the first attempt to develop a common language between chemists and physicists who explored Molecular Magnetism. From a more chemistry-based approach, Kahn's book *Molecular Magnetism* has been the unique tool allowing chemists to understand magnetism. There have been many other edited books covering the various aspects of the new research area, but it must be highlighted that the book that can be considered as the predecessor of the present one was *Molecular Nanomagnets* by D. Gatteschi, R. Sessoli, and J. Villain, which was focused on the role of the size of molecular magnets in determining the properties.

In the last few years, there has been an exponential growth of molecular magnets based on lanthanide ions, which had been neglected at the beginning. Having been among the first to explore molecular magnets we conceived the idea of writing a book, which reported the unique approach needed for Ln. The original format was limited to these ions, but the contact with the publisher convinced us to write something with a wider appeal. The title then became *Introduction to Molecular*

Magnets, which highlights that the book wants to cover the basic aspects of the field, and the specification "from transition metals to rare earths" clarifies that the dominant interest is on Ln, transition metals being the starting point.

The book has benefited from the comments and corrections provided by several colleagues, namely Roberta Sessoli, Federico Totti, Mauro Perfetti, Lorenzo Sorace, Lapo Bogani, and Alessandro Lascialfari. We thank Alessandro Barbieri and Matteo Mannini for their help in preparing photos and figures.

Given the age of the authors, the book is dedicated to our families: to sons and daughters, Luca and Clara Benelli, Silvia and Alessandra Gattesch, the grand children Duccio Benelli and Marta and Lorenzo Mencaroni and of course to the grandmothers Rossella and Ninetta.

Florence, January 6, 2015

1
Introduction

1.1
A Nano History of Molecular Magnetism

The two terms *molecular* and *magnetism* that appear in the title of this book are here used in a well-defined scientific and technological frame; on the other hand, both of them are also often used, with different meanings, that influences how the scientific version is understood by specialists. Here we will not present a history of the concept of a molecule or a magnet, but we will highlight some general concepts in a scientific field that is developing fast. In order to be understood, it is necessary to make clear immediately what is meant by the title.

Actually, there is a specification ("From transition metals to lanthanides") which is meant to indicate that the present book starts from what has been done in the last few years mainly using transition-metal ions. The novelty is the focus on lanthanides. Another possible subtitle could be "An f orbital approach to molecular magnetism".

Molecules, whatever the word means, are gaining space not only among specialists but also among lay people. The adjective "molecular" is attributed to an increasing number of scientific disciplines, and often the transition of a discipline to a molecular stage is a moment of its explosive development. Molecular biology, the branch of biology that deals with the chemical basis of biological activity, is a significant example. Chemistry is THE molecular science, covering the synthesis, reactivity, and functionality of matter down to the scale of 1 Å. There is no doubt that expressions containing "molecular" must be understood as a quality mark to the scientific approach, giving the impression of a set of activities investigating matter at the most fundamental scale, with as much detail as possible. The great success achieved so far in several molecular sciences is generating more and more molecular sciences. A short visit to Wikipedia shows as diverse substantives to go with "molecular," such as molecular pharmacology, psychiatry, therapy, endocrinology, microbiology, ecology, genomic, and so on. A tantalizing expression is "molecular foundry," but it has nothing to do with a workshop producing metal alloys with a molecular approach. In fact, it is a Department of Energy (DOE) program framed in nanoscience where the "foundry" provides researchers with instrumentation and expertise. Again, molecular implies something special.

Introduction to Molecular Magnetism: From Transition Metals to Lanthanides, First Edition.
Cristiano Benelli and Dante Gatteschi.
© 2015 Wiley-VCH Verlag GmbH & Co. KGaA. Published 2015 by Wiley-VCH Verlag GmbH & Co. KGaA.

The present book will deal with molecular systems that possess magnetic properties, beyond the ubiquitous presence of diamagnetism, and the term *molecular magnetism* (MM) is to be understood as an indication of detailed studies at the molecular level, and as a coming of age of a discipline. There is no doubt that magnets came about much earlier than molecules. The latter term has a well-defined origin, both in time and space: the modern concept of a molecule appeared in France in the early seventeenth century, mole meaning a small mass. The English word "molecule" is documented in 1678, while Gassendi used it in 1658. The concept of molecule was worked out by Descartes as "bodies so small that we cannot perceive them and of which everybody is composed." With time, the modern concept of molecule emerged, and it became apparent that the properties of matter rely on the structure and reactivity of molecules.

Magnetism is much older, and the meaning of the word is controversial, associating it either with the name of a shepherd who discovered the attraction between iron and lodestone, or to the region, Magnesia, where the discovery was made. Additionally, there is evidence of an early use of compasses in China. At any rate, magnetism attracted attention because it allows action at a distance, as exemplified by the magnetic interaction between lodestone and iron, and their reciprocal attraction.

This action at distance puzzled mankind for millennia, and, since movement was associated with the existence in the lodestone of a soul. After all, we are still using the expression "animal magnetism" to indicate the attraction between people. Pliny gave a more material description of the coupling, but in 1600 Gilbert still interpreted the phenomenology with the soul concept: "Magnetic attraction arises because the Loadstone hath a soul." A major breakthrough came rather unexpectedly by joining magnetism and molecules, when Coulomb tried to imagine how a molecule could become polarized in the process of magnetization. But it was the key experiment by Oersted, in 1820, that opened new perspectives in the understanding of magnetism by showing that an electric current influences the orientation of a compass needle. In fact, Ampere suggested that currents internal to the material were responsible of the magnetism and that the currents must be molecular, that is, microscopic rather than macroscopic.

The contribution by Faraday to the knowledge of magnetism cannot be underestimated. In fact, he found that magnetic properties of matter are much more widespread than just lodestone and iron. He discovered that almost the totality of substances is weakly repelled by an applied magnetic field and called these substances *diamagnets*. A less numerous class of compounds was weakly attracted by a magnetic field and was called *paramagnets*. After discovering and naming diamagnetism and paramagnetism, Faraday conceived the concept of a magnetic field, and this view provided an explanation for the action at a distance that startled so much the ancients. A visualization of a magnetic field is shown in Figure 1.1, as obtained with a network of magnetic needles.

The other giant step toward understanding magnetism was taken by Maxwell who provided the mathematical frame that allowed the description of electromagnetism. Pierre Curie investigated the temperature dependence of the

Figure 1.1 The power lines as described by an assembly of dipolar magnets. [Source: Prof. M. Verdaguer – Personal Communication].

magnetization, discovering the law that carries his name. The French title of his thesis, published in 1895, translates "Magnetic properties of matter at variable temperatures". Three types of magnetic bodies are introduced and a list of compounds corresponding to diamagnets, paramagnets, and ferromagnets are reported with a few examples. The only molecules listed are oxygen and nitric dioxide, which are present among paramagnets (weak magnets).

But one of the main actors on the magnetic scene was still missing: the electron. It took some time between the suggestion by Stoney (1874), the discovery by Thomson (1897) working with cathodic tubes and the understanding that the same electron was responsible for the chemical bond. Let us assign the merit for this to Lewis, who suggested the electron pair bond and substantially improved the ingenuous formalism of chemical formulas.

The last step was the development of quantum mechanics, which provided the tools for describing the magnetic properties, starting a revolution that we are still observing. Many new concepts were introduced, and some of them have had a fundamental impact on magnetism, most important among them spin and exchange. Today, with the centenary of quantum mechanics approaching (if we can assign an official date), there is an ever-increasing usage of quantum concepts and quantum phenomena, not only for basic science but for applications as well. Concepts such as quantum tunneling, coherence, decoherence, entanglement, and superposition, are no longer the initiatic jargon of a few scientists but the basic tools of everyday scientific life of chemists, physicists, materials scientists, biologists, and engineers. At the same time, there has been a shift in the size and number of objects under investigation. Typically, one investigates an ensemble containing a huge number of molecules, and what is obtained is an ensemble average. On the other hand, more

and more experimental and theoretical tools allow addressing single molecules – a long way from Descartes and a complete paradigmatic shift.

We hope to have kindled some interest in a field that brings together the physical origins of magnetism with the chemical nature of molecules. One of the questions the book will try to answer is the following: does the above remark about a field acquiring a quality mark when becoming a molecular science also apply to MM?

1.2 Molecules, Conductors, and Magnets

Organic matter is often associated to electronic insulators but recently organic conductors have been synthesized and studied. Research has moved from molecular electronics to molecular spintronics. We will discuss the new exciting opportunities associated with the coexistence of electronic conduction with magnetic properties which provide unique opportunities for addressing individual molecules, storing, writing, and reading information in a single molecule, exploiting the quantum nature.

Molecular electronics is an example of a multidisciplinary approach as is well explained by R. Friend, a physicist who is one of the protagonists of molecular electronics:

> One of the big opportunities in this science is that it crosses traditional divides between subject areas. There's communication between physics and chemistry and materials and divide physics. Managing that communication has been hard work, but it has been really rewarding, as well. It hasn't felt at all like the ordinary mode of activity for a research program in the physics department. In fact, I spend more of my time going to chemistry conferences than I do going to physics conferences. I find what I can pick up at chemistry conferences extremely valuable. I'm constantly trying to better understand what chemists are trying to do.
>
> *R. Friend*

Magnetism is a property traditionally associated with metallic and ionic lattices. Till very recently, magnets were exclusively metals (Fe, Co, Ni, Gd), alloys ($SmCo_5$, $Nd_2Fe_{14}B$), or oxides such as magnetite (Fe_3O_4). This does not mean that magnetic molecules do not exist, O_2 being a clear example. But oxygen is a paramagnet which needs an applied magnetic field to work as a magnet and low temperature. The inorganic materials referred to earlier have permanent magnetization below a critical temperature (often called the *Curie temperature*) that is well above room temperature.

The idea of using organic molecules to make a new type of magnet, that is, an "organic ferromagnet," is a logical consequence of an argument of the following type: if molecules can yield unusual properties such as electrical conductivity, why should they not be magnetic? A gold rush toward this goal started in the 1970s, and it seemed to be successful when a nitroxide radical was reported to

be ferromagnetic at room temperature. Unfortunately, the initial claim was never confirmed. More accurate measurements show that the magnetization was due to iron impurities present in very low concentrations. The lesson was clear: when measuring weak magnetic systems, it is necessary to be extremely cautious. Even the random contact of the sample with a metallic spatula may pollute the sample. Indeed, shortly after such misplaced claims, it was discovered that nitroxides can yield purely organic ferromagnets (Kinoshita, 2004) but with a critical temperature in the range of 1 K, about two orders of magnitude smaller than what was hoped for. Further efforts were made, and the critical temperature increased to about 35 K in a few years (Banister *et al.*, 1996).

By looking around, it was soon realized that relaxing the condition "organic" to "molecular," a whole world was ready to be explored. Let us also have a look at this new world.

1.3 Origin of Molecular Magnetism

MM soon developed as a vital area of interdisciplinary investigation, which produced novel types of magnetic materials. The development of a joint interest among chemists (who moved to understand the difficult theoretical and experimental techniques needed to characterize the complex magnetic properties of the new MM) and physicists (who needed help to unravel the complex molecular structures that chemical ingenuity was able to produce). A NATO ASI was held in Italy in 1983, and the book that was written on that occasion can be considered as the birth of MM (Willet, Gatteschi, and Kahn, 1985). The title of the ASI was "Magneto-structural correlation in exchange coupled systems" and it stressed the need to work out simple rules to understand how to design molecules capable of interacting ferromagnetically with other molecules. This at least was the goal of the organizers, Olivier Kahn, Roger Willett, and one of the authors of this book. On the other hand, the physicists who took part in the event were interested in low-dimensional magnets and obscure objects such as solitons or the Haldane gap (Haldane, 1983). Were the chemists able to synthesize compounds that might show them? The ASI was a good catalyst for joint action, and MM took off (Coronado and Mínguez Espallargas, 2013; Ratera and Veciana, 2012; Wang, Avendaño, and Dunbar, 2011; Zheng, Zheng, and Chen, 2014).

Whithout any doubt MM comes from "Magnetochemistry" (Carlin, 1986). This is the use of magnetic measurements to obtain structural information, and can be done in several different ways. It is important to stress that it is not only a technical exercise as the next example will show, hopefully. Let us consider a Ni^{2+} ion: it has eight valence electrons that occupy the five 3d orbitals following the *Aufbau* principle, as shown in Figure 1.2. The free ion has two unpaired electrons and a corresponding magnetic moment. If the ion is tetra-coordinated, the degeneracy of the five 3d orbitals is removed. The limit coordination is square planar or tetrahedral. In Figure 1.2 is shown the pattern of d levels for the two cases.

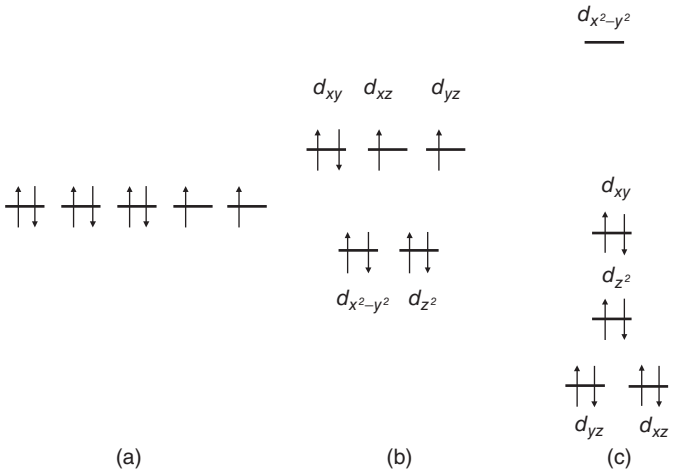

Figure 1.2 Electron configurations for $3d^8$ in (a) spherical, (b) tetrahedral, and (c) tetragonal symmetry.

Nickel(II) in a tetrahedral symmetry has two unpaired electrons and the square planar D_{4h} has zero. Therefore, the former has paramagnetic susceptibility while the latter has diamagnetic susceptibility. A simple measurement of the magnetic susceptibility may decide the coordination geometry.

This kind of research was useful but not particularly exciting, except when the exotic quantum mechanical models were used by chemists for the first time. At the beginning, when magnetic measurements were performed at room temperature, the only safe information came from the comparison of the magnetic moment with that of the free ion. Implicit was the assumption that (i) ions did not interact with one another and (ii) the symmetry of the complexes was not quenched. The noninteracting model, which was sufficient for the simple Ni^{2+} system described above, was not working in many cases. Real life required to go beyond paramagnetism, to explore the interacting systems in which the magnetic properties require the presence of unpaired electrons that must weakly interact with other unpaired electrons. The simplest case of two centers, with one unpaired electron each, gives rise to a singlet and a triplet state, originating from the interaction whose separation must be of the order of 1 – 1000 K. Higher interaction energies lead the system to the limit of a true chemical bond, while below, the lower limit interactions are so weak to be negligible at all but the lowest experimentally accessible temperatures. We will now show with many examples how efficient the theoretical and experimental techniques are that allow the design of tailor-made magnetic molecules.

The goal of obtaining a molecular ferromagnet produced a complete change in the systems to be investigated. Well-behaved paramagnets gave way to interacting systems chosen, at the beginning, using the Goodenough (1958) and Kanamori (1959) rules which were suggested by Anderson's theory of magnetic interactions (Anderson, 1959). The rules were written in a language borrowed from the valence

bond theory of the chemical bond, which was difficult to use for people with a molecular orbital (MO) background.

In the description of MM it is useful to characterize the interacting unpaired electrons with the nature of the half-filled orbitals s, p, d, and f. We will use this scheme extensively and hope to be convincing.

1.4 Playing with the Periodic Table

The intrinsic beauty of chemistry is that of creating new objects and a strong attraction for complexity. So new molecules were synthesized with 2, 3, and so on infinite magnetic centers, which showed interesting properties and waited for interpretation. The chemical way of thinking is intrinsically bottom-up, that is, going to the complex starting from the simple. MM is no exception. The procedure is, at the same time, a simple and a complex one. First of all, one has to choose the nature, size, shape, stability of reactivity, magnetic properties, and connectivity of the building blocks. These require the choice of the nature of the magnetic center. We will call the magnetic orbital the one that contains the unpaired electron, and one needs an efficient design to obtain a building of nice aspect. Molecules can make miracles, but they have severe limitations. The possibility of having bulk magnetic properties, for instance, ferro- or ferrimagnetism, requires an ordered array of 3d interaction. This proves to be difficult for molecules that are intrinsically of low symmetry, while it is easier for metallic and ionic lattices.

To determine the properties of the building blocks, let us start from using the magnetic orbitals. As stated previously, the magnetic orbitals are of p, d, and f nature. It is well known that p orbitals are external and reactive. As a consequence, magnetic organic compounds are generally unstable. On the opposite side, f orbitals are internal ones and very unreactive. In the middle stay the d orbitals. At the beginning of the MM era, the choice was for the p magnetic orbitals followed by d orbitals. The f orbitals were originally discarded, but in the last few years they have been intensively used for their unique properties. We will now have a look at the three types of magnetic orbitals, trying to understand the advantages and disadvantages as building blocks.

1.5 p Magnetic Orbitals

These are the most reactive and unstable orbitals. A pictorial view of selected molecules with electrons in p magnetic orbitals is provided in Figure 1.3. Among the building blocks we show, we can see nitroxides and nitronyl nitroxides, which have been studied as spin labels and spin probes (Jeschke, 2013) due to their good stability, which allows using them in solutions at room temperature. When used as spin probes, molecular moieties containing a paramagnetic group such as NO are

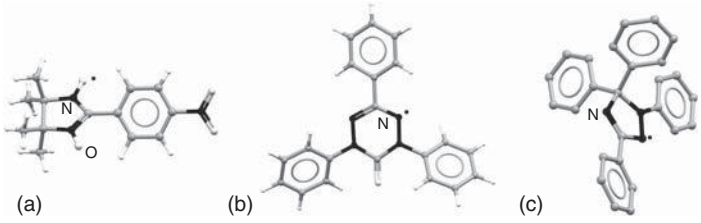

Figure 1.3 Examples of organic radicals: a) *p*-nitrophenyl nitronyl nitroxide; b) Verdazyl; c) 2,3,3,5-tetraphenyl-l H-1,2,4-triazol-1-yl. Hydrogen atoms are omitted for clarity.

selectively inserted into polymers and proteins (Tamura *et al.*, 2013). Electron spin resonance (ESR) spectroscopy is then used to get structural and dynamic information on the parts of the polymer or macromolecule. In both cases, the unpaired electron is mainly localized on the NO groups in a π orbital. The dimerization of the molecule through overlap of its π orbital or the π orbital of another molecule is hindered by the presence of bulky *t*-butyl groups (Figure 1.4a).

The interest in these systems is akin to the magnetochemistry approach outlined previously for the Ni compound: the magnetic properties are not relevant *per se*, but they provide structural information. But the organic ferromagnet revolution changed the interest in magnetic molecules focusing the attention on the magnetic orbitals and on their overlap. Figure 1.3 shows the formula of the first organic ferromagnet, which has a critical temperature of 0.6 K. The origin of the ferromagnetic behavior was interpreted as due to the overlap between positive and negative spin density regions in neighboring molecules (Takahashi *et al.*, 1991; Kinoshita, 2004). The lattice of magnetic centers is essentially three dimensional, as required for observing a transition to magnetic order. Unfortunately, the interactions are weak.

Organic ferromagnets were perhaps the first occasion for a stable collaboration between chemists and physicists in the field of magnetism, and the results were excellent. And with the results, the collaborations increased, producing even better results. The positive trend has been going on for 30 years now, and all indications seem to point to a bright future.

The other molecule of Figure 1.4 is a member of the family of TCNE, which in the reduced form $TCNE^{-}$ is magnetic and can interact with other magnetic orbitals. A TCNE derivative with vanadium turned out to be a magnet at room temperature (Miller and Epstein, 1998). It is not purely organic, but it showed that

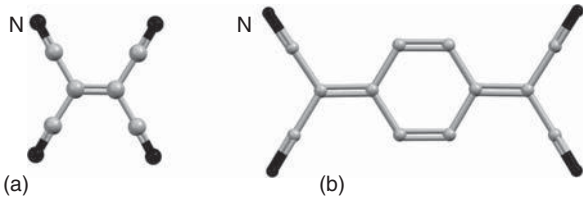

Figure 1.4 (a) Tetracyanoethylene (TCNE); (b) Tetracyanoquinodimethane (TCNQ).

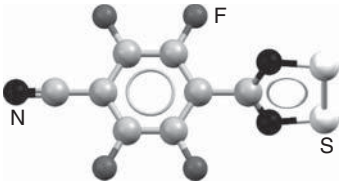

Figure 1.5 The dithiadiazolyl radical.

molecules can produce three-dimensional magnets. Before this result, the first organometallic ferromagnet was reported, where the interacting magnetic centers were again TCNE, organic, and $Fe(C_5Me_5)_2$, that is, metal-organic (Miller *et al.*, 1987). Purely organic is the thioradical shown in Figure 1.5, which is ordered as a weak ferromagnet below 35 K: the highest temperature achieved so far is found in a sulfur-containing radical (Banister *et al.*, 1996). The difficulty with them is that they tend to interact antiferromagnetically, often giving a covalent bond and a diamagnetic adduct. Furthermore, they have a very small magnetic anisotropy, which is an appealing property for TM (transition-metal) and even more for rare earth (RE) molecular magnets.

An appealing property of organic radicals is that they can bind TM or RE ions, showing strong couplings. We remind that Lanthanides refers to fifteen elements from La to Yb. Rare earths indicates lanthanides plus Sc and Y. Since the metal ions often have more than one unpaired electron, or $S > 1/2$ as we will learn to say, also an antiferromagnetic coupling can yield a magnetic adduct. We will see several examples in the following (Miller, 2011).

So far, we have referred to organic radicals, that is, systems with unpaired electrons that contain carbon atoms. The unpaired electron density, however, is often mainly localized on N and or O atoms. But the criteria are simple: the smaller the size, the larger the coupling. Inorganic radicals such as superoxide, which have been largely neglected for molecular magnets, are now appearing in dedicated studies. An interesting feature is the possibility of controlling the intermolecular interactions by changing the cation. In any case, the effective magnetic moments of superoxide ions are larger than the spin-only value because of contributions of the orbital momentum (Dietzel, Kremer, and Jansen, 2004). Furthermore, it has been demonstrated that the zigzag arrangement of the half-filled superoxide orbitals can form a spin chain, with a superexchange pathway mediated by the p_z orbitals of the alkaline ions (Riyadi *et al.*, 2012).

Recently, another radical has been introduced in MM, namely $(NN)^{3-}$, which had seen some history in the framework of the nitrogen fixation studies. It was found early that lanthanides are very efficient in the step reduction of nitrogen, and more recent results have isolated compounds of formula shown in Figure 1.6 (Evans *et al.*, 2009). Of course, the radical needs protecting groups such as *t*-butyl to quench intermolecular reactivity.

Various spectroscopic techniques including ESR confirmed the presence of the radical. More details will be provided in Chapter 20.

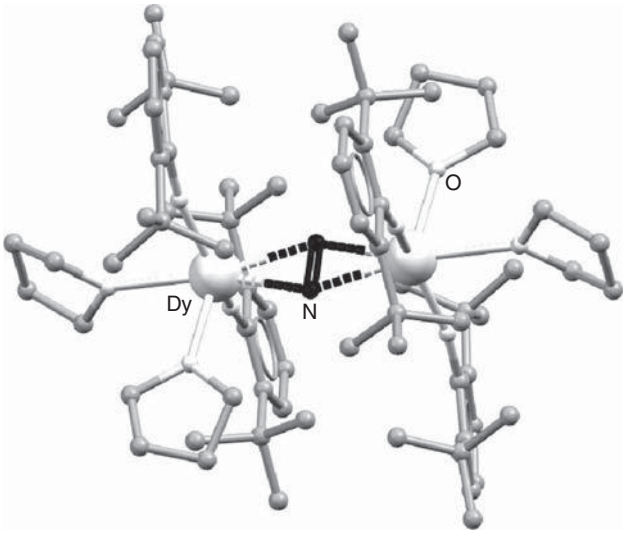

Figure 1.6 Asymmetric unit of $[(ArO)_2(THF)_2Dy]_2(\mu\text{-}\eta^2\text{:}\eta^2\text{-}N_2)$, (OAr $= OC_6H_3(CMe_3)_2$-2, 6). Hydrogen atoms have been omitted for clarity.

1.6 d Magnetic Orbitals

The d orbitals play a fundamental role in the field of MM. Their intrinsic features combined with the versatile chemistry of transition metals (Figure 1.7) offer the chance to synthesize compounds with a wide range of unusual magnetic properties. One class of systems that has been investigated for a long time for its peculiar magnetic properties is the so-called spin crossover (SCO) systems. It is based on the possibility of a metal to be stable in two coordination geometries which differ in the number of unpaired electrons. Let us consider an iron(III) ion in octahedral coordination. The 3d orbitals are split, with a set of three lying lower and a set of two lying higher, as shown in Figure 1.8. The former ones belong to the t_{2g} irreducible representation of the O_h group, while the latter to e_g. There are two possibilities to assign the five electrons to the five orbitals, one electron to each orbital, according to the configuration $t_{2g}^3\ e_g^2$ or, alternatively all five electrons are assigned to the t_{2g} orbitals to give t_{2g}^5.

The spin of the former configuration is 5/2, while for the latter it is just 1/2. The nature of the ground state depends on Δ_0, that is, the separation of the two sets of levels. A large Δ favors the low-spin (LS) arrangement, while a small Δ favors the high-spin (HS) arrangement. Generally a molecule is either HS or LS. In a few cases, the molecule can have both states populated, at a certain temperature, giving rise to what is called *spin equilibrium* or *spin crossover*, an observation first made by Cambi in the early 1930s (Cambi and Szegö, 1931). In a very simple schematization of the process, the HS molecule is favored by entropy, while

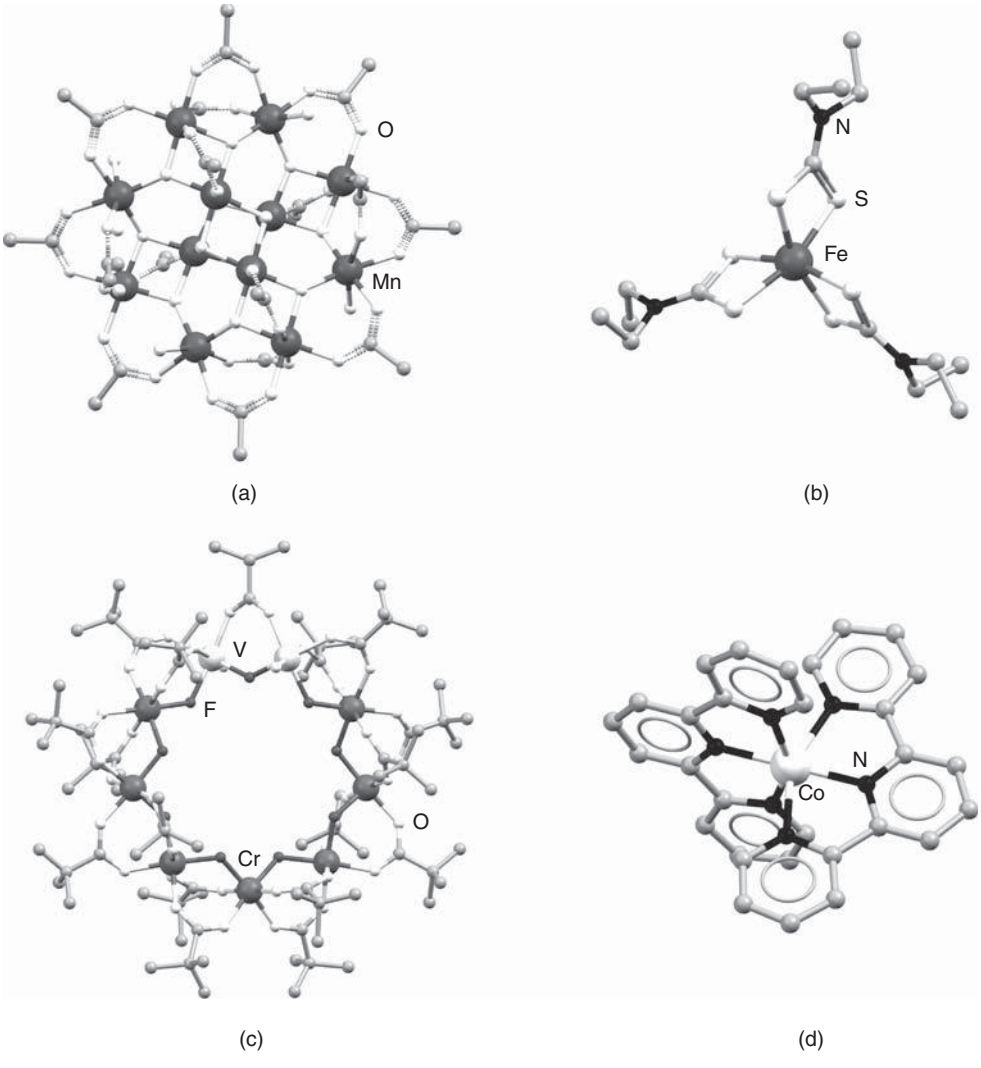

Figure 1.7 Some relevant molecules with *n*d magnetic orbitals. (a) Dodecakis(μ_3-oxo)-hexadecakis(μ_2-perdeuteroacetato-*O*,*O*′)-dodeca-manganese, (b) tris(*N*,*N*-diethyldithiocarbamato)-iron, (c) nonakis(μ_2-fluoro)-heptadecakis(μ_2-pivalato-*O*,*O*′)-dioxo-hepta-chromium-di-vanadium; and (d) bis(2,2′:6′,2″-terpyridine)-cobalt.

the LS one is favored by enthalpy. Recalling that the t_{2g} orbitals are nonbonding (or weakly π antibonding) while the e_g are σ antibonding, it must be expected that the LS has shorter bond distances and is favored at low temperature. The HS–LS transition can be gradual or sharp, and can be accompanied by hysteresis. The transition can be monitored by measuring some property that is different for the HS and LS, such as the magnetic moment or the color. Typical curves are shown in Figure 1.9, exemplifying the behaviors mentioned above. Perhaps

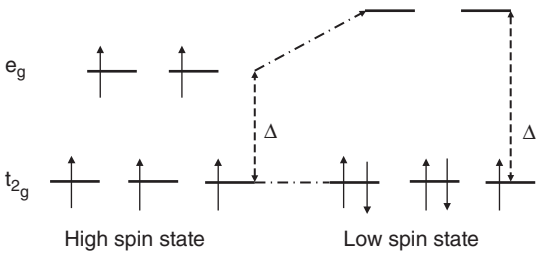

Figure 1.8 Fe^{3+} d orbitals in octahedral environments of different strengths.

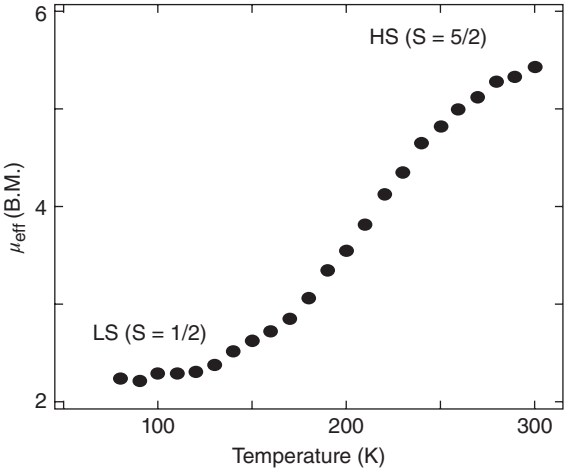

Figure 1.9 Temperature dependences of magnetic moment (μ_{eff}) of a typical iron(III) spin crossover compound. (Reproduced from: "Spin crossover iron(III) complexes", Coord. Chem. Rev., **2007**, *251*, 2606 by Nihei, M. *et al.* with permission from Elsevier B.V.)

the most important is the observation of thermal hysteresis, which makes the HS–LS bistable at a given temperature, with the actual status depending on the history of the sample. This is called *thermal hysteresis* because the variable causing it is temperature. Hysteresis is observed in magnets too, and it is caused by irreversible effects of the applied magnetic field. We will discuss at length the magnetic hysteresis in the following, because it is the basis for the implementation of devices – just think about the hard disk of your computer.

SCO properties have been reported for other ions in octahedral symmetry, such as iron(II), where the LS is diamagnetic and the HS has S = 2. These are perhaps some of the most currently investigated systems, and devices based on iron(II) have been tested for their use as memory cards. Iron(II) systems have also been found to undergo the so-called light-induced spin-state trapping (LIESST) effect. Flashing a laser on an LS molecule excites it to the HS form, as shown in Figure 1.10. There is a barrier for the molecule to revert to the ground state and the metastable HS state to survive at higher temperatures.

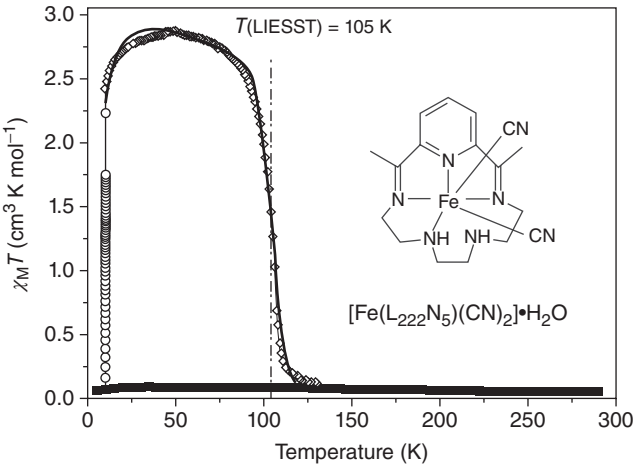

Figure 1.10 Magnetic and photomagnetic properties of a polycrystalline sample $[Fe(L_{222}N_5)(CN)_2]\cdot H_2O$ ($L_{222}N_5$ = 2,13-dimethyl-3,6,9,12,18-pentaazabicyclo[12.3.1] octadeca-1(18),2,12,14,16-pentaene). (Reproduced from Costa, J.S. *et al.* (2007) with permission from The American Chemical Society.)

A milestone in the development of MM was the discovery of the magnetic properties of the so-called Mn_{12} (Figure 1.7a). This cluster is a good example of zero-dimensional materials, and can be essentially regarded as a small piece of manganese oxide whose growth is blocked by the presence of carboxylates. It comprises 12 spin centers that are coupled to give a ground S = 10 state, with 8 Mn^{3+} having all the spins up and the 4 Mn^{4+} down. So far, there has been nothing particularly exciting. The real discovery was that, at low temperatures, the magnetization relaxes slowly and the molecule shows hysteresis like a tiny magnet. The phenomenon is called *single molecule magnetism*, and single molecule magnets (SMMs) have opened a new area of research (Aubin *et al.*, 1996)., where quantum tunneling of the magnetization, a long-sought phenomenon in mesoscopic magnets, was observed. What had led to the failure earlier was the impossibility to control precisely the size of the particles. Since the tunnel relaxation scales exponentially, even small deviations in size of the particles hide the effect completely. This is particularly true for small-sized particles for which the monodispersity should be absolute. Molecules can do the job because they are all identical to each other. When the properties of Mn_{12} were reported, there was the feeling that a fundamental tile was laid.

1.7
f Magnetic Orbitals

Lanthanides or lanthanoids, or REs, are the elements with 4f valence electrons. This gives them a rather dull chemistry which shows up in the dominance of the +3 oxidation state, in great similarity in reactivity and solubility which made

their isolation a difficult task. It seems fit the description of a group of slaves, all similar to each other and who do not dare to show differences. But it is only a false impression; under the uniform, they show rich and different dresses. Apart from the metaphor, the magnetic properties of Ln are unique because they have contributions from the spin and orbit motion of the electrons. The spin motion is, without fantasy, equal in the three directions in space, monitored by a proportionality constant between the intensity of the applied magnetic field and the generated magnetic moment, $g_e = 2.0023$. The orbital momentum, on the other hand, is different for different electrons, and it is in principle different in the different directions in space. Measuring the magnetic properties provides structural information, and this opportunity has been widely used in what can be described as the beginning of the molecular RE saga.

An important step was associated with the discovery that the presence of lanthanide complexes in solution induces shifts in the NMR spectra and increased resolution. In recent years, the discovery that molecular clusters behave as tiny magnets at low temperature has opened the stage of SMMs. The following steps were the extension to polymers, single chain magnets (SCMs), and, in the opposite direction, to single ion magnets (SIMs). With some delay compared to TM ions, lanthanides became one of the focal points of molecular spintronics where they provided the advantages of their unquenched orbital momentum. This new class of experiments requires a theoretical background, which is not trivial. It was worked out in the 1960s when the computer era was at the beginning and symmetry group theory was routinely used in a sophisticated way to reduce the size of the matrices required to calculate the properties. It is a very elegant way to write, and we recommend the interested reader to read Orbach's paper in which he introduces the magnetic relaxation mechanism which now is called after his name (Orbach, 1961).

1.8 The Goals of Molecular Magnetism

Classifying molecular magnets using the nature of the magnetic orbital is one possibility, but there are other options based on the definition of appealing goals that may develop toward exciting applications. As an example, SCO systems started as basic science, but now are pursued for magnetic bistability applications.

The development of strategies for organic (molecular) ferromagnets has produced two samples that are exciting achievements for basic science but rather removed from the expected applications. For instance, there were expectations for soluble magnets, which remain unachieved. The next appealing goals were bound to molecular spintronics, which developed in parallel to the development of spintronics and had a flash start with a Nobel Prize (Fert, 2008). The molecular aspects form a well-suited background in the so-called SMMs, which had been independently developed after a serendipitous discovery.

The current last step is toward quantum computing, that is, the use of quantum effects for developing a new type of computing. After many attempts to develop properties in hostile environments for molecules, the quantum realm appears to be favorable for molecules (Leuenberger and Loss, 2001).

1.9 Why a Book

In the last few years, there has been an exponential growth in interest on the magnetic properties of lanthanides. Their derivatives have found applications in new technologies widely diffused in our lives. Having worked in the field of magnetic properties of lanthanide ions for more than 30 years, we have personally experienced the difficulties inherent to the comprehension of these properties and dreamed to present a book that explains in a simple way the physics hidden beyond the quantum mechanical approaches. Since nobody had so far produced such a book, we decided to try to produce one ourselves. The last sentence is not quite correct; there are excellent edited books (Miller and Drillon 2006). Of course, the treatment of the matter for an edited book is more detailed, and we feel that there is room for both approaches. The idea was to keep the book short, using quantum mechanical approaches in a semiquantitative way, avoiding demonstrations as far as possible. But when we started writing, we realized that p, d, and f orbital systems are mixed in such a way that it is impossible to speak of one leaving out the others. So the menu changed for better food, becoming a general introduction to MM from the point of view of lanthanides. Of course, there is an overlap with Olivier Kahn's *Molecular Magnetism*, a perfect book (Kahn, 1993). But we chose the topics to have minimum overlap with that.

The new book has obviously some overlap with *Molecular Nanomagnets* by J. Villain, R. Sessoli, and one of us (Gatteschi, Sessoli, and Villain, 2006, GSV in the following). However, we feel that the focus on Ln of the present book will ensure the correct coverage.

The other points to critically discuss when starting to write a book are the following: Is it worthwhile? Is the area covered by other books? At which audience is it aimed – the expert, the beginner, chemists, physicists, or others? We could continue.

After this analysis, we decided that there should be room for a unitary book covering the main features of MM without trying to cover all the topics. We tried to integrate a historical approach, especially for the topics where we have given a personal contribution to the field, to a readable treatment of recent developments.

The conclusions are condensed in the title: we want to give an introductory coverage of MM but will do that from the point of view of Ln. There will be paragraphs dedicated to organic and TM, but there will be no attempt to cover these areas in detail. We will use them as an introduction to Ln-based MM.

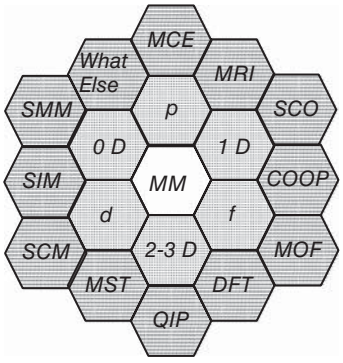

Figure 1.11 Scheme of the structure of this book as explained in the text. For acronyms, see Appendix A.

1.10 Outlook

The first step is to produce a graphic outline of the contents of the book shown in Figure 1.11.

The hexagonal tiles correspond to research areas, starting from the central one, which refers to *magnetochemistry* as the common origin. The first ring of growth reminds us of the relevance of the dimensionality and of the nature of the magnetic orbitals. Finally, ring 2 tries to highlight the main research areas.

We will try now to inform the reader on how the book is organized, giving the opportunity to decide whether to bypass chapters that he or she is already familiar with.

Chapter 2 deals with the electronic structures of the free ions, stressing the role of spin–orbit coupling and the differences between TM and Ln. The effect of applying a magnetic field on the spherical ions is also included.

Chapter 3 covers the coordinated ions working out the spin Hamiltonian approach to the energy levels trying to make clear the formalism and comparing the most common parametrization schemes. A series of compounds of Ln *aquo* ions are used as a test of magnetostructural correlation, also taking advantage of the angular overlap model that will be shown to be a useful tool for justifying the angular dependence of the bonding parameters. There is an introduction to the importance of magnetic anisotropy, which will be the leitmotiv throughout the book.

Chapter 4 describes in a very synthetic way some chemistry of the main family of derivatives whose magnetic properties are analyzed in depth in the other chapters of the book. The chapter is organized according to type of ligands: pyrazolylborates, phthalocyanines, cyclopentadiene and cyclooctatetraene, polyoxometalates, diketonates, nitronyl nitroxides, carboxylates, and Schiff bases.

Chapter 5 presents the basic magnetic properties of the individual magnetic building blocks, the anisotropy, and the strategies to design them correctly. The basic Curie and van Vleck equations are introduced, and their effects on the magnetic data of Ln are discussed with some suitable examples; particular

attention is given to the origin of the anisotropy, of the second, fourth, and sixth order.

Chapter 6 titled "Molecular orbital of isolated magnetic centers" introduces the MO approaches to the calculation of the magnetic properties of mononuclear compounds. The goal is to provide a minimum amount of information on the *ab initio* and DFT (density functional theory) techniques, while trying to define all the acronyms that make theoretical papers difficult to read. The two theoretical models are compared, and pedagogical examples are worked out with a TM in a very simple coordination environment and with Ln to obtain information on the magnetic relaxation showing the power of the method If one is asked which have been the most important theoretical and experimental techniques which in the last years have allowed breakthroughs in the developments in MM then computational chemistry would certainly be a top scorer. If one is asked which have been the most important theoretical and experimental techniques which in the last years have allowed breakthroughs in the developments in MM then computational chemistry would certainly be a top scorer.

Chapter 7, titled "Towards the molecular ferromagnet", is a central one, because it focuses on the description of the interaction between the magnetic building blocks, a key factor for designing molecular magnets. The treatment is made at the spin Hamiltonian level. The title of the chapter highlights one of the strategies that has had a stimulus for designing more and more complex arrangements of molecular magnetic building blocks to build a molecular magnet characterized by permanent magnetization. In fact, learning what the conditions are to induce a transition to magnetic order is stringent and difficult to meet with molecular building blocks. Complementary strategies aiming at building ferrimagnets, weak ferromagnets, and so on, are discussed, highlighting the interest for finite-sized molecular magnets.

Chapter 8 describes the MO treatment of exchange and superexchange interactions first introduced by Anderson, moving from semiempirical methods toward state-of-the-art *ab initio* and DFT calculations. We briefly comment on the techniques needed for discussing the MO approach to weakly coupled systems, such as the broken symmetry approach. We treat in some detail copper acetate because it has had an important role in the understanding of magnetic interactions.

Chapters 9 and 10 show real-life examples of the design, synthesis, and investigation of properties of compounds containing similar and different magnetic orbitals. In particular, Chapter 9 is about interactions involving p orbitals, highlighting the McConnell models, while Chapter 10 covers the d–d interactions not only 3d but considering heavier TMs. Interactions involving f orbitals are dealt with considering Gd–Cu derivatives.

Chapter 11 is the introduction of dynamics in the magnetic properties, or the revolution of Mn_{12}. Spin–lattice and spin–spin relaxation are introduced, together with the quantum tunneling mechanism and the interaction with the thermal bath.

Chapter 12 gives examples of SMM mainly based on TM, not covering in detail the literature but providing a critical view of what has been done and what

remains to be done. Chapter 13 does the same for f-based systems. Particular emphasis is given to the SIMs, which are typical of f electrons. This is one of the hottest topics in MM. Important properties including quantum effects are discussed in the frame of two classes of materials defined by Ln phthalocyanines and polyoxometalates.

Chapter 14 presents SMMs based on f magnetic orbitals, and Chapter 15 covers SCMs based on Ln. The discussion covers far-reaching arguments such as non-collinear axes and chirality, which are present also in other classes of compounds.

Chapter 16 is dedicated to Dy in order to cope with the wave of reports on this magic element.

In a sense, Chapter 17 is the opposite, focusing on individual molecules organized on surfaces and addressed with electric and magnetic fields. These are the hot topics where molecular spintronics, quantum computing, and so on, are covered together with the development in quantum computing (Chapter 18).

Chapter 19 underlines the conditions required to control the growth of 3D structures and covers the developing field of clusters of increasing size going to the limit which has so far been achieved with some indications of the techniques to analyze their magnetic properties. The strategies for 2D clusters are covered in the last section.

The final chapters cover the most used experimental techniques, namely ESR, NMR, some more or less direct application of molecular.

1.11 The Applications of Ln

Before closing this introductory chapter, it may be instructive to have a brief look at the main applications of REs, whose compounds now dominate a huge market in continuous expansion. The first industrial compounds involving lanthanides were produced by Carl Auer von Welsbach (the discoverer of neodymium and praseodymium) at the beginning of twentieth century. As he was already selling the gas mantle for obtaining a more intense gas light, he had problems in finding applications for all REs that remained after the treatment of monazite sands to extract thorium for his mantles (99% Th to 1% Ce). He started the production of "mischmetal" or Auer metal, which was a large success as a lighting flint. It was an alloy consisting of about 50% cerium, 25% lanthanum, 15% neodymium, 10% other RE metals, and iron which was added to increase the strength of the alloy. Mischmetals with similar composition are also used as deoxidizer in various alloys, to remove oxygen in vacuum tubes, sulfur impurities, and as an alloying agent with soft metal such as magnesium, because it provides high strength and creep resistance.

In the following years, the use of lanthanides increased continuously and, despite their cost and very similar chemical behavior, each of the 4f elements found a specific niche, making it fundamental for a number of different technological applications.

Their peculiar magnetic properties have been exploited in the production of alloys such as $SmCo_5$ and $Nd_2Fe_{14}B$, which constitute the majority of the permanent magnets. Molecular compounds are, today, irreplaceable contrast agent in MRI (magnetic resonance imaging). Moreover, the 4f ions play a relevant role in high-T_c superconductors.

Moreover, they are very versatile, offering the possibility to find the same element involved in very different applications. For example, Lanthanum is used to produce high refractive index glass, flint, hydrogen storage systems, battery electrodes, camera lenses, fluid catalysts, and cracking catalysts for oil refineries.

Their optical spectra show in visible and UV regions very sharp absorption lines, much sharper than those of usual transition elements, and this feature makes them essential in all application where bright colors are required. They have been used for a long time in staining glass and ceramics and, later to produce phosphors in classical cathode ray tube (CRT) monitors and TV devices. The possibility of using them in preparing OLED (organic light-emitting diode) screens is currently under study. Because of their optical properties, lanthanides are widely used in lasers (i.e., Nd:YAG) and as dopants in optical fiber amplifiers; for example, erbium is introduced in amplifiers used as repeaters in the terrestrial and submarine fiber-optic transmissions. Some lanthanide iron garnets are fundamental to producing tunable microwave resonators.

Another peculiar property derives from their ability to absorb neutrons and, therefore, they are used in nuclear reactors in control rods and as shielding and structural materials. For safety reasons, they have substituted thorium to improve the welding properties of tungsten.

As is shown in the following table, approximately 40% of the 125 000 tons of lanthanides produced in 2010 is employed in producing magnets and catalytic products. The fastest growing markets are permanent magnets, rechargeable batteries, phosphors, and polishing agents.

Application	Percentage
Magnets	25
Fluid cracking catalysts	15
Battery alloys	14
Polishing powder	14
Metallurgical	9
Auto catalysts	7
Glass additives	6
Phosphors	6
Others	4

Ln compounds are widely used in heterogeneous catalysis as metals, but more molecular systems such as triflates (they are considered among the most

promising catalysts for the so-called "green chemistry") and metallocenes are also widely used in homogeneous catalysis. The latter ones are under investigation also for their magnetic properties but, as far as we know, there is not much overlap between the two types of investigation. It might be useful to crash the barrier by importing magnetic techniques.

The largest end user of REs is the permanent magnet industry. This segment represents about 25% of total demand and is expected to grow to 30% by 2015. Lanthanides are in high demand due to their strength, heat resistance, and ability to maintain their magnetism over very long periods. Magnets made from RE elements such as neodymium, praseodymium, and dysprosium are the strongest known permanent magnets. Their higher performance and smaller size enables many miniature applications, such as personal electronic devices (smart phones, ear buds, MP3 music players). A miniature magnet made with neodymium causes the cell phone to vibrate when a call is received. Capacity utilization is one of the biggest challenges in the wind energy sector. Replacing gear-driven turbines with powerful direct-drive permanent magnet generators can increase efficiency by 25%, and some very large turbines require two tons of RE magnets.

One of the key features that determine the excellent behavior of $SmCo_5$ and $Nd_2Fe_{14}B$ as hard magnets is lanthanides magnetic anisotropy. The latter has been studied under many conditions to optimize the performance of the material. It must be recalled that the high-performance materials are used in many different ways, ranging from cell phones to wind mills and the automotive and aerospace industries. REs provide the so-called single ion anisotropies (magnetocrystalline anisotropy) which are associated with crystal-field and spin–orbit coupling. These factors have their influence on the orbital momentum of magnetoelasticity and magnetoresistance. In order to understand the differences and similarities between inorganic and molecular magnets, it will be necessary to introduce more detailed models. We are convinced that the bottom-up approach to magnetism can be extremely useful, and we will try to underline it whenever we will find some complementary approach between bottom-up and top-down schemes.

Applications can give rise to problems originating from the availability of the materials. Rare earths have a discouraging name, but in the practice they are actually rather abundant. The problem mainly lies in the fact that there are no mines containing one single metal, but ores contain many different metals, with extremely similar chemical properties.

Associated with the previous considerations is the world distribution of resources, which is far from uniform. Reserves are widespread, but the machinery and sophisticated equipment needed for the viable extraction of the elements from the ores are only available in a few countries such as the United States, India, Commonwealth of Independent States, and, above all, China. Owing to the less stringent environmental policies, in 2010, 94% of the global production of REs came from Chinese mines. In the last few years, the demand of lanthanides has been growing at 9–15% a year and the spreading of technologies strictly connected with RE derivatives is creating supply criticality especially for Nd, Dy, Eu, Tb, and Y.

1.12 Finally SI versus emu

Apparently, there should be no doubts on the units to be used in magnetism. The ninth General Conference on Weights and Measures in 1948 on taking the final decision on the electrical units indirectly defined the magnetic ones. According to the expression of Lorentz force, a particle of charge q moving with velocity $\boldsymbol{v}$ in the presence of an electric field $\boldsymbol{E}$ and a magnetic field $\boldsymbol{B}$ will experience a force f given by

$$f = q(\boldsymbol{E} + \boldsymbol{v} \times \boldsymbol{B})$$

Therefore, the electric and magnetic fields can be expressed in terms of the basic quantities of mass, length, time, and current. According to the *Systeme International* (SI), the units of $\boldsymbol{E}$ and $\boldsymbol{B}$ are, respectively, Newtons per coulomb ($\mathrm{N\,C^{-1}}$), and Newtons per coulomb per meter second ($\mathrm{N\,C^{-1}\,m^{-1}\,s}$), where a coulomb (C) is an ampere-second. The latter can be expressed either as kilogram per square second per ampere ($\mathrm{kg\,s^{-2}\,A^{-1}}$) or tesla (T). The tesla is a rather big unit. The largest continuous field ever produced in a laboratory is 45 T and the field at the Earth's surface is a few tens of microtesla.

Everything looks fine and clear, but in everyday practice things are different because in most reports on magnetism centimeter–gram–second (cgs) units are still used. Sometimes it is even worse, and mixtures appear, so that it is possible to find in the same paper "tesla" used when fields are strong and "oersted" when they are small. This is misleading not only because the two units belong to different systems but also because tesla measures the magnetic flux intensity (B) and oersted the magnetic field strength (H). Just to be more precise, in the cgs system the two quantities are related by the expression

$$B = H + 4\pi M$$

where B is measured in gauss, H in oersted, and the magnetization (M) in electrommagnetic unit per cubic centimeter ($\mathrm{emu\,cm^{-3}}$).

Through the book you will find the same mixed notation as is usually used in the literature. In an attempt to make reading easier, we report here the most useful conversion factor between SI and cgs units and a complete table in Appendix B.

1 T	=	10 kG
$1\ \mathrm{kA\,m^{-1}}$	=	12.57(≈12.5) Oe
$1\ \mathrm{A\,m^2}$	=	1000 emu
$1\ \mathrm{MJ\,m^{-3}}$	=	125.7 MG Oe
$1\ \mathrm{A\,m^2\,kg^{-1}}$	=	$1\ \mathrm{emu\,g^{-1}}$
1 G	=	0.1 mT
1 Oe	=	79.58 (≈80) $\mathrm{A\,m^{-1}}$
1 emu	=	$1\ \mathrm{mAm^2}$
1 MG Oe	=	$7.96\ \mathrm{kJ\,m^{-3}}$
$1\ \mathrm{kA\,m^{-1}}$	=	$1\ \mathrm{emu\,cm^{-3}}$

References

Anderson, P.W. (1959) New approach to the theory of superexchange interactions. *Phys. Rev.*, **115**, 2–13.

Aubin, S.M.J., Wemple, M.W., Adams, D.M., Tsai, H.L., Christou, G., and Hendrickson, D.N. (1996) Distorted Mn(IV)Mn(III)3 cubane complexes as single-molecule

Banister, A.J., Bricklebank, N., Lavender, I., Rawson, J.M., Gregory, C.I., Tanner, B.K., Clegg, W., Elsegood, M.R.J., and Palacio, F. (1996) Spontaneous magnetization in a sulfur–nitrogen radical at 36 K. *Angew. Chem., Int. Ed. Engl.*, **35**, 2533–2535.

Cambi, L. and Szegö, L. (1931) Über die magnetische Susceptibilität der komplexen Verbindungen. *Ber. Dtsch. Chem. Ges. (A and B Ser.)*, **64**, 2591–2598.

Carlin, R.L. (1986) *Magnetochemistry*, Spinger-Verlag, Berlin.

Coronado, E. and Mínguez Espallargas, G. (2013) Dynamic magnetic MOFs. *Chem. Soc. Rev.*, **42**, 1525–1539.

Costa, J.S., Balde, C., Carbonera, C., Denux, D., Wattiaux, A., Desplanches, C., Ader, J.P., Gütlich, P., and Létard, J.F. (2007) Photomagnetic properties of an iron(II) low-spin complex with an unusually long-lived metastable LIESST state. *Inorg. Chem.*, **46**, 4114–4119.

Dietzel, P.D.C., Kremer, R.K., and Jansen, M. (2004) Tetraorganylammonium superoxide compounds: close to unperturbed superoxide ions in the solid state. *J. Am. Chem. Soc.*, **126**, 4689–4696.

Evans, W.J., Fang, M., Zucchi, G.I., Furche, F., Ziller, J.W., Hoekstra, R.M., and Zink, J.I. (2009) Isolation of dysprosium and yttrium complexes of a three-electron reduction product in the activation of dinitrogen, the $(N_2)^{3-}$ radical. *J. Am. Chem. Soc.*, **131**, 11195–11202.

Fert, A. (2008) Nobel lecture: origin, development, and future of spintronics. *Rev. Mod. Phys.*, **80**, 1517–1530.

Gatteschi, D., Sessoli, R., and Villain, J. (2006) *Molecular Nanomagnets*, Oxford University Press, Oxford.

Goodenough, J.B. (1958) An interpretation of the magnetic properties of the perovskite-type mixed crystals $La_{1-x}Sr_xCoO_{3-\lambda}$. *J. Phys. Chem. Solid*, **6**, 287–297.

Haldane, F.D.M. (1983) Nonlinear field theory of large-spin Heisenberg antiferromagnets: semiclassically quantized solitons of the one-dimensional easy-axis Néel state. *Phys. Rev. Lett.*, **50**, 1153–1156.

Jeschke, G. (2013) Conformational dynamics and distribution of nitroxide spin labels. *Prog. Nucl. Magn. Reson. Spectrosc.*, **72**, 42–60.

Kahn, O. (1993) *Molecular Magnetism*, Vch Publishers, New York.

Kanamori, J. (1959) Superexchange interaction and symmetry properties of electron orbitals. *J. Phys. Chem. Solid*, **10**, 87–98.

Kinoshita, M. (2004) π-Electron ferromagnetism of a purely organic radical crystal. *Proc. Jpn. Acad. Ser. B Phys. Biol. Sci.*, **80**, 41–53.

Leuenberger, M.N. and Loss, D. (2001) Quantum computing in molecular magnets. *Nature*, **410**, 789–793.

Miller, J.S. (2011) Magnetically ordered molecule-based materials. *Chem. Soc. Rev.*, **40**, 3266–3296.

Miller, J.S., Calabrese, J.C., Rommelmann, H., Chittipeddi, S.R., Zhang, J.H., Reiff, W.M., and Epstein, A.J. (1987) Ferromagnetic behavior of $[Fe(C_5Me_5)_2]\bullet+[TCNE]\bullet-$. Structural and magnetic characterization of decamethylferrocenium tetracyanoethenide, $[Fe(C_5Me_5)_2]\bullet+[TCNE]\bullet+\cdot MeCN$, and decamethylferrocenium pentacyanopropenide, $[Fe(C_5Me_5)_2]^+.[C_3(CN)_5]^-$. *J. Am. Chem. Soc.*, **109**, 769–781.

Miller, J. S. and Drillon M. (2006) *Magnetism: Molecules to Materials V*, Wiley-VCH Verlag GmbH, Weinheim.

Miller, J.S. and Epstein, A.J. (1998) Tetracyanoethylene-based organic magnets. *Chem. Commun.*, 1319–1325.

Orbach, R. (1961) On the theory of spin-lattice relaxation in paramagnetic salts. *Proc. Phys. Soc.*, London, **77**, 821–826.

Ratera, I. and Veciana, J. (2012) Playing with organic radicals as building blocks for functional molecular materials. *Chem. Soc. Rev.*, **41**, 303–349.

Riyadi, S., Zhang, B., de Groot, R.A., Caretta, A., van Loosdrecht, P.H.M., Palstra, T.T.M., and Blake, G.R. (2012) Antiferromagnetic S = 1/2 spin chain driven by p-orbital ordering in CsO_2. *Phys. Rev. Lett.*, **108**, 217206.

Takahashi, M., Turek, P., Nakazawa, Y., Tamura, M., Nozawa, K., Shiomi, D., Ishikawa, M., and Kinoshita, M. (1991) Discovery of a quasi-1D organic ferromagnet, p-NPNN. *Phys. Rev. Lett.*, **67**, 746–748.

Tamura, R., Suzuki, K., Uchida, Y., and Noda, Y. (2013) *Electron Paramagnetic Resonance*, vol. 23, RSC Publishing, Cambridge, pp. 1–21.

Wang, X.Y., Avendaño, C., and Dunbar, K.R. (2011) Molecular magnetic materials based on 4d and 5d transition metals. *Chem. Soc. Rev.*, **40**, 3213–3238.

Willet, R.D., Gatteschi, D., and Kahn, O. (1985) *Magneto-Structural Correlations in Exchange Coupled Systems*, vol. C140, Reidel.

Zheng, Y.Z., Zheng, Z., and Chen, X.M. (2014) A symbol approach for classification of molecule-based magnetic materials exemplified by coordination polymers of metal carboxylates. *Coord. Chem. Rev.*, **258–259**, 1–15.

2
Electronic Structures of Free Ions

2.1
The Naked Ions

We will start by describing the procedure used to express the magnetic properties of molecular magnets, such as the ones described in Chapter 1, based on the concept of magnetic orbitals. For example, $[Ni(H_2O)_6]^{2+}$ is a charged molecule which can be described with computational chemistry approaches with high accuracy providing information on the properties including magnetic properties. It is the black box approach which is more and more diffuse thanks to increasing power of quantum mechanical calculations. No doubt that this is the future. But it is useful also to try to have more insight into the systems one is interested at. Continuing with the Ni example, one can assume that the interaction between the metal and the water molecules can be described as a weak one between a cation and electric dipoles. Now the magnetic properties of molecules depend on the presence of unpaired electrons. Because the water molecules have no unpaired electrons, it is the metal ion that gives the magnetic properties and the unpaired electrons are localized there. It is a brutal simplification but it works.

A useful approach to define the energy level distribution in a metal ion is to consider it as a formal gaseous ion of appropriate charge. This condition allows one to examine the in without the influence of other atoms or ions. Different ions have different magnetic properties. A simple approach is provided by the *Aufbau* principle, which is well known from introductory courses to describe the electron configuration. In a sense, the *Aufbau* configuration is the starting point of our itinerary to magnets. In a quantum mechanical scheme, relevant terms to be considered are the kinetic energy of the electrons in the field created by the nuclei, and the averaged electron–electron repulsion. The Hamiltonian can be expressed as a sum of terms

$$\mathcal{H} = \mathcal{H}_0 + \mathcal{H}_1 + \mathcal{H}_2 \tag{2.1}$$

where $\mathcal{H}_0$ accounts for electron–electron repulsions in a time average on a naked ion, $\mathcal{H}_1$ describes the residual electron–electron repulsion, and $\mathcal{H}_2$ the interaction between the spin and orbital motion. $\mathcal{H}_0$ is dominant and the other two are introduced as perturbations in which the effect of higher terms is considered first. We do not enter into the details on the methods used in deriving the eigenstates of

Introduction to Molecular Magnetism: From Transition Metals to Lanthanides, First Edition.
Cristiano Benelli and Dante Gatteschi.
© 2015 Wiley-VCH Verlag GmbH & Co. KGaA. Published 2015 by Wiley-VCH Verlag GmbH & Co. KGaA.

this Hamiltonian because there are several text books dealing with this argument (Carlin, 1986; Earnshaw, 1968). We want just to recall a few relevant points with special attention to 4f ions, as this field is less explored with respect to systems based on p or d orbitals.

The 14 ions that fill up the seven 4f orbitals can be described by the formalism familiar from the introductory courses describing the electronic structure of atoms and ions. These ions present some peculiarities, which can be useful to summarize. For instance, all the lanthanide elements form stable ions with the oxidation state +3. Some of them exhibit ions with oxidation states +2 and/or +4, and they are those lanthanides that in the anomalous oxidation states can attain the f^0, f^7, f^{14} configuration. The chemical behavior of this family of elements strongly differs from the chemistry of transition elements because of the fundamentally different behavior of f electrons compared to d ones. Actually, the 4f orbitals are shielded from interaction with surroundings by the external $5s^2$ and $5p^6$ shells. This feature has, as main consequence, the evidence that the various $4f^n$ configurations are slightly affected by the donor atoms around the lanthanide ions.

While the shapes of the s, p, and d orbitals are well known and routinely used to rationalize the bonding properties and magnetic properties of compounds, the f orbitals constitute a rarely explored field. In the last few years, the development of detailed approaches aiming to correlate the orbital structure with the magnetic and optical properties of the lanthanides has made the use of 4f orbitals more spread out (Li, Zhang, and Zhao, 2013). The low-lying electronic states can be labeled through the L and M quantum numbers, which depend on orbital moment. For one f electron, $L = 3, M_L = 0, \pm1, \pm2, \pm3$, yielding the imaginary orbitals. The corresponding real orbitals are z^3, (xz^2, yz^2), $(xyz, z(x^2 - y^2))$, $(x(x^2 - 3y^2))$, $(y(3x^2 - y^2))$. They are shown in Figure 2.1.

$\mathcal{H}_0$ is responsible of the fact that the energy depends on n, l quantum numbers and not only on n as in the hydrogen atom. In other words, $\mathcal{H}_0$ gives rise to the electron configuration $4f^n$. The states corresponding to a given configuration are $14!/((14 - n)!n!)$. The minimum degeneracy for a configuration f^1 is 14, which

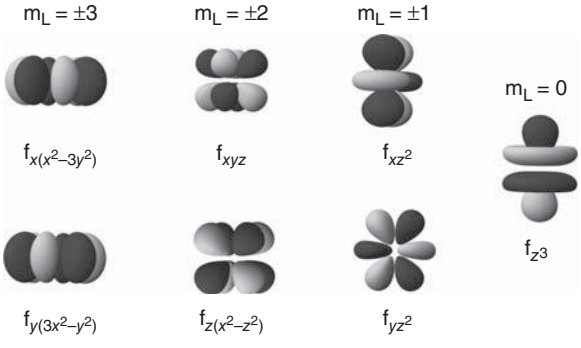

Figure 2.1 Shapes of the 4f orbitals.

becomes 3234 for $n = 7$. Applying $\mathscr{H}_1$, which introduces the electron repulsion terms that are not included in $\mathscr{H}_0$, partially removes the degeneracy of the configuration. Computing the energies of $\mathscr{H}_0 + \mathscr{H}_1$ for Ce^{3+}, which has one f electron, shows that the 14-fold degeneracy is partially removed in two blocks 8×8 and 6×6. The same calculations for Pr^{3+} show that the 91 degenerate states of the free ion ($n = 2$) yield a block-factorized matrix, with blocks of orders 1, 5, 9, 9, 13, 21, and 33. Numerical calculations are powerful, but the results are those of a black box. A deeper insight can be achieved using symmetry. The numbers given above are justified by the so-called Russell–Saunders coupling scheme, whose quantitative aspects will be discussed in the following. For the moment, we will introduce the ways to describe the eigenstates of the various ions.

The starting point can be one f electron, which corresponds to an orbital $L = 3$ state with the $7M_L$ states, $M_L = -3, -2, \ldots, +2, +3$. The spin functions are defined by $S = 1/2$, $M_S = \pm 1/2$. The 14 functions can be classified using L and S as ^2L where 2 indicates the spin multiplicity, $2S + 1$, $S = 2$. In $\mathscr{H}_1$, there is no energy operator associated with spin.

Let us move to $n = 2$, namely f^2. The functions will be characterized by the total orbital operators and total spin $L = L_1 + L_2$, $S = S_1 + S_2$ respectively. The allowed values of L are $|L_1 - L_2| \leq L \leq L_1 + L_2$, $L_1 = L_2 = 3$ and similarly for S. The allowed L values are 0, 1, 2, 3, 4, 5, 6 and the S values 0, 1. It is apparent, however, that assuming all the L values to correspond to a spin singlet and a spin triplet is not correct: the degeneracy calculated in this hypothesis is 196 (14×14: the possible configurations of seven orbitals with two electrons) and not 91 as we showed before. In fact, the ^{2S+1}L functions must be antisymmetric to the exchange of electrons (Fermi–Dirac statistics). Since the spin triplets are even, they require odd L states, and vice versa for the singlets. Therefore, the functions for f^2 are ^1S, ^3P, ^1D, ^3F, ^1G, ^3H, ^1I. The ground state is that with maximum orbital degeneracy and spin multiplicity, ^3H for $n = 2$. The states of $4f^n$ are the same as those of $4f^{14-n}$. The explanation is simple: the former is described as an electron configuration, and the latter as a hole configuration. Since the energies depend on the product of the charges, a pair of electrons is equivalent to a pair of holes. The eigenstates of H_2 are described by the quantum number $J = L + S$ and the functions are indicated as $^{2S+1}L_J$. The ground states for the Ln^{3+} ions are shown in Table 2.1.

Table 2.1 Paramagnetic lanthanides, number of their states according to S, L, J, and their ground multiplets.

n	1	2	3	4	5	6	7	8	9	10	11	12	13
Ion	Ce	Pr	Nd	Pm	Sm	Eu	Gd	Tb	Dy	Ho	Er	Tm	Yb
SL	1	7	17	47	73	119	119	119	73	47	17	7	1
SLJ	2	13	41	107	198	295	327	295	198	107	41	13	2
Total	14	91	364	1001	2002	3003	3432	3003	2002	1001	364	91	14
$^{2S+1}L_J$	$^2F_{5/2}$	$^3H_4$	$^4I_{9/2}$	$^5I_4$	$^6H_{5/2}$	$^7F_0$	$^8S_{7/2}$	$^7F_6$	$^6H_{15/2}$	$^5I_8$	$^4I_{15/2}$	$^3H_6$	$^2F_{7/2}$

SL is the number of L states and SLJ is the number of multiplets. For example, for Pr^{3+}, SL is 7 (^{1}S, ^{3}P, ^{1}D, ^{3}F, ^{1}G, ^{3}H, ^{1}I.); SLJ is 13 because the triplet states are split into three states (L + 1, L − 1, L). The total gives the total number of states of the configuration.

The energies of the low-lying levels determined by $\mathscr{H}_1$ are reported in the literature (Carnall, Fields, and Rajnak, 1968a,b,c; Peijzel *et al.*, 2005). Only the levels separated by less than 5000 cm^{-1} from the ground state are reported due to our interest for the magnetic properties which are well described by the low-lying levels. Matters are different for luminescence properties, which are extensively used to characterize the properties of the various ions.

2.2 Spin–Orbit Coupling

So far, the spin has been essentially a spectator or perhaps a tag which is useful for the identification of the electron state. Therefore, a crucial point in applying the Hamiltonian Eq. (2.1) is the role of the two terms that account for interelectronic repulsions and the coupling between the spin and orbital momenta of the electrons; that is, matters become different on introducing spin–orbit coupling. This is the interaction between the electron spin and orbit. Spin–orbit coupling becomes important for the heavy atoms, which require the inclusion of relativistic effects in calculating the energies. To have an idea of the energies involved, we show in Tables 2.2 and 2.3 the values of the spin–orbit coupling constants for some transition elements and for the 4f tripositive ions.

Table 2.2 Spin–orbit coupling constant ζ for transition metal ions.[a)]

Oxidation state	Ti	V	Cr	Mn	Fe	Co	Ni	Cu
+1	110	160	220	240	390	520	600	820
+2	121	167	230	347	410	533	649	829
+3	154	209	273	352	460	580	705	890
	Zr	**Nb**	**Mo**	**Tc**	**Ru**	**Rh**	**Pd**	**Ag**
+1	340	490	670	660	890	1210	1320	1830
+2	—	—	—	—	1000	1220	1600	1840
+3	500	670	820	—	1180	—	—	—
+4	—	750	950	—	1350	—	—	—
	Hf	**Ta**	**W**	**Re**	**Os**	**Ir**	**Pt**	**Au**
+1	—	—	—	—	—	—	(3400)	—
+2	—	—	(1500)	(2100)	—	—	—	(5000)
+3	—	(1400)	(1800)	(2500)	3000	—	—	—
+4	—	—	(2300)	(3300)	(4000)	(5000)	—	—
+5	—	—	(2700)	(3700)	(4500)	(5500)	—	—
+6	—	—	—	(4200)	(5000)	(6000)	—	—

a) Values are expressed in cm^{-1}. Values in parenthesis are only estimates.

Table 2.3 Spin–orbit coupling constants ζ for tripositive lanthanide ions.[a)]

Ce	Pr	Nd	Pm	Sm	Eu	Gd	Tb	Dy	Ho	Er	Tm	Yb
644	730	844	1070	1200	1320	1583	1705	1900	2163	2393	2656	2883

a) Values are expressed in cm^{-1}.

The reported values show some common features: the values of the spin–orbit coupling constants increase on passing from lighter to heavier elements in the same row; for the same element, the values increase on increasing the oxidation number; and the coupling effects are definitely more relevant for 4f ions than for 3d or 4d ions. The ζ constants for the 5d elements are reported but, with few exceptions, their values are not accurately defined.

For the transition-metal ions of the first and the second series, the spin–orbit coupling is small compared to the other effects and the energy structure can be defined by means of the Russell–Saunders coupling scheme and introducing spin–orbit coupling on the ^{2S+1}L states. The energies are computed using the Hamiltonian:

$$\mathscr{H}_{LS} = \lambda_{LS} \mathscr{L} \cdot \mathscr{S} \tag{2.2}$$

The energies of the J states are:

$$E(J) = \left(\frac{\lambda}{2}\right)[J\,(J+1) - L(L+1) - S(S+1)] \tag{2.3}$$

The effect of this perturbation is to split the energy levels into $2L + 1$ or $2S + 1$ states, whichever is smaller. Each state is characterized by a quantum number J, which determines the $2J + 1$ degeneracy of each state and assumes all the values in the $|L - S| - |L + S|$ range. The ^{2S+1}L states are now expressed as $^{2S+1}L_J$. The difference in energy between two states, which are characterized by J and $J + 1$ quantum number, is

$$\Delta E_{J,J+1} = \lambda_{LS}(J+1) \tag{2.4}$$

The λ_{LS} constant is defined by the single electron spin–orbit coupling constant ζ_{nl}, which is a positive quantity:

$$\lambda_{LS} = \frac{\pm\zeta_{nl}}{2S} \tag{2.5}$$

The positive sign is relative to a shell less than half filled, while the negative is for the opposite situation if the hole formalism is assumed. In this approach, the negative sign has the effect of placing at the lowest energy the state with the highest J with an inversion of the splitting with respect to the less than half filled shell. In the case of transition-metal ions, the electronic configurations of the ground state are described as

d^n configuration	d^1, d^9	d^2, d^8	d^3, d^7	d^4, d^6	d^5
Ground state	$^2D_{3/2,\,5/2}$	$^3F_{2,\,4}$	$^4F_{3/2,\,9/2}$	$^5D_{0,4}$	$^6S_{5/2}$

Larger effects are observed for lanthanides. For instance, the low-lying states of Ce^{3+} are $^2F_{5/2}$ and $^2F_{7/2}$. The former lies lower, the excited state being separated by $7\lambda/2$ or 2240 cm^{-1}. For the $4f^{13}$ (ytterbium), the two levels are reversed. Because the value of ζ dramatically increases on increasing n, the separation of the two low energy levels becomes 10 290 cm^{-1} for Yb. In general, the sign change of λ described in Eq. (2.4) stabilizes the states with L and S antiparallel for $n < 7$ and parallel for $n > 7$. As we will see, these properties are of paramount relevance in influencing the magnetic properties of Ln^{3+} derivatives.

Although Eq. (2.5) is enough to calculate the energies of the lowest multiplet, it is interesting to have an idea of how the individual 4f orbitals enter the ground multiplet. This has a number of consequences, of which the ion-dependent magnetic moment is perhaps the most relevant here. Another property is the charge distribution, which gives rise to lower than spherical symmetry. Indeed, the charge distribution is different for the different rare earth ions. We will exploit these schemes in Chapter 3, but we will introduce them now.

Let us take Dy as an example. It has $n = 9$, and therefore its configuration is equivalent to that of $14 - n = 5$ holes. Assigning the five holes to the m orbitals with $m = -3, -2, \ldots, 2, 3$, yields the lowest configuration described in Figure 2.2.

Introducing the spin, the corresponding function can be written as a Slater determinant $\prod |m_f, m_s\rangle$, where for the ground state all spin components are 1/2. $\left|3, \frac{1}{2}\right\rangle \left|2, \frac{1}{2}\right\rangle \left|1, \frac{1}{2}\right\rangle \left|0, \frac{1}{2}\right\rangle \left|-1, \frac{1}{2}\right\rangle$ can be labeled also with the components of the total orbital moment, of the total spin, and of the total J component. The sum of the m values gives $M = 5$ and the total spin $M_s = 5/2$. The corresponding M_j value is 15/2. If we repeat the classification of the levels for all the possible combinations, we discover that $\left|3, \frac{1}{2}\right\rangle \left|2, \frac{1}{2}\right\rangle \left|1, \frac{1}{2}\right\rangle \left|0, \frac{1}{2}\right\rangle \left|-1, \frac{1}{2}\right\rangle$ is the only one with $M = 5$, $M_s = 5/2$. But it can also be labeled with J and M_J. The function therefore is equivalent to

$$\left|J = \frac{15}{2}, M_j = \frac{15}{2}\right\rangle = \left|3, \frac{1}{2}\right\rangle \left|2, \frac{1}{2}\right\rangle \left|1, \frac{1}{2}\right\rangle \left|0, \frac{1}{2}\right\rangle \left|-1, \frac{1}{2}\right\rangle \tag{2.6}$$

A situation analogous to that depicted by Eq. (2.6), namely one Slater determinant needed to describe the largest component of the ground multiplet, holds for all the electron configurations with $n > 7$. Remembering that the orbitals have a radial and an angular part, the charge density is calculated through an expansion

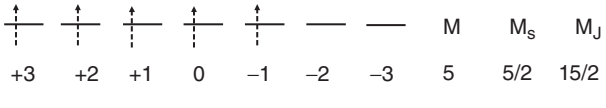

Figure 2.2 Distribution of five holes (dashed arrows) in seven f orbitals.

in a series of tesseral harmonics. The result for Dy is a charge density that is not spherical but an oblate ellipsoid. As we will see below, this has much importance in determining the sign of the magnetocrystalline anisotropy.

The degeneracy of the ground multiplet can be removed by the interaction with an electric and a magnetic field. The former will be treated in some detail in the next chapter.

The approach of considering the spin–orbit coupling as a perturbation of the system defined by the total spin–total orbit quantum numbers does not work for the heavier transition metals. The procedure to be followed is to start by applying spin–orbit coupling to individual electron total angular momenta couple together, and therefore for an ion with n electrons, $J = \sum_{i=1}^{n} j_i$. Actually, there is no spin–orbit coupling constant so large to make the relative phenomenon the dominant one. For most of these ions, it is more correct to deal with an intermediate j–j coupling scheme in which interelectronic repulsions and spin–orbit effects are considered of comparable magnitude. As a consequence, in each case, a non-approximate determination of the energy level structure for heavy ions requires a specific analysis.

2.3 Applying a Magnetic Field

The nature of the ground state influences the response to an external magnetic field, which completely removes the degeneracy. The interaction energy of a magnetic moment m with a magnetic field B is $U = -m \cdot B$. For an electron, one must consider both the spin and orbital contribution. The former is

$$m_{\mathrm{e}} = -g_{\mathrm{e}} \left(\frac{eh}{2m_{\mathrm{e}}} \right) s = -g_{\mathrm{e}} \mu_{\mathrm{B}}\, s \tag{2.6}$$

and the latter is

$$m_l = -\left(\frac{eh}{2m_e} \right) l = -\mu_{\mathrm{B}} l \tag{2.7}$$

where $g_{\mathrm{e}} = 2.0023$, which is determined by relativistic effects. Within a $^{2S+1}\mathrm{L}_{\mathrm{J}}$ state, the Hamiltonian can be written as

$$\mathscr{H} = \mu_{\mathrm{B}}(\mathscr{L} + g_{\mathrm{e}} \mathscr{S}) \cdot B \tag{2.8}$$

and the energy as

$$E_{\mathrm{M}} = g_{\mathrm{J}} \mu_{\mathrm{B}} B M_{\mathrm{J}} \tag{2.9}$$

where

$$g_{\mathrm{J}} = 1 + \frac{\mathrm{J(J+1)} + \mathrm{S(S+1)} - \mathrm{L(L+1)}}{2\mathrm{J(J+1)}} \tag{2.10}$$

with g_{J} the Landè factor.

Table 2.4 g_J values for the ground multiplets of lanthanides.

n	1	2	3	4	5	6	7	8	9	10	11	12	13
Ion	Ce	Pr	Nd	Pm	Sm	Eu	Gd	Tb	Dy	Ho	Er	Tm	Yb
g_J	6/7	4/5	8/11	3/5	2/7	—	2	3/2	4/3	5/4	6/5	7/6	8/7

The g_J values for the ground multiplets of the $4f^n$ configurations are shown in Table 2.4.

When the energies are expressed in wavenumbers, $\mu_B = 0.046693\ \text{cm}^{-1}\ \text{kOe}^{-1}$ and, therefore, for a field of 10 kOe (1 Tesla) the overall splitting of the ground doublet of Gd, which has $J = 7/2$ ($M_J = 7/2$) and $g_J = 2$, is, applying eq. (2.9), $6.5370\,\text{cm}^{-1}$.

References

Carlin, R.L. (1986) *Magnetochemistry*, Spinger-Verlag, Berlin.

Carnall, W.T., Fields, P.R., and Rajnak, K. (1968a) Electronic energy levels in the trivalent lanthanide aquo ions. I. Pr^{3+}, Nd^{3+}, Pm^{3+}, Sm^{3+}, Dy^{3+}, Ho^{3+}, Er^{3+}, and Tm^{3+}. *J. Chem. Phys.*, **49**, 4403–4406.

Carnall, W.T., Fields, P.R., and Rajnak, K. (1968b) Electronic energy levels of the trivalent lanthanide aquo ions. III. Tb^{3+}. *J. Chem. Phys.*, **49**, 4412–4423.

Carnall, W.T., Fields, P.R., and Rajnak, K. (1968c) Electronic energy levels of the trivalent lanthanide aquo ions. IV. Eu^{3+}. *J. Chem. Phys.*, **49**, 4424–4442.

Earnshaw, A. (1968) *Introduction to Magnetochemistry*, Academic Press.

Li, X., Zhang, F., and Zhao, D. (2013) Highly efficient lanthanide upconverting nanomaterials: progresses and challenges. *Nano Today*, **8**, 643–676.

Peijzel, P.S., Meijerink, A., Wegh, R.T., Reid, M.F., and Burdick, G.W. (2005) A complete $4f^n$ energy level diagram for all trivalent lanthanide ions. *J. Solid State Chem.*, **178**, 448–453.

3
Electronic Structure of Coordinated Ions

3.1
Dressing Ions

Understanding the energy levels of naked ions has been important, but real life begins only when the ions coordinate ligands. We recall that a ligand is any ion or molecule that interacts with at least one atom, the donor atom, with a metal ion. Examples of simple ligands are the oxide ions (O^{2-}), the hydroxide ions (OH^-), water (H_2O), carboxylate ($RCOO^-$, where R = H, CH_3, C_2H_5), and so on. In all these cases, oxygen is the donor atom. In the first four ligands, there is one donor atom, and they are said to be monodentate. For instance, the carboxylates can bind to metal ions in several different ways, as shown in Figure 3.1. When the two donor atoms bind to the same metal ion, they are said to be chelated, by analogy with the claws of lobster.

Because carboxylates have an important role in molecular magnetism (MM), we will present some typical cases in anticipation of what is going to come. The simplest way to coordinate is using one O to one metal M as in [K_5Tb(octakis(formato-O))] (Figure 3.2a) (Antsyshkina, Porai-Koshits, and Ostrikova, 1988). A symmetric alternative is chelating. Copper acetate is a prototype of metal ion coordination with four bridges with their well-known paddlewheel motif (Figure 3.2b).

The donor atoms tend to arrange themselves according to maximum symmetry. A convenient way of appreciating this is to refer to the polyhedron defined by the donor atoms. When a metal ion dissolves in water, it coordinates n water molecules. For transition-metal ions, $n = 6$ and the polyhedron is very often an octahedron, as shown in Figure 3.3. Rare earth (RE) ions are bigger than transition-metal ones and can coordinate nine water molecules which define a three-capped trigonal prism, as shown in Figure 3.3. The transition-metal *aquo* ions have O_h symmetry while RE has C_{3h}.

Historically, the first attempts to rationalize the electronic and magnetic properties of metal complexes have been performed by using the crystal field approach. The metal–ligand interaction is considered to be electrostatic in nature, and the ligand orbitals are not directly taken into consideration. For 4f electrons, the crystal field energies are of the order $10^2\ cm^{-1}$. We recall that

Introduction to Molecular Magnetism: From Transition Metals to Lanthanides, First Edition.
Cristiano Benelli and Dante Gatteschi.
© 2015 Wiley-VCH Verlag GmbH & Co. KGaA. Published 2015 by Wiley-VCH Verlag GmbH & Co. KGaA.

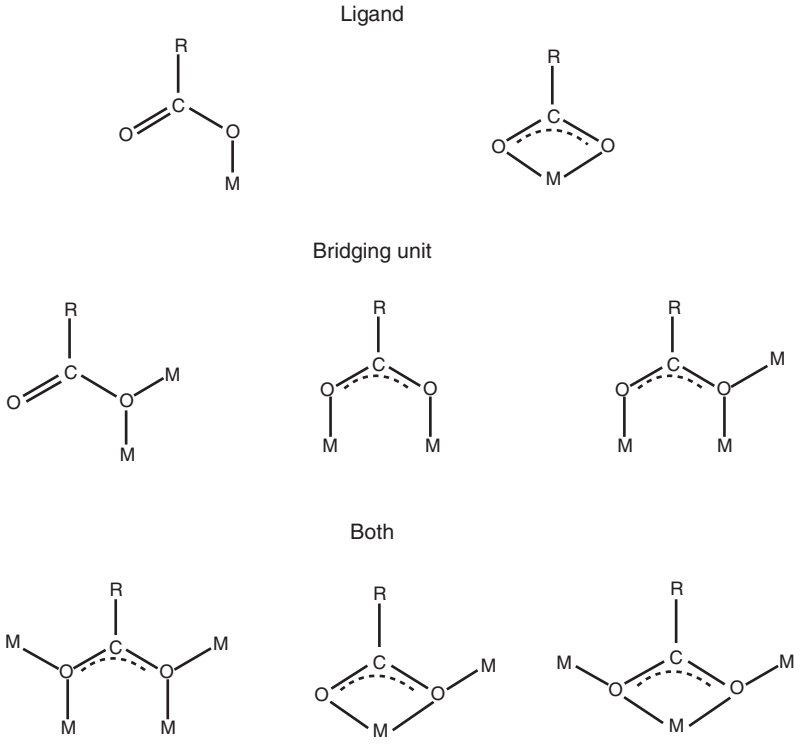

Figure 3.1 Ligand modes of a carboxylate group.

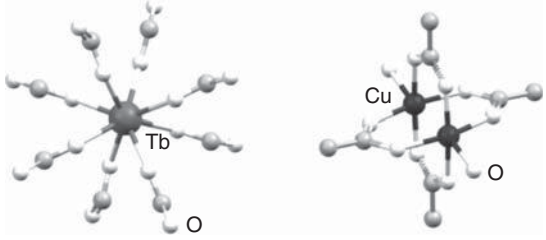

Figure 3.2 (a) [K_5Tb(octakis(formato-*O*))] and (b) copper(II) acetate hydrate.

for lanthanides the energies of the electron repulsion are of the order $10^4\,cm^{-1}$ and spin orbit coupling $10^3\,cm^{-1}$. Under these conditions, it seems a good approximation to introduce the effect of the ligands as a perturbation on the energies of the $^{2S+1}L_J$ multiplets. This is particularly true for the lowest lying J multiplets.

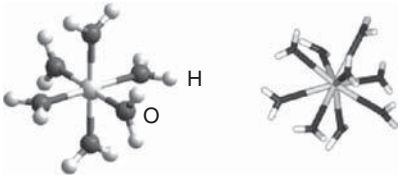

(a) (b)

Figure 3.3 (a) Transition-metal *aquo* ion with octahedral coordination geometry. (b) Lanthanide *aquo* ion with tricapped trigonal prism coordination geometry.

3.2 The Crystal Field

Assuming a rigorous electrostatic crystal field (CF) approach soon proved to be a catastrophe, in the sense that quantitative results were far from the experimental ones. The qualitative agreement was very promising, on the other hand. It was decided to keep what was properly working and to get rid of what was not working: CF became ligand field (LF). In the new model, the ligands produce a potential which is expressed by exploiting symmetry. The radial integrals, which did not work, are used as parameters. The spherical symmetry is broken by the ligands.

A convenient way of calculating the energies of the states originating from the $4f^n$ configuration is to expand in series an effective potential $\mathscr{V}$ which operates on the $|JM_J\rangle$ functions. The potential $\mathscr{V}$ is expressed using the Stevens operator equivalents, that is, operators that produce the same results as standard operators but contain angular momentum operators, which are relatively simple to calculate (Stevens, 1952). A convenient form of $\mathscr{V}$ is

$$\mathscr{V} = \sum_{0}^{\infty} \beta_k \sum_{q=-k}^{k} A_k^q \langle r^k \rangle \mathcal{O}_k^q \tag{3.1}$$

where $A_k^q \langle r^k \rangle$ is a parameter, $\mathcal{O}_k^q$ is the operator equivalent, and β_k is a number which depends on the number of f electrons and k is the rank operator. The operators with k even (0, 2, 4, 6) are responsible for the crystal field splitting, while those with k odd (1, 3, 5, 7) are responsible for the intensity of the induced electric dipole transitions (Görller-Walrand and Binnemans, 1996). We will neglect the latter in the following, since they do not affect magnetism. To have a complete description of the energy level distribution in any symmetry, the summation should include terms with $q < 0$, corresponding to imaginary matrix elements of the Stevens' operators. As these imaginary components are very often the source of very complicated fitting procedure and confusing parameters sets (Rudowicz, 1986), it is a common practice to approximate the real symmetry of the system to a higher one so that only $q > 0$ terms have to be considered.

The choice of the coordinate system used to describe the compound is at the same time relevant in determining the $A_k^q \langle r^k \rangle$ crystal field parameters. The $A_k^q \langle r^k \rangle$ parameters with $q \neq 0$ are not invariant under rotation of the reference frame: their sign and value depend on the choice of the coordinate system.

Table 3.1 Relations between the B_k^q and $A_k^q\langle r^k\rangle$ parameters (Stewart, 1985).

$A_2^0\langle r^2\rangle = \frac{1}{2}B_2^0$	$A_4^0\langle r^2\rangle = \frac{1}{8}B_4^0$	$A_6^0\langle r^6\rangle = \frac{1}{16}B_6^0$
$A_2^{\pm1}\langle r^2\rangle = \mp\sqrt{6}B_2^1$	$A_4^{\pm1}\langle r^4\rangle = \mp\frac{\sqrt{5}}{2}B_4^1$	$A_6^{\pm1}\langle r^6\rangle = \mp\frac{\sqrt{42}}{8}B_6^1$
$A_2^{\pm2}\langle r^2\rangle = \pm\frac{\sqrt{6}}{2}B_2^2$	$A_4^{\pm2}\langle r^4\rangle = \pm\frac{\sqrt{10}}{4}B_4^2$	$A_6^{\pm2}\langle r^6\rangle = \pm\frac{\sqrt{105}}{16}B_6^2$
—	$A_4^{\pm3}\langle r^4\rangle = \mp\frac{\sqrt{35}}{4}B_4^3$	$A_6^{\pm3}\langle r^6\rangle = \mp\frac{\sqrt{105}}{8}B_6^3$
—	$A_4^{\pm4}\langle r^4\rangle = \pm\frac{\sqrt{70}}{8}B_4^4$	$A_6^{\pm4}\langle r^6\rangle = \pm\frac{3\sqrt{14}}{16}B_6^4$
—	—	$A_6^{\pm5}\langle r^6\rangle = \mp\frac{3\sqrt{77}}{8}B_6^5$
—	—	$A_6^{\pm6}\langle r^6\rangle = \pm\frac{\sqrt{231}}{16}B_6^6$

Another important formalism has been developed by Wybourne using irreducible tensor operators. In Table 3.1 we show the relations between the two parameterizations in the fitting procedure of experimental data (Wybourne, 1965). Parameters based on either the Stevens or Wybourne approach can be used, as they are formally related as reported in the Table 3.1. We decided to apply in the following the Stevens formalism which is based on $A_k^q\langle r^k\rangle$ parameters.

The symmetry of the coordination sphere around the lanthanide ion is fundamental in the choice of the correct set of parameters. As symmetry operations cannot change the energy of the ion, the CF Hamiltonian has to transform as the totally symmetric representation of the point group of the molecules. Therefore the $A_k^q\langle r^k\rangle$ coefficients are different from zero if they correspond to the symmetry requirements reported in Table 3.2.

For instance, in a tetragonal environment, only the parameters with $q = 0, \pm4$ are different from zero, while for D_{4d} symmetry the terms with $q = \pm4$ are

Table 3.2 Symmetry restrictions on allowed q values (Görller-Walrand and Binnemans, 1996).

Symmetry	Restriction on q
C_n (parallel to main axis)	q is an integer multiple of the rotation number n, but $q \leq k$
σ_h (xy plane)	No terms with q = even for odd k values; no terms q = odd for k even values
σ_v (xz-plane)	No imaginary terms
i (inversion center)	No odd k values, thus no induced electric dipole intensity by mixing states of opposite parity
C'_2 (parallel to x-axis)	No terms with $q = 0$ for odd k values; no real terms with $k + \|q\|$ odd; no imaginary terms with $k + \|q\|$ even
C'_2 (parallel to y-axis)	No terms with $q = 0$ for odd k values; no real terms with $k + \|q\|$ odd; no imaginary terms with $k + \|q\|$ even
S_n (parallel to main crystal axis)	No terms with $q = 0$ for odd k values; no terms with $q = n$-fold and with $k + \|q\|$ odd; no terms with $q = (2x + 1)n/2$ ($x = 0, 1, 2, \ldots$) and $k + \|q\|$ even

also zero. If the symmetry is cubic as in a tetrahedral, octahedral, or cubic environment, the $\mathcal{O}_k^{\pm 4}$ and $\mathcal{O}_k^0$ terms with $k > 4$ must be included in a fixed ratio, which is determined by the symmetry. Group theory is extremely useful to define the form of the operators to be used in the description of these systems.

In Table 3.3 we report the nonvanishing B_k^q parameters for the 32 point groups which are compatible with crystal symmetry. With the same approach, it is

Table 3.3 Independent non-vanishing for B_k^q the 32 point groups.

Group	Non-vanishing B_k^q
C_1 C_i	All B_k^q (B_2^1 real)
C_2 $C_s(C_{1h})$ C_{2h}	B_2^0, Real $B_2^2, B_4^0, B_4^2, B_4^4, B_6^0, B_6^2, B_6^4, B_6^6$
D_2 C_{2v} D_{2h}	B_2^0, Real B_2^2, B_4^0, Real B_4^2, Real B_4^4, B_6^0, Real B_6^2, Real B_6^4, Real B_6^6
C_4 S_4 C_{4h}	B_2^0, B_4^0, Real B_4^4, B_6^0, B_6^4
D_4 C_{4v} D_{2d} D_{4h}	B_2^0, B_4^0, Real B_4^4, B_6^0, Real B_6^4
C_3 S_6 (C_{3h})	B_2^0, B_4^0, Real $B_4^3, B_6^0, B_6^3, B_6^6$
D_3 C_{3v} D_{3d}	B_2^0, B_4^0, Real B_4^3, B_6^0, Real B_6^3, Real B_6^6
C_6 C_{3h} C_{6h} D_6 C_{6v} D_{3h} D_{6h}	B_2^0, B_4^0, B_6^0, Real B_6^6
T T_d T_h O O_h	B_4^0, Real B_4^4, B_6^0, Real B_6^4

possible to select the operator equivalents whose explicit forms with $k = 2, 4, 6$ are reported in the literature (Abragam and Bleaney, 1970).

The above conditions apply for true symmetry. However, in many cases the system is close to symmetric and it is common to refer to the idealized symmetry.

We refer mainly to Ln because transition metals TM have been widely treated and, therefore, we wish to comment on the difference between the two types of metal ions. A great advantage of TM over Ln is that the former favors octahedral coordination which for d orbitals requires one parameter (Dq) to express the energies of the TMs. The catalog of Dq values for various TM and ligands give the spectrochemical series. Indeed, it was this simple parameter scheme that determined the success of LF for TM. Octahedral coordination is just one out of many for Ln, making life more difficult. Furthermore, f orbitals require two parameters in O_h symmetry, which, combined with the low sensitivity of Ln to LF, made the use of LF less spread out for Ln compared to TM.

3.3 The *aquo* Ions

The problems associated with the ligand field approach are well documented in many cases, so making a choice of picking up one series rather than another has many irrational features. We like to start from the *aquo* ions which are present in two intensively investigated series, namely the ethyl sulfates, $Ln(EtSO_4)_3(H_2O)_9$, and the bromates $Ln(H_2O)_9(BrO_3)_3$ (Table 3.4). The water molecules are organized in three triangles, the upper and lower ones being eclipsed, while the central one is rotated by $60° + \delta$ around the unique axis, Figure 3.4. The Ln ion is in the central of the middle triangle. $\delta = 0°$ for the bromates, yielding an overall D_{3h} symmetry. δ is different from zero (about 5°) for $EtSO_4$, with the symmetry lowering to

Figure 3.4 Coordination geometry around the Yb^{3+} ion in $Ln(H_2O)_9(BrO_3)_3$. Three coordinated oxygen atoms are hidden by the three atoms connected by the continuous line.

Table 3.4 Best fit parameters for some $Ln(H_2O)_9(BrO_3)_3$ in cm^{-1}.

Ion	$A_2^0\langle r^2\rangle$	$A_4^0\langle r^4\rangle$	$A_6^0\langle r^6\rangle$	$A_6^6\langle r^6\rangle$	References
Pr	115	−105	−48	650	Neogy, Purohit, and Chatterji (1986)
Nd	123	−24.5	−42	1018	Chatterji *et al.* (2004)
Gd	1.82×10^{-2}	5.3×10^{-9}	4.25×10^{-10}	—	Mukherjee and Neogy (1988)
Dy	122	−55	−47	553	Neogy and Purohit (1987)
Ho	65	−38	−24	551	Purohit, Neogy, and Saha (1992)
Er	60	−72.5	−22.5	665	Neogy *et al.* (1994)
Tm	95	−52.5	−26	835	Neogy *et al.* (1996b)
Yb	115	−50	−23	817	Neogy *et al.* (1996a)

C_{3h}. It is a useful exercise, which will help us to read the outputs of computer calculations as something different from a black box, to verify how the $\mathcal{O}_k^k$ operators span the irreducible representation of both C_{3h} and D_{3h}, while $\mathcal{O}_k^{\pm k}$ only for C_{3h}.

The terms to be included in the Hamiltonian Eq. (3.1) are the $\mathcal{O}_2^0$, $\mathcal{O}_4^0$, $\mathcal{O}_6^0$, $\mathcal{O}_6^{\pm 6}$ for D_{3h} while the number of symmetry operations of C_{3h} are 6 and their effects are the appropriate rotational parameter R, $\mathcal{O}_k^0 = \mathcal{O}_k^0$, $\mathcal{O}_4^{\pm 3}$, and $\mathcal{O}_6^{\pm 3}$ are not included because the presence of the symmetry plane requires that odd terms in z are zero. In other words, the $\mathcal{O}_k^{\pm 3}$ operators are the basis for the A_1'' A_2'' irreducible representations of D_{3h}, and only totally symmetric operators must be included. Matters do not change in C_{3h} symmetry: correlation tables show that the A_1'' A_2'' irreducible representations of D_{3h} become A''. Matters are different for the $\mathcal{O}_6^{\pm 6}$ operators, which span the A_1' A_2' representations in D_{3h} which become A' in C_{3h}. This means that only one parameter must be fitted in D_{3h}, whereas two are needed for C_{3h}.

The calculated levels for $Ln(H_2O)_9(BrO_3)_3$ were compared with experimental data, and the best fit factors, assuming D_{3h} symmetry, are collected 3.4.

Let us have a closer look at Ce^{3+} and Yb^{3+} ions, the first and the last of the paramagnetic series, respectively. The former in the free ion has a $J = 5/2$ ground state. The excited $J = 7/2$ is about 5000 cm^{-1} higher in energy, which in first approximation can be neglected in the interpretation of the magnetic properties. Only the diagonal matrix elements are different from zero because $\mathcal{O}_6^6$ only couples states differing by 6 in M_J, a situation which is not encountered for $J = 5/2$. The energies of the states are given in Table 3.5.

Yb, which has a ground $^2F_{7/2}$ has a nondiagonal matrix because $\mathcal{O}_6^6$ now couples $\pm 7/2$ with $\mp 5/2$. The matrix therefore is block-factorized 2, 2, 1, 1, 1, 1. The overall magnetic behavior is, in any case, determined by the nature of the doublet, which has the lowest energy. In the case of $Yb(EtSO_4)_3(H_2O)_9$, it has been derived by experiments a $g_{\|} = 3.335$, which is very close to the expected value of 3.429 for a $|\pm 3/2\rangle$ doublet with $g_J = 8/7$ (see Section 20.3 where a detailed procedure is worked out to the calculate the g-values). As shown in Table 3.5, the $|\pm 3/2\rangle$ doublet does not mix with any other state and therefore the experimental value $g_{\perp} \approx 0.01$ compares quite well with the expected value of zero.

Table 3.5 Ligand field matrix for Ce^{3+} and Yb^{3+}.

States	Ce	Yb	Ce	Yb	Ce	Yb
	B_2^0		B_4^0		B_6^0	
$\pm 1/2$	−4	−5	2	9	0	−5
$\pm 3/2$	−1	−3	−3	−3	0	9
$\pm 5/2$	5	1	1	−13	0	−5
$\pm 7/2$	—	7	—	7	—	1
Multiplying factor	2	3	60	60	—	1260
$\pm 7/2 \mp 5/2\ B_6^6$	—	$360\sqrt{7}$	—	—	—	—

For the Ce derivative, the $|\pm 5/2\rangle$ doublet is assumed as the ground one. In this case, the theory gives $g_{\|} = 4.29$ and $g_{\perp} = 0$. Experiments yielded $g_{||} = 3.72$ and $g_{\perp} = 0.20$: these discrepancies between the experimental and theoretical values are indicative of the fact that the assumption of pure states is no longer valid. Some additional components in the expression of the potential are required to justify the magnetic behavior.

The general strategy to determine the electronic structure of a metal ion starts with the correct definition of the symmetry around the ion under analysis. This step is fundamental for the choice of the nonvanishing terms in the Hamiltonian to be applied, at least in the first analysis, to the ground multiplet. At this stage, it is, in general, possible to compare this approach with some experimental evidence and, by using some fitting procedure, to extract information on the composition of the ground multiplet.

In many cases, a series of compounds are available in which the main geometrical parameter is an angular distortion. Let us imagine having a system where the central ion is bound to eight donor atoms in a square antiprismatic fashion (Figure 3.5). What happens if the geometrical structure is changed while keeping constant the tetragonal symmetry? And if the symmetry is changed from D_{4d} to C_{4v} by rotating one of the two squares formed by four nitrogen atoms by, say, five? An approach can be to expand the LF potential as a sum of contributions of the individual ligands.

3.4 The Angular Overlap Model

With the aim to correlate different sets of parameters with distortions of coordination polyhedra around the 4f ions, it is useful to look for Hamiltonian approaches based on the sum of local potential of each ligands ($V = \sum_L V_L$). On the market, there are, substantially, two models: the superposition model and the angular overlap model (AOM). Both models assume that the interaction is the product of a radial parameter and an angular factor that accounts for the geometry of the

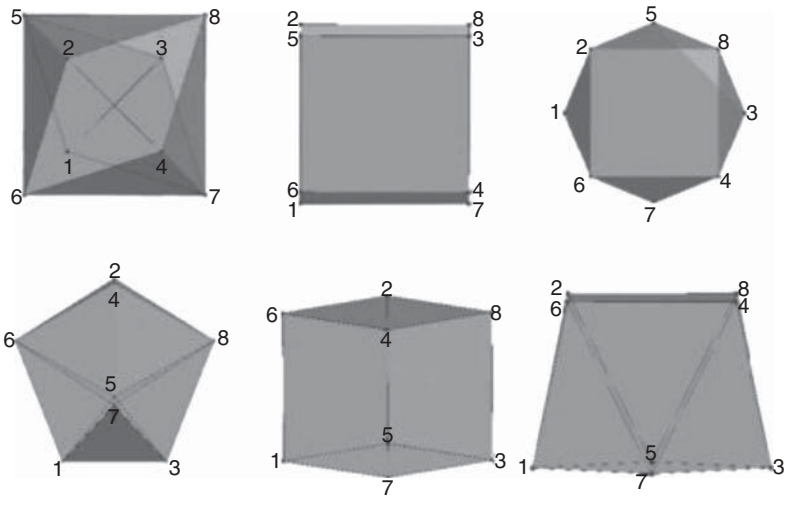

Figure 3.5 Sketch of the three regular polyhedra occurring for eight coordination, viewed along their higher symmetry axis (upper) and perpendicular to it (lower). From left to right: dodecahedron, cube, square antiprism.

system. The superposition model uses CF parameters, while AOM is based on a molecular orbital formalism. In this approach, the starting point is to consider the energies of the f orbitals' diagonal when under the influence of a ligand on the z-axis. The energies are defined by four parameters e_λ, where $\lambda = \sigma, \pi, \delta, \varphi$ referring to the symmetry of the interaction between the f and ligand orbitals. The relevance of each parameter can be defined by examining the actual molecular structure. Generally, e_σ and e_π are assumed to be the dominant terms. The assumption that the AOM parameters for different lanthanides are proportional to the eighth power of the bond length can help to further reduce the number of parameters. These properties of the AOM are useful to analyze the overall effects of angular variations in homologous series of compounds (Schäffer et al., 2009).

It is also possible to introduce additional parameters. Let us take into account the e_π parameter. In this form, it is assumed that the π interaction is isotropic in the plane perpendicular to the metal ligand direction. If one wants to consider anisotropic effects, two parameters must be used, namely $e_{\pi s}$ and $e_{\pi c}$, where s stands for sine and c for cosine, respectively. Given the general overparameterization of the model, generally isotropic interactions only are included.

The calculations of the f orbital energies are very simple, based on the following assumptions:

- The ligand orbitals are not explicitly considered;
- Their effect is a correction to their energies of the f (d) orbitals;
- The contributions of different ligands are additive;
- The energies of the f (d) orbitals for one ligand on the z-axis are diagonal;
- The energies of the f (d) orbitals for one ligand in general position are obtained by a rotation of the diagonal matrix.

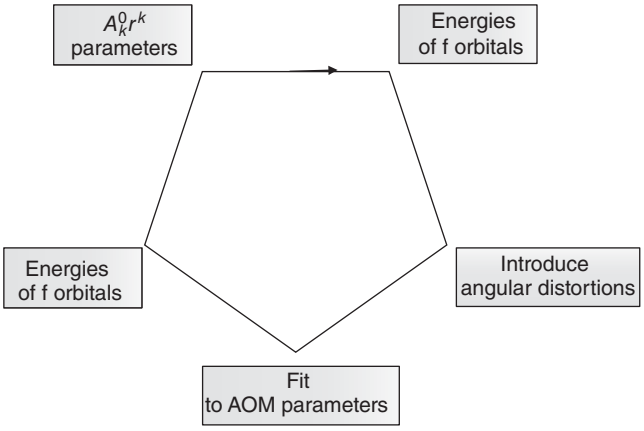

Figure 3.6 Diagram of a procedure to adopt for describing the effects of angular distortion on the electronic structure of lanthanide ions as explained in the text.

By using AOM in strict connection with the Stevens approach, it is possible to develop a strategy to describe the effects of angular distortion on the electronic structure of lanthanide ions. The overall strategy is schematized in Figure 3.6. We focus on a compound or on a series of compounds. Particularly interesting are the tetragonal systems described in Sections 3.5 and 3.6. The fit of several different properties will provide a set of Stevens' parameters $A_k^q\langle r^k\rangle$ (step 1); step 2 consists in the calculation of the energies of the f orbitals using

$$E(\pm \mathrm{M}) = \sum \frac{\hat{O}_3^0(3,\mathrm{M})}{\hat{O}_k^0(3,3)} F_k A_k^q \langle r^k \rangle \tag{3.2}$$

where $F_2 = -2/3$, $F_4 = 8/11$, and $F_6 = -80/429$ are the values assumed by the operator equivalents for $\mathrm{L} = 3$ while $\mathrm{M} = 0, 1, 2, 3$. Equation (3.2) requires the fit of the calculated energies using AOM. These energies are reproduced by using an appropriate set of e_λ parameters, which are fundamental for introducing directly angular distortions, step 4, and for calculating a new set of energies of the f orbitals. Step 5 – we are now ready to work out examples.

3.5
The Lantanum(III) with Phthalocyanine (Pc) and PolyOxoMetalates (POM)

From this new set to Stevens' parameters, the procedure is straightforward. In recent years, the compounds formed by Ln^{3+} with phthalocyanine (Pc) have been deeply investigated for some peculiar magnetic properties (Ishikawa *et al.*, 2003). In these systems, the metal ion is eightfold coordinated by the pyrrole nitrogen atoms of two phthalocyanine ligands parallel to each other, as sketched in Figure 3.7.

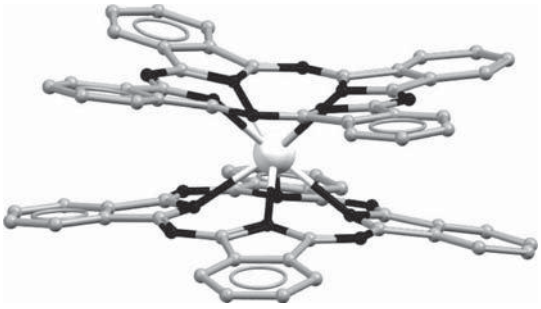

Figure 3.7 Simplified view of a phthalocyanine lanthanide complexes.

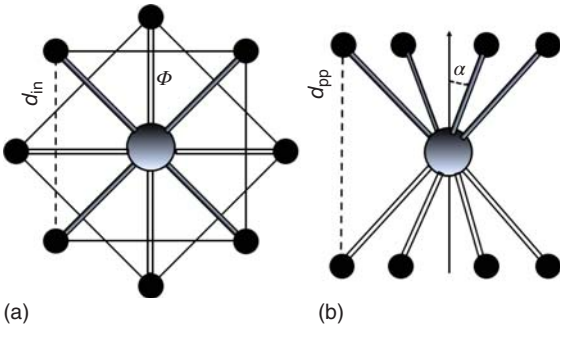

Figure 3.8 Details of the relevant structural parameters in a square antiprism. (a) (view along the S_8 axis). d_{in} is the shorter L–L distance in the L_4 square, and Φ is the skew angle between the diagonals of the two squares. (b) (Lateral view, perpendicular to the S_8 axis which is represented by the blue arrow). d_{pp} is the distance between the two parallel L_4 squares, and α is the angle between the S_8 axis and a RE–L direction.

More details on the synthesis and structure and properties of $Ln(Pc)_2$ will be given in Section 4.3; here we will only recall that the most common coordination polyhedral for eight-coordination are cube dodecahedron and squared antiprism (SAP) (Figure 3.5). Important structural parameters affecting the magnetic properties of the SAP are those depicted in Figure 3.8.

In a perfect, ideal SAP, the eight metal ion to donor atom bond distances, r, are all identical to each other. Therefore, only one parameter is needed. Φ is the angle between the diagonals of the squares. Φ is 0° for a regular SAP and 90° at the other limit. Other distortions consider the angle between the tetragonal axis and the r direction. For an ideal SAP $\alpha = 54.74°$. If $\alpha > 54.74°$ the SAP is elongated. The last parameter (d_{pp}) is for the shortest distance between donor atoms belonging to different squares.

The symmetry of a SAP is very close to D_{4d} and, therefore, the Hamiltonian includes only the $\mathcal{O}_2^0$, $\mathcal{O}_4^0$, $\mathcal{O}_6^0$ operators and the relative parameters. Recall that D_{4d} is not compatible with translational symmetry, and therefore only approximate symmetry can be observed in crystalline materials.

Table 3.6 Ligand field parameters (cm^{-1}) for $[Ln(phthalocyaninato)_2]^-$.

	$A_2^0\langle r^2\rangle$	$A_2^0\langle r^4\rangle$	$A_2^0\langle r^6\rangle$
Tb	420	30	−230
Dy	400	35	−210
Ho	370	40	−195
Er	350	44	−180
Tm	340	50	−160
Yb	320	53	−145

In comparing the values, it must be recalled that it is the energies that must be compared, and not the parameters. Anyway, there is not much to be learned. Matters are different with the calculated energies of the ground J multiplet. As reported in Table 2.1, the excited J states are neglected.

The overall splitting of the ground J multiplet ranges from about 600 cm^{-1} for Tb^{3+} to about 400 cm^{-1} for Ho^{3+}. The states defined by the J_z operator acting on $\pm M_J$ are degenerate in zero magnetic field. The levels' degeneracy is predicted by group theory either for Kramers and Non−Kramers but, actually, it is very uncommon for even electron configuration and real for odd electrons. The ground doublet corresponds to M_J values that are smaller than the maximum $M_J = J$, the only exception being Tb whose ground doublet is $M_J = 6$, equal to the maximum allowed for the ground multiplet. We will see later that a high M_J ground state is an important feature because it may give rise to a high magnetic anisotropy. In Table 3.6, the best fit parameters are reported, and in Figure 3.9 the calculated energy splittings for the various lanthanide ions are plotted.

There is another class of compounds where eight oxygen donor atoms form a similar environment around a Ln^{3+} ion, namely a polyoxometalate (POM) group. More chemical details will be provided in Section 4.5. The magnetic properties of DyPOM were found to be different from those of a $Dy(Pc)_2$ unit. Even at first glance, both systems are described in a SAP environment (AlDamen *et al.*, 2009). To understand the role of low symmetry components, the f orbital energies were calculated by using the $A_k^q\langle r^k\rangle$ parameters obtained by the best fit of the magnetic data of DyPOM. The minimum set of AOM e_λ parameter was used in the calculation to fit these energies. It was necessary to introduce e_σ, e_π, and e_δ for obtaining a good fit. The e_λ parameters were maintained constant, and a geometrical distortion was introduced to verify the behavior of the f orbital energies and the $A_k^q\langle r^k\rangle$ parameters with respect to elongation and compression of the coordination sphere along the C_4 axis. As reported in Table 3.7, a significant variation was calculated for $A_2^0\langle r^2\rangle$ which undergoes a change of sign on passing from the elongated ($\alpha = 50°$) to the compressed ($\alpha = 60°$) form of SAP with a value equal to zero for the magic angle.

To have more information on the electronic configuration and the magnetic behavior of the system, the same strategy was used to determine the energies of

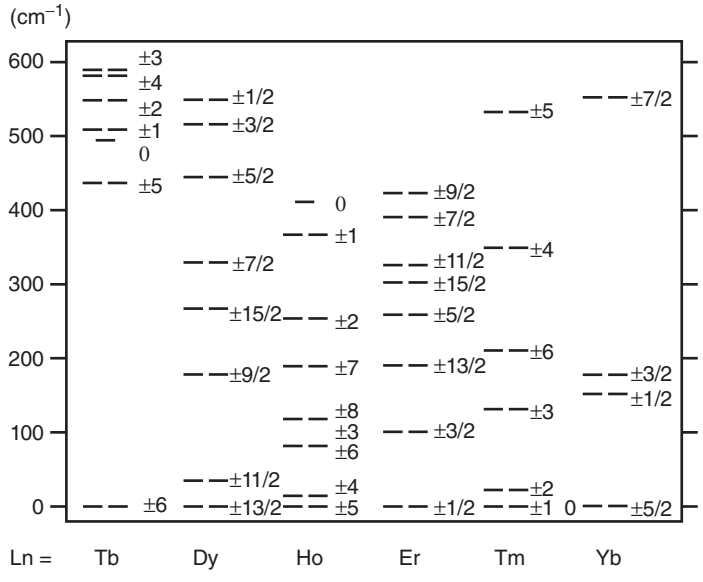

Figure 3.9 Energy diagram for the ground state multiplets of $[Ln(phthalocyaninato)_2]^-$. (Reproduced from Ishikawa, N. *et al.* (2003) with permission from The American Chemical Society.)

Table 3.7 Angle-dependent energies and parameters (cm^{-1}) for Dy POM.

α	$E(\pm3)$	$E(\pm2)$	$E(\pm1)$	$E(0)$	$A_2^0\langle r^4\rangle$	$A_4^0\langle r^4\rangle$	$A_6^0\langle r^6\rangle$	e_σ	e_π	e_δ
60°	−40	236	−87	−216	−88.3	−134.4	7	160	60	−78
54.7°	−132	312	−57	−245	0	−180	5	160	60	−78
50°	−209	339	−12	−236	96	−200	1	160	60	−78

the Kramers doublets of the ground $^6H_{15/2}$ multiplet in presence of the indicated geometrical distortions (Table 3.8). In any condition, the ground state is the one with $M_J = \pm 11/2$, which is characterized by a strong Ising anisotropy with $g_\parallel = 44/3$ and $g_\perp = 0$. The doublet closest in energy is the one with $M_J = \pm 9/2$, which is characterized also by an Ising feature with $g_\parallel = 36/3$ and $g_\perp = 0$. In presence of an elongation, the state with a higher M_J value becomes more stable with respect to the other one, as shown by an in increase in the energy difference.

Table 3.8 Calculated energies (cm^{-1}) for Dy POM.

α	$M_J = 15/2$	$M_J = 13/2$	$M_J = 11/2$	$M_J = 9/2$	$M_J = 7/2$	$M_J = 5/2$	$M_J = 3/2$	$M_J = 1/2$
60°	196	−20	−94	−92	−55	−10	27	47
54.7°	180	−66	−143	−124	−58	18	80	118
50°	138	−105	−174	−140	−54	44	126	171

A completely different pattern is observed if the geometrical perturbation is a rotation around the C_4 symmetry axis instead of the compression/elongation. The first effect is the loss of the D_{4d} symmetry, and therefore the $A_k^4\langle r^k\rangle$ parameters are no more forbidden and accordingly the states are no more pure eigenstates of $\hat{S}_z$ but linear combination of $m_i = M_J \pm 4n$. The present approach is helpful to evaluate the role of this kind of distortion in the magnetic behavior observed in Dy^{3+} and Er^{3+} derivatives with Pc ligands. By applying the above-described procedure, it was calculated that a 15° rotation around the tetragonal axis with respect a pure SAP geometry produces an inversion between the ground and the first excited state. Another interesting effect derives from the behavior of $A_k^q\langle r^k\rangle$ parameters under this type of rotation: $A_k^0\langle r^k\rangle$ components are invariant, while the generic $A_k^q\langle r^k\rangle$ type has a dependence on the angle of rotation of the type $a \times \sin^2\Phi$ with a and Φ equal to 0 for a perfect cubic symmetry. With the same general approach, the distortion of a pure cubic symmetry to a dodecahedron can be followed by using as variable parameters in the AOM calculations the angles θ_a and θ_b which vary during the flattening and the elongation of the tetrahedra composing the dodecahedron. This type of geometrical modification affects both axial and transverse parameters and, starting from POM data, it was found that the axial term has a nonzero and positive value while the transverse terms vary approximately proportional to $\cos^2(\theta_a - \theta_b)$.

A common result found for POM and Pc derivatives was the relationship among the $A_k^q\langle r^k\rangle$ of a best fit set of the type for lanthanide ions heavier than gadolinium (Ishikawa, 2007):

$$A_k^q\langle r^k\rangle = a_k + b_k(n-10) \quad n = 8, 9, \ldots, 13 \tag{3.3}$$

This correlation among parameters, which is fairly valid for LnPOM and $Ln(Pc)_2$ series, does not apply in the case of ethylsulfate derivatives, which have a trigonal symmetry, and seems to work only in the series for $A_2^0\langle r^2\rangle$ and $A_6^0\langle r^6\rangle$ parameters. Another specific feature for LnPOM and $Ln(Pc)_2$ derivatives is the increase of the absolute values of the LF parameters on passing from Tb to Yb. The easiest explanation is connected to the lanthanide contraction, that is, the reduction of the atomic radius on increasing the atomic number. On the other hand, this behavior does not apply to other series on lanthanide systems. For example, the trensal compounds (H_3 trensal = 2,2′,2″-tris (salicylideneimino) triethylenamine) which show a seven coordination with the RE ion in a site of C_3 symmetry (Flanagan *et al.*, 2002, Section 14.1). In this case, the LF approach requires nine parameters, while for the AOM calculations only five parameters are required, namely the e_σ and e_π for the three imino-nitrogen and oxygen donors which are related by the C_3 symmetry axis plus the e_σ for the apical tertiary N atom. The total is, therefore, five parameters. These compounds were analyzed, substantially, by optical techniques (NIR–vis–UV), and the LF parameters were extracted by fitting the relative spectra. The main difference with the parameters of POM and Pc derivatives is in the data used for fitting. In these two last systems, the studies were performed using magnetic susceptibilities and NMR spectra. These data are more sensitive to the actual composition of the ground multiplets. The strength of the LF has been related to the parameter:

$$\frac{N_v}{(4\pi)^{\frac{1}{2}}} = \left[\sum \frac{1}{2k+1} B_{k0}^2 + 2\sum |B_{kq}|^2\right]^{\frac{1}{2}} \tag{3.4}$$

where B_{kq} are the ligand field parameters expressed in the Wybourne notation, see Table 3.1. The expected decrease is, even in this case, connected to the atomic radius contraction with the consequence of a reduction of the overlap of f orbitals with the ligand ones. This effect is more efficient with respect of the increase of the overlap due to the reduction of the bond length.

3.6 Introducing Magnetic Anisotropy

The energy of a magnet depends on the orientation of the magnetization in the crystal axis frame, and therefore magnetic anisotropy is one of the key properties of a magnet. This is true for permanent magnets and, as we will show, it is true also for molecular magnets. Magnetic anisotropy is, for instance, responsible of hysteresis and coercivity, and lanthanides are very important for their unique properties. Magnetic anisotropy has multiple origins and we will try to introduce them by adjusting a language that was born and developed for permanent magnets. An interesting feature is that Ln enters the intermetallics showing strong magnetic properties as Ln^{3+} which can be easily compared with molecular systems.

The first term we introduce is *magnetocrystalline* anisotropy. This means the contribution of the CF and spin–orbit coupling, which generally is a dominant term. It may be associated with anisotropic g-values or with local anisotropy which removes the degeneracy of spin multiplets. An example of the former can be a Dy^{3+} ion in a low-symmetry environment in which the $J = 15/2$ ground state is split to give a well-separated ground Kramers doublet which can be described by the two $M = \pm 15/2$ functions. In a field parallel to the z-axis, the energies of the two levels are $\pm(15/2)g_J\mu_B B_z$. The g_J value is 4/3, as reported in Table 2.4. Treating the two levels as an effective $S = 1/2$ spin, the corresponding energies are $\pm\, 1/2 g\mu_B B_z$, which is equivalent to $g = 20$. If a moderate field is applied parallel to $x(y)$, the two levels do not split at all, that is, $g_{x(y)} = 0$. Therefore the Dy^{3+} ion introduces a strong anisotropy.

The other form of magnetocrystalline anisotropy is exemplified by the Mn^{3+} in the archetypal SMM (single molecular magnet) Mn12. Mn^{3+} has a d^4 configuration and a tetragonal coordination, which splits the ground $^5A_{2g}$ state in zero field leaving the $M = \pm 2$ as ground state. This means that, on cooling, the $M = 0, \pm 1$ levels are increasingly depopulated. The $M = \pm 2$ favor the spins parallel to z, and therefore they yield an easy axis of magnetization.

Other types of anisotropy can be referred to as *pair anisotropy*, which includes dipolar interactions and shape anisotropy. The latter is rather overlooked in molecular magnets, while the former is widely used as we will show in the following sections. The exchange interaction too can give rise to pair anisotropy. We will work out uniaxial anisotropy for the sake of simplicity.

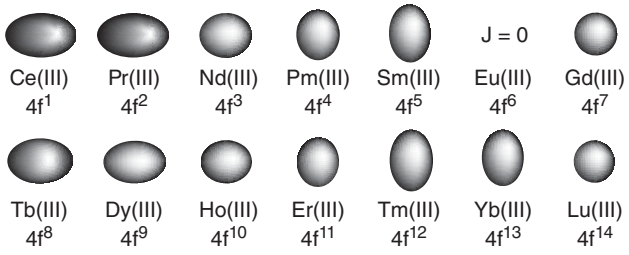

Figure 3.10 Quadrupole approximations of the 4f-shell electron distribution for the tripositive lanthanides. Values are calculated using the total angular momentum quantum number (J), the Stevens coefficient of second order (α), and the radius of the 4f-shell squared $\langle r^2 \rangle$. Europium is not depicted because of a J = 0 ground state. (Reproduced from Rinehart, J. D and Long, J. R. (2011) with permission from The Royal Society of Chemistry.)

The simplest way to express uniaxial anisotropy is

$$E_a = K_1 V \sin^2 \theta \tag{3.5}$$

where E_a is the anisotropy energy, V is the volume, K_1 is a constant, and θ the angle of the magnetic field with the unique axis. For K_1 positive, the minimum energy is for $\theta = 0$ (easy axis), while for K_1 negative the anisotropy is of the easy plane type. Often, instead of using the energy E_a one uses the field

$$H_a = \frac{2K_1}{M_s} \tag{3.6}$$

Let us now look in more detail the anisotropy of Ln. The anisotropy field of Sm in $SmCo_5$ is 17, and in $Sm_2Fe_{17}N_3$ it is 8.6, and that of Nd in $Nd_2Fe_{14}B$ is 4.9. Note that H_a for Fe is 0.05! It is apparent why lanthanides are so important in magnetism and why much effort has been made for optimizing the anisotropy fields. The starting point is to describe the charge distribution of the f orbitals. This can be done using the electric quadrupolar moment. A graphic representation of this type of anisotropy is shown in Figure 3.10 (Rinehart and Long, 2011).

The sphere, of course, corresponds to isotropy; the oblate, pancake-like, and the prolate, cigar-like, ellipsoids correspond to easy plane and easy axis, respectively. In the *Aufbau* scheme, the first f electron is assigned to the orbital with M = 3, obeying the Hund's rule. The shapes of the real f orbitals are shown in Figure 2.1. We recall that the real orbitals are linear combinations of $x^l y^m z^n$ functions, but in any case the shape maintains some feature of the starting f orbitals. The orbitals with M = 3 are ($x(x^2 - 3y^2)$, $y(3x^2 - y^2)$) and they develop in the xy plane, therefore the charge is the prolate ellipsoids. On passing to orbitals with lower M, the z component increases up to z_3, M = 0. The shape in this case is undoubtedly cigar-like. Therefore a change in the basic magnetic anisotropy must be expected while adding one electron at a time to describe the f^n configuration.

Beyond hand-waving arguments, several quantitative approaches have been attempted. Before proceeding, it is wise to stop to reflect on what we are doing. We are trying to express the shape of Ln ions using charge distributions due to f

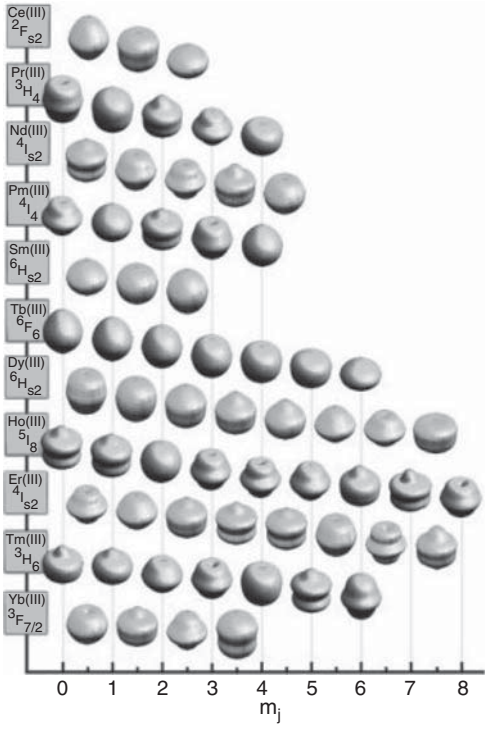

Figure 3.11 Approximations of the angular dependence of the total 4f charge density for M_J states composing the lowest spin–orbit coupled (J) state for each lanthanide. In the absence of a crystal field, all M_J states for each lanthanide ion are degenerate. Values are calculated from parameters derived in Ref. (Sievers, 1982). (Reproduced from Rinehart, J. D and Long, J. R. (2011) with permission from The Royal Society of Chemistry.)

electrons and crystal field. Nothing magnetic. The anisotropy is limited to second order. But experiments show fourth- and sixth-order effects. Anyway, after being neglected by MM, now it is being revisited. We will enter into more details in Chapter 14. Here we just show in Figure 3.11 the shape of $4f^n$ ions.

References

Abragam, A. and Bleaney, B. (1970) *Electron Paramagnetic Resonance of Transition Ions*, Oxford University Press, Oxford.

AlDamen, M.A., Cardona-Serra, S., Clemente-Juan, J.M., Coronado, E., Gaita-Ariño, A., Martí-Gastaldo, C., Luis, F., and Montero, O. (2009) Mononuclear lanthanide single molecule magnets based on the polyoxometalates $[Ln(W_5O_{18})_2]^{9-}$ and $[Ln(\beta 2\text{-}SiW_{11}O_{39})_2]^{13-}$ (Ln^{3+} = Tb, Dy, Ho, Er, Tm, and Yb). *Inorg. Chem.*, **48**, 3467–3479.

Antsyshkina, A.S., Porai-Koshits, M.A., and Ostrikova, V.N. (1988) Stereochemistry of binary formates. Crystal structure of tripotassium hexakis(formato)erbate(3-) dihydrate and pentapotassium octakis(formato) terbate(5-). *Koord. Khim.*, **14**, 850.

Chatterji, A., Chattopadhyay, K.N., Neogy, D., Paul, P., Chatterjee, R., and Chatterjee, S. (2004) Magnetic measurements on the single crystals of $Nd(BrO_3)_3 \cdot 9H_2O$ and a crystal field investigation of its properties. *J. Magn. Magn. Mater.*, **271**, 1–8.

Flanagan, B.M., Bernhardt, P.V., Krausz, E.R., Lüthi, S.R., and Riley, M.J. (2002) A ligand-field analysis of the trensal ($h_3$trensal = 2,2′,2″-tris(salicylideneimino)triethylamine) ligand. An application of the angular overlap model to lanthanides. *Inorg. Chem.*, **41**, 5024–5033.

Görller-Walrand, C. and Binnemans, K. (1996) in *Handbook on the Physics and Chemistry of Rare Earths*, Chapter 155, Vol. 23 (eds K.A. Gschneidner and L. Eyring), North-Holland, Amsterdam, pp. 121–283.

Ishikawa, N. (2007) Single molecule magnet with single lanthanide ion. *Polyhedron*, **26**, 2147–2153.

Ishikawa, N., Sugita, M., Okubo, T., Tanaka, N., Iino, T., and Kaizu, Y. (2003) Determination of ligand-field parameters and f-electronic structures of double-decker bis(phthalocyaninato)lanthanide complexes. *Inorg. Chem.*, **42**, 2440–2446.

Mukherjee, A.K. and Neogy, D. (1988) Magnetism and crystal field analysis of gadolinium bromate enneahydrate crystal. *Phys. Status Solidi B*, **146**, K45–K50.

Neogy, D. and Purohit, T. (1987) Magnetic behavior and crystal field of $Dy(BrO_3)_3.9H_2O$. *Phys. Rev. B*, **35**, 5849–5855.

Neogy, D., Purohit, T., and Chatterji, A. (1986) Magnetic measurements on $Pr(BrO_3)_3 \cdot 9H_2O$ single crystal and a study of the effects and origin of the crystal field. *J. Appl. Phys.*, **59**, 1272–1277.

Neogy, D., Chatterji, A., Chakrabarti, P.K., and Chattopadhyay, K.N. (1994) Magnetic studies on erbium bromate and the crystal field. *J. Magn. Magn. Mater.*, **136**, 118–126.

Neogy, D., Chakrabarti, P.K., Chattopadhyay, K.N., and Chatterji, A. (1996a) Magnetic measurements and crystal field investigations on $Yb(BrO_3)_3 \cdot 9H_2O$. *Phys. Status Solidi B*, **194**, 717–721.

Neogy, D., Saha, R.K., Chakrabarti, P.K., and Chattopadhyay, K.N. (1996b) The effects of crystal field on Tm(III) in $Tm(BrO_3)_3 \cdot 9H_2O$: an experimental and theoretical study. *J. Phys. Chem. Solid*, **57**, 1777–1782.

Purohit, T., Neogy, D., and Saha, R.K. (1992) Single crystal magnetic properties and crystal field investigation of $Ho(BrO_3)_3 \cdot 9H_2O$. *J. Magn. Magn. Mater.*, **117**, 399–404.

Rinehart, J.D. and Long, J.R. (2011) Exploiting single-ion anisotropy in the design of f-element single-molecule magnets. *Chem. Sci.*, **2**, 2078–2085.

Rudowicz, C. (1986) On standardization and algebraic symmetry of the ligand field Hamiltonian of rare earth ions at monoclinic symmetry sites. *J. Chem. Phys.*, **84**, 14.

Schäffer, C.E., Anthon, C., Bendix, J. (2009) Kohn–Sham DFT results projected on ligand-field models: Using DFT to supplement ligand-field descriptions and to supply ligand-field parameters. *Chem. Soc. Rev.*, **253**, 575–593.

Sievers, J. (1982) Asphericity of 4f-shells in their Hund's rule ground states. *Z. Phys. B: Condens. Matter*, **45**, 289–296.

Stevens, K.W.H. (1952) Matrix elements and operator equivalents connected with the magnetic properties of rare earth ions. *Proc. Phys. Soc. London, Sect. A*, **65**, 209–215.

Stewart, G.A. (1985) On the interpretation of nuclear quadrupole interaction data for rare-earth nuclei at low symmetry sites. *Hyperfine Interact.*, **23**, 1–16.

Wybourne, B.G. (1965) *Spectroscopic Properties of Rare Earths*, Kohn-Sham DFT results projected on ligand-field models: Using DFT to supplement ligand-field descriptions and to supply ligand-field parameters. Interscience John Wiley, New York.

4
Coordination Chemistry and Molecular Magnetism

4.1
Introduction

In the history of coordination chemistry, magnetism has been, from the very beginning, a powerful tool for understanding the electronic structures of the large number of synthesized systems with essentially infinite different characteristics such as coordination numbers, nature of the ligand atom, geometry, symmetry of the environment, and so on.

Nowadays, the role of synthetic strategies and magnetic studies is the opposite of the previously described state of the art. The chemical workbench is the place where many research groups are trying to develop preparative routes, which allow them to obtain tailor-made magnetic properties out of the designed molecular systems. The patrimony of knowledge acquired in the past is now vital in the attempt to obtain the required anisotropy of the ground state or a well-defined magnetic dimensionality in the three-dimensional solid structure.

The correlation between structure of TM coordination compounds and their magnetic properties has been widely investigated, as reported in the fundamental book by Kahn (1985) and many other books and review articles. We prefer here to stress more on the properties of lanthanides, which have been less systematically investigated so far compared to TMs but appear to be gaining interest in the last few years because of the success achieved in molecular magnetism.

As this is simply a chapter in a book and not a chemical encyclopedia, there is not enough space to deal with the chemical properties of coordination compounds. We want just to report some properties of a few classes of lanthanide derivatives stressing on one of the main features of RE coordination compounds.

The chemistry of 4f ions is largely different from that of TM ions mainly because the f orbitals do not contribute significantly to bonding in the complex formation involving the lanthanide. The very weak interaction between f and ligand orbitals leads to a less rich variety of coordination compounds: for instance, in the case of monodentate ligands, only atoms with a strong electronegativity are able to bind a lanthanide ion and, in the presence of water, complexes are formed by bidentate ligands able to form chelate rings. This limitation is very often compensated by the possibility of synthesizing the same complex with all the 14 4f ions without

Introduction to Molecular Magnetism: From Transition Metals to Lanthanides, First Edition.
Cristiano Benelli and Dante Gatteschi.
© 2015 Wiley-VCH Verlag GmbH & Co. KGaA. Published 2015 by Wiley-VCH Verlag GmbH & Co. KGaA.

observing substantial differences in the geometrical aspect of the environment around the metal ion. In the field of magnetism, this feature is extremely helpful, as it is possible to work on systems with the same symmetry operating on electronic structures substantially different from each other.

In the following, we will report some chemical properties of the classes of coordination compounds whose magnetic properties will be examined in detail along the chapters of this book. In choosing the examples, we will have in mind the type of functionalities to be developed, the first difference being the goal for which the molecules are designed. If the goal is obtaining single ion magnets (SIMs), a mononuclear molecule will probably be the best choice; if, on the other hand, single chain magnets (SCMs) and single molecular magnets (SMMs) are the goals, then it will be important to design systems that contain groups which can form extended structures.

4.2 Pyrazolylborates

The use of the family of ligands derived from the pyrazolylborate reported in Figure 4.1 was based on the flexibility of a ligand family that offers the chance of controlling through steric saturation the coordination number, geometry, and architecture of its complexes. Further, it is quite easy to introduce selected substituents in the R_1 and R_3 positions of the pyrazolyl rings, allowing, in such a way, the tuning of the ligand size and, therefore, controlling the metal coordination sphere. As the coordination sphere around the 4f ions is not saturated, there is the possibility to introduce with a certain degree of freedom ancillary ligands, which can be other pyrazolylborate moieties, spin carriers, or polyfunctional ligands able to increase the number of metal ions present in the final compounds (Marques, Sella, and Takats, 2002).

A very common strategy to synthesize pyrazolylborate derivatives is the reaction of a lanthanide halide or trifluoromethanesulfonate with the potassium or sodium salts of various pyrazolylborates. The final result of the chemical process is the synthesis of mono-, bis-, or tris-ligand complexes depending on the reaction conditions and the steric demand of the ligand. While for TM the coordination number does not exceed 6, for Ln, generally, higher coordination numbers are possible.

An example of a dysprosium(III) derivative fully coordinated by three pyrazolylborate molecules is shown in Figure 4.2 (Meihaus, Rinehart, and

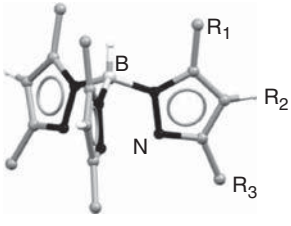

Figure 4.1 Scheme of the trispyrazolylborate anion. The R_1, R_2, and R_3 positions are occupied by various substituents such as H, $-C_2H_5$, $-C_4H_7$, and $-CF_3$. The three positions may be occupied by the same or different substituents.

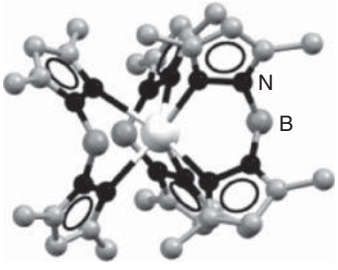

Figure 4.2 Structure of the trigonal prismatic complex $Dy(H_2BPzMe_2)_3$.

Long, 2011). The ligand binds two nitrogen atoms to the metal which therefore is hexa-coordinated with a trigonal prismatic geometry, approaching D_{3h} point symmetry. The bulky nature of the ligand provides a reasonably diluted magnetic environment, which enhances the possibility of SIM behavior.

4.3 Phthalocyanines

The Ln derivatives of phthalocyanine (Pc) had attracted the interest of researchers well before the discovery of the peculiar magnetic properties of some derivatives which are described in other chapters of this book. Actually, the ligands we are going to talk about belong to the aristocracy of ligands. In fact, porphyrins (RP) and Pcs have a rich chemistry with important applications and relevance to various fields ranging from biochemistry to semiconductors to molecular electronics (Elemans *et al.*, 2006; Hartinger and Dyson, 2009). The coordination chemistry of Ln^{3+} ions with RP and Pc is determined by the size of the ions which do not fit into the cavity of the ligand. The coordination is more relaxed if the metal ion coordinates two ligands in a sandwich-like geometry. This family of sandwich compounds displays peculiar physical, spectroscopic, and electrochemical properties, mainly originating from the $\pi-\pi$ interactions associated with these complexes.

The most used synthetic procedure for Pc derivatives requires several steps but can be outlined as a process where Ln^{3+} acetate in boiling 1-hexanol is mixed with substituted 1,2-dicyanobenzene in the presence of 1,8-diazabicyclo[5.4.0]undec-7-ene, DBU (see Scheme 4.1), and then purified by chromatography (De Cian *et al.*, 1985).

This procedure yields two products, namely the anionic $[LnPc_2]^-$ (generally blue), and the neutral $[LnPc_2]^0$ (generally green), which are obtained simultaneously; and it is well established that their relative ratio strongly depends on the heating gradients. Working on this parameter and on the chromatographic procedure, the anionic form is separated and stabilized by stoichiometric addition of

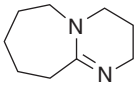

Scheme 4.1 DBU molecule.

some cation such as *n*-tetrabutylammonium $[TBA]^+$. The several reported crystal structures of these coordination complexes show a quasi-parallel arrangement of the Pc rings that incorporate, like in a sandwich, the metal ion which is, in most compounds, coordinated by eight nitrogen atoms belonging to the different phthalocyanine molecules.

The Pc family of derivatives offers a wide range of chemical strategies to modify the structural and electronic properties of the ligand molecule using the different precursor reagents to introduce suitable substituents in the aromatic rings (see Scheme 4.2).

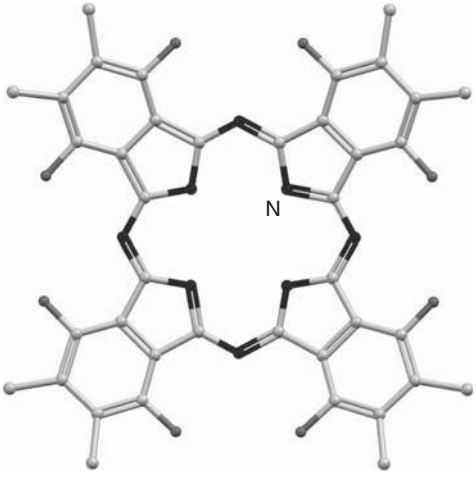

Scheme 4.2 A generic phthalocyanine.

As a consequence of this chemical flexibility, it is possible to produce compounds with different oxidation states involving the Ln^{3+} ion and/or ligand molecules and triple-decker sandwich derivatives including the same (Jiang *et al.*, 2001) or different lanthanide ions (Chabach *et al.*, 1996).

Of particular interest is the preparation of sandwich-type lanthanide triple-decker compounds where homo- or heterometallic pairs are formed by using different ligands such as RP and Pc. The synthesis starts with the reaction of $Ln(acac)_3$ and the selected porphyrin. Then, an $Ln'(Pc)_2$ is added, and the final mixed sandwich compound is extracted and purified. Some interesting magnetic properties are very often observed (Kan *et al.*, 2013).

4.4
Cyclopentadiene and Cyclooctatetraene

These two ligands are often considered together because of the similarity of the structures of the complexes that are possible to be synthesized with them and

even for historical reasons because they were used at the very beginning of the organometallic chemistry of lanthanide ions.

The cyclooctatetraene dianion (COT) came later than cyclopentadienyl derivatives: this molecule was used to confirm the possibility of forming coordination compounds of f elements with this class of ligands. The synthesis of most of the Ln^{3+} ions is quite straightforward: in an inert atmosphere (to avoid contact with oxygen and moisture), the potassium salt of cyclooctatetraene is prepared in degassed tetrahydrofuran (THF). The chloride salt of the chosen lanthanide is added, and then a cycle of extractions and recrystallizations is needed to separate the potassium salt of the general formula $K[Ln(C_8H_8)]\cdot THF$ from the dimer of formula $[Ln(C_8H_8)Cl\cdot 2THF]_2$ (Hodgson *et al.*, 1973) (Figure 4.3). An interesting behavior of the last compounds is the possibility of breaking the dimer to introduce a different ligand to complete the coordination sphere of the 4f ion. For instance, by reacting $[Ln(C_8H_8)Cl\cdot 2THF]_2$ with the sodium salt of pentamethylcyclopentadienyl it is possible to separate a compound with the formula $[(C_8H_8)Ln(C_5Me_5)]\cdot THF$ (Schumann *et al.*, 1989).

The crystal structure of $K[Ln(C_8H_8)]\cdot$(THF or diglyme) shows a classical sandwich structure as described for the Pcs. In most cases, the compounds crystallize in orthorhombic group and the molecular geometry is very close to D_{8d}, the rotomeric configuration which corresponds to an eclipsed geometry (Hodgson and Raymond, 1972b).

Even though cyclopentadienyl was used first in the synthesis of organometallic lanthanide complexes (Wilkinson and Birmingham, 1954), only recently this ligand has demonstrated the possibility to be used to produce SMM (Sulway *et al.*, 2012). Its chemistry is very similar to that of COT. The synthetic route is again based on the reaction of the sodium salt of variously substituted $C_5H_5^-$ ion in THF or other nonpolar solvents. Again, it is possible to obtain compounds with molecular structures such as those reported in Figure 4.3 even though the derivative of the reaction with $DyCl_3$ gave the polymeric compounds shown in Figure 4.4.

It is useful to remember that lanthanide cyclopentadienides act as strong Lewis acids. It is therefore possible to form adducts with molecules containing donor

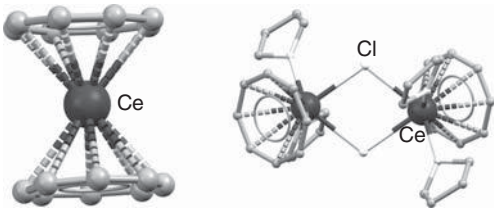

Figure 4.3 ORTEP view of the coordination sphere of $Ce(COT)_2$. (a) Diglyme (Hodgson and Raymond, 1972b) and (b) $[Ce(COT)Cl(THF)_2]_2$ (Hodgson and Raymond, 1972a). Hydrogen atoms are omitted for clarity.

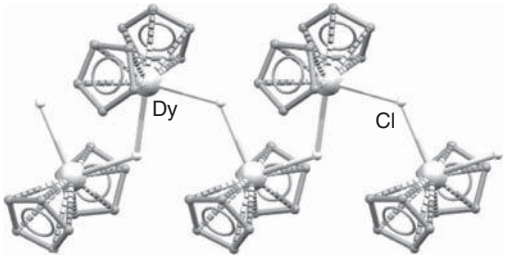

Figure 4.4 Structure of $[(\eta^5\text{-Cp})_2\text{Dy}(\mu\text{-Cl})]_\infty$. Hydrogen atoms are omitted for clarity.

atoms different from the most used nitrogen or oxygen atoms provided that the co-ligand molecule has some basic properties.

The similarity in the chemical behavior of these molecules is confirmed by the possibility to obtain by reacting $[\text{Ln}(C_5Me_5)\text{I}\cdot 2\text{THF}]_2$ with $\text{Na}(C_8H_8)$ in an inert atmosphere to obtain derivatives where the 4f ion is coordinated in a sandwich manner by either Cp and COT ligands (Evans *et al.*, 2000).

4.5 Polyoxometalates (POMs)

Chemistry met polyoxometalates (POMs) in 1778 when Carl Wilhelm Scheele described molybdenum blue. Since then, POMs have been a fascinating field of research just for the wealth of their chemical properties, for the palette of their colors, and for the aesthetic appeal of their molecular structure. Recently, the possibility of introducing magnetic ions into these systems raised a great interest, as it is possible to analyze the magnetic properties of molecular derivatives that could mimic the features of magnetic system such as metal oxide materials.

The strategy to prepare high-nuclearity POMs is not complex, as the procedure requires acidifying an aqueous solution containing the relevant metal oxide anions (molybdate, tungstate, vanadate, etc.). In the case of acidification, for example, a solution of sodium molybdate will give rise to metal oxide fragments whose nuclearity can be controlled by the pH. This offers in general a valid strategy in planning the overall structure of the POM derivatives. The introduction of magnetic ions can be achieved in two different ways: the first is based on the introduction of heteropolyanions in the clusters, while the second uses the POMs to encapsulate magnetic centers.

In the first procedure, it is important to control several variables such as the concentration/type of metal oxide anion and heteroatom concentration, pH and type of acid, and the type and concentration of electrolyte, as well as the possibility to introduce additional ligands. The second class of compounds is generally synthesized starting from a solution of the alkaline salt of the chosen POM. A solution of a 3d/4f salt is added, and the final product is precipitated by heating the whole pot. Very often, POM syntheses are carried out in aqueous solutions at room temperature or at elevated temperatures not higher than the boiling point of

the solvent. In addition to the traditional way, recently synthetic strategies based on a hydrothermal approach have been developed. To have a panoramic view of these aspects, we recommend the reader to the literature (Clemente-Juan and Coronado, 1999; Long, Burkholder, and Cronin, 2007).

Research based on the use of POMs as ligand toward spin carrier explores two different types of derivatives: the spin-delocalized mixed-valence POMs and the spin-localized ones (Clemente-Juan, Coronado, and Gaita-Ariño, 2012). For the synthesis of the mixed-valence derivatives, the electron-accepting ability of these metal oxide clusters is relevant: as a consequence, a variable number of electrons can undergo rapid transfer from one center to another of the POMs. These spin-delocalized clusters represent a formidable challenge in molecular magnetism because their electronic complexity is much higher than that encountered in the spin-localized magnetic clusters. An interesting example of the complex magnetic structure of this type of compounds is the family of $[V_{18}O_{48}]^{n-}$ cluster whose structure is shown in Figure 4.5 (Müller *et al.*, 1997).

In the second class of POMs, the magnetic moments remain localized on the magnetic metal ions. These compounds are produced by taking advantage of the capability of POMs to act as chelating ligands toward practically all 3d and 4f metal ions. This property allows to incorporate the magnetic ions at specific sites of the POMs structures. In such a way, it is possible, to some extent, to produce planned magnetic systems that contain either a single magnetic center or various magnetic centers connected though oxo-bridges. As these POM ligands are rigid, it is possible to analyze several derivatives using the same POM and changing the magnetic

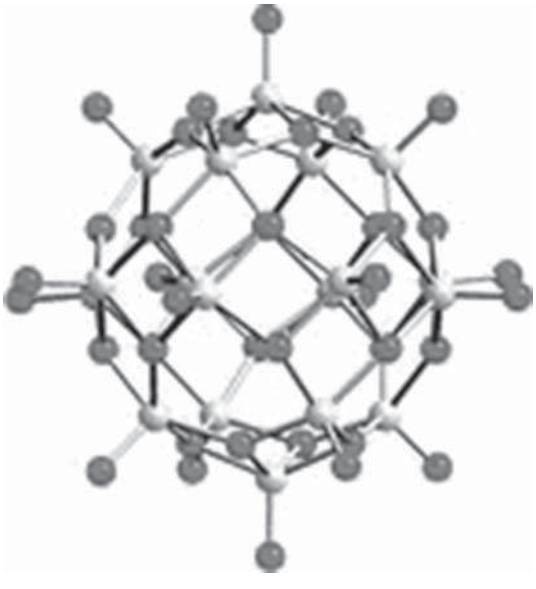

Figure 4.5 Structure of $[V_{18}O_{48}]^{n-}$ cluster. V is shown in light gray. (Reproduced from Clemente-Juan, J.M. *et al.* (2012) with permission from The Royal Society of Chemistry.)

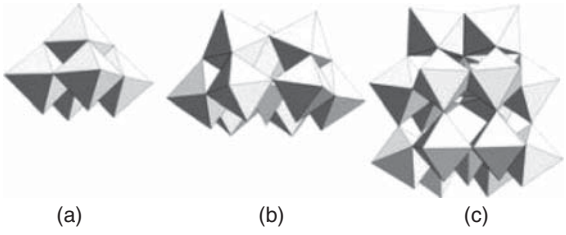

Figure 4.6 (a) $[W_5O_{18}]^{6-}$, (b) β-$[PW_9O_{34}]^{9-}$, and (c) $[P_2W_{15}O_{56}]^{12-}$. (Reproduced from Clemente-Juan, J.M. *et al.* (2012) with permission from The Royal Society of Chemistry.)

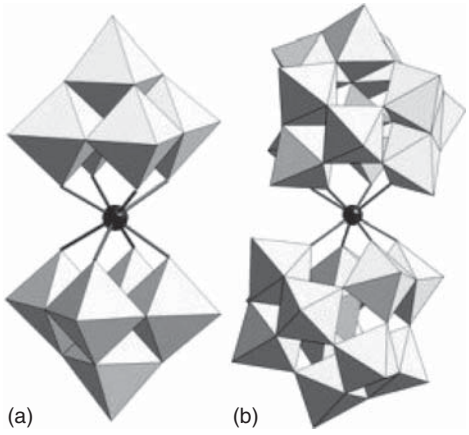

Figure 4.7 Structures of (a) $[Ln(W_5O_{18})_2]^{9-}$ and (b) $[Ln(\beta_2\text{-}SiW_{11}O_{39})_2]^{13-}$ derivatives. (Reproduced from Clemente-Juan, J.M. *et al.* (2012) with permission from The Royal Society of Chemistry.)

metal ions in the same structural feature. A few examples of the used POMs are shown in Figure 4.6.

Another relevant characteristic of these systems is the possibility to study the magnetic properties of the encapsulated ions or clusters as they are isolated systems due to the bulky nonmagnetic POM framework, with typical distances between the magnetic ions of the order of 1–2 nm. This aspect has suggested, recently, the possibility of using POMs in preparing compounds in which the correct choice of a highly anisotropic magnetic ion or cluster allows obtaining a system with a well-defined SIM behavior, as described in the dedicated chapters of this book. In Figure 4.7, examples are reported of the structure of systems containing the Ln^{3+} ion exhibiting the above-mentioned property.

4.6 Diketonates

In the field of molecular magnetism, the chemistry of simple or substituted acetylacetonate (R-acac) derivatives of Ln^{3+} is substantially based on the possibility to

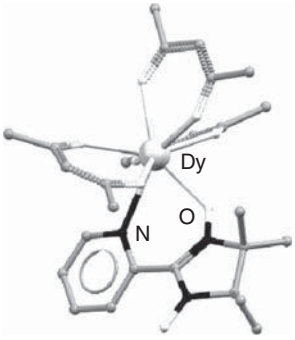

Figure 4.8 (a) View of the coordination environment of Dy^{3+} ion in $[Dy(hfac)_3(NIT_2Py)]$. Hydrogen and fluorine atoms are omitted for clarity.

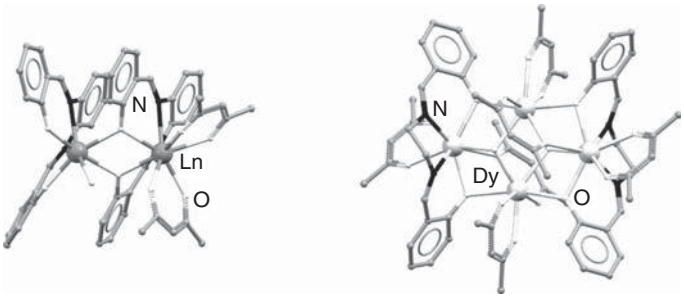

(a) (b)

Figure 4.9 Molecular structure of (a) $[Ln_2H_2L^1{}_2(acac)_2]$ and (b) $[Dy_4(\mu_3\text{-}OH)_2L^2{}_2(acac)_6]$ (b). All hydrogen atoms have been omitted for clarity.

use the tris-diketonates Ln^{3+} moieties to form adducts. The advantage of using acac derivatives is that they are effective Lewis bases whose properties can be enhanced by introducing electron-withdrawing groups such as $-CF_3$. As the three ligands supply only six oxygen donor atoms, it is relatively easy to complete the coordination sphere of the 4f ions with additional molecules suitable to form complexes containing one or more magnetic centers. The synthesis of these systems is rather simple: it requires refluxing in solvents such as methanol, acetonitrile, or dichloromethane $Ln(R\text{-}acac)_3{\cdot}H_2O$ and adding the co-ligand in the chosen stoichiometric amount.

For instance, using a nitronyl nitroxide (NIT) such as 2-(2-pyridyl)-4,4,5,5-tetramethylimidazolin-1-oxyl 3-oxide (NIT_2Py), is possible to synthesize a molecule containing only one Dy^{3+} ion, as shown in Figure 4.8 (Mei *et al.*, 2012). By using Schiff bases such as *N*,*N*′-bis(salicylidene)-*o*-phenylenediamine (H_2L^1) or *N*,*N*′-bis(salicylidene)-1,2-ethanediamine (H_2L^2), dimeric and tetranuclear systems have been described (Figure 4.9) (Sun *et al.*, 2013), while by choosing as the starting diketonate dibenzoylmethane (Ph_2acacH) the polymeric structure depicted in Figure 4.10 was obtained (Thielemann *et al.*, 2011).

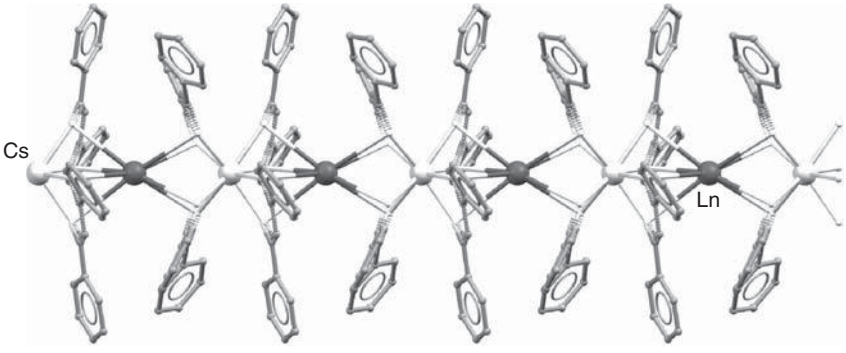

Figure 4.10 Schematic view of the chain in $[Cs(Ln(Ph_2acac)_4)]_n$ (Ln = Pr, Nd, Sm, Dy).

4.7 Nitronyl-nitroxides (NITs)

Beyond using various ligands to design the coordination geometry, the reactivity, and the spectroscopic and magnetic properties of coordination compounds taking advantage of the structure features, it is possible to use also ligands that contain magnetic centers such as organic radicals. Among the stable organic radicals, the NIT family exhibits some peculiarities. First of all, this kind of molecules has two oxygen atoms that can act as donor atoms to form coordination compounds with TM and lanthanide ions. The two oxygen atoms are located on opposite sides of the radical which can be used as a bidentate ligand or as a bridging molecule simultaneously linked to more than one metal ion. The synthesis of the organic radical allows the introduction in the molecule of functionalized groups leaving untouched the part of the radical where the unpaired electron is localized. Finally, the choice of the organic fragment bound to the penta-atomic ring allows tuning the distance between the magnetic molecules: large fragments can be useful to have well-separated molecules to reduce the intensity of intermolecular magnetic interaction. However, it is useful to stress that the oxygen atoms have weak Lewis basicity, and therefore they are poor ligands. This feature sets large limitations on the nature of the additional ligands around the metal ion because one must avoid co-ligands capable of kicking the nitroxide off.

The starting point in a project to prepare new molecular magnetic system by using an NIT is the synthesis of the radical itself. The preparation is rather straightforward and, at least in principle, it is not too difficult to draw on a piece of paper a new molecule. The initial reagents are 2,3-dimethyl-2,3-bis(hydroxylamine)butane and a well-chosen aliphatic aldehyde, and the reaction follows Scheme 4.3 (Ullman *et al.*, 1972).

The radical is obtained by treating the product of the first step with sodium periodate or lead dioxide followed by a separation via liquid chromatography. The final product is easily identified because the NITs derived from saturated aldehydes are generally red whereas unsaturated aldehydes yield violet or blue radicals depending on whether the solvent is polar or nonpolar.

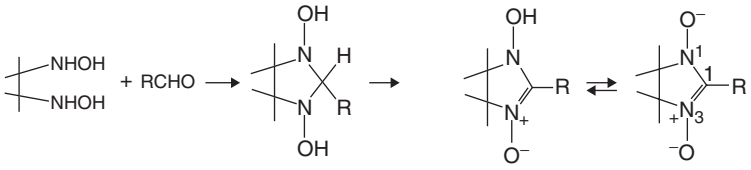

Scheme 4.3 A synthesis strategy for nitronyl nitroxides. (Reproduced from Ullman, E.F. *et al.* (1972) with permission from The American Chemical Society.)

From the above short description of the synthesis, the role of the substituent in the reacting aldehyde emerges. According to the nature of this fragment, it is possible to produce many different radicals. Just to give an idea of the flexibility of this kind of co-ligand, a few examples of NIT are summarized in Figure 4.11.

Since the first report of an NIT derivative with Gd^{3+}, several Ln^{3+}NIT derivatives have been described with different metal ion/radical ratios and structures ranging from a molecule containing a metal ion to compounds organized in infinite chains. It is evident that there is no single definite strategy to obtain the various derivatives. Anyhow, it is possible to indicate that a starting metal ion/NIT of 1 : 2 ratio will, probably, lead to the formation of the classical $Ln^{3+}NIT_2$ derivative (Benelli *et al.*, 1987). To obtain small clusters such as $[LnNIT]_2$, it may be useful to introduce a moiety with a ligand atom using an appropriate aldehyde such as

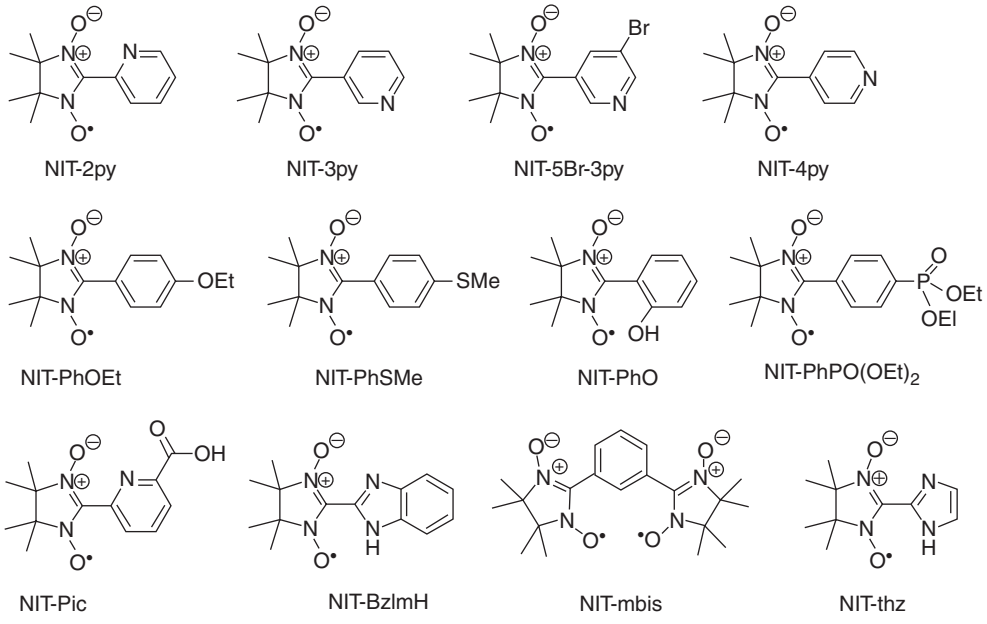

Figure 4.11 Some nitronyl-nitroxide ligands. (Reproduced from: "Lanthanide Single-Molecule Magnets", Chem. Rev., **2013**, *113*, 5110 by Woodruff, D.N., Winpenny, R.E.P. and Layfield, R.A. with permission from The American Chemical Society.)

NIT-*n*py or NIT-thz. Experimental evidence suggests that, with a metal ion/NIT ratio of 1 : 1, the formation of a linear chain assembly is favored to respect zero-dimensional systems by a reaction where the temperature is maintained as low as possible.

4.8 Carboxylates

On the shelf of any chemist, there will be a large amount of carboxylic acid, and therefore the possibility of synthesizing new coordination compounds is almost infinite. In general, the preparation of these systems is not very difficult, passing through the direct reaction of the selected acid with the appropriate metal oxide. The possibility offered by this type of ligand can be understood by two well-known examples: the dimeric structure of Cu^{2+} acetate whose magnetic properties changed the history of molecular magnetism, and the cluster formed again by acetic acid and 12 manganese ions which is a blockbuster in the recent study of magnetic properties of molecular systems.

As usual, some specific detail is useful to analyze the behavior of lanthanide-containing systems. The first point to stress is related to the fact that the ideal Ln^{3+}/acid ratio is 1 : 3, which gives a neutral compound: actually, the six oxygen atoms of three molecules of carboxylic acid are, generally, not enough to saturate the coordination around the 4f ion. Six-coordinated complexes are very uncommon in lanthanide chemistry. The first consequence is that the final structures of these derivatives show some additional complexity. For instance, if we consider the simplest system, namely the one formed with formic acid, the formula $[Ln(HCO_2)_3]$ (Ln = La, Ce, Tb, Tm, Gd, Sm) corresponds to an extended structure, as shown in Figure 4.12 (Xu *et al.*, 2006).

Therefore, the most common coordination complexes present an environment around the Ln^{3+} ion where additional ligand atoms are present with respect the three molecules of carboxylic acid. The simple acetate derivative presents a dimeric structure like the one shown in Figure 4.13 (Cañadillas-Delgado *et al.*, 2009).

As in the reported molecule, the carboxylic group is able to act as a bridging unit, and therefore it is often possible to produce extended structures. For instance, the previous compound reacts with fumaric acid, and the final product is an extended structure where the reported dimeric units are connected along two different directions by fumarate ligands.

4.9 Schiff Bases

Schiff bases are a category of ligands widely used in coordination chemistry. The basic reaction to produce the primary imine is very simple, and the variety

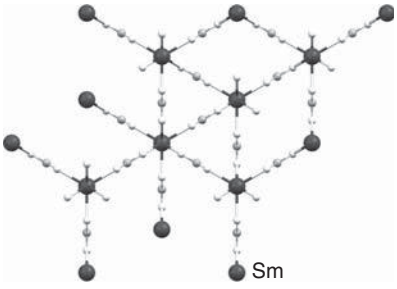

Figure 4.12 View along the *c*-axis of $[Sm(HCO_2)_3]_\infty$.

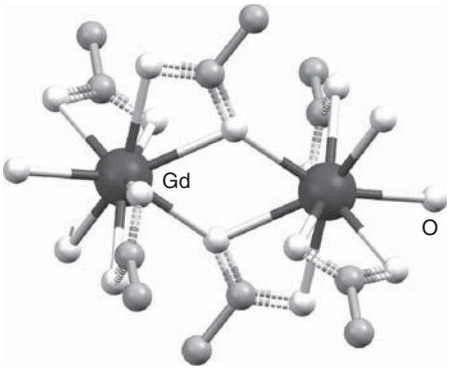

Figure 4.13 View of $[Gd_2(acetate)_6(H_2O)_4]\cdot 2H_2O$.

of ammines and aldehydes (or ketones) is so large that it is possible to produce an infinite series of ligand molecules (Vigato, Peruzzo, and Tamburini, 2012).

In the field of molecular magnetism, there are two classes of derivatives based on Schiff bases that are of particular interest. The first kind consists of derivatives obtained by the reaction of well-defined coordination compounds formed by a metal ion and a Schiff base with a different metal ion to produce hetero-bimetallic compounds. A second important class of poly-metallic compounds is based on the use of the so-called compartmental ligands, which are ligand molecules able to encapsulate different metal ions in different coordination spheres.

The first examples reporting the use of Ni^{2+} and Cu^{2+} Schiff base derivatives as ligands toward Ln^{3+} ions (Seminara *et al.*, 1984) opened the way to a very fruitful series of similar compounds whose magnetic properties gave new perspectives to the study of 3d–4f exchange interactions (Alexandropoulos *et al.*, 2013; Bencini *et al.*, 1985). The chemistry of these systems is generally simple. It is necessary to prepare a TM complex with the selected Schiff base and then to react it with a Ln^{3+} salt which contains a noncoordinated anion. If no other ligands are present, the need of a high coordination number produces compounds with a 3d/4f ratio different from 1 : 1, as in the example reported in Figure 4.14.

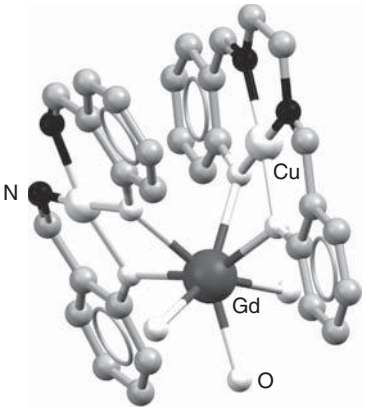

Figure 4.14 View of $[(CuHAPen)_2Gd(H_2O)_3]^{3+}$ ion. (HAPen = *N*,*N*′-ethylenebis(salicylaldiminato)).

Schiff bases are used to easily produce a class of ligands commonly denoted as "compartmental ligands": a simple example is shown in Scheme 4.4.

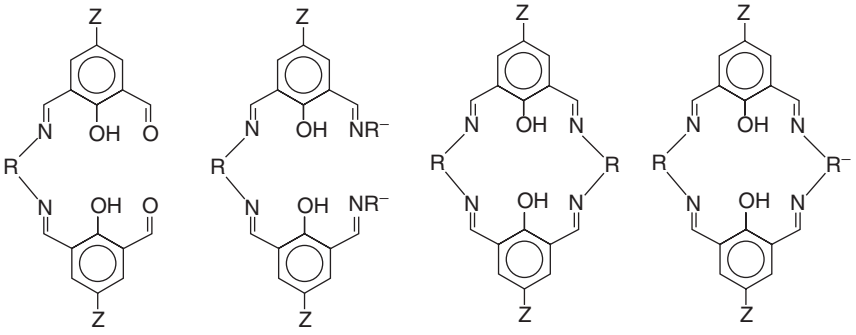

Scheme 4.4 Some examples of compartmental ligands.

In their synthesis, it is possible to choose the substituent R, R′, and Z to determine the size and the ligand atoms in the two "cavities" in such a way that it is possible to accommodate two different metal ions in suitable coordination spheres. The use of these types of ligands started with the simple synthesis of homo and heterobinuclear compounds with a wide typology of pairs: TM–TM, TM–Ln, Ln–Ln pairs with degenerate or nondegenerate ground states of one or both metal ions (Vigato and Tamburini, 2004).

Because of the relatively simple chemistry required to prepare this kind of ligands, in the last few years there have been several reports on the use of Schiff bases in the synthesis of complex clusters which in many cases exhibit an SMM behavior (Cimpoesu *et al.*, 2012; Gao *et al.*, 2013).

At the end of this rapid survey of ligands capable of forming SMM, SIM, and SCM, the conclusion is that the relevance of the ligands is rather low, the nature of the metal being much more important. This is rather expected, given the strong

influence of the environment on the metal properties and the moderate role of the ligands. We will work on this point in the following; at any rate, several classes of ligands have been identified and much work remains to be done.

References

Alexandropoulos, D.I., Nguyen, T.N., Cunha-Silva, L., Zafiropoulos, T.F., Escuer, A., Christou, G., and Stamatatos, T.C. (2013) Slow magnetization relaxation in unprecedented $Mn(III)_4Dy(III)_3$ and $Mn(III)_4Dy(III)_5$ clusters from the use of N-salicylidene-o-aminophenol. *Inorg. Chem.*, **52**, 1179–1181.

Bencini, A., Benelli, C., Caneschi, A., Carlin, R.L., Dei, A., and Gatteschi, D. (1985) Crystal and molecular structure of and magnetic coupling in two complexes containing gadolinium(III) and copper(II) ions. *J. Am. Chem. Soc.*, **107**, 8128–8136.

Benelli, C., Caneschi, A., Galleschi, D., Laugier, J., and Rey, P. (1987) Structure and magnetic properties of a gadolinium hexafluoroacetylacetonate adduct with the radical 4,4,5,5-tetramethyl-2-phenyl-4,5-dihydro-1H-imidazole 3-Oxide 1-Oxyl. *Angew. Chem., Int. Ed. Engl.*, **26**, 913–915.

Cañadillas-Delgado, L., Fabelo, O., Cano, J., Pasán, J., Delgado, F.S., Lloret, F., Julve, M., and Ruiz-Pérez, C. (2009) Dinuclear and two- and three-dimensional gadolinium(III) complexes with mono- and dicarboxylate ligands: synthesis, structure and magnetic properties. *CrystEngComm*, **11**, 2131–2142.

Chabach, D., De Cian, A., Fischer, J., Weiss, R., and Bibout, M.E.M. (1996) Mixed-metal triple-decker sandwich complexes with the porphyrin/phthalocyanine/porphyrin ligand system. *Angew. Chem., Int. Ed. Engl.*, **35**, 898–899.

Cimpoesu, F., Dahan, F., Ladeira, S., Ferbinteanu, M., and Costes, J.P. (2012) Chiral crystallization of a heterodinuclear Ni-Ln series: comprehensive analysis of the magnetic properties. *Inorg. Chem.*, **51**, 11279–11293.

Clemente-Juan, J.M. and Coronado, E. (1999) Magnetic clusters from polyoxometalate complexes. *Coord. Chem. Rev.*, **193–195**, 361–394.

Clemente-Juan, J.M., Coronado, E., and Gaita-Ariño, A. (2012) Magnetic polyoxometalates: from molecular magnetism to molecular spintronics and quantum computing. *Chem. Soc. Rev.*, **41**, 7464–7478.

De Cian, A., Moussavi, M., Fischer, J., and Weiss, R. (1985) Synthesis, structure, and spectroscopic and magnetic properties of lutetium(III) phthalocyanine derivatives: $LuPc_2 \cdot CH_2Cl_2$ and $[LuPc(OAc)(H_2O)_2] \cdot H_2O \cdot 2CH_3OH$. *Inorg. Chem.*, **24**, 3162–3167.

Elemans, J.A.A.W., Van Hameren, R., Nolte, R.J.M., and Rowan, A.E. (2006) Molecular materials by self-assembly of porphyrins, phthalocyanines, and perylenes. *Adv. Mater.*, **18**, 1251–1266.

Evans, W.J., Johnston, M.A., Clark, R.D., and Ziller, J.W. (2000) Variability of (ring centroid)-Ln-(ring centroid) Angles in the Mixed Ligand C_5Me_5/C_8H_8 Complexes $(C_5Me_5)Ln(C_8H_8)$ and $[(C_5Me_5)Yb(THF)](\mu\text{-}\eta_8\text{:}\eta_8\text{-}C_8H_8)[Yb(C_5Me_5)]$. *J. Chem. Soc., Dalton Trans.*, 1609–1612.

Gao, F., Cui, L., Liu, W., Hu, L., Zhong, Y.W., Li, Y.Z., and Zuo, J.L. (2013) Seven-coordinate lanthanide sandwich-type complexes with a tetrathiafulvalene-fused Schiff base ligand. *Inorg. Chem.*, **52**, 11164–11172.

Hartinger, C.G. and Dyson, P.J. (2009) Bioorganometallic chemistry – from teaching paradigms to medicinal applications. *Chem. Soc. Rev.*, **38**, 391–401.

Hodgson, K.O., Mares, F., Starks, D.F., and Streitwieser, A. (1973) Lanthanide(III) complexes with cyclooctatetraene dianion. Synthetic chemistry, characterization, and physical properties. *J. Am. Chem. Soc.*, **95**, 8650–8658.

Hodgson, K.O. and Raymond, K.N. (1972a) Dimeric π-cyclooctatetraene dianion complex of cerium(III). Crystal and molecular structure of $[Ce(C_8H_8)Cl.2OC_4H_8]_2$. *Inorg. Chem.*, **11**, 171–175.

Hodgson, K.O. and Raymond, K.N. (1972b) Ion pair complex formed between bis(cyclooctatetraenyl)cerium(III) anion and an ether-coordinated potassium cation. Crystal and molecular structure of $[K(CH_3OCH_2CH_2)_2O][Ce(C_8H_8)_2]$. *Inorg. Chem.*, **11**, 3030–3035.

Jiang, J., Bian, Y., Furuya, F., Liu, W., Choi, M.T.M., Kobayashi, N., Li, H.-W., Yang, Q., Mak, T.C.W., and Ng, D.K.P. (2001) Synthesis, structure, spectroscopic properties, and electrochemistry of rare earth sandwich compounds with mixed 2,3-naphthalocyaninato and octaethylporphyrinato ligands. *Chem. Eur. J*, **7**, 5059–5069.

Kahn, O. (1985) *Magneto-Structural Correlations in Exchange Coupled Systems*, vol. C140, Reidel.

Kan, J., Wang, H., Sun, W., Cao, W., Tao, J., and Jiang, J. (2013) Sandwich-type mixed tetrapyrrole rare-earth triple-decker compounds. Effect of the coordination geometry on the single-molecule-magnet nature. *Inorg. Chem.*, **52**, 8505–8510.

Long, D.-L., Burkholder, E., and Cronin, L. (2007) Polyoxometalate clusters, nanostructures and materials: from self assembly to designer materials and devices. *Chem. Soc. Rev.*, **36**, 105–121.

Marques, N., Sella, A., and Takats, J. (2002) Chemistry of the lanthanides using pyrazolylborate ligands. *Chem. Rev.*, **102**, 2137–2160.

Mei, X.-L., Ma, Y., Li, L.-C., and Liao, D.-Z. (2012) Ligand field-tuned single-molecule magnet behaviour of 2p-4f complexes. *Dalton Trans.*, **41**, 505–511.

Meihaus, K.R., Rinehart, J.D., and Long, J.R. (2011) Dilution-induced slow magnetic relaxation and anomalous hysteresis in trigonal prismatic dysprosium(III) and uranium(III) complexes. *Inorg. Chem.*, **50**, 8484–8489.

Müller, A., Sessoli, R., Krickemeyer, E., Bögge, H., Meyer, J., Gatteschi, D., Pardi, L., Westphal, J., Hovemeier, K., Rohlfing, R. *et al.* (1997) Polyoxovanadates: high-nuclearity spin clusters with interesting host–guest systems and different electron populations. Synthesis, spin organization, magnetochemistry, and spectroscopic studies. *Inorg. Chem.*, **36**, 5239–5250.

Schumann, H., Koehn, R.D., Reier, F.W., Dietrich, A., and Pickardt, J. (1989) Organometallic compounds of the lanthanides. 48. Cyclooctatetraenyl pentamethylcyclopentadienyl derivatives of the rare earths. *Organometallics*, **8**, 1388–1392.

Seminara, A., Giuffrida, S., Musumeci, A., and Fragalá, I. (1984) Polynuclear complexes of lanthanides with nickel and copper schiff bases as ligands. *Inorg. Chim. Acta*, **95**, 201–205.

Sulway, S.A., Layfield, R.A., Tuna, F., Wernsdorfer, W., and Winpenny, R.E.P. (2012) Single-molecule magnetism in cyclopentadienyl-dysprosium chlorides. *Chem. Commun.*, **48**, 1508–1510.

Sun, W.-B., Han, B.-L., Lin, P.-H., Li, H.-F., Chen, P., Tian, Y.-M., Murugesu, M., and Yan, P.-F. (2013) Series of dinuclear and tetranuclear lanthanide clusters encapsulated by salen-type and β-diketonate ligands: single-molecule magnet and fluorescence properties. *Dalton Trans.*, **42**, 13397–13403.

Thielemann, D.T., Klinger, M., Wolf, T.J.A., Lan, Y., Wernsdorfer, W., Busse, M., Roesky, P.W., Unterreiner, A.-N., Powell, A.K., Junk, P.C. *et al.* (2011) Novel lanthanide-based polymeric chains and corresponding ultrafast dynamics in solution. *Inorg. Chem.*, **50**, 11990–12000.

Ullman, E.F., Osiecki, J.H., Boocock, D.G.B., and Darcy, R. (1972) Stable free radicals. X. Nitronyl nitroxide monoradicals and biradicals as possible small molecule spin labels. *J. Am. Chem. Soc.*, **94**, 7049–7059.

Vigato, P.A., Peruzzo, V., and Tamburini, S. (2012) Acyclic and cyclic compartmental ligands: recent results and perspectives. *Coord. Chem. Rev.*, **256**, 953–1114.

Vigato, P.A. and Tamburini, S. (2004) The challenge of cyclic and acyclic schiff bases and related derivatives. *Coord. Chem. Rev.*, **248**, 1717–2128.

Wilkinson, G. and Birmingham, J.M. (1954) Cyclopentadienyl compounds of Sc, Y, La, Ce and some lanthanide elements. *J. Am. Chem. Soc.*, **76**, 6210–6210.

Xu, Y., Ding, S.H., Zhou, G.P., and Liu, Y.G. (2006) Samarium(III) formate. *Acta Crystallogr., Sect. E: Struct. Rep. Online*, **62**, m1749–m1750.

5
Magnetism of Ions

5.1
The Curie Law

In Chapter 2, we reported on how a system containing unpaired electrons responds to an applied magnetic field by introducing the Zeeman effect and the *g*-factor. We now start again from there, generalizing to define the magnetization. We will see some math, which can be avoided by going to Eq. (5.10).

When we apply a magnetic field H to a sample, it responds as

$$\boldsymbol{B} = \boldsymbol{H} + 4\pi\boldsymbol{M} \tag{5.1}$$

where $\boldsymbol{B}$ is a vector called the magnetic induction and $\boldsymbol{M}$ is the magnetization tensor. The simplest case is when $\boldsymbol{M}$ depends linearly on the field:

$$\boldsymbol{M} = \chi_v H \tag{5.2}$$

where χ_v is the dimensionless volume susceptibility. This occurs at low field and high temperature in systems with unpaired electrons that do not interact among themselves, which are called paramagnets. Actually, the experimental susceptibility is due to two contributions: χ_{para} and χ_{dia}. The former is due to the presence of unpaired electrons in the system. The latter originates from the interaction of the magnetic field with the motion of paired electrons in their orbitals. It is, therefore, a contribution that is present in all molecules because electron pairs are ubiquitous. The diamagnetic susceptibility is negative with rather small values, does not depend on the magnetic field strength, and is independent of temperature. If it is dominant, the substance is diamagnetic and it is repelled by the magnetic field. When it is necessary to get very accurate values of χ_{para} from an experiment on a metallo-organic molecule, it is necessary to separate the two contributions to χ. A very rough method is to consider

$$\chi_{\text{dia}} = -kM\,10^{-6}\ \text{emu}\ \text{mol}^{-1} \tag{5.3}$$

where M is the molecular weight and k an empirical value in the range 0.4–0.5. The correct strategy for determining the diamagnetic contribution is the Pascal's approach (Pascal, 1913), namely to consider χ_{dia} as the sum of the diamagnetic contributions of all the atoms, ions, functional groups, and bonds present in the

Introduction to Molecular Magnetism: From Transition Metals to Lanthanides, First Edition.
Cristiano Benelli and Dante Gatteschi.
© 2015 Wiley-VCH Verlag GmbH & Co. KGaA. Published 2015 by Wiley-VCH Verlag GmbH & Co. KGaA.

molecules. These values have been already determined and are reported in the literature (Bain and Berry, 2008).

The contribution of paramagnetic magnetization of an ensemble of N ions which have unpaired electrons is given by

$$M = N\frac{\sum \mu_n e^{\frac{-E_n}{kT}}}{\sum e^{\frac{-E_n}{kT}}} \tag{5.4}$$

where μ_n is the magnetic moment of the level n and E_n is its energy.

$$\mu_n = -\delta E_n/\delta H \tag{5.5}$$

and the sums are over all the thermally populated E_n states. We recall that for TMs the reference states are of the type ^{2S+1}L while for Ln these correspond to a J multiplet. As applied to Lns, Eq. (5.4) becomes the so-called Brillouin equation

$$M = N\mu_B \frac{\sum -g_J M_J e^{\frac{-g_J M_J \mu_B H}{kT}}}{e^{\frac{-g_J M_J \mu_B H}{kT}}} \tag{5.6}$$

It becomes

$$M = Ng_J\mu_B J\left\{\frac{2J+1}{2J}\coth\left(\frac{2J+1}{2J}\right)y - \frac{1}{2J}\coth\left(\frac{y}{2J}\right)\right\} \tag{5.7}$$

where $y = g_J\mu_B J H/kT$ Eq. (5.7). If $y \ll 1$, then $e^{-x} \approx (1 - x)$ and therefore

$$M = -Ng_J\mu_B \frac{\sum_{-J}^{J} M_J\,(1 - g_J\mu_B\,H/kT)}{\sum_{-J}^{J}(1 - g_J\mu_B\,H/kT)} = \frac{Ng_J^2\mu_B^2 H}{(2J+1)kT}\sum_{-J}^{J} M_J^2 \tag{5.8}$$

The summation equals to $\frac{1}{3}$ J(J + 1)(2J + 1), and on substitution the final form of the equation becomes

$$\chi = \frac{M}{H} = \frac{Ng_J^2\,\mu_B^2\,J(J+1)}{3kT} = \frac{C}{T} \tag{5.9}$$

which is commonly named the Curie law. Generally, molar magnetization is expressed as $cm^3\ mol^{-1}$ or emu mol^{-1}. Very often it is used the *effective magnetic moment* μ_{eff}:

$$\mu_{eff}^2 = \frac{3kT\,\chi}{N\mu_B^2} = g_J^2\,J(J+1) \tag{5.10}$$

where $N\mu_B^2/3k = 0.12505 \approx 1/8$. Nowadays, it is more common to refer to χT. A plot of χT versus T of a sample following the Curie law gives a line parallel to the T axis.

The Curie law is valid when the levels' splitting in a magnetic field is small with respect to kT (at 300 K, $kT \sim 200\,cm^{-1}$) and only one J state is populated.

Table 5.1 Basic magnetic information for Ln^{3+} ions.

Ion	$4f^n$	$^{2S+1}L_J$	g_J	ζ (cm^{-1})	$\chi_M T$	μ_{eff}	M (μ_B)
Ce^{3+}	1	$^2F_{5/2}$	6/7	644	0.80	2.54	2.14
Pr^{3+}	2	$^3H_4$	4/5	730	1.60	3.58	3.20
Nd^{3+}	3	$^4I_{9/2}$	8/11	844	1.64	3.13	3.27
Pm^{3+}	4	$^5I_4$	3/5	1070	0.90	2.68	2.4
Sm^{3+}	5	$^6H_{5/2}$	2/7	1200	0.09	0.85	0.71
Eu^{3+}	6	$^7F_0$	5	1320	0.00	—	—
Gd^{3+}	7	$^8S_{7/2}$	2	1583	7.88	7.94	7
Tb^{3+}	8	$^7F_6$	3/2	1705	11.82	9.72	9
Dy^{3+}	9	$^6H_{15/2}$	4/3	1900	14.17	10.65	10
Ho^{3+}	10	$^5I_8$	5/4	2163	14.07	10.61	10
Er^{3+}	11	$^4I_{15/2}$	6/5	2393	11.48	9.58	9
Tm^{3+}	12	$^3H_6$	7/6	2656	7.15	7.56	7
Yb^{3+}	13	$^2F_{7/2}$	8/7	2883	2.57	4.54	4

The reported data in Table 5.1 are the valence electron configuration (column 2), the nature of the ground multiplet (column 3), the calculated g_J (column 4), the SOC (spin–orbit coupling) constant of the free ion (column 5), χT of the free ion in the high-temperature limit (column 6), μ_{eff} of the free ion (column 7), and the saturation magnetization (column 8).

The equations are well suited for interpreting the magnetic properties of lanthanide complexes at high T and low field with few exceptions. The Curie law demands that a plot of χ^{-1} versus T is linear and goes to zero at $T = 0$. The slope of the curve provides C, which can be compared with the values calculated with Eq. (5.9) and shown in Table 5.1. Generally, however, there are deviations from the linear behavior at low temperature, and the extension of the high-temperature regime does not extrapolate to zero. The origin of this behavior is the breakdown of some basic assumptions used for obtaining Eq. (5.10). One is the equipartition of the population of the levels of the ground multiplet, that is, the breakdown of the high-temperature approximation. A simple way to cope with this is to introduce a correction in the Curie law:

$$\chi = C/(T - \theta) \tag{5.11}$$

This expression is the Curie–Weiss law, where θ is an adjustable parameter. Sometimes θ is called the *paramagnetic Weiss temperature*. In Chapter 7, we will see that analogous deviations from Curie law occur as a result of interactions between the magnetic centers. It is good to take note that, in order to obtain C and θ, it is more appropriate to fit χT rather than χ because the former gives similar numbers over a range of temperatures, while the latter gives different values. For $C = 0.375$, χT is 0.375 for every T value, while χ is 0.375/300 at room temperature and 0.375/4 at liquid helium temperature. In a fitting procedure, the bigger numbers have larger weights.

Equation (5.8) allows us to calculate the magnetization as a function of J (or S) and the external magnetic field for a system containing N atoms. Experimental results for the magnetization of Cr^{3+} (S = 3/2), Fe^{3+} (S = 5/2), and Gd^{3+} (J = 7/2) have been reported with the curves evaluated with Eq. (5.8) (Henry, 1952). The three metal ions were chosen because their ground state is relatively simple, as they have quenched orbital moment. The wave functions for the TM ions will be of the type |S, M>. For Gd, the seven f orbitals are singly occupied and the M_L orbital quantum number is given by $M_L = \sum m_l$ where m_l is ±3, ±2, ±1, 0, and $M_L = 0$. The spin quantum number of the ground state corresponds to spin +1/2 in all the orbitals, yielding S = 7/2. The situation is similar for Fe^{3+}, where the five d orbitals are singly occupied, yielding a ground L = 0 S = 5/2 state. For Cr^{3+}, the three degenerate orbitals are d_{xz}, d_{xy}, and d_{yz} appropriate for octahedral symmetry, yielding L = 0, S = 3/2. The agreement between experimental and expected values is excellent.

The magnetization on increasing the external magnetic field goes toward a saturation limit which corresponds to the orientation of all the spins parallel to the magnetic field.

$$M_{\text{sat}} = gS = g_j J \tag{5.12}$$

in μ_B units which correspond to 5585 emu mol^{-1}. So the saturation value in μ_B units for Cr^{3+} is 3, for Fe^{3+} 5, and for Gd^{3+} 7.

5.2 The Van Vleck Equation

The difficulty in using Eq. (5.5) to calculate the susceptibility is the need to know the energies E_n and their derivatives as a function of the field. As early as 1932, Van Vleck, an American physicist who in 1977 was awarded the Nobel Prize, suggested the expansion of the energies as a function of the field H (Van Vleck, 1932):

$$E_n = E_n^{(0)} + E_n^{(1)}H + E_n^{(2)}H^2 \ \ldots \tag{5.13}$$

where n identifies the energy level. In the assumption of low H and T not too small, the Van Vleck equation for the magnetic susceptibility becomes

$$\chi = \frac{M}{H} = \frac{N\sum_n \left(\frac{E_n^{(1)2}}{kT} - 2E_n^{(2)}\right) e^{\frac{-E_n^{(0)}}{kT}}}{\sum_n e^{\frac{-E_n^{(0)}}{kT}}} \tag{5.14}$$

When all the energies E_n are linear in H, the second-order Zeeman coefficients $E_n^{(2)}$ vanish, and the equation can be simplified and becomes

$$\chi = \frac{N\sum_n \frac{E_n^{(1)2}}{kT} e^{\frac{-E_n^{(0)}}{kT}}}{\sum_n e^{\frac{-E_n^{(0)}}{kT}}} \tag{5.15}$$

Let us get some practice by calculating the susceptibility of a Dy ion. In zero field, the ground multiplet for the $4f^9$ ground configuration is $^6H_{15/2}$. The populations of the other J multiplets can be neglected. Let us apply a weak field parallel to *z*. The $E_n^{(1)}$ energies required by Eq. (5.14) are

$$E_n^{(1)} = \mu_B \, g_J M_J \tag{5.16}$$

where g_J is given in Table 5.1 and $-J \leq M_J \leq J$.

Assuming the energy of the lowest doublet as the zero in the energies' scale ($E_n^0 = 0$), it is possible to derive from eq. (5.15) and neglecting the second order terms:

$$\chi = \frac{N g_J^2 \mu_B^2}{kT} \sum_{-J}^{J} \frac{M_J^2}{(2J+1)} \tag{5.17}$$

where $(2J + 1)$ accounts for the doublet degeneracy. Then

$$\chi = \frac{N g_J^2 \mu_B^2}{3kT} J(J+1) \tag{5.18}$$

which is the Curie law. The calculation of the magnetic susceptibility of the lowest doublet is straightforward.

It is possible to use the Van Vleck equation to estimate the contribution to the magnetic susceptibility of the mixing through the Zeeman perturbation of the excited states in a ground state without first-order angular momentum as long as the energy gaps between neighboring levels are not too large. This contribution is named *temperature-independent paramagnetism* (TIP) as its origin is not due to a thermal population of excited states. It is usually small – often the same order of magnitude as the diamagnetic susceptibility – but opposite in sign. For instance, octahedral Co^{3+} compounds have a $3d^6$ configuration. In octahedral symmetry, the d orbitals split into three states which are labeled as t_{2g} and two states which are labeled e_g. The labels are defined according to group theory. Since the ligand field (LF) is strong, the six electrons occupy the t_{2g} orbitals, yielding an orbitally non degenerate ground state which is indicated as $^1A_{1g}$ in the group theory language, and TIP is estimated around 200×10^{-6} emu mol^{-1}. Another example is the Eu^{3+} ion where the Zeeman perturbation mixes the ground $^7F_0$ state with the excited $^7F_1$ state, giving a nonzero susceptibility value as the low-temperature limit and the correct estimation of the room temperature value (Van Vleck, 1932). It is worth mentioning that a TIP contribution could be present even when the ground state is magnetic. The mechanism of mixing with non-thermally-populated states gives rise to a small contribution to the magnetic susceptibility, and for a correct analysis of the magnetic susceptibility this contribution must be evaluated together with any diamagnetic susceptibility.

Let us work out as an example the magnetic susceptibility of the *aquo* ion of Ce^{3+} using explicitly also the LF parameters. Table 5.1 tells us that the ground state is $^2F_{5/2}$ and that excited states can be neglected in first approximation. For the free ion in zero field, the $2J+1$ are degenerate and we can set $E_n^{(0)} = 0$. $E_n^{(1)}$ can be obtained from the Zeeman Hamiltonian with the field parallel to *z*. The addition

Table 5.2 Energies and eigenfunctions for Yb^{3+}.

Energies (cm^{-1})	Wavefunctions
0.0	$\|\pm 3/2\rangle$
44.1	$0.9496\|\pm 5/2\rangle - 0.3133\|\mp 7/2\rangle$
109.2	$\|\pm 1/2\rangle$
268.1	$0.9496\|\pm 7/2\rangle + 0.3133\|\mp 5/2\rangle$

of the CF makes the $E_n^{(0)}$ different from each other. The magnetic susceptibilty was calculated using the matrix described in Table 3.5 and the best fit parameters for the ethylsulfate were: $A_2^0 < r^2 >= -15\,cm^{-1}$, $A_4^0 < r^4 >= -40\,cm^{-1}$, $A_6^0 < r^6 >= -92\,cm^{-1}$, $A_6^6 < r^6 >= 1150\,cm^{-1}$ (Elliott and Stevens, 1952).

A similar treatment can be used for Yb^{3+}. The 8×8 zero-field matrix corresponding to the ground $^2F_{7/2}$ is transformed into two 2×2 blocks corresponding to two Kramers doublets ($\pm 1/2$ and $\pm 3/2$) and a 4×4 block ($\pm 5/2$ and $\pm 7/2$). Trivial diagonalization yields the energies and eigenfunctions, as shown in Table 5.2.

The g values reported below are the effective values calculated assuming that the splitting of the various doublets can be treated as $S' = 1/2$. This is the so-called spin Hamiltonian (SH) approach, which is widely used in magnetism and magnetic resonance. We will make ample use of this approach, so it is important that the reader familiarizes with it and that he or she has a full understanding of the assumptions that are introduced by the SH approach.

Let us suppose we have a $J = 3/2$ ground multiplet which is split in two Kramers doublets: the lowest doublet corresponds to $M_J = \pm 3/2$, which splits in a field H parallel to the z-axis as $E(\pm 3/2) = \pm 3/2 g_J \mu_B H$. We may neglect the excited doublet $M_J = \pm 1/2$ for the time being by assuming that the energy separation $M_J = \pm 3/2$ to $\pm 1/2$ is large compared to kT. In the SH formalism, the corresponding splitting is expressed as $E'(\pm 1/2) = \pm 1/2 g_{eff} \mu_B H$. Equalizing $E(\pm 3/2)$ and $E'(\pm 1/2)$ yields $g_{\|}^{\perp} = 3g_J$. Matters are different for a field perpendicular to z. In fact, a perpendicular field has nonzero matrix elements, with states differing in M_J by ± 1. The Hamiltonian for that can be written as $\mathcal{H} = g_J \mu_B H \mathcal{J}_x$, where $\mathcal{J}_x = 1/2(\mathcal{J}_+ + \mathcal{J}_-)$, with $\mathcal{J}_+$ and $\mathcal{J}_-$ being shift operators. Since the lowest Kramers doublet corresponds to $M_J = \pm 3/2$, the shift operators have no matrix element between them. In the SH formalism, this corresponds to $g_{\perp eff} = 0$. Therefore the ground state is strongly anisotropic. In this case, the magnetization is higher parallel to the z-axis, which is called the *easy axis*. This type of anisotropy is called also the Ising type. It must be stressed that $g_{||}$ and $g_{\perp}$ as calculated above assume that the perpendicular field is small. A more correct way requires taking into account the admixture of the $M_J = \pm 1/2$ excited levels into the $M_J = \pm 3/2$ ground one. The correct way is to diagonalize the 4×4 energy matrix of the $J = 3/2$ basis. The results are shown in Figure 5.1. In particular, the condition $g_{\perp} = 0$ is relaxed by the application of an external field.

Considering a zero-field separation of $0.3\,cm^{-1}$, the $g_{\perp eff}$ values are as shown below:

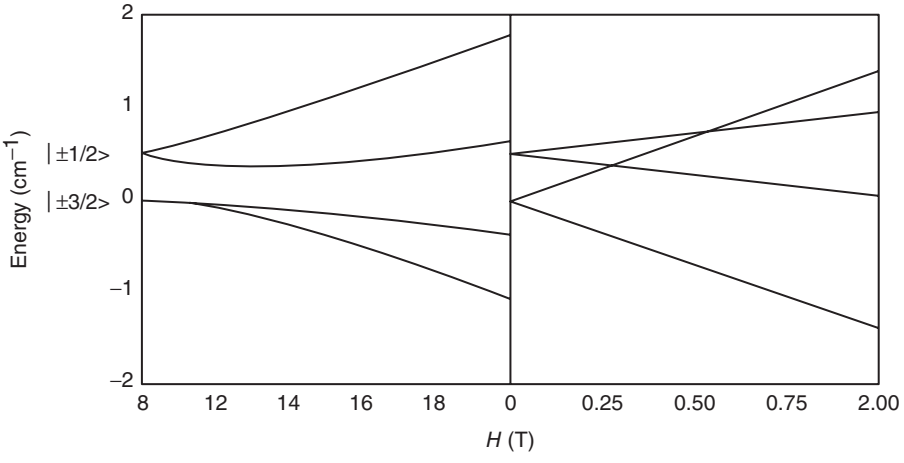

Figure 5.1 Field dependence of the energies of the M_J Kramers' doublets of a $J = 3/2$ multiplet: on the left the external field is along *x* while on the right is along *z*.

H (T)	0.1	0.2	0.3	0.4	0.5
$g_{\perp \text{eff}}$	0.03	0.18	0.31	0.50	0.69

An analogous treatment can be done for $M_J = \pm 1/2$ lying lowest. It is a simple exercise to check that $g_{\parallel} = g_J$ and $g_{\perp} = 2g_J$. This time, the favorite orientation is in the *xy* plane. The big difference in the energies along the *z* and *x* directions is due to the assumption that the two Kramers doublets are separated in zero field. The anisotropy of *g* is not needed to give anisotropic magnetic properties.

5.3 Anisotropy Steps in

The above described results show, generally, an angular dependence. It now the moment to have a better understanding of this behavior. The electron spin has a spherical symmetry, and therefore its properties are absolutely isotropic. If its behavior is observed inside an atom, the coupling of the spin with the orbital motion of the electron must be considered. The consequence of this distortion and the presence of SOC is a splitting of the energy levels, which, as a consequence, generates anisotropic behavior of the metal ions. That is, a magnetic field applied along a direction in the molecular frame has a different effect with respect to a magnetic field of the same intensity applied in plane orthogonal to the first one. It is useful to remember that we are dealing with magnetic molecular anisotropy which, in general, does not correspond to the crystal anisotropy. The magnetization values measured on a single crystal are related to the molecular ones by symmetry relationships, which are described in some detail in Chapter 16.

The major contributions to the magnetic anisotropy of a system are two: the zero-field splitting ZFS is the degeneracy removal for spin microstate in systems

with $S > 1/2$ with no applied magnetic field. The degeneracy is removed as a consequence of molecular electronic structure and/or spin density distribution and the Zeeman effect.

Let us consider first those metal ions whose electronic structure is well described by an orbitally nondegenerate wavefunction. In the previous paragraph, we considered Cr^{3+}, Fe^{3+}, and Gd^{3+}, which share the feature of a ground state with a quenched orbital moment. When a situation like this holds, it is possible to use the SH approach as defined in the previous section. This is the basis for developing the ZFS formalism.

ZFS is indicative of the fact that a given S multiplet, which under spherical symmetry is degenerate in zero external magnetic field, has its degeneracy removed under a lower symmetry. ZFS can originate either by the direct interaction of the magnetic dipoles of the unpaired electrons or from another contribution directly originated by SOC. For inorganic ions, the second mechanism is the dominant one, while the first is active in organic radicals giving rise to the small anisotropy. To deal with the ZFS, it is useful to use an SH of the form

$$\mathscr{H} = \mathcal{S} \cdot \boldsymbol{D} \cdot \mathcal{S} \tag{5.19}$$

where $\boldsymbol{D}$ is a traceless tensor. If it is possible to describe the asymmetry of the metal ion environment with a series expansion in magnetic multipoles, the first term is a quadrupolar one and, for system with $S \geq 1$, it depends on the second power of the spin operators. The relative SH can be written in the form

$$\mathscr{H} = D[\mathcal{S}_z^2 - S(S+1)/3] + E(\mathcal{S}_x^2 - \mathcal{S}_y^2) \tag{5.20}$$

The D parameter is different from zero for any symmetry lower than cubic, while E is different from zero only in the case of symmetry lower than axial. The energy of the split components of the S multiplet has a particularly simple formula for axial symmetry:

$$E(M) = D[M_s - S(S+1)/3] \tag{5.21}$$

where $S \leq M_s \leq S$. D has a sign; a positive value puts the states with smallest M (0 or 1/2) the lowest, and a negative D gives an $M = S$ ground state. This means that at low T the spin will be preferably oriented parallel to z, the unique axis for negative D, and positive D orients the spin perpendicular to z, yielding an easy plane system.

It is possible to estimate the sign and the intensity of the ZFS by using a simple formula where the principal g-values are used (see below):

$$D = \frac{\lambda}{2}\left[g_z - \frac{g_x + g_y}{2}\right] \quad E = \frac{\lambda}{4}(g_x - g_y) \tag{5.22}$$

where λ is the SOC constant within a given S multiplet defined in Eq. (2.2).

The second term in the series expansion is the hexadecapolar one, and it depends on the fourth power of the spin operators. It is operative for system with $S \geq 2$ and the relative Hamiltonian can be expressed through the Stevens operator equivalents

$$\mathscr{H} = \sum_k B_4^k \mathcal{O}_4^k \tag{5.23}$$

where B_4^k is an experimental parameter, $\mathcal{O}_4^k$ is a linear combination of spin operators at the fourth power, and k varies from 0 to 4. For tetragonal symmetry, only the terms with $k = 0$ and 4 are present; for trigonal symmetry terms with $k = 0$ and 3 are necessary, and for orthorhombic symmetry the required terms are $k = 0, 2,$ and 4. To have a full description of the system, the operators with negative k values should be included. In the practice, these operators are very often not included explicitly in calculations.

The second-order terms can also be expressed using the Stevens operators. The relation with D and E are

$$D = 3B_0^2 \quad E = B_2^2 \tag{5.24}$$

The Zeeman effect is generally defined with an SH

$$\mathscr{H} = \mu_B \boldsymbol{B} \cdot \boldsymbol{g} \cdot \mathcal{S} \tag{5.25}$$

where $\boldsymbol{g}$ is a tensor. Actually, the form of Eq. (5.25) is not correct because g connects an axial and a polar vector, and therefore is not a tensor. The problem has been simplified essentially by ignoring it, but recently the old problem has been revisited. We recommend the interested reader to the original literature (Chibotaru, Ceulemans, and Bolvin, 2008).

If the paramagnetic center is in an environment with a symmetry lower than cubic, g shows anisotropy. For electronic configurations such as d^9, low-spin d^7, and high-spin d^4, the ground state is an orbital doublet (E) in octahedral symmetry. This means that there are two orbitals at the same energy and the electron can pass freely from one to the other. Therefore, the orbital moment is different from zero and the orbital component is not completely quenched. But the coupling between the electron and the vibrations is generally operative and gives rise to large geometrical distortions which quench the orbital momentum. This is resumed in the Jahn–Teller theorem, which states that an electron system is unstable to any distortion lowering the symmetry. The ions that have a doubly degenerate E ground state are always found in a tetragonally elongated octahedral symmetry due to the Jahn–Teller effect. If the ground term is a triply degenerate T one, as observed in Fe^{2+} and Co^{2+}, the SOC is able to remove the degeneracy leaving, in any case, a large unquenched orbital momentum. A good example of this situation is the behavior of the high-spin Co^{2+} ion (d^7) in an octahedral environment. The electronic structure of the free ion consists of two energy levels one with seven states (^{4}F) and the other with three (^{4}P), with former state at the lower energy. On applying an octahedral field, the energy levels are reorganized as sketched in Figure 5.2. The ground state is ^{4}T, which means that there are three orbitals and four spin states. The presence of an SOC splits, to some extent, the multiplet, leaving Kramers doublets. If it is assumed that at low temperature only the lowest one is populated, the assumption of an effective $S = 1/2$ spin and an isotropic value g of 4.33 can be applied because of the unquenched orbital contribution.

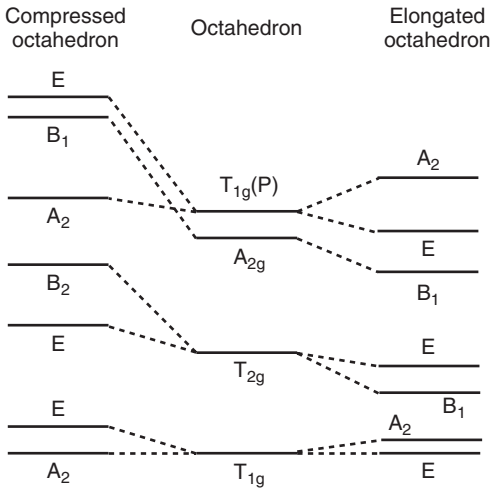

Figure 5.2 Effect on the ground multiplet of a Co^{2+} ion of various symmetries of the coordination sphere.

On lowering the symmetry, for instance by introducing a tetragonal distortion, the *g*-value varies with a dependence on the splitting of d orbitals with a specific relationship with t_{2g} orbitals. When the distortion splits the energy of the *xy*, *yz*, *xz* orbitals in such a way that the *xy* one is higher in energy, $g_{||}$ becomes smaller than 4.33 while $g_{\perp}$ value slightly increases. The limits for the two values in presence of strong distortions are $g_{||} = 2$ and $g_{\perp} = 4$. With an inverse distribution of the t_{1g} orbitals (i.e., $E_{yz,xz} > E_{xy}$), the strong distortion limits are $g_{||} = 8 - 9$ and $g_{\perp} = 0$ (see Figure 5.3).

As a consequence of this difference in the *g*-values, the system containing high-spin cobalt(II) ions exhibits a substantially different magnetic behaviors. In the

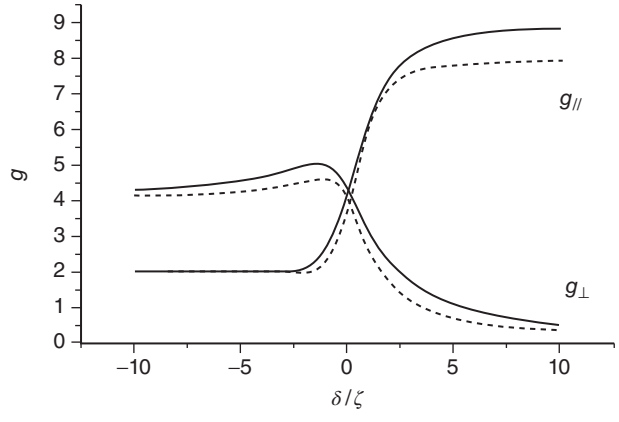

Figure 5.3 Range of *g*-values to be expected for distorted octahedral cobalt(II) complexes. Full line E/D = 0; dotted line E/D = 1/3.

first described case, their magnetism can be analyzed on the basis of an easy plane system as a magnetic field tends to orient the spin in the *xy* plane due to the higher *g*-value. In the presence of the second distortion, the system behaves like an Ising one, as the magnetic field preferentially orients the spin parallel to the *z*-axis.

When the system contains a lanthanide ion, the L, S, and J are good quantum numbers and the energy levels are discrete $^{2S+1}L_J$ multiplets. The presence of a CF is useful to fully or partly remove the degeneracy according to the symmetry of the coordination sphere around the ion. With the exception of Sm^{3+} and Eu^{3+}, multiplets are well separated in energy, and this feature allows us to treat at room temperature the ground level without considering, at least in first approximation, the other levels. The magnetic properties of lanthanide ions are mainly determined by the splitting of the ground multiplet by the action of CF, as described in Chapter 3.2. When an external magnetic field is applied to the compound, Zeeman effect becomes operative and the relative term must be added to the Hamiltonian:

$$\mathscr{H}_{\text{Zeeman}} = \mu_B(g_e 2\mathcal{S} + \mathcal{L}) \cdot \boldsymbol{B} \tag{5.26}$$

If the $^{2S+1}L_J$ multiplet is a pure J state, applying the Wigner–Eckart theorem, the Hamiltonian can be written as

$$\mathscr{H}_{\text{Zeeman}} = -\mu_B \mathcal{J} \cdot \boldsymbol{B} \tag{5.27}$$

For ions with an odd number of electrons, the ground state according to Kramers' theorem is a doublet and, if it is possible to work only on this doublet, it is, even in this case, to be consider an effective spin operator $S = 1/2$ and the Hamiltonian acquires the above-reported form.

Let us conclude this paragraph using again Dy^{3+} as an example. It has nine electrons in the f orbitals, and the Coulomb interactions among all these electrons give rise to sextuplets, quartets, and doublets distributed over a wide range of energies. The two lower terms are ^6H and ^6F terms which are separated by $\approx$7000 cm^{-1} in energy with the former being the ground term. The presence of SOC induces the splitting of these terms into multiplets. The ground ^6H generates six multiplets, the ^6F term six multiplets, and so on, according to the *L* and *S* values. As shown in Figure 5.4 in a qualitative manner, the distribution of the multiple energy levels may be extremely complex but, luckily, if the interest is focused on the magnetic properties, it is often enough to analyze the behavior of the $^6H_{15/2}$ ground state and, rarely, it is necessary to include even the one $^6H_{13/2}$ which is about 3000 cm^{-1} higher in energy.

In presence of a CF, the ground multiplet is split into eight doublets whose energies are strictly connected to the symmetry of the environment around the Dy^{3+} ion. Under cubic symmetry, all the doublets are well separated in energy, and therefore the magnetic properties are strictly connected with the nature of the ground doublet considering that there is no mixing of doublets. In this case, it is useful to apply the procedure used above for a multiplet $S = 3/2$. The calculation of effective *g*-values can be done as shown below. The expressions for the three components are

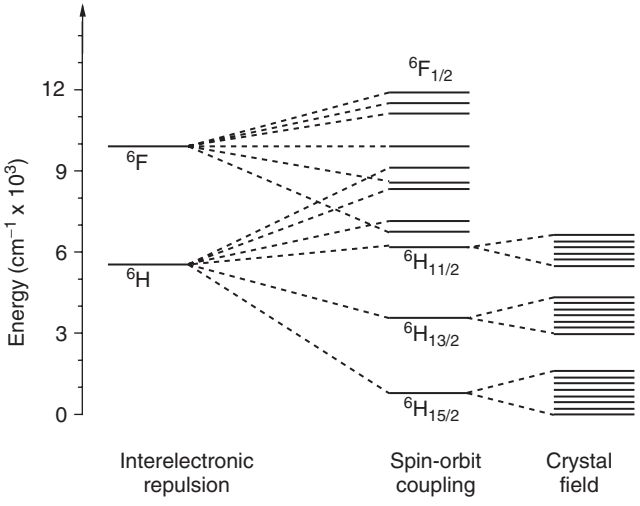

Figure 5.4 Energies of the lowest J multiplet states for a Dy^{3+} ion.

$$
\begin{aligned}
g_z &= 2g_J\langle M_J \mid \mathcal{J}_z \mid M_J\rangle \\
g_x &= 2g_J\langle M_J \mid \mathcal{J}_+ + \mathcal{J}_- \mid M_J\rangle \\
g_y &= 2g_J\langle M_J \mid \mathcal{J}_+ - \mathcal{J}_- \mid M_J\rangle
\end{aligned}
\tag{5.28}
$$

Considering that the Landé factor g_J for Dy^{3+} is 4/3, it is possible to evaluate, for instance, that in the case of the $|\pm 15/2>$ doublet as ground state $g_z = 20, g_x = g_y = 0$. This situation corresponds to an extremely high anisotropy of the Ising type. The ground doublet may change according to symmetry variations which change the nature of the $|\pm M_J>$ states and on the basis of the CF strength. Therefore, there is the possibility of ground states that are originated by the admixture of several doublets. An example of the first case has been observed in two series of compounds where the Dy^{3+} ion is eight-coordinated. In D_{4d} symmetry, the ground doublet may vary from $|\pm 11/2>$ ($g_z = 44/3, g_x = g_y = 0$) to $|\pm 9/2>$ ($g_z = 12, g_x = g_y = 0$) depending on the similarity of the environment to a cube or to a squared antiprism. With similar symmetry but different CF strength, the observed ground state may be either $|\pm 11/2>$ ($g_z = 44/3, g_x = g_y = 0$) or $|\pm 13/2>$ ($g_z = 52/3, g_x = g_y = 0$). In hexagonal symmetry environment, there is the possibility of a ground state which is a linear combination of different doublets which are mixed if they differ by 6 in M_J.

A useful instrument to predict, at least qualitatively, the anisotropy of rare earths derivatives in various coordination environments has been developed by Bleaney (1972). The magnetic anisotropy $\Delta\chi = \chi_z - (\chi_x + \chi_y)/2$ can be written as (Mironov *et al.*, 2002)

$$
\Delta\chi = -N\frac{\mu_B^2}{20(kT)^2}B_0^2(1+p)\xi \tag{5.29}
$$

Table 5.3 The parameters for magnetic anisotropy of Ln^{3+} in the Bleaney scheme.

	ξ	a	b	$kT/\Delta W$ at $T = 300$
Ce^{3+}	−11.8	−0.555	−0.0833	0.09
Pr^{3+}	−20.7	−0.497	−0.0353	0.095
Nd^{3+}	−8.08	−0.673	−0.0678	0.105
Sm^{3+}	0.943	−11.25	−3	0.20
Tb^{3+}	−157.5	−0.287	0.0139	0.10
Dy^{3+}	−181.0	−0.185	0.0081	0.07
Ho^{3+}	−71.2	−0.142	0.0062	0.05
Er^{3+}	58.8	−0.127	0.0061	0.03
Tm^{3+}	95.3	−0.133	0.0081	0.025
Yb^{3+}	39.2	−0.181	0.0188	0.02

where $p = a(kT/\Delta W) + b(kT/\Delta W)^2 \ldots$, and ΔW is the energy gap between the ground and the first excited multiplet of the lanthanide ion. ξ is defined as $g_J^2 <J\|\alpha\|J> J(J+1)(2J-1)(2J+3)$ where $<J\|\alpha\|J>$ is a numerical coefficient (Bleaney 1972).

The analysis of the expression for the magnetic anisotropy and of the values of the parameters reported in the Table 5.3 allows us to extract some common features valid for the whole series of 4f ions. First of all, a magnetic anisotropy is present if the rank-2 parameter B_0^2 is different from zero. Ranks 4 and 6 have no influence on the anisotropy whose relevance is proportional to B_0^2. According to the sign of the ξ-parameter, the magnetic anisotropy may have an opposite pattern on varying the metal ion. At least, the highest anisotropy is presented by dysprosium derivatives, followed by Tb^{3+} and Tm^{3+}.

The chapter has taken into account some of the features associated with magnetic anisotropy of the individuals ions. It is rather peculiar that these phenomena are collected with the tag anisotropy: using a negation (an- is the greek prefix for absence of) to define important properties, is not elegant. But it worked, and the origin of the negation is well understood: the orbital moment.

The main points that have been discussed are the basic treatment of magnetic ions which are based on the Brillouin function and the Curie law. These will be met very frequently as a standard of paramagnetic behavior. Of course, it will be informative to observe deviations from standard behavior because these will contain information on the structure and electronic structure. We will see many examples of these features. One of the fundamental issues that was described here is that of the anisotropy which will be stressed for all the investigated systems. Nomenclature such as Ising and XY are introduced here for the first time.

The treatment of the matter has been based on a simple scheme where the SH is the most useful one. It is introduced here, and it will be the leitmotiv throughout the coming chapters. The extensive use of operator equivalents should convince

the reader of the power of the method and induce him or her to practice the method.

References

Bain, G.A. and Berry, J.F. (2008) Diamagnetic corrections and Pascal's constants. *J. Chem. Educ.*, **85**, 532.

Bleaney, B. (1972) Nuclear magnetic resonance shifts in solution due to lanthanide ions. *J. Magn. Reson.*, **8**, 91–100.

Chibotaru, L.F., Ceulemans, A., and Bolvin, H. (2008) Unique definition of the Zeeman-splitting g tensor of a Kramers doublet. *Phys. Rev. Lett.*, **101**, 033003.

Elliott, R.J. and Stevens, K.W.H. (1952) The theory of the magnetic properties of rare earth salts: cerium ethyl sulphate. *Proc. R. Soc. London, Ser. A*, **215**, 437–453.

Henry, W.E. (1952) Spin paramagnetism of Cr^{3+}, Fe^{3+}, and Gd^{3+} at liquid helium temperatures and in strong magnetic fields. *Phys. Rev.*, **88**, 559–562.

Mironov, V.S., Galyametdinov, Y.G., Ceulemans, A., Görller-Walrand, C., and Binnemans, K. (2002) Room-temperature magnetic anisotropy of lanthanide complexes: a model study for various coordination polyhedra. *J. Chem. Phys.*, **116**, 4673–4685.

Neogy, D. and Purohit, T. (1987) Magnetic behavior and crystal field of $Dy(BrO_3)_3.9H_2O$. *Phys. Rev. B*, **35**, 5849–5855.

Pascal, P. (1913) Recherche Magnetochimiques (troisieme memoire). *Ann. Chim. Phys.*, **28**, 218–243.

Van Vleck, J.H. (1932) Theory of the variations in paramagnetic anisotropy among different salts of the iron group. *Phys. Rev.*, **41**, 208–215.

6
Molecular Orbital of Isolated Magnetic Centers

6.1
Moving to MO

So far the approach we chose to describe the electronic states of ions has been based on the spin Hamiltonian (SH) associated with the ligand field (LF) model, which allowed us to establish useful structural magnetic correlations, that is, the dependence of the magnetic properties on structural parameters, such as bond distances and bond angles. The exploitation of the role of symmetry in simplifying the description of the states cannot be overestimated. Anyway, this approach is a parametric one, and the need for having some fundamental treatment was felt by everybody working in the field. The difficulties associated with the use of quantum mechanical treatments on molecular magnets are that they have many electrons and open-shell configurations. Moreover, the magnetic properties, associated with the presence of unpaired electrons, are usually small and very sensitive to the level of the approximations included in the Hamiltonian and in the calculations themselves. Therefore, the mandatory use of extended basis sets, which till a few years ago were impossible to implement on existing computers, has nowadays become possible also for large systems. The improvements in computer performance and in the theoretical approach have substantially changed the scenario, making routine what was impossible a few years ago.

Quantitative calculations of the magnetic interactions require an accurate description of the multiplet structure of the molecules for the ground and the lowest excited states. This task can be accomplished by using extensive configuration interaction (CI) or by density functional theory (DFT) through broken symmetry approaches to correlate the magnetic electrons. The latter is less demanding in terms of computational requirements because the ground state properties of a many-electron system can be uniquely determined by an electron density that depends on only three spatial coordinates, thereby reducing the many-body problem of N electrons with $3N$ spatial coordinates to one with three spatial coordinates through the use of functionals of the electron density.

In this framework, we will treat essentially the properties of the ground state and of the low-lying levels, which in general are sufficient to compare the calculated magnetic properties with those obtained through the SH approach.

Introduction to Molecular Magnetism: From Transition Metals to Lanthanides, First Edition.
Cristiano Benelli and Dante Gatteschi.
© 2015 Wiley-VCH Verlag GmbH & Co. KGaA. Published 2015 by Wiley-VCH Verlag GmbH & Co. KGaA.

Although there is no true need to treat in separate ways systems that are formed by one type of building block and interact only weakly with each other and systems where at least two centers interact significantly, we will follow the scheme of starting from one center and introduce the interaction later. Therefore, we will start from systems that have a given number of unpaired electrons, which can be considered as based on one metal center. The unpaired electrons interact between themselves but not with electrons of different molecules, and we will show in the following how these systems can be treated.

6.2 Correlation Effects

We recall that one of the approaches to calculate the electronic structure of molecules uses the self-consistent field (SCF) in the Hartree–Fock (HF) approximation, where the ground state eigenfunction is described by a single Slater determinant (SD). The interactions between electrons are limited to those associated with their fermion nature, which keeps the electrons in different orbitals apart and attracts them in the same orbital. The difference between the HF energy and the lowest energy calculated with other methods is called the *electron correlation energy*. The correlation between opposite spins is called *Coulomb correlation*, and that between same spin is called *Fermi correlation*. Further types of correlation are the time static correlation when non sigle determinant approximation is possible for the ground state, between electrons in spatially different MOs (molecular orbitals) and the dynamic correlation when an interaction with excited states is needed, between electrons in the same orbital. Static correlation is the most difficult to calculate, especially for systems that are quasi-degenerate, such as metal ions. There are three ways of calculating the electron correlation, namely configuration interaction (CI), many-body perturbation theory (MBPT), and coupled cluster (CC).

For open-shell systems, such as the ones we are interested in, an improvement over HF is the unrestricted Hartree–Fock, UHF, where two different sets of molecular orbitals are allowed to relax self-consistently for the α and β electrons. A full CI, that is, including all the possible excitations starting from the reference state, is, of course, the most accurate choice but it is extremely demanding, if not impossible, except for very simple models and small basis sets (Bencini and Totti, 2008). A possible way of coping with the problem is by choosing a smaller space, according to guesses associated with the problem one is investigating. A reasonable alternative is the complete active space self-consistent field (CASSCF), which we will introduce in some detail in the following. The number of SDs to be included in the calculation dramatically increases with the basis set and the number of atoms.

Recently, a dramatic improvement was achieved in the possibility of using *ab initio* techniques to calculate the splitting of the lowest multiplet. This is extremely relevant for Lns (lanthanides) for which the LF treatment is not as efficient as for

TMs (transition metals) and the possibility to guess the SH parameters is rather poor. Therefore, using *ab initio* approaches may, for the first time, allow us to have insight into the magnetic properties of Lns. The difficulties are very large because the heavy Lns require a heavy relativistic treatment. In the Dirac approach, there are four Hamiltonians that must be used, but in general they are reduced in complexity in order to tackle the demanding Lns. The problems are associated with spin–orbit coupling (SOC) which mixes states with different spins requiring the simultaneous treatment with electron correlation. This still is too demanding and the two correlations are introduced one after the other. Several analyses are based on a "two-step" procedure where the initial quantum calculations are oriented toward determining the electron correlation and relativistic scalar effects while any spin–orbit contribution is explicitly neglected. With the second step, SOC is introduced by calculating the interactions among the different "spin-free" states. This strategy is based on the assumption that electron correlation and SOC can be decoupled: this starting point is valid if the radial shape of the orbitals is not substantially modified by SOC. This approximation is realistic both for TMs and Lns but not for the elements of the main group. A second condition for the validity of the approach is related to the contribution to SOC, which could be mainly generated by interactions among states close in energy. This assumption must be verified in each case with a good accuracy.

Among the "two-step" methods widely applied in this field, one of the most popular is the already mentioned CASSCF method. The first step is based on calculations that treat the static electronic correlation effects, followed by the introduction of dynamic electron correlation effects by means of the evaluation of the single and double excitation contributions in a second-order perturbative manner. If a full CI method is used, it is necessary to consider all the possible electronic configurations obtained by distributing electrons on the quantum system on the different molecular orbitals. The basic idea of this method is the reduction of the number of electronic configurations achieved by classifying the molecular orbitals into three categories: doubly occupied orbitals that are considered as inactive; unoccupied orbitals or inactive; and those orbitals that can be unoccupied, partially occupied, or fully occupied, namely the active orbitals. The different electronic configurations are derived by distributing the active electrons in the "active" molecular orbitals.

The CASSCF/CASPT2 states can be used to compute the SOC component of the Hamiltonian. To consider all those states that can have a relevant contribution on the energy of the lowest spin states, it would be necessary to take into account all the "spin-free" states in the Hamiltonian matrix of the SOC. In order to avoid CASSCF convergence problems on each single state, and mainly on the excited states, one single set of molecular orbitals is used to compute all the states of a given spatial and spin symmetry, the so-called state-averaged CASSCF calculation. This procedure is based on the possibility of computing several states in one step by optimizing the same molecular electronic wavefunctions for all the states instead of using specific optimized wavefunctions for each state. An additional advantage of this approach is a balanced description of all the computed

states and their energy differences. On the other side, an increase in the number of states included in the average calculation leads to lowering of the precision in the definition of the energies of the states.

The 4f orbitals present a peculiarity related to their localized nature close to the nucleus. As they are not involved in covalent bonds, to a first approximation the CASSCF calculations do not require the inclusion of the molecular orbitals of ligand molecules, and, as a consequence, the active space can be limited to 4f orbitals.

The radial shape of the orbitals is largely influenced by scalar relativistic terms, and therefore they are included in this first step through the optimization of the choice of the basis set. A commonly used quantum chemistry package for this kind of calculations is MOLCAS, where the relativistic ANO-RCC basis set is included. This set has been generated using the scalar relativistic terms of the Douglas–Krell–Hess (DKH) Hamiltonian (Pantazis *et al.*, 2008).

With the aim of reducing the calculation time of spin–orbit operators, a good approximation is introduced by treating the two electron terms as a screening correction of the dominating one-electron terms. A commonly used procedure is based on the application of the atomic mean field integrals (AMFIs), as this method eliminates the necessity of calculating multicenter electron integrals due the short-range nature of the spin–orbit interactions. A relevant point of this procedure is the negligible loss of accuracy of the treatment.

The final step of the process is the evaluation of some physical properties, such as magnetic susceptibility or the **g** tensor. In the case of Ln^{3+} ions, a SMM (single molecular magnet) behavior is observed only in the presence of a doublet as ground state with a large difference in energy with respect to the excited states. To compute the **g** tensor of the ground state, it is necessary to introduce the Zeeman effect by means of a perturbative approach. The diagonalization of the tensor gives the *g*-values and their orientation in the molecular frame. This procedure is limited by the size of the problem: as the computation time is proportional to the cluster dimension, it is necessary to reduce the molecular size of the cluster without losing accuracy in the calculation. For example, it could be useful to substitute the peripheral molecular residue with simpler fragments such as H atoms, maintaining the charge and saturating bonds. For the same reason, it is possible to treat 4f ion only one at a time. In presence of a multinuclear cluster, only the f orbitals for one Ln^{3+} ion can be considered in the active space. The other Ln ions can be considered using two different approaches. In one method, the 4f ion is substituted by a relativistic *ab initio* model potential (AIMP) which simulates their effects. Alternatively, the other 4f ions can be simulated by using similar ions without unpaired electrons (doping strategy). For instance, Y^{3+} is often used as diamagnetic host to dilute magnetic molecules because, when compared to 4f ions, it has a similar ionic radius, a similar chemistry, and no unpaired electron, and it is present in several isostructural series with the Ln ions. More details will be provided in the chapter regarding magnetically coupled systems.

6.3 DFT

DFT has its origin in a paper by Slater where he suggested an alternative to the HF formalism, the so-called Xα method. Here we make only a short resume because exhaustive reviews are available elsewhere (Cohen, Mori-Sánchez, Yang, 2012). DFT showed that the ground state energy of the system of interest is completely determined by the diagonal elements of the first-order density matrix, the charge density. The definitive step forward was taken in 1964 by Hohenberg and Kohn who showed that the ground state energy and density correspond to the minimum of some functional $E[\rho]$ (Hohenberg and Kohn, 1964). We recall that a functional is a function of function. By working out the functionals, the so-called Kohn–Sham equations needed for computing the energies are obtained (Sham and Kohn, 1966). The energy of a system of N electrons depends on $4N$ coordinates, namely three spatial plus one spin, for a wavefunction approach, while it depends on three coordinates independent of the number of electrons in DFT. Although an expansion is not mandatory, it turns out to be an efficient procedure to calculate the electron energy of the system. What seemed to be a dream, namely reliable quantum mechanical calculation of complex systems, is becoming real. There are problems, however, associated with the complexity of the schemes of calculation, but we will try to unravel the difficulties and provide a key to read the papers and to understand at a sufficient level what is done.

The electron density is usually expressed as a basis set expansion which can yield the involved orbitals by a self-consistent procedure. The energy of the system is calculated using the Kohn–Sham effective operator (Bencini, 2008)

$$\mathscr{H}_i^{\mathrm{KS}} = -\frac{1}{2}\nabla_1^2 - \sum_{A=1}^{M}\frac{Z_A}{r_{1A}} + \int\frac{\rho(r_2)}{r_{12}}\mathrm{d}r_2 + V_{\mathrm{XC}}^{\sigma}(r_1)c \tag{6.1}$$

where the first term on the right is the electron kinetic energy, second is the electron nucleus interaction, third is the Coulomb repulsion between electrons, and fourth is the exchange correlation energy. The exchange correlation part of the total energy functional remains, however, unknown and must be approximated, and this is the main reason why the results obtained by DFT depend mainly, on the approximated form of the used functional. The choice of the basic functions is, hoever, important as in the Hartree-Fock approximation.

Notwithstanding the difficulties, the advantage gained by DFT in terms of cost and time has transformed the technique into a quasi-routine technique which is a must in the analysis of the properties of complex molecules. The first applications were addressed to the calculation of binding energies of electrons in X-ray and UV spectroscopies, and it was early discovered that the Koopmans theorem does not work with DFT. The theorem assumes that the ionization energy of a closed shell is the energy of the HOMO (highest occupied molecular orbital) (Koopmans, 1934). The Koopmans theorem is correct within the RHF (Restricted Hartree-Fock) scheme. Obviously, the theorem is not accurate because it assumes that the HOMO is not relaxed when the number of electrons changes; the theorem is

not correct also because it neglects electron correlation. As in many other cases, theory is less strict than assumed, and the internal compensation of error makes inaccurate models acceptable. Corrections to the method were implemented by Slater by introducing the formalism of the transition state.

Another difficulty that had to be solved is associated with the need to calculate low-lying energy levels or multiplets.

In this chapter, we will cover the developments in the use of accurate quantum mechanical techniques to describe the isolated magnetic centers from the perspective of the calculation of the SH parameters. Analogous but unavoidably more complex treatments on di- and polynuclear system will be deferred to the next chapter.

6.4 The Complexity of Simple

Let us try to understand better what is hidden beneath the quantum mechanical language we have used. We move to test what type of complexity is hidden in seemingly simple systems. We start from TMs because this area has been explored in more detail. A rather accurate early approach is that pursued by Neese and Solomon for the calculation of the **g** and **D** tensors of iron(III) (Neese and Solomon, 1998) in $FeCl_4^-$. They made a detailed resume of the results obtained with the LF formalism and then went on to work out the formalism for MO. It must be clearly stressed that, from the very beginning, both methods (MO and LF) relied on the same assumption that the ground state is orbitally nondegenerate. We will come back on this point later. We recall that tetrahedral iron(III) has a ground $^6A_1$ ground state in $FeCl_4^-$, with the first excited state at 17 000 cm^{-1}. Among the numerous tetra-halo ferrates, $[PPh_4][FeCl_4]$ was chosen for a detailed investigation of pure and diluted samples. The compound crystallizes in the $I\bar{4}$ space group, the metal ion lying on an S_4 site. The symmetry of the ion is not far from D_{2d}. Using this symmetry, the LF is axial and, therefore, SH can be described as

$$\mathcal{H} = \mathcal{H}_{\text{Zeeman}} + \mathcal{H}_{\text{ZFS}} = \mu_B \boldsymbol{B} \cdot \boldsymbol{g} \cdot \mathcal{S} + \mathcal{S} \cdot \boldsymbol{D} \cdot \mathcal{S} \tag{6.2}$$

In Eq. (6.2), only the bilinear terms in the spin–spin interaction have been included for the sake of simplicity. However, a fourth-order term, which is widely used for quasi-cubic systems such as $FeCl_4^-$, must be added to assign the experimental properties using the **g** and **D** tensors. In T_d symmetry, the zero-field levels have the energies shown below:

$$E = \frac{a}{6}\left[S_x^4 + S_y^4 + S_z^4 - \frac{S(S+1)(3S^2+3S-1)}{5}\right] + \frac{F}{180}\left[35S_x^4 - 30S(S+1)S_z^2 + 25S_x^2 + 6S(S+1)\right] \tag{6.3}$$

with $F = 180B_4^0$ and $a = 24B_4^4$. ESR (electron paramagnetic resonance) gives a deep insight into the low-lying energy levels. The single-crystal spectra recorded

with the magnetic field parallel to the crystal tetragonal axis show five transitions as expected for an S = 5/2 ground state in the presence of zero-field splitting (ZFS) (Deaton, Gebhard, and Solomon, 1989). However, the pattern of transitions shows that fourth-order terms are dominant at high temperature. The dramatic change observed on cooling the sample is attributed to the T dependence of the D_{2d} distortion. These data show that the admixture of excited states in the ground state must be operative (Figure 6.1).

It is now necessary to try to relate the fitted values with those calculated with LF and with MO. The ground $^6A_1$ state has no orbital moment, so **g** is essentially isotropic and D is small. However, there are excited states ^4T which can be admixed into the ground state via SOC, which introduce orbital moment and magnetic anisotropy.

The best fit values are shown in Table 6.1.

A delicate problem is the calculation of the matrix elements of SOC. Just to have an idea of the complexity, we show the expressions to be elaborated. If the complex

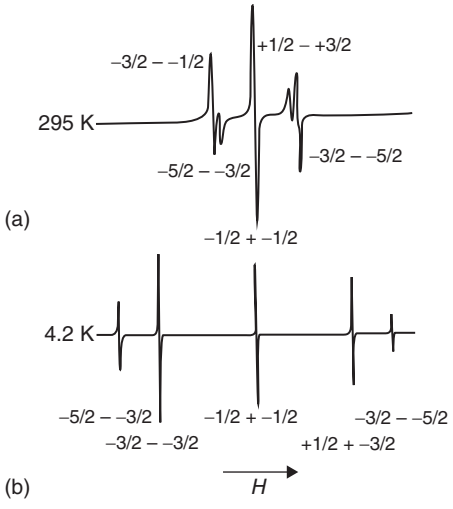

Figure 6.1 ESR spectra at 9.510 GHz of dilute $[PPh_4][FeCl_4]$ with H parallel to the S_4 crystal axis. (a) Room temperature, and (b) 4.2 K. (Reproduced from Deaton, J.C. *et al.* (1989) with permission from The American Chemical Society.)

Table 6.1 ZFS parameters for $FeCl_4^-$.

T (K)	D (cm^{-1})
295	−0.0109
185	−0.0253
120	−0.0316
4.2	−0.0419

formulas appear too difficult, shift to Eq. (6.7).

$$D_{pq}^{(0)} = -\frac{1}{S_a^2}\sum_b \delta_{S_a S_b}\Delta_b^{-1}\left\langle aS_aS_a\right| \sum_{A,i}\xi(r_{iA})l_{A,p}(i)s_0(i)\left|bS_bS_b\right\rangle x \left\langle bS_bS_b\right| \sum_{A,i}\xi(r_{iA})l_{A,q}(i)s_0(i)\left|aS_aS_a\right\rangle \tag{6.4}$$

This is the contribution for the ground state, and the following are the contributions for the first excited state.

$$D_{pq}^{(1)} = -\frac{1}{(S_a+1)(2S_a+1)}x\sum_b \delta_{S_bS_a+1}\Delta_b^{-1}\left\langle aS_aS_a\right| \sum_{i,A}\xi(r_{iA})l_{A,p}(i)s_{-1}(i)\left|bS_bS_b\right\rangle \times x\left\langle bS_bS_b\right| \sum_{i,A}\xi(r_{iA})l_{A,q}(i)s_{+1}(i)\left|aS_aS_a\right\rangle \tag{6.5}$$

where p and q refer to the Cartesian components of the **D** tensor. Repeating the process for excited states with $S_b = S_a = -1$ results in the following contribution to the **D** tensor:

$$D_{pq}^{(-1)} = -\frac{1}{S_a(2S_a+1)}\sum_b \delta_{S_bS_a-1}\Delta_b^{-1}\left\langle aS_aS_a\right| \sum_{i,A}\xi(r_{iA})l_{A,p}(i)s_{+1}(i)\left|bS_bS_b\right\rangle \times x\left\langle bS_bS_b\right| \sum_{i,A}\xi(r_{iA})l_{A,q}(i)s_{-1}(i)\left|aS_aS_a\right\rangle \tag{6.6}$$

After summing these terms, the second-order contributions to the ZFS from SOC are given by

$$D_{pq} = D_{pq}^{(0)} + D_{pq}^{(1)} + D_{pq}^{(-1)} \tag{6.7}$$

The calculations were performed using INDO (Intermediate Neglect of Differential Overlap) methods by varying the Cl–Fe–Cl angle from the tetrahedral angle 109.47°. The results for the **D** tensor are shown in Figure 6.2. They show that the best agreement for the value of D is achieved for axial compression, as experimentally observed.

6.5 DFT and Single Ions

One of the goals of molecular magnetism is following the growth of polynuclear structures and properties in a bottom-up manner. A well-established strategy to attempt the preparation of systems with, to some extent, planned characteristics is based on assembling mononuclear compounds selected with the aim of introducing in the final cluster some peculiar magnetic features. In this framework, it is relevant to understand the relationships between the properties of these mononuclear bricks and those offered by the final polynuclear system. In elaborating this strategy, DFT is very helpful in calculating the electronic and magnetic structure of the various systems and to write recipes for the most appropriate building blocks to arrange in a proper way. A true chemistry *in silico*! In a few cases such as the calculation of coupling constants, the *in silico*

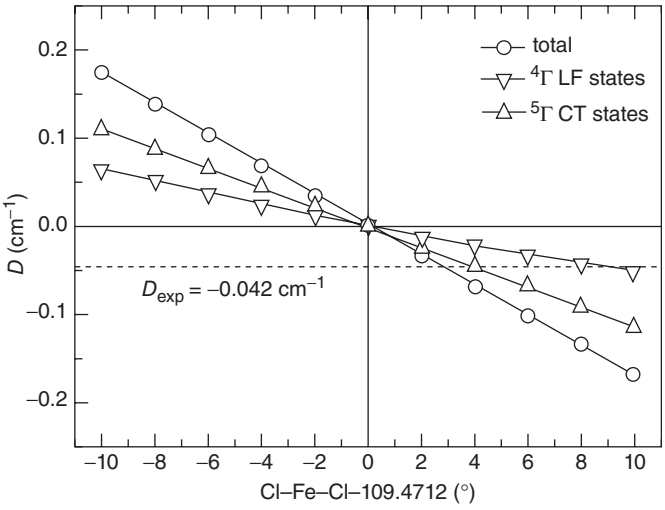

Figure 6.2 Calculated D value for $FeCl_4^-$ as a function of the $T_d \rightarrow D_{2d}$ distortion angle and charge-transfer and ligand-field contributions. (Reproduced from Neese, F. and Solomon, E.I. (1998) with permission from The American Chemical Society.)

approach can tell whether the developed models offer the possibility, at least in the isotropic system, to determine the nature of the magnetic coupling (Gatteschi and Sorace, 2001). An interesting property to investigate is the ZFS according to its relevance in influencing the magnetic anisotropy. For instance, it is commonly accepted (see Chapter 12) that the blocking temperature below which single molecule magnetic behavior is observed is associated with the presence of a negative D value. Indeed, the above results on $FeCl_4^-$ show an interesting correlation between the tetragonal distortion and the sign of D that is favored by a compression. An interesting feature is that, by comparing the parameters of the bricks, one can learn how to optimize the magnetic properties of the adducts. Experiments show that there is a large difference between the D value shown by a molecule such as $Mn_{12}O_{12}(CH_3COO)_{16}(H_2O)_4$ ($D = -0.46$ cm^{-1}) and a mononuclear Mn derivative such as Mn(acetylacetonate)$_3$ which shows a D value of -4.52 cm^{-1} (Krzystek *et al.*, 2003). In the search for computational approaches of ZFS for large molecules, it is helpful to start some calculation that can help in understanding the factors that lead to large D values in TM monomers or dimers. Moving from this idea, systematic approaches were made on a series of Mn and Fe compounds with different oxidation states in octahedral coordination (Cirera *et al.*, 2009), because it is the same observed around Mn^{3+} and Fe^{3+} in Mn_{12} (Barra *et al.*, 1999) and Fe_8 (Barra *et al.*, 1996) as shown by the structures of Figure 6.3.

The results are encouraging as shown in Table 6.2.

The analysis of the reported data shows that it is necessary to introduce the spin–spin contribution in the calculation to avoid underestimation in the D values. As expected from LF considerations, the ZFS in Mn^{3+} and Fe^{2+} are large, while for Fe^{3+} derivatives it is much smaller. Anyway, the differences

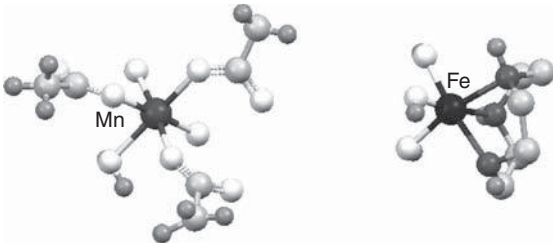

Figure 6.3 Octahedral environment on (a) Mn^{3+} and (b) Fe^{3+} in Mn_{12} and Fe_8 clusters.

Table 6.2 Calculated D values (cm^{-1}) for mononuclear Mn^{3+} and $Fe(^{3+}, ^{2+})$ complexes.

		$D_{calcd(SO)}$	$D_{calcd(SO+SS)}$	D_{exptl}	References
$Mn(dbm)_3$	Mn^{3+}	−2.43	−3.49	−4.57	Barra *et al.* (1997)
$Mn(acac)_3$	Mn^{3+}	−2.36	−3.28	−4.52	Krzystek *et al.* (2003)
MnF_3(terpy)	Mn^{3+}	−1.84	−2.65	−3.82	Mantel *et al.* (2003)
MnF_3(bpea)	Mn^{3+}	−1.84	−2.63	−3.67	Mantel *et al.* (2003)
$Mn(N_3)_3$(terpy)	Mn^{3+}	−1.65	−2.39	−3.29	Limburg *et al.* (2001)
MnCl(Py)(terpy)	Mn^{3+}	−1.28	−1.93	−3.00	Behere and Mitra (1980)
$Mn(bpea)(N_3)_3$	Mn^{3+}	+1.41	+2.07	+3.50	Mantel *et al.* (2003)
$Fe(dpm)_3$	Fe^{3+}	−0.19	+0.26	−0.18	Barra *et al.* (1999)
$Fe(mal)_3$	Fe^{3+}	−0.13	−0.11	±0.12	Collison and Powell (1990)
$Fe(acac)_3$	Fe^{3+}	+0.29	−0.22	+0.16	Collison and Powell (1990)
$[Fe(SPh)_3]^{2-}$	Fe^{2+}	+2.18	+3.14	6.48	Knapp *et al.* (1999)

Experimental data are provided for comparison. D values were computed by using DFT (Neese, F. 2009) and ORCA (Neese, 2012) approaches bpea = N,N-bis(2-pyridylmethyl)-ethylamine; Hdpm = dipivaloylmethane; Hdbm = 1,3-diphenyl-1,3-propanedione.

with experimental values are consistent, and even an investigation with several different functionals did not show significant improvements. The main reason is probably an intrinsic weakness due to the calculation techniques which are based on the generalized gradient approximations (GGAs) functionals. In any case, the method has relevant potentialities in calculating the ZFS as a function of the geometrical distortions in different coordination symmetries. For instance, the evaluation of D values has been described for octahedral d^4 ions in presence of Jahn–Teller distortions: for Mn^{4+} ions, an elongation of the coordination octahedron is accompanied by positive D values while a compression gives rise to negative D values. In presence of a Bailar twist, which accounts for the interconversion of an octahedron into a trigonal prism, for Mn^{4+} or Fe^{3+} ions the negative D values decrease on moving toward the trigonal prismatic geometry with a larger variation for Fe^{3+}. Analogously, it is possible to follow the D variation on passing from a square pyramidal environment to a trigonal bipyramidal one, with a higher positive value in presence of the former environment.

On passing from a tetrahedral coordination to the square planar one, the negative D values change according to the distortion, with the maximum anisotropy for intermediate geometries.

6.6 DOTA Complexes, Not Only Contrast

A good example of a practical application of these techniques is the study of magnetic anisotropies and luminescence of $Na[Dy(DOTA)(H_2O)]\cdot 4H_2O$ ($DOTA^{4-}$ = tetraaza-cyclododecane-tetraacetate) (Figure 6.4) (Cucinotta *et al.*, 2012).

These DOTA derivatives were widely studied for their properties as contrast agents in MRI (magnetic resonance imaging) and as luminescent systems (Woods and Sherry, 2003). To understand their behavior as contrast agents, the nuclear magnetic relaxation at room temperature has been investigated in depth, but only recently have their low-temperature magnetic properties been analyzed in any detail. It is rather surprising that it took so much time to decide the characterization of the low-temperature data. After all, they give an insight into the low-lying levels of the complex, which have an influence also at high temperatures. The compound $Na[Dy(DOTA)(H_2O)]\cdot 4H_2O$ shows an SMM behavior with a huge dependence of the relaxation time on the external magnetic field. The relaxation time increases by several orders of magnitude in the presence of an external magnetic field compared to the zero static field, and a thermally activated relaxation mechanism is observed with an effective barrier of about 60 K. Accurate work performed under a wide range of experimental and theoretical conditions suggest that this series of compounds are a pedagogical example of what can be done with Lns. It is not so important that an SMM behavior is observed; it is much more relevant that the concerted use of experimental and theoretical techniques provide a deep insight into the magnetic properties of molecular magnets formed by Ln.

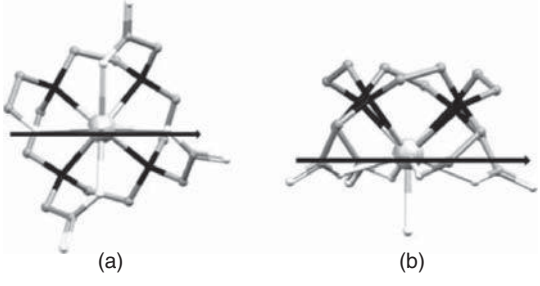

Figure 6.4 Two orthogonal views of $Na[Dy(DOTA)(H_2O)]\cdot 4H_2O$. (a) Parallel, and (b) orthogonal to the pseudo C_4 axis. The black arrows represent the direction of the easy axis of magnetization.

The first coordination sphere around Dy in $Na[Dy(DOTA)(H_2O)]\cdot 4H_2O$ is composed by four nitrogen atoms and four oxygen atoms situated at the vertices of a square antiprism with a water molecule capping a square lying on a pseudo C_4 symmetry axis. The overall symmetry can be assumed as C_{4v} based on the room-temperature data. Accurate experiments were performed to determine the T dependence of the magnetic susceptibility tensor using DC and AC techniques on single crystals taking advantage of the fact that the compound crystallizes in a triclinic space group. This ensures that the crystal's **g** tensor is the same as the molecular tensor, as we will analyze in Chapter 16. The symmetry of the low-temperature $\boldsymbol{\chi}$ tensor is very close to axial, and while the observed values are in nice agreement with an Ising anisotropy as often observed for the ground doublet of a Dy^{3+} ion, the easy axis direction is almost perpendicular to the idealized tetragonal symmetry axis of the complex.

With the final goal of determining the origin of this unexpected behavior, an analysis of the system was performed by following the above-sketched strategy. The CASSCF-CASPT2/RASSI-SO method was applied by varying slightly the model of the simplified system. The final result showed the dominant role of the water molecule that is capping a face of the square antiprism. This is a very interesting result because, generally, molecules belonging to the second coordination sphere do not influence the magnetic anisotropy of Ln^{3+} ions. It is a confirmation of the power of quantum chemical approaches to calculate the magnetic properties of Ln compounds, and the difficulties associated with hand-weaving arguments.

A more careful analysis of the structure shows that, in addition to the nearest neighbors, there are three Na ions which are not compatible with tetragonal symmetry. Although this is an important fact, it is hard to believe that a Dy–Na interaction is strong enough to drastically influence the magnetic properties. The water molecule, on the other hand, can be important depending on the orientation of the H–O–H plane in the Dy coordination sphere. This is confirmed by the computations which yield a ground Kramers doublet with a symmetry lower than axial. The experimental data fit reasonably well.

Having achieved a good success with Dy, Boulon *et al*. (2013) extended the treatment to the other heavy Lns. We must remember that in low symmetry the levels are grouped in pairs, namely Kramers' doublets, for compounds that have an odd number of unpaired electrons. Compounds that have even numbers of electrons give either singlets or quasi-degenerate doublets. The degeneracy of doublets in this case is accidental. The first point is the orientation of the easy axes, which are shown in Figure 6.5.

The g-values along the previous-reported easy axis and the energy level structure of the ground $^{2S+1}L_J$ multiplet from the relativistic *ab initio* calculations are reported in Table 6.3.

There is a gradual change of the orientation of the pseudo-tetragonal axis from parallel to orthogonal on lowering the size of the Ln. It is an amazingly good fit, showing the power of the method. Notice also the good agreement between experimental and calculated luminescence spectra, which allows us to

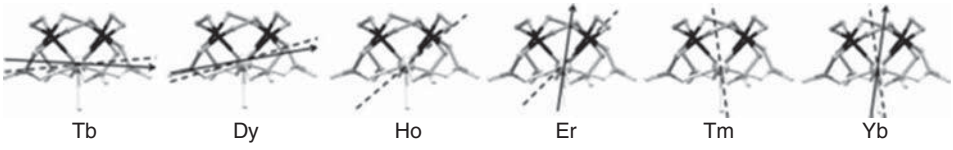

Figure 6.5 Experimental (full) and calculated (dotted) magnetization easy axis at $T = 2$ K for the series viewed perpendicular to the pseudo-fourfold symmetry axis of the molecules.

Table 6.3 *g* factors and energy levels for LnDOTA[a] .

		g_1	g_2		g_3	
Tb	12.7		2.1		0.5	
Ho	6.2		3.3		1.3	
Er	10.9		2.8		1.8	
Tm	12.02		1.02		0.95	
Yb	6.8		6.8		0.1	
Ground-state multiplet energy levels (cm^{-1})						
Tb	Singlets	0.0	1.6	25.4	29.8	115.6
	144.0	159.9	213.7	245.9	314.4	323.9
	379.9	384.4	—	—	—	—
Ho	Singlets	0.0	4.8	29.9	44.1	87.5
	145.8	155.6	172.2	185.5	192.9	214.0
	227.5	253.6	273.4	290.5	303.8	309.2
Er	Doublets	0.0	19.8	63.2	77.1	163.2
	228.8	317.5	427.0	—	—	—
Tm	Singlets	0.0	4.6	99.0	105.3	143.0
	173.0	206.6	225.5	260.6	307.5	325.5
	384.2	384.7	—	—	—	—
Yb	Doublets	0.0	197.2	379.3	416.2	—

a) For non-Kramers ions, gyromagnetic factors have been computed at $T = 2$ K.

have a wider look at the energies lying higher compared to what are required for magnetic data.

The observed levels give rise to slow relaxation at least for some ions. We will defer this exciting discussion on the possibility to cover all the facets till we cover Chapter 11 on the dynamics. Also, more details in the luminescence spectroscopy will be provided in Chapter 23.

The conclusion that we reach from the above selected examples is that LF and MO techniques provide a deep insight into single ion systems not only fitting the experimental data but also starting from scratch. We understand the nature and the origin of the ZFS and its impact on the asymmetry of the magnetic properties of systems that contain one magnetic center. It is now time to see what happens in multicenter systems.

References

Barra, A.L., Caneschi, A., Cornia, A., De Fabrizi Biani, F., Gatteschi, D., Sangregorio, C., Sessoli, R., and Sorace, L. (1999) Single-molecule magnet behavior of a tetranuclear iron(III) complex. The origin of slow magnetic relaxation in iron(III) clusters. *J. Am. Chem. Soc.*, **121**, 5302–5310.

Barra, A.L., Debrunner, P., Gatteschi, D., Schulz, C.E., and Sessoli, R. (1996) Superparamagnetic-like behavior in an octanuclear iron cluster. *Europhys. Lett.*, **35**, 133–138.

Barra, A.-L., Gatteschi, D., Sessoli, R., Abbati, G.L., Cornia, A., Fabretti, A.C., and Uytterhoeven, M.G. (1997) Electronic structure of manganese(III) compounds from high-frequency EPR spectra. *Angew. Chem., Int. Ed. Engl.*, **36**, 2329–2331.

Behere, D.V. and Mitra, S. (1980) Magnetic susceptibility study and ground-state zero-field splitting in manganese(III) porphyrins. *Inorg. Chem.*, **19**, 992–995.

Bencini, A. (2008) Some considerations on the proper use of computational tools in transition metal chemistry. *Inorg. Chim. Acta*, **361**, 3820–3831.

Bencini, A. and Totti, F. (2008) On the importance of the biquadratic terms in exchange coupled systems: a post-HF investigation. *Inorg. Chim. Acta*, **361**, 4153–4156.

Boulon, M.E., Cucinotta, G., Luzon, J., Degl'Innocenti, C., Perfetti, M., Bernot, K., Calvez, G., Caneschi, A., and Sessoli, R. (2013) Magnetic anisotropy and spin-parity effect along the series of lanthanide complexes with DOTA. *Angew. Chem. Int. Ed.*, **52**, 350–354.

Cirera, J., Ruiz, E., Alvarez, S., Neese, F., and Kortus, J. (2009) How to build molecules with large magnetic anisotropy. *Chem. Eur. J.*, **15**, 4078–4087.

Cohen, A.J., Mori-Sánchez, P., and Yang, W. (2012) Challenges for density functional theory. *Chem. Rev.*, **112**, 289–320.

Collison, D. and Powell, A.K. (1990) Electron spin resonance studies of "FeO6" tris chelate complexes: models for the effects of zero-field splitting in distorted S = 5/2 spin systems. *Inorg. Chem.*, **29**, 4735–4746.

Cucinotta, G., Perfetti, M., Luzon, J., Etienne, M., Car, P.-E., Caneschi, A., Calvez, G., Bernot, K., and Sessoli, R. (2012) Magnetic anisotropy in a dysprosium/DOTA single-molecule magnet: beyond simple magneto-structural correlations. *Angew. Chem., Int. Ed. Engl.*, **51**, 1606–1610.

Deaton, J.C., Gebhard, M.S., and Solomon, E.I. (1989) Transverse and longitudinal Zeeman effect on $[PPh_4][FeCl_4]$: assignment of the ligand field transitions and the origin of the $^6A_1$ ground-state zero-field splitting. *Inorg. Chem.*, **28**, 877–889.

Gatteschi, D. and Sorace, L. (2001) Hints for the control of magnetic anisotropy in molecular materials. *J. Solid State Chem.*, **159**, 253–261.

Hohenberg, P. and Kohn, W. (1964) Inhomogeneous electron gas. *Phys. Rev.*, **136**, B864–B871.

Knapp, M.J., Krzystek, J., Brunel, L.-C., and Hendrickson, D.N. (1999) High-frequency EPR study of the ferrous ion in the reduced rubredoxin model $[Fe(SPh)_4]_2$. *Inorg. Chem.*, **39**, 281–288.

Koopmans, T. (1934) Über die Zuordnung von Wellenfunktionen und Eigenwerten zu den Einzelnen Elektronen Eines Atoms. *Physica*, **1**, 104–113.

Krzystek, J., Yeagle, G.J., Park, J.-H., Britt, R.D., Meisel, M.W., Brunel, L.-C., and Telser, J. (2003) High-frequency and -field EPR spectroscopy of Tris(2,4-pentanedionato)manganese(III): investigation of solid-state versus solution Jahn – Teller Effects. *Inorg. Chem.*, **42**, 4610–4618.

Limburg, J., Vrettos, J.S., Crabtree, R.H., Brudvig, G.W., De Paula, J.C., Hassan, A., Barra, A.L., Duboc-Toia, C., and Collomb, M.N. (2001) High-frequency EPR study of a new mononuclear manganese(III) complex: $[(Terpy)Mn(N_3)_3]$ (terpy = 2,2′:6′,2′-terpyridine). *Inorg. Chem.*, **40**, 1698–1703.

Mantel, C., Hassan, A.K., Pécaut, J., Deronzier, A., Collomb, M.-N., and Duboc-Toia, C. (2003) A high-frequency and high-field EPR study of new azide and fluoride mononuclear Mn(III) complexes. *J. Am. Chem. Soc.*, **125**, 12337–12344.

Neese, F. (2012) The ORCA program system. *Wiley Interdisciplinary Reviews: Computational Molecular Science*, **2**, 73–78.

Nese, F. (2009) Prediction of molecular properties and molecular spectroscopy with density functional theory: From fundamental theory to exchange-coupling. *Coord. Chem. Rev.*, **253**, 526–563.

Neese, F. and Solomon, E.I. (1998) Calculation of zero-field splittings, g-values, and the relativistic nephelauxetic effect in transition metal complexes. application to high-spin ferric complexes. *Inorg. Chem.*, **37**, 6568–6582.

Pantazis, D.A., Chen, X.Y., Landis, C.R., and Neese, F. (2008) All-electron scalar relativistic basis sets for third-row transition metal atoms. *J. Chem. Theory Comput.*, **4**, 908–919.

Sham, L.J. and Kohn, W. (1966) One-particle properties of an inhomogeneous interacting electron gas. *Phys. Rev.*, **145**, 561–567.

Woods, M. and Sherry, A.D. (2003) Synthesis and luminescence studies of aryl substituted tetraamide complexes of europium(III): A new approach to pH responsive luminescent europium probes, *Inorg. Chem.*, **42**, 4401–4408.

7
Toward the Molecular Ferromagnet

7.1
Introduction

We are entering the important area that explains the nature of magnetism as a cooperative phenomenon, that is, justifies the observed bulk magnetization as due to a collective response of individual magnetic moments. In particular, we will concentrate on the peculiar aspects of molecular magnetism, essentially neglecting metallic and ionic magnets. Compared to inorganic magnets, which are based on metallic and ionic lattices, and behave as conductors or semiconductors, molecular magnets are generally to be considered as insulators. For the former, the cooperative behavior is generated by the moving electrons making fishing out the origin of the interaction between magnetic centers complicated. For MM, in general, it is sufficient to have a look at the nature of the orbitals with unpaired electrons, the so-called magnetic orbitals, and to guess the overlap between them. An example is provided by two Fe^{3+} ions bridged by an oxygen atom. It is an elementary example, well known to everybody, which hopefully reminds us the type of considerations that are needed to justify the origin of the magnetic interactions. A simple way to check the presence of a magnetic coupling is shown in Figure 7.1a. The spin of the unpaired electron on the left ion polarizes the doublet on the oxygen atom and, therefore, the unpaired electron on the right ion is forced to be antiparallel to the first one. If the angle Fe–O–Fe is 90°, the overlap between the left and right atoms is zero, forcing the second spin to be parallel to the first, one as shown in Figure 7.1b.

If, on the other hand, the overlap between the magnetic orbitals is zero, the exchange interaction will keep the individual moments parallel to each other. Of course, it is necessary that in some regions the overlap is positive and in others it is negative. Zero overlap everywhere gives zero interaction. Therefore, the coupling between magnetic orbitals and their overlap will be the key to understanding the origin of ferro- and antiferromagnetic (AFM) coupling.

We will liberally use the concept of molecular building block, developing a point of view that first simplifies the magnetic structure by recognizing elementary groups (the building blocks) whose local properties provide the starting point to give rise to cooperative phenomena and bulk behavior such as ferro-,

Introduction to Molecular Magnetism: From Transition Metals to Lanthanides, First Edition.
Cristiano Benelli and Dante Gatteschi.
© 2015 Wiley-VCH Verlag GmbH & Co. KGaA. Published 2015 by Wiley-VCH Verlag GmbH & Co. KGaA.

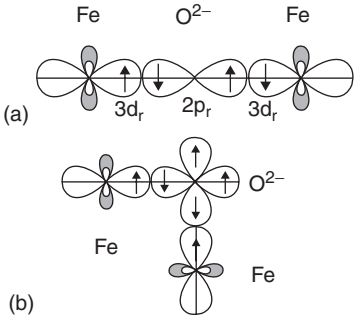

Figure 7.1 Spin orientation in a Fe–O–Fe group according to the geometry of the bridge a) parallel; b) antiparallel.

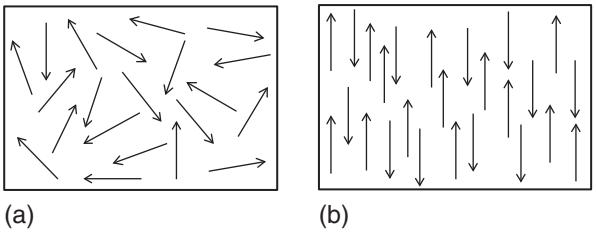

Figure 7.2 Paramagnetic system (a) in the absence and (b) in presence of a magnetic field.

ferri-, antiferromagnetism. There is a contrast between the interactions that tend to keep the individual magnetic moments ordered and thermal agitation that disorders them. It is intuitively clear that order dominates at low temperature.

Let us choose to use only one type of building block; there are many different ways to arrange them. First of all, we refer to solids so that we will consider infinite arrays. The simplest case is that of an assembly of noninteracting magnetic centers, as shown in Figure 7.2a, where the individual magnetic moments on the left flip freely and the time and space average of the magnetization are null in the absence of an applied magnetic field. This is the paramagnetic state described earlier. This is essentially an unrealistic case because the through-space interaction is impossible to quench. However, it may be an acceptable approximation when the interaction is weaker than thermal agitation. We can imagine as moving from the simple paramagnetic state which we recall corresponds to an ensemble of noninteracting moments to a magnetically ordered state. Switching on a magnetic field begins to orient the individual moments parallel to itself, inducing a nonzero magnetic moments, as shown in Figure 7.2b. The magnetization relaxes with a characteristic time, which we will discuss later.

At high temperature, the individual magnets will behave as isolated ones. If the interaction dominates, the order will consist of an infinite array of individual magnetic moments.

Let us represent, in a very simplified manner, the system as a collection of atoms which in the noninteraction limits are as shown below in Figure 7.3a.

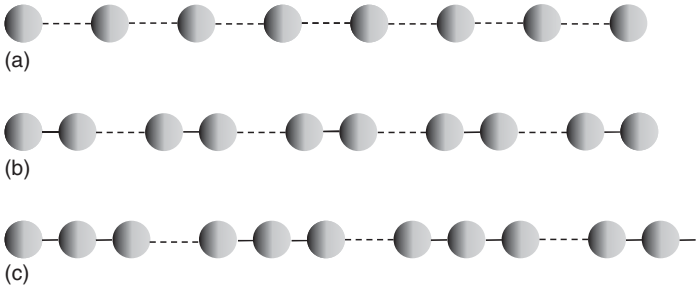

Figure 7.3 A collection of: non-interacting atoms (a), two by two interacting atoms (b), three by three interacting atoms (c).

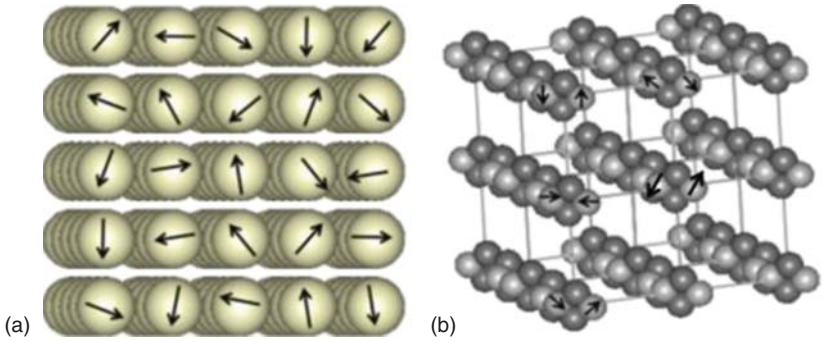

Figure 7.4 Building blocks and their spin arrangements: single atoms (left); interacting pairs (right).

For the sake of simplicity, we use a one-dimensional array. The first step toward complex structures is to switch on the interaction in pairs as shown in Figure 7.3b or in cluster (Figure 7.3c).

In schemes (b) and (c), there is a short and a long contact. The pair behaves like a paramagnet and, at low temperature the system behaves as a magnet of pairs. Instead of pairs, it is possible to use clusters and again the compound behaves as a paramagnet of clusters. One can continue to increase the size of the clusters to 3, 4, 5, and so on, up to more than 100. These are certainly exciting compounds, as we will see in the following, but their behavior is, in a sense, a complex paramagnet. A three-dimensional representation of the paramagnets is shown in Figure 7.4.

Matters become more interesting when the number of interacting centers becomes infinite. If it corresponds to a chain, it is named one-dimensional (the finite-sized systems are zero-dimensional). Further growth leads to two- and three-dimensional systems. The dimensionality of the magnets is important to determine the development of cooperative effects. These points will be worked out in Section 7.2.

Section 7.3 is one of the most important of the book because it tries to explain in a simple way the nature of the magnetic interactions. In order to start to practice with magnetic interactions, the relatively simple dipolar case will be treated at

some length. Section 7.4 is again a fundamental one because it treats the spin Hamiltonian (SH), which is the basic language of magnetism.

7.2 A Road to Infinite

Looking at some more detail a building block, let us choose the magnetic center as a metal ion, which can be a TM or an Ln. The brick will comprise also the ligands, which modulate the properties and allow putting the bricks together. These groups can be considered as the mortar that keeps the bricks together in the wall. Forgetting for the moment the single ions' properties, we assume that the ion is orbitally nondegenerate and has a spin multiplicity $2S + 1$. We must introduce the way the ions interact, because the bulk magnetic properties strongly depend on their interaction. The field to explore is vast and full of insidious structures, and requires treatments of increasing difficulty. We will try to use a step-by-step approach which we hope will make the path not too difficult. The first step is to recognize that magnetism is bound to the presence of unpaired electrons.

Let us now switch some interaction on, supposing that there is still an infinite number of bricks, but for the sake of simplicity we will assume that the interactions are limited to pairs, that is, each brick will interact with only one brick. The unpaired electrons of the two coupled atoms will interact, and the pairs will have different numbers of unpaired electrons. We have relaxed the condition of noninteraction only for pairs; therefore, the magnetic properties are dependent on an infinite array of pairs, as shown in the right part of Figure 7.4. The system is paramagnetic but, in general, more complex than that of isolated atoms. And we can continue going to 3, 4, and so on, interacting atoms. In passing, we note that the interaction among three bricks can be linear, or make an angle different from 180°, thereby introducing a shape factor in the magnetic properties.

In principle, it is chemically possible to build structures at will with a bottom-up approach. This step-by-step growth is fantastic, allowing us in principle to monitor the emerging properties and passing gradually from an isolated to a cooperative behavior. In this sense, MM are particularly well suited for nanoscience developments. This was one of the focal points of GSV. The treatment is much more complex there compared to the present one.

In the ideal process of building infinite structures of magnetic bricks, one can go to infinity in one, two, and three directions. Often, the systems are classified according to the number of directions along which infinite arrays of interacting centers are present. The systems having a finite number of bricks are called *zero-dimensional* or 0D.

One of the features of bulk magnets is that, below a critical temperature, they can be permanently magnetized. This is due to the fact that the interactions between the blocks, which tend to form a 3D ordered state, are stronger than the thermal agitation which tends to give a disordered state. There are many different types of order, the most common being ferromagnetic, antiferromagnetic, ferrimagnetic, and weak ferromagnetic, which are depicted in Figure 7.5.

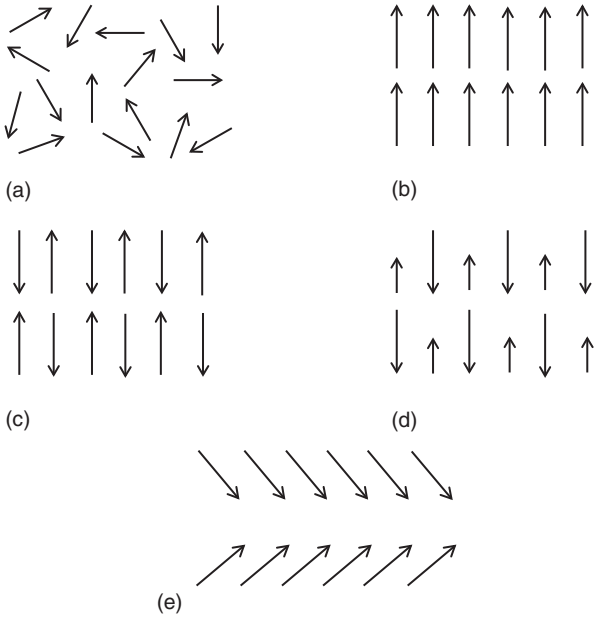

Figure 7.5 Relative orientations of the local spins in various classes of magnets. (a) Paramagnet. (b) Ferromagnet. (c) Antiferromagnet. (d) Ferrimagnet. (e) Canted ferromagnet.

The systems outlined in Figure 7.5b, d, and e have a nonzero magnetization below the critical temperature, while the system depicted in Figure 7.5c has null magnetization.

It must be stressed that to observe the ordered magnetic state it is necessary to have 3D magnetic arrays. It is not possible to have long-range magnetic order in low-dimensional systems. This can be understood intuitively for chains. If we have a 1D array of ferromagnetically coupled bricks, the breaking of one bond will cost something, but the entropy associated with the possibility to break in any position in the array will more than compensate it. Therefore, if a ferromagnet is the goal, it is necessary to design blocks that interact ferromagnetically with each other in three dimensions. Chemists starting the organic (molecular) ferromagnet adventure soon realized that if designing blocks that give rise to FM (ferromagnetic) coupling is difficult, demanding 3D magnetic arrays is a nightmare. Anyway several compounds were synthesized which show that strong ferromagnetic coupling in pairs is possible in MM and if room temperature molecular ferromagnets are still very rare, new exciting compounds can be obtained.

Going back to magnetic molecules, let us consider what happens on increasing their size. The answer is simple: the complications increase exponentially. One high-spin iron(III) has six magnetic degrees of freedom corresponding to the $2S+1$ spin states of a system with five unpaired electrons ($S = 5/2$). Thirty iron(III) ions, which can be assembled in a icosidodecahedral structure, shown in Figure 7.6, have $(2S+1)^{30}$ states. This corresponds to about $2.21 \times 10^{+23}$ or

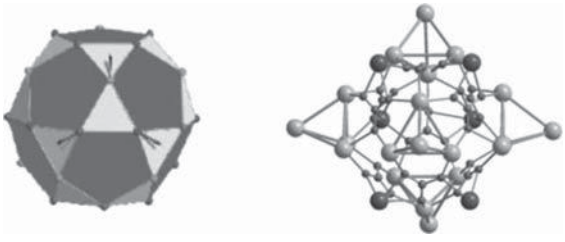

Figure 7.6 (a) Iron(III) core in $[Mo^{VI}_{72}Fe^{III}_{30}O_{252}(CH_3COO)_{20}(H_2O)_{92}]^{4-}$ (Reproduced from Müller *et al.*, 2006 with permission from The Royal Society of Chemistry). (b) Dy^{3+} core in $Dy_{30}I$ $(\mu_3\text{-}OH)_{24}(\mu_3\text{-}O)_6(NO_3)_9(IN)_{41}(OH)_3(H_2O)_{38}$. (Reproduced from Gu and Xue, 2007 with permission from The American Chemical Society.)

$1/3N_A$, where N_A is the Avogadro number. In other words, Fe_{30} has about 1 mol of spin levels. This is a good performance. Lns have even larger numbers of spin levels, therefore they develop easily large numbers of clusters. For instance, a cluster of Dy_{26}, whose structure is also shown in Figure 7.6, has 16 levels per ion or, if you prefer, 10^7 mol of levels per cluster.

7.3 Magnetic Interactions

The simplest approach to introduce magnetic interactions is to start from building blocks hat have an orbitally nondegenerate ground state. This condition is met because in many cases the LF (ligand field) reduces the degeneracy of the ground level. A Cr(III) free ion has a $3d^3$ configuration with a Russell–Saunders state with $2S + 1 = 4$ and $L = 3$, which corresponds to a sevenfold orbital degeneracy. On lowering the symmetry to octahedral, the orbital degeneracy is reduced to one, as we have shown above. We keep noticing the peculiar behavior of Lns due to their large, unquenched orbital component resulting from the fact that 4f electrons are internal electrons. This makes most of the basic assumptions used for describing the magnetic interactions invalid. In fact, the simplest approach to describe the interaction between two systems with a variable number of unpaired electrons is to use the HDVV Hamiltonian:

$$\mathscr{H} = J\mathcal{S}_1 \cdot \mathcal{S}_2 \tag{7.1}$$

It is an effective Hamiltonian that substitutes all the active coordinates with spin coordinates. The conditions required to apply this Hamiltonian correctly will be discussed in the following. We have already used SH for individual centers, and now we extend the formalism to *n* centers. It is legitimate to do so if the ground states are orbitally nondegenerate. S_i are the spin angular momentum operators centered on the site *i*. The use of Eq. (7.1) is relatively simple as we will soon verify. In fact, it is possible to write

$$2\mathcal{S}_1 \cdot \mathcal{S}_2 = \mathcal{S}^2 - \mathcal{S}_1^2 - \mathcal{S}_2^2 \tag{7.2}$$

where

$$|S_1 - S_2| \leq S \leq S_1 + S_2 \tag{7.3}$$

from which follows

$$E(S) = (J/2)[S(S+1) - S_1(S_1+1) - S_2(S_2+1)] \tag{7.4}$$

If $J < 0$, the ground state is one with the largest S and the coupling is ferromagnetic. A positive J requires the smallest S, as the ground state and the coupling is AFM. The S dependence of the energies is called the *Landé interval rule*.

For two spins $S_i = 1/2$, the coupled states are a singlet and a triplet. For two spins $S = 7/2$, say for gadolinium(III), the ground state is $S = 0$ if J is positive, and $S = 7$ if J is negative. The former case is referred to as *antiferromagnetic* and the latter *ferromagnetic* coupling.

As in many other cases the value of J has two contributions, one called *dipolar* and the other *exchange interaction*. The dipolar term depends on the product of the dipolar moments on the two centers and has an r^{-3} dependence on distance. The exchange interaction is more akin to the formation of a weak chemical bond, as we will discuss below. The exchange interaction is generally dominant, or, better, we will be more often interested to systems in which the strong exchange conditions are met. This means that S as defined in Eq. (7.3) is a reasonable starting point to describe the properties of the pair. We must introduce here a *caveat*. Often, the extent of the exchange interaction between two centers is guessed from the value of J, but, on comparing the J values of different pairs, the comparison can be made not between the simple J values but between the $JS(S+1)$ values of the pairs. However, the energy difference between the lowest and the highest S for pair i is $J\,S_i(S_i+1)$. The total spin S for a pair S_i gives an overall splitting $E(2S_i)$. This means that the splitting of the pair of levels for $S_i = 1/2$ is 3/4J, while for $S_i = 7/2$ it is 63/4J. To give similar effects, J of the doublet must be 21 times larger than that of the octet. We will work out an example below.

The Hamiltonian (7.1) is only one piece that is needed to describe the energy levels of the pair. For sure, one has to include the terms needed to define the single center's properties: the Zeeman terms, the low-symmetry terms, the electron–nucleus (hyperfine and superhyperfine) and the nuclear Zeeman terms, the nuclear quadrupole term, and so on. The description of the pair at the minimum level of complication, beyond Eq. (7.1), requires lower symmetry components which break the spherical symmetry of the isotropic term, adding anisotropic and antisymmetric components. This can be limited to the bilinear terms of S_1S_2 type, or one can include higher order terms some of which will be discussed in the following. The use of the Van Vleck equation on the states $E(S)$ defined in Eq. (7.4) yields

$$\chi = \frac{Ng^2\mu_B^2}{3kT} \frac{\sum_S S(S+1)(2S+1)\exp^{-\frac{E(S)}{kT}}}{\sum_S (2S+1)\exp^{-\frac{E(S)}{kT}}} \tag{7.5}$$

The S-values are those defined in Eq. (7.3).

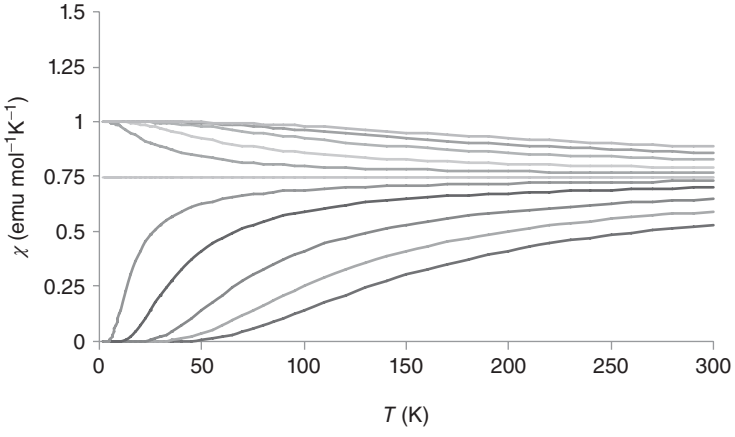

Figure 7.7 Temperature dependence of χT values for a dimer of S = 1/2 and with a coupling constant J varying from (top to bottom) between −200 and +200 cm^{-1}.

As very often the coupled system contains states with high S-values, it is useful to consider the possibility of intermolecular interactions by including their presence following a molecular field approach (McElearney *et al.*, 1973). Using Eq. (7.5), the magnetic susceptibility is calculated as

$$\chi_{\text{inter}} = \frac{Ng^2\mu_B^2\chi}{kT - zJ'\chi} \tag{7.6}$$

where zJ' accounts for the number of interacting centers (z) and the nature and intensity of the magnetic interaction (J'). Equation (7.6) recalls the Curie–Weiss law if we assume that

$$\theta = \frac{zJ'\chi}{k} \tag{7.7}$$

The temperature dependence of the χT product for pairs with $S_i = 1/2$ is shown in Figure 7.7.

If there is no interaction, the χT versus T plot is parallel to the T axis. Switching on the interaction leaves the same results for weak interactions ($JS^2 \ll kT$). When this condition is relaxed, the χT versus T plot increases (decreases) for ferro- (antiferro-) magnetic coupling on decreasing T. χ goes through a maximum when an AF interaction is present. The temperature of the maximum increases on either increasing the coupling constant (Figure 7.8) or increasing the spin value of the interacting magnetic center (Figure 7.9). The magnetic susceptibility provides easily the sign of J.

Indeed, the first step in the discussion of the magnetic properties of a new compound is the comparison of the calculated Curie constant (C) for the corresponding free ion with the observed χT value at room temperature which provides the basic information on the nature of the interaction in the pair. As an example,

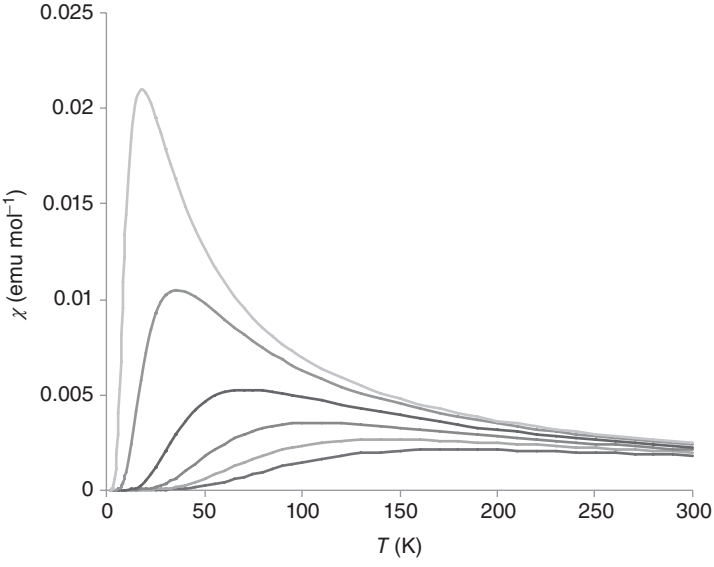

Figure 7.8 Temperature dependence of χ values for a dimer of S = 1/2 with an antiferromagnetic coupling constant J varying (from top to bottom) between 200 and 20 cm^{-1}.

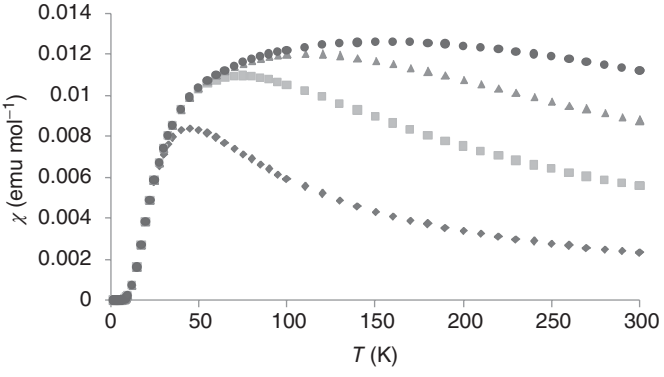

Figure 7.9 Temperature dependence of χ values for dimers with an antiferromagnetic coupling constant $J = 50\,cm^{-1}$ on varying the values of the coupling with S = 2 (●), 3/2(▲), 1(■), and 1/2(◆).

let us consider a di-gadolinium compound such as $[Gd_2(sal)_3(H_2O)]$ (Hsal = salicylic acid). The expected χT value for the pair in the high-temperature limit is 15.75 emu K mol^{-1}, corresponding to the sum of two free ions. The observed one is 15.7 emu K mol^{-1}, indicating that the high-T limit is a good approximation. Extending the measurements to low temperatures shows a positive deviation from the Curie law, suggesting that, at low temperature, states with larger spin are selectively populated (FM coupling). The value at 2 K is 18.9 emu K mol^{-1}, which is in

accordance with FM coupling. A fit with Eq. (7.5) gave $J = -0.05\,\mathrm{cm}^{-1}$, $g = 1.98$ (Costes *et al.*, 2002).

So far, for describing the magnetic interaction we have used spherical systems interacting in an isotropic way. The Hamiltonian, Eq. (7.1), is an example: S_1, S_2, and S refer to the irreducible representations of the spherical group. Actually, this is correct for integer spins. For half-integer spins (odd number of electrons), one must refer to the double groups in which the identity operator is not a rotation by 2π but by 4π. We recall that a rotation φ around z yields

$$R\varphi|\mathrm{SM}\rangle = \mathrm{e}^{iM\varphi}|\mathrm{SM}\rangle \tag{7.8}$$

where |SM> is an eigenfunction of a central field potential in the form of spherical harmonics. A rotation of 2π yields $\mathrm{e}^{iM2\pi}$, which for an integer M equals 1, while for a half-integer M it equals -1. Therefore, for the latter, the system is not invariant for a rotation of 2π. However, it is invariant for a rotation of 4π. From group theory, we can define a new group where a rotation by 2π is R, which can correspond to 1 or -1. The new group G* is obtained as a direct product of the original group G and the [E, R] group. The double group refers to the fact that G* contains twice as many elements as G. This intrinsic difference between integer and half integer is of paramount importance in magnetism.

The coupling depicted by Eq. (7.1) is isotropic, that is, $J_x = J_y = J_z$. This is not the only possibility. In fact, in a more general case, Eq. (7.1) can be rewritten as

$$\mathscr{H} = J_x \mathscr{S}_x + J_y \mathscr{S}_y + J_z \mathscr{S}_z \tag{7.9}$$

The relative values of the components of J determine the anisotropic components of the interaction. A type that we will discuss in many cases is given by $J_x = J_y = 0$; $J_z \neq 0$. This is called the *Ising case*, after the name of the German physicist who first introduced it in 1925 (Ising, 1925). Actually, the first introduction of the Ising Hamiltonian was done by Lenz, but with time Lenz dropped out. It must be stressed that the Ising approach is a classical one and only assumes two values, ±J. Compared to the HDVV Hamiltonian, which for two spins 1/2 gives a singlet and a triplet, the Ising approach gives the energies of the basis $|\sigma_i\, \sigma_k\rangle$, where σ_i is the z component of the spin. This condition can be met when a strong local field forces the spin to be parallel to z. This means that, for instance, the magnetic susceptibility is much larger parallel to z than perpendicular to it. The energies of the levels are given by $E(++) = E(--) = J$; $E(+-) = E(-+) = -J$.

The residual degeneracy of the Ising states is removed by an applied magnetic field. A simple way of treating the interaction is by the Zeeman Hamiltonian, which for a field parallel to z becomes

$$\mathscr{H} = g_z \mu_B \mathscr{S}_z H_z \tag{7.10}$$

In the simple treatment of the Ising interaction outlined so far, we have implicitly assumed that the z-axes of the interacting pairs are parallel to each other. However, it is an assumption which often fails, and several corrections have been suggested. We will treat the problem of noncollinear axes, that is, of the influence of the different orientation of the z-axes on the magnetic properties, both static and dynamic, in Chapter 11.

Table 7.1 Magnetic ordering as corresponding to the dimensionality of the lattice and order parameters.

	1d	2d	3d
Ising	No long Range order at $T = 0$ K	Magnetic order	Magnetic order
XY		K–T transition[a)]	
HDVV			

a) 2D *XY* systems show a Kosterlitz–Thouless transition (Kosterlitz and Thouless, 1973).

Stepping from paramagnets to correlated systems opens the opportunity for order–disorder transitions. In fact, the material will feel the magnetic interaction that tends to order the spins as well as thermal agitation that favors disorder. At low temperature, the ordered state is stable and the transition from disordered to order occurs at a well-defined temperature, which is called the *Curie temperature* for a ferromagnet and Neel temperature for an antiferromagnet. The conditions for the transition depend on several parameters that define the extent of the coupling, such as follows:

- nature of the spins
- dimensionality of the spins
- nature of the exchange interactions.

One thing is clear: to have long-range order, 3D interactions are needed. Some of the important conditions are summarized in Table 7.1.

The principal ordered states and the relative orientations of the spins are those shown in Figure 7.5. While ferro-, antiferro-, and ferrimagnets require angles 0–180° between spins, the canted ferrimagnet requires $180° - \alpha$. Typically, α is of the order of 1. If the main orientation of the two spins is parallel to z, it generates a noncompensation parallel to x (weak ferromagnetism), as shown in Figure 7.10.

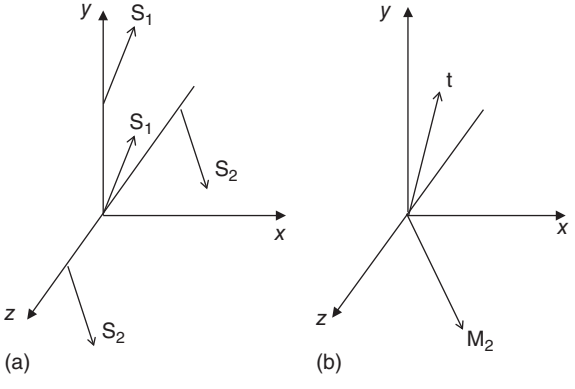

Figure 7.10 Spin alignment in a weak ferromagnet.

7.4
Introducing Interactions: Dipolar

Although it is possible to go a long way in understanding MM using *ad hoc* Hamiltonians, it is necessary to develop fundamental theories to be able to advance in the field, as we will show in the following. The present level is high and rapidly changing thanks to the impact of computer-aided chemistry in calculating complex molecular aggregates. We will work on these methods in the following. At the moment, we will simply stress that there are essentially two types of interactions responsible of the magnetic properties, namely dipolar and exchange. Although the two interactions can be described by the same SHs, they are much different from each other.

The interaction between two magnetic dipoles is a through-space interaction which decays slowly (as the inverse third power of the distance between the two magnets) and is simple to calculate using the point dipolar approximation. The interaction is calculated for pairs, and the calculated data are compared with the experimental data obtained from condensed matter systems. The slow decay with the distance between the dipoles requires that a check is made of the contribution by the next nearest neighbors. The interaction with far away dipoles is weak, but there are many interacting dipoles. Dropping out distant dipoles may be inaccurate.

Rather unsurprisingly, the first systematic approaches to rationalize the correlation between structure and magnetism of rare earth (RE) compounds used Gd^{3+}, either alone or connected with TM or organic radicals. We feel that starting from Gd can be pedagogical; therefore, we will review first the compounds that contain this ion.

Before proceeding, we want also to recall that dipolar interactions are important not only for pairs containing unpaired electrons but also for systems containing nonzero nuclear moments. There will be electron–electron, electron–nucleus, and nucleus–nucleus dipolar interactions, but we will be considering those involving electrons only, like the systems we are describing now. The formalism will be similar in all cases and it will be useful to develop a common point of view for different phenomena.

We recall that the Gd^{3+} ion can be treated as an $S = 7/2$ state. The large S-value, together with the quenched orbital component, promotes strong interaction. The first step requires the introduction of the nature of the interaction. In fact, Eq. (7.1) tells us, for example, that two spin 1/2 give a singlet and a triplet but does not tell the sign of the splitting and the separation. The fit of experimental data may give J, but some fundamental theory is needed because J by itself does not tell anything on the nature of the interaction. It was well known from Curie's time that the most obvious candidate to induce an interaction between two magnetic centers A and B is a dipolar interaction. A point magnetic dipole is associated to center A and B, and the interaction is calculated classically assuming that the distance R between the two dipoles is large compared to their spatial extension (point dipolar approximation). The calculated energies for TM ions, however, are

too weak to justify the observed data. In fact, dipolar energies are of the order of 1 K, at best, while experimental interaction energies range from 1 to 1000 K. Matters are less dramatic for RE ions, as shown by the following example.

We like to use a system that certainly does not belong to the molecular world. We like it because it gives us the opportunity to stress that the language is common and the methods to be used to understand the properties of matter are the same. Hearing people speaking a different scientific language enhances the opportunities of developing new points of view.

Here we are interested to a detailed study of the dipolar interaction between two Gd^{3+} ions in $Gd_{0.01}Y_{0.99}Ba_2Cu_3O_6$, which has been studied as single crystals. The compound is a perovskite, one of the classical typical ionic lattices, and a member of the YBCO family of high-T_c superconductors. The superconducting and magnetic properties depend on the stoichiometry $YBa_2Cu_3O_{6+x}$. The copper ions define bilayers which are antiferromagnetically coupled. The Y ions are in a site with eight oxygen atoms defining a square prism and possess tetragonal symmetry. They are sandwiched by the copper layers. The Gd^{3+} doped compounds have been intensively investigated because they give sharp lines in ESR and can be used as probes of the domain structure of the AFM coupling determined by the copper ions. The distance R between nearest neighbor Y ions is 0.386 nm, while the contact in the perpendicular direction is 1.168 nm. The anisotropic part of the dipolar interaction is well described by the Hamiltonian

$$\mathscr{H} = \mathcal{S}_1 \cdot \mathbf{D}_{12} \cdot \mathcal{S}_2 \tag{7.11}$$

The Hamiltonian (7.11) needs the $\mathbf{D_{12}}$ tensor, which depends on the individual dipoles and on their relative orientation and distance. The tensor is traceless. This condition can be made explicit using the equivalent Hamiltonian

$$\mathscr{H} = \mathrm{D}[\mathcal{S}_1 \cdot \mathcal{S}_2 - 3\mathcal{S}_{1z}\mathcal{S}_{2z}] \tag{7.12}$$

The two Hamiltonians are equivalent provided

$$\mathrm{D} = \mathrm{D}_{1x2x} = \mathrm{D}_{1y2y} = -\frac{1}{2}\mathrm{D}_{1z2z} \tag{7.13}$$

The corresponding tensor has axial symetry. Calculation of the energies with Eq. (7.11) requires the principal values and directions of the two **g** tensors, the R distance, and four angles relating the reference frames. A suitable expression for the calculation of the $\mathbf{D_{12}}$ tensor is

$$\mathrm{D}_{\mathbf{12}} = -\left[2g_z^2 + \frac{\left(g_x^2 + g_y^2\right)}{2}\right]\frac{\mu_\mathrm{B}^2}{2r_{12}^3} \tag{7.14}$$

A drastic simplification is possible when the two **g** tensors are isotropic. Two g-values are needed as in an magnetic field with arbitrary polar angles, pairs like A_1 and A_2 are not equivalent (Figure 7.11).

In a continuous lattice, there are infinite pairs: we take as models the pairs of Gd^{3+} along the a-axis. There are four such pairs, as shown in Figure 7.12. A sample calculation with $g = 2$, $R = 3.86$ Å yields an axial tensor with $D = -0.0602\,\mathrm{cm}^{-1}$

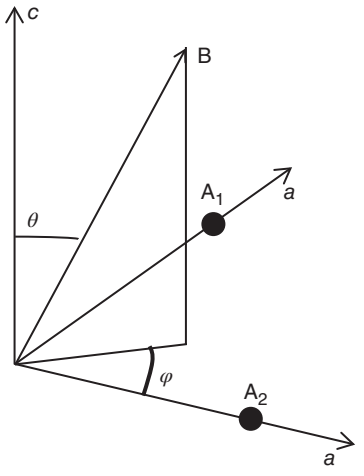

Figure 7.11 Definition of the polar coordinate system showing the position of two centers with respect the magnetic field.

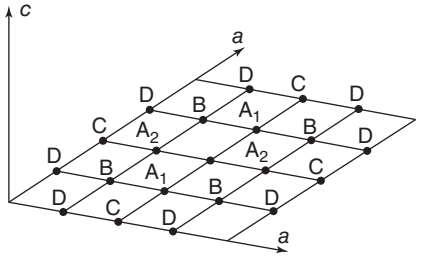

Figure 7.12 A, B, C, and D are sites of closest neighboring Gd^{3+} ions. A_1 and A_2 are in general not equivalent in arbitrarily oriented magnetic fields. (Reproduced from Simon, F. *et al.* (1999) with permission from The American Physical Society.)

($D = (g^2\mu_B{}^2)/R^3 = 0.433g^2/R^3$ for R in Ångstrom and D in cm^{-1}). The two individual magnetic dipoles are oriented along the direction connecting the two dipoles, which refer to the eigenvalues of $S_{z,i}$. There are 64 levels of the two ions, which are split dramatically. The levels can be labeled as M_1 and M_2, where M_i are the eigenvalues of S_{zi}. The lowest energy state is a doublet ($\pm 7/2$, $\pm 7/2$) at $-147D/4$, while the highest is (7/2, −7/2) whose energy is $147D/4$. The overall splitting for the calculated D value is 2.216 cm^{-1}. We recall that, when comparing different systems, it is not D the value to be used but rather DS^2. The detailed analysis of the dipolar field has been performed using a multifrequency ESR approach (Jánossy *et al.*, 1999; Simon *et al.*, 1999) which is very pedagogical and deserves an accurate treatment which we reserve for Chapter 21 where ESR experiments are discussed. Here we limit ourselves to the enunciation of the main results.

The information on the energies of the low-lying levels is assumed by recording the ESR spectra of a single crystal where gadolinium dopes the yttrium lattice with a formal concentration 1%. There will be Gd^{3+} ions that are isolated, that is, they have only diamagnetic nearest neighbors. Others have one Gd^{3+} two diamagnetic nearest neighbors, and so on. The dipolar fields of the various pairs are monitored

by ESR spectroscopy. Since the **D** tensors are expected to scale as r^{-3} and to have maxima along the direction Gd–Gd, the assignment of the signals to the pairs is easy. The appearance of forbidden transitions is a clear indication that dipolar interactions alone are not sufficient to explain the experimental data. Matters are dramatically improved if the isotropic exchange Hamiltonian Eq. (7.1) is taken into account i.e. adding the dipolar one (7.11) to the exchange term (7.1).

Our gadolinium example shows that the dipolar and exchange interactions are of the same order of magnitude. In fact, the fit of experimental data provided a J value of 0.105 cm^{-1} and D=0.036 cm^{-1}. The corresponding calculated J and D values within the point dipolar approximation are 0 and 0.030 cm^{-1}, respectively. This is a good result, making it appropriate to use the point dipolar approximation for Gd and, probably, for half-filled configurations such as f^7 and d^5.

7.5 Spin Hamiltonians

In the above treatment we have used only spin operators, following a well-defined procedure that is based on the so-called Spin Hamiltonian (SH) approach. One fundamental assumption of SH is that the ground states of both ions are orbitally nondegenerate. This is equivalent to saying that there is no orbital component in the ground state. It should be clear that we are in trouble with all the RE ions, except gadolinium, because the large orbital momentum of the free ions is only partially quenched by the weak LF. A simple approach is the one that has been reported for Yb pairs in $CsCdBr_3$. The interest for the system is that it shows intrinsic optical bistability (IOB).This means that for a single input intensity two stable transmission or emission intensity values are observed (Hehlen *et al.*, 1999). This is an interesting phenomenon for understanding optical switching. $CsCdBr_3$ has hexagonal structure containing linear arrays of face-sharing $CdBr_6$ octahedra, well separated from the other chains. The Yb ions enter the lattice only in pairs, with a majority of symmetric Yb ions separated by a vacancy, RE–vacancy–RE, due to strict charge compensation. The Gd pairs were also investigated, with the scheme described above. The isotropic component is exceedingly weak, and anisotropic one is significantly larger. The experimental data show a Gd–Gd distance of 6.0 Å, which is shorter than the Cd–Cd distance, due to the strain induced by charge compensation.

The ground state of the Yb center is a Kramers doublet, given by a linear combination of M components of the lowest multiplet $^2F_{7/2}$. The $J = 7/2$ ground state is split by the LF of trigonal symmetry into four Kramers doublets. If we neglect the other Kramers doublets, we can describe the properties of the ground one as if it were an $S = 1/2$ state with the two effective components $|\pm 1/2\rangle$. In this case, the g-values are no longer isotropic. If the external magnetic field makes an angle θ with the trigonal axis, and choosing a coordinate system x', y' and z', where the **g** tensors are diagonal, the effective Hamiltonian can be written as outlined in Section 7.6. The fit of the experimental data is excellent, and requires $R = 5.88$ Å,

which is rather close to what was found for Gd. Also, the isotropic exchange J is similar for Gd ($6 \times 10^{-4}\,cm^{-1}$) and Yb ($16 \times 10^{-4}\,cm^{-1}$). We notice that for isotropic **g** the tensor is traceless; on relaxing this condition, the trace becomes different from zero.

The best fit g-values are $g_{||} = 2.503$ and $g_{\perp} = 2.619$; the effective values are related to the true ones depending on the coefficients in the lowest Kramers doublet:

$$|\mp\rangle = \pm a \left|\frac{7}{2}, \pm\frac{1}{2}\right\rangle \pm b \left|\frac{7}{2}, \pm\frac{7}{2}\right\rangle \mp c \left|\frac{7}{2}, \mp\frac{5}{2}\right\rangle \tag{7.15}$$

where the functions are defined through the eigenvalues of J_z, M_j. States with $M_j = 3/2$ are excluded because they do not mix with the others in trigonal symmetry. Standard calculations yields

$$g_{||} = g_J(-a^2 - 7b^2 + 5c^2); \quad g_{\perp} = g_J(4a^2 - 2\sqrt{7}bc) \tag{7.16}$$

After having given a simple presentation of the spin case, the techniques used to cope with the problems of orbital contribution are described in Section 7.10.

7.6 The Giant Spin

In many cases, such as, for instance, in polynuclear systems, the SH is a sum of contributions centered on different ions or magnetic centers. For instance, it is quite common in SMMs (single molecule magnets) to use a SH that contains the interactions between the spins of the building blocks. It is also necessary to include terms that describe the properties of the individual building blocks. Let us have a look at what is going on in this field, what is definitely well defined and understood, and what requires further elaboration.

A general scheme for a system of N spins is based on the use of the Hamiltonian in Eq. (7.17), where $\mathcal{H}_i$ includes all the operators defined within the i-brick, while $\mathcal{H}_{ij}$ contains all those operating on the ij pair and the sum is extended to all the pairs of the system under investigation.

$$\mathcal{H} = \sum_i \mathcal{H}_i + \sum_{ij} \mathcal{H}_{ij} \tag{7.17}$$

For example, in $\mathcal{H}_i$ there are the i-brick Zeeman, ZFS (zero-field splitting), hyperfine, and so on, while in $\mathcal{H}_{ij}$ there all the terms related to the exchange magnetic interaction. The types of SH are numerous, but essentially all of them rely on states that depend on the LF.

They are defined on one center and provide the energies of the LF states in the assumption of a strong or a weak field. Strong and weak refer to LF, compared to electron repulsion. Generally they exploit symmetry. The operators refer to one or more centers. The single ion case is relatively simple, and generally provides the levels of the single ion to be compared with experimental data associated to magnetic properties, ESR, NMR, and so on.

7.7
Single Building Block

This is a rather well-defined area. It covers the description of the magnetic properties of isolated magnetic centers and, of course, is not limited to slowly relaxing systems. The relative roles of electron repulsion, spin–orbit coupling (SOC), and LF are well defined and understood. For describing the magnetic properties of Ln, usually the lowest lying J multiplet is sufficient, thereby keeping the complications to a minimum. Matters change if one is interested at luminescence properties, which require the energies of the excited states. While working on the ground J multiplet requires operating on relatively small basis sets, complete sets required for accurate calculations are much more demanding. But the current software and hardware facilities allow us to perform what is needed.

The common approach to LF formalism makes explicit use of operator equivalents and similar others. Beyond the intrinsic difficulties of a difficult technique, it is the use of so many different approaches by numerous authors that reminds one the Babel tower. Let us hope that the rapid improvement of *ab initio* techniques will convince people of the beauty of one language.

Additional terms are needed depending on the properties one is interested in. For magnetism, one needs the Zeeman term, which we should call *electron Zeeman*. Magnetic nuclei may be present: for instance, protons which are almost ubiquitous in molecular magnets. These require the introduction in H_i terms associated with nuclei-based interactions such as nuclear Zeeman, nucleus–electron, and nucleus–nucleus. A possible SH for one building block is

$$\mathscr{H} = \mathscr{H}_{\mathrm{z}} + \mathscr{H}_{\mathrm{zfs}} + \mathscr{H}_{\mathrm{hyp}} + \mathscr{H}_{\mathrm{Zn}} \tag{7.18}$$

where $\mathscr{H}_{\mathrm{z}}$ is the electron Zeeman term, $\mathscr{H}_{\mathrm{zfs}}$ is the single ion ZFS, $\mathscr{H}_{\mathrm{hyp}}$ is the hyperfine term, and $\mathscr{H}_{\mathrm{Zn}}$ is the nuclear Zeeman terms.

7.8
Multicenter Interactions

The field of interactions in principle contains all the Hamiltonians of the individual building blocks plus the new ones described by the interactions. So the terms described in the previous sections are certainly to be included. Concerning the pair interaction, instead of Eq. (7.1) one can also use a more general Hamiltonian:

$$\mathscr{H} = \mathrm{J}\mathscr{S}_1\mathscr{S}_2 + \mathscr{S}_1 \cdot \mathscr{D}_{12} \cdot \mathscr{S}_2 + \mathrm{d}_{12} \cdot \mathscr{S}_1 \mathrm{x} \mathscr{S}_2 \tag{7.19}$$

The first two terms have been already introduced and refer to isotropic and anisotropic interactions. The third is the antisymmetric interaction, which tends to orient the spins orthogonal to each other. While the isotropic and anisotropic interactions have no strict symmetry requirements, the antisymmetric one is incompatible with S_n operations. We recall that S_1 is equivalent to an inversion center and S_2 to C_s.

An important question to be answered is there any relation between the SH parameters of the pair and those of the individual centers. A simplified case is represented by the so-called strong exchange, which means that the $J\mathcal{S}_1 \cdot \mathcal{S}_2$ is dominant in determining the energies of the pair. The ground state is either $S = S_1 + S_2$ or $|S_1 - S_2|$, and the energies of the $2S + 1$ states can be calculated using perturbation approaches. In particular, the SH parameters of the pair can be calculated by projecting the corresponding parameters on the total spin.

$$g_{\text{pair}} = c_1 g_1 + c_2 g_2; \quad D_{\text{pair}} = d_1 D_1 + d_2 D_2 + d_{12} D_{\text{pair}} \tag{7.20}$$

with

$$c_1 = \frac{(1+c)}{2}; \quad c_2 = \frac{(1-c)}{2}$$

$$d_1 = \frac{(c_+ + c_-)}{2}; \quad d_2 = \frac{(c_+ - c_-)}{2}; \quad d_{12} = \frac{(1-c_+)}{2}$$

$$c = \frac{[S_1(S_1+1) - S_2(S_2+1)]}{S(S+1)}$$

$$c_+ = \{3[S_1(S_1+1) - S_2(S_2+1)]^2 + S(S+1)$$
$$[3S(S+1) - 3 - 2S_1(S_1+1) - 2S_2(S_2+1)]\}/[(2S+3)(2S-1)S(S+1)]$$

$$c_- = \left\{\left(4S(S+1)\left[S_1\left(S_1+1\right) - S_2\left(S_2+1\right)\right]\right) - 3\left[S_1\left(S_1+1\right) - S_2\left(S_2+1\right)\right]\right\}/$$
$$[(2S+3)(2S-1)S(S+1)]$$

The opposite case of weak exchange is more difficult to generalize, with each individual case being unique. The case of dominant dipolar interaction, however, is important because of the possibility of using it for obtaining structural information, as we will show below.

When we pass to three centers, there are two different possibilities which are not equivalent but can be used according to the knowledge one has of the compound under consideration. The first alternative is obvious: introduce the new centers considering the pairs 1–2, 1–3, and 2–3. It is a straightforward procedure which increases rapidly in complexity, the number of states to be included having been discussed above. The alternative is that of using hand-waving arguments to guess the nature of the ground state and assuming that its S-value affords a reasonable description of the properties that depend on the low-lying levels. This is generally called the *giant spin approach* and is widely used. In fact, it was used for the first time in Mn_{12}, because of the following considerations.

The system that has been most investigated with the big spin formalism is the archetypal SMM Mn_{12}. We recall that the molecule comprises 8 Mn^{3+} and 4 Mn^{4+} each with each with $S = 3/2$. The 12 centers have been divided into three sets: a core spin (S_{core}) consisting of four Mn^{4+} ions in an isotropic cubane core, a rim spin (S_{rim}) formed by seven Mn^{3+} coupled into a horseshoe shape, and a keystone Mn^{3+} spin (S_{JT}). The sketch of the structure is given in Figure 7.13. If we assume

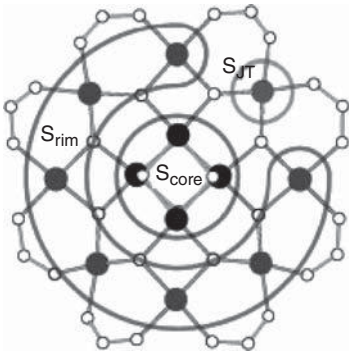

Figure 7.13 Grouping of component spins in a Mn_{12} molecule. (Reproduced from Nakano, M. and Oshio, H. (2011) with permission from The Royal Society of Chemistry.)

that the eight spin S = 2 are ferromagnetically coupled, they bring a contribution corresponding to S = 16 to the spin of the ground state (Nakano and Oshio, 2011).

By working out the same scheme for the Mn^{4+}, intra set ferromagnetic coupling yields an intermediate S = 6. Finally, an AFM coupling between the two sets yields the desired $S_T = 10$. The anisotropy of the system can be associated with the ZFS of the S_T, which is related to those of the individual spins.

It is important to gain knowledge of the anisotropy, which is due to the projection on the $S_T = 10$ giant spin of the anisotropy of the single Mn^{3+} ions. The Mn^{4+} ions are essentially isotropic and do not contribute much. The Mn^{3+} are axially symmetric due to the Jahn – Teller effect and the local D are essentially parallel to each other. The ZFS tensors are collinear, and it is possible to express the total D_T as a sum of local D_i using

$$\mathscr{H} = J\mathcal{S}_3 \cdot \mathcal{S}_4 \tag{7.21}$$

where $\mathcal{S}_3$ is the total spin operator on the eight Mn^{3+} ions, $\mathcal{S}_4$ is the analogous operator on the four Mn^{4+} ions. As a consequence $S_3 = 16$ and $S_4 = 6$ and, being J > 0, the S_T is equal to 10. In this simplified scheme, the $S_3 = 16$ state has $D = d_{16}$ D_i, where d_{16} is calculated by projecting the individual S of Mn^{3+} on S_3. The last step is the projection of S_3 on S_T, which yields

$$D = \frac{595D_3}{253} \tag{7.22}$$

It is apparent that it is a very approximate procedure, but it provides a rational approach. For instance, it allowed the calculation of the effect of flipping one D_i vector from the tetragonal axis to the perpendicular in order to justify the presence of impurities, which relax faster than the bulk in Mn_{12}.

7.9 Noncollinearity

The relative orientations of the local anisotropies are very important because they can give rise to unique properties. The noncollinear case is often met, and of

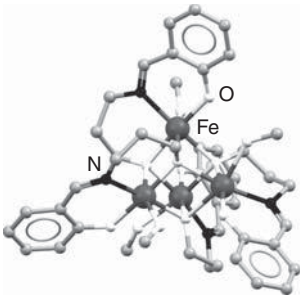

Figure 7.14 Structure of $[Fe_4(sae)_4(MeOH)_4]$ (H_2sae = 2-(4-hyroxysalicylidenamino)ethanol). Hydrogen atoms are omitted for clarity.

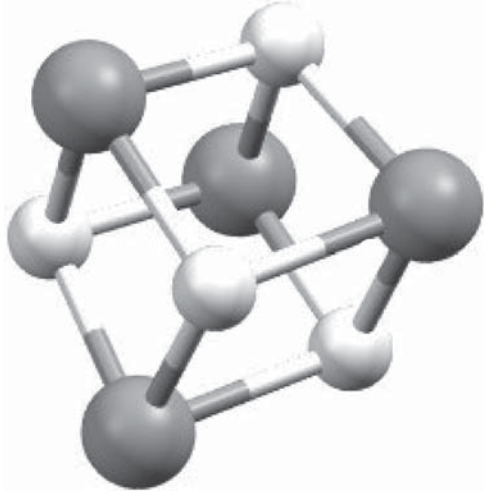

Figure 7.15 Fe_4O_4 core with a cubane arrangement.

course this gives rise to additional problems when trying to justify the anisotropy of the cluster, or of the chain, as a sum of contributions of local anisotropies. An interesting example of this behavior was found in some members of the cubane family (Shiga and Oshio, 2005). First of all, let us recall what noncollinear means. Imagine a tetrahedron of iron(II) ions bridged by four oxygen atoms forming a Fe_4O_4 cubane, as shown in Figure 7.14, while the Fe_4O_4 core is reported in Figure 7.15 (Oshio *et al.*, 2004). Each ion has an anisotropy axis which may or may not coincide with those of the other ions. The anisotropy of the cluster will depend on whether the local axes are collinear or not. In order to have an SMM, an easy-axis is required at the level of the cluster. A possible way to achieve this goal is by controlling the local anisotropy and then controlling the way these arrows are oriented in the clusters.

The above cubane has S_4 symmetry with local hard axes (Figure 7.16), and the Fe ions are ferromagnetically coupled to give an S = 8 spin ground state. The strong field approximation, which we have introduced in the previous paragraph, allows treating the system in some detail.

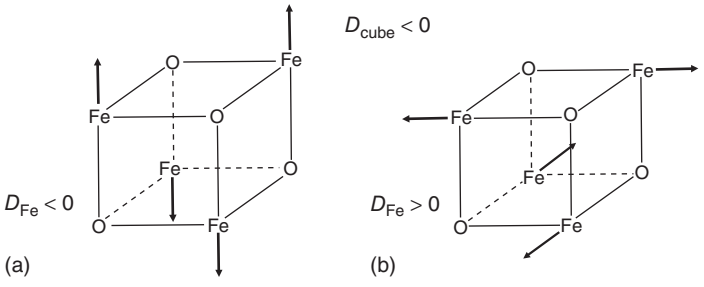

Figure 7.16 Collinear easy-axis ($D_{Fe} < 0$) alignment (a) and orthogonal hard-axis ($D_{Fe} > 0$) alignments (b) required for the negative D_{cube} value. (Reproduced from Oshio, H. *et al.* (2004) with permission from The American Chemical Society.)

The two limiting cases correspond to noncollinear and collinear axes, respectively. The interest for this type of clusters is in the design of molecules with a negative ZFS. Actually, the analysis of the magnetic measurements on the Fe_4O_4 derivative are consistent with a $D_{Cube} < 0$. This negative value might be originated either by a collinear easy axis arrangement ($D_{Fe} < 0$, Figure 7.16a) or by the presence of orthogonal hard axis ($D_{Fe} > 0$, Figure 7.16b). The D sign inversion is determined by the change in local orientation of the single ion tensors.

7.10 Introducing Orbital Degeneracy

We cannot conclude this section without saying something on the description of systems with orbital degeneracy in the ground state. It is just the case to repeat the old saying: *in cauda venenum.* Since there is not much systematic work done, we will report examples that look significant.

The assumption on which the SH is based is that the ground state is orbitally nondegenerate. If we look, for example, at first-row TMs in octahedral symmetry, we see that this condition is met only in cases that are reported in Table 7.2.

Table 7.2 Electronic ground states of transition-metal ions under O_h and D_{4h} environments.[a)]

	d^1	d^2	d^3	d^4	d^5	d^6	d^7	d^8	d^9
Elongated D_{4h}	^2E_g	$^3A_{2g}$ (+)	$^4B_{1g}$ (+)	$^5B_{1g}$ (−)	$^6A_{1g}$ (+)	^5E_g	$^4A_{2g}$ (+)	$^3B_{1g}$ (+)	$^2B_{1g}$
Octahedral O_h	$^2T_{2g}$	$^3T_{1g}$	$^4A_{2g}$	^5E_g	$^6A_{1g}$	$^5T_{2g}$	$^4T_{1g}$	$^3A_{2g}$	^2E_g
Compressed D_{4h}	$^2B_{2g}$	^3E_g	$^4B_{1g}$(−)	$^5A_{1g}$ (+)	$^6A_{1g}$ (−)	$^5B_{2g}$ (+)	^4Eg	$^3B_{1g}$(−)	$^2A_{1g}$

a) Metal ions with d^4-d^7 configurations are in the high-spin states. (+) and (−) signs denote ions possessing positive and negative *D* values, respectively, if the ground state is not a Kramers doublet and the orbital degeneracy is fully quenched.

The orbitally nondegenerate cases are seventeen, while the degenerate ones are ten. Of course, low-symmetry components may remove the degeneracy, and indeed the condition that justifies the SH approach previously introduced. Here we will report some examples where attempts have been made to obtain a view of the mechanism needed to justify the formalism

An efficient way of taking into account orbital degeneracy is due to Lines, and the method is generally called the *Lines model* (Lines, 1971). The model was worked out for a T level of octahedral symmetry, and in particular for high spin cobalt(II), whose ground state is $^4T_1$ in *O* symmetry, by introducing a formalism that is still used. The key assumption is that the ground state for the 12 states belonging to $^4T_1$ when SOC is included is a Kramers doublet, and the separation of the excited states is large. This seems to be hazardous, but it may be useful to tackle in some quantitative way the difficulties associated with orbital degeneracy. The SOC is calculated using the similarity of the T_1 state with the L orbital operator. The three orbital components of T_1 behave as the eigenfunctions of L_z, and the calculated energies in the two schemes give the same results if a correction $-kL$ is used where the parameter k is dimensionless and less than unity and represents a reduction of free-ion spin-orbit coupling.

Using the $|m_L m_S>$ notation for the eigenfunctions, the ground state of the single ions is a linear combination of $|\pm1\pm3/2\rangle$, $|0\pm1/2\rangle$, and $|\pm1\pm1/2\rangle$. In order to take into account the interaction between pairs, a Co–Co Heisenberg exchange between S_i and S_j is introduced. Additional terms allow for the existence of an external applied magnetic field H_0 (in a direction z, say), and the energies of the levels for $S = 3/2$ are obtained by diagonalizing the Hamiltonian

$$\mathcal{H} = \sum_{\text{pairs}} J\mathcal{S}_i \cdot \mathcal{S}_j - \sum_i \mu_B H_0 \left[2\mathcal{S}_i^z - \left(\frac{3}{2} k\mathcal{L}_i^z\right)\right] \tag{7.23}$$

Unfortunately, in view of the size of the matrix involved (formally $12^m \times 12^m$, although some reduction is possible), exact diagonalization is in general almost impossible and it becomes necessary to look for an adequate statistical approximation in order to attack the magnetic susceptibility problem.

A frequently used approximation involves focusing on the lowest Kramers doublet. Operating on the above-defined ground level, it is useful to use the Pauli matrices for spin 1/2:

$$S_x \equiv \begin{pmatrix} 0 & q \\ q & 0 \end{pmatrix} \quad S_y \equiv \begin{pmatrix} 0 & -iq \\ iq & 0 \end{pmatrix} \quad S_z \equiv \begin{pmatrix} q & 0 \\ 0 & -q \end{pmatrix} \tag{7.24}$$

where $q = 5/6$. The energies of the spin states are given by

$$E(S,\ M) = \left(\frac{25}{18}\right) J \left[S(S+1) - \left(\frac{3m}{4}\right)\right] - g_0 \mu_B H_0 M \tag{7.25}$$

where S for a pair is 0 and 1; for three spins 1/2, 1/2, and 3/2; and so on.

The model was felt to be inadequate and the results confirmed this view. Much better results were obtained by allowing for a temperature-dependent contribution from a fictitious ground doublet. This was done by replacing the fixed

Table 7.3 Matrix elements for an S = 3/2 isotropic system.

	$\|+3/2\rangle$	$\|+1/2\rangle$	$\|-1/2\rangle$	$\|-3/2\rangle$
$\|+3/2\rangle$	$D+\frac{9g\mu_B H_z}{4}$	$\frac{\sqrt{3}\mu_B H_x}{2}$	0	0
$\|+1/2\rangle$	$\frac{\sqrt{3}\mu_B H_x}{2}$	$-D+\frac{g\mu_B H_z}{4}$	$g\mu_B H_x$	0
$\|-1/2\rangle$	0	$g\mu_B H_x$	$-D-\frac{g\mu_B H_z}{4}$	$\frac{\sqrt{3}\mu_B H_x}{2}$
$\|-3/2\rangle$	0	0	$\frac{\sqrt{3}\mu_B H_x}{2}$	$D-\frac{9g\mu_B H_z}{4}$

g-value with a variable one determined by the temperature-dependent admixture of excited single ion states. The corresponding SH is

$$\mathscr{H} = \left(\frac{25}{9}\right)\sum_{i,j}\frac{1}{2}\mathrm{J}\,\mathcal{S}_i\cdot\mathcal{S}_\mathrm{J} - g(T)\mu_\mathrm{B}H_0\sum_i \mathcal{S}_i^z \tag{7.26}$$

and the results of fitting the experimental values were acceptable. The key feature is the use of effective g-values, which often are strongly anisotropic. We want to stress that the true g-values are not that much anisotropic. Let us try to explain what we mean by this. Let us suppose that we have a system with $\mathrm{S} = 3/2$, isotropic g, and axial ZFS. The SH is

$$H = \mathrm{D}\mathcal{S}_z^2 + g\mu_\mathrm{B}\cdot\mathcal{S}_z H_z \tag{7.27}$$

Let us suppose we scan a magnetic field in the xz plane. The matrix is given Table 7.3.

The calculated energies for fields parallel to the x- and z-axis are shown in Figure 5.1.

The Kramers doublets are symmetry-degenerate in zero field, while systems with even numbers of electrons are not symmetry-degenerate in pairs but can be accidentally degenerate. And one level is always nondegenerate.

The consideration that the Ln levels reduce to a ladder (irregular) of doublets (rigorous or casual) allows a great simplification for calculating the magnetic properties. For instance, the susceptibility of an isolated Ln is calculated as (Lukens and Walter, 2010):

$$\chi_{\mathrm{iso},\alpha} = \frac{N\mu_\mathrm{B}^2}{3kT}\frac{\sum_n (2\mathrm{S}_n+1)[\mathrm{S}_s(\mathrm{S}_n+1)^2\, g_{n,\alpha}^2 - 2Z_n kT]\mathrm{e}^{-\frac{E_n}{kT}}}{\sum_n (2\mathrm{S}_n+1)\mathrm{e}^{-\frac{E_n}{kT}}} \quad (\alpha = x \text{ or } z) \tag{7.28}$$

where the sum is over all the thermally populated states, S_n is the effective spin, g_n is the effective Zeeman factor, E_n is the energy of the doublet (singlet), and Z_n is the second-order Zeeman term. With these values, the coupled system is characterized by the interaction SH:

$$\mathscr{H}_\mathrm{ex} = \mathrm{J}\mathcal{S}_a\cdot\mathcal{S}_b - \mathcal{S}_a\cdot\Lambda\cdot\mathcal{S}_b \tag{7.29}$$

which corresponds to Eq. (7.19), after neglecting antisymmetric exchange and where Λ is the traceless anisotropy tensor with $-\Lambda zz/2 = \Lambda xx = \Lambda yy/2$. The off-diagonal elements are equal to 0 in presence of an axial symmetry. By adding the Zeeman term, finally one finds

$$\mathcal{H} = g_J \mu_B (H\mathcal{J}_a + H\mathcal{J}_b) + (g_J - 1)^2 (J\mathcal{J}_a \cdot \mathcal{J}_b - \mathcal{J}_a \Lambda \mathcal{J}_b) \tag{7.30}$$

where J_a and J_b are the projection of the individual spins on the angular momentum as $S_i = (g_J - 1)J_i$.

After a few steps, it is possible to reach the resolution of the SH in an explicit form which has the expression for the magnetic susceptibility reported below

$$J_z = \frac{D_{dd}}{3} + \frac{g_z^2 (g_J - 1)^2}{g_J^2} \left(J + \frac{\Lambda_{zz}}{2} \right) \tag{7.31}$$

$$= \frac{D_{dd}}{3} + \frac{g_z^2 (g_J - 1)^2}{g_J^2} (J - \Lambda_{xx}) \tag{7.32}$$

$$J_x = -\frac{D_{dd}}{6} + \frac{g_x^2 (g_J - 1)^2}{g_J^2} \left(J + \frac{\Lambda_{xx}}{2} \right) \tag{7.33}$$

$$D_{dd} = (2g_z^2 + g_x^2) \frac{\mu_B^2}{2r^3} \tag{7.34}$$

$$\chi_{\alpha,\text{pair}} = \frac{N\mu_B^2}{3kT} \frac{\sum_n F_\alpha(J_n, g_n, T)(2S_n + 1)[S_n(S_n + 1)g_{n,\alpha}^2 - 2Z_n kT] e^{-\frac{E_n}{kt}}}{\sum_n (2S_n + 1) e^{-\frac{E_n}{kt}}} \quad (\alpha = x \text{ or } z)$$

where a scheme of the low-lying levels of the pair is shown in Figure 7.17.

From the treatment outlined, it is possible to stress the relevance of the single ion anisotropy that can be expressed on the basis of the g_x/g_z ratio expressed with the γ parameter. An experimental investigation was made on $Ce_2(COT)_3$ (COT, cyclooctatetraene) and $[Ce(COT)_2]^-$ derivatives (Walter *et al.*, 2009). The latter is magnetically isolated corresponding to one Ce_{3+}, while the former corresponds to a pair of Ce_{3+}. The appealing feature is that both compounds are ESR active, a rather uncommon characteristic. The cerium derivative shows a spectrum that can be assigned to an effective $S' = 1/2$ with $g_z = 1.12$, $g_x = 2.27$, and $\gamma = 2.02$. Ce_{3+} is expected to have a $^2F_{5/2}$ ground state in a tetragonal LF, which is split into three Kramers doublets which are expected to have the following parameters:

M_J	$g_{\|\|}$	$g_\perp$
±1/2	6/7 = 0.86	18/7 = 2.57
±3/2	18/7 = 2.57	0
±5/2	30/7 = 4.29	0

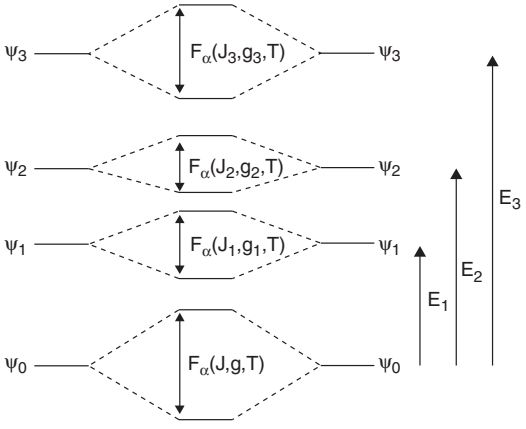

Figure 7.17 Qualitative diagram illustrating the splitting of the low-lying states of a pair of coupled f-ions along a given axis, α, where α is x, y, or z. The splitting due to coupling is exaggerated for clarity; J is generally much smaller than E_n. (Reproduced from Lukens, W.W. and Walter, M.D. (2010) with permission from The American Chemical Society.)

The experimental g-values are effective values. The values are close to those of the $M = 1/2$ Kramers doublet. In tetragonal symmetry, the three Kramers doublets are pure states because only states differing by 4 can be admixed. By introducing a binary symmetry in agreement with the structural data and the admixture with excited states, the corrected ground state becomes a $|1/2\rangle + b|1/2\rangle$, and the spectra of Ce_2 agree with a triplet whose fitting parameters are $g_{||} = 0.974$, $g_{\perp} = 2.335$.

A similar approach has been recently used for systems containing pairs of Ln where it is possible to have the mixed metal species containing a diamagnetic Ln. The idea was to obtain direct information on the isolated ion by diamagnetic dilution. The technique has been widely used, for instance, in the ESR of dinuclear systems. A variant was employed by Kahn *et al.* in polynuclear Ln nitroxide derivatives in which the diamagnetic effect is generated by the substitution of the nitroxide with a nitrone. More details are given in Chapter 9.

An attempt to investigate in detail some Cu–Ln (Ln = Tb, Dy, Ho, Er) deserves some consideration (Kajiwara *et al.*, 2011). The structure shown in Figure 7.18 has a copper coordinated by a Schiff base ligand bridging the Ln with two phenoxo groups. Copper is five-coordinated with an axial nitrate, while Ln_{3+} ion is nine-coordinated by oxygen atoms.

The four lanthanide derivatives are isomorphous, but their magnetic properties are different. The compounds containing Cu–Tb and Cu–Dy pairs showed SMM behavior, with energy barriers (U_{eff}) estimated from the Arrhenius plots as 22.9 and 18.1 cm^{-1} respectively. The Ho derivative exhibits a slow magnetic relaxation below 3.0 K, while the frequency-dependent behavior of the complex with Er indicated that easy-axis anisotropy was absent. Taking advantage of the fact that

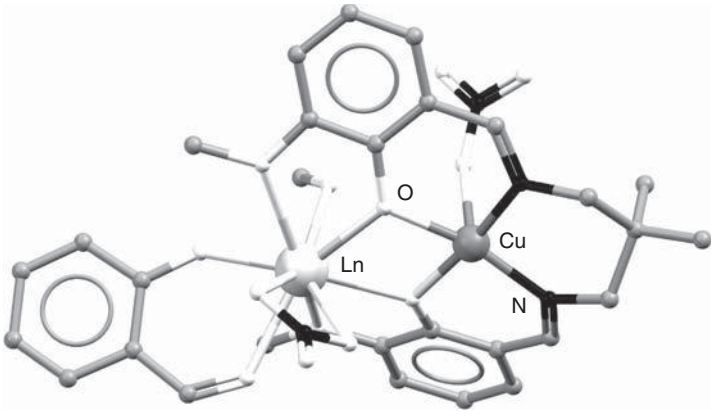

Figure 7.18 A view of the $[LnCu(NO_3)_3(L)(H_2O)]$ (L = *o*-vanilate anion). Hydrogen atoms are omitted for clarity.

the compounds crystallize in the triclinic group, a detailed analysis was performed to define the anisotropy properties of the magnetic susceptibility. The novelty of the study was that the measurement of the temperature dependences of the DC susceptibility were investigated for aligned microcrystalline samples with the aim of determining the magnetic anisotropy parameters in a CF (crystal field) framework. This approach was possible because, by crystallizing the complexes in $P\bar{1}$ space group, all the molecules in the crystal have the same molecular axis pointing in the same direction. The $A_n^0\langle r^n \rangle$ parameters derived by a fitting procedure of the magnetic data are representative of an easy-axis anisotropy for the Tb, Dy, and Ho derivatives and an easy-plane anisotropy for the Cu–Er pair.

This has been a hard chapter, which deserves some comment. The start has been the basic knowledge of the HDVV within the SH formalism. The isotropic and anisotropic terms were discussed, and the dipolar term was evaluated in an inorganic frame. The roles of exchange and dipolar terms in anisotropic contributions were shown to be comparable.

The SH was again taken into consideration, but it does not require further comments because its relevance is obvious. Some comments, instead, for noncollinearity seem obvious, but we will soon discover that it is a protagonist in many cases.

The introduction of orbital degeneracy makes an important point for Ln, and the reported examples a key to describing many compounds. In this case, more than in others, it would be possible, and perhaps should be possible, to write much more or much less.

References

Costes, J.-P., Clemente-Juan, J.M., Dahan, F., Nicodème, F., and Verelst, M. (2002) Unprecedented ferromagnetic interaction in homobinuclear erbium and gadolinium complexes: structural and magnetic studies. *Angew. Chem.*, **114**, 333–335.

Gu, X. and Xue, D. (2007) Surface modification of high-nuclearity lanthanide clusters:

two tetramers constructed by cage-shaped {Dy26} clusters and isonicotinate linkers. *Inorg. Chem.*, **46**, 3212–3216.

Hehlen, M.P., Kuditcher, A., Rand, S.C., and Lüthi, S.R. (1999) Site-selective, intrinsically bistable luminescence of Yb^{3+} ion pairs in $CsCdBr_3$. *Phys. Rev. Lett.*, **82**, 3050–3053.

Ising, E. (1925) Beitrag zur theorie des ferromagnetismus. *Z. Angew. Phys.*, **31**, 253–258.

Jánossy, A., Simon, F., Fehér, T., Rockenbauer, A., Korecz, L., Chen, C., Chowdhury, A.J.S., and Hodby, J.W. (1999) Antiferromagnetic domains in $YBa_2Cu_3O_{6+x}$ probed by Gd^{3+} ESR. *Phys. Rev. B: Condens. Matter*, **59**, 1176–1184.

Kajiwara, T., Nakano, M., Takahashi, K., Takaishi, S., and Yamashita, M. (2011) Structural design of easy-axis magnetic anisotropy and determination of anisotropic parameters of Ln(III)-Cu(II) single-molecule magnets. *Chem. Eur. J.*, **17**, 196–205.

Kosterlitz, J.M. and Thouless, D.J. (1973) Ordering, metastability and phase transitions in two-dimensional systems. *J. Phys. C: Solid State Phys.*, **6**, 1181–1203.

Lines, M.E. (1971) Orbital angular momentum in the theory of paramagnetic clusters. *J. Chem. Phys.*, **55**, 2977.

Lukens, W.W. and Walter, M.D. (2010) Quantifying exchange coupling in f-ion pairs using the diamagnetic substitution method. *Inorg. Chem.*, **49**, 4458–4465.

McElearney, J.N., Losee, D.B., Merchant, S., and Carlin, R.L. (1973) Antiferromagnetic ordering and crystal field behavior of $NiCl_2$ $4H_2$ O. *Phys. Rev. B*, **7**, 3314–3324.

Müller, A., Todea, A.M., Bögge, H., Van Slageren, J., Dressel, M., Stammler, A., and Rusu, M. (2006) Formation of a "less stable" polyanion directed and protected by electrophilic internal surface functionalities of a capsule in growth: $[(Mo_6O_{19})^{2-} \subset (Mo(VI)_{72}Fe(III)_{30}O_{252}(ac)_{20}(H_2O)_{92})]^{4-}$. *Chem. Commun.*, 3066–3068.

Nakano, M. and Oshio, H. (2011) Magnetic anisotropies in paramagnetic polynuclear metal complexes. *Chem. Soc. Rev.*, **40**, 3239–3248.

Oshio, H., Hoshino, N., Ito, T., and Nakano, M. (2004) Single-molecule magnets of ferrous cubes: structurally controlled magnetic anisotropy. *J. Am. Chem. Soc.*, **126**, 8805–8812.

Shiga, T. and Oshio, H. (2005) Molecular cubes with high-spin ground states. *Sci. Technol. Adv. Mater.*, **6**, 565–570.

Simon, F., Rockenbauer, A., Fehér, T., Jánossy, A., Chen, C., Chowdhury, A.J.S., and Hodby, J.W. (1999) Measurement of the Gd–Gd exchange and dipolar interactions in $Gd_{0.01}Y_{0.99}Ba_2Cu_3O_6$. *Phys. Rev. B: Condens. Matter*, **59**, 12072–12077.

Walter, M.D., Booth, C.H., Lukens, W.W., and Andersen, R.A. (2009) Cerocene revisited: the electronic structure of and interconversion between $Ce_2(C_8H_8)_3$ and $Ce(C_8H_8)_2$. *Organometallics*, **28**, 698–707.

8
Molecular Orbital of Coupled Systems

8.1
Exchange and Superexchange

In this chapter, we will focus on the results of calculations of spin Hamiltonian (SH) parameters using basic theories such as *ab initio* and density functional theory (DFT). This is a field that has been explored using adequate theoretical models only in the past few years but the obtained results are quite encouraging. The background needed to justify the nature of the interaction responsible of the cooperative phenomena that make all varieties of physical properties so fascinating is still the approach first taken by Anderson in the early 1950s (Anderson, 1950, 1959). Here we summarize Anderson's model essentially to introduce the language that has been used ever since the introduction.

At the simplest possible level, let us assume two systems characterized by having one unpaired electron each. The systems can be general, but we will start from metal-containing moieties. They can be schematized as shown in Figure 8.1. We may assume that the ground state of the two systems, in the absence of interaction, is given by two orbitals φ_A and φ_B, which we will call *magnetic orbitals*. The system in zero-order approximation is assumed to be orbitally nondegenerate. The interaction between A(B) and C is weak in such a way that the electron density is mainly concentrated on the metal centers A and B, but spin polarization will give a nonzero density also on the bridging ligands. As we will see, this can be of paramount importance in determining the mechanism of interaction and the magnetic properties.

Switching on the interaction requires us to define excited states and their admixture with the ground ones. This can be done by defining charge transfer processes in which one electron is transferred from an orbital localized on A to one centered on B (and/or vice versa). For the moment, we may assume that there is one unpaired electron on each atom. There are two types of charge transfer processes: (i) from a half-filled orbital to a half-filled orbital, and (ii) from a half-filled orbital to an empty one. The energies involved in the charge transfer are the electron–electron Coulomb repulsion U, due to the presence of two electrons in the same orbital with high density on one metal ion. The other contribution is the electron transfer that is associated with the transfer integral between the

Introduction to Molecular Magnetism: From Transition Metals to Lanthanides, First Edition.
Cristiano Benelli and Dante Gatteschi.
© 2015 Wiley-VCH Verlag GmbH & Co. KGaA. Published 2015 by Wiley-VCH Verlag GmbH & Co. KGaA.

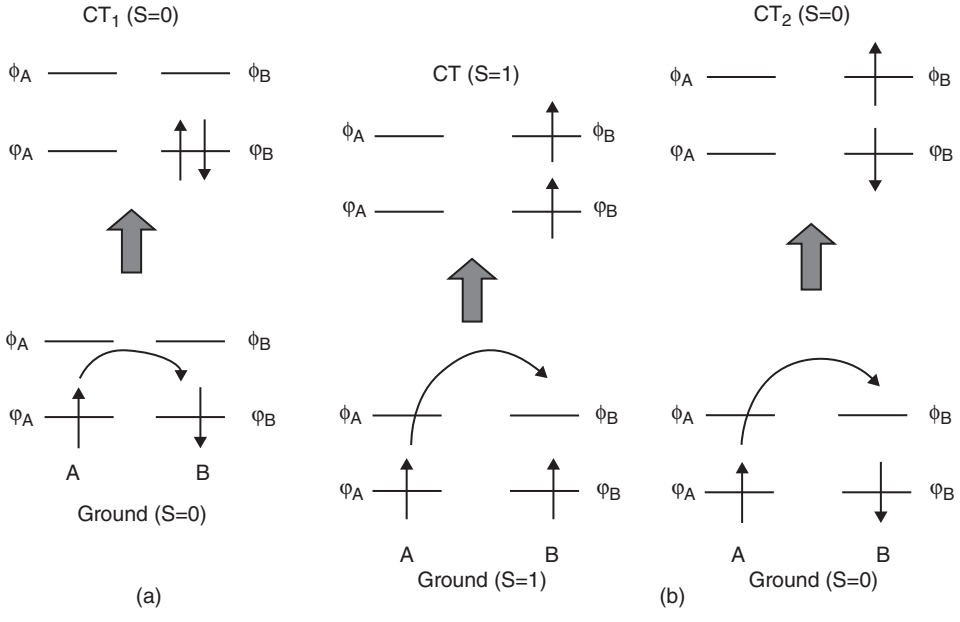

Figure 8.1 Schematic diagrams for the mechanism of the (a) antiferromagnetic and (b) ferromagnetic kinetic exchange: orbital population is in the ground spin-singlet state. (Reproduced from Palii, A. *et al.* (2011) with permission from The Royal Society of Chemistry.)

φ_A and φ_B orbitals, which is indicated by $t^2_{\varphi_A\varphi_B}$. This term depends on the kinetic energy of the electron and is called *kinetic exchange*. The excited state determined by charge transfer has an $S = 0$ state which is admixed with the corresponding one with $S = 0$ stabilizing it. For the charge transfer $\varphi_A \rightarrow \varphi_B$, the interaction energy is $\sqrt{2}t_{\varphi_A\varphi_B}$. The states generated by the transfer can be classified as singlet and triplet. By applying second-order perturbation theory, the contribution of the $\varphi_A \rightarrow \varphi_B$ charge transfer to the singlet–triplet separation is

$$E_{ST} = 4\, t^2_{\varphi_A\varphi_B}/U \tag{8.1}$$

where E_{ST} is the energy difference between the triplet and the singlet. This contribution is antiferromagnetic.

Other contributions arise from the other type of charge transfer, the one that involves a half-filled orbital and an empty one. The repulsion integral becomes U', and in the expression of the energy difference one must include the energy difference between the involved orbitals, Δ, and the intracenter exchange integral K. The calculated contribution to the single triplet separation is

$$E_{ST\varphi_A\rightarrow\varphi_B} = 2t^2_{\varphi_A\varphi_B}\left(\frac{1}{U'+\Delta-K} - \frac{1}{U'+\Delta+K}\right) \approx 4t^2_{\varphi_A\varphi_B}K/U^2 \tag{8.2}$$

This is the ferromagnetic contribution to the coupling.

Quite often, the AF term dominates because the two electrons occupy the same orbitals in a way that it is more efficient if the overlap between the two orbitals

is higher. We recall that one of the goals of molecular magnetism has historically been that of designing and synthesizing molecular ferromagnets. One can imagine the disappointment on obtaining antiferromagnetic coupling in most of the investigated systems. Strict control must be exerted to keep the magnetic orbitals orthogonal to each other and at the same time having regions in space where the overlap is nonzero. Equations (8.1) and (8.2) are qualitative guidance to imagine possible strategies in order to favor ferromagnetic coupling.

The model is strong for qualitative considerations and has opened the perspectives for designing molecular magnets. But Anderson's model was based on valence bond theory which was difficult to apply in chemistry. The development in the design of molecular magnets was based on models developed by Hay, Thibeault, and Hoffmann (1975) and by Kollmar and Kahn (1993). The vulgate made by the latter was of fundamental importance for bringing up a generation of chemists who were familiar with the qualitative molecular orbital (MO) model of exchange interaction.

The fundamental change was the development of DFT and *ab initio* techniques at the routine level. Let us have a look at these.

8.2
Structure and Magnetic Correlations: d Orbitals

Ferromagnetic coupling is necessary if one's aim is to obtain a molecular ferromagnet, but it is not mandatory if one wants to design systems with permanent magnetization. In fact, in this case it may be easier to design a molecular ferrimagnet by assembling two different magnetic moments. Even though they are antiferromagnetically coupled, the sum of the individual moments does not cancel to zero. In the 1980s, systematic attempts were made to develop correlations between structure and magnetic properties. The first attempts were using the Goodenough (1958) and Kanamori (1959) rules which summarized in a simple way the structural requirements to observe the required coupling: for the sake of simplicity, they are repeated here:

- The coupling between electrons in half-filled orbitals is antiferromagnetic and strong.
- The coupling between electrons in orthogonal orbitals is ferromagnetic and weak.
- The coupling between an electron in a half-filled orbital with zero (two) electrons in a filled (empty) orbital is weak ferromagnetic.

A variant was introduced by Kahn, who translated the Goodenough – Kanamori rules in a form more familiar to the MO-oriented language of coordination chemistry (Gillon *et al.*, 1989). The core of the Kahn's model is the overlap between the magnetic orbitals. It must be remarked that the language that is developed in this way is based on the use of natural orbitals, that is, of active orbitals that limit the number of correlated electrons. Actually, the treatment is semiquantitative at best,

but like ligand field (LF) all the types of guesses can be used. The impossibility of actually calculating the energies, and, even worse the electromagnetic properties, allows us to force the interpretations.

It must be stressed that the above rules hold if the overlap between the orbitals is direct or mediated by the overlap with formally full orbitals of the ligands. In the former case, one speaks of exchange; otherwise it is superexchange.

8.3 Quantum Chemical Calculations of SH Parameters

The first attempts to use quantum chemical calculations to obtain SH parameters in dinuclear species were focused on J_{AB}, the parameter defining the singlet–triplet separation in a system of two coupled $S = 1/2$ spins. For a long time, the only reported attempt was the pioneering *ab initio* work by De Loth (De Loth *et al.*, 1981). The difficulty was due to the need to accurately calculate a small number as the difference of two large numbers. This requires some assumptions which are difficult to control. The first positive signs were obtained using the B3LYP functional which provided reasonably good results at a reasonable price. One of the fundamental steps forward was the introduction of the so-called broken symmetry (BS) approach.

The most accurate treatment for the calculation of the low-lying levels of dinuclear, and in general polynuclear, magnetic systems is the so-called BS approach first suggested by Noodleman and Norman (1979). Within the BS approach, the energy of the low-spin state of the complex, that is the state mostly affected by static electron correlation effects, is approximately computed as a projection from a state of mixed spin and space symmetry (the BS state) obtained by an independent self-consistent field (SCF) calculation. The term *broken symmetry* refers to a state of the type $|S_A\ M_A\ S_B\ M_B\rangle$ which is not an eigenstate of the Hamiltonian. In this scheme, the value of J_{AB} is given by

$$J_{AB} = \frac{(E_{BS} - E_T)}{1 + S_{AB}^2} \tag{8.3}$$

where E_{BS} is the BS energy, E_T is the energy of the triplet, and S_{AB} is the overlap between the localized orbitals A and B.

For $S_1 = S_2 = 5/2$, the BS states are six. Explicitly, for the $S_i = 5/2$ case, the microstates involved are (5/2, −5/2), (−5/2, 5/2), (3/2, −3/2), (−3/2, 3/2), (1/2, −1/2), and (−1/2, 1/2), which can be rewritten as linear combinations of the total spin S eigenfunctions $|S_A\ M_A\ S_B\ M_B\ S\ M\rangle$, where $M = 0$ and $S = 0, 1, 2, 3, 4, 5$.

The value of the Heisenberg constant can be generalized to the case of two different spins:

$$J_{AB} = \frac{(E_{BS} - E_{HS})}{2S_AS_B + S_B} \tag{8.4}$$

where E_{HS} is the energy of the state of maximum multiplicity in the coupling. It was also assumed that $S_{AB} = 1$. The assumption on the overlap corresponds

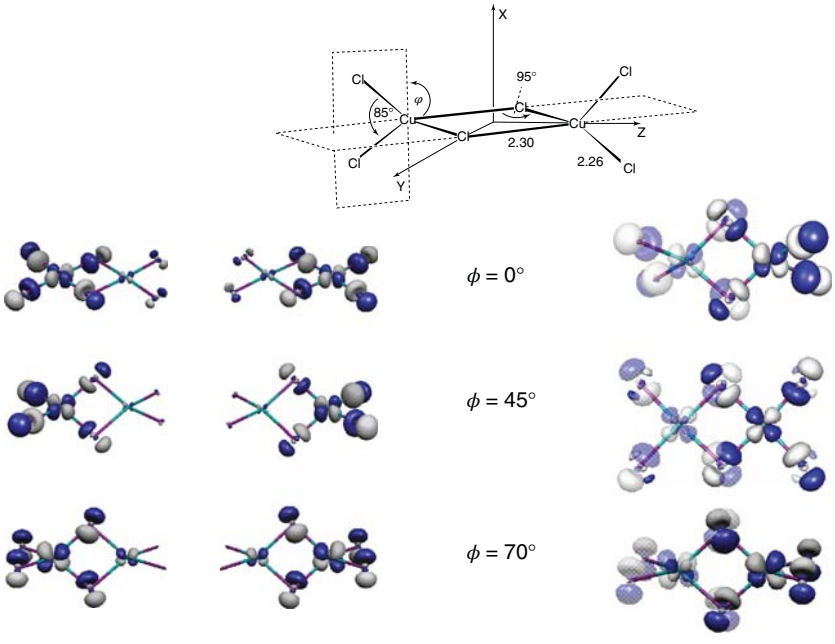

Figure 8.2 Isodensity surfaces of the magnetic orbitals of $[Cu_2Cl_6]^{2-}$ obtained from Xα-BS calculations at different φ values as defined molecular scheme in the top. Left: separate magnetic orbitals. Right: a representative view of the overlap between the magnetic orbitals (Bencini *et al.*, 1997). (Reproduced from Bencini, A. *et al.* (1997) with permission from The American Chemical Society.)

to maximum delocalization, or covalency effects. The opposed limit case corresponds to $S_{AB} = 0$, which gives the localized limit. An example of the two limit cases is provided in Figure 8.2 for $Cu_2Cl_6^{2-}$ dinuclear compounds. The results are based on the Xα method which was a precursor of DFT. We like to show them as a hommage to Alessandro (Sandro) Bencini whose early departure was a great loss for MM.

At the beginning, the results were disappointing because they were systematically larger than the experimental values. A modification was introduced in the way of projecting the BS UHF, which improved the agreement. The equation becomes

$$J_{AB} = \frac{2(E_{BS} - E_{HS})}{\langle S^2\rangle_{BS} + \langle S^2\rangle_{HS}} \tag{8.5}$$

where $\langle S^2\rangle_{BS}$ and $\langle S^2\rangle_{HS}$ are, respectively, the eigenvalues of the $\hat{S}^2$ operator for the BS and high-spin states.

Some examples of calculated results are shown for dinuclear species in Table 8.1.

The agreement between the observed and calculated values is satisfactory, and in some cases excellent. The agreement is so good using a simple approach that the possibility of error cancellation effects should be taken into account.

Table 8.1 Values of the through-bond J_{AB} exchange parameter computed using the B3LYP functional for some representative binuclear complexes. Novoa, Deumal, and Jornet-Somoza (2011).

Compound[a)]	J_{exp} (cm^{-1})	J_{DFT} (cm^{-1})
$[Cu_2(\mu\text{-}OH)_2(bipym)_2](NO_3)_2$	−114	−113
$[Ni_2(\mu\text{-}ox)(Medpt)_2(H_2O)_2](ClO_4)_2{\cdot}2H_2O$	+22	+27
$[CuVO(fsa)_2en]{\cdot}CH_3OH$	−118	−52
$[CuMn(obze)(H_2O)_4]{\cdot}2H_2O$	+34	+42

a) Bipym = 2,2′-bipyrimidine; Medpt = bis(3-aminopropyl)methylamine; $(fsa)_2$en = *N*,*N*′-(2-hydroxy-3-carboxybenzylidene)-1,2-diaminoethane; and obze = oxamido-*N*-benzoato-*N*′-ethanoato.

8.4 Copper Acetate!

In order to get familiar with the method, we find it extremely pedagogical to use copper acetate hydrate. Copper acetate has had a fundamental role in magnetochemistry and continues to provide deep insight into molecular magnetism. Let us go through the magnetic properties of copper acetate starting in 1951, when Guha reported the temperature-dependent magnetic susceptibility (Guha, 1951). It was completely different from what was expected for a d^9 ion with $S = 1/2$: it went through a broad maximum at about 300 K, and decreased below that rapidly, becoming diamagnetic. Bleaney and Bowers observed a triplet in the ESR spectrum and suggested a dinuclear structure which was confirmed in 1953 by X-ray data (Bleaney and Bowers, 1952; van Niekerk and Schoening, 1953). The T dependence of the susceptibility was fitted with the HDVV Hamiltonian to give $J = 300\ cm^{-1}$. There has been much work done trying to correlate the structures of carboxylates with the isotropic exchange, but without much success. At any rate, the interaction is mainly transmitted through the carboxylate groups and not by direct exchange. Rather obviously, copper acetate was investigated through *ab initio* techniques in the configuration interaction (CI) frame which produced good results. It must be stressed that the calculations required several *ad hoc* assumptions which made the efforts to produce them rather unappealing. The singlet–triplet separation was well calculated also within the DFT formalism. The ground state was calculated with complete active space self-consistent field (CASSCF), N-Electron Valence Perturbation Theory (NEVPT2), difference dedicated configuration interaction (DDCI2), and DDCI3. For normal people hating acronyms, a detailed discussion is provided in Appendix A.

The procedure worked out by Neese *et al.* to calculate the SH parameters is the one closest to the LF treatment (Sinnecker *et al.*, 2004). The energies of the magnetic interactions are calculated as differences between the first excited A_u triplet

state and ground-state singlet A_g spin orbit free states. The molecule is assumed to have D_{2h} symmetry. The difference in energy is compared with the expression obtained from the HDVV Hamiltonian $\Delta = J$. The J value is calculated as the difference between the lowest singlet state ^1A_g in the D_{2h} symmetry assumed for the molecule and the lowest ^3A_u. The energies are calculated by setting the spin–orbit coupling (SOC) contribution to zero. The calculated value is model dependent, which within DDCI3 is almost identical to the experimental one: 271 cm^{-1} versus 292 cm^{-1} (Maurice *et al.*, 2011).

The good agreement with experiment of DDCI3 is attributed to the inclusion of the excitations of three degrees of freedom which gave a better description of covalency effects (Calzado *et al.*, 2009),

The anisotropic components are defined in Eq. (7.11). The experimental value of $D/k = 240$ mK is expected to be the sum of two contributions:

$$D = 1/2(D_{12}^{dip} + D_{12}^{so}) \tag{8.6}$$

where D, D_{12}^{dip}, and D_{12}^{so} are tensors, 'dip' referring to dipolar and 'so' to spin–orbit components. Let us see the dipolar contribution first. This component is easily calculated within the point dipolar approximation, although also covalency effects may be needed. In general, the point dipolar approximation breaks down in the presence of spin delocalization. Copper acetate, however, is well behaved, and very similar results are obtained with the point dipolar and the *ab initio* calculations. A delicate point has been the determination of the sign of D, which has been finally achieved through high-field ESR. At a frequency of 400 GHz, the Zeeman energy is 60 K and the $-1 \rightarrow 0$ transition occurring at low field will gain intensity on decreasing T, showing the sign of D. The spectra are shown in Figure 8.3 (Ozarowski, 2008).

The SOC component is difficult to calculate within the LF formalism. The zero-field splitting (ZFS), on the other hand, is calculated using perturbation theory on the SOC and the dipolar Hamiltonian. In general, the two tensors have different principal axes, but this is not true for copper acetate where the two frames are, within error, parallel to each other. The assumption is that the wave function of the ground state can be obtained by correcting with the admixture of the excited states. This brings about the mixing of the ground state $|x^2 - y^2(a)x^2 - y^2(b)\rangle$ with excited states of the type $|x^2 - y^2(a)n(b)\rangle$. As a consequence, the energies of the lowest triplet depend on M, that is, D is different from zero (Maurice *et al.*, 2011). The elaboration of the perturbation yields for the SOC component

$$D = 2\frac{\zeta^2 J_{x^2-y^2,xy}}{\Delta E^2_{x^2-y^2,xy}} - \frac{1}{4}\frac{\zeta^2 J_{x^2-y^2,xz}}{\Delta E^2_{x^2-y^2,xz}} - \frac{1}{4}\frac{\zeta^2 J_{x^2-y^2,yz}}{\Delta E^2_{x^2-y^2,yz}} \tag{8.7}$$

where J is the coupling constant for one ion in the ground state and the other in an excited state, and Δ is the energy difference. A polite guess of the sign of the Js, assuming that the x^2-y^2 and n orbitals are orthogonal, shows it is negative. This is indeed confirmed by the calculations which for DDCI3 yield the results shown in Table 8.2.

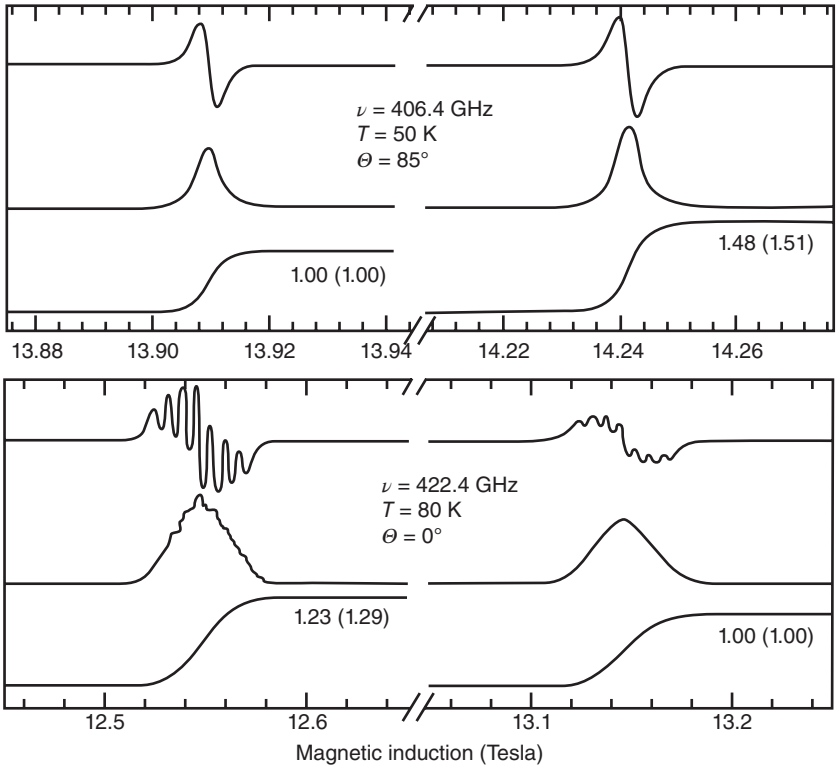

Figure 8.3 Single-crystal ESR spectra of $Cu_2(acetate)_4(pyrazine)_2$ measured with the frequency, temperature, and molecular orientation as indicated. The measured and calculated (in parentheses) relative intensities are shown. $A\|_{Cu} = 73.5 \times 10^{-4}\,cm^{-1}$. (Reproduced from Ozarowski, A. (2008) with permission from The American Chemical Society.)

The important feature of the calculated D is that the point dipolar contribution is about one-third of the experimental value and therefore is far from being negligible. The spin–orbit contribution has a negative sign, corresponding to a ferromagnetic coupling in the excited state. This result shows clearly that the Moryia approximation for the spin–orbit-determined ZFS, namely D proportional to the ground state J, is absolutely not correct. This had been observed in several cases, including copper acetate, but this is the first time that quantitative calculations provide clear evidence. The old copper acetate strikes again!

The following part can be skipped if you are not interested in the computational details. A correct approach to the calculations begins by considering the experimental atomic coordinates of the atoms present in the examined compound. At the very beginning, the often used strategy has been to consider as solutions of the nonrelativistic Born–Oppenheimer Hamiltonian the CASSCF and post-CASSCF methods, with a procedure that will include the SOC and SSC relativistic effects in a second step. The diagonalization of the state interaction (SI) matrix allows the

Table 8.2 Relative energies $\Delta E_{x^2-y^2,n}$ (in cm^{-1}) and excited-states magnetic couplings $J_{x^2-y^2,n}$ (in cm^{-1}) computed using different methods.

Method	$\Delta E^2_{x^2-y^2,xy}$	$\Delta E^2_{x^2-y^2,z^2}$	$\Delta E^2_{x^2-y^2,yz}$	$\Delta E^2_{x^2-y^2,xz}$
CASSCF	8 659	10 778	116 321	11 954
NEVPT2	11 272	12 851	14 049	14 447
DDCI1	8 628	10 253	11 418	11 728
DDCI2	10 180	11 701	13 153	13 521
DDCI3	12 280	13 313	15 510	15 090
Method	$J_{x^2-y^2,xy}$	$J_{x^2-y^2,z^2}$	$J_{x^2-y^2,yz}$	$J_{x^2-y^2,xz}$
CASSCF	−1.8	−53.5	−30.0	−35.4
NEVPT2	−0.6	−102.0	−16.2	−21.3
DDCI1	−1.4	−233.9	−31.5	−39.9
DDCI2	−15.9	−266.4	−31.5	−38.5
DDCI3	−29.9	−359.0	−63.9	−64.0

treatment of SOC and SCF variationally by using the Breit–Pauli SSC Hamiltonian and a mean-field SOC Hamiltonian.

The use of correlated energies in the diagonal elements of the SOC/SSC matrix is useful to introduce dynamic correlations effects. In this type of calculations, it is necessary to use accurate $J_{x^2-y^2,n}$ values, and therefore post-CASSCF methods are employed. To calculate correlated energies, the *n*-electron valence second-order perturbation theory (NEPTV2) method is used, while the DDCI is useful to determine both correlated wave functions and energies. DDCI1 considers one hole and one particle single excitation on the full active space; whereas DDCI2 accounts for both one hole and one particle single excitation and two holes and two particle excitations. At last, DDCI3 examined the case of two holes – one particle and one hole – two particles excitations.

On using CAS(2,2), the active space includes only the ground magnetic orbital which is substantially Cu-$3d_{x^2-y^2}$ in character; the alternative CAS(18,10) active space includes all the Cu-3d valence orbitals and electrons. The calculations of SOC and SSC interactions consider a basis that includes five triplet and four singlet states of A_u symmetry, that is, the lowest triplet and the eight excited singlet and triplet states $\Phi^{ST}_{x^2-y^2,n}$. As the actual symmetry is not a true D_{2h} one, the states $\Phi^{ST}_{x^2-y^2,n}$ do not contribute to the ZFS parameters and are also considered in the QDPT (Quasi Degenerate Perturbation Theory) matrix. In CAS(2,2), the orbitals were optimized in a state-average SCF calculation on the lowest singlet and triplet states. In the case of CAS(18,10), the orbitals were derived from an energy minimization of the average of the five lowest triplet and four lowest singlet states of A_u symmetry.

Use of the effective Hamiltonian theory allowed the extraction of the final ZFS parameters. The method is based on the use of *ab initio* energies and wave functions: by using a numerical approach, it is possible to determine the best matrix that represents the effective Hamiltonian working in a chosen model space. The

fulfillment of two conditions is useful in this phase: (i) its eigenvalues are the *ab initio* energies, and (ii) its eigenvectors are the orthonormalized projections of the *ab initio* wave functions in the model space. The comparison of each matrix element of the numerical matrix with the corresponding element of the analytical matrix of the model Hamiltonian gave the full **D** tensor. The diagonalization of the tensor allows defining the D and E values and the correct magnetic axes. The model has been used to analyze the behavior of several mononuclear and binuclear compounds (Olsen, 2011).

8.5 Mixed Pairs: Degenerate–Nondegenerate

We have kept repeating practically in all the chapters that unquenched orbital components require treatments different from those based on SH which are valid and can be applied only to orbital nondegenerate states. It is now time to have a look at what has been done to overcome this problem. It may be convenient to introduce the minimum possible complication in the system to be considered (Palii *et al.*, 2011). Let us take an A–B pair, where A is threefold orbitally degenerate, say its ground state is $^2T_{2g}$ in O_h symmetry, while B is orbitally nondegenerate, say in the ground state $^2B_{2g}$ of a tetragonally compressed D_{4h} symmetry. The orbital degeneracy is bound to the symmetry of the ion and of the number of electrons in the d orbitals. Anyway, the Jahn–Teller theorem should guarantee that the orbital degeneracy is removed by vibronic coupling. This, however, is an oversimplification, and actually one has to take into account also SOC and the relative roles of SOC and vibronic coupling to determine the nature of the ground and low-lying levels. Let us focus on the T level. The orbital degeneracy of the ground level can be removed by vibronic coupling and/or SOC. The T_{2g} ground state has a nonzero SOC splitting, and the six states yield four and two degenerate states, as sketched in Figure 8.4.

Vibronic coupling splits the T degeneracy. In principle, either scheme may be dominant, but it will depend on which electronic structural parameters that will dominate. It must also be remembered that, if the vibronic term dominates, it will quench the SOC splitting (Ham effect), while in the reverse scheme the SOC will quench the vibronic distortion. If we consider an E ground state, we see that the SOC is zero, so the vibronic coupling dominates and the E ground levels are strongly tetragonally distorted.

Let us go back to the example of Figure 8.4 and consider the changes to the treatment by Anderson. The key issue is the kinetic exchange, which is associated to the transfer of electrons from one half-filled orbital on A to an empty one on B. The allowed CT are $XZ \rightarrow xz$, $YZ \rightarrow yz$, and $XY \rightarrow xy$. A simple overlap argument suggests that the contribution of $XY \rightarrow xy$ can be neglected because the interaction of the A and B centers is of the δ type, whereas the other two are of the π type. A serious warning must be given, however: the overlap of the copper orbitals in copper acetate is of the δ type, but the exchange interaction is of 300 K! Continuing

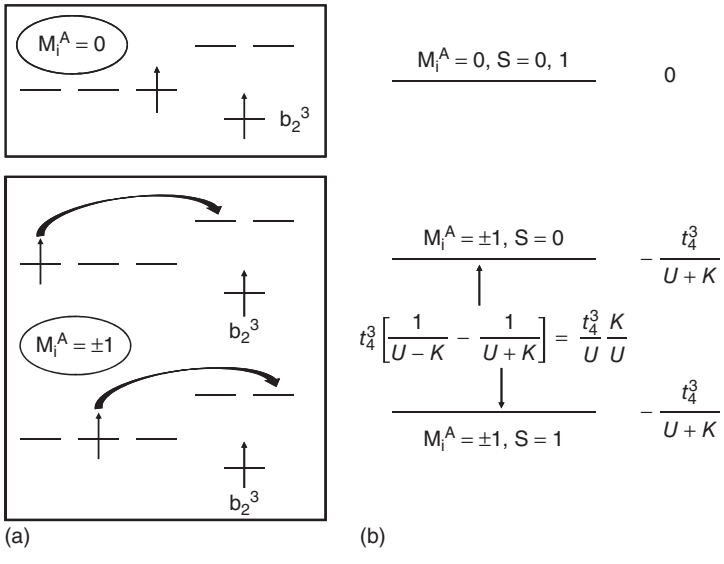

Figure 8.4 (a) Possible electron transfer processes and (b) energy pattern for the $^2T_{2g}(t_{2g}^1) \times {}^2B_{2g}(b_{2g}^1)$ exchange problem. Only the first steps of the two-step processes are shown. (Reproduced from Palii, A. *et al.* (2011) with permission from The Royal Society of Chemistry.)

with Anderson's scheme, the corrections to the energies of the low-lying levels depend on the occupation of the levels. Therefore, the simplicity of the HDVV spin Hamiltonian is lost.

The important feature is that the exchange splitting and the number of parameters increase. One of the early attempts to include orbit in the exchange mechanism is based on the so-called T–P isomorphism (Sugano, Tanabe, and Kamimura, 1970). The orbital angular momentum operators L_i, $i = x, y, z$, which operate on the LF functions can be substituted by the equivalent L operators defined on the p functions, yielding the same results within a proportionality constant. It is a well-established procedure to use effective Hamiltonians to simplify the use of quantum calculations. Using the T–P isomorphism, the low-lying levels can be expressed by the Hamiltonian

$$\mathscr{H}_{ex} = -\frac{1}{4}\left(\frac{3\,t_\pi^2}{U-K}\right)\ell_{ZA}^2 + \left(\frac{t_\pi^2}{U+K} - \frac{t_\pi^2}{U-K}\right)\ell_{ZA}^2 \jmath_A \jmath_B \tag{8.8}$$

whose eigenvalues have the following form:

$$E(m_l^A = 0; S) = 0$$
$$E(|m_l^A| = 1; S) = -\frac{t_\pi^2}{U+K} + \frac{1}{2}\left(\frac{t_\pi^2}{U+K} - \frac{t_\pi^2}{U-K}\right) S(S+1) \tag{8.9}$$

Another important feature emerging from the exploration of the degenerate orbital systems is that, even if the input is isotropic, the outcome can be anisotropic.

The principles used for working out Eq. (8.8) are of the type used here, and experiments were performed using single-crystal ESR. The systems were pairs of octahedra sharing an edge. It was possible to have Ni_2, Co_2, and Ni–Co pairs, but the last only at the impurity level (Banci *et al.*, 1982). We will come back to this later after discussing Yb.

8.6 f Orbitals and Orbital Degeneracy

It is now time to check whether the developing model we have been following up to now can give some insight into the Ln. A particularly pedagogical example is provided by a series of Ln compounds which have been puzzling for quite some time. The starting points were $Cs_3Ln_2X_9$, where X = Cl, Br, Ln = Tb, Dy, Ho, Yb. There is also a mixed metal derivative YbCr. The structure of the dinuclear species consists of two face-sharing octahedra of halides which coordinate the Yb ions with D_{3h} symmetry, as shown in Figure 8.5.

The system has been investigated with several different techniques, because of its fascinating perspective of a textbook example of interacting orbitally degenerate systems with high symmetry. A particularly efficient one is inelastic neutron scattering (INS) (Fultz, 2006; Skryabin, 2011), which can monitor the low-lying levels in good detail (Guedel, Furrer, and Blank, 1990). The expectation was to observe the evidence of deviations from the isotropic-exchange HDVV. But the spectral data provided no evidence for that. On the other hand, anisotropic effects were clearly observed in $Cs_3Ho_2Br_9$ and $YbCrBr_9^{3-}$. Having aroused the curiosity, it is now time to show the data.

For Yb^{3+}, the ground multiplet is $^2F_{7/2}$, which in octahedral symmetry splits into three levels, two Kramers doublets Γ_6 and Γ_7, and a quartet Γ_8, as shown in Figure 8.6.

The interesting feature is that different structures are available for different stoichiometries. In particular, the site symmetry is D_3 for $Cs_3Ho_2Br_9$ and exactly octahedral for $Cs_2NaHo_2Br_9$ (Furrer *et al.*, 1990). Measurements have been performed also on doped samples of $Cs_3Yb_2X_9$ with Cr, taking advantage of the similarity of the structures of the Cr and Ln derivatives (Mironov, Chibotaru, and

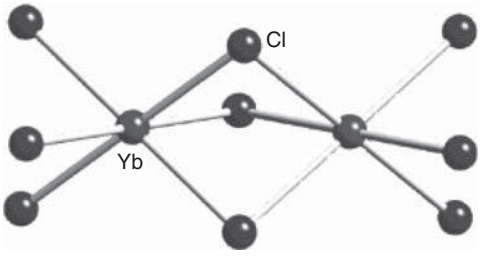

Figure 8.5 Schematic view of the $Yb_2Cl_9^{3-}$ ion.

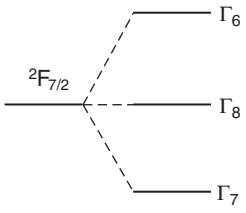

Figure 8.6 Splitting of the $^2F_{7/2}$ of Yb^{3+} in octahedral symmetry. The labels correspond to the irreducible representations of O*.

Ceulemans, 2003). In particular, a detailed attempt to put on a common frame the Yb–Yb and Yb–Cr dinuclear species was made by Mironov *et al.* An important piece of information is that the Yb–Cr pairs show a strong anisotropy. This is in contrast with the simple-minded expectation that the orbitally quenched Cr^{3+} should have only a small anisotropy. The data were analyzed for different schemes of exchange interaction, ranging from the isotropic HDVV to the highly anisotropic Ising. For the pure Yb^{3+} derivative, the sponsored method to calculate the low-lying levels of the Yb derivatives is an extension of the Goodenough treatment, which suggested the inclusion in the kinetic exchange the CT transition from $4f^N$ to 5d. For Yb, the CTs are $(4f^{13}5d^1)_A - (4f^{12}5d^0)_B$ and $(4f^{12}5d^0)_A - (4f^{13}5d^1)_B$ (Palii *et al.*, 2005).

The wave functions to be used to calculate the effect of exchange coupling are the four functions associated with the two lowest Kramers doublets. Their energies are calculated using the electron transfer formalism from A to B and vice versa. In fact, the experimental data were fitted to the Hamiltonian

$$\mathscr{H}_{\text{eff}} = J_x \mathcal{S}_x^A \mathcal{S}_x^B + J_y \mathcal{S}_y^A \mathcal{S}_y^B + J_z \mathcal{S}_z^A \mathcal{S}_z^B \tag{8.10}$$

where

$$J\alpha = (g\alpha/g_J)^2 (g_J - 1)^2 J \tag{8.11}$$

with $\alpha = x, \ y, \ z$ being the Cartesian components and g_J the Lande factor.

The fit of thee experimental data is in excellent agreement with the HDVV and rules out Ising. In fact, also the anisotropy of the *g*-values is small, again suggesting low anisotropy. In a detailed study using the same approach, we used under the heading old tools in a new field. Tsukerblat *et al.* reproduced the experimental data by fitting the f orbital configuration and taking into consideration the involvement of the empty 5d orbitals. This is, indeed, the key of the suggested treatment for taking into account orbital degeneracy.

The suggested treatment is far from general; it is just an example showing how it is possible to start a long and winding road. Anyway, the model fitted the experimental data with HDVV Hamiltonian parameters: $J = 6.50 \ \text{cm}^{-1}$ and $J = 5.74 \ \text{cm}^{-1}$ for the Cl and Br derivative, respectively.

Another pair that has been studied is Ho_2. Experiments were performed on diluted Ho in $Cs_3Ho_{0.2}Y_{1.8}Br_9$. The INS spectra of the pure Ho compounds yield two signals at 0.49 and 1.16 meV, which correspond to the transitions between the split components of the ground J = 8 state.

References

Anderson, P.W. (1950) Antiferromagnetism. Theory of superexchange interaction. *Phys. Rev.*, **79**, 350–356.

Anderson, P.W. (1959) New approach to the theory of superexchange interactions. *Phys. Rev.*, **115**, 2–13.

Banci, L., Bencini, A., Benelli, C., and Gatteschi, D. (1982) Exchange interactions in heterodinuclear complexes with one ion possessing an orbitally degenerate ground state. Nickel(II)-cobalt(II) pairs in diaquo(1,4-dihydrazinophthalazine)nickel(II) chloride hydrate. *Inorg. Chem.*, **21**, 3868–3872.

Bencini, A., Totti, F., Daul, C.A., Doclo, K., Fantucci, P., and Barone, V. (1997) Density functional calculations of magnetic exchange interactions in polynuclear transition metal complexes. *Inorg. Chem.*, **36**, 5022–5030.

Bleaney, B. and Bowers, K.D. (1952) Anomalous paramagnetism of copper acetate. *Proc. R. Soc. Lond. A Math. Phys. Sci.*, **214**, 451–465.

Calzado, C.J., Angeli, C., Taratiel, D., Caballol, R., and Malrieu, J.P. (2009) Analysis of the magnetic coupling in binuclear systems. III. The role of the ligand to metal charge transfer excitations revisited. *J. Chem. Phys.*, **131**, 044327.

De Loth, P., Cassoux, P., Daudey, J.P., and Malrieu, J.P. (1981) Ab initio direct calculation of the singlet-triplet separation in cupric acetate hydrate dimer. *J. Am. Chem. Soc.*, **103**, 4007–4016.

Fultz, B. (2006) Materials science applications of inelastic neutron scattering. *JOM*, **58**, 58–63.

Furrer, A., Güdel, H.U., Krausz, E.R., and Blank, H. (1990) Neutron spectroscopic study of anisotropic exchange in the dimer compound $Cs_3Ho_2Br_9$. *Phys. Rev. Lett.*, **64**, 68–71.

Gillon, B., Cavata, C., Schweiss, P., Journaux, Y., Kahn, O., and Schneider, D. (1989) Spin density in the heterodinuclear compound Cu(salen)Ni(hfa)$_2$: a polarized neutron diffraction study. *J. Am. Chem. Soc.*, **111**, 7124–7132.

Goodenough, J.B. (1958) An interpretation of the magnetic properties of the perovskite-type mixed crystals $La_{1-x}Sr_xCoO_{3-\lambda}$. *J. Phys. Chem. Solid*, **6**, 287–297.

Guedel, H.U., Furrer, A., and Blank, H. (1990) Exchange interactions in rare-earth-metal dimers. Neutron spectroscopy of cesium ytterbium halides, $Cs_3Yb_2Cl_9$ and $Cs_3Yb_2Br_9$. *Inorg. Chem.*, **29**, 4081–4084.

Guha, B.C. (1951) Magnetic properties of some paramagnetic crystals at low temperatures. *Proc. R. Soc. Lond. A Math. Phys. Sci.*, **206**, 353–373.

Hay, P.J., Thibeault, J.C., and Hoffmann, R. (1975) Orbital interactions in metal dimer complexes. *J. Am. Chem. Soc.*, **97**, 4884–4899.

Kanamori, J. (1959) Superexchange interaction and symmetry properties of electron orbitals. *J. Phys. Chem. Solid*, **10**, 87–98.

Kollmar, C. and Kahn, O. (1993) A Heisenberg Hamiltonian for intermolecular exchange interaction: spin delocalization and spin polarization. *J. Chem. Phys.*, **98**, 453–472.

Maurice, R.M., Sivalingam, K., Ganyushin, D., Guihéry, N., de Graaf, C., and Neese, F. (2011) Theoretical determination of the zero-field splitting in copper acetate monohydrate. *Inorg. Chem.*, **50**, 6229–6236.

Mironov, V.S., Chibotaru, L.F., and Ceulemans, A. (2003) Exchange interaction in the YbCrBr9 3- mixed dimer: the origin of a strong Yb^{3+}-C^{r3+} exchange anisotropy. *Phys. Rev. B: Condens. Matter*, **67**, 014424.

van Niekerk, J.N. and Schoening, F.R.L. (1953) A new type of copper complex as found in the crystal structure of cupric acetate, $Cu_2(CH_3COO)_4.2H_2O$. *Acta Crystallogr.*, **6**, 227–232.

Noodleman, L. and Norman, J.G. Jr., (1979) The Xα valence bond theory of weak electronic coupling. Application to the low-lying states of $Mo_2Cl_8^{4-}$. *J. Chem. Phys.*, **70**, 4903–4906.

Novoa, J.J., Deumal, M., and Jornet-Somoza, J. (2011) Calculation of microscopic exchange interactions and modelling of macroscopic magnetic properties in molecule-based magnets. *Chem. Soc. Rev.*, **40**, 3182–3212.

Olsen, J. (2011) The CASSCF method: a perspective and commentary. *Int. J. Quantum Chem.*, **111**, 3267–3272.

Ozarowski, A. (2008) The zero-field-splitting parameter D in binuclear copper(II) carboxylates is negative. *Inorg. Chem.*, **47**, 9760–9762.

Palii, A.V., Tsukerblat, B.S., Clemente-Juan, J.M., and Coronado, E. (2005) Isotropic magnetic exchange between anisotropic Yb(III) ions. Study of $Cs_3Yb_2Cl_9$ and $Cs_3Yb_2Br_9$ crystals. *Inorg. Chem.*, **44**, 3984–3992.

Palii, A., Tsukerblat, B., Klokishner, S., Dunbar, K.R., Clemente-Juan, J.M., and Coronado, E. (2011) Beyond the spin model: exchange coupling in molecular magnets with unquenched orbital angular momenta. *Chem. Soc. Rev.*, **40**, 3130–3156.

Sinnecker, S., Neese, F., Noodleman, L., and Lubitz, W. (2004) Calculating the electron paramagnetic resonance parameters of exchange coupled transition metal complexes using broken symmetry density functional theory: application to a Mn^{III}/Mn^{IV} model compound. *J. Am. Chem. Soc.*, **126**, 2613–2622.

Skryabin, Y.N. (2011) Theory of neutron scattering in magnets. *Theor. Math. Phys.*, **168**, 1330–1346.

Sugano, S., Tanabe, Y., and Kamimura, H. (1970) *Multiplets of Transition-Metal Ions in Crystals*, Academic Press.

9
Structure and Properties of *p* Magnetic Orbitals Systems

9.1
Magnetic Coupling in Organics

The interest in understanding the mechanism of the interaction between organic radicals is associated with the dream of a room-temperature organic ferromagnet. Historically, this has been a milestone in molecular magnetism but interest in organic magnetism was existent even prior to that. A particularly well-developed field was the use of dipolar interactions between stable organic radicals such as nitroxides, which depend on the inverse third power of the distance, as the probes to measure distances in spin-labeled proteins. The new interest in understanding the mechanism of interaction between organic radicals prompted a renewed interest in spin labeling, as we will see in some detail in the following.

If the goal is the synthesis of organic ferromagnets, a three-dimensional (3D) network of ferromagnetic (FM) interactions must be designed. Unfortunately, this is a very difficult task: designing pairs of ferromagnetically coupled organic molecules is extremely difficult, but arranging 3D ferromagnetic arrays is (almost) hopeless. An excellent example is the polycarbenes, whose structure is shown in Figure 9.1. Several oligomers were synthesized showing strong ferromagnetic coupling ($|J| > 300$ K) but no 3D magnetic properties (Iwamura, 2013).

The compound in Figure 9.1 has not been synthesized yet, but even on achieving that, the bulk magnetism would not be granted unless additional interactions between the planes could be switched on. Indeed, the dipolar interaction is always present, and in the presence of strong in-plane correlations it might be enough to produce a transition to long-range magnetic order.

It must also be remembered that the ferrimagnetic approach, that is, exploiting antiferromagnetic (AFM) coupling between different spins, which is an efficient tool to install permanent magnetization in molecular magnets containing transition metals (TMs) or Lns, is hardly usable for radicals because the systems with $S > 1/2$ are extremely rare. Let us start by considering the basic features responsible of the coupling between the radicals, and in particular of ferromagnetic coupling. It is apparent that there must be important differences between the rules for metals and for radicals. The former are the Goodenough–Kanamori rules, reported in Section 8.2. For the latter, reference is made to the McConnell I (production of

Introduction to Molecular Magnetism: From Transition Metals to Lanthanides, First Edition.
Cristiano Benelli and Dante Gatteschi.
© 2015 Wiley-VCH Verlag GmbH & Co. KGaA. Published 2015 by Wiley-VCH Verlag GmbH & Co. KGaA.

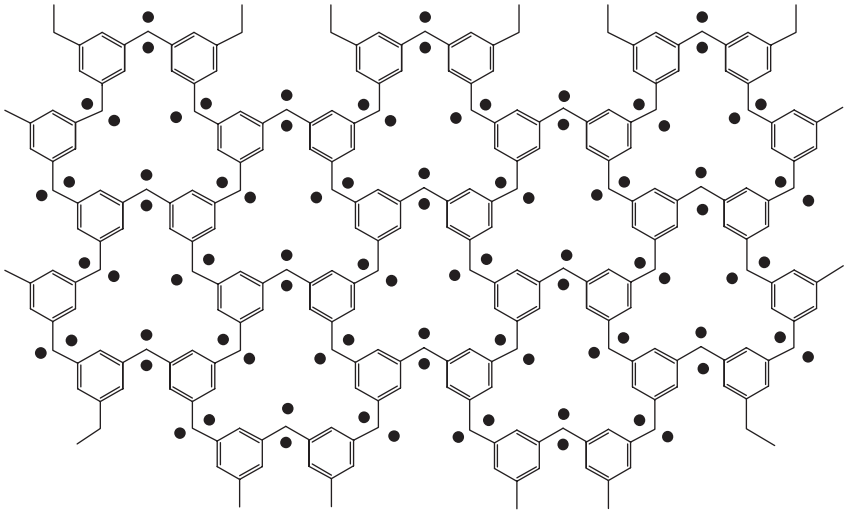

Figure 9.1 Example of a polycarbene. (Reproduced from Iwamura, H. (2013) with permission from Elsevier B.V.)

intermolecular ferromagnetic interactions in organic solids (McConnell, 1963)) and II schemes (ferromagnetic spin alignment using ionic charge-transfer salts (McConnell, 1967)).

The McConnell I scheme is intuitively clear, as shown by Figure 9.2 (Novoa, Deumal, and Jornet-Somoza, 2011). Let us assume a molecule such as the allyl radical, which is spin-polarized + − +: it will interact with an identical one in such a way that the shortest contact is + +. The coupling is AFM, while if the shortest contact is + −, the coupling is FM.

The number of possible pitfalls is enormous, and the use of the model is justified only if nothing better is available. Attempts to establish structural magnetic

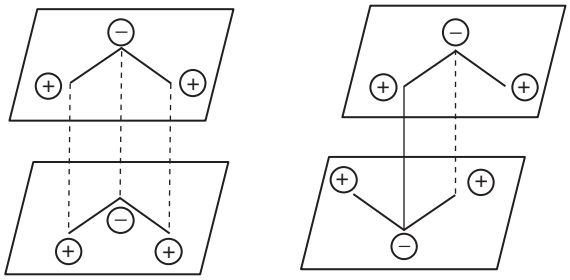

Figure 9.2 Antiferromagnetic (on the left) and ferromagnetic (on the right) interactions in a couple of allyl radicals. The prediction is based on the McConnell I model.

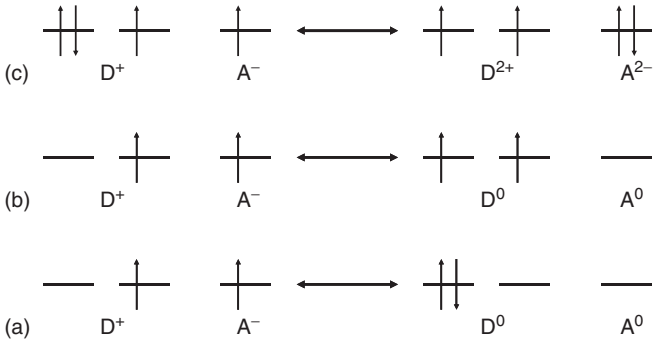

Figure 9.3 Charge-transfer mixing in: (a) normal ionic charge-transfer dimer, (b) McConnell II model; (c) Breslow's modification (LePage and Breslow, 1987).

correlations in a series of nitroxides failed to provide any evidence for various sets of distances and angles with FM coupling.

Designing synthetic strategies on this basis requires a lot of good luck. At any rate, the model is formalized by defining a Hamiltonian

$$\mathscr{H}^{AB} = \mathcal{S}^{A}\mathcal{S}^{B}\sum_{i\in A, j\in B} J_{ij}^{AB}\rho_i^A\rho_j^B \tag{9.1}$$

where J_{ij}^{AB} is the exchange integral between atom i of molecule A and atom j of molecule B, $\mathcal{S}^{A}$ and $\mathcal{S}^{B}$ are the total spin operators of molecules A and B, and ρ_i^A and ρ_j^B the spin densities on atom i of molecule A and atom j of molecule B, respectively. As J_{ij}^{AB} is generally negative, the interaction is ferromagnetic only when the product $\rho_i^A\rho_j^B$ is negative. In this hypothesis, a ferromagnetic interaction is possible only when the closer atoms of the interacting molecules have atomic spin population with opposite signs.

The two interacting allyl radicals sketched in Figure 9.2 are a simple example of a system described with the McConnell-I model. Even though there are experimental (Izuoka *et al.*, 1987) and theoretical (Yamaguchi, Toyoda, and Fueno, 1989) studies that demonstrate the validity of this approach, its application in systems where the magnetic interaction is based on a through-space mechanism requires great caution.

The McConnell II model is based on a charge-transfer mechanism. In the normal way, the ground state is a singlet. But if the excited state is a triplet, as sketched in Figure 9.3, then a triplet state can be induced.

9.2
Magnetism in Nitroxides

An important issue is the need for a 3D network of interactions in order to have a bulk ferromagnet. While with metal ions it is relatively simple to individuate

possible exchange pathways, this is more difficult for organic magnets. Recently, an automatized method has been suggested to monitor the mechanism of interaction in pairs of radicals, and we wish to present here the results of the analysis performed on the radical *p*-nitrophenyl nitronyl nitroxide (NIT*p*PhNO$_2$) sketched in (Scheme 9.1), which orders as ferromagnet up to 0.60 K (Takahashi *et al.*, 1991).

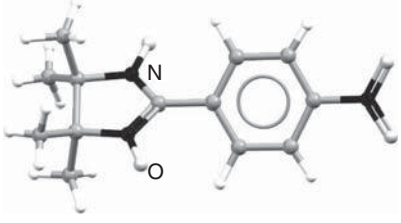

Scheme 9.1 *p*-nitrophenyl nitronyl nitroxide radical.

The nitronyl nitroxides are characterized by what can be called a *structural instability*: the solids crystallize in several different cells. The four known polymorphs of the *p*-nitrophenyl derivative, whose structure is shown in Figure 9.4, are indicated as α (monoclinic, space group: $P2_1/c$), β (orthorhombic, space group: $F2dd$), γ (triclinic, space group: $P\bar{1}$), and δ (monoclinic, space group: $P2_1/c$). The β form is a ferromagnet and the γ form is an AFM, while no evidence of deviation from paramagnetic behavior is observed in the α and δ forms. In the literature, there is an early attempt to calculate the magnetic coupling using the model put forward by Hay, Thibeault, and Hoffmann (1975), but the relevant analysis has been performed in the last few years with the approach described in the following (Novoa, Deumal, and Jornet-Somoza, 2011). The method is called the *first-principles bottom-up* approach. The first step of this approach corresponds to an

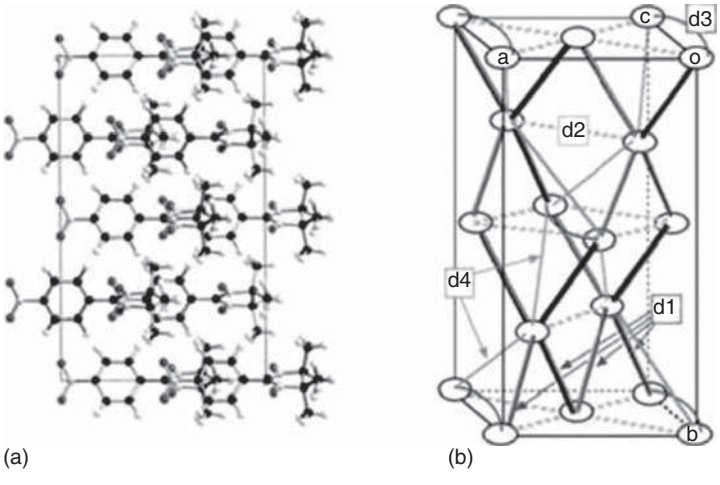

Figure 9.4 (a) Packing of the β-phase crystals of the NITpPhNO$_2$. (b) Arrangement of the four (d1–d4) symmetry-unique pairs of radicals within the crystal unit cell. (Reproduced from Novoa J.J. *et al.* (2011) with permission from The Royal Society of Chemistry.)

analysis for finding all unique radical contacts between pairs of radicals. The analysis of the crystal structure of the radical shows the presence of four symmetry-related pairs of radicals (Figure 9.4) (Awaga *et al.*, 1990).

The second step is the computation of J_{AB} for all the pairs. By using the UB3LYP/6-31+G(d) level (Deumal *et al.*, 2002), two different relevant magnetic interactions have been computed. The reliability of the obtained J_{AB} values is confirmed if, on changing DFT functional, the individual J_{AB} values might change but the ratio between the two constants is preserved. The presence of two different interactions allows, by examining the crystal structure, the construction of the magnetic topology of the system, which showed the presence of ferromagnetic interactions in all directions. This is the third step in the sketched procedure. Finally, the thermodynamic properties are derived by using the Van Vleck equation for magnetic susceptibility Eq. (5.15) and for specific heat Eq. (9.2):

$$C_{\mathrm{p}}(T) = \frac{N}{k_{\mathrm{B}}T^2}\left[\frac{\sum_n \left(2\mathrm{S}_n+1\right)\left(\mathrm{E}_n-\mathrm{E}_0\right)^2 \exp\left[-\frac{\mathrm{E}_n-\mathrm{E}_0}{k_{\mathrm{B}}T}\right]}{\sum_n (2\mathrm{S}_n+1)\exp\left[-\frac{\mathrm{E}_n-\mathrm{E}_0}{k_{\mathrm{B}}T}\right]} - \frac{\left(\sum_n \left(2\mathrm{S}_n+1\right)\left(\mathrm{E}_n-\mathrm{E}_0\right)\exp\left[-\frac{\mathrm{E}_n-\mathrm{E}_0}{k_{\mathrm{B}}T}\right]\right)^2}{\left(\sum_n \left(2\mathrm{S}_n+1\right)\exp\left[-\frac{\mathrm{E}_n-\mathrm{E}_0}{k_{\mathrm{B}}T}\right]\right)^2}\right] \tag{9.2}$$

where N is the Avogadro number, H is the external applied field, E_0 and S_0 are the energy and the spin of the magnetic ground state, and k_{B} is the Boltzmann constant. The calculated magnetic susceptibility approaches nicely the experimental values on increasing the magnetic model space size. The computed curves for specific heat show a maximum, which corresponds to a ferromagnetic transition temperature of 0.45 K, in qualitative agreement with the experimental value of 0.60 K (Figure 9.5).

The result of this analysis is that ferromagnetic coupling between NITR is possible, but weak. No simple rule has emerged to correlate the spin density with the coupling.

9.3 Thioradicals

In the field of purely organic free radicals that show a transition to an ordered magnetic phase, the surprisingly high temperature of 35.5 K has been reported for a dithiadiazolyl radical (Banister *et al.*, 1996) which orders as a weak ferromagnet. The radical has the structure shown in Scheme 9.2 and the packing shown in Figure 9.6. The coupling between the thioradicals is AFM, but deviations from

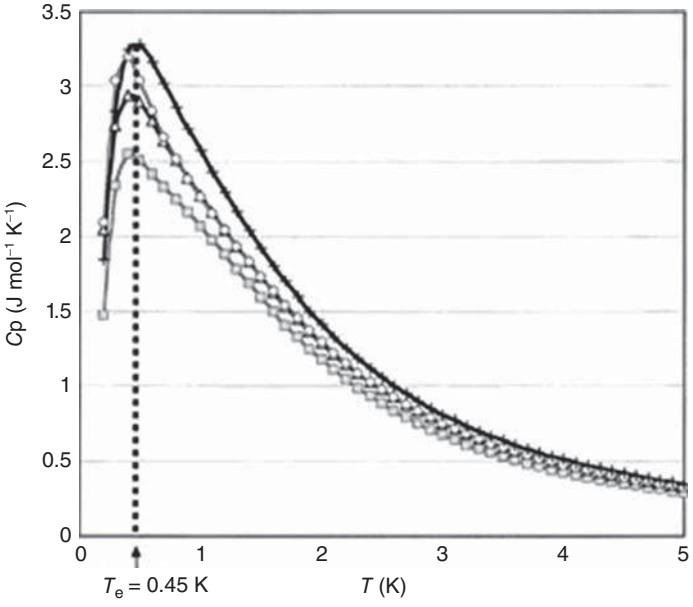

Figure 9.5 Simulated *Cp*(*T*) data for NIT*p*PhNO2 using a three-dimensional minimal sites model (■) and its extension along the crystallographic axes *a* (□), *c* (∘), and *b* (+). (Reproduced from Deumal, M. *et al.* (2002) with permission from The American Chemical Society.)

collinearity are possible due to spin–orbit coupling (SOC) associated with the S atoms. This means that the angle between the two spins is different from 180°. The justification of the deviation from 180° is given by the antisymmetric exchange which tends to orient the coupled spins at 90°. A deviation from antiparallel orientation of less than 1° (0.085 ± 0.005°) generates a nonzero resulting spin in the orthogonal direction. The system behaves as a ferromagnet, but only a fraction of the spin is involved, as shown by the saturation magnetization which is much smaller than expected for one unpaired electron; therefore the system is called a *weak ferromagnet*.

The spin densities are mainly concentrated on the S and N atoms as calculated with DFT techniques. This result supports the idea that the magnetic interaction is transmitted in the crystal through the intermolecular contacts which involve the two atoms (Palacio *et al.*, 1997).

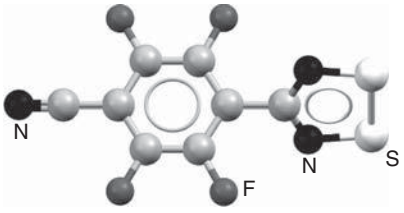

Scheme 9.2 The dithiadiazolyl radical.

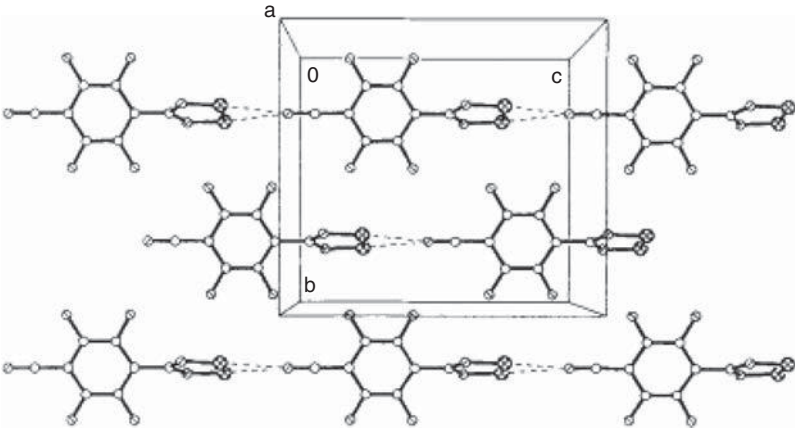

Figure 9.6 Molecular packing of the dithiadiazolyl radical, illustrating the parallel alignment of radical chains. (Reproduced from Banister A.J. *et al.* (1996) with permission from John Wiley & Sons, Inc.)

The success has suggested that heavier atoms such as S, Se, and Te might be usefully employed for higher order temperature.

Otherwise, one can attempt to use hybrid systems comprising organic radicals and metal ions, both TM and Ln. This will be referred to in the next sections.

9.4 Metallorganic Magnets

In this section, we will report some examples of magnetic hybrid systems. By "hybrid" we indicate systems that contain at least two types of magnetic orbitals, for instance p and d, p, and f, and so on. A *caveat* must be issued on the nomenclature. In the way used by nonchemists, metal-organic and organometallic are equivalent terms, while for chemists metallorganic implies that M–C bonds are present. We will follow the chemistry convention.

Hybrid systems can, in principle, provide more opportunities than the pure ones. There are several good reasons for that. The first one is rather obvious: in metal-based magnets, the unpaired electrons can be assumed to be in metal-centered magnetic orbitals, while in organic materials the unpaired electron can be delocalized on many C, N, O, and so on atoms. The different types of magnetic orbitals provide more opportunities for the magnetic orbitals to interact with each other. Also, in many cases the interaction between different types of orbitals is fairly strong.

A pictorial example is shown in Figure 9.7. The molecule is obtained using as building blocks $[Mn^{III}(TPP)]$ and tetracyanoethylene (TCNE), where TPP is tetraphenyl-porphyrine and $TCNE^{-}$ is the anion of ethenetetracarbonitrile (Miller and Epstein, 2011).

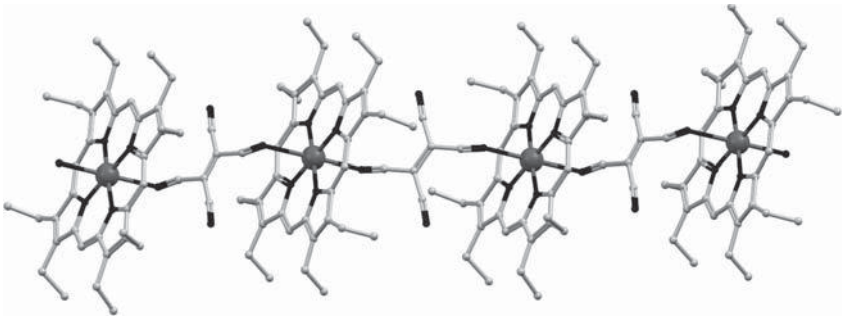

Figure 9.7 Segment of a uniform chain of the ferrimagnetic [Mn^{III}TPP]–[TCNE] · 2PhMe coordination polymer (the solvent is omitted for clarity). The TCNE anions are bridging Mn^{III}TPP moieties.

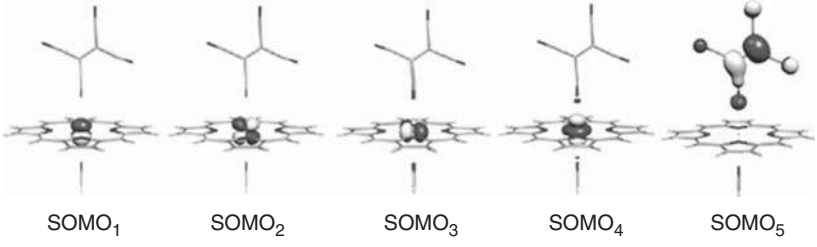

Figure 9.8 Shapes of the five SOMO orbitals of the system [Mn^{III}(TPP)]TCNE computed by using the B3LYP approach (Ribas-Arino, Novoa, and Miller, 2006). (Reproduced from Novoa J.J. *et al.* (2011) with permission from The Royal Society of Chemistry.)

Some metal ion radical compounds were already reported in Section 1.1. The present compound is a coordination polymer of the formula [Mn^{III}(TPP)]TCNE. The metal ion has a $3d^4$ electron configuration with four unpaired electrons in the *xz*, *yz*, *xy*, and z^2 orbitals. The $TCNE^-$ molecule has spin density on all atoms even though the density is not the same on all atoms. The type of d orbitals involved is qualitatively obtained by considering that the symmetry is elongated octahedral as generally observed in pseudo-octahedral coordination for manganese(III). The $t_{2g}{}^3e_{2g}$ configuration yields a ground ^5E_gwhich is unstable because of orbital degeneracy. Jahn–Teller theorem requires that vibronic coupling remove the degeneracy. The magnetic orbitals associated with the metal are SOMO 1–4, and that of the radical is SOMO 5 (Figure 9.8). The magnetic properties of the molecule depend on the exchange interactions involving the magnetic orbitals.

The simplest approach is to treat the compound as an alternating chain of $S_1 = 2$ and $S_2 = 1/2$. Assuming that S_1 can be treated as a classic spin, it is possible to calculate the magnetic susceptibility using the formulas elaborated by Seiden for the high-temperature limit and assuming negligible interchain coupling (Seiden, 1983). We recall that a classic spin is better approximated by a higher S, and therefore the present system is not the ideal one. Also, the Seiden model

assumes Heisenberg exchange, while the compound is better approximated by Ising exchange.

The magnetic data show a good approximation to a one-dimensional ferrimagnet, with interchain interactions that eventually determine the transition to magnetic order. We do not enter into the chemical details, which would make the production of a reasonably well-characterized system rather problematic.

TCNE compounds have been reported with several metal ions such as Fe, Mn, and V (Miller, 2011). The last yielded at room temperature a ferromagnet which as yet represents one of the few molecular ferrimagnets.

Similar compounds were also reported, among which $Fe(C_5Me_5)_2(TCNQ)$ (C_5Me_5 = (η_5-pentamethyl-cyclopentadienyl); TCNQ = tetracyanoquinodimethane) has a unique role (Scheme 9.3).

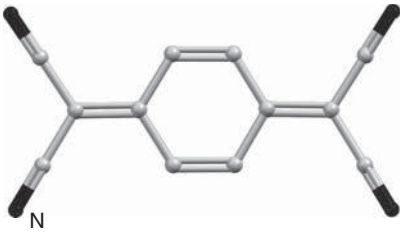

Scheme 9.3 3 Tetracyanoquinodimethane (TCNQ).

Several different possibilities were suggested, but perhaps the most famous, and controversial, case was that of $Fe(C_5Me_5)_2(TCNQ)$ whose structure is shown in Figure 9.9. The compound orders as a ferromagnet, and the magnetic orbitals are localized on $Fe(C_5Me_5)$ and on TCNQ (Broderick *et al.*, 1995). One feature is agreed upon by the groups working the field, namely that the Ising-type anisotropy has a key role in determining the relatively high critical temperature. This is clearly something that is associated to the metal ion. Therefore, the system is far away

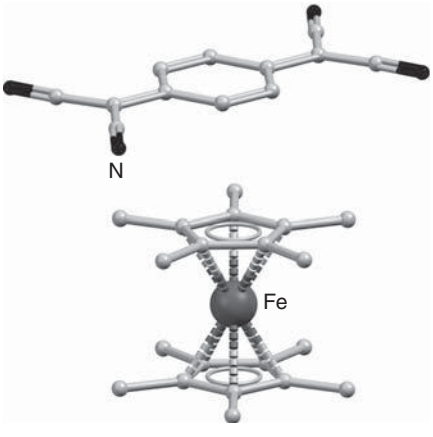

Figure 9.9 Schematic view of $Fe(C_5Me_5)_2(TCNQ)$.

from pure organic magnetism. And the hybrid nature is mandatory to determine the properties.

9.5 Semiquinone Radicals

The first examples reported in the literature on the nature of the magnetic interaction of gadolinium(III) and stable organic radicals, generally different nitronyl nitroxides, showed in all cases the presence of a ferromagnetic interaction whose coupling mechanism was estimated in the range $0.5-10\,cm^{-1}$. By using a chelating nitronyl nitroxide as ligand, an AFM interaction was observed for the first time (Lescop *et al.*, 1999). With the aim of investigating the exchange mechanism that gives rise to the two possible different couplings, other systems were synthesized with radicals different from nitronyl nitroxides.

An appealing series of organic radicals that can act as ligands toward TM and Ln is that of dioxolenes, which have the structures shown in Figure 9.10. They are stable in three different oxidation states: Cat, SQ, and Q (see the figure for explanation of the acronyms). We will not spend time on the TM: some derivatives such as the cobalt ones can be stable in two charge-transfer states of the type $Co^{III}Cat^{2-}$ and $Gd^{II}SQ$. The former is diamagnetic and the latter is paramagnetic. The phenomenon is akin to spin crossover, and is called *valence tautomerism* (Adams *et al.*, 1993; Gütlich and Dei, 1997).

We will spend some more time on dioxolene Ln derivatives. The original interest in Ln 3,5-di-*tert*-butylsemiquinonato (DTBSQ) was bound to the possibility to observe ferromagnetic coupling. An AFM coupling in fact was observed in the complex $[Gd(Hbpz_3)_2(DTBSQ)] \cdot 2CHCl_3$ ($Hbpz_3$ = hydrotris(pyrazolyl)borate), whose asymmetric unit is shown in Figure 9.11 (Caneschi *et al.*, 2000).

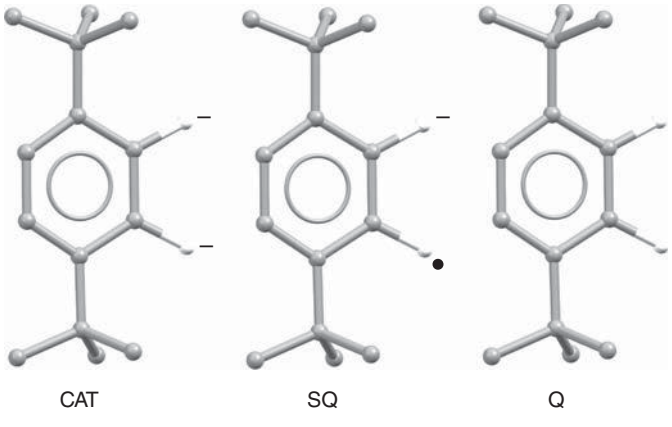

Figure 9.10 Cathecolate dianion (CAT), semiquinonate anion (SQ), and the quinone (Q). (From left to right).

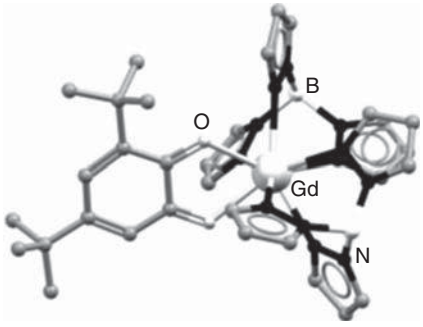

Figure 9.11 Sketch of the asymmetric unit of $[Gd(Hbpz_3)_2(DTBSQ)] \cdot 2CHCl_3$. Hydrogen atoms and solvating molecules are omitted for clarity.

The magnetization pattern measured at 2.15 and 4.5 K in an external magnetic field up to 8 T was nicely reproduced by using a Brillouin function for an S = 3 system, while the magnetic susceptibility values measured in the 10–245 K range were interpreted on the basis of an AFM coupling with $J = 11.4$ cm^{-1}. The energy separation between the ground S = 3 state and the first excited S = 4 state is 45.6 cm^{-1}, which is a quite remarkable value.

With the aim of elucidating the origin of these strong AFM interaction, the analogous coordination complexes were synthesized substituting Gd^{3+} with Sm^{3+}, Eu^{3+}, Dy^{3+}, Ho^{3+}, Er^{3+}, and Yb^{3+} (Caneschi *et al.*, 2004). Furthermore, the DTBSQ radical was substituted in the series, including in this case also Gd^{3+}, with the tropolonate ligand (see Scheme 9.4). This can be considered as a diamagnetic substituent of DTBSQ. The tropolonate derivatives show a marked similarity in structure with the semiquinonate derivative.

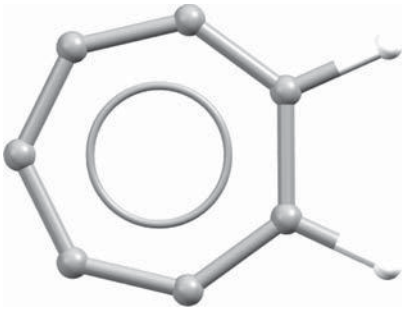

Scheme 9.4 Tropolonate ligand.

The goal of this approach can be schematized as indicated below: in a pair A–B where both bricks are magnetic, B is substituted by the diamagnetic D. The A–D pair provides information on the SH parameters in the assumption that substituting B with D changes only the magnetic properties of B, leaving those of A unchanged. It is a bold assumption justified by the small ligand field (LF) of Ln which has been used in Ln–Cu pairs in dinuclear and polynuclear species where B is copper and D can be square-planar nickel(II) or tetrahedral Zn^{2+}. A similar approach can be used for NITR radicals by using a diamagnetic nitrone ligand (Kahn *et al.*, 2000).

A detailed analysis of the Ln semiquinone series was performed by using both magnetic measurement and ESR spectroscopy, comparing the magnetic behavior of the various lanthanide ions with the radical and in the compounds with the tropolonate. The experimental data used were not quite conventional, as they were obtained through the measurement of the charge density using high-resolution X-ray diffraction experiments at 106 K and determining the spin density through polarized neutron diffraction experiments at 1.9 K on the $[Y(Hbpz_3)_2(DTBSQ)]$ compound (Claiser *et al.*, 2005). The crystal structure data at 106 and 10 K are very close to each other, suggesting a relatively robust structure.

The static deformation density map shows that the SQ is highly polarized. Formally, the Y ion carries a +3 charge, and the experiment says +1.53, while the N and O atoms of pyrazolyl borate, which are all expected to carry a −1 charge, are found to have −1.13 and −1.07 on N and +0.91 on SQ. The data provided also the spin densities, as shown in Figure 9.12.

All these data suggest a sizeable delocalization from the radical to the rare earth. These data are in agreement with the DFT calculations, allowing the suggestion of a model for exchange interaction in presence of Gd^{3+} ion and an organic radical. The nature of the magnetic interaction is substantially the result of two contributions: one from the direct overlap of the radical π orbital with the 4f orbitals resulting in AFM coupling, and the other due to the 4f orbitals' polarization by the spin delocalized from the radical toward the unoccupied 5d or 6s Gd^{3+} orbitals leading to ferromagnetic coupling. The difference observed in the magnetic behavior of DTBSQ and, generally, nitronyl nitroxides may, therefore, be related to the increased donor strength of the semiquinone ligand (Caneschi *et al.*, 2000).

As is often the case, the data of the other Ln derivatives are less conclusive because they need more data to gather the information needed. The features of

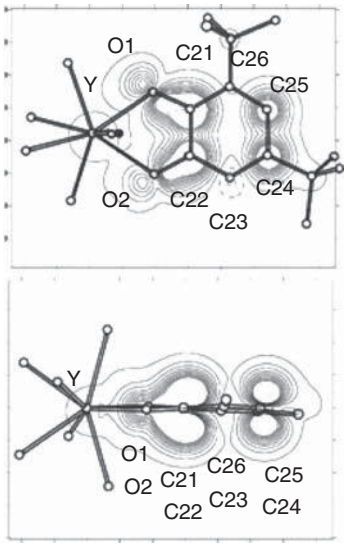

Figure 9.12 Projection of the induced spin density at 1.9 K under 9.5 T in $Y(HBPz_3)_2(DTBSQ)$ obtained by multipole model A reconstruction. (Top) Along the perpendicular to the mean plane of the semiquinonate ring. (Bottom) Along the C_{21}–C_{22} direction. Low levels only: $\pm 0.005\ \mu_B\ Å^{-2}$ with steps of $0.010\ \mu_B\ Å^{-2}$. Negative levels are dashed lines.

the ESR spectrum for the tropolonate derivative, which are analyzed in Section 21.3, suggest that the main contribution to the Yb^{3+} ground doublet comes from an f orbital of δ symmetry. As the magnetic orbital of the semiquinone has π symmetry, the orthogonality of the magnetic orbitals on the two magnetic centers should induce a weak ferromagnetic interaction. On the other side, the magnetic data suggest the presence of a dominant AFM contribution at low temperature. The nature of the interaction may be generated by the contribution of the low-lying first excited doublet, but different contributions may be active in determining the actual sign of the magnetic coupling. In any case, a more appropriate model is needed to analyze the origin of the exchange mechanism in this family of compounds, which could take into account explicit electron–electron correlation, crystal field effects, and SOC. For instance, the analysis of Cu^{2+}–Ln^{3+} pairs showed that the relevant factors in determining the nature of the coupling are the inter-orbital 4f electron repulsion integrals and the splitting of the f orbitals induced by the ligand field. In particular, it was shown that a ferromagnetic coupling is more probable for $n < 7$, while an AFM coupling is expected for the second half in the lanthanide series (Rudra, Raghu, and Ramasesha, 2002). For systems with parameters near the critical values, small changes due to differences in the ligand field can affect the magnetic properties even when belonging to the same half of the lanthanide series. According to this model, the low-spin state for all the above-described LnSQ systems may be originating from the smaller electron–electron repulsion in these systems with respect to the nitronyl-nitroxide derivatives. This is in agreement with the larger covalent character of the semiquinone–rare earth adduct compared to the latter ones.

9.6
NITR Radicals with Metals

Systems comprising metal ions and organic radicals are very numerous and have already been referred to in a number of cases including in the previous sections. We wish to report here some other examples in which organic radicals and their reduction products have been used to simplify the analysis of the coupled system where the p orbitals are involved. Let us start from a simple example Ln–R, where a Ln ion is bound to a radical which can be a nitronyl nitroxide (NITR). The system is simple but still far from amenable to immediate understanding. Let us suppose at the beginning that the Ln–NITR interaction can be neglected. The χT product for the organic radical is temperature independent and equal to 0.375 emu mol^{-1} K (S = 1/2). The Ln contribution, on the other hand, is temperature dependent as a result of the ZFS of the ground J multiplet. Focusing on Dy and assuming tetragonal symmetry, and giving test parameters to the ligand field, yields the energies of the Kramers doublets of the ground multiplet, as reported in Table 9.1, and the temperature dependence of χT, in Figure 9.13.

The behavior of χT values on decreasing T is due to the thermal depopulation of the energy levels according to their M_J values. For instance, the high-T

Table 9.1 Energy levels for a Dy^{3+} in a tetragonal field.

M_J	11/2	13/2	9/2	7/2	15/2	5/2	3/2	1/2
E (cm^{-1})	0	9.1	81.8	189.7	214.7	288.7	360.6	397.6

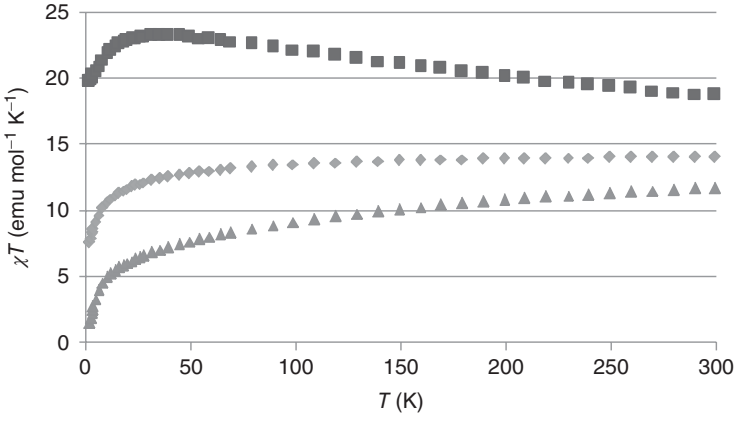

Figure 9.13 Temperature dependence of the χT values for a Dy^{3+} ion in a tetragonal coordination environment ($\chi_z T$ (■); $\chi_x T$, $\chi_y T$ (▲); mean value (◆)).

average χT of the Ln moiety is 13.75 emu mol^{-1} K. At low temperature, only the $M_J = \pm 9/2$ Kramers doublet is populated, which gives $\chi_{||} T = 19.78$ mol^{-1} K, $\chi_\perp$, $\chi T = 1.33$ mol^{-1} K at $T = 2$ K.

Switching on the Ln–NITR interaction changes the low-temperature limit. Assuming that the separation between the lowest and second lowest Kramers doublet of Ln is large compared to the Ln–NITR interaction, the approximate energies of the lowest four levels are given by the solution of the Hamiltonian

$$\mathcal{H} = J_z \mathcal{S}_z \mathcal{J}_z + g_{\mathrm{Ln},z} \mu_B \mathcal{S}_z H_z + g_{\mathrm{NITR},z} \mu_B \mathcal{J}_z H_z + H_x \tag{9.3}$$

which gives the energies of the four Kramers doublets present at zero magnetic field as

$$E_{1,2} = \pm g_{\mathrm{Ln},z} \mu_B H_z$$
$$E_{3,4} = \frac{1}{2} J_z \pm \left(g_{\mathrm{NITR},z} + \frac{1}{2} g_{\mathrm{Ln},z} \right) \mu_B H_z$$

From these expressions, an analytical formula to reproduce the field and temperature dependence of the magnetization along the easy axis can easily be derived.

It is all very simple if one knows the LF parameters, as in the above example. But in real life, the information is not available and fitting the data requires determining a large number of parameters. It would be good to have independent information on the Ln and NITR contributions.

In order to gain information, it may be useful to switch the radical off by substituting the NITR with the corresponding diamagnetic nitrone whose structure is

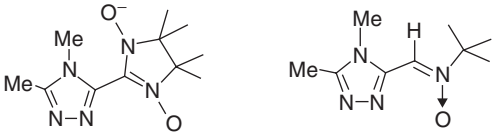

Figure 9.14 (Left) The organic radical 2-(4′,5′-dimethyl-1′,2′,3′-triazolyl)-4,4,5,5-tetramethyl-4,5-dihydro-1*H*-imidazolyl-1-oxy-3-oxide (TRZ), and (right) the derived nitrone. (Reproduced from Kahn, M.L. *et al.* (2000) with permission from The American Chemical Society.)

shown in Figure 9.14 together with the chosen nitroxide. Both ligands are chelated through N and O, but there are differences. The chelate ring of NITR is similar to that of nitrone. The differences between the two ligands are to be seen in the periphery, where the former has two *tert*-butyl groups and the latter one. At any rate, nitrone seems to be a reasonable diamagnetic approximation of NITR.

The idea is that the nitrone derivative provides the T dependence of χT of the Ln complex:

$$\Delta\chi T = \chi\text{Ln(organic radical)} \times T - \chi\,\text{Ln(nitrone)} \times T \tag{9.4}$$

An example taken from the work by Kahn and Sutter is particularly didactic (Sutter, Kahn, and Kahn, 1999). Let us start from Ho, which is coordinated by two NITR entities which can be substituted by two nitrones. The temperature dependence of χT of the NITR derivative is shown in Figure 9.15. At high temperature, χT is quasi constant at the value expected for one Ho and two radicals. The decrease observed at low T may be due to the depopulation of Stark levels or to the AFM coupling NITR–Ho or NITR–NITR. The data of the Ho nitrone derivative provide some qualitative information. The nitrone curve subtracted from the NITR gives information on the intrinsic data of Ho. Figure 9.16 shows that, down to 100 K, the difference is practically constant, it decreases to a minimum at 20 K,

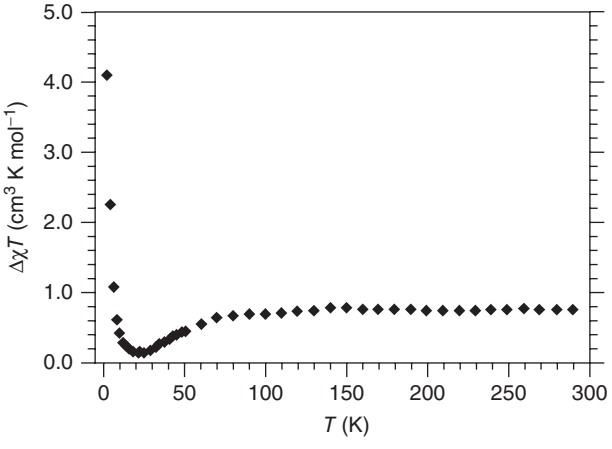

Figure 9.15 $\Delta\chi T$ versus T plot for $Ho(TRZ)_2(NO_3)_3$ calculated according to Eq. (9.4). (Reproduced from Sutter, J.P. *et al.* (1999) with permission from WILEY-VCH Verlag GmbH.)

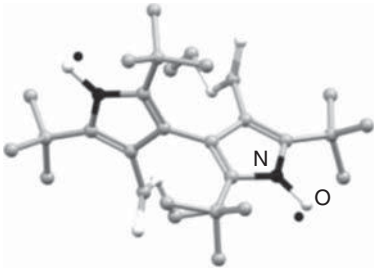

Figure 9.16 Structure of dinitroxyl (Bertrand *et al.*, 1994).

and then increases rapidly to 5 emu K mol^{-1} at 2 K. This is taken as evidence of ferromagnetic coupling between Ho and NITR. An analogous experiment with other 4f ions derivative showed that for the Ln^{3+} with $4f^1$ to $4f^5$ electronic configurations the interaction is AFM, and the interaction was found ferromagnetic for the configurations $4f^7$ to $4f^{10}$ (Kahn *et al.*, 2000).

9.7
Long Distance Interactions in Nitroxides

The use of nitroxides as spin labels and spin probes dates back to more than 50 years and many useful applications have been based on the assumption that the distance between two spins S_1 and S_2 can be measured assuming that they

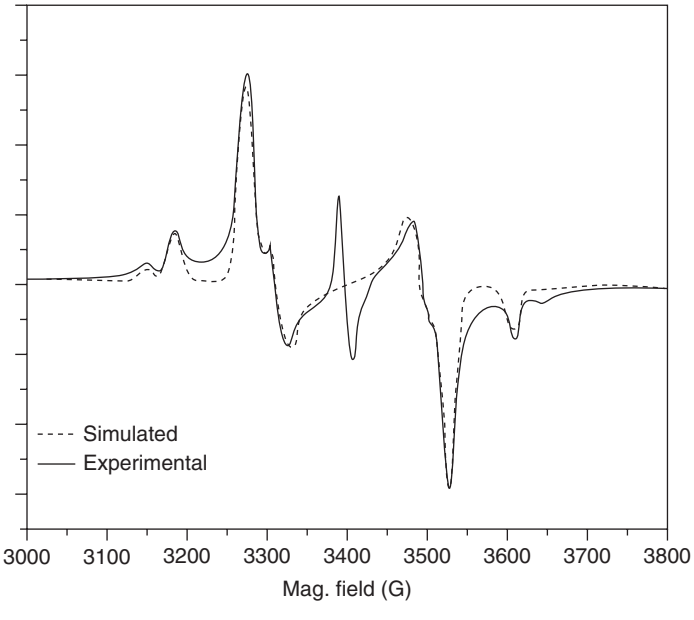

Figure 9.17 X-band spectrum of dinitroxyl in glassy decalin at 89 K. (Reproduced from Riplinger C. *et al.* (2009) with permission from The American Chemical Society.)

behave as classical spins. If the usual ESR studies are integrated with pulsed electron–electron double resonance (PELDOR) and double quantum coherence (DQC), it is possible to measure inter-spin distances or distributions of distances larger than 50 Å. This feature is relevant in defining the nature of the exchange mechanism as demonstrated in study on 2,2′,5,5′-tetra(*tert*-butyl)-4,4′-bis(ethoxy-carbonyl)-3,3′-bipyrrolyl-1,1′-dioxyl (dinitroxyl) (Figure 9.16) (Riplinger *et al.*, 2009).

The X-band ESR spectrum of the dinitroxyl is reported in Figure 9.17. To reproduce all the features of the spectrum, it is necessary to assume the presence of two conformations. The point-dipole approximation is able to reproduce the D and E values of the conformations which correspond to inter-spin distances of 5.1 and 4.8 Å, respectively, which is significantly shorter than the 7.0 Å distance between the centroids of the N–O bonds observed in the structure derived by X-ray crystallography. The molecular structure suggests that extensive delocalization of the unpaired electron might be contributing to this discrepancy. To analyze this possibility, it is necessary to develop a more detailed computational analysis.

It has been demonstrated that the ZFS of organic triplets and biradicals is dominated by the spin–spin contribution D^{SS}:

$$D_{KL}^{(SS)} = -\frac{g_e^2}{16}\frac{\alpha^2}{S(2S-1)}\sum_{\mu\nu}\sum_{\kappa\tau} P_{\mu\nu}^{\alpha-\beta} P_{\kappa\tau}^{\alpha-\beta}\left[\mu\nu\left|g^{KL}\right|\kappa\tau - \mu\kappa\left|g^{KL}\right|\nu\tau\right] \quad (9.5)$$

where g_e is the free-electron g-value (2.002 319), α is the fine structure constant ($\approx$1/137 in atomic units), the indices μ, ν, κ, τ refer to the basis functions, $P_{\mu\nu}^{\alpha-\beta}$

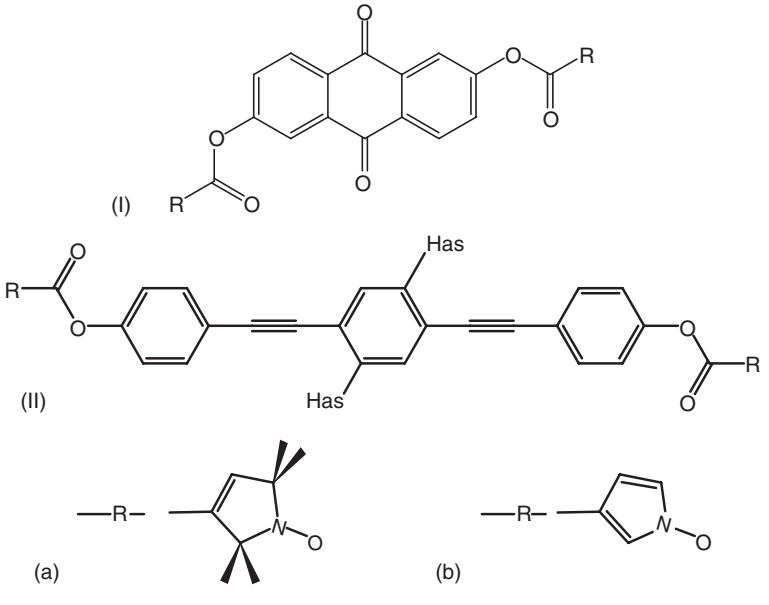

Scheme 9.5 Structural Diagram of Biradical (I) and Biradical (II).

Table 9.2 N–N distances for biradicals I and II measured experimentally from the molecular structure (with nitroxyl ring a) and determined via DFT calculations from D^{I} (with nitroxyl rings a and b).

System	Biradical I			Biradical II		
	D (cm^{-1})	Interspin (Å)	N–N distance (Å)	D (cm^{-1})	Interspin distance (Å)	N–N distance (Å)
Experimental results[a)]	−0.000341 ± 0.000005	19.73 ± 0.14	—	−0.000115 ± 0.000006	29.3 ± 0.5	27.84 ± 0.01[b)]
DFT model (a)	−0.000335	19.8	19.11[b)]	−0.000109	28.8	28.46[c)]
DFT model (b)	−0.000455	17.9	18.93[b)]	−0.000357	19.4	28.29[c)]

a) Available only for systems Ia and IIa.
b) N–N distance from X-ray diffraction, from (Pannier *et al.*, 2000).
c) From optimized structure.

is an element of the spin-density matrix, and $g^{KL} = r_{12}^{-5}(3r_{12K}r_{12L} - \delta_{KL}r_{12}^2)$ is the operator for the electron–electron magnetic dipole–dipole interaction. The final expression, even though not unique, shows the Coulombic contribution to the spin–spin interaction.

$$D_{KL}^{PDJ} = -\frac{g_e^2}{8}\frac{\alpha^2}{S(2S-1)} R_{i_L j_L}^{-5}[3R_{i_L j_L K}R_{i_L j_L L} - \delta_{KL}R_{i_L j_L}^2] \tag{9.6}$$

To confirm the correctness of the model, two different biradicals whose structures are depicted below were analyzed (Scheme 9.5).

The quality of the model can be appreciated on examining the experimental and calculated distances, reported in Table 9.2.

This important chapter has defined the basis of magnetism of compounds that contain at least one type of p orbital. The role of this type of magnetic orbitals perhaps deserves more intensive investigation now that *ab initio* techniques have become so diffuse.

References

Adams, D.M., Dei, A., Rheingold, A.L., and Hendrickson, D.N. (1993) Bistability in the [CoII(semiquinonate)$_2$] to [CoIII(catecholate)(semiquinonate)] valence-tautomeric conversion.

Awaga, K., Inabe, T., Nagashima, U., and Maruyama, Y. (1990) Two-dimensional network of the ferromagnetic organic radical, 2-(4-nitrophenyl)-4,4,5,5-tetramethyl-4,5-dihydro-1H-imiadzol-1-oxyl 3-N-oxide. *J. Chem. Soc., Chem. Commun.*, 520–520.

Banister, A.J., Bricklebank, N., Lavender, I., Rawson, J.M., Gregory, C.I., Tanner, B.K., Clegg, W., Elsegood, M.R.J., and Palacio, F. (1996) Spontaneous magnetization in a sulfur–nitrogen radical at 36 K. *Angew. Chem., Int. Ed. Engl.*, **35**, 2533–2535.

Bertrand, P., More, C., Guigliarelli, B., Fournel, A., Bennett, B., and Howes, B. (1994) Biological polynuclear clusters coupled by magnetic interactions: from the point dipole approximation to a

local spin model. *J. Am. Chem. Soc.*, **116**, 3078–3086.

Broderick, W.E., Eichhorn, D.M., Liu, X., Toscano, P.J., Owens, S.M., and Hoffman, B.M. (1995) Three phases of $[Fe(C_5Me_5)_2]^+[TCNQ]^-$: Ferromagnetism in a new structural phase. *J. Am. Chem. Soc.*, **117**, 3641–3642.

Caneschi, A., Dei, A., Gatteschi, D., Poussereau, S., and Sorace, L. (2004) Antiferromagnetic coupling between rare earth ions and semiquinones in a series of 1: 1 complexes. *Dalton Trans.*, 1048–1055.

Caneschi, A., Dei, A., Gatteschi, D., Sorace, L., and Vostrikova, K. (2000) Antiferromagnetic coupling in a gadolinium(III) semiquinonato complex. *Angew. Chem. Int. Ed.*, **39**, 246–248.

Claiser, N., Souhassou, M., Lecomte, C., Gillon, B., Carbonera, C., Caneschi, A., Dei, A., Gatteschi, D., Bencini, A., Pontillon, Y. *et al.* (2005) Combined charge and spin density experimental study of the yttrium(III) semiquinonato complex $Y(HBPz_3)_2$(DTBSQ) and DFT calculations. *J. Phys. Chem. B*, **109**, 2723–2732.

Deumal, M., Bearpark, M.J., Novoa, J.J., and Robb, M.A. (2002) Magnetic properties of organic molecular crystals via an algebraic Heisenberg Hamiltonian. Applications to WILVIW, TOLKEK, and KAXHAS nitronyl nitroxide crystals. *J. Phys. Chem. A*, **106**, 1299–1315.

Gütlich, P. and Dei, A. (1997) Valence tautomeric interconversion in transition metal 1,2-benzoquinone complexes. *Angew. Chem., Int. Ed. Engl.*, **36**, 2734–2736.

Hay, P.J., Thibeault, J.C., and Hoffmann, R. (1975) Orbital interactions in metal dimer complexes. *J. Am. Chem. Soc.*, **97**, 4884–4899.

Iwamura, H. (2013) What role has organic chemistry played in the development of molecule-based magnets? *Polyhedron*, **66**, 3–14.

Izuoka, A., Murata, S., Sugawara, T., and Iwamura, H. (1987) Molecular design and model experiments of ferromagnetic intermolecular interaction in the assembly of high-spin organic molecules. Generation and characterization of the spin states of isomeric bis(phenylmethylenyl)[2.2] paracyclophanes. *J. Am. Chem. Soc.*, **109**, 2631–2639.

Kahn, M.L., Sutter, J.P., Golhen, S., Guionneau, P., Ouahab, L., Kahn, O., and Chasseau, D. (2000) Systematic investigation of the nature of the coupling between a Ln(III) ion (Ln = Ce(III) to Dy(III)) and its aminoxyl radical ligands. Structural and magnetic characteristics of a series of $\{Ln(organic\ radical)_2\}$ compounds and the related $\{Ln(Nitrone)_2\}$ derivatives. *J. Am. Chem. Soc.*, **122**, 3413–3421.

LePage, T.J., Breslow, R. (1987) Charge-transfer complexes as potential organic ferromagnets. *J. Am. Chem. Soc.*, **109**, 6412–6421.

Lescop, C., Luneau, D., Belorizky, E., Fries, P., Guillot, M., and Rey, P. (1999) Unprecedented antiferromagnetic metal–ligand interactions in gadolinium–nitroxide derivatives. *Inorg. Chem.*, **38**, 5472–5473.

McConnell, H.M. (1963) Ferromagnetism in solid free radicals. *J. Chem. Phys.*, **39**, 1910.

McConnell, H. (1967) Ferromagnetic coupling in charge-transfer complexes. *Proc. R. A. Welch Found. Chem. Res.*, **11**, 144.

Miller, J.S. and Epstein, A.J. (1998) Tetracyanoethylene-based organic magnets. *Chem. Commun.*, 1319–1325.

Miller, J.S. (2011) Magnetically ordered molecule-based materials. *Chem. Soc. Rev.*, **40**, 3266–3296.

Novoa, J.J., Deumal, M., and Jornet-Somoza, J. (2011) Calculation of microscopic exchange interactions and modelling of macroscopic magnetic properties in molecule-based magnets. *Chem. Soc. Rev.*, **40**, 3182–3212.

Palacio, F., Antorrena, G., Castro, M., Burriel, R., Rawson, J., Smith, J.N.B., Bricklebank, N., Novoa, J., and Ritter, C. (1997) High-temperature magnetic ordering in a new organic magnet. *Phys. Rev. Lett.*, **79**, 2336–2339.

Pannier, M., Veit, S., Godt, A., Jeschke, G., and Spiess, H.W. (2000) Dead-time free measurement of dipole–dipole interactions between electron spins. *J. Magn. Reson.*, **142**, 331–340.

Ribas-Arino, J., Novoa, J.J., and Miller, J.S. (2006) Analysis of the magneto-structural correlations in the meso-tetraphenylporphyrinatomanganese(III) tetracyanoethenide family of molecule-based magnets. *J. Mater. Chem.*, **16**, 2600–2611.

Riplinger, C., Kao, J.P.Y., Rosen, G.M., Kathirvelu, V., Eaton, G.R., Eaton, S.S., Kutateladze, A., and Neese, F. (2009) Interaction of radical pairs through-bond and through-space: scope and limitations of the point-dipole approximation in electron paramagnetic resonance spectroscopy. *J. Am. Chem. Soc.*, **131**, 10092–10106.

Rudra, I., Raghu, C., and Ramasesha, S. (2002) Exchange interaction in binuclear complexes with rare-earth and copper ions: a many-body model study. *Phys. Rev. B: Condens. Matter*, **65**, 2244111–2244119.

Seiden, J. (1983) Propriétés statiques d'une chaîne isotrope alternée de spins quantiques 1/2 et de spins classiques. *J. Phys. Lett.*, **44**, 947–953.

Sutter, J.P., Kahn, M.L., and Kahn, O. (1999) Conclusive demonstration of the ferromagnetic nature of the interaction between holmium(III) and aminoxyl radicals. *Adv. Mater.*, **11**, 863–865.

Takahashi, M., Turek, P., Nakazawa, Y., Tamura, M., Nozawa, K., Shiomi, D., Ishikawa, M., and Kinoshita, M. (1991) Discovery of a quasi-1D organic ferromagnet, p-NPNN. *Phys. Rev. Lett.*, **67**, 746–748.

Yamaguchi, K., Toyoda, Y., and Fueno, T. (1989) Ab initio calculations of effective exchange integrals for triplet carbene clusters. Importance of stacking modes for ferromagnetic interactions. *Chem. Phys. Lett.*, **159**, 459–464.

10
Structure and Properties of Coupled Systems: d, f

10.1
d Orbitals

Molecular magnetism has birth with transition metals (TMs), in particular 3d, and at the beginning it was the detailed study of copper(II) dinuclear compounds which provided a key to understand how it could be possible to design tailor made magnetic interactions. An early success in magneto structural correlation was achieved with oxo bridged copper(II) dimers where a linear relation between J and Cu-O-Cu angle α was discovered. The cross over from ferro- to antiferromagnetic coupling occurs at $\alpha = 94°$ (Crawford *et al.*, 1976). After copper other ions started to be explored with the goal to understand the conditions which must be met to optimize the coupling between the building blocks. In the quasi totality of cases isotropic exchange is used. As yet there is a large impact of 3d metal ions even if heavier TM are now attracting increasing interest. Several reviews are available on corellations of magnetic properties and structural features of TM (Sieklucka *et al.*, 2011; Malrieu *et al.*, 2014). We will treat only few cases which we hope will be emblematic of the behavior of nd metal ions. In Table 10.1 the ground states for octahedral coordination are reported as derived by a simple *aufbau* approach.

For each configuration, the first row refers to the high spin (HS) or low spin (LS) state, the second to the number of unpaired electrons, the third to the total spin value, and the fourth to the orbital symmetry in octahedral coordination. A refers to an orbitally non-degenerate state, for which the spin Hamiltonian approximation holds. *E* indicates a state which is orbitally double degenerate Jahn-Teller theorem states that the coupling between the electron and vibration, vibronic coupling, may remove the orbital degeneracy by lowering the symmetry. Vibronic coupling is particularly efficient for E states. T corresponds to states with comparable phonon and spin orbit coupling (SOC) can remove orbital degeneracy. Correspondingly the treatment of the two perturbations is very delicate. A small difference between the two effects quenches the succumbing one. The two phenomena are referred to as Ham effect and dynamic Jahn-Teller. The Ham effect is based on the possibility that vibronic coupling may quench the SOC.

Introduction to Molecular Magnetism: From Transition Metals to Lanthanides, First Edition.
Cristiano Benelli and Dante Gatteschi.
© 2015 Wiley-VCH Verlag GmbH & Co. KGaA. Published 2015 by Wiley-VCH Verlag GmbH & Co. KGaA.

Table 10.1 Electronic configurations of d^n octahedral complexes.

d^1	d^2	d^3	d^4		d^5		d^6		d^7		d^8	d^9
			HS	LS	HS	LS	HS	LS	HS	LS		
1	2	3	4	2	5	1	6	0	3	1	2	1
$^2T_{2g}$	$^3T_{1g}$	$^4A_{2g}$	^5E_g	$^3T_{1g}$	$^6A_{1g}$	$^2T_{2g}$	$^5T_{2g}$	$^1A_{1g}$	$^4T_{1g}$	^2E_g	$^3A_{2g}$	^2E_g

Other classes of paramagnets which are actively investigated are single molecule magnet (SMM), single chain magnet (SCM), single ion magnet (SIM) and they will be treated in full detail in Chapters 12, 15, and 13 respectively.

Switching on an interaction between the magnetic building blocks will give at low temperature a transition to magnetic order, which can be ferro-, ferri-, antiferro-, weak ferro-magnetic in nature just to cite the most diffuse ones.

10.2 3d

The coordination compounds containing first row TM ions have attracted researchers' attention as their magnetic properties *y* are easier to handle with respect to 4d and 5d congeners. Most of the examples in the following are based on 3d derivatives. Therefore, here, we want just to stress a few examples which can be considered relevant in the development of MM. Table 10.2 shows the main magnetic ions with some basic information referred to stable oxidation numbers.

The first examples of molecular ferrimagnets were described as one dimensional – Cu-Mn-Cu-Mn arrays bridged by oxalates which give rise to 1D ferrimagnets thanks to the strong AF coupling transferred by the anion. The long range magnetic correlation switches on the interaction between chains and the system orders ferrimagnetically in the 4 K range (Kahn *et al.*, 1988).

Perhaps the most exploited ligand to yield bulk magnets is CN^- ion, which has the advantage to form strong bonds with metal ions; to bridge between pairs of

Table 10.2 3d metal ions with magnetic properties.

Metal Ion	Oxidation State	d Electrons	S	Metal Ion	Oxidation State	d Elecytons	S
V	+4	d^1	1/2	Cr	+3	d^3	3/2
Mn	2+	d^5	5/2	Fe	2+	d^6, HS	2
Mn	3+	d^4	2	Fe	3+	d^5, HS	5/2
Mn	4+	d^3	3/2	Fe	3+	d^5, LS	1/2
Co	2+	d^7, HS	3/2				
Co	2+	d^7, LS	1/2	Ni	2+	d^8	1
Co	3+	d^6, HS	2				
Co	3+	d^6, LS	0	Cu	+2	d^9	1/2

metal ions; to have two different donors which may preferentially bind to the M or M′ metal ions depending on the relative affinity. It must be remembered that to this series belongs one of the two room temperature molecular magnets (Miller, 2014).

A notable increase in the number of molecular magnets is achieved if we include in the list also systems containing radicals. Beyond the $Fe(cp)_2$ (cp = cyclopentadienyl) and the $V(TCNE)_2$ (TCNE = tetracyanoethylene) already mentioned $Fe(C_5Me_5)(TCNE)$ and TCNQ (TCNQ = tetracyanoquinodimethane) yield ferromagnets and metamagnet. A long detailed list is available (Miller, 2011).

$M(hfac)_2$ NITR have been investigated with several metal ions. The Co^{2+} derivative will be discussed as the first discovered SCM. Beyond compounds in which the strong interactions are one dimensional a few cooperative systems have two dimensional starting point. $[Fe^{II}(TCNE)(NCMe)_2][FeCl_4]$ show transition at 80 K. Ordered states are observed also in hydroxo, phosphonates, and thiophosphonates bridged compounds.

10.3
4d and 5d

It may be convenient to start from telling which are the features which diversify the 4d and 5d ions from 3d metal ones (Wang, Avendaño, and Dunbar, 2011). The wave functions are radially expanded and SOC and ligand field effects are larger for the former. All the interactions are stronger and so are the SH parameters, and the *J* coupling constants. We are going to show how the heavy metal ions must be treated in a different way compared to 3d. The difference is not only quantitative but qualitative.

The chemistry is different. While in 3d coordination octahedra and tetrahedra polyhedral dominate and coordination numbers are very rarely larger than 6 for heavier ions more coordination numbers are possible. The heavy TM have many oxidation states which can be switched also by external stimuli like light irradiation opening exciting perspectives in photomagnetism.

The approach used for obtaining new compounds at the simplest level is to mix in solution standard compounds and ligands and try to obtain something new. Serendipity is beautiful but one never know when it works. The problem is that many starting materials are rather inert therefore the building block strategy has been widely sed. In Table 10.3 are given the same type of information as in Table 10.2 considering that for 4d and 5d metal ion the LS configuration is more commonly found with respect 3d ions.

A nice example of the features of heavier TM is shown by the relevance of temperature independent paramagnetism (TIP) in the magnetic susceptibility. A trigonal bipyramidal pentanuclear cluster Os_2Ni_3 was synthesized, whose structure is shown in Figure 10.1 (Hilfiger *et al.*, 2008).

The Os^{3+} can be considered as equivalent to each other. The ions are in an octahedral coordination as shown in Figure 10.2.

Table 10.3 4d and 5d metal ions with magnetic properties.

4d							
Metal Ion	**Oxidation State**	**d Electrons**	**S**	**Metal Ion**	**Oxidation State**	**d Elecytons**	**S**
Nb	+4	d^1	1/2	Pd	+2	d^8, LS	1
Mo	+1	d^5	5/2				
Mo	+3	d^3	3/2	Ag	+2	d^9	1/2
Ru	+3	d^5, LS	1/2				
Ru	+3	d^4, LS	1				
5d							
Ta	+4	d^1	1/2	Os	+3	d^5, LS	1/2
W	+4	d^2	1	Os	+4	d^4, LS	1
W	+5	d^1	1/2				
Re	+4	d^3	3/2	Ir	+4	d^5, LS	1/2
Re	+5	d^2	1	Pt	+2	d^8	1

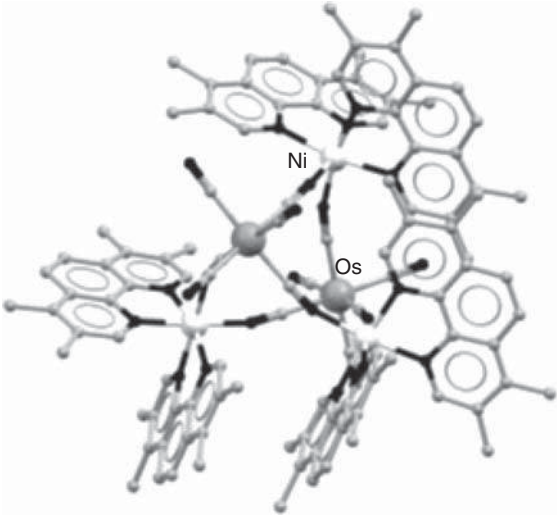

Figure 10.1 View of the molecular structure of $[Ni(tmphen)_2]_3[Os(CN)_6]_2 \cdot 6CH_3CN$ (tmphen = 3,4,7,8-tetramethyl-1,10-phenanthroline). Hydrogen atoms have been removed for the sake of clarity.

The three Ni are on the vertices of an equilateral triangle orthogonal to the Os-Os direction. The six donor atoms for Ni are four N of two from the tmphen ligand and two N of two bridging cyanides. The six carbon donors come from three bridging and three terminal CN. The ground state for nickel(II) in Oh symmetry is $t_{2g}^6 e_g^2 ({}^3A_{2g})$ while for osmium(III) it is $t_{2g}^5 ({}^2T_{1g})$. Clearly osmium(III) is orbitally degenerate and this makes impossible to use the spin Hamiltonian approach. Let us check in some detail the involved magnetic orbitals.

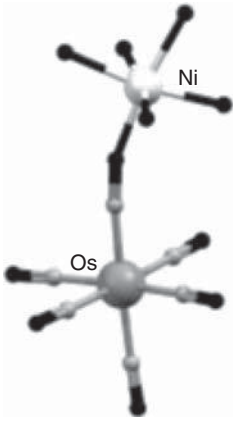

Figure 10.2 Local frame for $(NC)_5Os(\mu\text{-}CN)NiN_5$ bioctahedral fragment in the $[Ni(tmphen)_2]_3\ [Os(CN)_6]_2 \cdot 6CH_3CN$ derivative.

As it is always the case for a T_2 ground state the orbital degeneracy can be removed either by SOC or by Jahn Teller distortion. A large SOC gives rise to a large splitting which quenches the JT effect. A qualitative group theory argument tells that SOC switched on in the ground state $^2T_1$ induces the representation $T_1 \times E' = E' + U'$ of the double group O* (Section 7.3). We remind that for system with odd number of electrons the standard groups are not correct because the $S = \frac{1}{2}$ functions are not invariant to a rotation of 2π and the identity corresponds to a rotation of 4π. Therefore it is necessary to use the double groups which are obtained by the direct product G with (Em R) where R is the rotation by 2π. Please notice that for the irreducible representation we use the notation a′, e′, and so on, while it is more common Γ.

The SOC constant of Os free ion is larger than 5000 cm^{-1} therefore the ground doublet can be described as an effective $S = \frac{1}{2}$, and the U state is neglected because it has high energy. The involved magnetic orbitals therefore are two effective spins S(Os) for Os and three true S(Ni) = 1 for nickel. In this way it is possible to treat the problem forgetting orbital degeneracy in the ground state. The Hamiltonian is written as a sum of contributions from all the six Os-Ni pairs. Writing it is not trivial, because it is necessary to take into account the different orientations of the six pairs. Another case of non collinear axes. This kind of problem will be met again in Ln system where a similar solution.

$$\mathscr{H}_{\text{ex}} = \sum_{i=1,2} \sum_{j=3,4,5} \sum_{\alpha,\beta=X,Y,Z} \left\{ J_{\alpha\beta}(i,j)\, \tau_\alpha(i) \mathscr{s}_\beta(j) + \mu_B \left[g_{\text{eff}}(\text{Os})\, \tau_{12} + g(\text{Ni}) \mathscr{s}_{345} \right] H \right\} \tag{10.1}$$

where $\tau_{12} = \tau_1 + \tau_2$ is the pseudo-spin operator of the Os pair, $\mathscr{s}_{345} = \mathscr{s}_3 + \mathscr{s}_4 + \mathscr{s}_5$ is the spin operator of the Ni triad, and H is the magnetic field. The exchange parameters $J_{\alpha\beta}(i,j)$ are expressed in terms of the exchange integrals $J_\parallel$ and $J_\perp$. By assuming an anisotropic J or ever interaction and exploiting symmetry for the calculation of the Hamiltonian for the whole cluster a good fit was made of the powder susceptibility (Palii *et al.*, 2009).

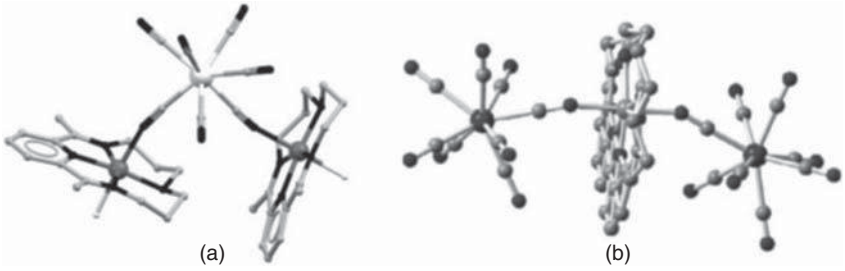

Figure 10.3 (a) View of the cationic $[(NiL^2)_2(M(CN)_8)]^+$ unit and (b) view of the anionic $[(NiL^2)(M(CN)_8)_2]^{4-}$ (M = Mo(V), W(V)).

A series of compounds which use a $[M(CN)_8]^{n-}$ building block with M = Mo^{5+}, W^{5+} is interesting for the magnetic properties of the adducts it can form (Sieklucka *et al.*, 2011). It is also interesting to compare with compounds of Ln where the metal ion is eight coordinate, a coordination with is rare with 3d ions. Eight coordination can correspond to various geometries. The limit ones have been introduced in Chapter 3. The coordination polyhedra are fluctuating and it is very demanding to unravel the electronic structure and the spin density because in every case it is mandatory to have detailed investigations with experimental and theoretical treatments. A nice example is provided by two compounds $[MNi_2]$ with $(Mo/W)(CN_8)^{3-}$ ion (M) (Visinescu *et al.*, 2006). Another set has stoichiometry $[M_2Ni]^{4-}$. The synthesis is trivial, 1 mol $M(CN)_8{}^{3-}$ is reacted with 2 mol NiL_2 (L_2 = 2,12-dimethyl-3,7,11,17-tetrazabicyclo[11.3.1]heptadeca-1(17),2,11,13,15-pentaene) in the presence of $HClO_4$ to yield the Ni_2M adduct. If the same reaction is made without $HClO_4$ the NiM_2 adduct is obtained (Figure 10.3). The Ni coordinates four nitrogen in a plane and has an octahedral coordination binding one cyanide and one water in the Ni_2M and two N in NiM_2. The trimeric units form chains by hydrogen bonding of the terminal water molecules for the Ni_2M and cyanide moieties for NiM_2.

The magnetic data show a ferromagnetic (FM) coupling which causes an increase of χT on decreasing temperature down to about 20 K for Ni_2M and NiM_2. The data were fitted with the standard treatment including parameters for intermolecular AFM coupling. The best fit parameters are given in Table 10.4.

Table 10.4 Exchange coupling constants and g values of some Ni_2M or NiM_2 (M = Mo, W) compounds.

	Ni_2Mo	Ni_2W	$NiMo_2$	NiW_2
J (cm^{-1})	−27	−37	−15	−14
zJ′ (cm^{-1})	−1	−0.86	−0.6	−0.7
g_{Ni}	2.14	2.11	2.12	2.25
g_M	2.00	2.00	2.00	2.00

Some comments: the difference between the J parameter of the Mo and W compounds is very small, being essentially zero for the NiM_2 compounds. At the same time, it is more important for Ni_2M. A detailed analysis was performed starting from looking for the best geometrical description of the $M(CN)_8$ polyhedra. By comparing the experimental angles with the ones expected for squared antiprism (SAP), bicapped trigonal prism (BTP), and dodecahedron (DD) it is concluded that the closest geometry is that of the DD.

The LF analysis for eight coordination shows that for all the limit geometries the ground state is orbitally non degenerate. For the DD the ground state is B_1. DFT calculations were performed on several coordination polyhedra and on the experimental structure – the calculations confirm the nature of the ground state has been confirmed. Also the calculated values of the J are in line with the experimental ones, confirming the validity of the DFT calculations also for clusters containing 4d and 5d ions.

10.4 Introducing Chirality

The three dimensional metal oxalates provide the opportunity to speak of chirality which is one of the fundamental properties of matter. In fact we live in a chiral world including ourselves. An object is chiral if it is not superimposable to its mirror image like the left and right hand. Referring to symmetry an object is chiral if it does not admit any improper rotation. This can be considered structural chirality and is familiar to all chemists because it affects the reactivity of chemicals. It is also well known that nature favors one type of chiral objects. Some properties bound to chirality are frequently measured like optical activity and circular dichroism.

There is another type of chirality which sometimes is called magnetic chirality. It is observed for instance when a spin system is placed in a magnetic field and circularly polarized light is propagated parallel to the field. The observed difference in absorption of left and right polarized light is called Magnetic Circular Dichroism, (MCD), and it does not require structural chirality to be observed. The wavelength of the radiation can be any, the most common being UV-Vis and X-ray (XMCD, Funk *et al.*, 2005) respectively.

Spin chirality is used to describe the properties of frustrated spins. If three spins on the vertices of an equilateral triangle are AFM coupled it is impossible to put them up and down (spin frustration). It is not a catastrophe the remedy is to orient the spins as detailed discussed in Section 16.2. The two orientations are the mirror image of each other; therefore the system is an example of spin chirality.

There is much interest in understanding structural chirality and learning how to make Enantiopure Chiral Magnets (ECMs). The idea is that ECM can be better than non-enantiopure materials. Another reason to move toward ECM is that they are expected to give rise to Magneto Chiral Effect (MChE). As we will show shortly the effect demands ECM. This goal can be achieved in several different pathways. The first is the less strategic one, namely spontaneous resolution. It is

rare but after Pascal it has occurred quite a few times. For instance we observed the phenomenon in CoNITPhOMe which yielded crystals belonging to the $P3/_1$ space group. More strategic approaches require chiral ligands or chiral bridge ligands. More sophisticate strategies associate the chiral coligand with not chiral connectors and master the configuration of intrinsically chiral networks.

Well, this statement might be a little pessimistic as recent results about crystal structure data base checking seem to indicate. Space groups are cataloged in three classes depending on their chirality properties. Class I collects 165 groups which contain at least an improper rotation (Ci, Cs, or Sn). They are all non-chiral.

Class II has 22 groups corresponding to two sets of 11 groups. They are enantiometric pairs. These are always chiral. The groups contain at least one symmetry axis.

Class III has 43 groups. They contain proper rotations and 21. Even if they have no improper axis they are achiral. But the crystals which pack by them are achiral.

Avnir *et al.* suggest the following classification (Alvarez, Alemany, and Avnir, 2005):

Class	N of groups	Groups	Crystals
Class I	165	Improper achiral	Achiral
Class II	22	Helical chiral	Chiral
Class III	43	Proper achiral	Chiral

The analysis of the reported structures identified 574 000 non biological of which 131 000 were chiral. The number of structures which were reported as chiral is only 35 000: about 100 000 are missing. This may mean that the serendipity approach even for chirality is rather efficient.

Once the ECM is obtained one waits to be sure that the effort was worthwhile. In a few cases it was found that subtle differences in the spin orientation were observed which produced a non-zero contribution to the magnetization. An interesting result but not particularly exciting.

MChD (Magneto-Chiral-Dichroism) in principle has the novelty of a new phenomenon which can produce new types of phenomena. Beyond the circular dichroism (CD) and MCD, MChD was suggested to be operative as a cross effect between CD and MCD. Shortly the absorption coefficient of a chiral molecule can be made different for an unpolarized light beam by applying a magnetic field parallel or antiparallel to the propagation direction. The interest for this exotic property is that it has been suggested to be responsible of the biased distribution of the L amino acids and D sugars some attempts to find evidence were made but evidence is lacking.

Without entering in detailed calculations it is sufficient to explain that the global dielectric tensor depends on the wave vector of light and the magnetization of the medium. The terms entering the development are the refraction and absorption; natural circular birefringence and natural circular dichroism; magnetic circular birefringence, and magnetic circular dichroism and finally the term comprising

magneto-chiral effects namely magneto-chiral and MChD. The implementation of the MChD requires to have an enantiomerically pure sample in order to be sure that the small expected effect is not by accident. A high magnetization is needed for the same reason. Spectral ranges must be available which are free from interactions with light. Preliminary data have been obtained on systems containing Eu (Train, Gruselle, and Verdaguer, 2011).

10.5 f-d Interactions

The rationalization of the magnetic properties of pairs of metal ions, of which at least one is a Ln, is a strategy which aims to move from simple to complex. Therefore, the first step must be to choose Ln, which must be as simple as possible. Second the partner must be chosen. It is better to use building blocks characterized by p or d magnetic orbitals because they have been intensively studied and magneto-structural correlations are available which hopefully can be extended to f magnetic orbitals. Therefore let us start from d-f pairs.

Among the first examples of attempts to correlate structure and magnetic properties of systems with coupled Ln and TM the Gd-Cu species have had a key role. The choice of Gd was almost a must, being the only Ln with orbitally not degenerate ground state, allowing relatively simple effective Hamiltonian approach, which is of the HDVV type. Similar considerations apply for copper which is also characterized by a rich coordination chemistry which had produced efficient correlations between structure and magnetic properties.

It was with some surprise that it was found that in most cases the Gd-Cu coupling is ferromagnetic (Bencini *et al.*, 1985; Benelli and Gatteschi, 2002). The naïve scheme we had in mind was: Cu has one magnetic orbital, Gd has seven, a small overlap of the Cu with one or more Gd magnetic orbital should be enough to develop AFM coupling. After all Gd with half-filled $4f^7$ configuration is analogous to Fe^{3+} and Mn^{2+} with their $3d^5$ configuration and the coupling observed in Cu, Mn, and Cu-Fe is generally AFM. The current understanding of the origin of the FM coupling is the polarization mechanism by which a fraction of unpaired electron is transferred from a copper orbital to an empty one of Gd. After some discussion the choice fell on the 5d orbitals. The mechanism is that associated to the rule of Goodenough-Kanamori: the 5d orbital housing the fraction of unpaired electron is orthogonal to the 4f orbital, and the exchange interaction will keep the spins of the two electrons parallel to each other.

The ferromagnetic coupling constants are small, typically of the order of 1 K. Please remember that on comparing couplings one should use the energies, not the coupling constants. In a Gd-Cu pair the total spin will be $S = 3, 4$, the latter being the ground state for FM coupling. It is apparent that the systems are very delicate when attempting to rationalize properties which are measured by small numbers and depend on many parameters which up to few years ago were brutally assumed with little or null support for calculations. The above alluded

to suggested mechanism for FM coupling in Cu-Gd systems was originally suggested by the Florence group (Bencini *et al.*, 1986). We observed that a possible mechanism for the ubiquitous FM observed experimentally was described by a polarization mechanism requiring the partial transfer from a Cu orbital to an empty Gd orbital. We suggested 6*s*, but it was more an example than a statement. After long discussions DFT provided a quantitative basis for a correct analysis.

10.6 A Model DFT Calculation

The use of DFT for calculating the magnetic coupling in Cu-Gd systems started with an epochal paper by Cimpoesu and Hirao which provided a deep insight in the mechanism of interaction (Paulovič *et al.*, 2004). The calculations were performed on a model molecule containing copper and lutetium to avoid at the beginning the complications of the seven unpaired electrons.

A structure of the molecule together with the polarized spin density is shown in Figure 10.4.

Recalling that he ground state of Gd^{3+} is $4f^7$, $^8S_{7/2}$, the SOC, and low symmetry components of the LF remove the degeneracy of the ground multiplet yielding a zero field splitting (ZFS). The FT value compares well with the experimental ones. Another point is that here cannot be any admixture of the $4f^7$ states with the $4f^6s$ or $4f^6d$ because of parity effects. The calculated parameters for the electron repulsion compare well with the experimental ones.

The interest, once the calculations have been shown to yield a feasible view of the molecule, is then moved to the mechanism of exchange interaction. The

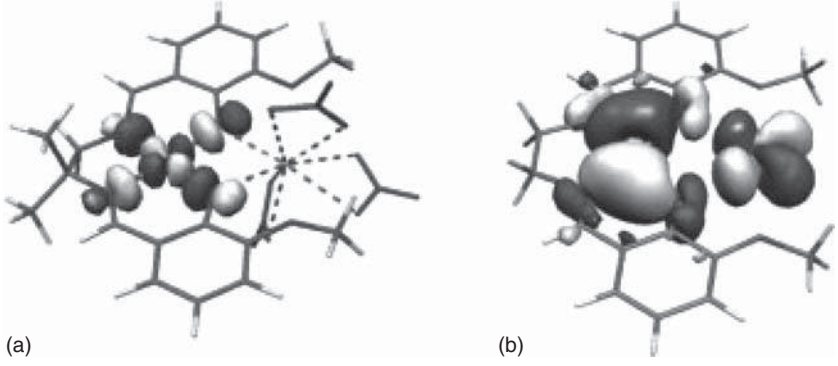

Figure 10.4 Orbitals of quasi-C_{2v} symmetry in Cu–Ln complexes with binucleating ligands. (a) The natural orbital resulting from complete active space self-consistent field (CASSCF). The departure from true C_{2v} symmetry comes from asymmetric ligand substitution and the placement of semi-coordinated NO_3^- counterions. (b) The orbital density difference map for the orbital centered on [CuL]. (Reproduced from Paulovič, J. *et al.* (2004) with permission from The American Chemical Society.)

polarization mechanism through the 5d orbitals suggested by Kahn appeared to be more appropriate (Andruh *et al.*, 1993).

10.7
Magneto-Structural Correlations in Gd-Cu

DFT proved to be useful to calculate FM coupling in [LCuGd$(O_2CF_3)_3$ $(C_2H_5OH)_2$], where L = N,N′-bis(3-ethoxy-salicylidene)-1,2-diamino-2-methyl-propanato) whose structure is shown in Figure 10.5. The copper is square pyramidal while Gd is eight-coordinated (Novitchi *et al.*, 2004). The metal ions are separated by 0.32959 nm and are bridged by two phenoxo and one carboxylate groups.

The DFT calculations were performed on the whole structure using the BS approach (Rajaraman *et al.*, 2009). The experimental data showed a ferromagnetic coupling constant J = $-4.42\ cm^{-1}$ and the calculations with several different functionals gave J values ranging from -3.6 to $-8.8\ cm^{-1}$. This is certainly an important result but more insight must be achieved by further analysis. This shows that the magnetic orbital of Cu is very far from the magnetic orbitals of Gd, while it is relatively close to the empty 5d and 6s. The natural bond orbital analysis (NBO) shows the presence of significant electron density in these orbitals. Overall the mechanism of exchange can be schematized as shown in Figure 10.6. The energies of the 5d orbitals cluster in a set of two lying lower and another of three lying higher. The former are determined by the CT from $d_{x^2-y^2}$ of Cu to the 5d, while the latter gain density through f delocalization. The suggestion is that the former give AF coupling, the others the F contribution.

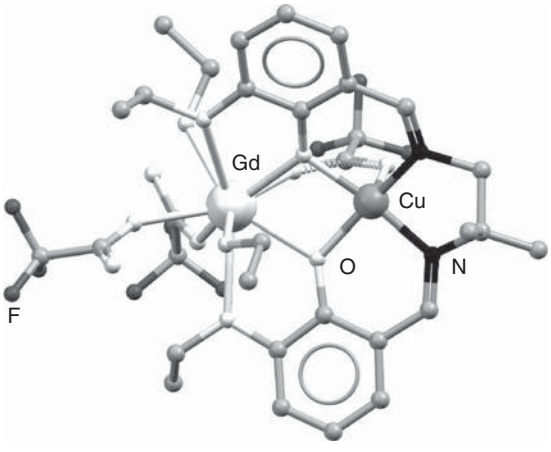

Figure 10.5 Ball and stick representation of [LCuGd$(O_2CF_3)_3(C_2H_5OH)_2$] (L = N,N′-bis(3-ethoxy-salicylidene)-1,2-diamino-2-methyl-propanato). Hydrogen atoms are omitted for clarity.

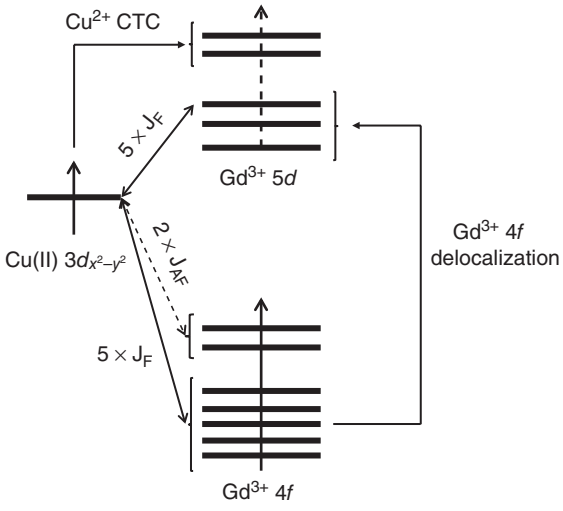

Figure 10.6 A schematic mechanism for the magnetic coupling on the [GdCu] pair obtained from the DFT calculations. The nature and the number of interactions between the Cu^{2+} and the Gd^{3+} are shown by double headed arrows. The Gd^{3+} 5d orbitals gain density via the Cu^{2+} charge transfer and also via the 4f delocalization.

The above results can be used to verify the suggested magneto structural correlations which were based simply on an empirical basis. Historically the first suggestion was made by Winpenny who attempted a correlation with the Cu-Gd distance, but the comparison with structural data was unsuccessful (Winpenny, 1998). Costes suggested the dihedral angle α between the GdO_2 and the O_2Cu planes, where O_2 are the bridging oxygen atoms (Costes, Dahan, and Dupuis, 1999). The fit was made to an exponential dependence:

$$J = A \ \exp(B\alpha) \tag{10.2}$$

where $A = 11.5\ \text{cm}^{-1}$ and $B = -0.054$ for α in degrees. The agreement is pretty good but there is not much discussion possible. But the advantage of having the possibility of calculating model molecules using DFT allows to use tailor made molecules to discuss the effect of various parameters on the magnetic coupling (Rajaraman *et al.*, 2009). So calculating molecules with Cu-Gd distance r varying from 0.26 to 0.48 nm Morse curve was obtained which does not match with the experimental data which do not give evidence of the AF coupling suggested by the calculations. A better agreement is obtained with the dihedral angle dependence. J becomes increasingly AF on increasing α as shown in Figure 10.7.

The calculated values are fitted to:

$$J = A + B \exp(\alpha/p) \tag{10.3}$$

where $A = -9.599\ \text{cm}^{-1}$; $B = 2.651\ \text{cm}^{-1}$; $p = 31.20°$.

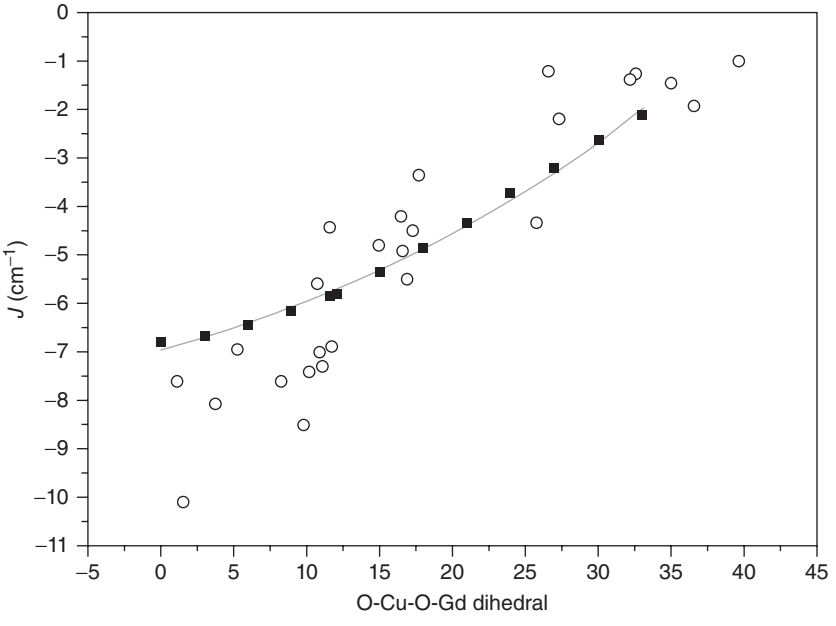

Figure 10.7 Magneto-structural correlations developed by DFT calculations by varying the O-Cu-O-Gd dihedral angle. The open circles represent the experimental points obtained from the crystal structure and *J* from the magnetic susceptibility measurements. The line on graph is the exponential growth fit for the DFT points.

Having limited the number of parameters needed for describing the exchange interactions the fit is very good but it appears that in the real world matters are different and many small changes in hidden parameters determine the dispersion of points in Figure 10.7.

Beyond copper other TM have been investigated in pairs. Both 3d and 4d/5d have been taken into consideration. Ferromagnetic coupling was observed for manganese(III), iron(II), cobalt(II) nickel(II). Antiferromagnetic coupling was observed with chromium(III) and iron(III).

Particularly elegant are the derivatives obtained using $W(CN)_8^{3-}$ as building blocks together whit $Gd(DMF)_6$ DMF = *N*,*N*′-dimethylformamide (Ikeda *et al.*, 2005). The compound is a textbook example of one dimensional ferrimagnet with high temperature data following the Curie law. The AFM coupling yields a minimum at about 7 K and then increases rapidly. A simple treatment of the susceptibility has been suggested by Seiden who considers the chain as the alternation of classic and quantum spins. The approximation is reasonable given the big Gd spin. Indeed a good fit was obtained with $J = 1.4\ cm^{-1}$. Terpy (2,2 : 6,2-terpyridine) is used to synthesize Ln(terpy) $W(CN)_8$ chains, with Ln = Gd, Sm (Przychodzen *et al.*, 2006). The Gd derivatative behaves as regular ferrimagnetic chains dominated by next neighbor (NN) (see Chapter 15) interaction with a coupling constant of $1.6\ cm^{-1}$. The Sm derivative shows a 1-D magnetic behavior

and the magnetic properties are nicely reproduced in the Seiden approach with a $J = -1.4\ \mathrm{cm}^{-1}$ and $g_{\mathrm{Sm}} = 0.13$. The effective coupling constant J between the total angular momentum of Sm^{3+} center and the spin of the W^{5+} ion indicates a net ferromagnetic coupling.

Several examples of Gd-Gd interactions have been reported, in general with antiferromagnetic coupling, J ranging from 0.05 to $0.21\ \mathrm{cm}^{-1}$. An exception was reported with a ferromagnetic coupling $-0.05\ \mathrm{cm}^{-1}$ observed in a salicylate derivative. It must be stressed that the above reported J values assume that the ZFS due to the LF can be neglected, an over simplifying assumption. The problem has been tackled by Long *et al.* (2011) on a dinuclear Gd with valdien (H_2valdien = N_1, N_3-bis(3-methoxysalicylidene)diethylenetriamine) by fitting the temperature dependence of χT with the exchange model and comparing with the values obtained with *ab initio* calculations of the ZFS. The exchange value is $-0.08\ \mathrm{cm}^{-1}$ while the fitted parameter of the isotropic exchange $J_{\mathrm{iso}} = 0.178\ \mathrm{cm}^{-1}$ the difference being due to the ZFS. Therefore the ZFS cannot be neglected.

10.8 f Orbital Systems and Orbital Degeneracy

So far we have avoided the complications associated with orbital degeneracy, except for the concise considerations of Section 8.6. We will re-consider now the orbitally degenerate case in a simple way. From now on we will have to accept the challenge and see what must be done to treat at an acceptable degree of accuracy. The simplest case is that of an isolated Ln, where one assumes that the interaction between neighboring ions can be neglected. Since the LF is small and the dipolar magnetic interactions although small must be summed on many neighbors, the assumption of isolated ions may not be trivial to confirm.

Under these conditions one can expect that the ground multiplet $^{2S+1}L_J$ is split by the LF. We will by necessity consider only examples since the number of Gd-Ln pairs where Ln is a paramagnetic lanthanide different from Gd is 12 and the number of Ln-Ln′ pairs is 78! A test treatment will be done of pairs with valdien ligand similar to the Gd pairs described above. The ions for which data are available are Eu, Tb, Dy, and Ho. The data were interpreted using the so called Lines model which was originally developed for HS cobalt(II) in octahedral symmetry (Lines, 1971) and was introduced in Section 10.3. In this approach the exchange interaction between different spin terms in the absence of SOC is modeled by a single parameter exchange Hamiltonian. This is written on the basis of the *ab initio* computed spin orbit multiplets of the metal fragments and then diagonalized. The results of the calculation yield the anisotropic exchange Hamiltonian for the complex. This is much better than the simplest bilinear approximation which requires the calculation of a 3×3 matrix requiring nine parameters.

This approach has been used for the pairs described above. Calculations of the energies of the levels of Eu show that the first excited state is lower in energy than expected for the free ion ($231.4\ \mathrm{cm}^{-1}$ compared to $400\ \mathrm{cm}^{-1}$).

Table 10.5 Calculated exchange coupling constants (cm^{-}) for Ln_2 complexes.

Ion	Eu	Gd	Tb	Dy	Ho
J (Lines)	—	0.08	0.1	0.21	0.44
J (Ising)	—	—	3.60	5.25	7.04
Ln-Ln	3.830	3.811	3.788	3.768	3.754
Ln-O-Ln	107.26	107.76	108.05	108.22	108.17

The calculation of the Tb derivative yields for the Lines parameter 0.1 cm^{-1} in good agreement with the experimental one. Similar good fits were obtained for the other metal ions as shown in Table 10.5 where it is possible to compare the values of coupling constants evaluated in the Lines and Ising approaches.

The analysis of the computations takes into account as structural parameters the Ln-O distance and the Ln-O-Ln angle. Both the Lines and the Ising model show an increase of J on moving from left to the right in the Periodic Table. It seems also that the exchange coupling increases on decreasing the Ln-Ln distance, but this does not really seem to be a rational correlation because the same *J* value gives different spectrum of levels and magnetic properties.

References

Alvarez, S., Alemany, P., and Avnir, D. (2005) Continuous chirality measures in transition metal chemistry. *Chem. Soc. Rev.*, **34**, 313–326.

Andruh, M., Ramade, I., Codjovi, E., Guillou, O., Kahn, O., and Trombe, J.C. (1993) Crystal structure and magnetic properties of $[Ln_2Cu_4]$ hexanuclear clusters (where Ln = trivalent lanthanide). Mechanism of the Gd(III)-Cu(II) magnetic interaction. *J. Am. Chem. Soc.*, **115**, 1822–1829.

Bencini, A., Benelli, C., Caneschi, A., Carlin, R.L., Dei, A., and Gatteschi, D. (1985) Crystal and molecular structure of and magnetic coupling in two complexes containing gadolinium(III) and copper(II) ions. *J. Am. Chem. Soc.*, **107**, 8128–8136.

Bencini, A., Benelli, C., Caneschi, A., Dei, A., and Gatteschi, D. (1986) Crystal and molecular structure and magnetic properties of a trinuclear complex containing exchange-coupled $GdCu_2$ species. *Inorg. Chem.*, **25**, 572–575.

Benelli, C. and Gatteschi, D. (2002) Magnetism of lanthanides in molecular materials with transition-metal ions and organic radicals. *Chem. Rev.*, **102**, 2369–2387.

Costes, J.-P., Dahan, F., and Dupuis, A. (1999) Influence of anionic ligands (X) on the nature and magnetic properties of dinuclear $LCuGdX_3 \cdot nH_2O$ Complexes (LH_2 standing for tetradentate schiff base ligands deriving from 2-hydroxy-3-methoxybenzaldehyde and X Being Cl, N_3C_2, and CF_3COO). *Inorg. Chem.*, **39**, 165–168.

Crawford, V.H., Richardson, H.W., Wasson, J.R., Hodgson, D.J., and Hatfield, W.E. (1976) Relationship between the singlet-triplet splitting and the Cu-O-Cu bridge angle in hydroxo-bridged copper dimers. *Inorg. Chem.*, **15**, 2107–2110.

Funk, T., Deb, A., George, S.J., Wang, H., and Cramer, S.P. (2005) X-ray magnetic circular dichroism – A high energy probe of magnetic properties. *Coord. Chem. Rev.*, **249**, 3–30.

Hilfiger, M.G., Shatruk, M., Prosvirin, A., and Dunbar, K.R. (2008) Hexacyanoosmate(III) chemistry: preparation and magnetic properties of a pentanuclear

cluster and a Prussian blue analogue with Ni(II). *Chem. Commun.*, 5752–5754.

Ikeda, S., Hozumi, T., Hashimoto, K., and Ohkoshi, S.-i. (2005) Cyano-bridged gadolinium(III)-tungstate(V) bimetallic assembly with a one-dimensional chain structure. *Dalton Trans.*, 2120–2123.

Kahn, O., Pei, Y., Verdaguer, M., Renard, J.P., and Sletten, J. (1988) Magnetic ordering of manganese(II) copper(II) bimetallic chains; design of a molecular based ferromagnet. *J. Am. Chem. Soc.*, **110**, 782–789.

Lines, M.E. (1971) Orbital angular momentum in the theory of paramagnetic clusters. *J. Chem. Phys.*, **55**, 2977.

Long, J., Habib, F., Lin, P.-H., Korobkov, I., Enright, G., Ungur, L., Wernsdorfer, W., Chibotaru, L.F., and Murugesu, M. (2011) Single-molecule magnet behavior for an antiferromagnetically superexchange-coupled dinuclear dysprosium(III) complex. *J. Am. Chem. Soc.*, **133**, 5319–5328.

Malrieu, J.P., Caballol, R., Calzado, C.J., De Graaf, C., Guihéry, N. (2014) Magnetic interactions in molecules and highly correlated materials: Physical content, analytical derivation, and rigorous extraction of magnetic hamiltonians. *Chem. Rev.*, **114**, 429–492.

Miller, J.S. (2011) Magnetically ordered molecule-based materials. *Chem. Soc. Rev.*, **40**, 3266–3296.

Miller, J.S. (2014) Organic and molecule-based magnets. *Mater. Todays.*, **17**, 224–235.

Novitchi, G., Shova, S., Caneschi, A., Costes, J.P., Gdaniec, M., and Stanica, N. (2004) Hetero di- and trinuclear Cu-Gd complexes with trifluoroacetate bridges: synthesis, structural and magnetic studies. *Dalton Trans.*, 1194–1200.

Palii, A.V., Reu, O.S., Ostrovsky, S.M., Klokishner, S.I., Tsukerblat, B.S., Hilfiger, M., Shatruk, M., Prosvirin, A., and Dunbar, K.R. (2009) Highly anisotropic exchange interactions in a trigonal bipyramidal cyanide-bridged $Ni(II)_3Os(III)_2$ cluster. *J. Phys. Chem. A*, **113**, 6886–6890.

Paulovič, J., Cimpoesu, F., Ferbinteanu, M., and Hirao, K. (2004) Mechanism of ferromagnetic coupling in copper(II)-gadolinium(III) complexes. *J. Am. Chem. Soc.*, **126**, 3321–3331.

Przychodzen, P., Lewinski, K., Pelka, R., Balanda, M., Tomala, K., and Sieklucka, B. (2006) $[Ln(terpy)]^{3+}$ (Ln = Sm, Gd) entity forms isolated magnetic chains with $[W(CN)_8]_3$. *Dalton Trans.*, 625–628.

Rajaraman, G., Totti, F., Bencini, A., Caneschi, A., Sessoli, R., and Gatteschi, D. (2009) Density functional studies on the exchange interaction of a dinuclear Gd(III)-Cu(II) complex: method assessment, magnetic coupling mechanism and magneto-structural correlations. *Dalton Trans.*, 3153–3161.

Sieklucka, B., Podgajny, R., Korzeniak, T., Nowicka, B., Pinkowicz, D., and Kozieł, M. (2011) A decade of octacyanides in polynuclear molecular materials. *Eur. J. Inorg. Chem.*, **2011**, 305–326.

Train, C., Gruselle, M., and Verdaguer, M. (2011) The fruitful introduction of chirality and control of absolute configurations in molecular magnets. *Chem. Soc. Rev.*, **40**, 3297–3312.

Visinescu, D., Desplanches, C., Imaz, I., Bahers, V., Pradhan, R., Villamena, F.A., Guionneau, P., and Sutter, J.-P. (2006) Evidence for increased exchange interactions with 5d compared to 4d metal ions. Experimental and theoretical insights into the ferromagnetic interactions of a series of trinuclear $[(M(CN)_8)^{3-}/Ni(II)]$ compounds (M = Mo(V) or W(V)). *J. Am. Chem. Soc.*, **128**, 10202–10212.

Wang, X.Y., Avendaño, C., and Dunbar, K.R. (2011) Molecular magnetic materials based on 4d and 5d transition metals. *Chem. Soc. Rev.*, **40**, 3213–3238.

Winpenny, R.E.P. (1998) The structures and magnetic properties of complexes containing 3d- and 4f-metals. *Chem. Soc. Rev.*, **27**, 447–452.

11
Dynamic Properties

11.1
Introductory Remarks

Relaxation is the magic word to describe spin dynamics. Spin can be referred to electrons and nuclei, and relaxation will be electronic and nuclear. One type of relaxation will influence the other. On relaxation of the electron, that is, the change of the magnetization, Zeeman level of the electron will generate a fluctuating field which will influence nuclear relaxation. On the other hand, the fluctuations of the nuclear spin will influence electron relaxation. In this book, we will be more interested in electron relaxation, so we start focusing on electrons.

The unpaired electron may be localized on a metal ion or delocalized on a number of atoms, as shown in Figure 11.1. The former case applies to many TMs (transition metals) and Ln compounds, and the latter to organic radicals such as nitronyl nitroxides. It is apparent that in a metal ion there is a very localized spin density, which is very intense at the ion location and zero elsewhere, while in a radical there is low density everywhere.

It must be stressed that the assumption of metal localization should be checked through experiments because partial delocalization on the ligands must be expected.

The relaxation depends on the nature of the relaxing spin and on the environment where it is embedded. We will refer to solid-state systems where the relevant interactions determining the relaxation are the dipolar interaction between spins, exchange interaction, and phonon (vibronic) coupling. Matters would be different for fluid solution relaxation where all the degrees of freedom of the molecule must be taken into account together with chemical exchange.

On the other hand, one can be interested at nuclear relaxation which depends on the spin density on the resonating nucleus through the contact term, that is, on the unpaired spin on the nucleus. An additional term is provided by the dipolar coupling generated by the electron. We will not be interested in the relaxation behavior of systems that have zero spin. We recall, however, that NMR of diamagnetic materials has achieved an incredible step forward in the determination of the structure of macromolecules including proteins.

Introduction to Molecular Magnetism: From Transition Metals to Lanthanides, First Edition.
Cristiano Benelli and Dante Gatteschi.
© 2015 Wiley-VCH Verlag GmbH & Co. KGaA. Published 2015 by Wiley-VCH Verlag GmbH & Co. KGaA.

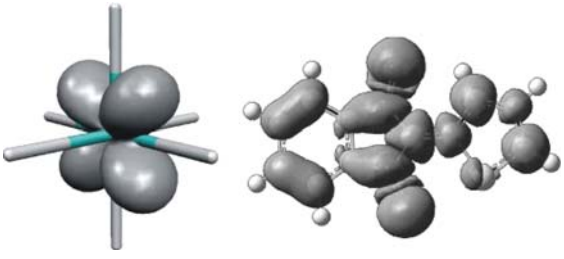

Figure 11.1 Cartoon showing the various types of spin density in molecular paramagnets. (a) Spin density distribution for octahedral d^1 and (b) spin density of a nitroxide. (Reproduced from Bowles, S.E. (2009) with permission from Elsevier B.V.)

We will start by going in some detail into the properties of Ln due the excitement created by these ions in the recent years.

One of the key points in the magnetic properties of rare earth ions is their time dependence. This is not peculiar of rare earths, but it has important features that are bound to their largely unquenched orbital contribution. Investigating the magnetic dynamics means exploring an extremely appealing territory, which clarifies some fundamental issues of magnetism. Beyond the great importance of dynamics in magnetic resonance, the last few years have seen a dramatic increase in interest about dynamics of magnetization. The interest started already in the 1930s; actually, at the beginning it was more focused on the TM ions. However, the first attempts to understand the experimental data were unsuccessful until Orbach in his two seminal papers published in 1961 worked out the basic theory which is still used today (Orbach, 1961a,b). After being used for many years, in an increasingly routine fashion the model has been rejuvenated after the discovery that some systems containing one rare earth ion behave as single molecule magnets. They are called also *single ion magnet*s, *SIM*s, and a significant part of the book is dedicated to them.

In order to figure out the temperature dependence of the magnetic properties, it is necessary to define which magnetic properties are considered, which measurement techniques are used, which temperature range is to be chosen, and so on. Perhaps the most investigated properties for Ln compounds are the dynamic magnetic susceptibility (magnetization), which is the focus of a large cumulative effort to understand the features that can give rise to slow relaxation in molecules. We will briefly go through Orbach's treatment, using his examples of holmium and dysprosium for non-Kramers and Kramers ions, respectively. We will not enter into the theoretical details but will try to stress the assumptions that underlie the formulae that are widely used. In this chapter, we will limit ourselves to cover simple experiments.

The first systematic work on the dynamics of paramagnetic Ln derivatives was performed in isomorphous series such as the ethyl sulfates hydrates, $M(EtSO_4)_3(H_2O)_3$, whose structure was shown in Figure 3.4 The RE ions are nine-coordinate, with the nine water molecules defining two octahedra sharing a

face. The overall symmetry is C_{3h}. We will suppose that the energies of the split components of the ground J multiplet are known through different techniques such as static magnetic measurements, absorption, luminescence spectra, and so on.

11.2
Spin–Lattice Relaxation and T_1

We will work out the relaxation of magnetization and susceptibility. Relaxation in magnetic resonance will be treated in the corresponding chapters. We will limit to a minimum the experimental details, which will be treated in Chapters 20–22.

Let us suppose we excite a transition in a magnetic system, for instance, by applying an external magnetic field. When the stimulus is quenched, the system will return to equilibrium with a characteristic time T_1 associated with the inversion of the magnetization. In order to go back to equilibrium, the system must emit a quantum of energy δ to be exchanged with the environment (the lattice). The decay of the magnetization follows an exponential behavior, as shown in Figure 11.2.

$$M(\tau) = M(0)\exp(-\tau/T_1) \tag{11.1}$$

T_1 is called the *spin–lattice relaxation time*, the name alluding to the fact that the relaxing spin exchanges energy with a bath formed by the environment in which the spin is embedded. The involved energies depend on the nature of the paramagnetic center, on the measurement technique, and on temperature.

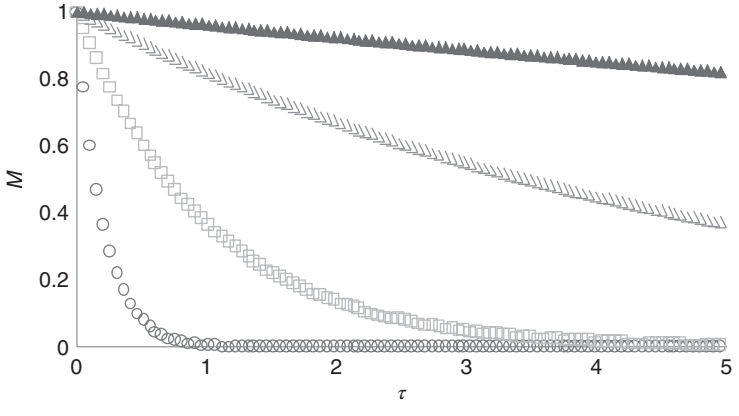

Figure 11.2 Exponential decay of the magnetization of a paramagnet. The magnetization is assumed to be unitary. The curves are calculated by assigning to T_1 the values of 0.04 s (full triangles), 0.2 s (open triangles), 1.0 s (open squares), and 5 s (open circles).

The time dependence of the relaxation is also determined by what is called the *spin–spin relaxation time* T_2. It is associated with transverse interactions, that is, with the decay of magnetization, and will be treated in Section 11.7.

11.3 Phonons and Direct Mechanism

Magnetic relaxation requires an interaction between the states involved in the phenomenon. As we will see, there are different possible mechanisms. A very common mechanism of relaxation is based on the modulation of the crystal field (CF) by the vibrations. We are considering a solid whose lattice vibrations are described by normal modes of the crystal. In the continuum limit, waves are formed which, like photons, follow the Bose–Einstein statistics. The wavelength is long compared to atomic distances. These waves are called *phonons* and, according to the model first proposed by Debye, their spectrum has an upper limit defined by the Debye temperature

$$k\theta_D = \hbar\omega_{max} \tag{11.2}$$

where θ_D is the Debye temperature and ω_{max} is the highest angular frequency. Physically, TD can be associated at the temperature above which all modes begin to be excited. At a fixed temperature, the number of phonons of angular frequency ω is $[\exp(\hbar\omega/kT) - 1]^{-1}$. It must be said that no particular improvement has been done for adjusting the Debye model to the molecular systems. We recall that for a quantum such that $kT > \hbar\omega$, the number of phonons is about $kT/\hbar\omega$ and small otherwise. It must also be recalled that in low-symmetry compounds, such as the ones we are interested in, there is not one Debye temperature but three. Just to give a flavor, θ_D for typical inorganic materials like Fe it is 470 K and for diamond 2200 K, and for the archetypal SMM (single molecular magnet) (Mn_{12}ac), calculation results give 15–35 K.

The mechanism for relaxation is different for Kramers and non-Kramers ions. In the absence of a magnetic field, the former has a minimum degeneracy of two, while the latter can be completely nondegenerate. However, for RE it is rather frequent to have a quasi-degenerate ground doublet such as, for instance, observed in $Ho(EtSO_4)_3$. We will treat a two-level ground state, as shown in Figure 11.3.

The process involves the $|a\rangle$ and $|b\rangle$ levels. The relaxation within the lowest spin doublet requires phonon coupling which corresponds, at the simplest possible level, to the emission of one phonon of energy δ. This is the so-called direct process, which is schematically shown in Figure 11.3. The system is prepared in off-equilibrium and monitored as it returns to equilibrium. The process to be calculated is the transition probability from $|b\rangle$ to $|a\rangle$ and from $|a\rangle$ to $|b\rangle$ and take the difference. The assumptions demand that the heat bath in contact with the relaxing system has infinite heat capacity. The assumption is sound but not always valid. A well-documented case of the breakdown of the assumption is the so-called phonon bottleneck. It can be simply described by the fact that the phonon transfer

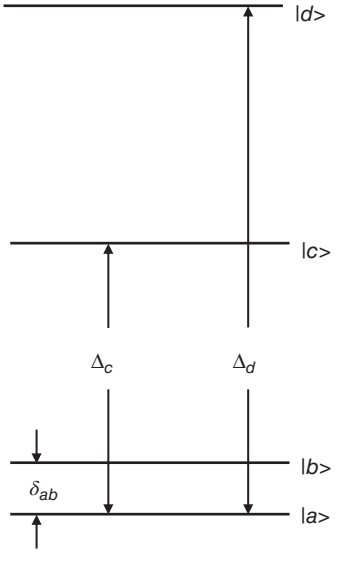

Figure 11.3 Scheme of the relaxation in a two-level system. The process on the left corresponds to the direct process.

is slow at low T and that the bath does not succeed in following the system. See, for instance, an early report by Scott and Jeffries (1962). Another assumption is that the external magnetic field is larger than the dipolar (and exchange) field produced by the neighboring metal ions. As we will see, the direct process is effective only at very low temperature. This is because the phonons of energy corresponding to the separation of the two states involved in the relaxation that are required and they are of low abundance.

The calculation of the orbit–lattice coupling, which describes the variation of the CF potential felt by the ion during the vibration, is conveniently done by expanding the potential in a series of strain using the same formalism used for the static potential generated by the CF. The result is indicated below:

$$T_1^{-1} = C\delta^2 kT \tag{11.3}$$

where C depends on the sound velocity to the power 5 and on the density of final states. The remarkable result is that the relaxation rate is directly proportional to temperature. The density of states depends on the coupling $\langle b|\sum V_{nm}|a\rangle$, where V_{nm} are operator equivalents describing the orbit–lattice coupling.

Let us look in some detail at $Ho(EtSO_4)_3$ which should clarify the formalism. We recall that Ho has a J = 8 ground state. In Orbach's example, $Ho(EtSO_4)_3$ has a ground state $|a\rangle = 0.933|+7\rangle + 0.342|+1\rangle + 0.111|-5\rangle$, which gives rise to a transition to $|b\rangle = 0.5|+6\rangle + 0.5|-6\rangle + 0.71|0\rangle$. The $|+7>$ function has nonzero matrix element with $|+6>$ through $V_{n,1}$; the other nonzero matrix elements are $\langle 6|V_{n5}|1\rangle, \langle 0|V_{n1}|1\rangle, \langle -6|V_{n-1}|-5\rangle$. Calculating the matrix elements is trivial but feeding values to the parameters and feeding the other constants make the calculation rather tricky. T_1 was calculated as

$$T_1 = 2 \times 10^{-5} \tanh(\delta/T) \tag{11.4}$$

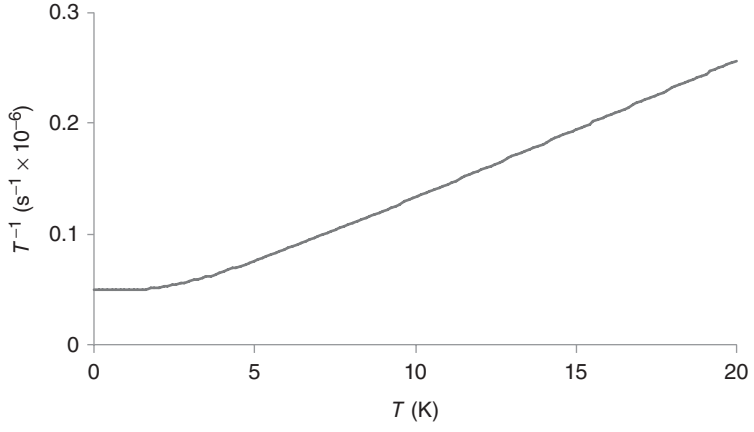

Figure 11.4 Temperature dependence of T_1^{-1} calculated for $Ho(EtSO_4)_3$.

In Figure 11.4, we plot T_1^{-1} versus T. Below 3 K, corresponding to $T_1^{-1} < 5.8 \times 10^4\ s^{-1}$, the relaxation rate is essentially independent of temperature, a regime that has been recently described as *quantum tunneling*. More details will be provided in the next chapter. Above 5 K, T_1^{-1} varies linearly with a slope 1.23×10^{-4}.

The results are good, but the quantitative results were obtained at the expense of several approximations, particularly for the matrix element. An appropriate conclusion is that, for non-Kramers ions, the spin–lattice relaxation rate is proportional to T, that is, $T_1^{-1} = AT$. A is of the order of $10\ K^{-1}\ s^{-1}$ for $Ho(EtSO_4)_3$. Now, the above results give some hint to control the relaxation, or to design tailor-made magnetic molecules. The relaxation rate increases quadratically with δ, so separation is small for slow relaxation. Another possible physical quantity to handle is the orbit–phonon coupling: trying to quench requires the control of the symmetry of the lowest levels.

For Kramers ions, an external field is used to remove the degeneracy of the ground doublet of Ytterbium(III), as shown in Figure 11.5.

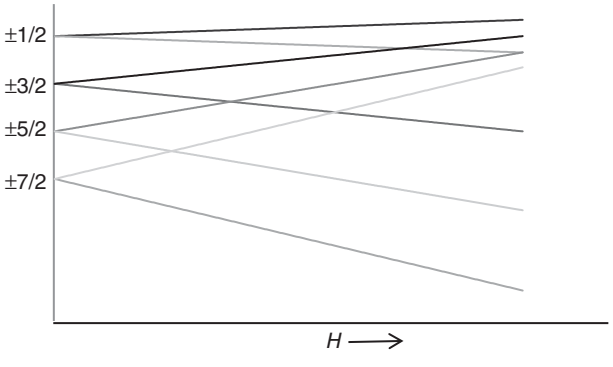

Figure 11.5 The splitting of Kramers doublets produced by an external magnetic field.

By proceeding as described above for the non-Kramers case, the result for Kramers is more complex because of the presence of a magnetic field introduces magnetic anisotropy. A rather general expression is provided by Eq. (11.5), which shows the linear dependence on T of the spin lattice relaxation rate and a fourth power dependence on H. The relaxation regards the transition between the splitted components of the ground Kramers doublet. For the limit $g\mu_B H < kT$, the relaxation rate is given by

$$T_1^{-1} = g^2 H^4 k T C' F_{voc} \tag{11.5}$$

where C' is a product of constants and sound velocity, while F_{voc} is the orbit coupling. Using Eq. (11.5), for Dy the ground state is a very anisotropic Kramers doublet, with $g_{||}$ close to 11 and $g_{\perp}$ close to zero. The first excited doublets are at 23, 31, and 87 K, respectively, and g^2 becomes $g_{||}{}^2 \sin^2\theta \cos^2\theta$. Substituting, the calculated spin–orbit coupling that come out is $T_1^{-1} = 1.7 \times 10^{-11} H^4 T$. The important feature is the field control of the relaxation rate. With no field applied the relaxation rate goes to zero. We will go back to this point while talking of SIM (Chapter 13).

Concluding one-phonon processes are efficient only at low temperatures because of the low abundance of small-wavelength phonons. At higher temperatures, other processes become more efficient.

11.4
Two Is Better than One

Two-phonon processes provide the possibility of exploiting more abundant phonons, as shown in Figure 11.6. The mechanism requires an excited level at energy Δ: the system absorbs a phonon of energy Δ and emits one at $\Delta - b$. In fact, there are two types of two-phonon process depending on the nature of the excited state: if it is real, the Δ/k is within the Debye temperature and the process is called the *Orbach* process. If the excited state is virtual, the process is

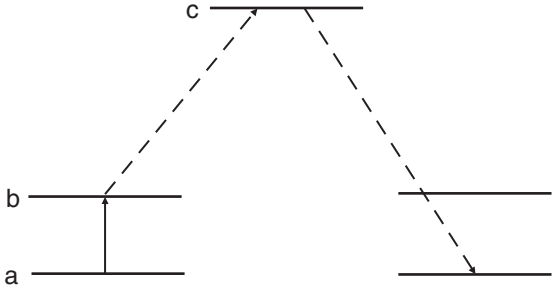

Figure 11.6 Two-phonon processes. A phonon induces the b→c transition. A phonon is emitted and the c→a transition occurs, completing the process.

referred to as the *Raman* process. Again, there is a difference between Kramers and non-Kramers ions. We start from the latter.

One of the key conditions used for calculating the two-phonon relaxation rate is that there is only one excited level involved in the relaxation mechanism located at Δ_c. It is also assumed that $\delta \ll kT$, Δ_c and it must be decided whether Δ_c is smaller or larger than the Debye energy $k\theta_D$. In the latter case, the spin–lattice relaxation time is given by

$$1/T_1 = 9(6!)/(4\pi^3\rho^2 v^{10}\Delta_c^2)(kT/\hbar)^7 |\sum_{n,m}\sum_{n',m'} \langle a|V_n^m|c\rangle\langle c|V_{n'}^{m'}|b\rangle|^2 \qquad (11.6)$$

Apart from the constants, the relaxation rate depends on the seventh power of T. The other important feature is the ${\Delta_c}^{-2}$ dependence: a large separation of the $|c\rangle$ level gives a slow relaxation. The last relevant term is the orbit–phonon coupling, which is given by the sum of products of the matrix elements involving a, b, and c.

A comparison of the relaxation rate for the one- and two-phonon mechanisms helps in understanding why the latter is more efficient than the former at moderate T. The number of phonons of frequency $h\nu$ at a fixed temperature is

$$n = (R/[\exp(h\nu/kT) - 1])\nu^2 \mathrm{d}\nu \qquad (11.7)$$

Small frequency means small number of available phonons, so the relaxation of the system is inefficient. Two-phonon processes can choose from a wider set of phonons; therefore they fully exploit the opportunities.

The other limit for two-phonon mechanism, namely that in which the intermediate state is below the Debye energy, gives rise to two different regimes, one which is analogous to the Raman process and another which is referred to as the Orbach process. The contribution of the Orbach process to the relaxation rate is

$${T_1}^{-1} = R\Delta^3/[\exp(\Delta/kT) - 1] \qquad (11.8)$$

In the limit $\Delta \gg kT$, the relaxation rate is $R\Delta^3 \exp(-\Delta/kT)$. This is a thermally activated Arrhenius behavior, with Δ having the role of the barrier. We will see that an Orbach-type process is the current justification of the slow relaxation of SMM.

The extension of the previous procedure to Kramers ions finally gives

$$1/T_1 = 9!\hbar^2/(\pi^3\rho^2 v^{10}\Delta_q^4)(kT/\hbar)^9 \times \left|\sum_{n,m}\sum_{n',m'} \left\langle -1/2p|V_n^m|\,1/2q\right\rangle \langle 1/2q|V_{n'}^{m'}|1/2p\rangle\right|^2 \qquad (11.9)$$

For an excited level higher than the Debye temperature, a simplified formula is given by

$$T_1 \propto T^{-7} \qquad (11.10)$$

while a more complete form (which may be safely dropped out) is

$$1/T_1 = \left| \sum_{n,m} \sum_{n',m'} \left\langle -\frac{1}{2}p \right| V_n^m \left| \frac{1}{2}q \right\rangle \left\langle \frac{1}{2}q \right| V_{n'}^{m'} \left| \frac{1}{2}p \right\rangle \right|^2 \left[9!\hbar^2/(\pi^3\rho^2 v^{10}\Delta_q^4)\,(kT/\hbar)^9 \right.$$
$$+ \left. 3/(2\pi\rho v^5 h)(\Delta_q/h)^3 \left[\exp\left(\Delta_q/kT\right) - 1\right]^{-1} \right.$$
$$\times \left. \left[\left| \sum_{n,m} \left\langle -\frac{1}{2}p \right| V_n^m \left| \frac{1}{2}q \right\rangle \right|^2 + \left| \sum_{n',m'} \left\langle \frac{1}{2}q \right| V_{n'}^{m'} \left| \frac{1}{2}p \right\rangle \right|^2 \right]^{-1} \right] \tag{11.11}$$

Applying the above formula to DyETS, we see that the direct process is dominant up to about 2.5 K. Above this temperature, it is the Orbach process that dominates. At any rate, the relaxation times are not particularly long: for instance, at 2.7 K the relaxation time is 1 ms. Since Dy has become a superstar in the field of slow magnetic relaxation, this is an important piece of information. If one looks for high-temperature slowly relaxing systems, it is not sufficient to design high barriers but it is necessary to efficiently quench also the Raman and the direct processes.

The Raman relaxation process owes its name to its similarity to incoherent scattering in optics: in the real process, a phonon with energy ε_1 is adsorbed, and simultaneously another one of energy $\varepsilon_1 + \delta$ is emitted together with a spin flip. With a perturbative approach, it is possible to demonstrate that the relaxation time $T_{1\text{Raman}}$ is proportional to the temperature according to the expression (Scott and Jeffries, 1962)

$$\frac{1}{T_{1\text{Raman}}} \propto \left(\int_0^{k\Theta} \varepsilon_1^n \frac{e^{\frac{\varepsilon_1}{kT}}}{\left(e^{\frac{\varepsilon_1}{kT}} - 1\right)^2} d\varepsilon_1 \right) T^{n+1} \tag{11.12}$$

where Θ denotes the Debye temperature of the lattice. For non-Kramers doublets, $n = 6$, while in presence of Kramers doublets $n = 8$. Generally, the integral is a constant for low temperatures and it is proportional to T^{1-n} at high temperatures.

11.5 Playing with Fields

We will now add the effects of external and internal fields, namely the dipolar interaction with neighboring spins and the hyperfine interaction with magnetic nuclei. The external field described by the Zeeman term $\mathscr{V}_Z$ is assumed to be large compared to hyperfine and dipolar terms.

$$\mathscr{V}' = \mathscr{V}_Z + \mathscr{V}_{\text{hyp}} + \mathscr{V}_{\text{dip}} \tag{11.13}$$

The dipolar interaction is usually used in the point dipolar approximation, that is, assuming that the distance between two magnetic dipoles is large compared to their spatial extension. The corresponding Hamiltonian takes the form (Orbach, 1961a)

$$\mathscr{V}_{\text{dip}} = \sum_{(i,\,j)} \left[\frac{(\mu_i \cdot \mu_j)}{r_{ij}^3} - \frac{3(\mu_i \cdot r_{ij})(\mu_j \cdot r_{ij})}{r_{ij}^5} \right] \tag{11.14}$$

where μ_i and μ_j are magnetic dipoles at a distance r_{ij}.

$$\mathscr{V}_{\text{dip}} = \mu_{\text{B}}^2 \Lambda^2 \sum_{(i,j)} (1/r_{ij}^3)(\mathscr{A} + \mathscr{B} + \mathscr{D} + \mathscr{E} + \mathscr{F}) \tag{11.15}$$

where

$$\mathscr{A} = \mathscr{J}_z^{(i)} \mathscr{J}_z^{(j)} (1 - 3\ \cos^2\theta_{ij})$$

$$\mathscr{V} = -\frac{1}{4} \left[\mathscr{J}_-^{(i)} \mathscr{J}_+^{(j)} + \mathscr{J}_+^{(i)} \mathscr{J}_-^{(j)} \right] (1 - 3\cos^2\theta_{ij})$$

$$\mathscr{C} = -\frac{3}{2} \left[\mathscr{J}_+^{(i)} \mathscr{J}_z^{(j)} + \mathscr{J}_z^{(i)} \mathscr{J}_+^{(j)} \right] \sin\theta_{ij} \cos\theta_{ij} \exp(-i\varphi_{ij})$$

$$\mathscr{D} = -\frac{3}{2} \left[\mathscr{J}_-^{(i)} \mathscr{J}_z^{(j)} + \mathscr{J}_z^{(i)} \mathscr{J}_-^{(j)} \right] \sin\theta_{ij} \cos\theta_{ij} \exp(i\varphi_{ij})$$

$$\mathscr{E} = -\frac{3}{4} \left[\mathscr{J}_+^{(i)} \mathscr{J}_+^{(j)} \right] \sin^2\theta_{ij} \exp(-2i\varphi_{ij})$$

$$\mathscr{F} = -\frac{3}{4} \left[\mathscr{J}_-^{(i)} \mathscr{J}_-^{(j)} \right] \sin^2\theta_{ij} \exp(2i\varphi_{ij}) :$$

So that $\mathscr{V}_{\text{dip}} = \sum_{p,q} \sum_{(i,j)} a_{pq}^{ij} \mathscr{O}_j^p(i) \mathscr{O}_i^q(j)\ Y_2^{p+q}(ij)$. The a_{pq}^{ij} are the appropriate coefficients in the previous expansion, $p, q = 0, \pm 1$, $\mathscr{O}_j^p(i) = \mathscr{J}_z^i$ and $\mathscr{O}_1^{\pm 1}(i) = \mp \mathscr{J}_\pm^{(i)}$.

For two spins with $g = 2$, the energy of interaction at a distance of 0.5 nm is $2.77 \times 10^{-2}\ \text{cm}^{-1}$, which becomes $3.46 \times 10^{-3}\ \text{cm}^{-1}$ at 1 nm. The interaction is weak but decreases slowly with the distance, so many spins must be considered to interact with the relaxing spin.

The hyperfine interaction couples the magnetic moment of the relaxing electron with the nuclear spin. We will come back to hyperfine role in relaxation later on Chapter 21, as seen from the nucleus point of view. Here we show the Hamiltonian used for calculating T_1:

$$\mathscr{V}_{\text{hyp}} = \sum_i (2\mu_{\text{B}} \beta_{\text{n}} \mu_{\text{n}} / I) \langle r^{-3} \rangle (\mathscr{J}_i \cdot N_i) \tag{11.16}$$

where β_{n} is the nuclear magneton, μ_{n} is the nuclear magnetic moment in nuclear magnetons, I the nuclear spin, and the sum is over all spin states. From Abragam and Pryce (1951)

$$N = \sum [l - s + 3\ (r \cdot s) r / (r^2)] \tag{11.17}$$

where the sum is over all electrons in the f shell.

The analysis of the field dependence of the two-phonon relaxation process has revealed that there is a difference in the behavior according to values assumed by $g_\perp$. When $g_\perp = 0$, then the final expression for T_1 is

$$\frac{1}{T_1} = \left(\frac{1}{T_1}\right)_I \frac{\left(H^2 + H_{\text{hyp}}^2 + H_{\text{dip}}^2\right)}{\left(H^2 + H_{\text{hyp}}^2 + \frac{1}{2}H_{\text{dip}}^2\right)} \tag{11.18}$$

where $\left(\frac{1}{T_1}\right)_I = 2c_{jj}\left|\sum_{n\ m\ n'm'} \langle \alpha|\ V_n^m|1/2q\rangle\langle 1/2q|\beta_{n'}^{m'}\rangle\right|^2$ and H_{hyp}^2, H_{dip}^2 are the mean square internal hyperfine and dipolar fields, respectively.

The expression to be applied when $g_\perp \neq 0$ is

$$\begin{aligned} 1/T_1 &= (1/T_1)_I \left\{ \frac{tr\ V_z^2 + \ \mu\ tr\ V_{\text{hyp}}^2 + \ \mu' trV_{\text{dip}}^2}{tr\ V_z^2 + tr\ V_{\text{hyp}}^2 + trV_{\text{dip}}^2} \right\} \\ &= (1/T_1)\left(H^2 + \mu H_{\text{hyp}}^2 + \mu' \frac{1}{2}H_{\text{dip}}^2\right) \Big/ \left(H^2 + H_{\text{hyp}}^2 + \frac{1}{2}\ H_{\text{dip}}^2\right) \end{aligned} \tag{11.19}$$

where μ has a value that depends only on the orbit–lattice parameters while μ' depends on the orbit–lattice parameters as well as on temperature and concentration. According to the Van Vleck approach on the effective fields approximation, μ must be equal to 1 and $\mu' = 2$. The experiments gave values of $\mu < 1$, and μ' may assume values greater than 2 and it generally decreases with increasing temperature for Raman processes but it is temperature independent for resonant processes.

11.6 Something Real

A typical method to study the dynamical properties of magnetic molecular systems is the AC susceptibility measurement in which the sample is placed between two coils through which a current flows at an angular frequency ω. It is therefore useful to determine the dynamic or differential susceptibility $\delta M/\delta H$ by applying a small oscillating magnetic field. The crucial point, in this kind of experiments, is the presence of magnetic dipoles, which may not be able to follow immediately the change in the direction of the oscillating magnetic field. In this case, the redistribution of spins over the energy levels follows a relaxation process which will be characterized by a relaxation time τ. If the magnetic field oscillates sinusoidally

$$H(t) = \ H_0 + he^{i\omega t} \tag{11.20}$$

H_0 is the static field, and $\omega = 2\pi\nu$ is the angular frequency of the alternating field. As a consequence, the magnetization follows a similar pattern:

$$M(t) = M_0 + m(\omega)e^{i\omega t} \tag{11.21}$$

In the presence of a relaxation phenomenon, $H(t)$ and $M(t)$ cannot be in phase and, therefore, $m(\omega)$ is a complex quantity. As $\chi(\omega) = m(\omega)/h$, the susceptibility

is formed by one real (called dispersion) and one imaginary (named absorption) component:

$$\chi(\omega) = \chi'(\omega) - i\chi''(\omega) \tag{11.22}$$

There is a strict correlation between the frequency ω and the relaxation time τ. When the magnetic field is oscillating at a low frequency, $\omega\tau \ll 1$ and the measured susceptibility coincides with the static one. In these experimental conditions, the differential susceptibility is called *isothermal* or χ_T to indicate the thermal equilibrium between the spin system and the lattice. The other limit corresponds to the high-frequency condition, $\omega\tau \gg 1$, when the spin system is no more able to redistribute in accordance with the frequency alternation and, therefore, is uncoupled with the lattice. The measured susceptibility is called *adiabatic* or χ_S, and it depends on the intensity of the magnetic field. For very strong fields $\chi_S = 0$.

It is possible to demonstrate that

$$\chi'(\omega) = \frac{\chi_T - \chi_S}{1 + \omega^2\tau^2} + \chi_S \quad \chi''(\omega) = \frac{\omega\tau(\chi_T - \chi_S)}{1 + \omega^2\tau^2} \tag{11.23}$$

The frequency dependence of χ' and χ'' is schematically shown in Figure 11.7.

Alternatively, it is possible to report data in the form of the so-called Argand diagram, which is equivalent in the field of magnetism to the Cole–Cole plot for dielectrics (Cole and Cole, 1941). In the plot, χ'' is reported versus χ', and Eq. (11.24) gives a semicircle where at its top the condition $\omega^{-1} = \tau$ is satisfied (Figure 11.8).

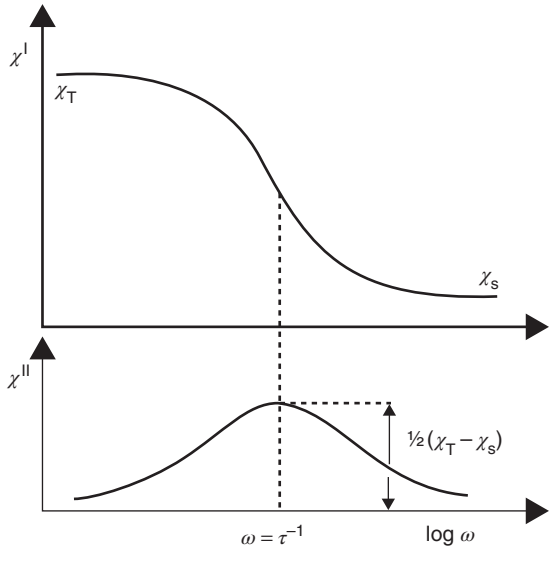

Figure 11.7 The high and low limits of the in-phase susceptibility corresponding to the adiabatic and thermal susceptibility, while a relevant feature of the out-phase susceptibility is the possibility of determine the relaxation time.

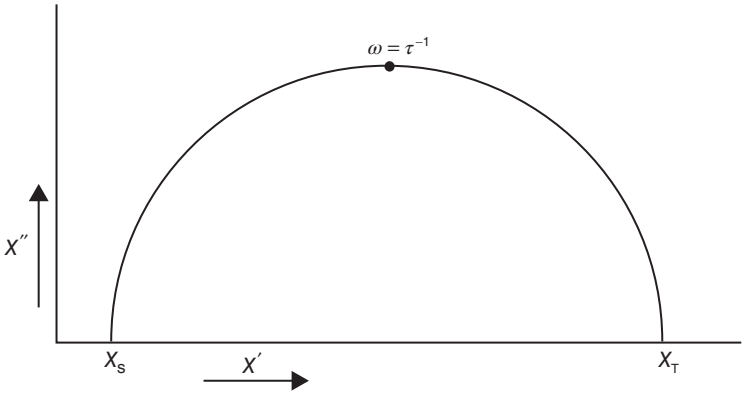

Figure 11.8 A typical Cole–Cole plot.

If the dynamic properties depend on a distribution of τ values, it is possible to analyze the phenomenon by using the relations

$$\chi(\omega) = \chi_S + \frac{\chi_T - \chi_S}{1 + (i\omega\tau)^{1-\alpha}}$$

and

$$\chi''(\omega) = (\chi_T - \chi_S)\frac{\left((\omega\tau)^{1-\alpha}\cos\left(\frac{\pi\alpha}{2}\right)\right)}{1 + 2(\omega\tau)^{1-\alpha}\sin\left(\frac{\pi\alpha}{2}\right) + (\omega\tau)^{2-2\alpha}} \tag{11.24a}$$

$$\chi'(\omega) = \chi_S + (\chi_T - \chi_S)\frac{1 + (\omega\tau)^{1-\alpha}\sin\left(\frac{\pi\alpha}{2}\right)}{1 + 2(\omega\tau)^{1-\alpha}\sin\left(\frac{\pi\alpha}{2}\right) + (\omega\tau)^{2-2\alpha}} \tag{11.24b}$$

α is a parameter related to the distribution of the relaxation times: a large distribution gives a large α value. It is possible to determine this parameter by using the Argand plot: the angle that subtends the arc is given by $\pi(1 - \alpha)$. It is often possible to observe more complex behaviors which show more semicircles and even partially merged ones (Grahl, Keozler, and Sessler, 1990).

11.7 Spin–Spin Relaxation and T_2

The most common parameter used to identify the spin–spin relaxation mechanism is T_2. This notation is useful to mark the difference with the spin–lattice relaxation which is identified by T_1 as described above. In the solid state, the relaxation rate by spin–spin interactions shows different mechanisms if the system under observation is in an ordered magnetic phase or in a pure paramagnetic region. In the first case, the mechanism is dominated by exchange interactions, and very often this situation is examined by using an approach based

on the Suhl–Nakamura model (Nakamura, 1958; Suhl, 1958), while in the latter situation there are two possible contributions due to dipole–dipole interaction.

The dipole–dipole interaction is treated by using the classical Hamiltonian reported in Eq. (11.25). This applies to a system comprising ions M with levels m_s and N with levels n_s (Bonville *et al.*, 1978):

$$
\begin{aligned}
A &= \mu_B^2 \sum_N \frac{1}{r_N^3} g_M^z g_N^z \left(1 - 3\cos^2\theta_N\right) S_M^z S_N^z \\
B &= -\frac{1}{4}\mu_B^2 \sum_N \frac{1}{r_N^3} g_M^\perp g_N^\perp \left(1 - 3\cos^2\theta_N\right) \times \left(S_M^+ S_N^- + S_M^- S_N^+\right) \\
C &= -\frac{3}{2}\mu_B^2 \sum_N \frac{1}{r_N^3} g_M^z g_N^\perp \sin\theta_N \cos\theta_N \times e^{-i\varphi_N} \left(S_M^z S_N^+ + S_M^+ S_N^z\right) \\
D &= -\frac{3}{2}\mu_B^2 \sum_N \frac{1}{r_N^3} g_M^z g_N^\perp \sin\theta_N \cos\theta_N \times e^{i\varphi_N} \left(S_M^z S_N^- + S_M^- S_N^z\right) \\
E &= -\frac{3}{4}\mu_B^2 \sum_N \frac{1}{r_N^3} g_M^\perp g_N^\perp \sin^2\theta_N e^{-2i\varphi_N} S_M^+ S_N^+ \\
F &= -\frac{3}{4}\mu_B^2 \sum_N \frac{1}{r_N^3} g_M^\perp g_N^\perp \sin^2\theta_N e^{2i\varphi_N} S_M^- S_N^-
\end{aligned}
\tag{11.25}
$$

where θ and φ are the polar coordinates of the vector $\boldsymbol{r}$ describing the relative position of the M and N ions. The off-diagonal terms are conventionally labeled flip–flop (B), flip–diagonal (C, D), and flip–flip (E, F). The relaxation rate W is calculated by using Fermi's golden rule which determines the transition probability as

$$
W^{MN}_{m_s n_s \to m'_s n'_s} = \frac{2\pi}{h} \left| \left\langle m'_s n'_s \right| \mathscr{V}_{dip} \left| m_s n_s \right\rangle \right|^2 \times \rho\left(E_{m_s n_s} - E_{m'_s n'_s}\right) \tag{11.26}
$$

where $\rho(E_{m_s n_s} - E_{m'_s n'_s})$ is the density of final states available for the transition and can be expressed by using the appropriate Boltzmann distribution. Further, it is possible write

$$
|\langle m'_S n'_S | \mathscr{V}_{dip} | m_S n_S \rangle|^2 = |\langle |B| \rangle|^2 + \ldots + |\langle |F| \rangle|^2 \tag{11.27}
$$

and since A–F have different selections rules, there are no cross terms.

The reported expression shows that there is a dependence of the relaxation rate related to dipolar relaxation on $g_\perp^2$. This means that, for $g_\perp^2 = 0$, the dipole–dipole relaxation vanishes. As for many rare earth ions very low values of $g_\perp^2$ have been observed, the dominant processes are the flip – diagonal ones (C, D) which depend on $(g_z g_\perp)^2$. In any case, the dipolar mechanism, whose relevance decreases on increasing the temperature, contributes only partially to the total relaxation mechanism.

The relaxation mechanism in systems influenced by molecular motions will be described in Chapter 19.

This has been a heavy chapter which we tried to simplify but, we fear, without success. Maybe it is useful to introduce a resume of the formulae relating the various mechanisms of magnetic relaxation for Kramers and non-Kramers ions,

which will be examined in Chapter 13:

$$\tau^{-1} = R_{\mathrm{d}}(h\upsilon)^5 \coth(h\upsilon/2kT) + R_{\mathrm{Or}}\Delta^3[\exp(\Delta/kT) - 1]^{-1} + R_{\mathrm{R}}T^9 + R'_{\mathrm{R}}(h\upsilon/k)^5T^9 \tag{11.28}$$

and

$$\tau^{-1} = R_{\mathrm{d}}(h\upsilon)^3 \coth(h\upsilon/2kT) + R_{\mathrm{Or}}\Delta^3[\exp(\Delta/kT) - 1]^{-1} + R_{\mathrm{R}}T^7 \tag{11.29}$$

At this stage, it is useful to stress that the direct mechanism dominates at low temperature and has a linear dependence on T. At high temperature, it is the Raman mechanism that dominates and it is competitive with the Orbach process.

References

Abragam, A. and Pryce, M.H.L. (1951) Theory of the nuclear hyperfine structure of paramagnetic resonance spectra in crystals. *Proc. R. Soc. London, Ser. A: Math., Phys. Eng. Sci.*, **205**, 135–153.

Bonville, P., Hodges, J.A., Imbert, P., and Hartmann-Boutron, F. (1978) Spin-spin and spin–lattice relaxation of ytterbium(3+) in ytterbium aluminate, ytterbium-doped thulium aluminate and ytterbium-doped yttrium aluminate and magnetic ordering in ytterbium aluminate measured by the Moessbauer effect. *Phys. Rev. B*, **18**, 2196–2208.

Bowles, S.E., Dooley, B.M., Benedict, J.B., Kaminsky, W., and Frank, N.L. (2009) The competing roles of topology and spin density in the magnetic behavior of spin-delocalized radicals: donor-acceptor annelated nitronyl nitroxides. *Polyhedron*, **28**, 1704–1709.

Cole, K.S. and Cole, R.H. (1941) Dispersion and absorption in dielectrics I. Alternating current characteristics. *J. Chem. Phys.*, **9**, 341–351.

Grahl, M., Keozler, J., and Sessler, I. (1990) Correlation between domain-wall dynamics and spin-spin relaxation in uniaxial ferromagnets. *J. Magn. Magn. Mater.*, **90**(Pt. 91), 187–188.

Nakamura, T. (1958) Indirect coupling of nuclear spins in antiferromagnet with particular reference to MnF_2 at very low temperatures. *Prog. Theor. Phys.*, **20**, 542–552.

Orbach, R. (1961a) Spin–lattice relaxation in rare-earth salts: field dependence of the two-phonon process. *Proc. R. Soc. London, Ser. A: Math., Phys. Eng. Sci.*, **264**, 485–495.

Orbach, R. (1961b) Spin–lattice relaxation in rare earth salts. *Proc. R. Soc. London, Ser. A*, **264**, 458–484.

Scott, P.L. and Jeffries, C.D. (1962) Spin–lattice relaxation in some rare-earths salts at helium temperature; observation of the phonon bottleneck. *Phys. Rev.*, **127**, 32–51.

Suhl, H. (1958) Effective nuclear spin interactions in ferromagnets. *Phys. Rev.*, **109**, 606.

12
SMM Past and Present

12.1
Mn_{12}, the Start

A very short resume of how the revolution of the single molecule magnet (SMM) started was given in the Introduction (Chapter 1). The unusual spin state S = 10 of a Mn_{12} cluster was confirmed by several techniques (Gatteschi and Sessoli, 2003). In particular the high-field magnetization was determined (Caneschi *et al.*, 1991). It was the collaboration between our group and the Grenoble group that made the difference, allowing the use of high magnetic fields, both for static magnetization and ESR measurements. It was the latter that provided the key information on the nature of the zero-field splitting of the ground S = 10 state. We believe it was one of the first spectra recorded on the spectrometer built by Brunel; the quality was rather poor but sufficient to reach an important conclusion.

And Figure 12.1 is a good witness. Note that the exciting waves are characterized by the wavelength in micrometers, as opposed to the frequency in gigahertz or the wavenumber in cm^{-1} as generally used. There is a main signal which goes to zero field for a wavelength of about 1100 μm or a wave number of 9 cm^{-1}. We soon realized that a detailed interpretation of the spectra was not needed; the relevant information was easy to obtain. In fact, the absorption at zero field for a frequency of 10 cm^{-1} shows that there is a pair of levels separated by that energy in zero field. Assuming an S ground state in tetragonal symmetry, the differences between the E(S) and the E(S − 1) levels correspond to the resonance frequency at

$$D = h\nu/(1-2S) \tag{12.1}$$

where $h\nu$ is the resonance frequency. With the above parameters, D is about 5.0 cm^{-1} and the overall splitting of the lowest multiplet is 50 cm^{-1}.

Since the relations between the different units are never available when we need them, we report them again in Table 12.1. The first column reports the wavelengths.

The possible solutions suggest D in the range of 0.05 cm^{-1}, which compares well with that obtained by the analysis of the temperature dependence of the magnetic susceptibility. The ground state was S = 10. It seemed to be the end of the story, but it was only the beginning.

Introduction to Molecular Magnetism: From Transition Metals to Lanthanides, First Edition.
Cristiano Benelli and Dante Gatteschi.
© 2015 Wiley-VCH Verlag GmbH & Co. KGaA. Published 2015 by Wiley-VCH Verlag GmbH & Co. KGaA.

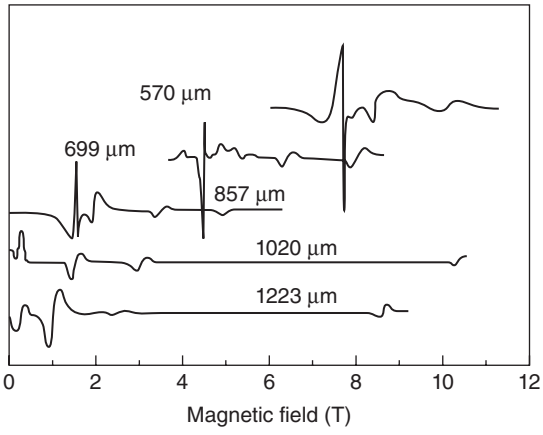

Figure 12.1 Wavelength dependence of the ESR spectra of $Mn_{12}Ac$ polycrystalline powder at 4 K.

Table 12.1 Energy quanta of ESR spectra of Figure 12.1.

λ (μm)	$h\nu$ (GHz)	H_0 (T)	λ^{-1} (cm^{-1})
1223	254.3	8.756	8.1766
1020	294.1	10.499	9.8039
857	350.1	12.495	12.6696
699	429.2	15.319	14.3062
570	526.3	18.787	17.5440

At that time, Gatteschi's opinion was that the research had achieved the result of characterizing the ground state of the complex cluster, and he suggested Roberta Sessoli to look for some other interesting problem. She said yes, and continued to work on Mn_{12}, obtaining the exciting results that formed the basis for the SMM era (Sessoli *et al.*, 1993). The one that was most exciting was the observation of magnetic hysteresis of molecular origin.

Indeed, what the new measurements showed was slow relaxation of the magnetization which gave rise to magnetic hysteresis. This is often the signature of three-dimensional magnetic order but nothing of that kind occurred in Mn_{12}. The phenomenon was molecular. Three years later, the quantum relaxation was reported (Thomas *et al.*, 1996), reaching a full success.

The developments of the SMM up to 2005 are reported in the book *Molecular NanoMagnets* (Gatteschi, Sessoli, and Villain, 2006) and in many review articles (Aromí and Brechin, 2006; Woodruff, Winpenny, and Layfield, 2013); so here we keep the treatment of those topics to a bare minimum. We notice that a simple search of SMM yielded 5287 answers in the Web of Knowledge in 2014.

The start was pretty slow, because many developments were needed before synthetic chemists could develop the necessary concepts allowing the synthesis of

SMM. From the analysis of $Mn_{12}Ac$, it was clear that a high anisotropy was needed in a strongly coupled system. The source of anisotropy for the archetypal compound is bound to the removal of degeneracy in zero field of the S = 2 ground state of manganese(III). The sign of the splitting of the ground S = 2 state, that is, either elongation or compression of the coordination polyhedron, is associated with the Jahn – Teller distortion which favors the tetragonally elongated geometry. For some time, there were simple variations on the theme of Mn_{12} (Rogez *et al.*, 2009) but no improvement on the serendipitous first SMM.

Also Fe_8, the second discovered SMM, was obtained by chance using an ion-like high-spin iron(III) which does not have a very strong anisotropy. However, it was found to show quantum tunneling of the magnetization, QTM and oscillations associated with the application of transverse magnetic fields (Sangregorio *et al.*, 1997). Similar effects were known for conductors, with the name *Berry phase effects*, but they had not been observed for magnets. This is another of the fundamental aspects that were discovered in SMM (Wernsdorfer and Sessoli, 1999).

The basic aspects of SMM have initially been clarified on Mn_{12}, Fe_8, and Mn_4 The last system was described by Aubin, Wemple, Adams, Tsai, Christou, and Hendrickson. (Aubin *et al.*, 1996). The SMMs are characterized by a magnetic relaxation that is thermally activated. The first approximate model assumed that at low temperature the system could be described by a spin S, that is, it is possible to assume a "giant" spin as the ground state whose ZFS levels follow the double-well distribution of Figure 12.2. The energies of the states with positive M are plotted in the left well, and those with negative M in the right. If a magnetic field is applied parallel to z, the states with negative M go to lower energies, and those with positive M go to higher energies. On switching the field off, the system goes back to equilibrium through a series of steps $S \rightarrow S-1, S-1 \rightarrow S-2, \ldots -1 \rightarrow 0 \ldots -S+1 \rightarrow -S$. It is apparent that the approximation is crude, but its success made it to be used in many cases. It took a few years before some brave attempts succeeded in improving the description of the magnetic properties of SMM.

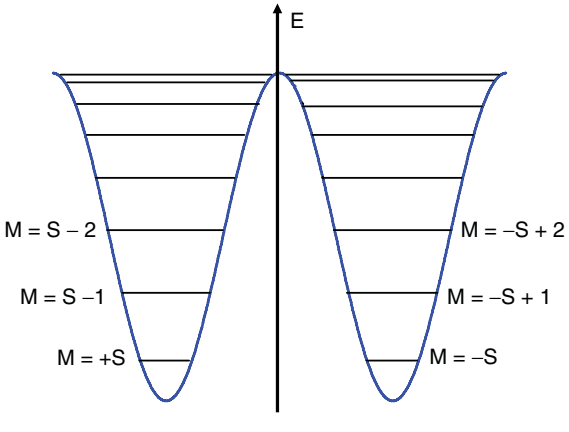

Figure 12.2 Energies of the spin levels M belonging to a ground manifold S, $-S \leq M \leq +S$. The lowest lying levels are $M = \pm S$, the highest one is $M = 0$.

The relaxation follows an Arrhenius plot with activation energy U_{eff}, which at the simplest level of complication corresponds to the energy difference between the lowest and highest levels of the ZFS, Δ:

$$\tau = \tau_0 \exp(U_{\text{eff}}/T) \tag{12.2}$$

Arrhenius plots have been observed in many cases, but in general the agreement of the experimental barrier with that obtained from the ZFS, Δ, is moderate. We remind that Δ is given by the difference between the highest state DS^2 and the lowest, M_S for integer spin and $D[S^2 - 1/4]$ for half-integer spin. The possible explanation is that the spins can shortcut by avoiding climbing the ladders and tunnel into the other well, as shown in Figure 12.2. We will come back to the quantum tunneling behavior shortly. Some SMMs with U_{eff}, Δ, $\tau_{0,}$ and blocking temperature are shown in Table 12.2. The blocking temperature τ_b corresponds to the temperature at which the relaxation time becomes equal to the characteristic time τ_b of the used measurement technique. For a DC experiment, τ_b can be 1 s; for an NMR experiment the frequency is of the order of 100 MHz and τ_{b4} is 10^{-4} s; and for an X-band EPR experiment, τ_b is of the order 10^{-9} s. It is apparent that the blocking temperature has not increased much in 20 years. While appealing models are available for designing the barrier, the pre-exponential factor is a black box and no model for it is available. And for some obscure reason, in many cases an increase in the value of the barrier is accompanied by a decrease in the value of τ_0 leaving τ substantially unaltered.

12.2 Some Basic Magnetism

The observed behavior of Mn_{12} is similar to that of superparamagnets. It is important to make this and other basic concepts available to the readers to let them

Table 12.2 U_{eff} and τ_0 for some SMM.

	U_{eff} (cm^{-1})	τ_0 (s)	References
$[Dy_7(OH)_6(thmeH_2)_5(thmeH)(tpa)_6(MeCN)_2][NO_3]_2$	97	7.2×10^{-9}	Sharples *et al.* (2011)
$[Dy_5O(OiPr)_{13}]$	367	4.7×10^{-10}	Blagg *et al.* (2011)
$[(NMe_4)_3Na(Co_4(cit)_4[Co(H_2O)_5]_2)] \cdot 11H_2O$	18	8.2×10^{-9}	Murrie *et al.* (2003)
$[Mn_{21}DyO_{20}(OH)_2(Bu^tCO_2)_{20}(HCO_2)_4(NO_3)_3(H_2O)_7]$	51	2.0×10^{-12}	Papatriantafyll-opoulou *et al.* (2010)
$[Mn_6O_2(Et\text{-}sao)_6(O_2CPh(Me)_2)_2(EtOH)_6]$	86.4	2.0×10^{-10}	Milios *et al.* (2007)
$[Mn_{12}O_{12}(O_2CCH_3)_{16}(CH_3OH)_4]CH_3OH$	50	9.8×10^{-9}	Redler *et al.* (2009)
$[Mn_{84}O_{72}(O_2CMe)_{78}(OMe)_{24}(MeOH)_{12} - (H_2O)_{42}(OH)_6]$	12.5	5.7×10^{-9}	Tasiopoulos *et al.* (2004)
$[Fe_8O_2(OH)_{12}(tacn)_6]^{8+}$	17	3.4×10^{-8}	Sangregorio *et al.* (1997)

$thmeH_3$ = tris(hydroxymethyl)ethane; tpa = triphenylacetic acid; OiPr = iso-propoxide; cit = citrate; sao = 2-hydroxybenzaldehyde oxime; and tacn = 1,4,7-triazacyclononane.

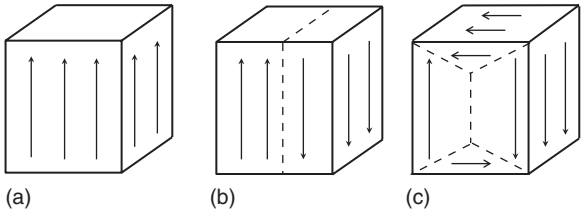

Figure 12.3 Domain formation in a ferromagnet. The energy is minimized when domains are formed. (a) The domains are kept parallel by a magnetic field. On switching off the field, the domains start to randomize (b) until the magnetization goes to zero (c).

appreciate the new behavior associated with SMM. So far, we have considered systems characterized by short-range magnetic order, but it is well known that a transition to long-range order can occur when the interaction between the magnetic centers becomes larger than thermal agitations. The blocking of thermal motion gives rise to an order–disorder transition which occurs at a well-defined temperature. For a ferromagnet, the critical temperature is called the *Curie temperature*. Under these conditions, the magnetization is blocked (Figure 12.3a). Let us start from a ferromagnet below the Curie temperature. The spontaneous magnetization is blocked in domains that minimize the magnetic energy of the sample, as is shown in Figure 12.3c.

If we now apply an external magnetic field, the number of grains with magnetization parallel to the field will increase up to saturation, as shown in Figure 12.3b. Finally, at higher fields all the domains will become magnetically aligned. The magnetization reaches the saturation value (Figure 12.4).

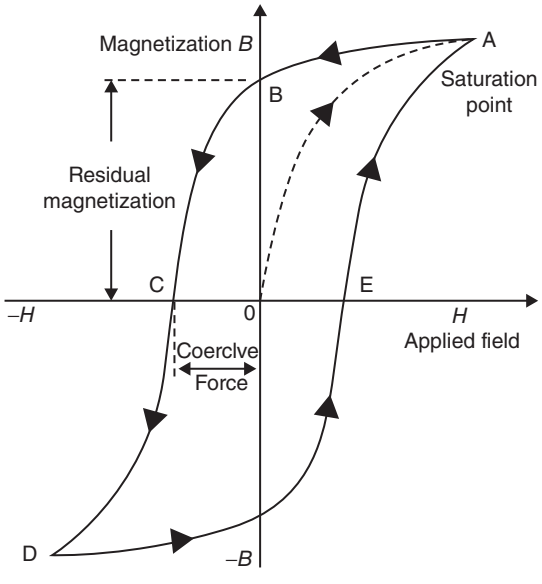

Figure 12.4 Typical magnetic hysteresis loop.

On decreasing the field, the magnetization decreases, but at zero field it is not zero because irreversible phenomena step in. The magnetization at zero field is called *remnant magnetization*. If we continue to decrease the field, the magnetization goes to zero at a field which is called the *coercive field*.

A large coercive field characterizes a hard ferromagnet, and a weak field is characteristic of a soft ferromagnet. The curve of Figure 12.4 is called hysteresis (retard) and is typical of ordered magnets. The overall process corresponds to the inversion of the magnetization, which is determined by the magnetic anisotropy. The background information needed for understanding magnetic anisotropy has been provided in Sections 3.6, 5.3, 7.9, and 7.10.

Before proceeding further, let us recall that it is possible to observe a paramagnet–antiferromagnet transition and the critical temperature is called the *Néel temperature*. We are now ready to work out one of the important issues, namely that of the size dependence. Let us imagine a magnetic particle of large size. Below the Curie temperature, the magnetization is blocked. On decreasing the size, the energy needed to reorient the magnetization decreases linearly with the volume V of the particle, in fact a decrease of the size of the particles makes the reorientation of the magnetization easier and faster. A simple way of describing this behavior is to assume that the relaxation of the magnetization depends exponentially on the anisotropy of the grain. A high barrier blocks the magnetization, and when the barrier becomes comparable to thermal energy, the magnetization reorients fast imitating a paramagnetic behavior. Since the moment is large, because it corresponds to a concerted reorientation of all the spins of the grain, the phenomenon is called *superparamagnetism*. The way the superparamagnetic behavior is indicated is through a double-well curve, as shown in Figure 12.2. The height of the barrier is, of course, proportional to N^{-3} where N is the number of spins. The typical region to observe superparamagnetic behavior is the nanometer region, and the K_1 (see eq. (3.5)) value depends on the nature of the particle. For instance, the blocking temperature for magnetite is 45 K, while that for Co is 65 K. The higher blocking temperature observed for Co is due to its high anisotropy.

For superparamagnetic nanoparticles (NPs), τ_0 is of the order of $10^{-12}-10^{-6}$ s. There is another class of particles that has a time dependence of the magnetization as given by Eq. (12.2) but with much shorter τ_0, of the order $10^{-15}-10^{-17}$ s. They are called *spin glass*, and as suggested by the name, their magnetization freezes, that is, it is blocked without giving rise to long-range order (see also Section 15.4). This is due to the fact that the magnetic centers have a very flat range of energies close to the ground state like in a glass, that is, spin-glass-like (SGL) materials. The origin of the behavior may be disorder, spin frustration, or slow magnetic relaxation, which may block in a thermodynamically unstable orientation. Well-ordered crystal structures produce either ferromagnetic or antiferromagnetic order (except for some geometrically frustrated lattices) and disorder is needed, in either the site occupations or the exchange interactions, to prevent a uniquely ordered ground state. On the other hand, a blocked magnetization state may also originate from slow relaxation of the magnetization, without breaking ergodicity.

Since most work on SGL behavior on molecular magnets has been done on single chain magnets (SCMs), more considerations will be discussed briefly in Chapter 15.

The behavior of a system such as Mn_{12} can be described as shown in Figure 12.2: the difference is that for the clusters the levels are quantized but for the NPs it is continuous.

The other important feature of SMM is the tunnel effect of the magnetization. This is a resonant tunneling that occurs when pairs of levels in different wells have the same energy, and becomes relevant only at very low temperature. While thermally activated relaxation is reasonably well understood, tunneling demands more work.

In order to describe the magnetic properties of SMM, we prefer to refer to a well-defined set of molecules. Instead of using Mn_{12}, here we prefer to focus on another system which in the recent years has provided new insight into SMM and afforded basic information on the problems and opportunities to address individual molecules. We state that this is bound to the developments in the field of molecular spintronics, which we will describe in Chapters 17 and 18.

12.3 Fe_4 Structure and Magnetic Properties

The second SMM to be discovered and investigated was a cluster comprising eight high-spin iron(III) ions, which also turned out to have slow relaxation of the ground $S = 10$ state. The system is slightly less complex than Mn_{12}: the size of the Hilbert space is 10^8 for Mn_{12} and 1 679 616 for Fe_8. The success obtained with iron(III) induced much work on similar compounds. It was realized that iron(III) was not well suited for high blocking temperature, because the single ion anisotropy is small. But in order to try to understand the mechanisms responsible of SMM behavior, it had advantages. For instance, the isotropy of $\mathbf{g}$ was an advantage because it simplified the treatment of the anisotropy. Another positive point of iron(III) clusters was that they have long been studied in the frame of modeling ferritin and other biologically relevant clusters (Gatteschi *et al.*, 2012). Fe_8 was originally synthesized for the interest in ferritin. Several different compounds were investigated, but we focus here on a family that has provided a deep understanding, which we label as the Fe_4 family (Barra *et al.*, 1999; Cornia *et al.*, 2004). Reducing to a simple scheme, Fe_4 has the structure sketched in Figure 12.5. The size of the Hilbert space is now only 1296×1296. The system is also simplified by the presence of a binary axis passing through the central and one peripheral iron. An initial description of the magnetic properties of Fe_4 was reported by Gatteschi, Sessoli, and Villain (2006). Here we will add an improved version.

A series of compounds were made by changing the ancillary ligands with the goal to learn how to fine-tune the magnetic properties and the SMM behavior. A systematic approach was made using the tripodal ligands H_3L shown in

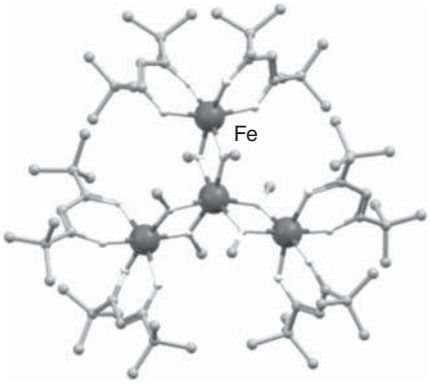

Figure 12.5 Sketch of the structure of [Fe_4(hexakis(μ_2-methoxo)-hexakis(dpm))].

Figure 12.5. The structure is based on a central iron ion which is octahedrally coordinated to six alkoxo groups of two H_3L ligands. The three oxygen atoms define the face of the octahedron. Each alkoxo group is bridging the central iron with one of the peripheral ions. The latter are octahedrally coordinated by two dpm (H_{dpm} = dipivaloylmethane) and two alkoxo ligands. The overall structure can be described as a trigonal propeller (Accorsi *et al.*, 2006). One of the geometrical factors needed to describe the propeller is the helical pitch γ. This is shown in Figure 12.6. This is the dihedral angle between the (average) plane of the four iron ions and the Fe_2O_2 planes of the bridges. In a regular octahedron, the angle is 60°.

The local symmetry around the iron ions is determined by the angles θ the Fe–O bond direction makes with the trigonal axis (octahedral angle 54.47°) and φ, the angle between the two opposed triangles (octahedral 60°; trigonal prism 0°).

Assuming that the deviation from trigonal symmetry is small, the spin Hamiltonian can be written as

$$\mathcal{H} = J\mathcal{S}_1 \cdot (\mathcal{S}_2 + \mathcal{S}_3 + \mathcal{S}_4) + J'(\mathcal{S}_2 \cdot \mathcal{S}_3 + \mathcal{S}_3 \cdot \mathcal{S}_4 + \mathcal{S}_4 \cdot \mathcal{S}_2) \tag{12.3}$$

S_1 is the spin at the center of the triangle, and S_2, S_3, and S_4 define the vertexes. Trivial considerations on the feasible exchange interactions suggest that J′ is small, and in a first approximation it may be neglected. J, on the other hand, must be AFM. This means that the ground state can be described as using S and S_T, where $S_T = S_2 + S_3 + S_4 = 15/2$ and $S = S_T - S_1$. The ground state therefore is S = 5.

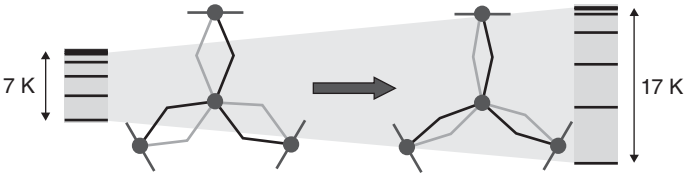

Figure 12.6 Propeller structure of Fe_4 compounds and energies of the low-lying levels.

Table 12.3 Selected geometric and magnetic parameters for $[Fe_4(L^1)_2(dpm)_6]$ (**1**) and $[Fe_4(L^3)_2(dpm)_6] \cdot Et_2O$ ($3Et_2O$) (**2**)[a] with estimated standard deviations in parentheses.

	1	**2**
$Fe_1 \cdots Fe_2$ (Å)	3.0858(4)	3.074(3)
$Fe_2 \cdots Fe_2'$ (Å)	5.3448(7)	5.32(6)
$\langle Fe_1 - O_1 \rangle$ (Å)	1.9810(12)	1.975(8)
$\langle Fe_2 - O_1 \rangle$ (Å)	1.9639(12)	1.974(3)
$\alpha = \langle O_1 - Fe_1 - O_1' \rangle$(°)	89.16(5)	89.2(6)
$\beta = \langle O_1 - Fe_1 - O_1'' \rangle$(°)	76.68(7)	77.7(2)
$\langle O_1 - Fe_2 - O_1'' \rangle$(°)	77.47(7)	77.79(8)
$\langle Fe_2 - O_1 - Fe_1 \rangle$ (°)	102.92(5)	102.23(17)
J_1 (cm^{-1})[b]	16.51(8)	16.37(12)
J_2 (cm^{-1})[b]	−0.62(8)	0.29(11)
D (cm^{-1})[c]	−0.445	−0.421, −0.415
B_4^0 (cm^{-1})	1.0×10^{-5}	8×10^{-6}
U_{eff}/k_B,[d] U/k_B[e] (K)	17.0, 16.0	15.6, 15.0
τ_0 (s)[d]	2.1×10^{-8}	1.9×10^{-8}

a) Idealized D_3 symmetry is assumed, unless otherwise noted.
b) From variable-temperature DC susceptibility data, at $T \geq 30$ K for **1**, at $T \geq 23$ K for $\mathbf{2} \cdot Et_2O$ (with correction for intermolecular interactions).
c) From HF-ESR or W-band ESR.
d) From variable-temperature AC susceptibility data.
e) Calculated as $(|D|/k_B)S^2$.

From the analysis of the temperature dependence of the magnetic susceptibility, J indeed turns out to be AFM while J′ is much smaller and the ground state has S = 5. The values of the fit are shown in Table 12.3. The (5, 15/2) ground state is separated from the first excited state by about 50 cm^{-1}. The trend of the value of J is in agreement with early results in dinuclear oxo-bridged iron(III) species, which showed an increase in J on increasing the Fe–O–Fe angle.

The difference in energy between the ground state and the lowest excited levels allow the detailed investigation of the lowest S = 5 level. The ZFS gives rise to a barrier ranging from 16 to 7 K in the various members of the series. It was found indeed that the D parameter is negative throughout the series but with significant variations. Using the Orbach model, the separation between the lowest M = ±5 doublet and the top M = 0 acts as a barrier for the reorientation of the magnetization. In the Fe_4 series, it is about 10–20 K, not much but sufficient to observe slow relaxation at low temperature, magnetic hysteresis, and quantum tunneling. Indeed, the relaxation was found to follow an Arrhenius dependence with the U_{eff} and τ_0 parameters reported in Table 12.3. The slow magnetic relaxation was monitored through the AC measurements, as shown in Chapter 11.

Attempts were made to relate the D values to geometrical parameters. In fact, the geometrical origin of the anisotropy was not obvious and several attempts were made until eventually good results were obtained by taking into consideration the helical pitch γ. Notwithstanding that the variations of the

value of γ are small, they are accompanied by concomitant variations in the coordination geometry of the central iron and produce sizeable shifts in the value of the barrier.

Several attempts were made to rationalize the observed D values in terms of dipolar and exchange interactions. We recall that a convenient way to express the ZFS is to start from a Hamiltonian of the type

$$\mathscr{H} = \mathscr{H}_0 + \sum_i \mathscr{S}_i \cdot \mathbf{D}_i \cdot \mathscr{S}_i + \sum_{i<j} \mathscr{S}_i \cdot \mathbf{D}_{ij} \cdot \mathscr{S}_j \tag{12.4}$$

where the first term contains the isotropic and Zeeman components, the second is the single ion anisotropy, and the third is the spin–spin anisotropy. In the generally accepted strong exchange limit, that is, when D is small compared to J, it is possible to project the local parameters on the total spin. For instance, using D_3 symmetry for Fe_4, we have to take care of the three equivalent D_i, $i = 2, 3, 4$, located on the three ions defining the triangle and D_1. Indeed, the (slightly) idealized D_3 symmetry ion one has the full symmetry of the cluster, while the other three ions have C_2 symmetry. The local symmetry requires a principal axis parallel to the binary axis. In Figure 12.7, we show the local axes.

The local binary axes of the 2–4 ions are labeled as x_i, and z_i is orthogonal to the Fe_i–Fe_1 direction. The y_i-axes are local easy axes, while z_i are hard, and x_i intermediate. The local z-axis of Fe_1 is parallel to the trigonal axis. In this way, the projections of the individual spins on the total spin yield the coefficients reported below:

$$D = (5/39)D_1 + (51/182)[D_2(3\cos^2\beta - 1 + 3E_2 \sin^2\beta \cos 2\gamma] \tag{12.5}$$

where D_1 is the axial ZFS parameter of the central iron(III) ion, which lies on the threefold z-axis and must consequently have a rigorously axial anisotropy; D_2 and E_2 are the axial and rhombic ZFS parameters of the peripheral metal centers. The coefficients were calculated as previously reported (Gregoli *et al.*, 2009). The omitted spin–spin terms will be mentioned later. Concerning D_1, AOM (angular overlap model) and DFT (density functional theory) agree in indicating a negative value for a trigonally distorted octahedron. In order to gain more insight, some model compound was needed to confirm the values of the parameters. The

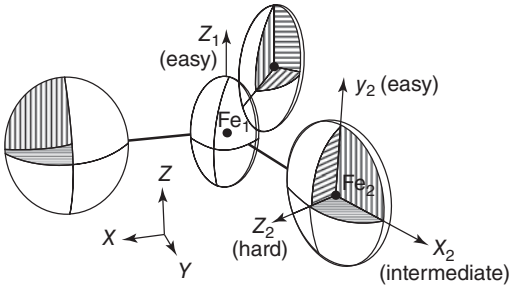

Figure 12.7 Sketch of the Fe_4 cluster with the local components of the local **D** tensors. (Reproduced from Accorsi, S. *et al.* (2006) with permission from The American Chemical Society.)

unique feature of Fe_4 is the stability of the cluster, which allows its deposition on surfaces permitting measurements on isolated molecules. We will come back on this point soon. For the peripheral ions, there is an ESR evidence for a positive D_2 in $[Fe_2(OCH_3)_2(dpm)_4]$. The principal direction along which the positive D_2 value is observed is very close to the z_2 direction of Figure 12.7. Using the mentioned values and Eq. (12.5), a D parameter of $-0.4\,cm^{-1}$ is calculated, which is in good agreement with the experimental one.

The robustness of the structure allows the formation of solid solutions of Fe_4 in the diamagnetic isomorphous Ga_4 (Abbati *et al.*, 2001). Before proceeding, we want to stress the difficulties we met with to prove doping the diamagnetic Ga_4 with Fe_4 avoiding metal scramble. A key experiment was the spectra of deuterated dpm Fe_4. The species was dissolved in the presence of Ga_4 in the ratio 1 : 1. The spectra were essentially unchanged for 18 h, showing no signal at the frequency of deuterium in the isolated Fe(dpm). On this basis, the crystallization was tuned to last no more than 10 h.

So far we have neglected the higher order single ion contributions. By extending the above model to include the B_4^0 parameters, the fit is improved and good agreement is achieved. Two spin interactions can be easily calculated for the dipolar terms, but the values are small and can be neglected. The exchange-determined contribution is expected to be small for the iron(III) terms because it has no spin–orbit coupling (SOC) in the ground state.

12.4
Fe_4 Relaxation and Quantum Tunneling

The observation of Arrhenius relaxation was interesting and expected on the basis of the similarity with Mn_{12} and Fe_8. However, to comply with the information provided by Mn_{12} and Fe_8, magnetic hysteresis had to be observed and QTM proved.

After overcoming some problems with the first investigated Fe_4, which were due to the coexistence of different isomers in the lattice, single-crystal magnetic data were collected which are shown in Figure 12.8. The sample was found to yield magnetic hysteresis.

The measurements were performed at 40 mK with a micro-SQUID (superconducting quantum interference device) (Wernsdorfer *et al.*, 1995; Wernsdorfer *et al.*, 2000). An external field was applied parallel to the z-axis of a single crystal and clear stepped hysteresis was observed. This had previously been observed in Mn_{12} (and Fe_8), and the experimental data were fitted assuming that the steps occur when two levels cross. The same model is used here. As the energy of the +MS level increases while that of the −MS+n level decreases, they will have to meet somewhere, restoring the conditions for resonant tunneling. The field at which this occurs, for axial symmetry and considering only second-order anisotropy terms, is given by

$$H_n = nD' \tag{12.6}$$

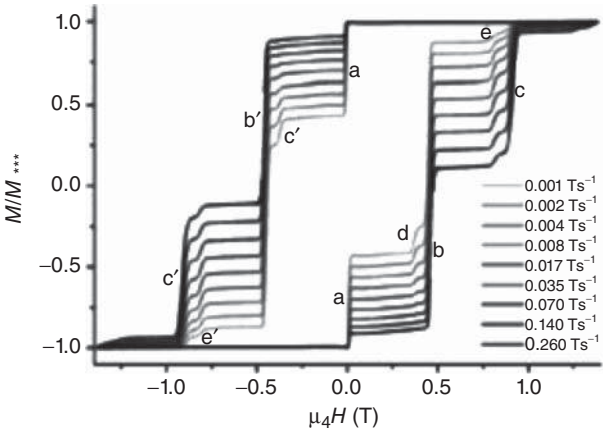

Figure 12.8 Magnetic hysteresis of Fe_4 recorded on single crystals at 40 mK with the applied fields parallel to the *z*-axis. The curves correspond to different field scan velocities. (Reproduced from Vergnani, L. *et al.* (2012) with permission from Wiley-VCH Verlag 3390 GmbH & Co. KGaA.)

where $n = 0, 1, 2 \ldots$ and $D' = D/\mu B = 0.41\ \text{cm}^{-1}$. Of course, the sharpness of the transitions is due to the low temperature. Equation (12.6) can be made more general by including also the tunnel splitting involving the pairs of levels $-M_s$ and $M_s - n$ generated by an off-diagonal perturbation which can couple states differing by a factor $\pm p$ in the value of m (Giraud, Tkachuk, and Barbara, 2003).

A qualitative interpretation is that at H_n the relaxation is fast and the magnetization varies rapidly. On the other hand, the flat region of the plot corresponds to fields where the relaxation is extremely slow. The fast relaxation is associated with

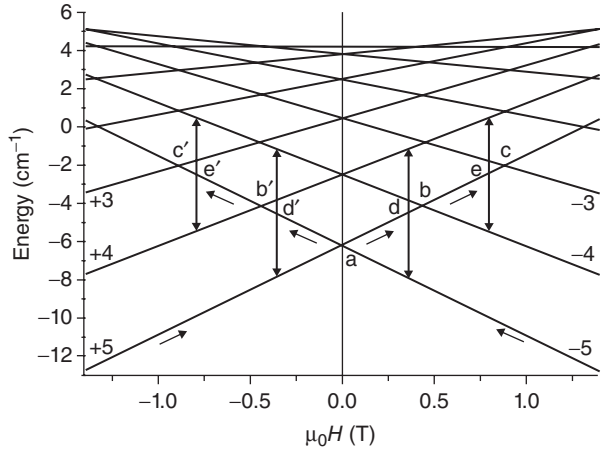

Figure 12.9 Field dependence of the energies of the components of the ground S multiplet of Fe_4. The field is parallel to the *c* crystal axis. $T = 40$ mK. (Reproduced from Vergnani, L. *et al.* (2012) with permission from Wiley-VCH Verlag 3390 GmbH & Co. KGaA.)

resonant QTM which operates when two levels are degenerate. Equation (12.6) is perfectly justified by using the D' value obtained from spectroscopic data. Therefore, there is no doubt that Fe_4 is an SMM like Mn_{12} and that it shows QTM. Additional information could be gathered by measuring the field dependence of the split levels of the ground S = 5 multiplet, reported in Figure 12.9. c and c′ correspond to transitions between states located in different wells. The step at zero field correspond to resonant tunneling between $M_s = \pm 5$; the others are attributed as shown in Figure 12.9.

12.5 And τ_0?

While structural correlations to understand the features influencing U_{eff} have been successfully worked out, much less has been done to understand the factors affecting the pre-exponential factor of the Arrhenius plot, τ_0. This is not rational because experimentally τ_0 values of $10^{-5}-10^{-11}$ are typically observed, and if it were possible to "design" τ_0, more efficient systems might be implemented. A rather convincing treatment has been performed on Fe_4 by taking advantage of the detailed studies performed on a series of compounds.

Perusal of Table 12.3 clearly shows a trend: the value of U_{eff} increases on increasing J, while τ_0 decreases. The efforts to increase the blocking temperature are frustrated by the decrease of τ_0. Since a relevant factor is phonon coupling, let us start from the expression adequate for that:

$$\tau_0^{-1} \approx \frac{1}{h_4 c_S^5 \rho} \left| \left\langle M_S = \pm 1 \right| V_{sp} \left| M_S = 0 \right\rangle \right|^2 (E_0 - E_{\pm 1})^3 \tag{12.7}$$

where c_S is the speed of sound in the material, ρ is the density of the material, and V_{sp} is the Hamiltonian describing spin–phonon interaction.

It contains only h topmost levels which act as the rate-determining steps. These features are expected to have an inverse power of 3 dependence on the energy difference between E_0 and $E_{\pm 1}$. Since the corresponding phonons are not numerous, the relaxation is slow. Equation (12.7) suggests for τ_0 a D^{-3} dependence. The agreement in the Fe_4 series is only qualitative but offers a rationalization of the inverse dependence observed in the parameters defined for describing the relaxation time.

12.6 Deep in the Tunnel

The low T relaxation of a SMM is dominated by tunneling, which requires a transverse field. In fact, if we assume two spin levels whose energies depend on a variable applied magnetic field parallel to z, the ground state will be a combination of the two states. The mixing will be determined by a quantum coupling between the states. If there is no coupling, there is no admixture of states and the system

is localized. In the presence of coupling, the system will oscillate between at least two levels.

The reference model is the Landau–Zener–Stuckelberg, LZS model (Wernsdorfer *et al.*, 2005; Földi *et al.*, 2007), which relates the tunneling probability P_k of monodisperse noninteracting clusters with the quantum splitting of the levels at resonance Δ_k:

$$P_k = 1 - \exp[(\pi {\Delta_k}^2)/(2|\varepsilon|)] \tag{12.8}$$

where $|\varepsilon| = g\mu_B\hbar(2S - |k|)\nu$ is the time derivative of the difference in Zeeman energy of the states involved in the resonance. A method to measure P_k is based on the height of the step in the hysteresis loop, which is proportional to the difference in magnetization divided by the difference between the equilibrium magnetization. Measurements performed on the $k = 0$ transition in the pure and doped samples show that undiluted samples have a large P compared to pure samples. In other words, the increase in paramagnetic species determines less efficient relaxation, thus showing that magnetic dilution can improve the memory effect. This is an important result to be taken into account when trying to move in the direction of molecular spintronic devices where isolated molecules are addressed.

A detailed analysis of the low-temperature relaxation of cluster was performed by Prokof'ev and Stamp (2006). The required transverse field is so small that static dipolar interaction of electronic and nuclear origin and hyperfine interaction are much larger than Δ. In this condition, the effect of the static fields would be that of pushing all the clusters out of resonance, quenching the relaxation. Since relaxation is observed, something must be added to the scene including the dynamics that changes the conditions: by varying the bias at each cluster in time, more spins are brought in resonance. Developing this model shows that the relaxation at low temperature and low field requires initially a fast hyperfine fluctuation that puts a few molecules in resonance: this causes other molecules in the solid to undergo relaxation, and so on. Calculating the relaxation yields

$$M(r,t) = 1 - \sqrt{t/\tau} \tag{12.9}$$

where $M(r,t)$ is the magnetization and τ is the characteristic time at low temperature. Since the process depends on the shape, this must be taken into account.

Monte Carlo simulations of the relaxation of samples of different geometries are performed as the time step is decided, which is much shorter than the characteristic time. A number of cluster magnetization are flipped and the dipolar field distribution recalculated to take into account the flip for ensembles of clusters of 50^3 spheres and cubes (Prokof'ev and Stamp, 1998). As shown in Figure 12.10, the agreement is fairly good.

The model was applied to Fe_4 by calculating the magnetic properties in the point-dipolar approximation mimicking a small crystal containing Fe_4 (Vergnani *et al.*, 2012). The symmetry of the clusters is forced to be D_3, with the principal directions shown in Figure 12.10.

The propeller-like core of the molecule is used as a starting point to evaluate the influence of molecular symmetry on the origin of magnetic anisotropy. Three

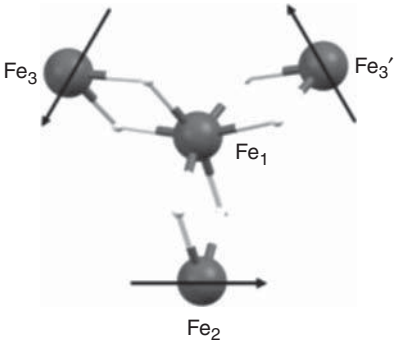

Figure 12.10 Fe_4 core of $[Fe_4(L^1)_2(dpm)_6]$. The black arrows define the hard axes (Z) of the anisotropy tensors for the three peripheral ions.

different geometries are used as models in the calculations. In all the models, a C_2 symmetry is, at least, preserved and, therefore, the 3 and 3′ iron ions are related by symmetry, and the binary axis is parallel to the $Fe_1 - Fe_2$ direction which corresponds to Y as in the crystal structure. In model 1, the symmetry is strictly D_3 and this feature forces the hard axes of the three tensors (z) to lie exactly in the molecular plane. In the Prokof'ev and Stamp approach, this model failed to reproduce the experimental quantum splitting of the levels. Models 2 and model 3 were developed by introducing rhombic distortions, which are varied in the two models by simply changing the sign of the angles of deformation.

The calculation in a lower symmetry showed better agreement with the experiments and were indicative that the differences between model 1 and the other two must be related to the effect of the dipolar transverse field. The crucial experiment is the application of a transverse field **B** in the XY plane either in the pure or diluted system. The distribution of dipolar fields can be responsible for the magnetic behavior. Indeed, using the models described above, it is apparent that the molecules have their tunneling enhanced by the transverse fields. Therefore rhombic anisotropy is responsible of the tunneling of the diluted sample.

These results provided direct evidence of the role of intermolecular magnetic interactions on the properties of SMMs. The steps present in the hysteresis loops of the pure Fe_4 are due to two-molecule tunneling effects, as they disappear in the diluted samples. The calculations performed with a multispin model have clarified the role of internal dipolar fields on the position and efficiency of single molecule tunneling resonances. The decreased tunneling probability in zero field observed in the pure Fe_4 phase was attributed to a dipolar shuffling mechanism involving the longitudinal component of internal fields. On the other side, the faster tunneling displayed by the pure Fe_4 phase was found to be consistent with the distribution of transverse internal fields in the crystal. The observation of faster zero-field relaxation in magnetically diluted SMMs requires additional experiments for a better understanding the role of interactions in SMM behavior.

12.7 Magnetic Dilution Effects

So far so good. As mentioned above, it is useful to monitor the influence of the intercluster interactions on the tunneling mechanisms. This kind of studies offers another opportunity to perform new experiments on Fe_4 diluted with Ga_4 reported in Section 12.3.

We recall that one of the stringent requirements to observe the SMM behavior is the minimization of the intercluster interactions, be they exchange or dipolar in nature. As suggested above, a possibility is substituting magnetic Fe^{3+} with diamagnetic Ga^{3+}, but unfortunately this can be done only in a random way. On the other hand, it is possible to apply some chemistry and make derivatives with the central Fe substituted with another trivalent ion, such as Cr, obtaining different ground states (Tancini *et al.*, 2010). Cr^{3+} is magnetic but it is rather inert, and it lasts in the central position for sufficient time to form $CrGa_3$ species.

There are two other features in the hysteresis plots marked as d and e (Figure 12.9) which cannot be attributed to single molecule tunneling. A similar behavior was previously observed in a manganese-based SMM $[Mn_4O_3(OSiMe_3)(OAc)_3(dbm)_3]$ (Hdbm = 1,3-diphenyl-1,3-propanedione), and was assigned to two-molecule tunnel transition allowed by intermolecular exchange interactions (Wernsdorfer *et al.*, 2002, 2005). The cluster is formed by one manganese(IV) and three manganese(III) arranged in a distorted cubane structure, the manganese(IV) lying on a trigonal axis. The AFM coupling between Mn^{3+} and Mn^{4+} gives S = 9/2 ground state, with the first excited state lying at about $5.5\,cm^{-1}$ above the ground level. The ZFS is described by $D = -0.72$ K, $E/D = 0.046$. This corresponds to $U_{eff} = 14\ K$. The point made in the analysis of the hysteresis loop recorded at low T is that the intercluster interactions cannot be neglected. The interactions can be observed as additional steps. They are attributed to spin–spin cross relaxation, SSCR. Rather obviously, the presence of many magnetic clusters in the lattice has some consequences on the magnetic properties of the considered cluster. The problem is a many-body problem which can become very complex. Matters become tractable if it is possible to consider only pairs of clusters; in Mn_4 the shortest intercluster distance is 0.803 nm along the trigonal axis, while the shortest distance in the trigonal plane is 1.692 nm. Therefore, a two-cluster model can be used. Also in this case, by limiting to low temperatures, a number of transitions are observed, as shown in Table 12.4.

Transition 1 corresponds the ground state tunneling: one of the spins reverses while the other remains unaltered. The energy of the dipolar interaction is calculated as 100 Oe, rather different from the experimental 360 Oe. Focusing of SSCR transitions 7 is a good example. It corresponds to a spin making a tunnel transition −9/2 to 9/2 within the ground state while the other making a transition to an excited state.

A similar behavior is observed for Fe_4, but this time it was possible to perform experiments by doping with diamagnetic Ga_4 (Wernsdorfer *et al.*, 2002; Repollés, Cornia, and Luis, 2014). The results speak for themselves; the c, n, d features

Table 12.4 The 13 tunnel transitions for two coupled SMMs with S = 9/2.

N	IS[a)]	FS[b)]	Type[c)]
1	(−9/2, −9/2)	(−9/2, 9/2)	GS → GS
2	(−9/2, 5/2)	(7/2, 7/2)	ES → SSCR
3	(−5/2, 9/2)	(7/2, 7/2)	ES → SSCR
4	(−9/2, 5/2)	(9/2, 3/2)	ES → SSCR
5	(−9/2, −7/2)	(9/2, −5/2)	ES → SSCR
6	(−9/2, 7/2)	(9/2, 5/2)	ES → SSCR
7	(−9/2, −9/2)	(−7/2, 9/2)	SSCR
8	(−9/2, 9/2)	(7/2, 9/2)	GS → ES
9	(−9/2, −9/2)	(−9/2, 7/2)	GS → ES
10	(−7/2, 9/2)	(7/2, 7/2)	ES → SSCR
11	(−9/2, −9/2)	(−7/2, 7/2)	SSCR
12	(−9/2, 9/2)	(5/2, 9/2)	GS → ES
13	(−9/2, 9/2)	(7/2, 7/2)	SSCR

a) IS: Initial state.
b) FS: final state.
c) Type: GS = ground state, ES = excited state, and SSCR = spin – spin cross relaxation.

disappear, indicating that a two-cluster mechanism is needed to observe them. Evidence for the existence of doping-dependent magnetic interactions comes from the difference in the states observed when the magnetic field crosses zero, which is 0 for magnetization at zero field. In 1, the transition occurs at 81 Oe, showing that the clusters sense a nonzero field while the doped samples have transition at zero. In order to obtain deeper insight into the mechanism of SSCR, the assumption was made that the perturbing interaction is dipolar in nature.

12.8 Single Molecule Magnetism

What we have in mind is experiments performed on individual molecule magnets. Given the previous experience, a Fe_4 derivative was designed to be well suited to be deposited on Au(111). The topological measurements evidenced a monolayer of objects of the correct size, to be described as Fe_4. One of the desirable features of Fe_4 is its stability which allows the measurement of the response of the individual molecules organized on suitable surfaces. These must be conducting in order that the molecules are individually addressable to the scanning probe. Good evidence of the possibility to organize molecules on suitable surfaces was achieved relatively early, but the crucial experimental step was the use synchrotron radiation in XMCD (X-ray magnetic circular dichroism) experiments. The choice of the surface was Au(111) to organize derivatives of Fe_4 possessing tails with a sulfur donor. The tail can have variable lengths monitored by the length of the aliphatic chains connecting the Fe_4 body to the S atoms. It is also possible to have

two tails instead of one. In order to avoid errors, it is necessary accurately examine that the SMM behavior is mantained after grafting. For this purpose XMCD has to be considered a powerful tool because it has the sensitivity to monitor the magnetization of molecular submonolayers. In the successful results of Sessoli *et al.* on Fe_4C_5 (5 is the number of carbon atoms of the aliphatic chain used to lock the cluster to the surface), the preliminary measurements were of XAS (X-ray absorption spectroscopy) type (Mannini *et al.*, 2010). The experiments were performed at sub-Kelvin temperatures at an applied field of 30 kOe. The XAS and XMCD results were identical within error to those of the bulk samples. In order to record the magnetic hysteresis, XMCD was measured at 0.650 K and with different orientations of the magnetic field. The curves are shown in Figure 12.11. The $T = 1.0$ K spectra do not show evidence of deviation from paramagnetic behavior, while those at 0.65 K clearly show evidence of stepped hysteresis. The evidence of SMM behavior on monolayers has been achieved. The self-assembly process the authors used allowed to obtaining arrays of intact and fully functional SMMs chemically grafted to gold. The control of orientation is relevant for any application of SMMs in single-molecule spintronic devices and can be achieved by a rational chemical approach. Further, it is worth of mention that SMMs and QTM effects, having constituted a milestone in the history of spin, are proving useful in learning how complex matter organizes at the nanoscale.

This has been an important chapter where some examples of SMM have been worked out. Of course, Mn_{12} and Fe_8 have been mentioned, but more details were dedicated to Fe_4 and Mn_4. The conditions to observe the SMM behavior emerge quite clearly from the discussion of the magnetic data.

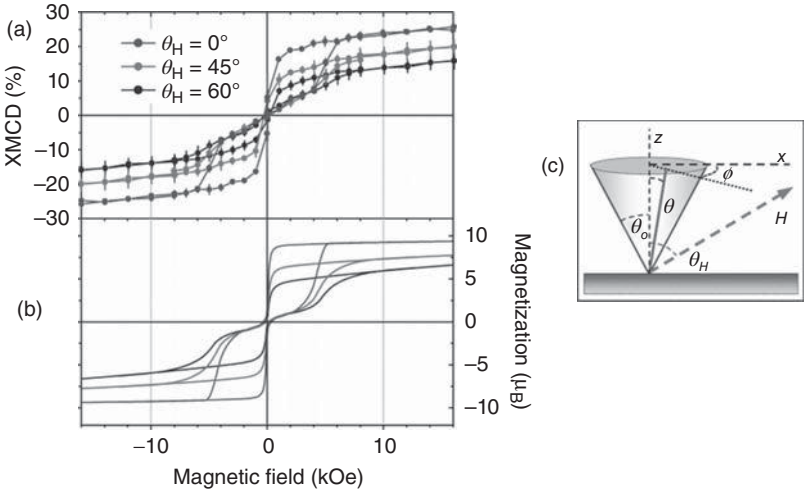

Figure 12.11 (a) Angle-resolved hysteresis loops for the Fe_4C_5 monolayer obtained from the XMCD at 709.2 eV and $T = 650(50)$ mK. (b) Calculated hysteresis loops. (c) Geometrical parameters describing the orientation of molecular axis (full line) on the surface. (Reproduced from Mannini, M. *et al.* (2010) with permission from Macmillan Publishers Limited.)

The simplest way to measure slow magnetic relaxation is through AC susceptibility measurements. The observation of an out-of-phase susceptibility is an indication of slow magnetic relaxation. The correlation between the Fe–Fe coupling and the helical pitch is a beautiful example of the structural–magnetic correlations that can be established in TM compounds. Other important results are the possibility of measuring the effects of magnetic dilution by exploiting diamagnetic ions such as Ga^{3+}. Simple models provide evidence of the relative role of dipolar and exchange in influencing the relaxation.

QTM is the other relevant parameter that can be investigated. Here we limit the treatment to one example. More details will be provided in Chapter 17. After the enthusiasm for observing QTM in mesoscopic matter Mn_{12}, which after all was a little exaggerated, the stepped hysteresis of Fe_4 was not really a surprise: quantum size produces quantum effects. In the case of a Kramers doublet, the relaxation is very fast because the two levels are degenerate. In order to slow down the relaxation, it is necessary to break down the degeneracy, for instance, by adding an external field.

Finally, the modern techniques allow the measurement of individual molecules, opening completely new worlds which change our point of view of matter.

References

Abbati, G.L., Brunel, L.-C., Casalta, H., Cornia, A., Fabretti, A.C., Gatteschi, D., Hassan, A.K., Jansen, A.G.M., Maniero, A.L., Pardi, L. *et al.* (2001) Single-Ion versus dipolar origin of the magnetic anisotropy in iron(III)-oxo clusters: a case study. *Chem. Eur. J.*, **7**, 1796–1807.

Accorsi, S., Barra, A.L., Caneschi, A., Chastanet, G., Cornia, A., Fabretti, A.C., Gatteschi, D., Mortalò, C., Olivieri, E., Parenti, F. *et al.* (2006) Tuning anisotropy barriers in a family of tetrairon(III) single-molecule magnets with an S = 5 ground state. *J. Am. Chem. Soc.*, **128**, 4742–4755.

Aromí, G. and Brechin, E. (2006) in *Single-Molecule Magnets and Related Phenomena* (ed. R. Winpenny), Springer, Berlin, Heidelberg, pp. 1–67.

Aubin, S.M.J., Wemple, M.W., Adams, D.M., Tsai, H.L., Christou, G., and Hendrickson, D.N. (1996) Distorted $Mn(IV)Mn(III)_3$ cubane complexes as single-molecule magnets. *J. Am. Chem. Soc.*, **118**, 7746–7754.

Barra, A.L., Caneschi, A., Cornia, A., De Fabrizi Biani, F., Gatteschi, D., Sangregorio, C., Sessoli, R., and Sorace, L. (1999) Single-molecule magnet behavior of a tetranuclear iron(III) complex. The origin of slow magnetic relaxation in iron(III) clusters. *J. Am. Chem. Soc.*, **121**, 5302–5310.

Blagg, R.J., Muryn, C.A., McInnes, E.J.L., Tuna, F., and Winpenny, R.E.P. (2011) Single pyramid magnets: Dy_5 pyramids with slow magnetic relaxation to 40 K. *Angew. Chem. Int. Ed.*, **50**, 6530–6533.

Caneschi, A., Gatteschi, D., Sessoli, R., Barra, A.L., Brunel, L.C., and Guillot, M. (1991) Alternating current susceptibility, high field magnetization, and millimeter band EPR evidence for a ground S = 10 state in $[Mn_{12}O_{12}(CH_3COO)_{16}(H_2O)_4] \cdot 2CH_3COOH \cdot 4H_2O$. *J. Am. Chem. Soc.*, **113**, 5873–5874.

Cornia, A., Fabretti, A.C., Garrisi, P., Mortalò, C., Bonacchi, D., Gatteschi, D., Sessoli, R., Sorace, L., Wernsdorfer, W., and Barra, A.L. (2004) Energy-barrier enhancement by ligand substitution in tetrairon(III) single-molecule magnets. *Angew. Chem. Int. Ed.*, **43**, 1136–1139.

Földi, P., Benedict, M.G., Pereira, J.M. Jr., and Peeters, F.M. (2007) Dynamics

of molecular nanomagnets in time-dependent external magnetic fields: beyond the Landau-Zener-Stückelberg model. *Phys. Rev. B: Condens. Matter Mater. Phys.*, **75**, 104430.

Gatteschi, D., Fittipaldi, M., Sangregorio, C., and Sorace, L. (2012) Exploring the no-man's land between molecular nanomagnets and magnetic nanoparticles. *Angew. Chem. Int. Ed.*, **51**, 4792–4800.

Gatteschi, D. and Sessoli, R. (2003) Quantum tunneling of magnetization and related phenomena in molecular materials. *Angew. Chem. Int. Ed.*, **42**, 268–297.

Gatteschi, D., Sessoli, R., and Villain, J. (2006) *Molecular Nanomagnets*, Oxford University Press, Oxford.

Giraud, R., Tkachuk, A.M., and Barbara, B. (2003) Quantum dynamics of atomic magnets: cotunneling and dipolar-biased tunneling. *Phys. Rev. Lett.*, **91**, 2572041–2572044.

Gregoli, L., Danieli, C., Barra, A.-L., Neugebauer, P., Pellegrino, G., Poneti, G., Sessoli, R., and Cornia, A. (2009) Magnetostructural correlations in Tetra-iron(III) single-molecule magnets. *Chem. Eur. J.*, **15**, 6456–6467.

Mannini, M., Pineider, F., Danieli, C., Totti, F., Sorace, L., Sainctavit, P., Arrio, M.A., Otero, E., Joly, L., Cezar, J.C. *et al.* (2010) Quantum tunnelling of the magnetization in a monolayer of oriented single-molecule magnets. *Nature*, **468**, 417–421.

Milios, C.J., Inglis, R., Vinslava, A., Bagai, R., Wernsdorfer, W., Parsons, S., Perlepes, S.P., Christou, G., and Brechin, E.K. (2007) Toward a magnetostructural correlation for a family of Mn_6 SMMs. *J. Am. Chem. Soc.*, **129**, 12505–12511.

Murrie, M., Teat, S.J., Stœckli-Evans, H., and Güdel, H.U. (2003) Synthesis and characterization of a cobalt(II) single-molecule magnet. *Angew. Chem. Int. Ed.*, **42**, 4653–4656.

Papatriantafyllopoulou, C., Wernsdorfer, W., Abboud, K.A., and Christou, G. (2010) $Mn_{21}Dy$ cluster with a record magnetization reversal barrier for a mixed 3d/4f single-molecule magnet. *Inorg. Chem.*, **50**, 421–423.

Prokof'ev, N. and Stamp, P. (1998) Low-temperature quantum relaxation in a system of magnetic nanomolecules. *Phys. Rev. Lett.*, **80**, 5794–5797.

Prokof'ev, N.V. and Stamp, P.C.E. (2006) Decoherence and quantum walks: anomalous diffusion and ballistic tails. *Phys. Rev. A: At. Mol. Opt. Phys.*, **74**, 020102(R).

Redler, G., Lampropoulos, C., Datta, S., Koo, C., Stamatatos, T.C., Chakov, N.E., Christou, G., and Hill, S. (2009) Crystal lattice desolvation effects on the magnetic quantum tunneling of single-molecule magnets. *Phys. Rev. B*, **80**, 094408.

Repollés, A., Cornia, A., and Luis, F. (2014) Spin–lattice relaxation via quantum tunneling in diluted crystals of Fe_4 single-molecule magnets. *Phys. Rev. B*, **89**, 054429.

Rogez, G., Donnio, B., Terazzi, E., Gallani, J.L., Kappler, J.P., Bucher, J.P., and Drillon, M. (2009) The quest for nanoscale magnets: the example of Mn_{12} single molecule magnets. *Adv. Mater.*, **21**, 4323–4333.

Sangregorio, C., Ohm, T., Paulsen, C., Sessoli, R., and Gatteschi, D. (1997) Quantum tunneling of the magnetization in an iron cluster nanomagnet. *Phys. Rev. Lett.*, **78**, 4645–4648.

Sessoli, R., Gatteschi, D., Caneschi, A., and Novak, M.A. (1993) Magnetic bistability in a metal-ion cluster. *Nature*, **365**, 141–143.

Sharples, J.W., Zheng, Y.-Z., Tuna, F., McInnes, E.J.L., and Collison, D. (2011) Lanthanide discs chill well and relax slowly. *Chem. Commun.*, **47**, 7650–7652.

Tancini, E., Jesus Rodriguez-Douton, M., Sorace, L., Barra, A.L., Sessoli, R., and Cornia, A. (2010) Slow magnetic relaxation from hard-axis metal ions in tetranuclear single-molecule magnets. *Chem. Eur. J.*, **16**, 10482–10493.

Tasiopoulos, A.J., Vinslava, A., Wernsdorfer, W., Abboud, K.A., and Christou, G. (2004) Giant single-molecule magnets: a {Mn84} torus and its supramolecular nanotubes. *Angew. Chem. Int. Ed.*, **43**, 2117–2121.

Thomas, L., Lionti, F., Ballou, R., Gatteschi, D., Sessoli, R., and Barbara, B. (1996) Macroscopic quantum tunnelling of magnetization in a single crystal of nanomagnets. *Nature*, **383**, 145–147.

Vergnani, L., Barra, A.L., Neugebauer, P., Rodriguez-Douton, M.J., Sessoli, R., Sorace, L., Wernsdorfer, W., and

Cornia, A. (2012) Magnetic bistability of isolated giant-spin centers in a diamagnetic crystalline matrix. *Chem. Eur. J.*, **18**, 3390–3398.

Wernsdorfer, W., Hasselbach, K., Mailly, D., Barbara, B., Benoit, A., Thomas, L., and Suran, G. (1995) DC-SQUID magnetization measurements of single magnetic particles. *J. Magn. Magn. Mat.*, **145**, 33–39.

Wernsdorfer, W., Bonet Orozco, E., Barbara, B., Benoit, A., and Mailly, D. (2000) Classical and quantum magnetisation reversal studied in single nanometer-sized particles and clusters using micro-SQUIDs. *Phys. B: Condens. Matt.*, **280**, 264–268.

Wernsdorfer, W., Bhaduri, S., Tiron, R., Hendrickson, D.N., and Christou, G. (2002) Spin-spin cross relaxation in single-molecule magnets. *Phys. Rev. Lett.*, **89**, 197201.

Wernsdorfer, W., Bhaduri, S., Vinslava, A., and Christou, G. (2005) Landau-Zener tunneling in the presence of weak intermolecular interactions in a crystal of Mn_4 single-molecule magnets. *Phys. Rev. B*, **72**, 214429.

Wernsdorfer, W. and Sessoli, R. (1999) Quantum phase interference and parity effects in magnetic molecular clusters. *Science*, **284**, 133–135.

Woodruff, D.N., Winpenny, R.E.P., and Layfield, R.A. (2013) Lanthanide single-molecule magnets. *Chem. Rev.*, **113**, 5110–5148.

13
Single Ion Magnet (SIM)

13.1
Why Single

It is now the right time to enter into the details of the field of research that focuses on the properties of molecule-based systems whose magnetization relaxes slowly not due to cooperative phenomena but due to intrinsic properties of the metal ions that are present in a molecular structure. As stated in Chapter 1, the role of Ln in MM has been a marginal one till the beginning of this century. The main reasons for the lack of interest were (i) weak magnetic interactions, (ii) the difficulties associated with a large unquenched orbital contribution which demands high doses of quantum mechanics, (iii) the need for routine magnetic measurements below 4 K which were not available in chemistry labs, (iv) the lack of interest for the samples where the instrumentation was available, such as in specialized physics laboratories, and (v) the worrying doubt of whether it was worthwhile. But worst of all was the fact that there are 13 paramagnetic Lns and there was always a reviewer asking why all of them were not investigated!

The change in attitude toward all the above issues came at the beginning of this century when two reports on completely different materials showed that indeed isolated Ln ions can give rise to slow magnetic relaxation analogous to what was observed in SMMs (single molecule magnets). The compounds were Ho-doped $YLiF_4$, a typical solid-state material, and $[Ln(Pc)_2]^-$, whose structure is shown in Figure 3.7, a typical molecular material. They showed that, beyond prejudice, Ln ions can be appealing for systems where the single ion anisotropy can provide unique properties appealing to chemistry, physics, and materials science. It was the start of single ion magnets (SIMs), even though the name was coined later.

In the same years, SCMs (single chain magnets) were discovered, as we report in Chapter 15, showing that molecules provide a new point of view toward magnetism and suggesting for the first time that zero-dimensional, or better single ion, systems may be exciting. In short, Lns are not very appealing for magnetic interactions because the f orbitals are internal ones and are strongly shielded from the environment but they easily produce large anisotropy due to unquenched orbital moment. Let us check if going single is rewarding.

Introduction to Molecular Magnetism: From Transition Metals to Lanthanides, First Edition.
Cristiano Benelli and Dante Gatteschi.
© 2015 Wiley-VCH Verlag GmbH & Co. KGaA. Published 2015 by Wiley-VCH Verlag GmbH & Co. KGaA.

13.2
Slow Relaxation in Ho in Inorganic Lattice

The observation of slow magnetic relaxation in Ho^{3+} was surprising but in line with previous results (Wu *et al.*, 1991). The novelty was the magnetic hysteresis in a paramagnet and the clear evidence for quantum effects. But let us go in order. There was an interest on doped single crystals of $YLiF_4$ for possible applications in high-power laser diodes, so there was experience of growing good single crystals and controlling the doping extent of holmium (Agladze *et al.*, 1991). The magnetic properties of the Ho-doped crystals had been investigated for monitoring dipolar interactions. The host material crystallizes in the tetragonal space group $I4_1/a$, and the Ln ion has S_4 symmetry. The coordination is dodecahedral with a twist angle of about 2°, which justifies the lowering of the symmetry from D_{2d} to S_4. The relevant interactions to be considered are CF (crystal field) and SOC (spin–orbit coupling) (Griffith, 1961). The ground J = 8 manifold was taken into consideration. The CF was used in the Stevens formalism (Stevens, 1952) with five parameters B_k^q corresponding to $k = 2, 4, 6$ and $q = 0, 4$. $g_J = 5/4$ was taken from the free ion.

It is a useful exercise to classify the CF and the M_J basis functions using group theory. Those who are not familiar with group theory can safely skip this paragraph. The irreducible representations, (IRs) of S_4 are A, B, and E. We prefer this notation to the one that classifies the IRs as Γ_i. The 17 functions of the ground J = 8 multiplet give the IRs 5A + 4B + 4E. The basis for A is $M_J = 0, \pm4, \pm8$; for B it is $M_J = \pm2, \pm6$, and for E it is $M_J = \pm1, \pm3, \pm5, \pm7$. In this symmetry, the presence of transverse CF terms $B_4^4O_4^4$ and $B_6^4O_6^4$ mixes free ion states, with $\Delta M_J = \pm4$.

The energies of the M_J states were obtained from high-resolution optical data and single-crystal ESR spectra in the frequency range 70–600 GHz. The spectra were recorded parallel to *c* and *a* (Magariño *et al.*, 1976). Several signals were observed in each crystal orientation. The assignments were performed by extrapolating the resonance fields to zero. The spectra yielded a ground doublet, which was degenerate in zero field mainly corresponding to

$$\Psi_{1,2} = \alpha_1|\pm7\rangle + \alpha_2|\pm3\rangle \tag{13.1}$$

The wave functions are labeled using the M_J components of J, the number of the ground multiplet.

Using an effective spin S = 1/2 for describing the behavior of the lowest doublet, the energies are given by

$$E_{1,2} = \pm1/2\, g_{\text{eff}\,||}\ \mu_B H; \quad g_{\text{eff}||} = 2g_J(7\alpha_1^2 + 3\alpha_2^2) \tag{13.2}$$

The expected $g_{\text{eff}||}$ values range from 17.5 to 7.5. Since the experimental value is 13.3(1), the region where $\alpha_1^2 = \alpha_2^2 = 0.5$ seems to be appropriate. The spectra parallel to *a* show only a small splitting. The first excited state is a singlet at about 6.6 cm^{-1}, which is a linear combination of $|\pm6\rangle$ and $|\pm2\rangle$. The next excited state is a singlet at 23.8 cm^{-1}.

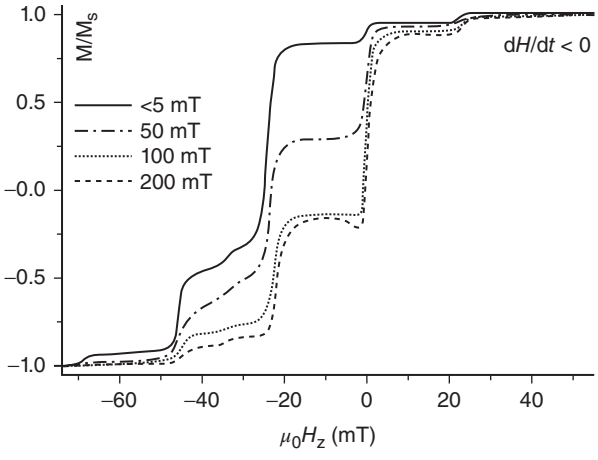

Figure 13.1 Hysteresis loops in a constant transverse field at $T = 50$ mK and for $\upsilon = 0.55$ mT s^{-1}. A transverse field enhances the quantum fluctuations in zero longitudinal applied field, leading to a larger magnetization step. (Reproduced from Giraud, R. *et al.* (2001) with permission from The American Physical Society.)

The magnetic properties of this system were measured with a micro-SQUID in the range 40 mK to 2 K. The sample was prepared by applying a field up to 2 T parallel to the tetragonal crystal axis. Then the field was cycled at variable speeds. At slow field sweep, the staircase hysteresis loop shown in Figure 13.1 was observed (Giraud *et al.*, 2001).

The hysteresis signals irreversibility and slow relaxation, as we have described in the previous chapter. It is not unexpected below 300 mK, where the dynamics is very slow. Hysteresis is a typical indication of bulk magnetic behavior, but a transition to magnetic order must be excluded here because the concentration of the magnetic Ho^{3+} is low in the sample. The overall appearance of the plot is similar to that reported in Chapter 12 for the SMM Fe_4 but the origin is different as we are going to show. The steps on the hysteresis curve represent discontinuity points where the relaxation properties vary rapidly as a result of rapid changes of the energies of quantized levels. The properties of the system in the vicinity of the crossing depend on the coupling of the two levels. If the crossing levels are not coupled, the interaction is zero and the two levels cross without any deviation, while if the interaction is different from zero, the two levels repel each other, opening a gap as shown in Figure 13.2.

13.3
Quantum Tunneling of the Magnetization: the Role of Nuclei

We have already introduced resonant tunneling in Chapter 12, where we have shown that when two levels meet it is an occasion for exchanging quanta and

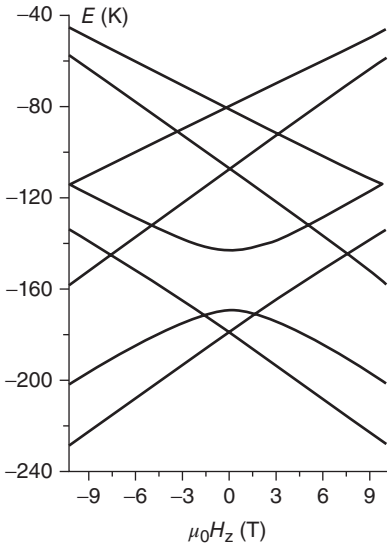

Figure 13.2 Low-energy part of the Zeeman diagram of Ho^{3+} in $LiYF_4$ with crossing and noncrossing levels according to thermally activated tunneling. (Reproduced from Giraud, R. *et al.* (2001) with permission from The American Physical Society.)

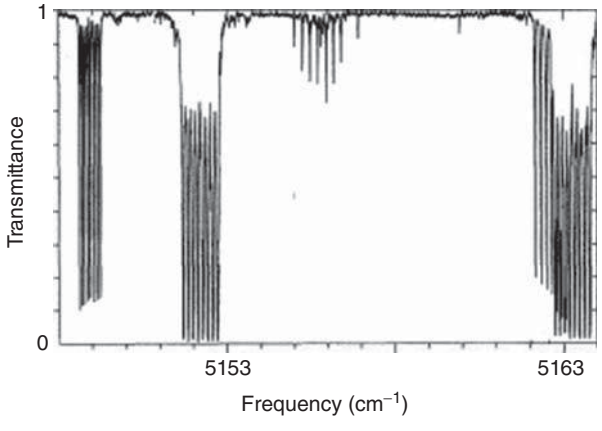

Figure 13.3 The low-frequency part of the transition $^5I_8 \rightarrow {}^5I_7$ of Ho^{3+} in $LiYF_4$. Ho (0.1 at.%) at 2.0 K. $E, H \perp c$ polarization. The spectral resolution is 0.004 cm^{-1}. (Reproduced from Agladze, N.I. *et al.* (1991) with permission from The American Physical Society.)

relaxing. Of course, we must remember that the experiments we are talking of now occur below 1 K: in order to have relaxation, we need something moving at that temperature. The magnetization of nuclei is a good candidate, and the behavior of ^{165}Ho can be monitored in a direct way by measuring the optical absorption of $YLiF_4$ doped with 1% Ho as we mentioned previously (Giraud, Tkachuk, and Barbara, 2003). The spectra showed evidence of nonzero ^{165}Ho hyperfine interactions ($A_J = 812$ MHz). In fact, the material was under investigation for its optical properties in the infrared, and the transitions were so sharp that the hyperfine structure was clearly resolved (see Figure 13.3).

Table 13.1 Hyperfine constant values (in MHz) for stable lanthanide isotopes.

^{141}Pr	^{143}Nd	^{147}Sm	^{151}Eu	^{155}Gd	^{159}Tb	^{161}Dy	^{165}Ho	^{167}Er	^{169}Tm	^{171}Yb
1765.2	634.7	623.4	104.3	12.1	530.0	896.1	812	558.3	687	2055
—	^{145}Nd	^{149}Sm	^{153}Eu	^{157}Gd	—	^{163}Dy	—	—	—	^{173}Yb
—	393.0	458.5	45.9	15.0	—	625.4	—	—	—	580

This is indeed an important feature of the material. It is useful to remember that in the system, there are magnetic nuclei, such as ^{19}F, that have I = 1/2 and ^{165}Ho with I = 7/2 and natural abundance 100%. The latter is centered on the relaxing Ln, therefore it may have an important role in the magnetic relaxation. It is necessary therefore to switch on the nuclei; the appropriate form to do this is the introduction of the hyperfine term. The hyperfine term regards the interaction between the unpaired electron and the nuclear spin of ^{165}Ho. The relevant Hamiltonian is

$$\mathscr{H} = \mathscr{J} \cdot \mathbf{A}_{\mathrm{IJ}} \cdot \mathscr{J} \tag{13.3}$$

We recall that the hyperfine tensor has essentially three contributions, namely the contact, the spin dipolar, and the orbit component (often called the *pseudo-contact term*) (Bertini, Luchinat, and Parigi, 2002). The first term depends on the unpaired spin density on the nucleus. As is well known, only the s orbitals have nonzero spin density on the nucleus. Therefore, the lanthanides have no contact contribution to the hyperfine term at zero-order approximation. However, some spin density is transferred from the f to the s orbitals by a spin polarization mechanism.

The dipolar contribution due to the through-space interaction provides information on the nuclei–electron distance. The last contribution introduces the dipolar interaction involving the orbital moment. The dipolar term is traceless. Other terms have been neglected, such as nuclear Zeeman, nuclear quadrupole, and so on.

Each energy level of the J = 8 ground multiplet are split into 2J + 1 components on introducing the hyperfine coupling. In a simple perturbative way, the energy of the hyperfine levels, for a magnetic field parallel to the tetragonal axis, is given by

$$E_{\mathrm{MJ,MI}} = g\mathrm{M_J}\mu_{\mathrm{B}}H + \mathrm{AM_IM_J} \tag{13.4}$$

No direct measurement of the relaxation time of the magnetization has been reported, but evidence that it must be long is clear. Considering the lowest doublet, loosely described by $\mathrm{M_J} = \pm\mathrm{J}$, as the two-level system of the Orbach treatment, a barrier of the order of 10^2 K is anticipated, but the possibility of shortcuts via quantum relaxation must be taken into account (Giraud *et al.*, 2001). After all, quantum tunneling of the magnetization is well documented in the SMM of d clusters.

The hyperfine interaction in Lns is, in most cases, larger than that of 3d metal ions (Table 13.1) (e.g., ^{51}V ≈ 240 MHz; ^{53}Cr ≈ 195 MHz; ^{55}Mn ≈ 270 MHz; ^{63}Cu ≈ 350 MHz), and therefore they are much better suited for the

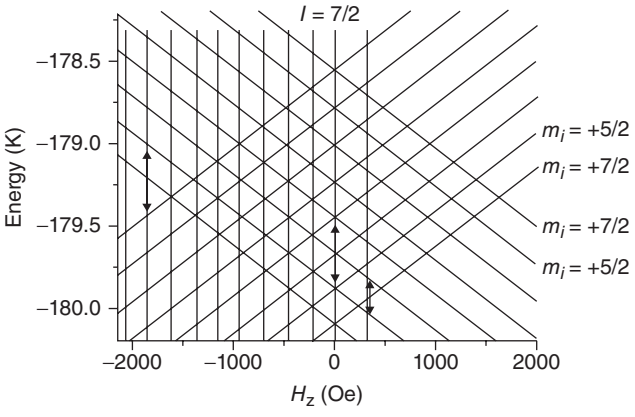

Figure 13.4 Electronuclear energy levels calculated within the single-ion representation. Equally spaced levels in the Zeeman diagram allow for nondissipative cross spin relaxation (CSR) processes in the tunneling regime for $LiHoF_4$. (Reproduced from Giraud, R. *et al.* (2003) with permission from The American Physical Society.)

investigation of entanglement of electron and nuclear moments. The energy levels available at low temperature are the product of electron and nuclear functions. Continuing with the Ho example, the electron states are a ground doublet and a singlet at about 10 K. Therefore, the low-T limit is a two-level system with a barrier of 10 K. Under these conditions, there are no avoided crossing and no tunneling. On switching on the hyperfine interactions, the energies of the electronic levels split into eight levels. The number of crossings increases, as shown in Figure 13.4. Since the hyperfine levels can be admixed by transverse fields, avoided crossings can be anticipated.

13.4 Back to Magnets

The observed steps in the magnetization require crossing levels. The magnetic experiments performed at 50 mK show hysteresis and at least four steps. The separation between the steps is given by $H_n = n \times 23$ mT $(-7 < n < 7)$. The candidates to justify the observed behavior are the hyperfine levels, that is, those generated by the interaction between the electron and nuclear spin. In fact, the experimental H_n values are in excellent agreement with the calculated hyperfine contribution. This may be induced by the transverse component of the hyperfine $A_J/2(I^+J^- + I^-J^+)$. By applying the transverse operator to the $|\pm M_I\rangle$ functions, avoided crossing is expected when the difference in absolute value of the nuclear quantum numbers M_I is 2, 6, 10, …, and so on. This has indeed been observed, lending credibility to the role of hyperfine interactions. Additional effects have been suggested and, in some cases, observed operating with AC susceptibility at higher T.

The experiments were also performed on variously doped $LiHo_{1-x}Y_xF_4$ crystals. In this way, it was possible to measure the properties of dimers, trimers, and so on, the best technique to employ is pulsed ESR, which provides the signals of the various species.

The above-described results were certainly interesting but failed to produce high excitement, the main reason being that they do not correspond to molecular magnets. Nevertheless, the obtained results had shown that Lns can give surprising physics and that slow relaxation can be observed even in single ions. This observation showed that one of the strategies for attaining a high blocking temperature was based on a prejudice, namely that polynuclear species were mandatory.

Similar relevant quantum effects were observed in a system where $CaWO_4$ was doped with Er^{3+}. The properties are relevant in the field of quantum computation and therefore they are described in detail in Section 18.6. At any rate, they confirmed that single ions can behave as magnets.

13.5
The Phthalocyanine Family: Some More Chemistry

The previous results are certainly very interesting but they look much more a lecture in quantum mechanics than anything else. After all, observing quantum effects in a single ion below 1 K is not that surprising. It is now time to go back to MM and, after long, introduce some nontrivial chemistry. One of the relevant features of the chemistry of porphyrins (RP) and phthalocyanines (Pcs) is the use of four nitrogen donor atoms (N4) to coordinate to the metal ions. There are essentially two ways to do that, namely with the metal ions in the plane of the four nitrogen atoms, or outside, as shown in Figure 13.5.

The M–N4 moiety can complete the coordination polyhedron with additional ligands. The manner that is relevant to SIM is that the additional ligands are provided by Pc and/or RP, as shown in Figure 13.6. The simplest structure is one in which two N4 rings bind one metal ion forming a sandwich structure, in which two tetraindole moieties form two deckers with the metal ion being the meat ball. The two-charge on the ring favors $M(N4)_2$ with M^{4+} ions. Charge compensation arguments suggest also a triple decker (N4)–M–(N4)–M(N4) with trivalent cations. Trivalent cations were also found to yield $M(P4)_2$ compounds. After some

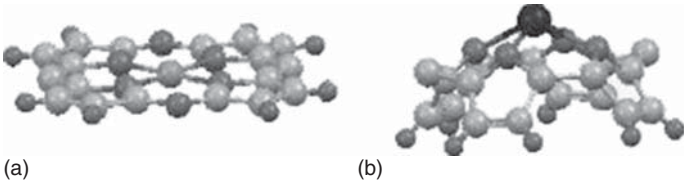

Figure 13.5 A metal coordinated (a) inside or (b) outside the pyrrole plane.

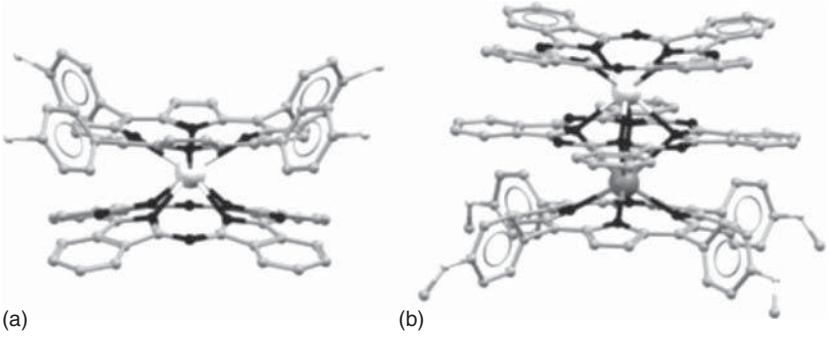

Figure 13.6 Schematic view of a sandwich-type mixed (phthalocyaninato)(porphyrinato) dirare earth (a) double and (b) triple decker complex.

controversy, it was finally agreed that one N4 group is binegative while the other is a mono-charged radical anion. Finally, anion double decker species were reported.

The advantage of this type of compounds is the versatility of the tetrapyrrole moiety, which can be really tailored by playing on its charge, solubility, steric hindrance, and redox properties. The first sandwich structure $Sn(Pc)_2$ was reported in 1936 (Linstead and Robertson, 1936) and the X-ray structure in 1973 (Bennett, Broberg, and Baenziger, 1973). In the 1980s when the Ln sandwiches were first synthesized, the interest of chemists was for their electrochromic properties and the new compounds were appealing because they could sublime, in general, unchanged. They could be deposited on optically transparent electrodes and used in electrochromic displays. They were of no particular interest for MM because at that time the focus was for molecular ferromagnets and the bulk molecules were the opposite compared to what was needed to build a ferromagnet. One of the authors (DG) remembers to have talked with Buchler, one of the pioneers of double decker compounds (Buchler *et al.*, 1986), and agreed with him that there was not much to expect from their paramagnetic properties. A nice example of having a vision.

13.6 The Anionic Double Decker

An investigation on $[Ln(Pc)_2]^-$ showed, on the contrary, that the magnetic properties of double decker anions are unique, behaving as SMMs with relatively high blocking temperature. An exciting alternative was available to the clusters of TMs which had dominated the scene of high T blocking temperature. It was a revolution which apparently occurred serendipitously as often happens in science and MM was no exception. But the key to understanding what was going on was NMR, which is a basic technique in chemistry in order to understand the structures of molecules in solution. The use of NMR in the solid state is rather rare and extremely limited in the investigation of paramagnetic species.

TBA[Ln(Pc)$_2$] (TBA is tetra-butyl-ammonium ion) were investigated to observe the crystal structure (Ln = Nd, Gd, Ho, Lu). Rather surprisingly, the structures are similar to each other but different in several important features. The four compounds crystallize in tetragonal space groups: Nd in *P*4/*ncc*; Gd and Ho in $P42_12$; and Lu in *P*4/*nmm*. All the metal ions at any rate are in a tetragonal site. The large difference in the structure is in the skew angle between the two tetragonal planes: it is 6° for Nd, 34° for Gd, 43° for Ho, and 45° for Lu. A correlation was attempted between the skew angle and the $\pi-\pi$ interaction between the Pc planes, as measured by the distance between the planes. The smaller the interaction, the smaller was the angle. Detailed data obtained on other series of M(Pc)$_2$ compounds showed that the structural correlation was not confirmed, small lattice effects being able to influence the skew angle in a hard-to-control way (Koike *et al.*, 1996).

The AC magnetic properties of TBA[Ln(Pc)$_2$] (Ln = Tb, Dy, Ho, Er, Tm, Yb) were examined in polycrystalline powders. Evidence of slow relaxation, as provided by nonzero out-of-phase susceptibility, was observed in the Tb and Dy derivatives. For sure, that was a surprise, but even more surprising was the fact that slow relaxation was observed at 50 K while with SMM and SCM it never exceeded 15 K. It is now time to try to enter into the details, focusing on what is clear and trying to use it as a bridgehead to understand how it works (Ishikawa *et al.*, 2003a):

1) The relaxation must be referred to the model worked out by Orbach.
2) In this frame, the relaxation of the single ion must be given by the sum of three mechanisms, namely direct, Raman, and Orbach. Further, the role of QTM must also be considered.
3) In order to work out this model, it is necessary to have an idea of the energies of the low-lying levels.

13.7 CF Aspects

We have already discussed in some detail the CF parameters of the Pc family in Section 3.5. In fact, the first step forward in understanding the electronic structure of the double decker compounds was the implementation of an efficient method to calculate the energies of the CF levels by using not only the temperature dependence of the magnetic susceptibility in the solid phase but also NMR spectra in fluid solution. Further, it was assumed that the CF parameters of the Lns vary linearly with the number of 4f electrons. Let us start from this assumption, which had already been used in several cases. Each metal ion requires a number of B_k^q parameters to be fitted, which for tetragonal symmetry range from 3 to 5. In D_{4d} symmetry, only the $q = 0$ operators are needed. A problem is that the temperature dependence of χ is not very informative, and therefore some additional assumption must be made. Although paramagnetic

Table 13.2 Energies and wave functions of the ground state multiplets of $[Pc_2Ln]^-$.

Tb^{3+}		Dy^{3+}		Ho^{3+}	
Energy (cm^{-1})	**Wave function**	**Energy (cm^{-1})**	**Wave function**	**Energy (cm^{-1})**	**Wave function**
0	$\|6\rangle, \|6\rangle$	0	$\|13/2\rangle, \|-13/2\rangle$	0	$\|5\rangle, \|-5\rangle$
436	$\|5\rangle, \|5\rangle$	35	$\|11/2\rangle, \|-11/2\rangle$	15	$\|4\rangle, \|-4\rangle$
494	$\|0\rangle$	179	$\|9/2\rangle, \|-9/2\rangle$	82	$\|6\rangle, \|-6\rangle$
509	$\|1\rangle, \|-1\rangle$	268	$\|15/2\rangle, \|-15/2\rangle$	117	$\|3\rangle, \|-3\rangle$
548	$\|2\rangle, \|-2\rangle$	330	$\|7/2\rangle, \|-7/2\rangle$	121	$\|8\rangle, \|-8\rangle$
581	$\|4\rangle, \|-4\rangle$	445	$\|5/2\rangle, \|-5/2\rangle$	190	$\|7\rangle, \|-7\rangle$
589	$\|3\rangle, \|-3\rangle$	517	$\|3/2\rangle, \|-3/2\rangle$	254	$\|2\rangle, \|-2\rangle$
		550	$\|1/2\rangle, \|-1/2\rangle$	367	$\|1\rangle, \|-1\rangle$
				410	$\|0\rangle$
Er^{3+}		Tm^{3+}		Yb^{3+}	
0	$\|1/2\rangle, \|-1/2\rangle$	0	$\|1\rangle, \|-1\rangle$	0	$\|5/2\rangle, \|-5/2\rangle$
102	$\|3/2\rangle, \|-3/2\rangle$	2	$\|0\rangle$	153	$\|1/2\rangle, \|-1/2\rangle$
191	$\|13/2\rangle, \|-13/2\rangle$	23	$\|2\rangle, \|-2\rangle$	178	$\|3/2\rangle, \|-3/2\rangle$
259	$\|5/2\rangle, \|-5/2\rangle$	132	$\|3\rangle, \|-3\rangle$	552	$\|7/2\rangle, \|-7/2\rangle$
302	$\|15/2\rangle, \|-15/2\rangle$	211	$\|6\rangle, \|-6\rangle$		
327	$\|11/2\rangle, \|-11/2\rangle$	349	$\|4\rangle, \|-4\rangle$		
391	$\|7/2\rangle, \|-7/2\rangle$	532	$\|5\rangle, \|-5\rangle$		
423	$\|9/2\rangle, \|-9/2\rangle$				

shifts in the NMR spectra of molecules containing Lns have long been known, their systematic use in MM has been advocated by Ishikawa *et al.* (2003b). The details concerning paramagnetic NMR will be discussed in Chapter 21; here it is sufficient to remember that the presence of a paramagnet perturbs the field felt by the protons and generates a shift of the signals which depends on the system structure.

The combined use of magnetic susceptibility and NMR allows us to calculate the energies of the levels in the form of an interesting tool to describe the lowest multiplet, whose energies and wave functions are reported in Table 13.2 (Ishikawa *et al.*, 2003b).

The doublet of lowest energy is that with $M_J = \pm J$ for Tb^{3+}, and that with $m = \pm 1/2$, that is, with the smallest component, for Er^{3+}. The former corresponds to an Ising-type magnetic anisotropy and the latter to the XY type.

13.8 The Breakthrough

The breakthrough was reported in 2003 (Ishikawa *et al.*, 2003a). The series was $Ln(Pc)^-$, where Ln is the series from Tb to Yb. The results of AC susceptibility clearly showed slow magnetic relaxation in the Tb and Dy derivatives. The heights of the barriers are 331 and 40 K for Tb and Dy, respectively, while the blocking

temperatures are 2.0 and 3.3 K. The calculations outlined above suggest as the ground state for Tb $M_J = \pm 6$, and the first excited state $M_J = \pm 5$ at more than 400 cm^{-1}. For Dy, the ground state is $M_J = \pm 13/2$ with $M_J = \pm 11/2$ at 28 cm^{-1}. It is interesting to note that the barrier for Tb is the highest reported till then. Beyond the brilliant result, there were exciting chemical opportunities opening as outlined above. The discovery that a simple mononuclear compound behaves like a magnet opened the possibility of designing at will the structure in order to optimize the blocking temperature. The first idea that occurred in the minds researchers was that of using single molecules for storing information. In order to do that, detailed preparative work was needed for optimizing the substrate on which to organize the molecules, controlling the magnetization of the system, and devising techniques needed for addressing the individual molecules. These require exciting new perspectives in chemistry, physics, and materials science. But it is not enough; the possibility of addressing single molecules allows us to go deep inside in the roots of quantum mechanics and science philosophy.

Let us have a look in some detail the properties of Tb and Dy molecules with Pc to try to understand why the magnetization relaxes slowly. In fact, χ'' goes to frequency dependent maxima, and at low T it reaches the lowest T (was introduced in Section 11.6). The plot of the relaxation frequency of Ln versus $1/T$ can be fitted using the standard formulae valid for Kramers (Dy) and non-Kramers (Tb), Eqs. (13.5) and (13.6), respectively (Ishikawa *et al.*, 2004):

$$\tau^{-1} = R_d(h\upsilon)^5 \coth(h\upsilon/2kT) + R_{Or}\Delta^3[\exp(\Delta/kT) - 1]^{-1} + R_R T^9 + R'_R(h\upsilon/k)^5 T^7 \tag{13.5}$$

and

$$\tau^{-1} = R_d(h\upsilon)^3 \coth(h\upsilon/2kT) + R_{Or}\Delta^3[\exp(\Delta/kT) - 1]^{-1} + R_R T^7 \tag{13.6}$$

where the suffixes d, Or, R indicate the direct, Orbach, and Raman contributions, respectively. The Arrhenius plot for Dy is dominated by the Orbach process in the range 3–12 K with $\Delta = 45$ K, $\tau_0 = 3 \times 10^{-6}$ s. The same plot for Tb follows the Orbach mechanism only in the range 25–50 K. Below 25 K, either a Raman or direct mechanisms are dominant. The calculated barrier is 374 K and $\tau_0 = 2.0 \times 10^{-8}$ s. It is certainly important that the Arrhenius barrier correlates well with the energy difference between the lowest and second lowest level for the Ln: 700 K for Tb and 40 K for Dy. Of course, a correlation as simple as the one just presented cannot stand elementary criticisms: why does Yb, which has an energy difference much larger than Dy, not show slow relaxation? An answer might be that the nature of the lowest levels can be relevant. The matrix elements involving the two lowest levels depend on the (product) of the M_J values, and therefore Yb, which involves 5/2 and 1/2, relaxes faster than Dy which involves 13/2 and 11/2. More data is needed. In fact, Murugesu *et al.* some years later titled their paper "Ytterbium can relax slowly too: a field-induced Yb_2 single molecule magnet" (Lin *et al.*, 2012). The compound they addressed was a dinuclear compound with acac ligands, and the model used for the Pc derivatives works well.

Notwithstanding the relative structural simplicity, the interpretation of the magnetic susceptibility is not without difficulties. In order to use a didactic approach, we will first use the approach by the Moldavian scientists (Reu *et al.*, 2012) who use what can be called *old fashioned treatment of the data*. They use a basic LF technique which provides the energy of the levels and the relaxation times. What is lost in rigor is obtained in terms of transparency. We will not go to discuss the details, but will recall the key points.

The first step is the introduction of the CF on the Tb derivative. The data of the experimental structure are used with bond distances $Tb-N_i = 0.244$ nm in one plane and $Tb-N_i = 0.243$ nm in the other parallel plane, which define a distorted tetragonal prism. The two planes are rotated by 34.5° with respect to each other. The other distortion angles are defined by the azimuthal angles $\theta_1 = 53.8°$ and $\theta_2 = 126.5°$. These angles indicate a tetragonally compressed geometry. The Stevens formalism is used. The magnetic susceptibility and the hyperfine NMR spectra are calculated. The calculations were performed by exploiting symmetry using IRs of the D_{2d} group. The best fit yields a ground doublet, which can be reasonably described as $|\pm 6\rangle$ with the first excited singlet $|0\rangle$ at about 300 cm^{-1}. But the most important feature of the developed model is the calculation of the electron–phonon interaction. In fact, although the vibronic formalism is continuously advocated, attempts to theoretically or experimentally obtain it have been extremely rare. Therefore, attempts like the one we are describing are certainly welcome.

What is needed is a model for the electron–phonon interaction and for the phonon dispersion law, that is, the frequency dependence of the number of phonons. The electron–phonon interaction is defined through the derivative of the potential energy of the interactions of the Tb electrons and the N electrons. The type of relaxation process is limited to one-phonon transitions, and the effects are limited to low temperature. The active modes are defined by the Debye model, and finally an expression is achieved for one-phonon transitions between Tb levels. The relaxation times are calculated, which are shown in Table 13.3.

The calculated values compare well with the experimental ones except for the lowest available temperature.

Table 13.3 Calculated and experimental values of the relaxation times (τ) of the TBA[$TbPc_2$] cluster.

T	Theory	Experimental (Ishikawa *et al.*, 2004)
14	9.5×10^{5}	0.157
27	3.20×10^{-2}	1.58×10^{-2}
34	1.11×10^{-3}	1.57×10^{-3}
40	1.52×10^{-4}	1.61×10^{-4}

Table 13.4 LF parameters defined in Eq. (13.8) (in cm^{-1}) for "Site 1" (Ishikawa, Iino, and Kaizu, 2002) and "Site 2" (Ishikawa *et al.*, 2003b).

	Site 1	Site2		Site 1	Site2
a_2^0	252	244	b_4^4	−22.5	−35.5
b_2^0	−18.7	−24.4	a_6^0	21	15
a_4^0	−191	−183	b_6^0	−0.08	−0.06
b_4^0	9.0	7.0	a_6^4	366	296
a_4^4	643	792	b_6^4	−52.0	−30.6

13.9 Multiple Deckers

Then next step is the triple decker, which allows two coordination sites where it is possible to place two identical or different Ln ions. Since the two sites are very close to each other, it is possible to use them to monitor the Ln–Ln interaction by taking advantage of the availability of the Y–Ln where the diamagnetic Y quenches the intramolecular interactions. A beautiful series was synthesized using two types of ligands, namely Pc and 2,3,9,10,16,17,23,24-octabutoxy-phthalocyanine, (Pc*). The series is of the type [PcLnPcLn′Pc*], where Pc* can occupy only an external position. We will use the symbol (LnLn′) to indicate that Ln′ is in the compartment Pc*. The characterization was made using the same strategy highlighted above for the double decker: for every compound, the T dependence of χ down to 2 K is measured and the solution NMR (Ishikawa, Iino, and Kaizu, 2002).

The analysis of the magnetic susceptibility is resumed in

$$\Delta\chi T = \chi(\mathrm{LnLn})T - [\chi(\mathrm{LnY})T + \chi(\mathrm{YLn})T] \tag{13.7}$$

The first step to compare the CF parameters for $[\chi(\mathrm{LnY}) - \chi(\mathrm{YLn})]T$. The a_k^q and b_k^q parameters obtained by the best fit are shown in Table 13.4 according to

$$A_k^q\langle r^k\rangle(n) = a_k^q + b_k^q(n - 10) \tag{13.8}$$

where $n(\text{number of f electrons}) = 8, 9, \ldots, 13$.

As expected, the variation between the two types of molecules is small but significant. In order to give a feeling of the involved energies, we show the calculated energies for Tb, Dy, Ho, Er, Tm, and Yb trivalent ions in the dimer containing Y^{3+} as second metal ion in the dimer (Figure 13.7).

The $[\chi(\mathrm{LnLn})]T$ curves shown in Figure 13.8 provide some qualitative information on the existence of interactions between the two Lns. For Tb, Dy, and Ho, the evidence is for FM (ferromagnetic) coupling, for Tm FM, for Er AFM (antiferromagnetic), and for Yb very weak. Starting from the analysis of the dipolar contribution is an obvious strategy because it can be done without introducing additional parameters. What is needed is the structure of the compound, which can be obtained from the optimization of DFT. The results are excellent, as shown in Figure 13.8, both qualitatively and quantitatively. The differences between the

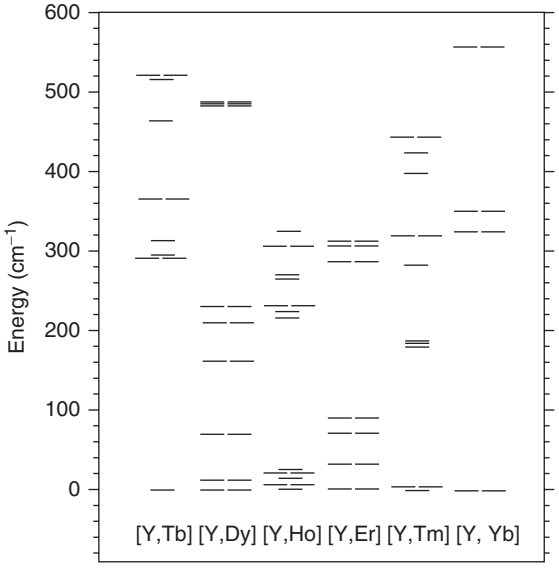

Figure 13.7 Energy diagram for the ground state multiplets of [Y, Ln]. (Reproduced from Ishikawa, N. *et al.* (2002) with permission from The American Chemical Society.)

various Lns arise from the different anisotropies of their magnetic susceptibility, namely cigar- and pancake-like in the language introduced in Section 3.6. No further attempt was made to introduce exchange contributions.

The other relevant question regarding triple decker compounds is the relation, if any, of the relaxation behavior with that of the corresponding double decker (Ishikawa, Otsuka, and Kaizu, 2005a). The Tb double decker shows a strong SMM behavior and the corresponding triple decker as well. The out-of-phase susceptibility of (Y–Tb), (Tb–Y), and (Tb–Tb) are shown in Figure 13.9. At an AC frequency of 997 Hz, the maxima are observed at 7, 18, and 27 at 20 K, respectively (Tb 11.5 K). There are several issues to discuss. Tb has the maximum τ_0 at intermediate T compared to the two Y derivatives.

On the other hand, (Tb–Tb) in zero DC field has a relaxation time definitely higher than that of (Y–Tb) or (Tb–Y). Another relevant observation is that (Tb–Tb) has two maxima that do not shift with an applied DC magnetic field, while the maxima of (Y–Tb) and (Tb–Y) do. It is rather surprising that the mutual influence is not obviously there. This behavior suggests, in the assumption that the dominant mechanism is the f–f interaction, that the relaxation processes in the two $4f^8$ systems occur somewhat independently of each other, at least at temperatures above 20 K.

Before changing the systems under analysis, it is worth mentioning that even the $[(Pc)_2Ho]^-$ derivative behaves as a SIM (Ishikawa, Sugita, and Wernsdorfer, 2005b). The analysis of the magnetic behavior confirmed that in this case the quantum process is due to resonant quantum tunneling between the entangled states of the electronic and nuclear spin systems.

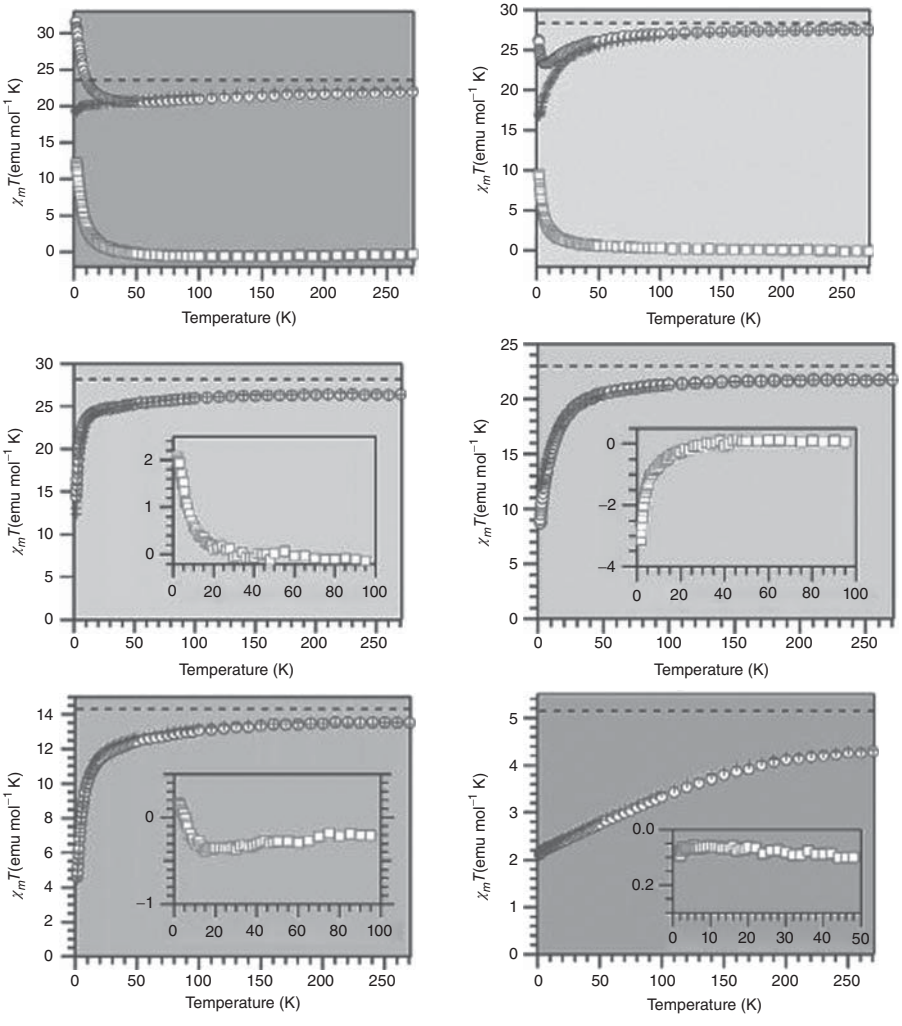

Figure 13.8 Plots of $\chi_M([Ln, Ln])T$ (circles) and $\chi_M([Y, Ln])T + \chi_M([Ln, Y])T$ (crosses) against temperature T. The differences between the two, $\Delta\chi_M T$, are shown in each inset. The Ln ions are (from left to right and from the top to the bottom) Tb, Dy, Ho, Er, Tm, and Yb. (Reproduced from Ishikawa, N. *et al.* (2002) with permission from The American Chemical Society.)

13.10 The Polyoxometalate Family

The second family of SIM is not a molecular family if we associate the molecule with a relevant organic component. In fact, our tour on the periodic table now brings us in the region of molybdates, tungstates, and so on, which have long been known to yield clusters of increasing size and complexity and are referred

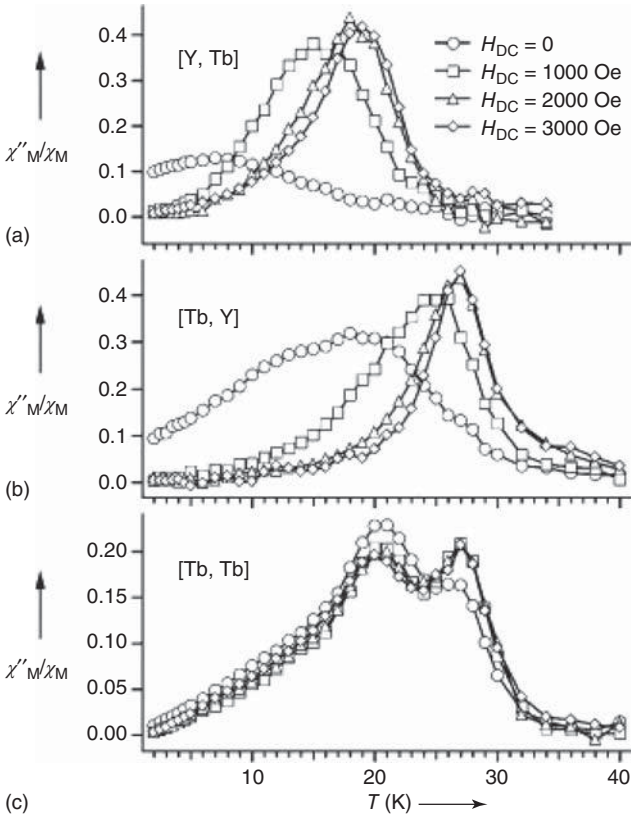

Figure 13.9 Plots of χ''_M/χ_M against temperature of (a) [Y–Tb], (b) [Tb–Y], and (c) [Tb–Tb] measured in a 5 G AC magnetic field of 997 Hz with DC field H_{DC} of indicated magnitudes. (Reproduced from: "Single molecule magnet with single lanthanide ion" in Polyhedron, **2007**, *26*, 2147 by Ishikawa, N. with permission from Elsevier Ltd.)

to as polyoxometalates (POMs) (AlDamen *et al.*, 2008). Some calculations on the electronic structure of POM with Ln have been described in Section 3.5. Here we aim to introduce some magnetic properties. The versatility of POMs in yielding complex structures and hosting heteroatoms has been compared with that of proteins. Beyond the interest for the esthetic beauty for clusters such as $Mo_{12}O_{72}$ shown in Figure 13.10, the POMs are studied for the possibility of analyzing the magnetic properties of single clusters because the large inter-cluster distances offered by hindrance of the POMs ensure the magnetic insulation of each paramagnetic center.

A class of POMs that have attracted attention is $[Ln(W_5O_{18})_2]$, which have a sandwich structure with two W_5O_{18} deckers wrapping an Ln pickle (AlDamen *et al.*, 2008). The similarity with the Pc double deckers is obvious. The Ln is eight-coordinated in a square antiprism geometry with four oxygen atoms on a square of the upper W_2O_5 and four from the lower. The angle φ of rotation of the

Figure 13.10 The structure of a generic β-Keggin anion.

two squares ranges from 39° to 47° or the compounds whose X-ray structures have been reported. Focusing on the derivatives with nine Na^+ ions, however, the angles are much closer to 45°, that is, 46.7° for Eu, 44.0° for Dy, and 44.5° for Er (Figure 13.11).

We will focus on Ho because it has been investigated with both magnetic measurements and ESR (Ghosh *et al.*, 2012). In both cases, the hyperfine coupling with ^{165}Ho (100% natural abundance) plays a relevant role. The SQUID measurements show tunnel splitting, which requires transverse fields that mix states differing by eight in the states. The interesting details of the ESR spectra deserve a more elaborate treatment, as given in Chapter 21.

13.11 More SIM

Among coordination compounds with a sandwich-like structure with a SIM behavior, (Cp*)Er(COT) (Cp* = pentamethylcyclopentadienide [$C_5Me_5^-$], COT = cyclooctatetraenide [$C_8H_8^{2-}$]), whose structure is shown in Figure 13.12, possesses some peculiarities (Jiang *et al.*, 2011). First, the two radicals coordinated to the central atom are different and, second, the number of non-hydrogen atoms in the system is very small (19 atoms) with respect to the majority of SIM.

Two evident sets of peaks were observed in the χ'' versus temperature plot in the 2–30 K range. These data were interpreted as an indication of the existence of two relaxation processes, and magnetic site-dilution measurement indicated the single-ion origin of such relaxation behavior. Arrhenius analysis showed that both are thermally activated, with $\Delta E = 323$ K and $\tau_0 = 8.17 \times 10^{-11}$ s for one set, and $\Delta E = 197$ K and $\tau_0 = 3.13 \times 10^{-9}$ s for the other. The ring-shaped aromatic ligands generate a high local symmetry which could be responsible for the observed magnetic properties (magnetization hysteresis, two thermal relaxation processes with high energy barriers). The tilting of the two rings induces a deviation from

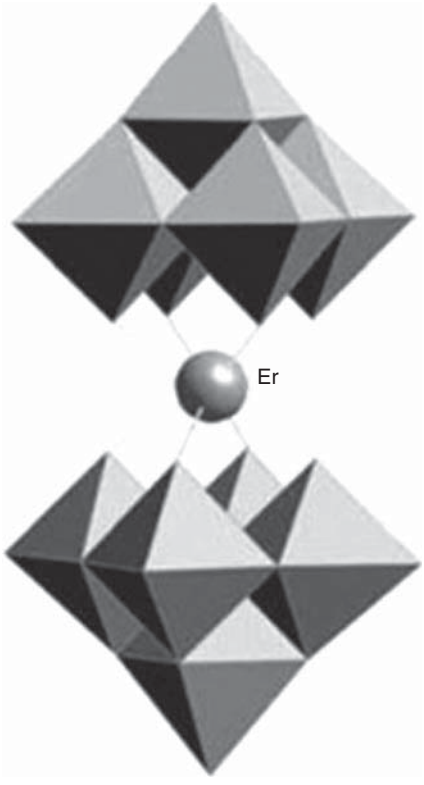

Figure 13.11 Structure of a POM: $[ErW_{10}O_{36}]^{9-}$. (Reproduced from AlDamen, M.A. *et al.* (2008) with permission from The American Chemical Society.)

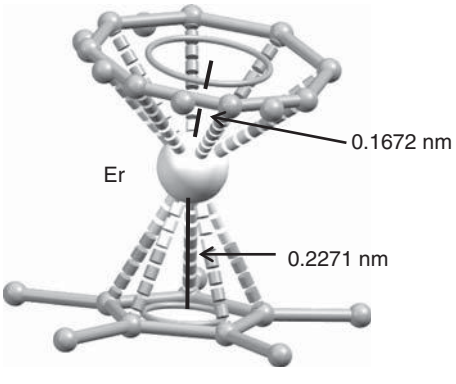

Figure 13.12 Schematic view of the title compound $(Cp^*)Er(COT)$. The two rings are Cp^* (below Er^{3+}) and COT (above Er^{3+}), respectively. Hydrogen atoms are omitted for clarity.

the axial symmetry and may give rise to the quantum tunneling at zero static field and low temperature. The analysis of magnetic behavior of analogous compounds with Tb, Dy, Ho, Er, Tm, and Y showed that, among these new derivatives, only the Dy and Ho derivatives behave like SIM (Jiang *et al.*, 2012). The Ho derivative too showed the presence of two relaxation processes but only when this compound was highly diluted in the isomorphous diamagnetic Y^{3+} analogs. The quantum tunneling decoherence relaxation rate increases from Er to Ho to Dy: this behavior may be due to the transverse anisotropy originating from the tilting of the two aromatic rings within one molecule. LF analyzes suggest that the Ising-type ground state of Dy, Ho, and Er may be responsible for the single-ion magnet behavior.

13.12 Perspectives

Much has been done in the field of SIM, but much remains to be done. There are beautiful molecules that remain to be discovered and, if they are POMs, it is all right. An example is the fivefold geometry of the series of POMs $[LnP_5W_{30}O_{110}]^{12-}$ with Ln = Tb, Dy, Ho, Er, Tm, and Yb, which is shown in Figure 13.13 (Cardona-Serra *et al.*, 2012).

The fields to be explored are molecular spintronics and quantum computing, where it is of fundamental importance to be able to arrange active blocks, buffer blocks, and minority properties blocks. Let us imagine that our goal is assembling the fivefold symmetry molecule in order to use it as SIM. The key block is the metal ion. In principle, we have a lot of ions available in the periodic table, but we want to try an Ln. Previous experience suggests an electronic configuration $4f^{8-13}$. Finally, we decide on Er. A second aspect is the choice of the ligands which give

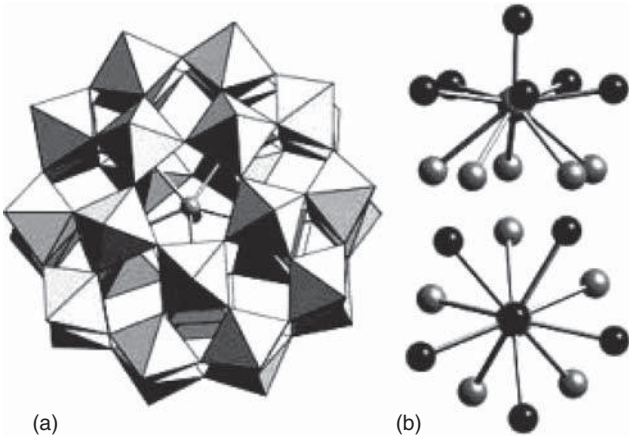

Figure 13.13 (a) Structure of the $[LnP_5W_{30}O_{110}]^{12-}$ anion and (b) top and lateral views showing the near-C_{5v} coordination of the lanthanide ion in a fivefold environment. (Reproduced from Cardona-Serra, S. *et al.* (2012) with permission from The American Chemical Society.)

stability, shape symmetry, and so on. It is certainly good news that SIMs can now introduce so many sophisticated properties.

References

Agladze, N.I., Popova, M.N., Zhizhin, G.N., Egorov, V.J., and Petrova, M.A. (1991) Isotope structure in optical spectra of $LiYF_4$:Ho(III). *Phys. Rev. Lett.*, **66**, 477–480.

AlDamen, M.A., Clemente-Juan, J.M., Coronado, E., Martí-Gastaldo, C., and Gaita-Ariño, A. (2008) Mononuclear lanthanide single-molecule magnets based on polyoxometalates. *J. Am. Chem. Soc.*, **130**, 8874–8875.

Bennett, W.E., Broberg, D.E., and Baenziger, N.C. (1973) Crystal structure of stannic phthalocyanine, an eight-coordinated tin complex. *Inorg. Chem.*, **12**, 930–936.

Bertini, I., Luchinat, C., and Parigi, G. (2002) Magnetic susceptibility in paramagnetic NMR. *Prog. Nucl. Magn. Reson. Spectrosc.*, **40**, 249–273.

Buchler, J.W., De Cian, A., Fischer, J., Kihn-Botulinski, M., Paulus, H., and Weiss, R. (1986) Metal complexes with tetrapyrrole ligands. 40. Cerium(IV) bis(octaethylporphyrinate) and dicerium(III) tris(octaethylporphyrinate): parents of a new family of lanthanoid double-decker and triple-decker molecules. *J. Am. Chem. Soc.*, **108**, 3652–3659.

Cardona-Serra, S., Clemente-Juan, J.M., Coronado, E., Gaita-Ariño, A., Camón, A., Evangelisti, M., Luis, F., Martínez-Pérez, M.J., and Sesé, J. (2012) Lanthanoid single-ion magnets based on polyoxometalates with a 5-fold symmetry: the series $[LnP_5W_{30}O_{110}]^{12-}$ (Ln^{3+} = Tb, Dy, Ho, Er, Tm, and Yb). *J. Am. Chem. Soc.*, **134**, 14982–14990.

Ghosh, S., Datta, S., Friend, L., Cardona-Serra, S., Gaita-Arino, A., Coronado, E., and Hill, S. (2012) Multi-frequency EPR studies of a mononuclear holmium single-molecule magnet based on the polyoxometalate $[Ho(III)(W_5O_{18})_2]^{9-}$. *Dalton Trans.*, **41**, 13697–13704.

Giraud, R., Tkachuk, A.M., and Barbara, B. (2003) Quantum dynamics of atomic magnets: cotunneling and dipolar-biased tunneling. *Phys. Rev. Lett.*, **91**, 2572041–2572044.

Giraud, R., Wernsdorfer, W., Tkachuk, A.M., Mailly, D., and Barbara, B. (2001) Nuclear spin driven quantum relaxation in $LiY_{0.998}Ho_{0.002}F_4$. *Phys. Rev. Lett.*, **87**, 057203/057201–057203/057204.

Griffith, J.S. (1961) *The Theory of Transition-Metal Ions*, Cambridge University Press, Cambridge.

Ishikawa, N., Iino, T., and Kaizu, Y. (2002) Interaction between f-electronic systems in dinuclear lanthanide complexes with phthalocyanines. *J. Am. Chem. Soc.*, **124**, 11440–11447.

Ishikawa, N., Otsuka, S., and Kaizu, Y. (2005a) The effect of the f–f interaction on the dynamic magnetism of a coupled $4f^8$ system in a dinuclear terbium complex with phthalocyanines. *Angew. Chem. Int. Ed.*, **44**, 731–733.

Ishikawa, N., Sugita, M., and Wernsdorfer, W. (2005b) Nuclear spin driven quantum tunneling of magnetization in a new lanthanide single-molecule magnet: bis(phthalocyaninato)holmium anion. *J. Am. Chem. Soc.*, **127**, 3650–3651.

Ishikawa, N., Sugita, M., Ishikawa, T., Koshihara, S.Y., and Kaizu, Y. (2003a) Lanthanide double-decker complexes functioning as magnets at the single-molecular level. *J. Am. Chem. Soc.*, **125**, 8694–8695.

Ishikawa, N., Sugita, M., Okubo, T., Tanaka, N., Iino, T., and Kaizu, Y. (2003b) Determination of ligand-field parameters and f-electronic structures of double-decker bis(phthalocyaninato)lanthanide complexes. *Inorg. Chem.*, **42**, 2440–2446.

Ishikawa, N., Sugita, M., Ishikawa, T., Koshihara, S.-Y., and Kaizu, Y. (2004) Mononuclear lanthanide complexes with a long magnetization relaxation time at high temperatures: a new category of magnets at the single-molecular level. *J. Phys. Chem. B*, **108**, 11265–11271.

Jiang, S.-D., Liu, S.-S., Zhou, L.-N., Wang, B.-W., Wang, Z.-M., and Gao, S. (2012) Series of lanthanide organometallic single-Ion magnets. *Inorg. Chem.*, **51**, 3079–3087.

Jiang, S.-D., Wang, B.-W., Sun, H.-L., Wang, Z.-M., and Gao, S. (2011) An organometallic single-Ion magnet. *J. Am. Chem. Soc.*, **133**, 4730–4733.

Koike, N., Uekusa, H., Ohashi, Y., Harnoode, C., Kitamura, F., Ohsaka, T., and Tokuda, K. (1996) Relationship between the Skew Angle and Interplanar Distance in Four Bis(phthalocyaninato)lanthanide(III) Tetrabutylammonium Salts ($[NBu^{n}_{4}][Ln(III)Pc_{2}]$; Ln = Nd, Gd, Ho, Lu). *Inorg. Chem.*, **35**, 5798–5804.

Lin, P.H., Sun, W.B., Tian, Y.M., Yan, P.F., Ungur, L., Chibotaru, L.F., and Murugesu, M. (2012) Ytterbium can relax slowly too: a field-induced Yb_2 single-molecule magnet. *Dalton Trans.*, **41**, 12349–12352.

Linstead, R.P. and Robertson, J.M. (1936) The stereochemistry of metallic phthalocyanines. *J. Chem. Soc. (Resumed)*, 1736–1738.

Magariño, J., Tuchendler, J., D'Haenens, J.P., and Linz, A. (1976) Submillimeter resonance spectroscopy of Ho^{3+} in lithium yttrium fluoride. *Phys. Rev. B*, **13**, 2805–2808.

Reu, O.S., Palii, A.V., Ostrovsky, S.M., Tregenna-Piggott, P.L.W., and Klokishner, S.I. (2012) A model of magnetic and relaxation properties of the mononuclear [Pc2Tb] – TBA + complex. *Inorg. Chem.*, **51**, 10955–10965.

Stevens, K.W.H. (1952) Matrix elements and operator equivalents connected with the magnetic properties of rare earth ions. *Proc. Phys. Soc. London, Sect. A*, **65**, 209–215.

Wu, W., Ellman, B., Rosenbaum, T.F., Aeppli, G., and Reich, D.H. (1991) From classical to quantum glass. *Phys. Rev. Lett.*, **67**, 2076–2079.

14
SMM with Lanthanides

14.1
SMM with Lanthanides

The so-called giant spin model of single-molecule magnet (SMM) has, for a long time, dominated the scene of (true or potential) Ln-based SMM, notwithstanding the great success of the single-ion magnet (SIM) highlighted in Chapter 13. What was understood from the investigation of Ln-containing SIM was that, to achieve high-temperature molecular magnets, the way is not of making big spins but rather introducing big anisotropy. The famous $Tb(Pc)_2$ example tells what is needed to observe slow magnetic relaxation: exploit the prolate geometry available on the metal ion and strengthen it with an appropriate ligand field. If we look at recent reviews that report Ln-containing SMMs, we see that their number is rapidly growing (Sievers, 1982; Woodruff, Winpenny, and Layfield, 2013). Many different mechanisms are discovered, which give rise to slow relaxation. Here we will start from a short history of Ln-based SMMs referring to systems containing more than one Ln and perhaps another magnetic center. The use of Ln was looked at as rather improbable due to the weak interactions expected for the 4f orbitals with other orbitals of any kind. New types of compounds, however, soon showed that the above opinion was not quite correct, and it was found that SMMs containing Lns can be obtained also beyond the limit of SIM. It must also be recalled that the so-called giant spin approach is based on the strong field assumption, that is, the total spin is a (quasi) good quantum number. This is hardly the case for Lns, while it may be acceptable for TMs.

The first SMM containing Ln ions to be reported was a $[CuTb]_2$ cluster in which the four metal ions define a ring connected by L ligands (H_3L = 1-(2-hydroxybenzamido)-2-(2-hydroxy-3-methoxy-benzylidene-amino) ethane) (Osa *et al.*, 2004) (Scheme 14.1).

The structure of $[CuTb]_2$ is shown in Figure 14.1. The isostructural $[NiTb]_2$ contains a diamagnetic square-planar coordinated Ni^{2+}, which provides the opportunity to perform magnetic dilution experiments.

The oxidation states and the square planar coordination of TM ion shown in Figure 14.1 are confirmed by room-temperature magnetic measurements which yielded $\chi T = 23.12\,\text{emu mol}^{-1}\,\text{K}$ for the Ni derivative and $\chi T = 26.42\,\text{emu mol}^{-1}\,\text{K}$

Introduction to Molecular Magnetism: From Transition Metals to Lanthanides, First Edition.
Cristiano Benelli and Dante Gatteschi.
© 2015 Wiley-VCH Verlag GmbH & Co. KGaA. Published 2015 by Wiley-VCH Verlag GmbH & Co. KGaA.

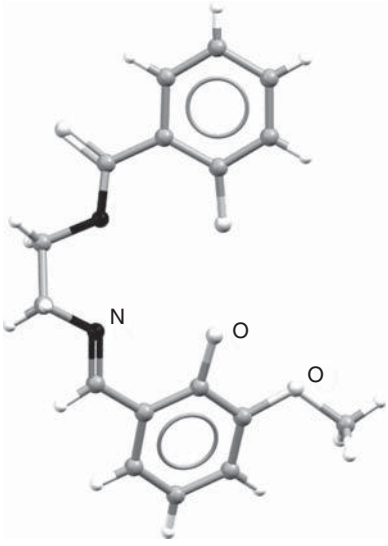

Scheme 14.1

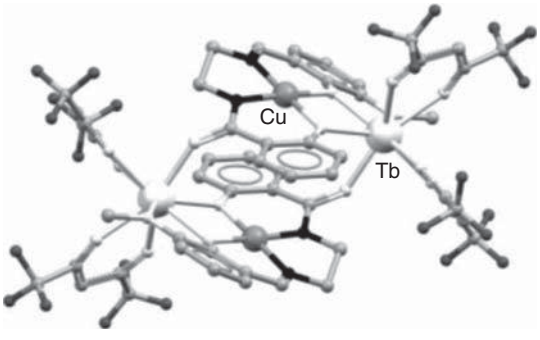

Figure 14.1 Ball-and-stick representation of the molecular structure of the compound $[Cu^{II}LTb^{III}(hfac)_2]_2$. The hydrogen atoms are omitted for clarity.

for the Cu derivative. The Ni derivative value of χT agrees with the free-ion value of 23.64 emu mol^{-1} K for two Tb ions, and that of the Cu derivative is slightly higher than the sum of Tb and Cu contributions, in agreement with a weak ferromagnetic coupling. Clear evidence of ferromagnetic coupling between Cu and Tb was achieved by the T dependence of χT. In fact, χT increases on decreasing T, reaching a maximum of 38.97 emu mol^{-1} K at 10 K, below which χT decreases to about 15 emu mol^{-1} K. AC magnetic susceptibility measurements provided unequivocal evidence of slow magnetic relaxation, with $U_{eff} = 21$ K and a blocking temperature $T = 1.2$ K. The results were surprising because the blocking temperatures were in the range observed with TMs, and the expectation was for lower temperature for Ln. The analysis of the data suggested that the ferromagnetic coupling must be due to Cu–Tb interactions

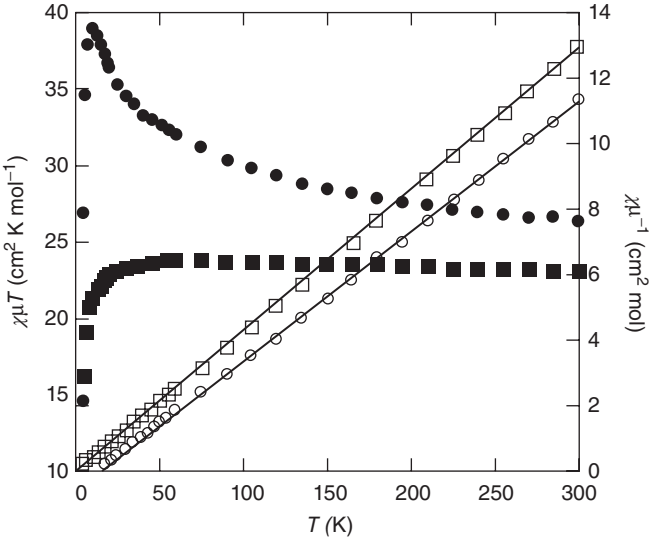

Figure 14.2 Plots of $\chi_M T$ versus T and $1/\chi_M$ versus T for $[Cu^{II}LTb^{III}(hfac)_2]_2$ (closed circle, open circle) and $[Ni^{II}LTb^{III}(hfac)_2]_2$ (closed square, open square). (Reproduced from Osa, S. *et al.* (2004) with permission from The American Chemical Society.)

because no ferromagnetic coupling was evidenced in NiTb in which Cu was substituted by the diamagnetic Ni (Figure 14.2). Similar results were achieved with Dy

The versatility of the structure of tetranuclear compounds suggested a systematic approach, which was attempted to monitor the occurrence of SMM behavior employing at some stage all the Ln ions except Pm. The idea was to check the presence of ferromagnetic coupling, as observed in the Tb and Dy derivatives, as a prerequisite for the observation of SMM behavior, but no other Ln was found to show similar dynamics.

The results were not surprising Lns with less than seven electrons showed antiferromagnetic (AFM) coupling, while those with seven and more electrons show ferromagnetic coupling. Immediately after the paper by Re *et al.* (Osa *et al.*, 2004), Pecoraro *et al.* reported a Dy_6Mn_6 cluster in which there are four Mn^{3+} and two Mn^{4+}, the protagonists of the Mn_{12} saga (Zaleski *et al.*, 2004) which are present in the same ratio of Mn^{3+}/Mn^{4+} as in Mn_{12}. The compound was isolated by using metallacrown ligands designed to synthesize large clusters. The spin topology of the compound is, however, much different from that of Mn_{12}. The six Dy ions define a quasi-regular hexagon, the Mn_3 groups capping either end of the ring. The ligands are a salicylideneiminate (SAL) derivatives. There is some evidence of SMM behavior but not enough to reach the blocking T. Finally, another cluster, $Mn_{11}Dy_4$, with a blocking T of 0.55 K (Mishra *et al.*, 2004) was reported the same year. This time, the manganese ions are in the +3 oxidation state – beautiful structures but of moderate magnetic interest.

A more successful attempt was made with Mn and Ln together with mdeaH (H_3mdea = 1-(2-hydroxybenzamido)-2-(2-hydroxy-3-methoxy-benzyli deneamino)-ethane), which yields Ln_4Mn_5 clusters, where Ln = Tb, Dy, Ho, or Y (Mereacre *et al.*, 2008). There is one Mn^{4+} and four Mn^{3+} ions. The Mn^{4+} sits on an inversion center of a triclinic cell. The Jahn–Teller elongation axis of the four Mn^{3+} ions are not parallel to each other, and therefore a strong SMM contribution from the Mn subcluster seems improbable. The interesting feature of the cluster is the Y derivative, which can provide side information on the manganese subcluster. Taking into account only the manganese spins, the spin Hamiltonian can be written as

$$H = J_1 \mathcal{S}_5 \cdot (\mathcal{S}_1 + \mathcal{S}_3) + J_2 \mathcal{S}_5 \cdot (\mathcal{S}_2 + \mathcal{S}_4) + J_3 \cdot (\mathcal{S}_1 \cdot \mathcal{S}_2 + \mathcal{S}_3 \cdot \mathcal{S}_4) \qquad (14.1)$$

where J_1, J_2, and J_3 are the exchange interactions between Mn^{3+} and Mn^{4+} sites through double O bridges between Mn^{3+} and Mn^{4+} ions, through single O bridges, and between Mn^{3+} ions through single alkoxo bridges, respectively, and S_i are the spin vectors for each of the metal ions ($S_i = 2$ for Mn^{3+} with $i = 1-4$ and $S_5 = 3/2$ for Mn^{4+}). The matrix is large, but it can be solved numerically.

The experimental information show a decrease from $\chi T = 10.5$ to 1.8 emu K mol^{-1}. in the range 300 - 1.8 K The spin topology is illustrated in Figure 14.3. The best fit of the χT values of Y_4Mn_5 yields a ground S = 3/2 state. The low T value of χT at 1.8 K is not far from what is expected for a total spin S = 3/2, but additional work is needed. The AC measurements of Y were performed with and without an applied field. The presence of an external magnetic field produced a substantial slowing down of the relaxation from >1500 Hz in zero field to 77 Hz in an optimum DC field of about 4500 Oe.

The data of the Tb, Dy, and Ho derivatives are completely different from that of the Y derivative. All of them display room-temperature χT values which are in agreement with the free-ion values. On decreasing T, χT goes through a minimum, but increase again. Accurate AC susceptibility measurements were made in the range 0.1–15 000 Hz and 1.8–7 K. The Arrhenius plot was found to work well. The relevant parameters are shown in Table 14.1. At a qualitative level, it can be concluded that anisotropic ions can indeed work well and

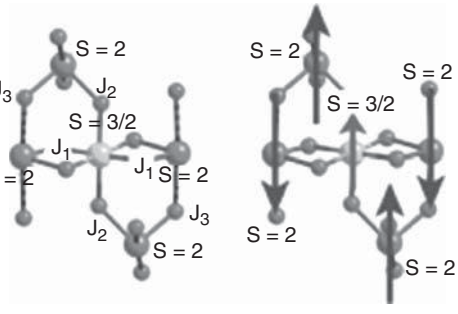

Figure 14.3 Topology of the intra-complex magnetic interactions in Ln_4Mn_5. (Reproduced from Mereacre, V. *et al.* (2008) with permission from WILEY-VCH Verlag GmbH & Co. KGaA.)

Table 14.1 Static and dynamic parameters for Ln complexes, Ln = Y, Tb, Dy, Ho.

Ion	U_{eff} (cm^{-1})	τ_0 (s)	χT	χT
			Room *T*	Free ion
Y	20.2	2.6×10^{-8}	10.5	13.9
Tb	33	4.5×10^{-9}	67.8	66.1
Dy	38.6	3×10^{-9}	62.2	70.6
Ho	—	—	60.9	70.1

that more than half-filled f orbitals work very well. The Ho derivative is more similar to Y than to the other paramagnetic species. In particular, no out-of-phase χ was observed, suggesting that the Ho contribution to the anisotropy is weak.

A powerful tool for determining the dynamic magnetic properties of a system is the analysis of the frequency dependence of the AC susceptibility. The utility of this kind of experiments is well supported by the results of studies performed on Ln(trensal) (Ln = Dy^{3+}, Er^{3+}; H_3trensal = 2,2′,2″-tris-(salicylideneimino) triethyl-amine), which has a trigonal symmetry imposed by crystallographic features, as reported in Chapter 3 (Lucaccini *et al.*, 2014; Pedersen *et al.*, 2014; Rigamonti *et al.*, 2014). AC susceptibility experiments were performed at various frequencies as a function of temperature, and under no circumstances the out-of-phase magnetic susceptibility χ'' was observed. When DC fields in the range 200–2400 Oe at 1.9 K were applied, a slow relaxation process was observed for both the derivatives, with a maximum of the relaxation time at an applied field of about 800–900 Oe. Attempts to reproduce the temperature dependence of the relaxation mechanism were not satisfactory at low temperature, and the usual Arrhenius approach yielded estimated barriers for Dy^{3+} and Er^{3+} derivatives as 22 ± 1 and $7 \pm 1\ cm^{-1}$, respectively, which did not match the energy difference between the ground and the first excited doublet obtained from luminescence data (around $50\ cm^{-1}$ for both the complexes). This discrepancy suggests that the observed barrier cannot be connected with an Orbach process. In an attempt to have a more detailed understanding of the process, the magnetic field dependence of the relaxation time was explicitly taken into account by using the relationship by adding three terms to the usual Raman and Orbach terms (Section 13.8):

$$\tau^{-1} = \frac{B_1}{1 + B_2 H^2} + A_1 H^4 T + A_2 H^2 T \tag{14.2}$$

where the first term represents the field dependence of quantum tunneling (QT) process, the second is the direct process for a Kramers ion without hyperfine interactions, and the third one is the direct process for a Kramers ion in the presence of hyperfine interaction. A_i and B_i are empirical parameters.

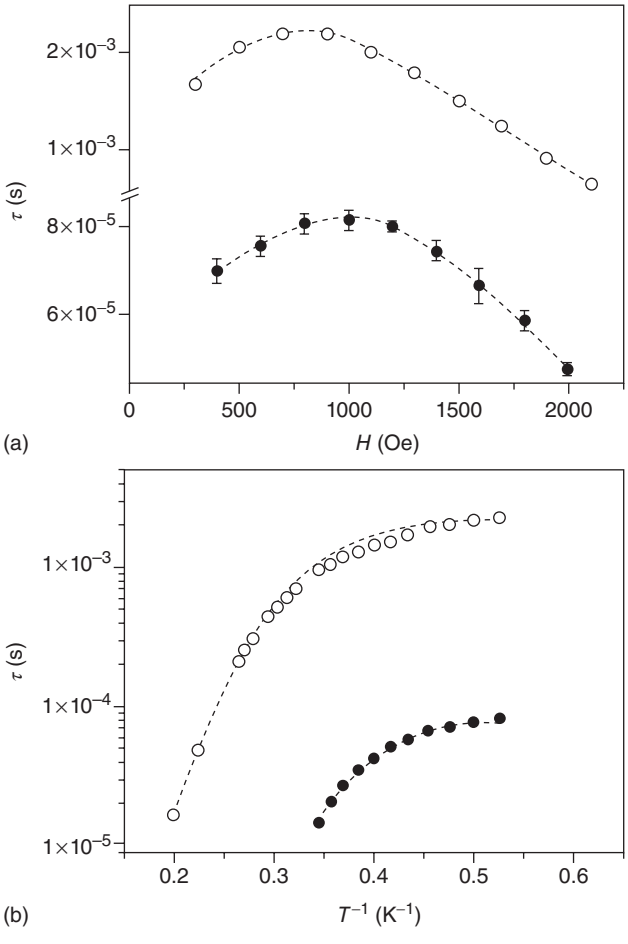

Figure 14.4 (a) Field and (b) temperature dependence of the relaxation times of Er(trensal) (empty circles) and Dy(trensal) (full circles) and best fit curves. The experiments were performed on samples in which the Ln complexes were diluted in the isomorphous Y(trensal) to rule out the possibility of effects due to intermolecular interactions. (Reproduced from Lucaccini, E. *et al.* (2014) with permission from The Royal Chemical Society of Chemistry.)

The overall fitting procedure was performed by considering the contribution of each of the five terms (the three in Eq. (14.2) and the Orbach and Raman contributions), and the possibility of reproducing the experimental data (Figure 14.4) was, in any case, possible by not including Orbach processes in addition to the direct and QT ones, while a Raman process, with variable exponent n, provided reasonable reproduction of the data. Therefore, the final conclusion was that the relaxation was not occurring via the first excited doublet.

14.2
More Details on SMM with Lanthanides

After starting from the time of discovery of the 4f-based SMM, let us follow a different route trying to move from simple to complex systems, provided we accept that in Ln something simple exists. Neglecting Pc and POM (polyoxometalate), described in some detail elsewhere, we will spend some time on dinuclear species of the type Ln_2 and Ln–Ln′ to monitor the reciprocal influence of the two ions in the relaxation mechanism. Indeed, it is of vital relevance to understand the step-by-step growth of the complex properties starting from the compound described below.

The systems we present now are dinuclear Ln compounds that contain diamagnetic Y and Dy in all proportions. The rationale for the investigation of these systems is the following: One of the important features of magnetic relaxation is QT, and in order to understand the QT of magnetization (QTM) in polynuclear systems, it is vital to understand how the mechanism of transition from level M to M′ occurs and what is the effect of an applied field, which offers an additional handle to invent devices.

Three valdien complexes (H_2valdien = *N*1,*N*3-bis(3-methoxysalicylidene) diethylene-triamine) with Dy^{3+} and Y^{3+} have been investigated for exploring the effects of doping in diamagnetic lattices (Habib *et al.*, 2011). The concentrations of the doped samples have been observed to correspond to the values of the synthesis, confirming that the occupation of the sites occurs on a statistical basis. The relative weights of the YY, YDy, and DyDy species for dilution x are $(1-x)^2, 2x(1-x)$, and x^2, respectively. The values of the Arrhenius parameters on varying x are shown in Table 14.2. The height of the barrier decreases on increasing the Dy content, suggesting that adding a neighboring Dy favors the relaxation. As noted before, τ_0 evidences a reverse trend, increasing on increasing x. The blocking temperature (T_b) decreases with U_{eff}, showing that the reversed changes of τ_0 and U_{eff} do not compensate.

Additional information stems from the analysis of the single-crystal magnetic hysteresis performed with the μ-SQUID (superconducting quantum interference device) technique. Steps are observed at zero field for $x = 0.05, 0.10, 0.50$ samples, which were attributed to QTM. As x increases, the step at zero field decreases, eventually disappearing for $x = 1$. In a parallel way, a new step increases at ±0.3 T.

Table 14.2 Arrhenius plot parameters for different Y/Dy ratios.

x	τ_0 ($\times 10^{-7}$ s)	U_{eff} (cm^{-1})	T_b (K)
0.05	2.88	88.5	5.9
0.10	3.16	87.8	5.9
0.50	3.90	85.1	5.8
1.00	6.04	76.0	5.3

This is due to the mutual exchange interaction between the two Dy^{3+} which are AFM-coupled.

With the same ligand, an interesting series of dinuclear compounds with the general formula $[Ln^{3+}{}_2(valdien)_2(NO_3)_2]$ ($Ln^{3+} = Eu^{3+}$, Gd^{3+}, Tb^{3+}, Dy^{3+}, Ho^{3+}) have been reported (Long *et al.*, 2011). The distances within the pairs are long.

Again, it is Dy which is the star of the movie but this time a good costarring role is reserved for Yb. This ion has not been very popular in the last few years of SMM hunt because it is not as easy as Tb and Dy to show Ising-type anisotropy. However, never say never, and recently Yb has been reported exploiting XY-type anisotropy (Liu *et al.*, 2012). The first noteworthy feature is that the Yb is octahedrally coordinated with C_i symmetry, but not far from D_{3d} symmetry. The combined efforts of using LF and *ab initio* approaches provided the energies of the low-lying Kramers doublets. The separations of the calculated doublets from the ground one are about 230, 332, and 398 cm^{-1}. The nature of the ground state suggests XY type of anisotropy. In fact, *ab initio* calculations suggest an admixture of $\pm 5/2$ and $\pm 3/2$ and $g_{\|} = 0.5$ and $g_{\perp} = 3$. No evidence of slow relaxation is observed in the absence of an applied magnetic field, which is a clear indication of efficient QTM, as previously observed. Applying a static field removes the degeneracy of the levels and quenches the relaxation. Under these conditions, the relaxation becomes slow and phenomena like QTM become unobservable.

Four dinuclear Dy species were investigated as ovph complexes (H_2ovph = *o*-vanillin picolinoylhydrazone) (Guo *et al.*, 2011). The structure shown in Figure 14.5 contains two Dy ions, one in a pentagonal bipyramidal seven-coordinate environment, and the other in an eight-coordinate environment with a cyclic structure dubbed a hula hoop. The T dependence of χT was fitted with a simple model using isotropic $J = 5.88\,cm^{-1}$ and a molecular field correction. Contrary to many Lns, the relaxation in zero applied DC field is slow, a result that usually requires a field to be observed. The usual procedure for obtaining information on the dynamics was followed, and evidence for *two* relaxation processes was achieved. In particular, the AC susceptibilities of both follow

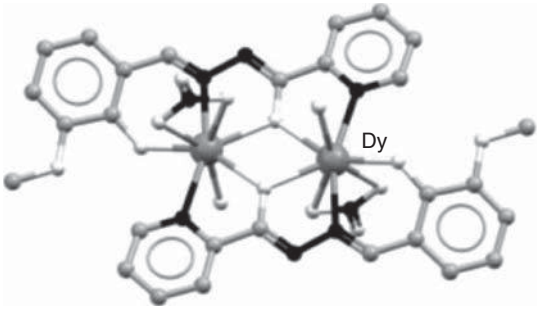

Figure 14.5 Molecular structure of the complex $[Dy_2(ovph)_2(NO_3)_2(H_2O)_2] \cdot 2H_2O$. Hydrogen atoms and lattice water are omitted for clarity.

Arrhenius law, with $U_{eff} = 150$ and 198 K, respectively. The calculated blocking temperatures are 8.5 and 10.0 K, respectively.

14.3 New Opportunities

A new opportunity has arisen with the discovery of a new radical bridge capable of forming the dinuclear species $[([(Me_3Si)_2N]_2Ln(THF))_2(\mu\text{-}\eta^2:\eta^2\text{-}N_2)]^{2-}$ where $Ln^{3+} = Gd^{3+}$, Dy^{3+}, Y^{3+} and THF = tetrahydrofuran. The bridge can be formulated as N_2^{3-}, as confirmed by several experimental and theoretical techniques (Evans *et al.*, 2009; Rinehart *et al.*, 2011). The structure of the compound is shown in Figure 14.6. The coordination of the Ln is tetrahedral, an unusual one for Ln. The N_2 bridge has S = 1/2 spin localized on a π orbital perpendicular to the Ln–N_2–Ln plane.

The magnetic coupling can be described by the SH

$$H = J\mathcal{S}_{rad} \cdot (\mathcal{S}_{Gd1} + \mathcal{S}_{Gd2}) + zJ' < S_z > \mathcal{S}_z \tag{14.3}$$

where the Heisenberg–Dirac–van Vleck Hamiltonian (HDVV) has been proposed as appropriate for an isotropic radical and Gd^{3+}. The energies of the states are

$$\begin{aligned} E = {} & J/2\,[S(S+1) - S_{Gd12}(S_{Gd12}+1) - S_{rad}(S_{rad}+1)] \\ & + J'/2\,[S_{Gd12}(S_{Gd12}+1) - S_{Gd1}(S_{Gd1}+1) - S_{Gd2}(S_{Gd2}+1)] \end{aligned} \tag{14.4}$$

The exciting feature is that the Gd derivative shows an AFM coupling with the radical with $J = 54\,cm^{-1}$ and $zJ' = -0.07\,cm^{-1}$. This means that for dominant J, the energies of the states $|S\ S_{12}\rangle$ are given by kJ, with k an integer ranging from 7 to −8 with a ground state with S = 13/2. In order to check the possible role of Gd–Gd interaction, a derivative with the N_2^{3-} radical substituted by the diamagnetic N_2^{2-} was synthesized and the magnetic properties were measured. The

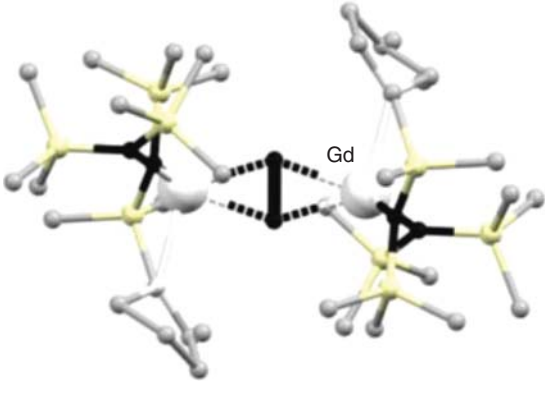

Figure 14.6 Structure of the centrosymmetric $[([(Me_3Si)_2N]_2Gd(THF))_2(\mu\text{-}\eta^2:\eta^2\text{-}N_2)]^{2-}$ anion.

compound has been found to be AFM-coupled with a small coupling constant. Therefore, the ferromagnetic coupling is associated with the radical species. The observed ferromagnetic coupling constant is the largest reported so far for a Gd species.

These results are certainly exciting, but the results obtained on the Dy analog are even more. The overall look of the magnetic properties of the N_2^{3-} and N_2^{2-} Dy derivatives are similar to that of the Gd derivative: χT increasing on decreasing temperature for the radical and decreasing for the diamagnetic ligand. Dynamic measurements showed that the DyN_2^{3-} derivative follows an Arrhenius law with $U_{\text{eff}} = 123\,\text{cm}^{-1}$, $\tau_0 = 8 \times 10^{-9}\,\text{s}$. The barrier is the highest observed till then. It was also shown that the compound undergoes to a magnetic hysteresis of molecular origin, which was open up to 8 K. Even more exciting are the results of the Tb derivative, which showed a record blocking temperature of 14 K, which was much better than reported in TM giant spins.

The radical, however, is not very versatile because it is extremely reactive. Another more stable radical is bipyrimidyl, which was tested with cyclopentadienyl coligands (Cp*) (Demir *et al.*, 2012). The structure is shown in Figure 14.7.

Again, the coupling between the Gd ions is ferromagnetic and large. The Tb derivative shows Orbach relaxation down to 3 K, below which the relaxation time becomes independent of temperature due to QTM. The calculated barrier is $U_{\text{eff}} = 44.2\,\text{cm}^{-1}$ with $\tau_0 = 4(1) \times 10^{-8}\,\text{s}$, while for the Dy derivative $U_{\text{eff}} = 87.8(3)\,\text{cm}^{-1}$ and $\tau_0 = 1.03(4) \times 10^{-7}\,\text{s}$. The Dy derivative shows magnetic hysteresis behavior. Below 2 K and an average sweep rate less than $0.003\,\text{T s}^{-1}$, Tb^{3+} derivative does not show hysteresis at zero field but a loop slightly opens on increasing the external field. This behavior is in agreement with the observed relaxation times in the AC susceptibility experiments and with a tunneling at zero applied DC field. On the other side, the measurements on a polycrystalline sample of Dy^{3+} complex exhibited the hysteresis loops at zero field for temperatures up to 6.5 K.

This section has provided a broad overview of SMMs containing at least two ions, one of which is an Ln. We have partly used a chronological approach, which

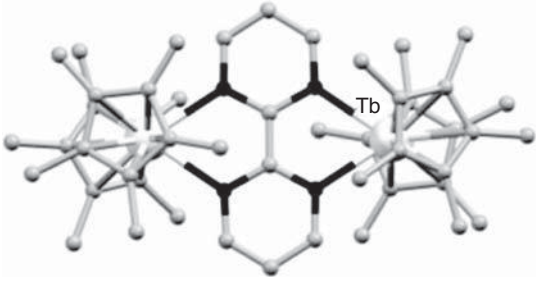

Figure 14.7 Structure of the bipyrimidyl radical-bridged cation in a crystal of $[(Cp^*_2Tb)_2(\mu\text{-bpym}^\bullet)](BPh_4)$.

is a not costly way of connecting different items. The result is highlighting a few systems that provide a more detailed understanding of Ln molecular magnets.

References

Demir, S., Zadrozny, J.M., Nippe, M., and Long, J.R. (2012) Exchange coupling and magnetic blocking in bipyrimidyl radical-bridged dilanthanide complexes. *J. Am. Chem. Soc.*, **134**, 18546–18549.

Evans, W.J., Fang, M., Zucchi, G.l., Furche, F., Ziller, J.W., Hoekstra, R.M., and Zink, J.I. (2009) Isolation of dysprosium and yttrium complexes of a three-electron reduction product in the activation of dinitrogen, the $(N_2)3-$ radical. *J. Am. Chem. Soc.*, **131**, 11195–11202.

Guo, Y.-N., Chen, X.-H., Xue, S., and Tang, J. (2011) Modulating magnetic dynamics of three Dy_2 complexes through keto–enol tautomerism of the o-vanillin picolinoylhydrazone ligand. *Inorg. Chem.*, **50**, 9705–9713.

Habib, F., Lin, P.-H., Long, J., Korobkov, I., Wernsdorfer, W., and Murugesu, M. (2011) The use of magnetic dilution to elucidate the slow magnetic relaxation effects of a Dy_2 single-molecule magnet. *J. Am. Chem. Soc.*, **133**, 8830–8833.

Liu, J.-L., Yuan, K., Leng, J.-D., Ungur, L., Wernsdorfer, W., Guo, F.-S., Chibotaru, L.F., and Tong, M.-L. (2012) A six-coordinate ytterbium complex exhibiting easy-plane anisotropy and field-induced single-ion magnet behavior. *Inorg. Chem.*, **51**, 8538–8544.

Long, J., Habib, F., Lin, P.-H., Korobkov, I., Enright, G., Ungur, L., Wernsdorfer, W., Chibotaru, L.F., and Murugesu, M. (2011) Single-molecule magnet behavior for an antiferromagnetically superexchange-coupled dinuclear dysprosium(III) complex. *J. Am. Chem. Soc.*, **133**, 5319–5328.

Lucaccini, E., Sorace, L., Perfetti, M., Costes, J.-P., and Sessoli, R. (2014) Beyond the anisotropy barrier: slow relaxation of the magnetization in both easy-axis and easy-plane Ln(trensal) complexes. *Chem. Commun. (Camb.)*, **50**, 1648–1651.

Mereacre, V., Ako, A.M., Clérac, R., Wernsdorfer, W., Hewitt, I.J., Anson, C.E., and Powell, A.K. (2008) Heterometallic $[Mn_5\text{-}Ln_4]$ single-molecule magnets with high anisotropy barriers. *Chem. Eur. J.*, **14**, 3577–3584.

Mishra, A., Wernsdorfer, W., Abboud, K.A., and Christou, G. (2004) Initial observation of magnetization hysteresis and quantum tunneling in mixed manganese – Lanthanide single-molecule magnets. *J. Am. Chem. Soc.*, **126**, 15648–15649.

Osa, S., Kido, T., Matsumoto, N., Re, N., Pochaba, A., and Mrozinski, J. (2004) A tetranuclear 3d-4f single molecule magnet: $[Cu(II)LTb(III)(hfac)_2]_2$. *J. Am. Chem. Soc.*, **126**, 420–421.

Pedersen, K.S., Ungur, L., Sigrist, M., Sundt, A., Schau-Magnussen, M., Vieru, V., Mutka, H., Rols, S., Weihe, H., Waldmann, O. *et al.* (2014) Modifying the properties of 4f single-ion magnets by peripheral ligand functionalisation. *Chem. Sci.*, **5**, 1650.

Rigamonti, L., Cornia, A., Nava, A., Perfetti, M., Boulon, M.E., Barra, A.L., Zhong, X., Park, K., Sessoli, R. (2014) Mapping of single-site magnetic anisotropy tensors in weakly coupled spin clusters by torque magnetometry. *Chem. Phys. Phys. Chem.*, **16**, 17220–17230.

Rinehart, J.D., Fang, M., Evans, W.J., and Long, J.R. (2011) Strong exchange and magnetic blocking in $(N_2)^{3-}$ radical-bridged lanthanide complexes. *Nat. Chem.*, **3**, 538–542.

Sievers, J. (1982) Asphericity of 4 f-shells in their Hund's rule ground states. *Z. Phys. B*, **45**, 289–296.

Woodruff, D.N., Winpenny, R.E.P., and Layfield, R.A. (2013) Lanthanide single-molecule magnets. *Chem. Rev.*, **113**, 5110–5148.

Zaleski, C.M., Depperman, E.C., Kampf, J.W., Kirk, M.L., and Pecoraro, V.L. (2004) Synthesis, structure, and magnetic properties of a large lanthanide-transition-metal single-molecule magnet. *Angew. Chem. Int. Ed.*, **43**, 3912–3914.

15
Single Chain Magnets (SCM) and More

15.1
Why 1D

The focus of the book so far has been on finite-size sets, which from a magnetic point of view can be considered as zero-dimensional. Time has come to move to infinity, at least in one direction, focusing on one-dimensional magnets. With this expression, we define systems that are connected by a network of interactions which define *an infinite chain*. The nodes are magnetic centers, such as a metal ion or a radical, which, independently of the structure, is topologically one-dimensional as far as the *magnetic* interactions are concerned. A linear chain and a zigzag chain are both one-dimensional (Figure 15.1). If the chain has a neighboring chain parallel to itself in a plane but the chain-to-chain interaction is weak, the system is one-dimensional. An adequate chain-to-chain interaction will transform the system into a two-dimensional one.

The interest for the magnetic properties of one-dimensional materials started with the goal of investigating relatively simple systems which should lend themselves to relatively more detailed investigations as compared to classical three-dimensional materials. One of the problems that was debated was the so-called Haldane conjecture (Haldane, 1983). The question was simple: The spin levels of a one-dimensional system form a band: is it gapped? The expression means that a simple minded view may lead one to imagine that there is a continuum of levels in contact with the ground $S = 0$ ($S = 1/2$) level of an antiferromagnetic (AFM) chain. The answer by Haldane was that the band gap is between the lowest $S = 0$ and the first triplet, but only for chains formed by integer individual spins. The chains with half-integer spins are not gapped. A confirmation of the correctness of the conjecture came from a molecular nickel(II) chain (Yamashita, Ishii, and Matsuzaka, 2000). This was in fact one of the first examples of the potentialities of molecular magnetism (MM) in providing samples on which to test theories.

Another field of intense activity was that of spin dynamics in one-dimensional Heisenberg AFM. This is a feature different from the ones we have discussed where Ising spins are needed. The first attempts to characterize the unique properties in 1D required isotropic spins. This shows the exchange influence on the magnetic relaxation, which in one-dimensional systems is less efficient than in higher

Introduction to Molecular Magnetism: From Transition Metals to Lanthanides, First Edition.
Cristiano Benelli and Dante Gatteschi.
© 2015 Wiley-VCH Verlag GmbH & Co. KGaA. Published 2015 by Wiley-VCH Verlag GmbH & Co. KGaA.

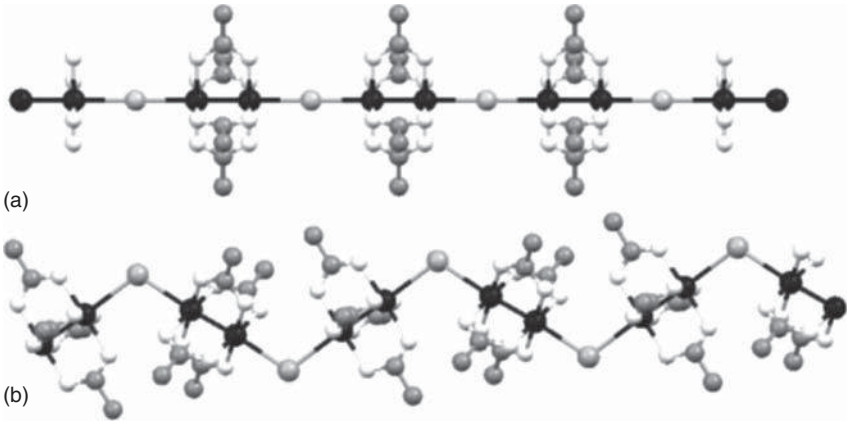

Figure 15.1 Linear (a) and zig-zag (b) molecular chains. (From Ref. (Delgado-Martinez *et al.*, 2014).)

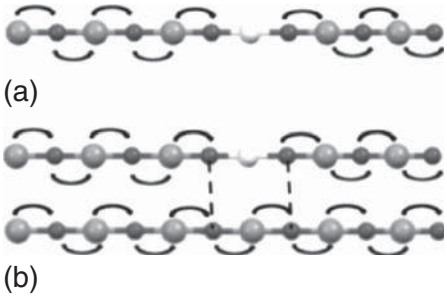

Figure 15.2 A sketch of 1D/2D magnetic structures in presence of a diamagnetic defect: the correlation is transmitted through the nearest neighbor exchange interaction (a). A break in the extended interaction cannot be avoided (b).

dimensional magnets. The reason is obvious, as shown in Figure 15.2: in 1D, there is only one way to transmit the excitation, and one break in the lattice blocks it. In 2D, it is possible to avoid the break by jumping on the neighbor chains. In order to investigate the relaxation of 1D AFM, the MM approach can provide reasonably isolated chains due to the presence of bulk organic groups shielding the magnetic interactions between chains.

The characterization of the spin dynamics requires (i) a good 1D system, that is, weakly interacting chains; (ii) strong intrachain interaction; and (iii) isotropic exchange. The three points are satisfied by Tetramethylammonium Manganese Chain (TMMC), which has the structure shown in Figure 15.3 and has been investigated in all possible ways. The structure is rather elementary, but when chemists realized that they could do something better, it was too late and essentially all was done.

The spin correlation function of a 3D system yields a characteristic time τ_c, which is inversely proportional to J. This means that the correlation time goes to

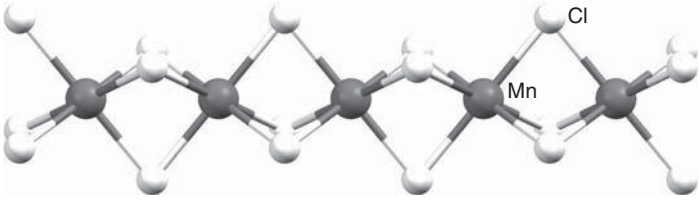

Figure 15.3 Sketch of the linear chains found in $N(CH_3)_4MnCl_3$ (TMMC). The octahedral environment about the manganese atom is slightly distorted, corresponding to a lengthening along the chain (Morosin and Graber, 1967).

zero rather rapidly. In1D, the correlation function decays more slowly and the long time tail must be investigated. The functions to be used are of the type $\tau^{-D/2}$, and the techniques to be used magnetic resonance, both electronic and nuclear. ESR in the weak exchange regime yields Gaussian lines, whereas the lines are Lorentzian in the strong exchange regime. In 1D systems, the line shapes are intermediate between Gaussian and Lorentzian (Boucher *et al.*, 1976).

In the previous chapters, we have shown the excitement provided by the SMM and the SIM, and now we will start with single chain magnets (SCMs), which we recall are 1D systems that relax slowly below a blocking temperature. It is instructive to reflect on the requirements needed to increase the blocking temperature below which slow relaxation sets in. The organization of SMM and SIM in 1D structure is an efficient way to introduce an internal field that reduces the tunneling thus increasing the blocking temperature. Indeed, it was found that 1D Ising ferrimagnets show a magnetic behavior similar to that of SMM and were called *single chain magnets* (Clérac *et al.*, 2002; Caneschi *et al.*, 2002; Bogani *et al.*, 2004). The key difference on the required spin dynamics between SCM and the 1D material highlighted above is that the latter requires isotropic interaction while the former needs an Ising-type interaction.

The rationalization of the observed magnetic behavior was made using the so-called Glauber model. This was originally suggested for 1D ferromagnets and is very pedagogic, which provides a good opportunity for getting acquainted with spin dynamics in 1D (Glauber, 1963). Actually, the model has been used also in totally different systems such as social dynamics (Stauffer, 2005), chemical reactivity (Skinner, 1983), and neural networks (Schneidman, Berry II, Segev, R., and Bialek, 2006). It was never applied to the original target of the model, namely the 1D ferromagnet, because of the lack of suitable systems. MM provided an almost ideal test ground, as we will show presently, even though the test ground was a ferrimagnet and not a ferromagnet.

15.2 The Glauber Model

The model starts from defining a configuration, that is, assigning to each center either a magnetization +1 or −1, according to the Ising scheme. We use the case

Table 15.1 Configurations of four Ising spins.

1	+	+	+	+	2	−	−	−	−
3	+	+	+	−	4	−	−	−	+
5	+	+	−	+	6	−	−	+	−
7	+	−	+	+	8	−	+	−	−
9	−	+	+	+	10	+	−	−	−
11	+	+	−	−	12	−	−	+	+
13	+	−	+	−	14	−	+	−	+
15	−	+	−	+	16	+	−	+	−

of four spins because they are simpler to visualize than infinite array. The 16 configurations are enumerated in Table 15.1.

The dynamics is determined by transitions where one spin flips from −1 to +1, or vice versa. An example could be the transition 5 → 1. The spin to be flipped is the third of the configuration 5 to the corresponding spin of configuration 1. The time evolution of a given configuration, say (+1, +1, −1, +1), depends on the sum of the probabilities of flipping one spin, as shown by Coulon, Miyasaka, and Clérac (2006).

The probability of reversing a spin, leaving the others unchanged, can be expressed with parameters comprising the coupling constant J. In the absence of a field, the probability is proportional to $[1 - \tanh(2J/kT)(\sigma_p(\sigma_{p_{-1}} + \sigma_{p+1}))]$, where σ_p (two-valued classical variables $\sigma_p = \pm 1$) is the ith spin flipping from σ_p to $-\sigma_p$ and σ_{p-1}, σ_{p+1} the neighboring spins. At low temperatures, the transition probability is maximum for transitions that move toward parallel orientation of neighboring spins and decreases on increasing the temperature. Continuing with the above example, the transition 5 → 1 goes in the right direction because two AFM interactions are broken to form two FM interactions. The opposite behavior is expected for transitions which move to AFM from parallel orientation. An example is the transition 5 → 15. A temperature-independent behavior is expected for transitions that move from AFM to AFM as in the 9 → 12 transition where from FM-AFM one goes to AFM-FM.

Using the standard stochastic techniques requires the knowledge of the pair spin correlation. We recall that $\langle \sigma_p \sigma_l \rangle$ gives information on the value of σ_l at time $t + \tau$ starting from σ_p at time t. The calculation of the dynamics is strongly affected by the length of the segments of correlated spins, which in its turn depends on defects and/or impurities, as we anticipated previously, are very efficient to alter the properties of 1D magnets. The procedure is similar to that alluded to for the spin dynamics above.

On preparing the system with all the spins parallel to each other at low temperature, the return to equilibrium will be exponential with a characteristic time τ which diverges exponentially as $\exp(2J/kT)$. The model is similar to the Orbach mechanism worked out for SMM. In fact, the expression for τ is

$$\tau = [\alpha(1 - \gamma + 2\gamma \tanh^2(h_0))]^{-1} \tag{15.1}$$

where $\gamma = \tanh(2J/kT)$, $h_0 = \mu_B B_0 g/kT$, and α is a parameter. Equation (15.1) yields also the field dependence assuming identical isotropic spins. We will stress this point in the following when treating the problem of noncollinearity, which is important for TMs and much more so for Ln. τ_0 enters into the expression relating the transition probability of inverting the spin of the p center, and it is the inverse of the attempt frequency, that is, the transition probability without exchange. As usual, the expression containing the tanh can be replaced by $\exp(2J/kT)$.

The problem of the sensitivity to defects is hardly mentioned in the case of SMM, but there is ample evidence of dramatic effects in clusters. We have mentioned in many cases copper acetate. The dinuclear copper compound is AFM-coupled and is diamagnetic at low temperature, but the magnetization has a paramagnetic tail at low temperature and the ESR spectra are typical of single copper ion. The problem was expected theoretically and has been experimentally observed. The most probable model is that in pair a copper ion is substituted by a diamagnetic ion or by nothing.

It must also be remembered that molecular lattices may host complex impurity. In a dinuclear copper(II) compound, strongly AFM-coupled ESR spectra at low temperature can show the presence of an impurity more weakly coupled. On the basis of the comparison with the spectra of dinuclear species, the structure of host and impurity can be defined as shown in Figure 15.4. The asymmetric dimer at room temperature behaves as an asymmetric triplet as shown in the ESR spectra. On cooling the asymmetric species signal disappears due to the strong AFM coupling. A new symmetryc species is detected providing evidence that the asymmetrc species lattice hosts a compound with a higher symmetry.

In an infinite array, all the spins are equivalent, and in finite size the sites can be classified as internal or external which are very different in terms of

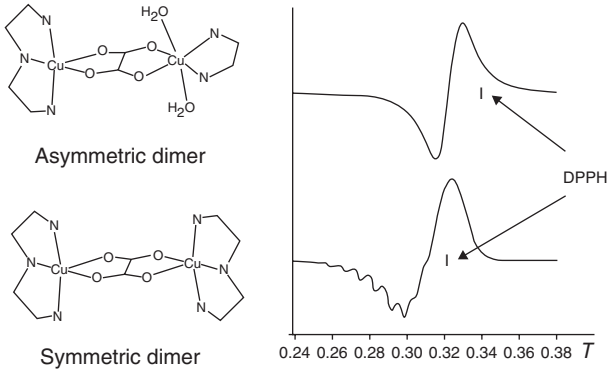

Figure 15.4 Polycrystalline powder ESR spectra of a Cu dimer at X-band frequency and room temperature (upper line) and at 4.2 K (lower line). The low-temperature spectrum indicates the presence of a triplet spin species containing two equivalent copper atoms (Bencini *et al.*, 1986).

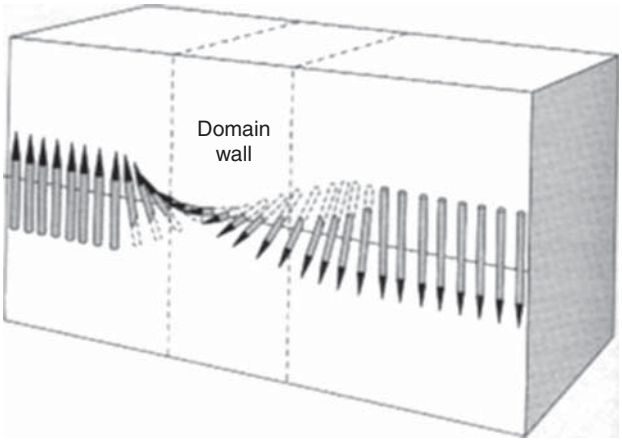

Figure 15.5 Formation of a domain wall (DW) in a one-dimensional magnet.

interactions. In fact, internal sites have two neighbors to interact with, while the external ones have only one. Expanding as for the perfect chain, two regimes are predicted depending on the length of the segments and on the average correlation length. Let us consider a segment of N sites: the two regimes can be defined when the correlation length is much longer than N sites (low-temperature regime) and when it is much shorter (high-temperature regime). The relaxation time is expected to diverge as $\exp(4J/kT)$ at high T and as $\exp(2J/kT)$ at low temperature.

Let us go more into the detail of the relaxation mechanism. A nucleation is generated by reverting a spin at a boundary, Figure 15.5. This corresponds to the formation of a domain wall (DW). In a perfect Ising case, the wall has the depth of one step, but also thicker walls have been considered. The relaxation occurs with the migration of the wall toward the other boundary, which will be successful with a $1/N$ chance. τ_0 is expected to scale with N. The average value of N depends on many factors, its typical value being 10 – 10 000.

The relaxation time of a segment N is expected to scale as

$$\frac{\tau_N}{\tau} = f(x) = \frac{1}{1 + (\omega(x)/x)^2} \tag{15.2}$$

where $x = N/\xi$ and $\omega(x)$ is the smallest root of $\omega \tan(\omega/2) = x$. $f(x)$ goes to 1 for $x \gg 1$ and for $x \ll 1$ it is about $x/2$. The field dependence was reported by Coulon *et al.* (2007) as

$$\frac{\tau_N(B_0 = 0)}{\tau_N(B_0 \neq 0)} = 1 + a^2 h_0^2 \tag{15.3}$$

where $a = 2\xi f(x\sqrt{2}/3)$, with $f(x)$ the scaling function defined in Eq. (15.2) and $h_0 = \mu_B B_0 g/kT$. The parameter ξ is related to the correlation length of spin in the chain and, consequently, to the dimension of the DWs (Gatteschi and Vindigni, 2014).

15.3
SCM: the d and p Way

So far, we have only described what theory suggests for 1D ferromagnets. Time has come to describe some experimental results. We will start from the discovery of SCM, which regards d and p orbitals, and then we will focus on the original contribution of the f orbitals. We will focus on the class of compounds analogous to that of the first SCM, and try to obtain as much information as can be available in them without attempting to cover the matter in detail. Excellent reviews are available, including a strategic one that provides interesting ideas for a successful chemical approach to SCM (Sun, Wang, and Gao, 2010; Nakano and Oshio, 2011; Palii *et al.*, 2011).

The discovery of what was called the *single chain magnet* happened in the frame of synthesis of compounds of 3d metal ions with nitronyl nitroxides, the NITR radicals. They can bind to metal ions with their oxygen atoms, and one radical can bridge two metal ions. In the studies made on systems formed by metal hexafluoroacetylacetonate (hfac) with NITR radicals with the goal to obtain molecular ferromagnets a cobalt(II) derivative at the beginning, it was difficult to obtain reproducible results, but showed appealing indications of high magnetization at low temperature (Caneschi *et al.*, 2001). Eventually, chemistry produced crystals that showed the chain structure, Figure 15.6. Some structural details are mandatory because they are responsible of the magnetic properties. CoPhOMe ($[Co(hfac)_2(NITPhOMe)]$) (NITPhOMe = 4′-methoxy-phenyl-4,4,5,5-tetramethylimidazoline-1-oxyl-3-oxide) crystallizes in the $P3_1$ space group which is chiral, showing that there is spontaneous resolution. The helix grows as a trigonal axis, generating three cobalt ions which are identical to each other but with the features such as the z-axis of the octahedron which is rotated by 120°. Therefore there are three magnetically nonequivalent sites in the unit cell, which may give important effects as we will see later.

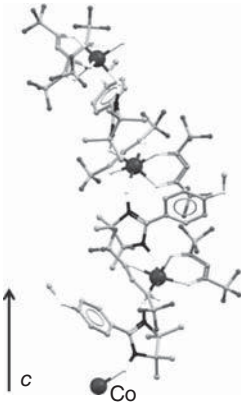

Figure 15.6 Simplified view of the content of the unit cell of CoPhOMe. For the sake of clarity, hydrogen and fluorine atoms are omitted.

From the magnetic point of view, CoPhOMe is a one-dimensional ferrimagnet due to the AFM coupling between the high-spin cobalt(II) and the radical. The former is octahedrally coordinated. In O_h, symmetry the ground state of cobalt(II) is $^4T_{1g}$, which is split by spin orbit coupling (SOC) and low symmetry components to give a ground Kramers doublet, separated by about 150–200 K from the first excited doublet. By treating the ground doublet as an effective $S = 1/2$ state in O_h symmetry, $g_x = g_y = g_z = 4.3$. This means that, even though the coupling between Co^{2+} and the radical is AF, the two magnetizations do not compensate to give zero. The magnetic data of a mononuclear compound with two radicals shows AFM coupling. Since CoPhOMe has a low symmetry the **g** tensor will be anisotropic. The limiting cases for trigonal symmetry of the Ising type is $g_x = g_y = 0, g_z = 9$ as sketched in Section 5.3.

Indeed, the temperature dependence of χT values of single crystals with the field parallel and perpendicular to the trigonal axis clearly indicated an Ising-type magnetic anisotropy. The temperature dependence was fitted with a Hamiltonian which contains the Ising interaction between the spin of cobalt and radical and the Zeeman component of the two spins parallel to the trigonal axis. The fit yielded g_z of Co^{2+} equal to 7.4, in good agreement with the expected value and $J = 224$ K.

The magnetic relaxation becomes slow below 20 K, as shown by both DC and AC measurements. The former show a stepped hysteresis analogous to that observed in SMM, while the AC measurements showed out-of-phase χ'' below 15 K following an Arrhenius plot with $\tau_0 = 3 \times 10^{-11}$ s and $\Delta = 154$ K.

The first paper was soon followed by a report by a combined Franco-Japanese team, which, instead of using cobalt, used manganese and nickel and induced Ising symmetry through zero-field splitting (ZFS) rather than with **g**. The described system consisted of a heterometallic chain $[Mn_2(saltmen)_2\ Ni(pao)_2(py)_2](ClO_4)_2$ (saltmen^{2-} = *N*,*N*′-(1,1,2,2-tetramethylethylene)bis(salicylideneiminate) and pao = pyridine-2-aldoximate), whose spatial arrangement is shown in Figure 15.7 (Clérac *et al.*, 2002).

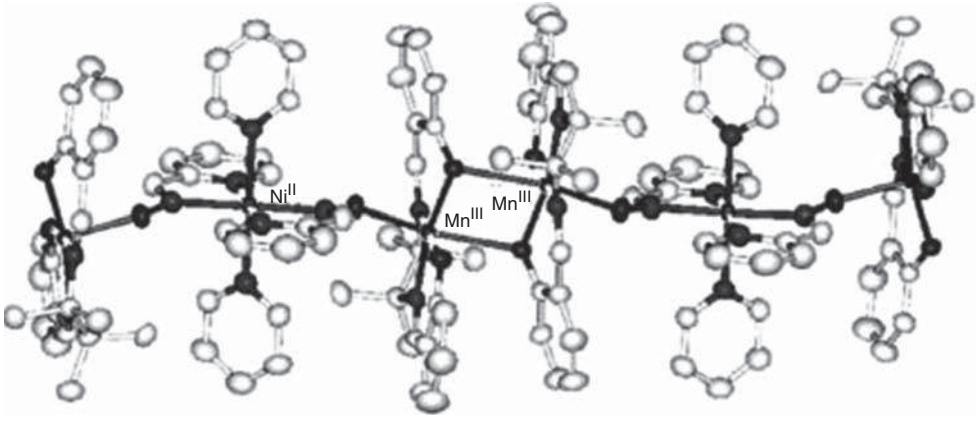

Figure 15.7 Isolated chain of $[Mn_2(saltmen)_2Ni(pao)_2(py)_2]^{2-}$. (Reproduced from Clérac, R. *et al.* (2002) with permission from The American Chemical Society.)

The crystal structure is indicative of a good magnetic isolation of the chains. For the magnetic properties, the one-dimensional compound is formed by an assembly of trinuclear species (Mn–Ni–Mn) with a Ni^{2+}–Mn^{3+} AFM interaction (J = 21 K). The trinuclear species are connected through a FM Mn^{3+}–Mn^{3+} interaction ($J' = -7$ K). Below 3.5 K, a hysteresis loop was observed, and combined AC and DC measurements showed a slow relaxation of the magnetization.

The spin dynamics of one-dimensional ferromagnets had been calculated by Glauber, but no check could be done because of the lack of suitable materials. Time had come to use the experimental systems. The Glauber treatment yielded an Arrhenius behavior with the barrier 2J, and the comparison with experiment was positive.

Several improvements including detailed evaluation of the interactions between centers have been introduced justifying the expression "beyond Glauber" (Zhang *et al.*, 2013). The initial assumption of the Glauber model is that the DWs are extended to one lattice unit, in accordance with the Ising model. Relaxing this condition can be done, referring to the so-called anisotropic Heisenberg Hamiltonian

$$\mathscr{H} = \mathrm{J}\Sigma\mathcal{S}_i\mathcal{S}_{i+1} + D\Sigma\mathcal{S}_i{}^2 - g\mu_{\mathrm{B}}H\Sigma\mathcal{S}_i \tag{15.4}$$

As long as $|D/\mathrm{J}| \gg 2/3$ Eq. (15.4) is equivalent to the Ising Hamiltonian, and the Glauber model works. The first term favors large DWs and the second sharp ones. The energy associated with a broad DW is

$$E_{\mathrm{dw}} = 2(2D\mathrm{J})^{\frac{1}{2}} \tag{15.5}$$

The energy needed to create a soliton, as described in the study of one-dimensional dynamics.

Another important factor to describe the SCM dynamics is associated with finite-size effects. We have already noticed that 1D systems are very sensitive to defects, as sketched in Figure 15.2. In an infinite chain, every spin has two nearest neighbors (NNs). Flipping one spin requires spending twice the energy of the interaction between NNs. However, if there is a defect, the flipping energy is only equivalent to spending one quantum. There are therefore two regimes, the pure chain and the broken chain, and which of them will be dominant depends on the number of defects. An extention of the Glauber treatment to finite size clusters suggests an Arrhenius type behavior but with a slope corresponding to the half of the value of a system without defects. Evidence for the two types of behavior has been observed (Bogani *et al.*, 2004).

15.4 Spin Glass

The treatment we have made so far of SMM, SIM, and SCM has been based on the superparamagnetic model; that is, the slowly relaxing system can be considered as

a collection of non interacting grains inside which the spins respond collectively to the stimuli. In a system of ferromagnetic or ferrimagnetic fine particles whose volume V is so small that the product KuV (Ku is the anisotropy constant) is less than or comparable to the thermal energy kT the total sum moment of all the coupled atoms fluctuates randomly like that of a large paramagnetic atom. The susceptibility follows a Curie law with a huge value of C. The relaxation depends on the size of the grains, and the total spin behaves as a giant spin, or, if you wish, as a superparamagnet. The derived model has been excellent for justifying the magnetic properties. We must mention, however, that there is an another class of systems, which has some similarity with superparamagnetic properties. These systems are called Spin Glass and are characterized by disorder and competing interactions, which offer the system many opportunities for different behavior. The ideal pathway from the initial to the final depends in a series of steps which provide a number of different opportunities. In other words, the system has a very shallow potential energy, which will make it impossible to move twice on the same pathway. The behavior of SG will depend on the temperature. At low temperature, the mobility is frozen and the system may undergo a magnetic hysteresis without ordering. This means that there are many different relaxation behaviors. An important variable to characterize the system is the distribution of relaxation times $G(\tau)$. Its size depends on the presence of random structures and frustration (see Section 16.2). Close to the glass temperature, $G(\tau)$ is narrow, but it becomes very broad at low T. The dependence of the magnetization on T follows an Arrhenius dependence, but the barrier Δ has no physical meaning. Consequently, τ_0 can have very small values, $10^{-15}-10^{-17}$ s. Indeed, the value of τ_0 is quite often used to decide whether the sample corresponds to superparamagnetic or SG.

15.5
Noncollinear One-dimensional Systems

Assembling systems that contain noncollinear moieties is an efficient way to envisage complex behavior. We have already met noncollinear systems, and in Section 7.9 we had detailed the effects that can originate from this structural condition. A useful definition of noncollinearity is a system in which the local properties, such as the local anisotropy, the **g** and **J** tensors, and so on, are defined on different axes in an external frame, which typically is the crystal frame. CoPhOMe is a typical example, as already shown in Figure 15.6 (Caneschi *et al.*, 2001).

Let us suppose that a system is defined in a coordinate frame X, Y, Z. The local principal directions x, y, z are related by rotations that can be performed using the Euler angles. We recall that they refer to standard rotation matrices defined by three angles: φ which refers to a rotation by φ around Z followed by a rotation by θ around x', where x' is the axis generated by the rotation by φ. Finally, ψ corresponds to a rotation around z''. The matrices are shown in Table 15.2.

Table 15.2 Generalized rotation matrix.[a)]

$\cos\theta\cos\varphi$	$\sin\psi\sin\theta\cos\varphi - \cos\psi\sin\varphi$	$\cos\psi\sin\theta\cos\varphi + \sin\psi\sin\varphi$
$\cos\theta\sin\varphi$	$\sin\psi\sin\theta\sin\varphi + \cos\psi\sin\varphi$	$\cos\psi\sin\theta\sin\varphi - \sin\psi\cos\varphi$
$-\sin\theta$	$\sin\psi\cos\theta$	$\cos\psi\cos\theta$

a) Using this rotation matrix, it is possible to compute the Euler angles φ, θ, and ψ by equating each element in the matrix with the corresponding element in the matrix product $R_z(\varphi)R_y(\theta)R_x(\psi)$. The resulting nine equations can be used to find the Euler angles.

Let us refer to systems with a trigonal axis such as CoPhOMe. The X-axis is chosen to lie in the plane containing the local z-axis of the chosen molecule.

A treatment of the chains in the Ising formalism requires taking into account the relative orientation of the local z-axis. The simplest case would be with all the spins parallel to the z-axis: this would be the classical Ising model. The spin Hamiltonian can be expressed as

$$\mathcal{H} = \sum_i J(\mathcal{S}_i^z\mathcal{S}_{i+1}^z + \mathcal{S}_i^z\mathcal{S}_{i-1}^z) - \mu_B H_z \sum_i (g_{Co}\mathcal{S}_i^z + g_{\text{rad}}\mathcal{S}_{i-1}^z) \tag{15.6}$$

$\mathcal{S}_i^z$ refers to Co and $\mathcal{S}_{i+1}^z$ to the radical. It encompasses only the interactions, and the interaction of a spin with its right and left neighbor is the same. The effect of a field on Co g and on radical are included in the second part of the Hamiltonian.

An SCM behavior has been reported in a system where the metal ion is the same but in an alternating different oxidation state, as described in Figure 15.8 (Kajiwara *et al.*, 2005).

The compound, an alternating high-spin Fe^{2+} and low-spin Fe^{3+} chain complex, *catena*-$[Fe^{II}(ClO_4)_2(Fe^{III}(bpca)_2)]ClO_4$ (Hbpca = bis(2-pyridylcarbonyl)amine),

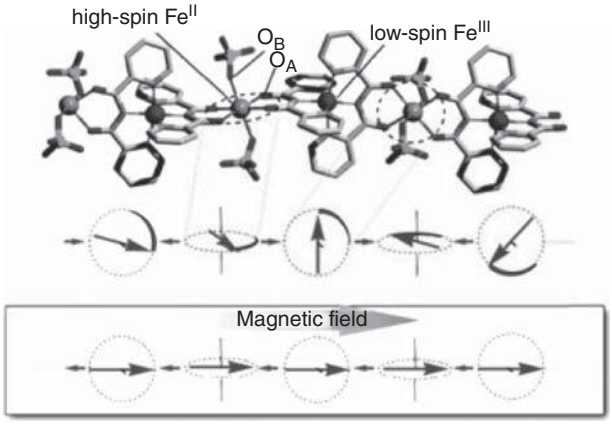

Figure 15.8 Spin arrangement of high-spin Fe^{2+} and low-spin Fe^{3+} alternating chain complex *catena*-$[Fe^{II}(ClO_4)_2(Fe^{III}(bpca)_2)]ClO_4$. (Reproduced from Kajiwara, T. *et al.* (2005) with permission from The American Chemical Society.)

behaves as an SCM with $\Delta = 27(1)\,\mathrm{K}$, $\tau_0 = 100\,\mathrm{s}$, and a blocking temperature estimated as $T_B = 1.3\,\mathrm{K}$. The observed Δ value is smaller than the one expected for pure Glauber's dynamics, suggesting that the transverse magnetization of the Fe^{2+} spins in an easy plane is responsible for the magnetic relaxation in connection with the presence of twisted arrangement of easy planes along the chain axis.

15.6 f Orbitals in Chains: Gd

Before entering the field of SCMs based on lanthanide ions, it is useful to describe some special features that are relevant in determining the overall magnetic behavior of low-dimensional systems. Let us start with the basic magnetic properties observed in quasi-one-dimensiona compounds built with 4f ions and organic radicals, such as the already mentioned nitronyl nitroxide. Though low-dimensional magnetic systems containing TM ions have been known for many years, the same is not true for lanthanide containing systems.

The first attempts to design molecular magnets containing Ln ions had the goal to obtain true magnets characterized by long-range order, remnant magnetization, magnetic hysteresis, and so on. In other words, the goal was the synthesis of ferro- or ferrimagnets based on molecules. The difficulty is that there are three-dimensions in space and to have a magnet it is mandatory to have strong interactions in all of them. The difficulty that had emerged with TM and RE was no better. Anyway, systematic attempts were made to design one-, two-, and three-dimensional MMs, and $Gd(hfac)_3$ and NITR were the obvious choice to start from one-dimension.

The first example of this class of compounds was described in 1989 (Benelli *et al.*, 1989b). The choice of the ligands was derived from the work on synthesizing chain of alternating TM ions and an organic radical (Benelli *et al.*, 1985; Caneschi *et al.*, 1989). These derivatives contain Gd^{3+} ions that alternate with nitronyl nitroxide radicals to form regular chains, as shown in Figure 15.9.

From a magnetic point of view, the system consists of an arrangement of different spin ($S = 1/2$ for nitronyl nitroxides, $S = 7/2$ for Gd^{3+}), as described in the following with a spin organization strictly dependent on the nature of the exchange interaction. A first hypothesis is to assume a FM interaction as

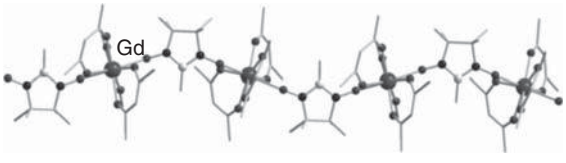

Figure 15.9 Representation of a cell of $Gd(hfac)_3$NITR chain (R = ethyl, isopropyl). H and F atoms are omitted for clarity.

observed in similar zero-dimensional derivatives (Benelli *et al.*, 1987). Furthermore, the room-temperature single-crystal ESR spectra unambiguously indicate the magnetic monodimensionality of the Gd(hfac)NITEt derivative, excluding the presence of relevant intrachain interactions. The spin arrangement in the chain is the one reported in the following, and a one-dimensional FM behavior could be confirmed if the χT values increase on decreasing the temperature (Scheme 15.1).

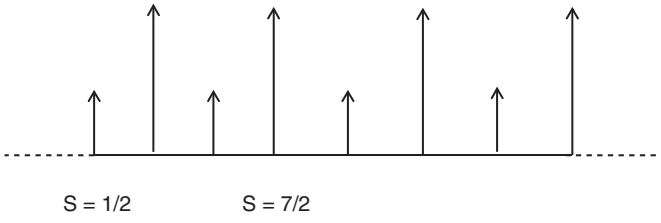

Scheme 15.1 Ferromagnetic spin alignment in a Radical-Gd Chain

On the other hand, AFM coupling gives a ferrimagnet, and again an increase in χT values on decreasing temperature should be observed after an initial decrease (Scheme 15.2).

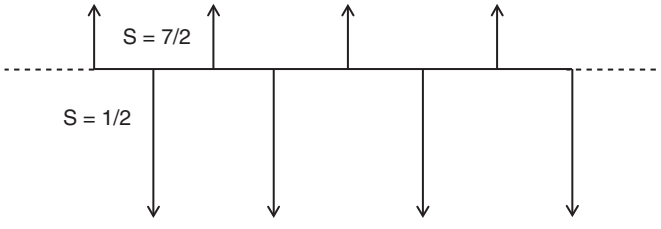

Scheme 15.2 Antierromagnetic spin alignment in a Radical-Gd Chain

The experimental data, shown in Figure 15.10, were completely disappointing. χT values were found to decrease on decreasing temperature. Actually, by varying the radical it was also possible to have χT increasing on decreasing temperature but much less than anticipated for F coupling. In the analysis of different Ln–nitronyl nitroxides systems, an AFM interaction, on the order of $10\,cm^{-1}$, was observed to be operative between the radicals in a linear-chain yttrium nitronyl nitroxide complex (Benelli *et al.*, 1989a), which has a structure very similar to that of the gadolinium derivatives described here. Weak AFM interactions between the gadolinium ions were observed in the dinuclear species containing semiquinone ligands (Dei *et al.*, 2000). These experimental evidences suggested an additional next-nearest-neighbor (NNN) AF interactions operative between radicals and Gd^{3+} ions pairs. This new exchange mechanism gives rise to the frustrated spin structure, as shown in Scheme 15.3.

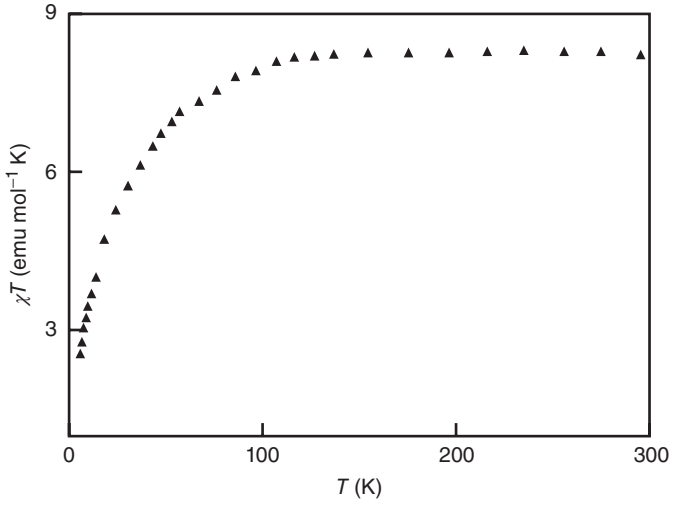

Figure 15.10 Temperature dependence of the observed χT product of $Gd(hfac)_3NITEt$ in the 5–300 K range.

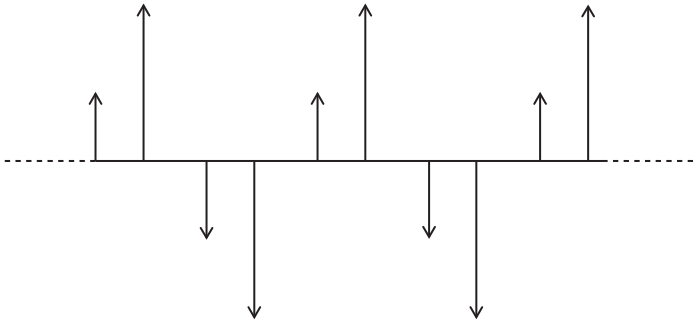

Scheme 15.3 Spin alignment in a Radical-Gd Chain in presence of NNN interactions

The magnetic behavior of this system was analyzed by using the following Hamiltonian in the approximation of considering the system with an Ising approach:

$$\mathcal{H} = J_{\text{Gd-NIT}} \sum_{NN} \mathcal{S}_{\text{Gd}^z} \mathcal{S}_{\text{NIT}^z} + J_{\text{NIT-NIT}} \sum_{NNN} \mathcal{S}_{\text{NIT}^z} \mathcal{S}_{\text{NIT}^z} + J_{\text{Gd-Gd}} \sum_{NNN} \mathcal{S}_{\text{Gd}^z} \mathcal{S}_{\text{Gd}^z} - g\mu_B H_z \sum (\mathcal{S}_{\text{NIT}^z} + \mathcal{S}_{\text{Gd}^z}) \quad (15.7)$$

where $J_{\text{Gd-NIT}}$ is the NN coupling constant between the gadolinium ion and the adjacent radical; $J_{\text{Gd-Gd,}}$ and $J_{\text{NIT-NIT}}$ are the NNN coupling constants, and S_z^i are the spin angular momentum components of the i species along the quantization axis z. The fitting procedure gave satisfactory results, even for the system made up of highly isotropic species, with the following parameters: $J_{\text{Gd-NIT}} = -0.41\,\text{cm}^{-1}$, $J_{\text{NIT-NIT}} = 5.08\,\text{cm}^{-1}$, and $J_{\text{Gd-Gd}} = 0.98\,\text{cm}^{-1}$ for

Gd(hfac)·NITEt and $J_{Gd-NIT} = -0.42\,cm^{-1}$, $J_{NIT-NIT} = 5.32\,cm^{-1}$, and $J_{Gd-Gd} = 0.38\,cm^{-1}$ for Gd(hfac)·NIT*i*Pr. The sets of data are not very surprising in the obtained values: the novelty is the relevance in these systems of the NNN magnetic interactions at least when Ising species are present.

In a nonrealistic Ising approach, the ground state is in a two spin-up, two spin-down configuration. The nature of the magnetic centers suggests an anisotropic exchange, but quantitative calculations within that scheme are too complex. Therefore, an *XY* scheme was used as an acceptable compromise. If a more realistic easy plane is assumed, a helix is formed and the chains behave as 1D helimagnets, as shown in Figure 15.11.

The pitch of the helix depends on the J values for the various spin pairs, the single ion anisotropy, and the inter chain interaction. The pitch Q is given by the expression

$$Q = \cos^{-1}(1/(2(\delta + \delta'))) \tag{15.8}$$

where $\delta' = |J_{z2}|S^2/(J_{z1}sS)$ and $\delta' = |J_{z2}|S^2/(J_{z1}sS)$, where the J's are the coupling constants, s is the radical and Gd spin, respectively. The helical order is possible only if the ratio between NNN and NN exchange coupling exceeds the threshold value $(\delta + \delta') > 1/2$.

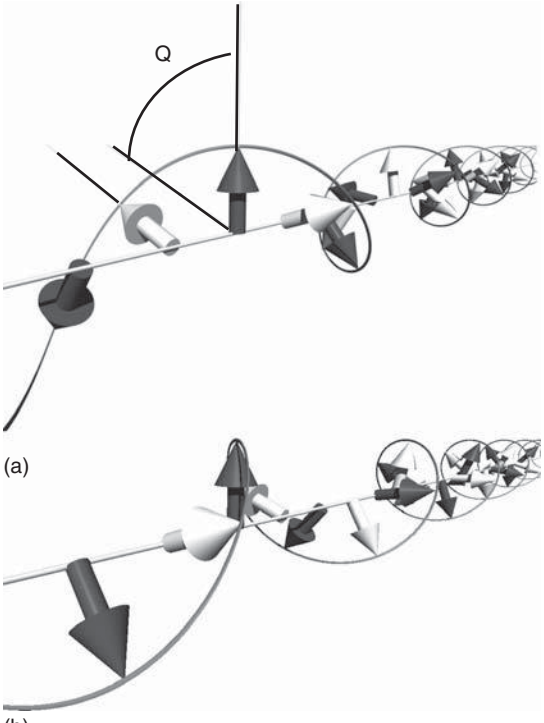

Figure 15.11 Spin arrangement in a chain with different spins. (a) Positive pitch Q; (b) Negative pitch Q.

Table 15.3 Calculated pitch Q for different NITR radicals.

R	*Q*	Magnetic interaction
*i*Pr	72	AF
Et	71	AF
Me	37	F
Ph	32	F

Different behaviors of χT are calculated depending on Q at 0 K. For $Q = \pi/2$ the system is fully frustrated and χT decreases on decreasing T, highlighting an AFM behavior. For Q significantly smaller than $\pi/2$, the FM behavior is observed. In Table 15.3, we report the calculated pitches. We recall that the pitch Q is the wave vector which defines the angle formed by two first neighbors spin. It is not relevant if the spins are equal of different like in the above described Gd chains. If $Q = 0°$ spins are parallel and we have a ferromagnetic ground state while if $Q = 180°$ this one is AFM. If $Q = 90°$ and the first spin is up, the third spin is down and the fifth is up again. (Pini and Rettori, 1993; Cinti *et al.*, 2010).

The paramagnetic phase is characterized by increasing chiral correlation on decreasing temperature. This means that longer helices are present in which the chirality is preserved. At low temperature, an ordered state is reached where all the chains are identical from the spin point of view. We can call it a *spin solid*. Many years ago, Villain (1978) suggested that an intermediate phase can exist in which all the chains have the same chirality but in every chain the phases are random. This is a *spin liquid*. The intermediate phase is stabilized by the fact that the spin correlation increases more slowly than the chiral correlation on decreasing the temperature. It is like having a set of corkscrews which all turn clockwise or anti-clockwise but with random phases. The two transitions can be monitored using standard techniques such as specific heat, magnetic susceptibility, NMR, and, less standard, like muon spin rotation (μSR).

15.7 f Orbitals in Chains: Dy

The first report of an SCM involving 4f orbitals was about a derivative of an NIT radical with a highly anisotropic 4f ion such as Dy^{3+}. The new chapter of the story starts with the synthesis of $[Dy(hfac)_3NITEt]_n$, which is a member of the same family as CoPhOMe whose properties have been described previously. It is characterized by relatively strong intrachain interactions between the radicals and the Dy ion (Benelli *et al.*, 1992). As observed in other cases, the $^6H_{15/2}$ ground multiplet is widely split, leaving a ground doublet, which generates a strong Ising anisotropy. At low temperature, the Dy doublet can be treated as an effective $S = 1/2$ system with a highly anisotropic **g** tensor. The AFM coupling with the spin of the radical

yields a one-dimensional ferrimagnet. Dipolar interactions trigger the transition to 3D order at 4.3 K. In order to favor the SCM, the strategy was obvious: decrease the interchain dipolar interactions by increasing the inter-chain distances.

The chosen radical was NIT-C_6H_4OPh (NIT-C_6H_4OPh = 2,4′-benzoxo-4,4,5,5-tetramethylimidazoline-1-oxyl-3-oxide) whose structure is shown in Scheme 15.4 (Bogani *et al.*, 1992; Bernot *et al.*, 2006).

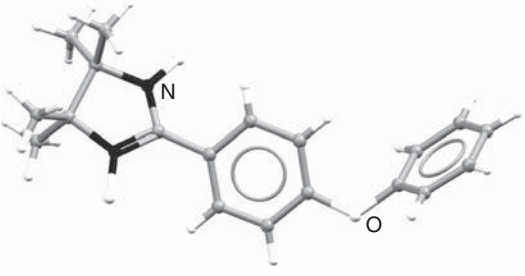

Scheme 15.4 Molecular structure of 2,4′-benzoxo-4,4,5,5-tetramethylimidazoline-1-oxyl-3-oxide (NIT-C_6H_4OPh).

The presence of two phenyl groups provides supramolecular interactions stabilizing the structure and enhancing the electron density on the rings. In fact, the X-ray structure of $[Dy(hfac)_3(NIT\text{-}C_6H_4OPh)]_n$ shows that the Dy ions and the radicals are organized on a binary screw axis forming a helix, as shown in Figure 15.12. The shortest Dy–Dy distance increases to 1.135 nm, and the interchain dipolar interaction energy decreases by 15%. The Ln atoms are eight-coordinated by six oxygen atoms of hfac and two oxygen atoms of two radicals.

It is useful to compare the coordination environments of the polymer $[Dy(hfac)_3(NIT\text{-}C_6H_4OPh)]_n$ and the monomer $[Dy(hfac)_3(NIT\text{-}C_6H_4OEt)_2]$ (Bernot *et al.*, 2009a). The structures are very similar to each other, as confirmed

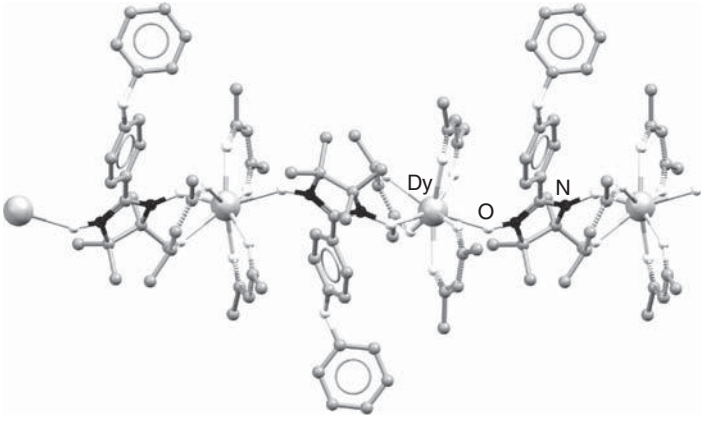

Figure 15.12 View of the crystal structure of $[Dy(hfac)_3(NIT\text{-}C_6H_4OPh)]_n$ at 150 K. Fluorine and hydrogen atoms are omitted for clarity.

Table 15.4 Geometry of the coordination sphere of Dy-NITR derivatives.

	$[Dy(hfac)_3(NIT\text{-}C_6H_4OEt)_2]$	$[Dy(hfac)_3(NIT\text{-}C_6H_4OPh)]_n$
Bond length (Å)		
$Dy–O_1$	2.336(5)	2.373(1)
$Dy–O_2$	2.322(5)	2.343(1)
$Dy–O_3$	2.358(5)	2.329(2)
$Dy–O_4$	2.375(3)	2.343(2)
$Dy–O_5$	2.349(3)	2.328(2)
$Dy–O_6$	2.368(1)	2.361(2)
$Dy–O_{NIT1}$	2.351(7)	2.385 (1)
$Dy–O_{NIT2}$	2.316(7)	2.329(1)
Bond angles (°)		
$O_1–Dy–O_2$	73.52	72.39
$O_1–Dy–O_3$	126.64	127.55
$O_1–Dy–O_4$	132.83	132.76
$O_1–Dy–O_5$	73.90	73.34
$O_1–Dy–O_6$	73.52	74.76
$O_1–Dy–O_{NIT}$	146.77	146.03

The O1 – O6 oxygen atoms belong, two by two, to three hfac molecules.

by the X-ray data. These data reflect the low sensitivity of lanthanide to the environment. Indeed, one of the driving forces for determining the coordination beyond the metal donor interactions is the stacking interactions between the aromatic rings. A comparison between the monomer and polynuclear systems is shown in Table 15.4.

In order to describe the coordination environment of Ln^{3+}, it is possible to use polytopal analysis to decide which coordination polyhedron best describes the metal ion's environment (Casanova *et al.*, 2004). For an eight-coordinate complex, such as the one we are considering, the three most important coordination polyhedra are the square antiprism (SAPR), DD, and bicapped trigonal prism (TPRS) (see Figure 3.5). The geometry of the coordination polyhedra of the two compounds is reasonably close to that of a distorted DD with triangular faces, where the two radical oxygen atoms occupy the apical positions of two distorted pentagons. Essentially the same geometry is observed in other DyNITR derivatives. It is interesting to reflect on the symmetry aspects of the coordination polyhedra, which in the ideal case favor tetragonal, pentagonal, and trigonal symmetry for SAPR, DD, and TPRS, respectively. Regular DD is not compatible with crystal symmetry; therefore distorted geometries must be expected for DD. For these systems, the actual molecular structure is slightly different from the idealized one. In the case of $[Dy(hfac)_3(NIT\text{-}C_6H_4OEt)_2]$, the coordination polyhedra can be schematized as a distorted SAPR, while for $[Dy(hfac)_3(NIT\text{-}C_6H_4OPh)]_n$ is a distorted DD.

The comparison of the structure with that of CoPhOMe shows a great difference in the parameters, which are sensitive for magnetic properties. We refer to the Ln-ON direction, which indicates the local *z* direction, that is, the axis of local

anisotropy. In the Co^{2+} derivative, the chain is formed by the operation of the trigonal screw axis that yields three local axes which make an angle θ with the trigonal axis, while the projection of z_i corresponds to $\varphi = 0°, 120°, 240°$. For Ln, the space group is orthorhombic $P2_12_12_1$ and the screw axis is binary. Let us train to see the orthorhombic cell and the limitations this symmetry determines. Let us start from the *b*-axis which is the chain axis. Let us suppose that the axis connecting Dy with the external NIT oxygen makes an angle θ_1 with the screw axis and the direction cosines are $l_1 = \sin(\theta_1)$, $m_1 = 0$, $n = \cos(\theta_1)$ for z_1 and $-\sin(\theta_1), 0, \cos(\theta_1)$ for z_2. Symmetry requires a z_2-axis with direction cosines $-l, m, -n$. However, there are two other symmetry axes that transform l, m, n into $-l, -m, n$, and $-l, m, -n$ respectively. So the relevant vectors are defined by symmetry: they are equivalent by symmetry but different in the geometrical properties.

The AC measurements showed a frequency-dependent out-of-phase susceptibility, which is compatible with the SCM behavior. In fact, the experimental data could be fitted with an Arrhenius law, with $\tau_0 = 1.9 \times 10^{-12}$ s and $\Delta = 69 \pm 1\,\text{cm}^{-1}$. The height of the barrier is comparable with those observed in compounds containing TMs.

In a slightly optimistic way, we can start from the *ab initio* calculations of the energy levels and the magnetic properties of a "mononuclear" species, which modifies NIT-C_6H_4OPh as reported in the following (Bernot *et al.*, 2009b). A model compound was used in which NIT-C_6H_4OPh transformed into NITPh, eventually transforming the external NO into NOH killing the radicals. The results provided the energies of the low-lying multiplets and the effective *g*-values. They confirmed a quasi-axial *g* tensor with $g_\parallel = 18, g_\perp = 1.5$. The comparison with the experimental data is very good, including the directions of the easy axes which differ by 7°.

A view along *b*, which defines the *Y* laboratory axis, shows that there are two chains related by a twofold axis. The *Z*-axis is perpendicular to the (101) crystal face. The magnetic data were obtained at 2.5 K by measuring the DC susceptibility in three planes, namely by rotating around *X*, *Y*, and *Z*. The results are shown in Figure 15.13. The rotation around *Z* is essentially independent of the angle. Qualitatively, matters are simple, the extreme in the rotations being observed parallel to the *a*- and *c*-axes, which in the *XY* reference frame are observed at 45° from the axes of the experimental reference frame.

The puzzling result is provided by the T dependence of M/H. χ_z decreases dramatically on increasing T while χ_x varies very little. Already at 9 K, there is a crossover in the magnetic anisotropy, with χ_z becoming the hard axis. The field dependence of the magnetization parallel and perpendicular to the chain axis is very different. When the field is parallel to *Z*, the magnetization saturates rapidly to $9\,\mu_B$, while when it is orthogonal, the magnetization increases with a step similar to a metamagnetic transition. This is certainly an interesting property, which demands an explanation. Before proceeding further, we recall that "metamagnetic" indicates a change in magnetization due to a change in relative spin orientation as a result of the application of a magnetic field which is stronger than the interaction of the spins. The tentative interpretation of the magnetic properties starts from the assumption that AFM coupling is operative

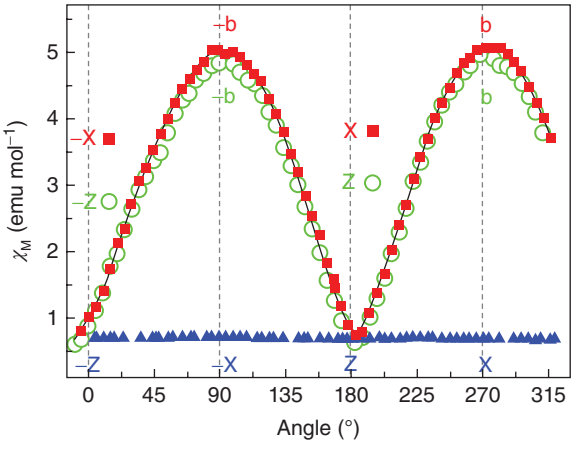

Figure 15.13 Angular variation of the molar susceptibility, χ^M, for three orthogonal rotations at 2.8 K, measured in a 1 kOe external field. Rotations were performed around *X* (circles), *b* (triangles), and *Z* (squares).

between NNN Dy. This idea comes from the comparison with a system that is based on a 1D AFM.

Let us check if this is the right idea to understand $[Dy(hfac)_3(NIT\text{-}C_6H_4OPh)]_n$. We introduce some additional geometry first. The two chains are symmetry-related by a screw axis along *b* and therefore the easy axis for Dy^{3+} ions in the two chains about orthogonal to each other (Figure 15.14). By applying a field parallel to the *Z* direction for one chain, it will be parallel to *X* for the other one. The effect, therefore, will be very different for the two chains. When the applied field is strong enough, one chain readily saturates. We can take this as an encouragement to explore this model. This was done by measuring the magnetization in the *ac* plane with fields of 1 and 30 kOe. The high field measurements show a strong

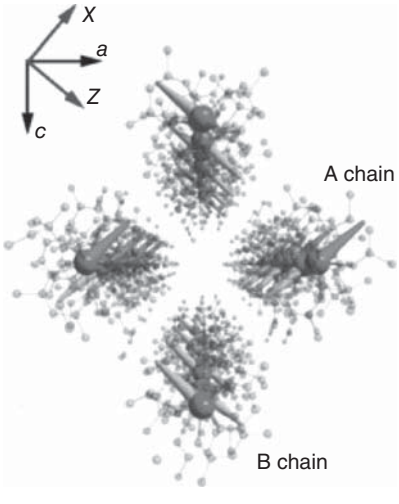

Figure 15.14 Views of the structure of $[Dy(hfac)_3(NIT\text{-}C_6H_4OPh)]_n$ along the *b* crystallographic axis of the crystal packing, showing the two symmetry-related types of chains. The orientation of the *X*- and *Z*-axes in the *ac* plane is also represented.

angular dependence. In the rotation, the chains parallel to the strong field have strong magnetization. Since the chains are separated by about 90°, a periodicity of 90° is observed for the high maxima. Also, weaker maxima are observed roughly halfway between the maxima.

The 1D system permits some calculation of the static magnetic properties using the transfer matrix formalism. This uses interactions between classical vectors to describe exchange, single-ion, and Zeeman interactions. The drastic approximation is to include only the Dy spins, assuming that the role of the radical can be neglected because they are isotropic. There are two Dy ions in the chain, which have coordinates $\theta = 75°$, $\varphi = 135° \pm 45°$ for their z_i-axes. The spins and the SH parameters are compared as required in the laboratory and the local frames. The results of the calculations can be compared with the experimental results, producing a qualitative semiquantitative description of the magnetic properties of $[Dy(hfac)_3(NIT\text{-}C_6H_4OPh)]_n$.

The calculation of the field at which the flip of the spin occurs is about 15 kOe, which is in good agreement with experiment. At high T, that is, for T larger than $\Delta/2$, the correlation length is very short and the chains behave as simple paramagnets. The calculations give good agreement with experiments. Finally, we check the puzzling angular dependence with strong fields in the *ac* plane. Since there are two chains with principal axes rotated by 90°, when the magnetization of one chain goes to a minimum the other goes through a maximum. A similar behavior was reported in a Mn^{3+} chain connected through phenylphosphinic acidanion, which are rather efficient in transmitting AFM coupling (Bernot *et al.*, 2008). Single-crystal measurements revealed a field dependence, which, when the field is parallel to the *c*-axis of the monoclinic cell, has the stepped behavior typical of metamagnetic transition. In fact, the field becomes strong enough to break the AFM coupling between the Mn ions. The system shows also slow magnetic relaxation with $\tau_0 = 1.6 \times 10^{-10}$ s and $U_{\text{eff}} = 36.8$ K. This is also a unexpected feature because the SCM behavior is observed not in an FM, as required by Glauber, or in a ferrimagnet, but in an AFM provided the local anisotropies are not collinear.

15.8
Back to Family

With the detailed knowledge of the magnetic properties of $[Dy(hfac)_3(NIT\text{-}C_6H_4OPh)]_n$, let us now go back to the family $[Ln(hfac)_3(NIT\text{-}C_6H_4OPh)]_n$ (Ln = Gd, Tb, Dy, Ho, Er, Tm, Yb) (Bernot *et al.*, 2006; Bernot *et al.*, 2009a). First of all, what must be expected is an interaction between Ln and NITR with a high probability of being FM. Assuming the presence of both NN and NNN interaction, as observed in Gd derivatives, the presence of only NN interaction gives three possibilities to expect for a 1D system, namely (i) a simple paramagnet if the NN interaction is zero; (ii) a 1D ferromagnet if J is FM; and (iii) a 1D ferrimagnet if J is AFM. The χT versus T plots of the six compounds can be read as indicating a weak ferromagnetic interaction for Dy, FiM for Tb, Ho, Er, and AFM for Gd and Yb. Clearly, in Gd and Yb some assumptions break down,

Table 15.5 Main static and dynamic properties for $[Ln(hfac)_3(NIT\text{-}C_6H_4OPh)]_n$.

	χT, 300K (emu/mol)	M at 120 kOe (μ_B)	M_{satur} (μ_B)	Ueff (cm^{-1})	τ_0 (s)
Gd	8.20	6.38	7	—	—
Tb	11.10	4.78	9	45±1	$(9.6 \pm 0.4) \times 10^{-9}$
Dy	12.2	5.53	10	69±1	$(1.9 \pm 0.4) \times 10^{-12}$
Ho	14.4	6.14	10	34±2	$(2.6 \pm 0.6) \times 10^{-11}$
Er	11.37	5.73	7	—	—
Yb	3.0	2.56	4	—	—

because the use of only NN does not allow AFM behavior as noticed in Section 15.6. The model was corrected by introducing the NNN AFM interactions which may result in an AFM. More details can be found in Chapter 19, where cooperativity effects will be discussed. In the present series, also Yb shows an AFM behavior. This seems to point out a discriminating role of the anisotropy: in the dysprosium derivative the NNN interaction between AFM coupled Dy ions has a dominant role. For holmium and terbium derivatives, the presence of steps in the magnetization suggests weak ferromagnet interaction in the chains. A deeper analysis of these systems requires a more detailed magnetic characterization.

Some relevant parameters are collected in Table 15.5 with analogous data of the other investigated Ln. The first column reports the ratio between χ of the free ion and that of the compound. The second and third columns show the saturation magnetization and the experimental magnetization at 1.45 K in a field of 100 kOe. In almost all cases, the experimental magnetization is much smaller than the saturation magnetization reported in the fourth column. A plot of the magnetization versus field, 0–100 kOe, at 1.55 K clearly show hysteresis, the coercive field being 3 kOe.

It is instructive to have a more accurate look at the field dependence of the magnetization, which is shown in Figure 15.15 in the form of the derivative of the magnetization versus field for the six Ln derivatives. The data show a step at 13.77 kOe, which is independent of the field sweep rate. Analogous results were obtained for Dy, Ho, and Er. The field dependence of the magnetization M shows three steps and a small hysteresis loop. The derivatives of M by H are shown in Figure 15.15. The AC susceptibility was measured down to 1.55 K in the 55–25 kHz frequency range. The data clearly indicate SCM behavior with $\Delta = 45\,\text{K}, \tau_0 = 1 \times 10^{-8}\,\text{s}$. Using the reported slope in the range of 5 K, the correlation length is about 6 spins. Therefore the system must be considered in the infinite regime.

The exponential divergence may be masked by the presence of defects, which cut the chains into segments which are longer than the correlation length ζ. If it is shorter on decreasing temperature, ζ does not become infinite but stops to a constant value.

A graphic procedure to obtain information on the magnetic properties of a series of compounds is the scaling plot. One assumes that χT depends on

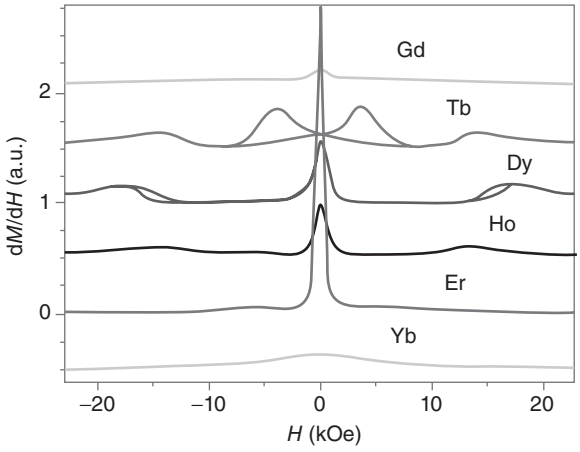

Figure 15.15 Derivatives of the magnetization curves for the Gd, Tb, Dy, Ho, Er, and Yb chains. Magnetization curves were all recorded at 1.55 K and with a field sweep rate of 12 kOe min^{-1}. The first peak observed for the Tb compound around 5 kOe is obviously due to the hysteresis.

exp(2J/kT) where J is the coupling constant. By plotting ln(χT) versus $1/T$, one should obtain a straight line with the slope proportional to J. In Figure 15.16, the scaling plots for the six investigated Ln are reported, and it is immediately apparent that Gd and Yb are completely different from the others presumably due to the anisotropy. The "saturation magnetization" is comparatively closer to the expected one in the Gd and Yb where $M_{\|}$ and $M_{\perp}$ are similar to each other than in Tb–Er where $M_{\perp}$ is small. The anisotropic systems show evidence of field-induced jumps in the magnetization, which in principle provides information on the energy levels. Tb has free-ion χT down to about 50 K, at which point it starts to decrease to a minimum of 6.08 emu K mol^{-1} at 6.9 K. Below, there is a rapid increase, reaching 81 emu K mol^{-1} at 1.89 K. This is the signature of the 1D behavior.

The important feature of these systems is that an Ising behavior is needed for SCM in these f–p chains. The series is long, but at least for the structures of these Ln complexes only the f^8–f^{13} configuration yields the Ising behavior. The Glauber model is good as a first approximation. Additional contributions bound to the individual bricks must be included, as already suggested f or d orbitals. A particularly relevant one is the that of NNN, which in addition to introducing appealing spin frustration effects may dramatically change the anisotropy.

Mixed metal chains were reported also involving Cu and Ln. some of them correspond to systems which presents SCM behavior where there is interacting 3d and 4f ions (Costes *et al.*, 2004). Chemical analysis is consistent with the formula $[(LCu)_2Ln(NO_3)]$ (Ln = Gd^{3+}, Tb^{3+}; LH_3 = 2-hydroxy-*N*-{2-[(2-hydroxyethyl)amino]ethyl]benzamide)) but, unfortunately, it was not possible to study the crystal structure by X-ray diffraction. The analysis of the magnetic properties of the lanthanide derivatives were performed on the basis of the crystal

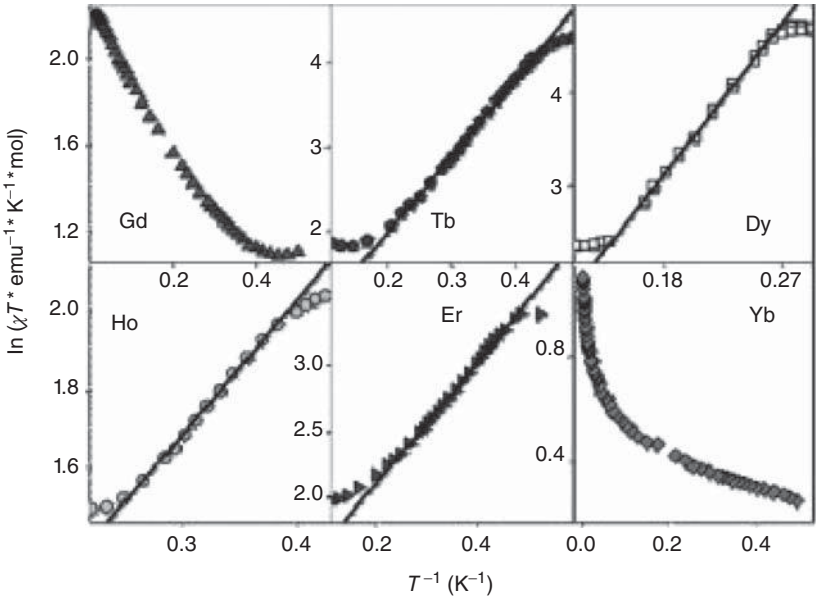

Figure 15.16 Scaling of the data for all the compounds using an Ising temperature dependence of the susceptibility and plotting $\ln(\chi T\,\mathrm{mol\,K^{-1}\,emu^{-1}})$ versus $1/T$. Data for Tb, Dy, Ho, and Er compounds display the predicted scaling behavior. The corresponding fits to the regions with the linear regime are shown as lines. The behavior of Gd and Yb compounds does not agree with the scaling procedure.

structure of the chemically similar $[(LCu)_2Mg(H_2O)_6]\cdot 3H_2O$ complex where Cu^{2+} ions are in a planar environment alternating with octahedral $Mg(H_2O)_6$ moieties. The magnetic properties of the Gd^{3+} were nicely reproduced by assuming a model where a chain of tetranuclear Gd_2Cu_2 units are linked through the gadolinium ions located at the opposite vertices, leading to a good agreement between experimental and observed data by assuming FM Gd–Cu interactions on the order of $1.75-2.5\,\mathrm{cm^{-1}}$. For the terbium derivative, the behavior of the in-phase and out-of-phase susceptibilities and the symmetrical shape of the Cole–Cole plot are characteristic of a SCM with $\tau_0 = 3.8\times10^{-8}\,\mathrm{s}$ and $\Delta = 28.5\,\mathrm{K}$. Apparently, the differences in anisotropy of the two 4f ions seem to play a relevant role in determining the overall magnetic properties of the two compounds.

References

Bencini, A., Gatteschi, D., Zanchini, C., Kahn, O., Verdaguer, M., and Julve, M. (1986) EPR evidence for an unexpected symmetric dinuclear species present in the lattice of an asymmetric dinuclear copper complex. *Inorg. Chem.*, **25**, 3181–3183.

Benelli, C., Caneschi, A., Galleschi, D., Laugier, J., and Rey, P. (1987) Structure and magnetic properties of a gadolinium hexafluoroacetylacetonate adduct with the radical 4,4,5,5-tetramethyl-2-phenyl-4,5-dihydro-1H-imidazole 3-oxide 1-oxyl. *Angew. Chem. Int. Ed. Engl.*, **26**, 913–915.

Benelli, C., Caneschi, A., Gatteschi, D., Pardi, L., and Rey, P. (1989a) One-dimensional magnetism of a linear chain compound containing yttrium(III) and a nitronyl nitroxide radical. *Inorg. Chem.*, **28**, 3230–3234.

Benelli, C., Caneschi, A., Gatteschi, D., Pardi, L., and Rey, P. (1989b) Structure and magnetic properties of linear-chain complexes of rare-earth ions (gadolinium, europium) with nitronyl nitroxides. *Inorg. Chem.*, **28**, 275–280.

Benelli, C., Gatteschi, D., Carnegie, D.W., and Carlin, R.L. (1985) A linear chain with alternating ferromagnetic and antiferromagnetic exchange: Cu(hfac)2.cntdot.TEMPOL. *J. Am. Chem. Soc.*, **107**, 2560–2561.

Benelli, C., Caneschi, A., Gatteschi, D., Sessoli, R. (1992) Magnetic ordering in a molecular material containing dysprosium(III) and a nitronyl nitroxide. *Adv. Mater.*, **4**, 504–505.

Bernot, K., Bogani, L., Caneschi, A., Gatteschi, D., and Sessoli, R. (2006) A family of rare-earth-based single chain magnets: playing with anisotropy. *J. Am. Chem. Soc.*, **128**, 7947–7956.

Bernot, K., Luzon, J., Bogani, L., Etienne, M., Sangregorio, C., Shanmugam, M., Caneschi, A., Sessoli, R., and Gatteschi, D. (2009a) Magnetic anisotropy of dysprosium(III) in a low-symmetry environment: a theoretical and experimental investigation. *J. Am. Chem. Soc.*, **131**, 5573–5579.

Bernot, K., Luzon, J., Caneschi, A., Gatteschi, D., Sessoli, R., Bogani, L., Vindigni, A., Rettori, A., and Pini, M.G. (2009b) Spin canting in a Dy-based single-chain magnet with dominant next-nearest-neighbor antiferromagnetic interactions. *Phys. Rev. B: Condens. Matter Mater. Phys.*, **79**, 134419.

Bernot, K., Luzon, J., Sessoli, R., Vindigni, A., Thion, J., Richeter, S., Leclercq, D., Larionova, J., and van der Lee, A. (2008) The canted antiferromagnetic approach to single-chain magnets. *J. Am. Chem. Soc.*, **130**, 1619–1627.

Bogani, L., Caneschi, A., Fedi, M., Gatteschi, D., Massi, M., Novak, M.A., Pini, M.G., Rettori, A., Sessoli, R., and Vindigni, A. (2004) Finite-size effects in single chain magnets: an experimental and theoretical study. *Phys. Rev. Lett.*, **92**, 207204.

Bogani, L., Sangregorio, C., Sessoli, R., and Gatteschi, D. (2005) Molecular engineering for single-chain-magnet behavior in a one-dimensional dysprosium-nitronyl nitroxide compound. *Angew. Chem. Int. Ed.*, **44**, 5817–5821.

Boucher, J.P., Bakheit, M.A., Nechtschein, M., Villa, M., Bonera, G., and Borsa, F. (1976) High-temperature spin dynamics in the one-dimensional Heisenberg system $(CH_3)_4MnCl_3$ (TMMC): spin diffusion, intra- and interchain cutoff effects. *Phys. Rev. B*, **13**, 4098–4118.

Caneschi, A., Gatteschi, D., Lalioti, N., Sangregorio, C., Sessoli, R., Venturi, G., Vindigni, A., Rettori, A., Pini, M.G., and Novak, M.A. (2001) Cobalt(II)-nitronyl nitroxide chains as molecular magnetic nanowires. *Angew. Chem. Int. Ed.*, **40**, 1760–1763.

Caneschi, A., Gatteschi, D., Lalioti, N., Sangregorio, C., Sessoli, R., Venturi, G., Vindigni, A., Rettori, A., Pini, M.G., and Novak, M.A. (2002) Glauber slow dynamics of the magnetization in a molecular Ising chain. *Europhys. Lett.*, **58**, 771–777.

Caneschi, A., Gatteschi, D., Renard, J.P., Rey, P., and Sessoli, R. (1989) Magnetic coupling in zero- and one-dimensional magnetic systems formed by nickel(II) and nitronyl nitroxides. Magnetic phase transition of a ferrimagnetic chain. *Inorg. Chem.*, **28**, 2940–2944.

Casanova, D., Cirera, J., Llunell, M., Alemany, P., Avnir, D., and Alvarez, S. (2004) Minimal distortion pathways in polyhedral rearrangements. *J. Am. Chem. Soc.*, **126**, 1755–1763.

Cinti, F., Rettori, A., Pini, M.G., Mariani, M., Micotti, E., Lascialfari, A., Papinutto, N., Amato, A., Caneschi, A., Gatteschi, D. *et al.* (2010) Experimental validation of Villain's conjecture about magnetic ordering in quasi-1D helimagnets. *J. Magn. Magn. Mater.*, **322**, 1259–1261.

Clérac, R., Miyasaka, H., Yamashita, M., and Coulon, C. (2002) Evidence for single-chain magnet behavior in a MnIII – NiII chain designed with high spin magnetic units: a route to high temperature metastable magnets. *J. Am. Chem. Soc.*, **124**, 12837–12844.

Costes, J.-P., Clemente-Juan, J.M., Dahan, F., and Milon, J. (2004) Unprecedented $(Cu_2Ln)_n$ complexes ($Ln = Gd^{3+}$, Tb^{3+}): a New "single chain magnet". *Inorg. Chem.*, **43**, 8200–8202.

Coulon, C., Clérac, R., Wernsdorfer, W., Colin, T., Saitoh, A., Motokawa, N., and Miyasaka, H. (2007) Effect of an applied magnetic field on the relaxation time of single-chain magnets. *Phys. Rev. B: Condens. Matter Mater. Phys.*, **76**, 214422, 1–15.

Coulon, C., Miyasaka, H., and Clérac, R. (2006) Single-chain magnets: theoretical approach and experimental systems. *Struct. Bond.*, **122**, 163–206.

Dei, A., Gatteschi, D., Massa, C.A., Pardi, L.A., Poussereau, S., and Sorace, L. (2000) Spontaneous symmetry breaking in the formation of a dinuclear gadolinium semiquinonato complex: synthesis, high-field EPR studies, and magnetic properties. *Chem. Eur. J.*, **6**, 4580–4586.

Delgado-Martinez, P., Gonzalez-Prieto, R., Gomez-Garcia, C.J., Jimenez-Aparicio, R., Priego, J.L., and Torres, M.R. (2014) Structural, magnetic and electrical properties of one-dimensional tetraamidatodiruthenium compounds. *Dalton Trans.*, **43**, 3227–3237.

Gatteschi, D. and Vindigni, A. (2014) in *Molecular Magnets* (eds J. Bartolomé, F. Luis, and J.F. Fernandez), Springer-Verlag, Berlin, Heidelberg, pp. 191–220.

Glauber, R.J. (1963) Time-dependent statistics of the Ising model. *J. Math. Phys.*, **4**, 294–307.

Haldane, F.D.M. (1983) Nonlinear field theory of large-spin Heisenberg antiferromagnets: semiclassically quantized solitons of the one-dimensional easy-axis Néel state. *Phys. Rev. Lett.*, **50**, 1153–1156.

Kajiwara, T., Nakano, M., Kaneko, Y., Takaishi, S., Ito, T., Yamashita, M., Igashira-Kamiyama, A., Nojiri, H., Ono, Y., and Kojima, N. (2005) A single-chain magnet formed by a twisted arrangement of ions with easy-plane magnetic anisotropy. *J. Am. Chem. Soc.*, **127**, 10150–10151.

Morosin, B. and Graber, E.J. (1967) Crystal structure of tetramethylammonium manganese(II) chloride. *Acta Crystallogr.*, **23**, 766–770.

Nakano, M. and Oshio, H. (2011) Magnetic anisotropies in paramagnetic polynuclear metal complexes. *Chem. Soc. Rev.*, **40**, 3239–3248.

Palii, A., Tsukerblat, B., Klokishner, S., Dunbar, K.R., Clemente-Juan, J.M., and Coronado, E. (2011) Beyond the spin model: exchange coupling in molecular magnets with unquenched orbital angular momenta. *Chem. Soc. Rev.*, **40**, 3130–3156.

Pini, M., Rettori, A. (1993) Thermodynamics of alternating spin chains with competing nearest- and next-nearest-neighbor interactions: Ising model. *Phys. Rev. B*, **48**, 3240–3248.

Skinner, J.L. (1983) Kinetic Ising model for polymer dynamics: Applications to dielectric relaxation and dynamic depolarized light scattering. *J. Chem. Phys.*, **79**, 1965–1974.

Schneidman, E., Berry II, M.J., Segev, R., Bialek, (2006) Weak pairwise correlations imply strongly correlated network states in a neural population, *Nature*, **440**, 1007.

Stauffer, D. (2005) Teaching computational bio-socio-econo-physics. *Eur. J. Phys.*, **26**, S79.

Sun, H.L., Wang, Z.M., and Gao, S. (2010) Strategies towards single-chain magnets. *Coord. Chem. Rev.*, **254**, 1081–1100.

Villain, J. (1978) Chiral order in helimagnets. *Ann. Isr. Phys. Soc.*, **2**, 565.

Yamashita, M., Ishii, T., and Matsuzaka, H. (2000) Haldane gap systems. *Coord. Chem. Rev.*, **198**, 347–366.

Zhang, W.X., Ishikawa, R., Breedlove, B., and Yamashita, M. (2013) Single-chain magnets: beyond the Glauber model. *RSC Adv.*, **3**, 3772–3798.

16
Magic Dysprosium

16.1
Exploring Single Crystals

To study in more detail the properties of molecular magnetism (MM) based on Ln requires the ability to manage sophisticated experimental and theoretical techniques. Topics that were the hunting reserve of very few people, due to their complexity, nowadays are routine techniques that are mandatory if one wants to gain a minimum of information needed to understand the magnetic properties. We have already mentioned these techniques in the previous chapters when introducing concepts such as single molecule magnets (SMMs), single chain magnets (SCMs). We wish to explore the techniques to be handled, but instead of doing that in a systematic way we prefer to introduce a series of connected examples by referring to Dy. We choose Dy for several good reasons, the first being the abundance of materials containing that metal ion and of techniques covering many different fields that are being used for their characterization. The unique features of Dy (Gatteschi, 2011) were pointed out by one of us in a short note in *Nature* entitled "Anisotropic Dysprosium"; the conclusion was that a system such as that of the Dy compounds whose properties are so sensitive to many subtle features is a challenge for chemists. It seems that the challenge is being met.

The anisotropy of Dy has several components, one of which is associated with the splitting of the ground $J = 15/2$ multiplet into a series of Kramers doublets. The splitting can be justified by the Hamiltonian associated with the ligand field (LF) interaction, which depends on the nature of the ligands and their location in the coordination sphere. The LF is responsible for the magnetic properties and, vice versa, the fit of the magnetic properties provides a view of the symmetry of the compound. This is often wishful thinking, because the LF treatment is parametric and having reliable values of the parameters is problematic. Luckily, in the past years *ab initio* techniques have become very efficient (Chibotaru, Ungur, and Soncini, 2008; Cucinotta *et al.*, 2012), yielding basic information that allows several problems to be solved from the outset.

The analysis of the magnetic properties of DyNITR derivatives in two similar coordination environments can provide information on the next-nearest-neighbor (NNN) (For the definition of NNN, see Chapter 15) interaction between

Introduction to Molecular Magnetism: From Transition Metals to Lanthanides, First Edition.
Cristiano Benelli and Dante Gatteschi.
© 2015 Wiley-VCH Verlag GmbH & Co. KGaA. Published 2015 by Wiley-VCH Verlag GmbH & Co. KGaA.

radicals and Dy. To produce an accurate analysis, it is fundamental to perform measurements on single crystals as we have discussed in Chapter 15. This technique requires attention to avoid misfit of data. The information on the magnetic properties can be obtained with several different techniques, which ideally should provide static and dynamic properties, space orientation, and so on. A clear example is magnetic susceptibility, which is the linear response of the material to an applied magnetic field. It has a spatial dependence that provides a lot of information, but which must be obtained at some cost. And sometimes money alone is not enough! The most accurate way to obtain insight into the electronic structure of molecular systems is by performing measurements on single crystals, because in principle this can provide the values of the susceptibility in the molecular frame. But this is strongly dependent on the molecular and crystal structure. The magnetic susceptibility of molecules can be described by a tensor, which has principal directions and values. The tensors respond to crystal symmetry requirements, which dictate the number and the relative orientation of the tensors. In a weak field, it is not possible to obtain the individual tensors, but only the crystal averages.

Let us consider how the crystallographic symmetry may influence the susceptibility pattern. Monoclinic lattices are quite common in MM, so we use monoclinic symmetry as an example. In a monoclinic cell with C_2 symmetry, the possible local symmetries of the metal ions are C_1, C_i, C_s, and C_2. If one molecule is in a C_1 site, the χ_1 tensor has no limitation, so in principle χ_{ij1} can have all the values, as shown in Figure 16.1. There must be an equivalent molecule related through the C_2 axis parallel to the $b(y)$ crystal axis. The tensor of the second molecule will be referred to that of the first molecule according to $\chi_{ii1} = \chi_{ii2}$; $\chi_{xy1} = -\chi_{xy2}$; $\chi_{yz1} = -\chi_{yz2}$; and $\chi_{xz1} = \chi_{xz2}$. The two tensors are the same but have different orientations. This case is often referred to as *magnetically not equivalent tensors*. Magnetic measurements on a single crystal will find one tensor with a principal direction parallel

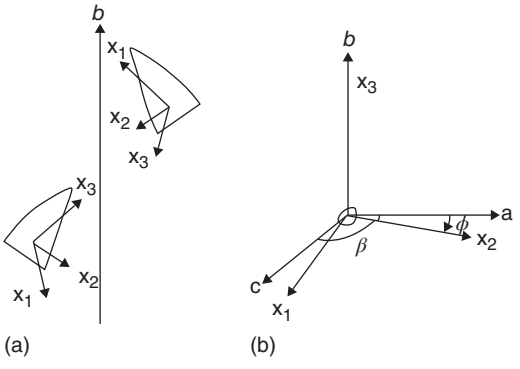

Figure 16.1 (a) Principal molecular magnetic axes related by a C_2 axis parallel to the crystal axis *b* and (b) one principal crystal susceptibility is constrained to lie along *b* by symmetry.

to b, the other two axes being at arbitrary angles in the ac plane. The observed χ, which is the crystal susceptibility, is the sum of the two molecular χi's.

Although the two molecular χi's have no symmetry, the crystal susceptibility χ has binary symmetry. Let us try to use some numbers. Suppose we want to explore the values of magnetic susceptibility in the bc plane. The principal values of the molecular magnetic susceptibility for molecule 1 make an angle α with the b axis and an angle $180° - \alpha$ with the c^* axis. The corresponding values for the molecule 2 form an angle $-\alpha$ with the b axis being this one a binary axis of symmetry. The experimental measured susceptibility is the sum of the two molecular contributions. The two symmetry related projections mentioned above form, therefore, a 2α angle. In the particular case of $\alpha = 45°$, the system exhibits a quasi-axial behavior which is originated by the crystalline symmetry but not by the molecular one. It is apparent that neglecting this problem may lead to erroneous interpretations, such as assuming an axial molecular symmetry while the actual symmetry is lower. In order to avoid mistakes, the structure must be known and, if several polymorphs are available, the one with the most suitable orientation of the molecules must be chosen. "Best oriented" means the system where the local tensors are as parallel as possible to each other. This condition, for instance, is met in a tetragonal crystal if the molecule lies in a tetragonal site (remember the Mn_{12} cluster lies on an S_4 site in a tetragonal crystal). A tetragonal site in a cubic crystal, on the other hand, does not meet the orientation requirement. Space groups that meet the requirement are the triclinic ones, where there is either one or two sites related by an inversion center. The orientation of the magnetic tensor in the cell is not fixed and must be experimentally determined to gather the principal values and the principal directions. If the two molecules are referred by C_i they are equivalent and the molecular susceptibility will be identical to the crystal susceptibility.

A good example is that of $[Dy(hfac)_3(NITPhOEt)_2]$, where a preliminary analysis found that it crystallizes in the triclinic space group $P\overline{1}$ (N.2), with two molecules in the unit cell. The molecules are related by an inversion center, that is, there is only one tensor and the molecular and crystal χ values are identical. The experimental procedure to measure the magnetization of a triclinic crystal may be delicate, but if correctly made a reliable result is guaranteed.

The static magnetization of $[Dy(hfac)_3(NITPhOEt)_2]$ was measured with the field rotated in three laboratory planes defined by the X, Y, and Z axes. X is parallel to a, Z is parallel to $c^* = a \times b$, and b' is orthogonal to X and Y (Bernot *et al.*, 2009). The magnetizations shown in Figure 16.2 were measured at 2.5 K. It is apparent that the χ tensor is very anisotropic in the XZ plane, with minimum anisotropy in the XY plane. The angular dependence in the planes follows the tensorial dependence:

$$M(\theta) = \chi_{\alpha\alpha} H(\cos\theta)^2 + \chi_{\beta\beta} H(\sin\theta)^2 + 2\chi_{\alpha\beta} H \sin\theta \cos\theta \tag{16.1}$$

Standard techniques provide the principal values and directions, which are shown in Figure 16.2. At least three orthogonal rotations are needed to reconstruct the **M** tensor.

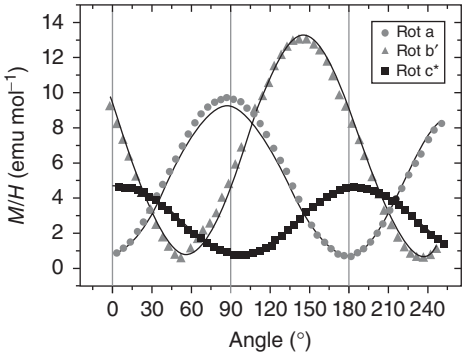

Figure 16.2 Angular variation of the molar susceptibility (*M*/*H* ratio) of $[Dy(hfac)_3(NITPhOEt)_2]$ at $T = 2.5$ K along the three axes of the laboratory frame. At $\theta = 0$ and 90°, respectively, *H* is parallel to *b*′ and c* for the rotation around a, c* and a for the b′ rotation, and a and b′ for c* rotation.

The easy axis corresponds to $\chi T = 33.0$ emu K mol^{-1}, while the hard and intermediate axis correspond to $\chi T = 0.5$ and $\chi T = 3.25$ emu K mol^{-1}, respectively. This corresponds to Ising-type anisotropy. The easy axis corresponds to the pseudo C_2 axis of the coordination polyhedron, giving some opportunity to the qualitative appreciation of the LF effects in the 4f orbital.

Nowadays, *ab initio* calculations are becoming relatively easy to use at acceptable computational costs even of complex systems such as Ln complexes (Bernot *et al.*, 2009). In the case under discussion, complete active space self-consistent field (CASSCF) calculations were performed on a simplified molecular model which provided sufficient understanding of the Dy ion (Table 16.1).

The calculations suggest that the lowest Kramers doublet is described by a wave function characterized by $M_J = \pm 15/2$. This shows a strong Ising-type anisotropy of the Dy ion, as already observed in similar compounds. Assuming that the antiferromagnetic (AFM) coupling between the NNN radicals is large, the two spins of the radicals are paired and the *g*-value of the complex is equal to the value of the ion. The Kramers doublet is treated as an effective spin $S = 1/2$. In a field parallel to *z*, the levels split as $g_{zeff}\mu_B m_J H$ where $g_{zeff} = 15/2 g_J$. The value of g_J is 4/3, therefore $g_{zeff} = 2g_J\ 15/2 = 20$. A weak field parallel to *x* or *y* does not remove the degeneracy of the doublet, and therefore $g_{xeff} = g_{yeff} = 0$. It is necessary, though, to have a better view of the physics of the system in order to have a detailed view of the factors influencing the energies of the low-lying levels, which are of fundamental importance for the magnetic properties. It is, thus, necessary to perform some more experiments.

Field dependence in the range 2.5–15 K was measured parallel to the easy and hard axis, respectively. The anisotropy remains constant and χT goes through a broad maximum. Field dependence of magnetization at 1.6 K up to 120 kOe was measured on polycrystalline powders. It seems adequate to assume that the Dy has a ground doublet the separation of which from the first excited doublet is

Table 16.1 Energy levels of the $^6H_{15/2}$ multiplet and principal gyromagnetic factors for the ground Kramers doublet state computed for Dy^{3+} in $[Dy(hfac)_3(NITPhOEt)_2]$ using the CASSCF–RASSI-SO *ab initio* method (Bernot *et al.*, 2009).

	A[a)]	B[b)]	C[c)]	D[d)]
Energy levels (cm^{-1})				
E_1	30.2	30.3	29.9	40.4
E_2	62.1	63.0	62.6	75.0
E_3	66.6	67.4	67.4	79.1
E_4	99.6	101.5	101.5	111.4
E_5	114.7	116.0	115.8	128.9
E_6	215.9	220.6	221.0	237.8
E_7	372.8	380.2	380.0	411.1
Principal *g*-values				
g_x	1.5	1.7	1.8	1.0
g_y	1.3	1.4	1.4	0.9
g_z	17.6	17.5	17.4	18.2

a) Includes in the RASSI-SO calculation all of the CASSCF roots in the 0–40 000 cm^{-1} energy range.
b) Same as A, except that only the sextet roots are considered.
c) Considers only the ^6H roots from a CASSCF state average calculation with a total of 18 sextet roots.
d) Same as C, but using a CASSCF state average calculation with the 11 lowest sextet roots.

large compared to kT below 4 K. The magnetic data reported previously suggest that the ground state can be described by three interacting doublets through the spin Hamiltonian:

$$\mathcal{H} = J\mathcal{S}_{R1}\mathcal{S}_{R2} + J'(\mathcal{S}_{R1z} + \mathcal{S}_{R2z})\sigma + g_{R1z}\mathcal{S}_{R1z}\,\mu_B H_z + g_{R2z}\mathcal{S}_{R2z}\,\mu_B H_z + g_{Dy}\mu_B\sigma H_z \tag{16.2}$$

where the Ising nature of Dy is taken into account by $\sigma = \pm 1/2$. The energies of the four Kramers doublets are given by

$$\begin{aligned} E_{1,2} &= \pm\frac{1}{2}\, g_{Dy}\mu_B H \\ E_{3,4} &= J_{NNN} + \frac{1}{2}\, J_{NN} \pm \left(g_R + \frac{1}{2}\, g_{Dy}\right)\mu_B H \\ E_{5,6} &= J_{NNN} \pm \frac{1}{2}\, g_{Dy}\mu_B H \\ E_{7,8} &= J_{NNN} - \frac{1}{2}J_{NN} \pm \left(g_R - \frac{1}{2}g_{Dy}\right)\mu_B H \end{aligned} \tag{16.3}$$

For a field parallel to the easy axis, it is easy to calculate analytical expressions for magnetization. Assuming that the **g** tensor of the radical is isotropic and equal to 2.00, only three parameters are needed. Beyond the NN coupling constant, the analysis of the magnetic data of an analogous Gd derivative proved the need to introduce the NNN interaction (Benelli *et al.*, 1990). Detailed studies of the effects of spin frustration yielding chiral magnetic order will be reported in Chapter 19.

A limit to the value of NITR J_{NNN} could be given by measuring the Y derivative, which showed an AFM behavior (Benelli *et al.*, 1989) between the radicals interacting with the same radical. Fitting the T dependence of χ yielded $J_{NNN} = 15\ \text{cm}^{-1}$. Using this and by varying the other two parameters, the best fit gave $g_{Dy} = 19.7$, $J\,J_{NN} = -13.5\,\text{cm}^{-1}$. Expectedly, there is a large correlation between the J_{NN} and J_{NNN} values. The value of g_{Dy} is an effective one. If we assume that the J_{NNN} between the radical spins is dominant at low temperature, the system is in the ground state, that is, it is nonmagnetic. Then the g_{Dy} for the ground doublet is given by $g_J J$ for $g_{\|}$ and zero for $g_{\perp}$.

16.2 The Role of Excited States

An early example of Dy's versatility was provided by a series of trinuclear compounds with the formula $[Dy_3(\mu_3OH)_2L_3Cl(H_2O)_5]Cl_3$ where L is the anion of *o*-vanillin(2-hydroxy-3-methoxybenzaldehyde) sketched in Scheme 16.1 (Tang *et al.*, 2006).

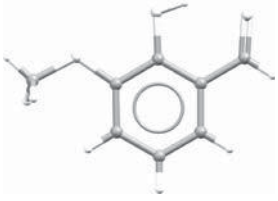

Scheme 16.1 *o*-vanillin anion.

In the presence of AFM coupling, triangles immediately give rise to frustration, chirality, and all sorts of complex phenomena (Baker *et al.*, 1991; Coronado *et al.*, 2007; Liu *et al.*, 2011; Demir *et al.*, 2012). Given the increasing interest for all systems that show complex behavior, Ln-based systems were taken into consideration and a Dy trinuclear complex was found to give rise to novel properties. As we will soon see, the molecule has a toroidal dipolar magnetic behavior. All the words need to be explained and more must be introduced, all of which will require additional explanation. The Dy_3 cluster is often called the prototype Dy_3 to highlight that and, like Mn_{12}, it has been the beginning of a new scientific field which has much promise for the future.

As everybody knows, a torus is a donut but many people perhaps ignore its scientific relevance. Electric dipoles correspond to a charge separation, and magnetic dipoles correspond to a current flowing along a loop. Currents flowing on a surface of a torus along its meridians (poloidal currents) generate a toroidal dipole. The toroidal dipole can also be represented as a closed loop of magnetic dipoles arranged head to tail. Tori were early applied to nuclear physics, but more recently they have been used in the field of multiferroics. From multiferroics to molecular materials, there is only a little step and indeed the interplay between the two types of materials is under increasing attention.

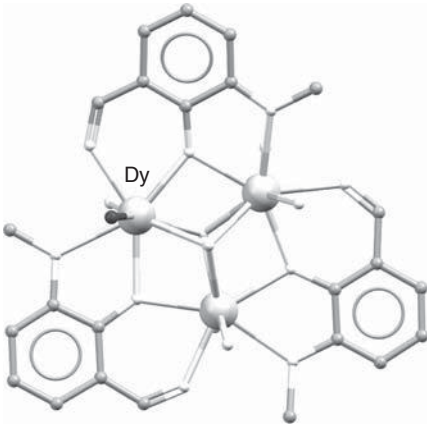

Figure 16.3 View of the molecular structure of $[Dy_3(\mu_3OH)_2L_3Cl(H_2O)_5]Cl_3$ (Oxygen = white; Chlorine = black).

Toroidal dipoles have been detected in molecules, by calculations, and now they are observed in molecular magnets. There are expectations that molecular materials are akin to multiferroics because the properties have a feeling of partially localized systems.

The structure of the archetypal Dy_3 is shown in Figure 16.3. The core is formed by a triangle of Dy in which the metal ions are connected by a μ_3OH bridge above and a μ_3OH bridge below the plane. Three additional μ_2OR of three vanillin bridges along the Dy–Dy directions are present. The compound crystallizes in the monoclinic space group $C2/c$ but the cluster has C_1 symmetry.

By and large, the triangle can be considered as isosceles, with intra-triangle Dy–Dy distances in the range 3.50–3.53 Å. Magnetic measurements show evidence of AFM coupling (Tang *et al.*, 2006) with the usual observation of decreasing χT on decreasing T. So far so good, but a big surprise was found, namely the observation that the susceptibility goes through a maximum at about 6.5 K and χT tends to zero at $T = 0$ K. These data indicate a nonmagnetic ground state, which is not expected for three spins, at least for a Heisenberg cluster (Luzon *et al.*, 2008). Now the problem is to understand the origin of such a behavior in a system with an odd number of Kramers' doublets.

A possibility is that intermolecular AFM interactions are present, which pair the spins. The observed maximum in χ is rather broad, excluding a transition to long-range magnetic order. Further, no short contact is observed between Dy ions of different triangles, so the AFM interaction between triangles possibility breaks down. The explanation of the magnetic properties must be found inside the triangles.

Additional information comes from the field dependence of the magnetization ($\boldsymbol{M}$) of an ensemble of polycrystalline powders at $T = 1.8$ K. From 0 to about 0.95 T, $\boldsymbol{M}$ increases slowly, then more rapidly to reach 15.6 μ_B at 7 T. This value compares well with that expected for three uncorrelated magnetic moments for

the Dy^{3+} ion. Single-crystal magnetizations with the magnetic field parallel and perpendicular to the Dy_3 plane show a very small $\boldsymbol{M}$ value for the latter and the maximum for the former. It is well known that Dy has a ground state described by an effective $S = 1/2$ with easy axis of magnetization. This view has been confirmed by CASSCF calculations.

It may be instructive to work out in some detail the difference between the Heisenberg and Ising models for triangular clusters. Let us assume trigonal symmetry D_3 for the sake of simplicity. In both cases the system is frustrated. The Heisenberg model splits the eight levels into a quartet and two degenerate doublets of lowest energy. Using group theory, the levels can be labeled as $^4A_2$ and ^2E. A_2 and E describe the orbital contribution introduced by the presence of three ions.

For the Ising model, one can use the Hamiltonian in the form

$$\mathscr{H} = \sum_{i<k} J_z \sigma_i \sigma_k \tag{16.4}$$

where σ_i are the Pauli matrices. The eight states are split in zero field into six and two degenerate states.

The data show that the strong anisotropy localizes the moments in the plane perpendicular to the trigonal axis. Let us assume that the system can be considered as formed by three ions weakly antiferromagnetically coupled. Each ion has a ground Kramers doublet, which is characterized by a very anisotropic g. The temperature and field dependence of the magnetic properties can now be understood, at least at a qualitative level. Assume that the easy axes of each spin can be described by ↑ and ↓, which means that we will read, for instance, (↑↑↑) as indicating that the three vectors are parallel to their $+z_i$ axes. A possible orientation of the spins is shown in Figure 16.4.

The possible microstates are given in Table 16.2. The energies of the lowest lying doublets can be easily calculated using an Ising approach. The energies of the eight states in the absence and presence of a field are as reported in Table 16.2. The first column shows the microstates of the 1, 2, and 3 Dy ions. The second reports the result of introducing the exchange $J\mathcal{S}_i\mathcal{S}_k$ and applying it to all the states. It is apparent that the Ising splitting into two and six levels is completely different from the Heisenberg exchange splitting into 4 + 2 + 2. Assuming that the three easy axes make angles of 120° between them, it is impossible to excite only one of them. There are two limiting cases depending on the position where the

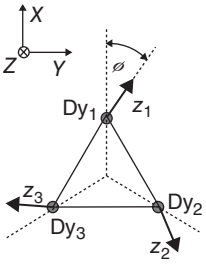

Figure 16.4 Schematic view of the spin structure of the triangular cluster. (Reproduced from Luzon, J. *et al.* (2008) with permission from The American Physical Society.)

Table 16.2 Energies of a triangle of Ising spins.

Basis set[a)]	Energy at zero field	Energy correction in a magnetic field
$\|\uparrow\uparrow\uparrow\rangle$	3J/4	0
$\|\downarrow\uparrow\uparrow\rangle$	−J/4	$g\mu_B H$
$\|\uparrow\downarrow\uparrow\rangle$	−J/4	$g\mu_B H$
$\|\uparrow\uparrow\downarrow\rangle$	−J/4	$-2g\mu_B H$
$\|\uparrow\downarrow\downarrow\rangle$	−J/4	$-g\mu_B H$
$\|\downarrow\uparrow\downarrow\rangle$	−J/4	$-g\mu_B H$
$\|\downarrow\downarrow\uparrow\rangle$	−J/4	$2g\mu_B H$
$\|\downarrow\downarrow\downarrow\rangle$	3J/4	0

a) Up and down refer to the local z-axes.

easy axes are placed, namely parallel to the bisectors or the edges of the triangles. The results are different but similar. In both cases, a jump in the magnetization is expected as experimentally observed (Figure 16.5). Given the great simplicity of the model, it is very rewarding that so many features of the experimental data find justification.

The attempts to fit the structural and magnetic properties were increasing in detail step after step. After establishing that the ground state can be described as the combination of three S = 1/2 states which are AFM coupled, using the structural coordinates slightly arranged to justify trigonal symmetry the parameters obtained by Sessoli *et al.* were acceptable (Luzon *et al.*, 2008). In particular, $g_x = 20$ and all the other components being zero agree well with what was expected.

Although at first glance surprising, a number of hand-waving arguments give a first hint which can be tested. First of all, the S = 0 ground state can be justified if we allow for nonparallel orientation of the spins, as shown in Figure 16.4 (Zhang, Guo, and Tang, 2013).

The model is very simple, and the key feature is the orientation of the individual vectors that define a torus. It is an exciting perspective to see how easily Dy ions provide a sophisticated spin arrangement. Several results have already been reported, starting from the more detailed description of the properties of Dy_3.

On the basis of the above description, it is possible to fit M versus H and χ versus T, assuming that the eight states originating from the three local doublets provide a good starting point. The interaction Hamiltonian includes an Ising term and a Zeeman term which sets $g_\perp = 0$.

$$\mathscr{H} = \sum_{i,k=1,2,3}^{i>k} J_{zz}\mathcal{S}_{zi}\mathcal{S}_{zk} - \mu_B \sum_{i=1,2,3} g_z H_z \mathcal{S}_{zi} \tag{16.5}$$

The best fit values are $J_{zz} = 10.6(4)$ K, $g_z = 20.7(1)$. In zero field, the eight levels are grouped in six, with two the lowest being a Kramers doublet. We recall that in HDVV the eight levels split into a quartet and two degenerate Kramers

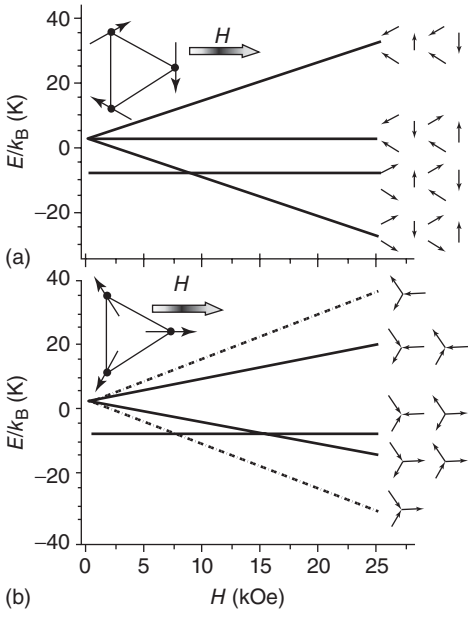

Figure 16.5 (a) Zeeman splitting of the levels due to the application of the field along the *X*-axis (bisector) calculated with the spin Hamiltonian (Eq. 16.5) and the parameters indicated in the text, assuming $\Phi = 90°$. (b) Same diagram calculated with $\Phi = 0$. The spin structure for each state is schematized by the arrows. The nondegenerate states are highlighted by dashed lines. (Reproduced from Luzon, J. *et al.* (2008) with permission from The American Physical Society.)

doublets. Triangles are possible candidates for revealing antisymmetric exchange. But the expected effect is to remove the accidental degeneracy of the two Kramers doublets. So the Ising model is unique.

The calculated levels for a field applied parallel to the easy axes of one Dy are shown in Figure 16.5.

The agreement is good, but in order to reproduce the increase of the magnetization for fields larger than 20 kOe, some improvement is needed. A good one is obtained introducing an excited Kramers doublet for the individual Dy characterized by $M_J = \pm 13/2$ at a distance Δ from the ground. The improvement in the fit is dramatic, with the parameters $J = -0.092(2)$ K, $g = 1.35(1)$, and $\Delta = 102(5)$ K.

The dynamic properties are even more interesting. In fact, the AC susceptibility shows evidence of slow relaxation which can be fitted with the Arrhenius law, with $\tau_0 = 2.5(5) \times 10^{-7}$ s, $\Delta = 36(2)$ K. This is a clear indication of SMM behavior, but the ground state is nonmagnetic. Therefore, this must be considered as SMM behavior in the excited state. Further, the relaxation can occur also by tunneling, and Dy_3 has been proven to be an excellent material for investigating quantum phenomena.

We recall that the lowest doublet is formed by two states that differ in spin chirality: that is, one connects the Dy ions by a left-polarized wave and the other

a right-polarized one. The overall tunneling is particularly efficient close to zero field. The application of a weak field dramatically changes the relaxation time because it splits the doublet and quenches the possibility of resonant tunneling. This, indeed, is a feature that emerges in many cases and is often referred to as *quantum tunneling*. The same phenomenon is observed at level crossing, because again the underbarrier mechanism becomes prominent. In the intermediate region, on the other hand, the system goes back to thermally activated behavior with a barrier as high as 120 K.

Another fascinating aspect of Dy_3 is that it can be used as a starting point to obtain more complex systems. In a bottom-up approach, the first step may correspond to add a second triangle yielding a doubled structure Dy_6 (Hewitt *et al.*, 2010). From the chemical point of view, the key is the partial replacement of HL of the *o*-vanilline ligand with a new one as indicated below (Scheme 16.2).

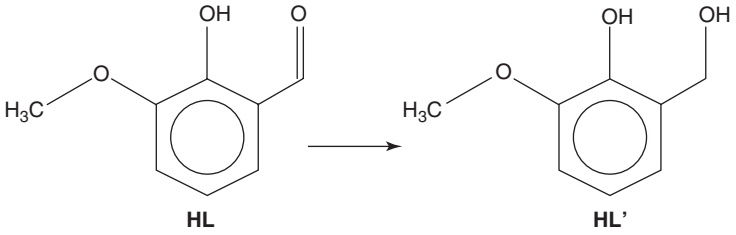

Scheme 16.2 HL (*o*-vanillin, left) and H_2L' (2-hydrox-ymethyl-6-methoxyphenol, right).

The scheme of the structure as far as the Dy_3 moieties are concerned is shown in Figure 16.6.

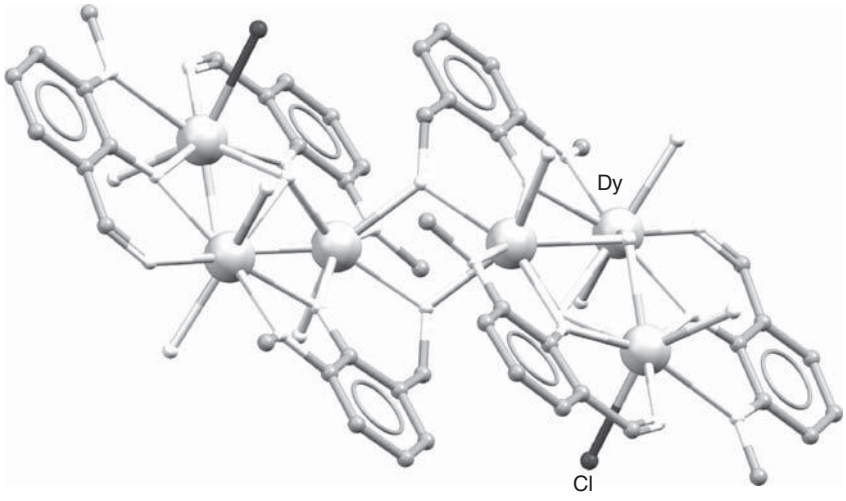

Figure 16.6 Structure of the $[Dy_6(\mu_3\text{-}OH)_4L_4L'_2Cl(H_2O)_9]^{5+}$ cation.

The planes of the two Dy_3 triangles are strictly parallel, but not coplanar: the perpendicular distance between them is 0.248 nm with the $Dy_3 \ldots Dy_3'$ vector at 48.4° to the normal of the Dy_3 planes. The static magnetic susceptibility agrees with the values expected for two Dy_3. A peculiar feature in the temperature dependence of the magnetic susceptibility is a maximum in χ observed at 3 K under an applied field of 10 kOe to be compared to 7 K observed in Dy_3. The use of a CASSCF approach for the three different Dy^{3+} ions, including the effect of the spin–orbit coupling (Bernot *et al.*, 2009), provide information on a large anisotropy of the gyromagnetic factors ($g_z \gg g_x, g_y$), and a large energy gap between the ground and first excited Kramer's doublet justified the Ising approximation used.

The computed single-ion easy anisotropy axes, where θ is the angle subtended by an easy axis with respect to the plane of the triangle and ϕ is the angle between the projection of each easy axis on to the plane of the triangle, and the corresponding bisector of the triangle are reported in Figure 16.7 where the same approach described for Dy_3 is extended to two triangles.

As the system crystallizes in a triclinic space group, to evaluate the effects of breaking the trigonal symmetry characteristic of Dy_3, a single-crystal magnetic characterization was performed. The collected data showed that, in the large angular dependence of the magnetization, the positions of the maxima and minima change significantly on going from 1.9 to 10 K, but remain almost unaltered up to the highest investigated temperature (25 K) in contrast to what was observed in Dy_3 and monomeric Dy systems. This pattern can be attributed to the way in which the two triangles have been linked. To validate this hypothesis,

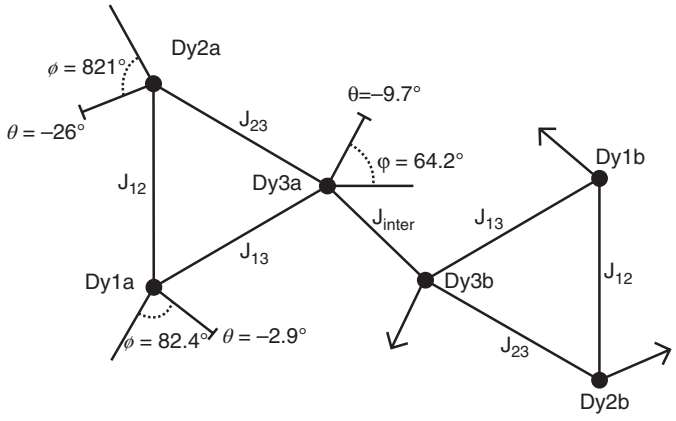

Figure 16.7 The calculated easy axes. The arrows represent the positive directions of the associated local *z*-axes used in the spin Hamiltonian (16.6) and the angles of these to the plane defined by the triangular moiety (θ). The angles of their projections on to the triangular plane with the bisector of the triangle (ϕ) are also indicated. The shape of the arrows is indicative of their relative orientation with respect to the plane the page. The magnetic interactions derived from the spin Hamiltonian are also shown. (Reproduced from Hewitt, I.J. *et al.* (2010) with permission from Wiley-VCH Verlag GmbH & Co. KGaA.)

the single-crystal magnetic data were fitted with an Ising spin Hamiltonian by considering each Dy^{3+} as an Ising spin with S = 1/2, as we previously mentioned for Dy_3:

$$\mathcal{H} = -J^{z}_{\text{int}} \mathcal{S}^{3a}_{z_3} \mathcal{S}^{3b}_{z_3} - \sum_{i,j=1,2,3}^{n=a,b} \sum_{i<j} J^{zz}_{ij} \mathcal{S}^{in}_{z_i} \mathcal{S}^{in}_{z_j} - \sum_{i=1,2,3}^{n=a,b} g_{z_i} \mathcal{S}^{in}_{z_i} H_{z_i} \tag{16.6}$$

where the index n refers to the two different triangular moieties, denoted as a and b, and the indexes i and j refer to the three different Dy^{3+} ions in each triangle (Figure 16.7). $S^{in}_{z_i}$ denotes the spin operator for the inth Dy ions inside the n Dy_3 triangle (Dy_3) along its local easy anisotropy axis z_i. J^{zz}_{ij} corresponds to the Ising magnetic interactions within the triangular moiety, and J^{z}_{int} is the magnetic interaction between the two connected Dy_3 ions in different triangles. Finally, g_{z_i} and H_{z_i} are the gyromagnetic factors and the applied magnetic field, respectively, along the z_i local axes. The two triangular moieties are related by an inversion center, and therefore the local axes z_i and the parameters J^{zz}_{ij} and g_{z_i} do not depend on the triangle index n. Using the g_{z_i} the gyromagnetic factors ($g_{z_1} = 19.8, g_{z_2} = 19.7$, $g_{z_3} = 19.3$) and the directions of the z_i local axes previously obtained from *ab initio* calculations, the unknown parameters of the Hamiltonian model are the four independent magnetic interactions indicated in Figure 16.7. The simulation of the angle-resolved magnetic susceptibility data gives AFM interactions with $J^{zz}_{12} = 5.3\,\text{cm}^{-1}$, $J^{zz}_{13} = 4.2\,\text{cm}^{-1}$, $J^{zz}_{23} = 3.5\,\text{cm}^{-1}$, and $J^{z}_{\text{int}} = 0.8\ \text{cm}^{-1}$.

16.3 A Comparative Look

Valdien (H_2valdien = N_1,N_3-bis(3-methoxysalicylidene)diethylenetriamine) can be used for obtaining dinuclear derivatives and to compare the magnetic interactions in pairs of Eu, Gd, Tb, Dy, and Ho (Long *et al.*, 2011). A sketch of the structure of $[Dy_2(\text{valdien})_2(NO_3)_2]$ is shown in Figure 16.8.

The triclinic crystals, as stated several times, are useful because there is only one orientation per molecule per cell. The Dy^{3+} ions are 8-coordinate, and SHAPE (Casanova *et al.*, 2005) analysis suggests an intermediate geometry between a squared antiprism (SAP) and a dodecahedron. High-T magnetic measurements show the usual boring behavior with a slowly decreasing χT versus T. At low temperature, however, matters become more interesting. AC measurements in the range 2–12 K show slow relaxation of the magnetization, with evidence of one species as expected for the triclinic cell (Figure 16.9).

Measurements performed at 0.04 K show magnetization steps for applied fields in the range −0.3 to 0.3 T. This is a clear indication that the ground state is nonmagnetic. By varying the field, M increases, providing evidence of an excited state that can be populated under these conditions. Indeed, the experiments at 0.04 K performed at different sweep rates show two steps at ±0.3 T, evidencing the presence of an excited level corresponding to a spin flip of the AFM coupled Dy_2 (Figure 16.10).

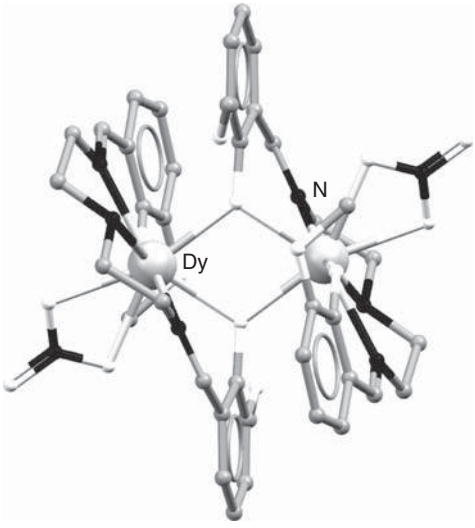

Figure 16.8 Molecular structure of $[Dy_2(valdien)_2(NO_3)_2]$.

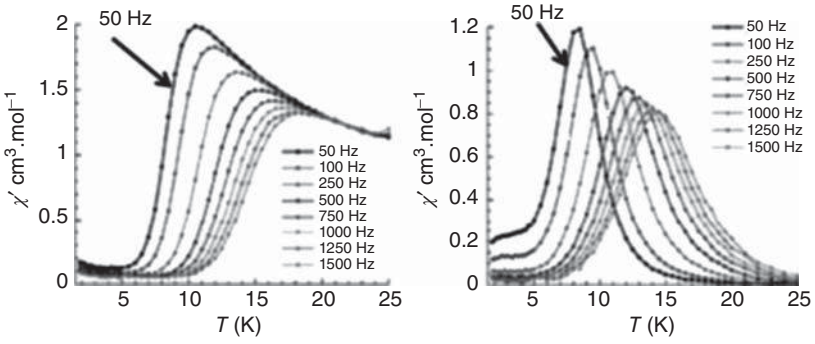

Figure 16.9 Temperature dependence of the in-phase χ' (a) and out-of-phase χ'' (b) AC susceptibility signals under zero DC field for of $[Dy_2(valdien)_2(NO_3)_2]$. (Reproduced from Long, J. *et al.* (2011) with permission from The American Chemical Society.)

The low-T, high-field experiments saturate with some hysteresis. The observation of hysteresis suggests that, on going back to "hot" temperatures such as 20 K, the usual Arrhenius behavior is observed with $U_{eff} = 76$ K, a result very close to that observed for Mn_{12} and for a long time the highest blocking temperature and the dream of every SMM researcher. Below 4 K, the relaxation becomes independent of T, which is the signature of the quantum tunneling of the magnetization (QTM). A similar behavior was previously observed in $[Mn_4O_3Cl_4(O_2CCH_3)_4(pyridine)_3]$, where two Mn_4 clusters are entangled. In this complex, the QTM is the consequence of a collective behavior of the complete S = 0 dimer derived by the exchange-coupled S = 9/2 of the Mn_4 cluster. The coupling is manifested as an exchange bias of all tunneling transitions, and the

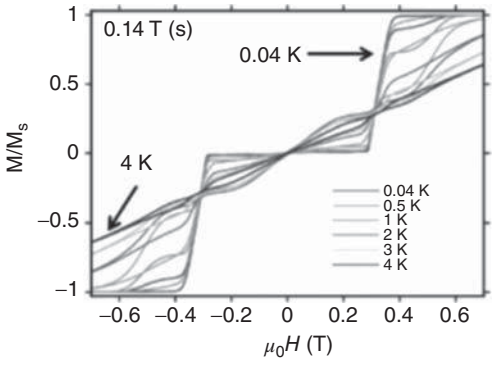

Figure 16.10 Field dependence of the normalized magnetization of $[Dy_2(valdien)_2(NO_3)_2]$ between 0.04 and 4 K for DC applied field ranging from −1.5 to 1.5 T. (Reproduced from Long, J. *et al.* (2011)with permission from The American Chemical Society.)

hysteresis loops consequently display the unique features of the absence in an SMM of a QTM step at zero field (Wernsdorfer *et al.*, 2002).

The other ions have been less accurately investigated. Anyway, quantum mechanical studies have been performed that have given good results in the fit of X^T for the five metal ions introducing Ln–Ln interactions. The best fit parameters are given in Table 16.3.

An interesting feature of the attention is devoted to Eu^{3+}. The magnetic properties depend on the relative population of the ground $^8F_0$ and the first excited $^8F_1$. Because the ground state is nonmagnetic and for Ln only low temperatures allow interesting behaviors, Eu^{3+} is rather neglected. The present series reports magnetic data for Eu^{3+}, showing that the room-temperature X^T value is larger than usually observed. *Ab initio* calculations indeed show a separation between the lowest levels, about 200 cm^{-1}, which is lower than the separation measured in the free ion, namely 400 cm^{-1}. This discrepancy may be due to the selected wave function. The need for the use of more extended sets could be satisfied but with too costly computations.

The results for the other ions are rather goods in terms of fit of the magnetic properties but there is no systematic trend evolving

Table 16.3 Calculated exchange coupling constants for dinuclear complexes.

Ln^{3+}	Gd^{3+}–Ln^{3+} (Å)	Ln^{3+}–O–Ln^{3+} (°)	Lines J (cm^{-1})	Ising J′ (cm^{-1})
Eu	3.830(3)	107.26(6)	—	—
Gd	3.811(1)	107.76(8)	−0.08	—
Tb	3.788(1)	108.05(8)	−0.10	−3.60
Dy	3.768(3)	108.22(3)	−0.21	−5.25
Ho	3.754(3)	108.17(5)	−0.44	−7.04

16.4
Dy as a Perturbation

One of the trends in the use of Dy is certainly that of using it to build large clusters and exploiting its anisotropy in a concerted manner. A different approach uses Dy as a doping species to add to clusters of different metal ions (Ako *et al.*, 2009). A beautiful example of the latter strategy is the synthesis of a Mn_{18} Dy cluster starting from Mn_{19} (Ako *et al.*, 2006). Mn_{19} contains seven Mn^{2+} and 12 Mn^{3+}. Some chemical structural consideration is in order now. The structure of Mn_{19} can be described starting from the Mn^{2+} ions that are on the vertices of two tetrahedra which share a vertex, as shown in Figure 16.11. A Mn^{2+} ion connects two supertetrahedra with 3-1-3 Mn ions. Inside the tetrahedral, 12 Mn^{3+} ions are hosted, defining two octahedra. The interesting feature is that the dominant coupling between the metal ions is ferromagnetic and the ground state has $S = 7 \times 5/2 + 6 \times 2 = 83/2$, the biggest spin so far reported. An example of chemical ingenuity is the development of a strategy to exchange the bridging Mn with a Ln. The approach of using preformed building blocks worked well, while the attempts to start from Mn_{19} were unsuccessful. The final product of this strategy is schematized in Figure 16.11.

The magnetic data of Mn_{19} confirm the presence of strong ferromagnetic coupling resulting in χT much higher than expected for uncoupled free ions at room temperature (93 emu mol K^{-1} vs the free ion value of 66.6 emu mol^{-1} K). The ferromagnetic coupling is confirmed by the increase of χT on decreasing T. The data of $Mn_{18}Dy$ are less unequivocal. In fact, the room temperature value of χT is larger than that expected for free ions (observed for $Mn_{18}Dy$, 105.1 emu K mol^{-1}, expected 76.4 for 12 Mn^{3+} with $S = 2$, six Mn^{2+} with $S = 5/2$, and one Dy^{3+} metal ion with $C = 14.17$ cm^3 K mol^{-1}). But it decreases on decreasing T. On lowering the temperature, the χT product decreases to reach 58.2 emu K mol^{-1} at 1.8 K. This behavior is indicative of some AFM coupling in the Mn^{2+}/Dy^{3+} interaction.

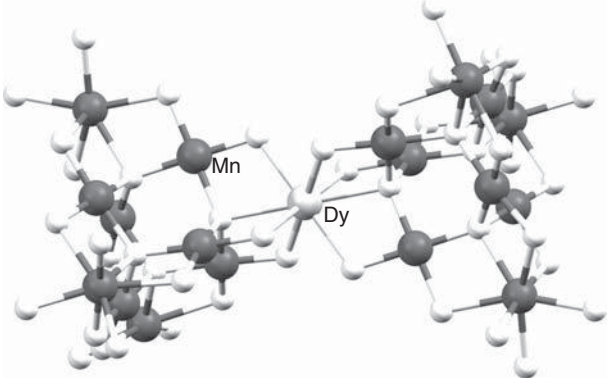

Figure 16.11 Simplified metallic core of $[Mn^{III}{}_{12}Mn^{II}{}_{6}Dy^{III}(\mu_4\text{-}O)_8(\mu_3\text{-}Cl)_{6.5}(\mu_3\text{-}N_3)_{1.5}(HL)_{12}(MeOH)_6]Cl_3 \cdot 25MeOH$ (H_3L = 2,6-bis(hydroxymethyl)-4-methylphenol).

In any case, a ground state with a large spin is expected even though it was not possible to determine this value as the magnetization at 1.85 K does not saturate up to 7 T. It is well known that a large spin and anisotropy can induce a slow relaxation of the magnetization. In this $Mn_{18}Dy$ cluster, both these features are present and the AC measurements seem to confirm this hypothesis. Further, the presence of a magnetic hysteresis observed by working on an oriented single crystal with a μ-SQUID apparatus suggests a behavior compatible with a SMM one.

In the authors' opinion, this is one of the important chapters in which many concepts are worked out by taking advantage of the peculiarity of lanthanides. The more employed technique to study these systems must be the single crystal magnetometry either with the standard technique or by using cantilever magnetomety, even if in some cases ambiguous results can be obtained.

Dysprosium has indeed something magical about it, and one can forecast that the Dy mine is not yet empty. For sure, it will be necessary to open different caves finding something good also in the other lanthanides.

References

Ako, A.M., Hewitt, I.J., Mereacre, V., Clérac, R., Wernsdorfer, W., Anson, C.E., and Powell, A.K. (2006) A ferromagnetically coupled Mn_{19} aggregate with a record S = 83/2 ground spin state. *Angew. Chem.*, **118**, 5048–5051.

Ako, A.M., Mereacre, V., Clérac, R., Wernsdorfer, W., Hewitt, I.J., Anson, C.E., and Powell, A.K. (2009) A $[Mn_{18}Dy]$ SMM resulting from the targeted replacement of the central MnII in the S = 83/2 $[Mn_{19}]$-aggregate with Dy III. *Chem. Commun.*, 544–546.

Baker, J.M., Cook, M.I., Hutchison, C.A., Martineau, P.M., Tronconi, A.L., and Weber, R.T. (1991) Magnetic resonance studies of Dy^{3+} and Er^{3+} in lanthanum nicotinate dihydrate. *Proc. R. Soc. London, Ser. A*, **434**, 707–717.

Benelli, C., Caneschi, A., Gatteschi, D., Pardi, L., and Rey, P. (1989) One-dimensional magnetism of a linear chain compound containing yttrium(III) and a nitronyl nitroxide radical. *Inorg. Chem.*, **28**, 3230–3234.

Benelli, C., Caneschi, A., Gatteschi, D., Pardi, L., and Rey, P. (1990) Linear-chain gadolinium(III) nitronyl nitroxide complexes with dominant next-nearest-neighbor magnetic interactions. *Inorg. Chem.*, **29**, 4223–4228.

Bernot, K., Luzon, J., Bogani, L., Etienne, M., Sangregorio, C., Shanmugam, M., Caneschi, A., Sessoli, R., and Gatteschi, D. (2009) Magnetic anisotropy of dysprosium(III) in a low-symmetry environment: a theoretical and experimental investigation. *J. Am. Chem. Soc.*, **131**, 5573–5579.

Casanova, D., Llunell, M., Alemany, P., and Alvarez, S. (2005) The rich stereochemistry of eight-vertex polyhedra: a continuous shape measures study. *Chem. Eur. J.*, **11**, 1479–1494.

Chibotaru, L.F., Ungur, L., and Soncini, A. (2008) The origin of nonmagnetic kramers doublets in the ground state of dysprosium triangles: evidence for a toroidal magnetic moment. *Angew. Chem. Int. Ed.*, **47**, 4126–4129.

Coronado, E., Curreli, S., Giménez-Saiz, C., Gómez-García, C.J., Deplano, P., Mercuri, M.L., Serpe, A., Pilia, L., Faulmann, C., and Canadell, E. (2007) New BEDT-TTF/$[Fe(C_5O_5)_5]^{3-}$ hybrid system: synthesis, crystal structure, and physical properties of a chirality-induced α phase and a novel magnetic molecular metal. *Inorg. Chem.*, **46**, 4446–4457.

Cucinotta, G., Perfetti, M., Luzon, J., Etienne, M., Car, P.E., Caneschi, A., Calvez, G., Bernot, K., and Sessoli, R. (2012) Magnetic anisotropy in a dysprosium/DOTA single-molecule magnet:

beyond simple magneto-structural correlations. *Angew. Chem. Int. Ed.*, **51**, 1606–1610.

Demir, S., Zadrozny, J.M., Nippe, M., and Long, J.R. (2012) Exchange coupling and magnetic blocking in bipyrimidyl radical-bridged dilanthanide complexes. *J. Am. Chem. Soc.*, **134**, 18546–18549.

Gatteschi, D. (2011) Anisotropic dysprosium. *Nat. Chem.*, **3**, 830.

Hewitt, I.J., Tang, J., Madhu, N.T., Anson, C.E., Lan, Y., Luzon, J., Etienne, M., Sessoli, R., and Powell, A.K. (2010) Coupling Dy_3 triangles enhances their slow magnetic relaxation. *Angew. Chem. Int. Ed.*, **49**, 6352–6356.

Liu, J., Koo, C., Amjad, A., Feng, P.L., Choi, E.S., Del Barco, E., Hendrickson, D.N., and Hill, S. (2011) Relieving frustration: the case of antiferromagnetic Mn_3 molecular triangles. *Phys. Rev. B: Condens. Matter Mater. Phys.*, **84**, 094443.

Long, J., Habib, F., Lin, P.-H., Korobkov, I., Enright, G., Ungur, L., Wernsdorfer, W., Chibotaru, L.F., and Murugesu, M. (2011) Single-molecule magnet behavior for an antiferromagnetically superexchange-coupled dinuclear dysprosium(III) complex. *J. Am. Chem. Soc.*, **133**, 5319–5328.

Luzon, J., Bernot, K., Hewitt, I.J., Anson, C.E., Powell, A.K., and Sessoli, R. (2008) Spin chirality in a molecular dysprosium triangle: the archetype of the noncollinear Ising model. *Phys. Rev. Lett.*, **100**, 247205.

Tang, J., Hewitt, I., Madhu, N.T., Chastanet, G., Wernsdorfer, W., Anson, C.E., Benelli, C., Sessoli, R., and Powell, A.K. (2006) Dysprosium triangles showing single-molecule magnet behavior of thermally excited spin states. *Angew. Chem. Int. Ed.*, **45**, 1729–1733.

Wernsdorfer, W., Aliaga-Alcalde, N., Hendrickson, D.N., and Christou, G. (2002) Exchange-biased quantum tunnelling in a supramolecular dimer of single-molecule magnets. *Nature*, **416**, 406–409.

Zhang, P., Guo, Y.N., and Tang, J. (2013) Recent advances in dysprosium-based single molecule magnets: structural overview and synthetic strategies. *Coord. Chem. Rev.*, **257**, 1728–1763.

17
Molecular Spintronics

17.1
What?

In the previous chapters, we laid out the fundamental knowledge of the magnetic properties of molecular magnets. Although in many cases we evoked possible applications, the main bulk of research has been of fundamental type. In the last few years, the rising interest in sophisticated systems and devices, which one could once only dream of, is starting to give exciting results, and has determined a new approach where molecular magnetism (MM) can bring an important contribution. The research areas can be tagged as spintronics and quantum information processing (QIP), to which the adjective "molecular" can be added.

The use of molecules in designing electronic devices has a long story, and has produced also important applications. Just to mention a few of them, let us remember organic semiconductors, organic light-emitting diodes (OLEDs) (Lee, Kim, and Lee, 2014), organic spin valves, organic photovoltaic cells, and organic field-effect transistors. The success obtained in molecular electronics has pushed the interest in the application of MMs for devices.

Spintronics is one of the exciting areas of development of science where several different techniques merge to produce breakthroughs of fundamental and applicative relevance. The name is a composite term including "spin" and "electronics", which states the novelty of the research field, namely that, for the first time, electronics gets interested at the charge and the spin of the electron. Electronics, complex as it may be, mainly deals with the electronic charge, and has historically neglected the magnetic properties, that is, the spin that electrons carry. Spin electronics starts with the idea to exploit not only the transport of charge but also this magnetic part. The start was excellent, with the Nobel Prize being awarded to Grünberg (Binasch *et al.*, 1989) and Fert (Baibich *et al.*, 1988) in 2007, only 12 years after the discovery that in nanostructured magnetic devices it is possible to control the electronic resistance to enhance the possibility to store information in the nanostructures. The short time from the scientific discovery to market was amazing. The breakthrough discovery was that by arranging nanolayers of ferromagnets (Fe) and antiferromagnets (Cr) it is possible to control the transport of charge by an applied magnetic field, as schematically

Introduction to Molecular Magnetism: From Transition Metals to Lanthanides, First Edition.
Cristiano Benelli and Dante Gatteschi.
© 2015 Wiley-VCH Verlag GmbH & Co. KGaA. Published 2015 by Wiley-VCH Verlag GmbH & Co. KGaA.

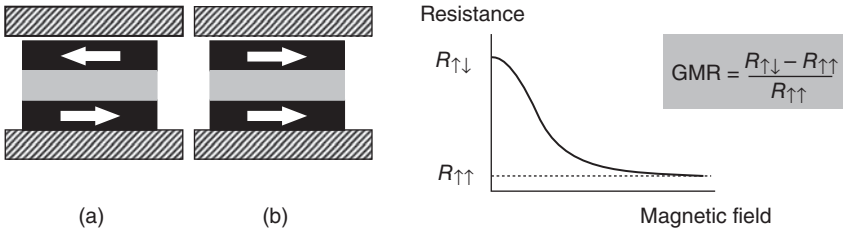

Figure 17.1 A schematic diagram of the core of a system showing giant magnetoresistance (GMR). (a) Antiparallel spin alignment. (b) Parallel spin alignment. On the right the field dependence of GMR.

indicated in Figure 17.1. The physical property used was magnetoresistance, which had been known for more than a century.

The influence of a magnetic field on the resistance of a metal conductor was noticed for the first time by Lord Thompson who, in a paper of 1857 titled "On the Electro-Dynamic Qualities of Metals: Effects of Magnetization on the Electric Conductivity of Nickel and of Iron" in the *Proceedings of the Royal Society of London*, **8**, pp. 546–550 (1856–1857), stated: "I found that iron, when subjected to a magnetic force, acquires an increase of resistance to the conduction of electricity along, and a diminution of resistance to the conduction of electricity across, the lines of magnetization." The phenomenon was dubbed magnetoresistance, but it was a small effect and for 130 years or so it remained a scientific curiosity. Standard materials are characterized by variations of resistance of a few percent at room temperature, making them unsuitable for applications. The larger the effect, the smaller the size of the device needed for observing it and the higher the density of information. Matters changed with the advent of nanotechnology.

Both Fert and Grünberg were interested in the properties of magnetic multilayers. They experimented with Fe layers, separated by a Cr layer, which could be prepared either with parallel or antiparallel magnetization. The Cr layers are antiferromagnetic (AF). The electrons traveling in the Fe layers with spins parallel to the magnetization move well while with opposing spins the transport is less efficient. At the AF layers and interfaces, the electrons are scattered. If the geometry of the layers is as shown in Figure 17.1a, the electrons move well and the resistance is low. On the other hand, in the geometry of Figure 17.1b, the resistance is high. In the new systems used by Fert and Grünberg, the ratio of variation is 1800% at low temperatures and 400% at room temperature. Since in general magnetoresistance is of the order of 1%, the new phenomenon was called giant magnetoresistance (GMR). The new phenomenon was immediately investigated for designing a new generation of magnetic memories.

Making magnetic field sensors requires a more complex device structuring. For instance, the spin valve structure requires a cap (Ta), a pinning layer (FeMn), a pinned layer (Co), a spacer (Cu), a free layer (NiFe), a buffer (Ta), and a substrate (Si). The whole structure corresponds to 30 nm. The active part is 10 nm. Devices like this now constitute the core of hard disks. It must be stressed that there

is nothing molecular in all these; they are just top-down techniques applied to inorganic materials.

Realizing that exploiting also spin opened many new possibilities was the start of spintronics, which is producing new physics and also new novel applications. Just to mention a few new exciting results, we refer to colossal magnetoresistance (CMR), where the transition from AFM (antiferromagnet) to ferrimagnet in manganese oxides is exploited. It is interesting to notice that the magnetic actors are the same as in Mn_{12}. Other interesting acronyms are TMR, which stands for tunnel magnetoresistance, where the middle layer is an insulator instead of a conductor. The current tunnels through the insulator as in a SQUID (superconducting quantum interference device).

That was only a start, and new phenomena were discovered that opened a new field, namely spintronics. Several different types of devices were implemented taking advantage of the possibility to use both electric and magnetic field in a concerted way. Particularly appealing are the opportunities provided by GMR biosensors which are compatible with standard silicon technology, are cheap, portable, and operable at room temperature, and are integrable in a lab-on-chip approach.

17.2 Molecules and Mobile Electrons

Among the current developments in spintronics, an important role is played by conducting islands with the size of a few nanometers called quantum dots (QD)s. As the size of the particles introduces a discretization of the energy spectrum, the electronic properties of QDs can be interpreted as due to a number of orbitals, and can thus be considered comparable to those of molecules; therefore interesting overlap between the two types of objects can give rise to new physics and new chemistry to explore the novel perspectives associated with molecular materials. Given the similarity, at least for the electronics, between QD and molecules, we will use the two terms interchangeably. If there is a difference between the two, then we will notice that.

MM started with the attempt to check what could be done using molecules instead of, or in addition to, metallic and ionic systems. It is rather obvious that the developments of spintronics would have created excitement in the MM community for the perspectives of new systems that could open up using molecules. And finding a name for the new area was easy: molecular spintronics was born.

Up to now, we have been playing with variations on the theme of infinite arrays of the SMM in crystals, powders, and frozen solutions. The interest was on individual molecules, but playing with them is still a difficult task that requires the implementation of new techniques with the possibility of addressing individual molecules and the sensitivity to record their response to external stimuli. The first idea that came to the mind was, of course, of using SMM for building nanosized memories, and we have discussed the progress made in the field on many occasions. On the experimental level, this is certainly a challenging goal. So far we

have considered the magnetic properties of molecules in some detail, but we have essentially neglected the electric charge transport properties. We will now try to fill the gap. In particular, we will make a short detour to define the background needed to generate electric transport in the absence and presence of molecules.

Molecular electronics has been developed for quite some time without caring for the influence of magnets. The basic breakthrough has been the increasing interest in nanosized objects, which has made the quantum size effects relevant for possible applications. The basic science is rather similar for molecules and QDs.

The simplest possible device requires a source electrode, from which the electron flux enters, and a drain electrode, from which the flux exits. Slightly more complex is the transistor, which comprises an additional electrode, the gate. The function of the gate is that of controlling the electron flow by applying a potential to the device, for example, by shifting the levels of the QD with respect to the Fermi energy of the leads. The possibility to measure the properties of individual molecules has become real with the implementation of new instrumentation with high sensitivity. Just to mention a well-known example, let us think of the scanning tunneling microscope (STM), which can work like an electrode and measure the structure of the molecule on the substrate. STM belongs to the more general class of scanning probe microscopies, SPM, is a general word for denoting several different techniques, among which one can refer to the photon scanning tunneling microscopy (PSTM), which uses an optical tip to tunnel photons; the scanning tunneling potentiometry (STP), which measures the electric potential across a surface; spin-polarized scanning tunneling microscopy (SPSTM), which uses a ferromagnetic tip to tunnel spin-polarized electrons into a magnetic sample, and AFM, another SPM technique, in which the force caused by the interaction between the tip and sample is measured. The appealing features of STM are the lateral resolution of 0.1 nm and depth resolution of 0.01 nm, and the possibility of performing measurements under many different experimental conditions. When STM is used at low temperature to measure conductivity under variable bias voltage it provide access to the energy levels of the investigated system as in standard spectroscopy, and is thus referred to as Scanning Tunnel Spectroscopy (STS).

An example of the use of STM is shown in Figure 17.2 where the STM images of a monolayer of a sublimated of Fe_4 on Au(111), which we have discussed in Chapter 12, are shown. A careful analysis provides a statistical distribution of molecular diameters following a log-normal distribution.

The use of molecules for spintronics requires the understanding of the interaction of molecules with electrodes which are magnetic. It is therefore necessary to focus on the molecule–electrode interaction to understand how the electrons move, or to precisely determine what leads to the transport. The simplest approach demands a direct interaction between the molecules and the electrode.

Let us consider a simple system as starting point. Namely, we may consider a source and a drain connected through a suitable molecule or QD. In the bulk of the metallic electrodes, electrons are delocalized and circulate freely, as determined by the band structure. In the molecule, the levels are quantized and the transport depends on the interaction between the electrodes and the

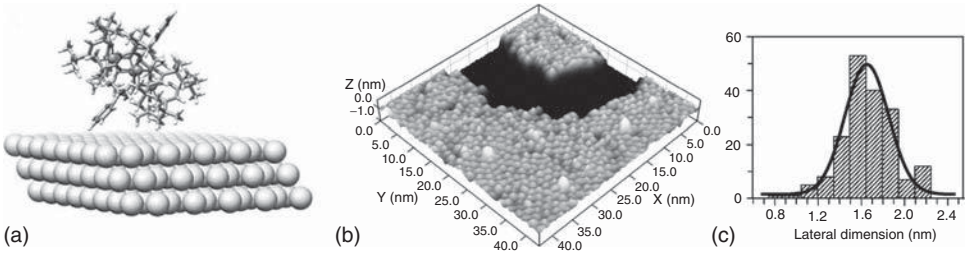

Figure 17.2 (a) DFT optimized geometry of the Fe_4 molecule deposited on Au substrate, showing that the idealized C_3 axis forms an angle of ca. 35° with the normal to the surface. (b) STM image of Fe_4 sublimated on Au(111) ($50 \times 50\,nm^2$, 10 pA, 2.0 V). (c) Lateral size distribution of the Fe_4 molecules extracted from image (b) along with its Gaussian fit (Malavolti *et al.*, 2015). (Reproduced from Malavolti, L. *et al.* (2015) with permission from The American Chemical Society.)

molecule. The way in which the molecule "feels" the electrode may be complex, and can lead to hybridization effects between the lead and molecular wave functions. On the other hand, there are often substantial energy barriers between the leads and the molecule, which prevent appreciable hybridization. In these cases, it is usually enough to consider that transport through the device is determined by the quantized energy spectrum of the molecule. Under these conditions, many transport features can be described by the properties of the (highest occupied molecular orbital) HOMO and the lowest unoccupied molecular orbital (LUMO) of the system. The interaction of the quantized orbitals of the molecule determines the properties of what can be called *quantized transport*.

The interaction between the molecule and the leads is fundamentally determined by the presence of an energy barrier, often called a *Schottky barrier*. The height and width of these barriers determine the extent of the hybridization between the leads and molecular wave functions, with three main regimes found in the literature, called *weak*, *strong*, and *intermediate coupling regimes*. In weak coupling, the barrier is sufficiently high to leave the wave functions of the molecule substantially unchanged and to imply a step charging the molecule for the current to flow. The electrons can then become strongly localized on the molecular object, and to increase the current the transport mechanism requires overcoming the charging energy needed to add additional electrons to the molecule. In the strong coupling regime, there is large admixture of the molecular and electrode wave functions and the transport can occur practically without a barrier, close to the Fermi energy. Finally, the intermediate coupling region is a mixed regime in which molecular charging still takes place but direct electrode–electrode effects can also take place (e.g., co-tunneling through both Schottky barriers), providing a great number of opportunities for different properties.

The reference point to classify the devices is the quantum of conductance $G_0 = e^2/h$, which is the conductance of a single channel through a nanoscale device. The overall current can then be understood as the sum of all the possible channels of the particular device. In the weak coupling regime, which is the most

common one, the important quantities are the spacing of the quantized levels of the molecule, δ, and the energy needed to add one electron to a charged system, EC. The region of main interest for MM is that for which $G < G_0$. If $G \ll G_0$ and $E \gg$ EC, there is strong localization of electron excitations and the conduction mechanism is dominated by hopping. Moving to lower energies, we enter the Coulomb blockade regime. In this regime, electrons tunnel through the Schottky barrier from the leads to the molecule whenever a molecular state comes into resonance with the Fermi energy of the leads. This situation can be achieved in two ways: by sweeping a gate voltage that changes the position of the molecular orbitals, or by adjusting the source–drain potential. As the electrons become localized on the molecular object, the only possible way to increase the current is by overcoming the charging energy needed to add more electrons to the molecule. This energy is related to the classical Coulomb repulsion potential (hence the name Coulomb blockade), which is usually negligible for single electrons in bulk systems but becomes important when the size of the QD is in the nanometer range. In such nanodevices, the charging energy, EC, is the fundamental energy scale. The other relevant parameter is δ, which is the original electronic spacing between the quantized levels of the molecule. The fact that, in principle, the transport can occur coherently is certainly an appealing feature given the current interest for all sorts of quantum effects. Electrons must remain coherent to observe their tunneling between electrodes. The coherence is lost immediately after (ps) the passage as a consequence of the scattering with other electrons.

The strong coupling regime, corresponding to low energy and low conductance, can lead to the system entering the Kondo regime (Kondo, 1968). The name is that of the Japanese physicist who discovered it when investigating the low-temperature resistivity of metals with magnetic impurities. The interaction of the mobile electrons with the magnetic impurity determines a large increase of the electric resistance at low temperatures. In recent years, the effect has been observed also in molecules and QDs, where the role of the magnetic impurity is taken by the electrons in the QD quantized states. The interest for the Kondo regime is that it defines a strongly coupled state between the molecular and flowing electrons. The molecular spin state can then screen the flowing charges, giving rise to a large density of states close to zero bias with respect to the Fermi energy of the leads. The experiment thus consists in measuring the differential conductance $G = \mathrm{d}I/\mathrm{d}V$ as a function of the bias voltage V_b. The Kondo effect is observed as a peak in G, and can be detected with a number of techniques, most prominently STM and transport measurements. The Kondo behavior is then characterized by a number of variables, such as the Kondo temperature, which depends on the energy relative to the Fermi energy. If using the gate voltage, the molecular level becomes higher than the highest filled band level, interaction disappears and the Kondo effect is lost. What is the interest in investigating the Kondo effect? The issue is that the physics of the screening interactions is still poorly understood, and involves the presence of virtual electronic states that are difficult to model qualitatively and quantitatively. Additionally, it is sensitive to the mutual influence of conduction electrons and localized spins.

At this stage, it might be interesting to provide some examples, which, we hope, will clarify the concepts introduced previously. It is first of all useful to point out the role of the chemistry of the compounds. In fact, the use of molecules requires a detailed knowledge of the structure in solution and how it can be modified by the interaction with the electrodes. Classical chemical tools can be used to tune the coupling between the leads and the molecule, by altering the height and width of the Schottky barrier. An interesting example is found in an early experiment by Park *et al.*, who used gold electrodes connected by a magnetic molecule $Co(terpy(CH_2)_nSH)_2^{2+}$, with $n = 0, 5$. Thiols, or molecules functionalized with pending thiols had extensively been used in the frame of molecular electronics to create self-assembled monolayers (SAMs), as thiolates have high affinity for gold and can organize layers of molecules. It is possible to control the transport properties by varying the number n of the CH_2 groups connecting the terpyridine molecule with the sulfur. Studies on the Co molecule with $n = 1$ deposited on gold electrodes showed evidence of the strong coupling regime: a Kondo peak appeared at zero bias, with the predicted possibility of tuning the Kondo effect by sequentially adding electrons to the molecule. If a longer tether, with $n = 5$, is used, the system shifts to the weak coupling, and standard Coulomb blockade dominates the behavior (Park *et al.*, 2002) (Figure 17.3).

To reach these conclusions, however, much delicate work was needed. The transistor was assembled on a silica layer, and gold wires of size $200\,nm \times 300\,nm \times 15\,nm$ were fabricated by electron beam lithography. The wires were coated with molecules and broken by electromigration. This fabrication technique involved a sequential burning of the gap until only the tunneling signal was detected, indicating the presence of gapped structures of $1-2\,nm$ between the electrodes, which could host the target molecules. Measurements were then performed at 100 mK, and the application of a magnetic field provided information on the presence of low-spin cobalt(II), albeit with rarely observed g-values (Park *et al.*, 2002).

Similar results were obtained by using the dinuclear vanadium complex (Liang *et al.*, 2002). An example is shown in Figure 17.4 (Shores and Long, 2002).

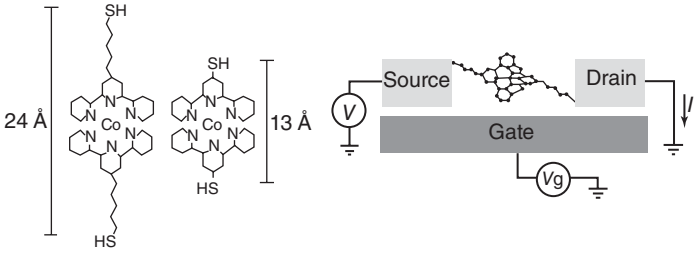

Figure 17.3 Scheme of the structure of $[Co(terpy\text{-}(CH_2)_5\text{-}SH)_2]^{2+}$ (terpy-$(CH_2)_5$-SH = 4′-(5-mercaptopentyl)-2,2′:6′,2″-terpyridinyl) and $[Co(terpy\text{-}SH)_2]^{2+}$ (terpy-SH = 4′-(mercapto)-2,2′:6′,2″-terpyridinyl) (a). Schematic diagram of the device (b). (Reproduced from Park, J. *et al.* (2002) with permission from Nature Publishing Group.)

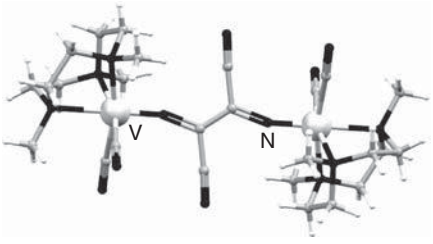

Figure 17.4 Molecular structure of $[(Me_3tacn)_2V_2(CN)_4(\mu\text{-}C_4N_4)]$ ($Me_3tacn = N,N',N''$-trimethyl-1,4,7-triazacyclononane).

Let us now look at the mechanism by which the transport through the molecule occurs. If there is no match between the molecular energies and the bias window, no current is observed, as shown in Figure 17.5a (left). The number of electrons on the dot is fixed (N) and it is in Coulomb blockade. Increasing V_g lowers the chemical potentials, and when one of the levels is aligned within the Fermi energy of the leads, electrons tunnel across the dot and a nonzero current I_{dot} is measured. By operating with the gate potential V_g, the two levels eventually match, Figure 17.5a (middle), and electrons tunnel from the source to the drain. The current will be observed only in the proximity of matching energies. The periodic jumps in current are called *Coulomb oscillations*. Instead of using V_{g}, it is possible to use V_{b}, and similar results are obtained as shown in Figure 17.5.

17.3 Of Molecules and Surfaces

While spintronics is already providing useful applications, the field of molecular spintronics is still in the science stage and has yet to produce a mature technology. A fundamental work, however, is developing and producing much new physics and chemistry and suggesting new horizons to reach. The field is fully in the development phase, a fact that makes writing these pages particularly difficult, as exciting discoveries appear every day. By and large, there are three approaches that are widely used. The first starts from the obvious observation that, if one wants to investigate transport through magnetic molecules, it is useful to have a clarified mechanism for molecules in general. In the language used previously, the first step has been that of using simple molecules.

There are essentially three ways to organize and address molecules for transport:

1) Organizing the molecules on suitable surfaces and use the tip of an STM as a lead;
2) Digging a hole in a metal to generate a gap in which to arrange a molecule;
3) Using the molecule for its spin, while transport occurs through an electronic QD (double dot scheme).

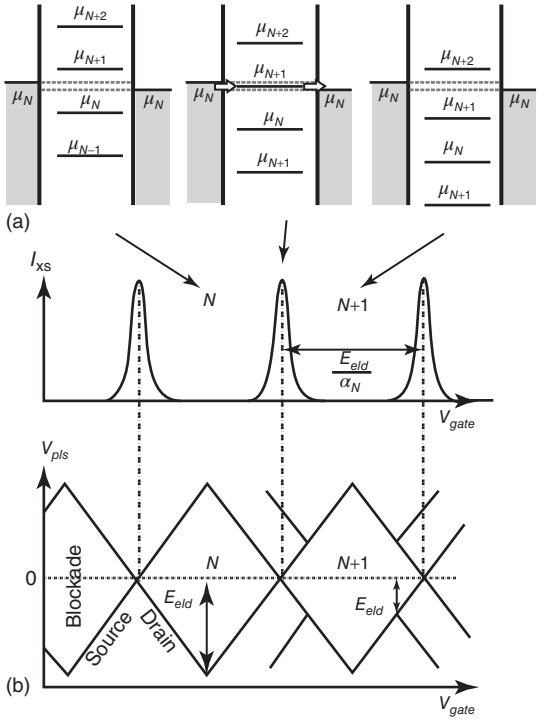

Figure 17.5 (a) Schematic of the quantized states of the electrochemical potential of a quantum dot for three different level alignments. (b) Coulomb oscillations in the current I_{dot} across the QD. (c) Schematic differential conductance dI_{dot}/dV_{bias} plot exhibiting Coulomb diamonds and excited state resonances. The addition energy E_{add} and the energy E_{exc} of an excited state are indicated. (Reproduced from "An introduction to molecular spintronics", Sci. China Chem., **2012**, *55*, 867 by Jiang, S.D., *et al*. with permission from Science China Press and Springer-Verlag.)

In order to behave as an electronic QD, the size of the objects must be reduced to a few nanometers for metals while for single-walled carbon nanotubes (SWCNTs) quantum effects can be observed up to 10^2 nm.

The three possible ways of operations are shown in Figure 17.6.

It is possible to organize the active molecules on surfaces and address them with an STM tip, as shown in Figure 17.6a. The magnetic molecule can be inserted between two electrodes, as in Figure 17.6b. Finally, it is possible to introduce an additional QD as a carbon nanotube, as shown in Figure 17.6c, so as to avoid electron transport directly through the molecule.

It is now time to tackle the status of the molecular organization on surfaces. Several steps can be envisaged:

1) *Choice of the active molecules* and their characterization in bulk. We can start with SMM:Fe_4, Mn_{12}, $LnPc_2$, or POM (polyoxometallate). There are several criteria to be met. Ideally, the chosen molecules must be stable enough to survive the treatment used for the organization on the surfaces. Typical

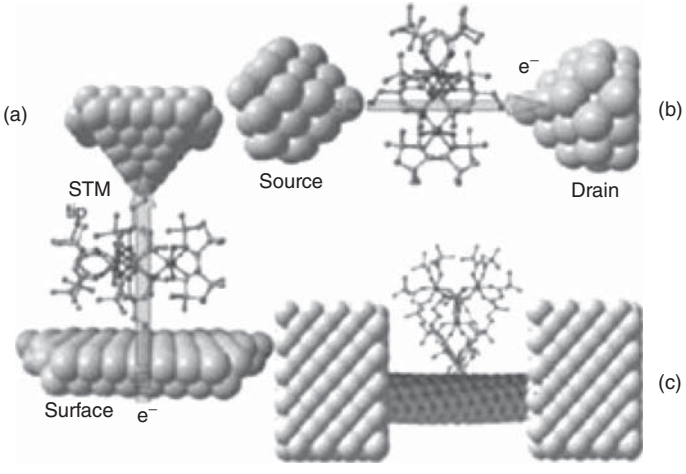

Figure 17.6 Detection schemes for molecular spintronics. (a) Detection scheme using a conducting tip; (b) molecular junction device; (c) double magnetic QD scheme. The molecule is attached onto a second, electronic QD (in this case a carbon nanotube). (Reproduced from "An introduction to molecular spintronics", Sci. China Chem., **2012**, *55*, 867 by Jiang, S.D., *et al*. with permission from Science China Press and Springer-Verlag.)

surface chemistry treatments require ultrahigh vacuum (UHV) treatments, which not many molecules can stand, or the use of solutions and several SMMs is not possible without breaking a large percentage of the molecules. One example is Mn_{12}, which has been found to be unstable when attached to a surface. Another factor is the shape of molecules: flat ones, such as $LnPc_2$, are better suited than puckered ones.

2) *Choice of substrates* to allow individual addressing of the molecules. The first condition is that the surface reactivity be compatible with the molecular stability. Molecules must be hosted while keeping as far as possible their properties. In other words, the host surface must interact weakly with the molecule so as to keep it ordered without reacting, or reacting in a controlled way. Another point that must be taken into consideration is the magnetic properties of the substrate. Examples of magnetically inert surfaces are provided by Au, BN, Cu, highly oriented pyrolitic graphite (HOPG), and graphene, while magnetically active supports are provided by Fe, Co, or Ni.
3) *Addressing individual molecules.* This is the most delicate issue because there are problems of sensitivity, the type of instrumentation, and the interaction of the measurement with the quantum system. This requires new techniques such as STM–STS that are capable of addressing the molecule in an atom-to-atom way. Additionally, new theoretical models are needed to actually model the properties, observe them with such techniques, and distinguish the molecular behavior from the interference of the substrate. For STM, for example, calculations are necessary to simulate the observed images in order to extract the relevant information. Eventually, it is important to remember

that it is not only desirable to measure the single-molecule properties but is also important to provide new ways of manipulating the spins, in order to achieve control over the molecular system.

Two additional points must be mentioned, which are of fundamental importance for molecular spintronics.

4) The transition from bulk to single molecules: that is, the passage from bulk material to isolated molecules requires accurate checks of the "purity" and integrity of each system that is investigated.
5) One must eventually be able to create devices out of such system: this might actually be the most difficult part, as the systems work at low temperatures and the devices are somehow fragile when operated.

17.4 Choosing Molecules and Surfaces

Surfaces are intrinsically reactive, and this reactivity is exploited for depositing molecules. Surface chemistry has been a major research field in chemistry much before the interest in spintronics started appearing, with catalysis being one of the major focuses of interest in the study of surfaces. The driving force for the interaction between molecules and surfaces can be provided by van der Waals or other weak interactions, and in this case one talks of physisorption. Moreover, the molecules can also interact, producing true chemical bonds with the surface, and in this case one talks of chemisorption. In both cases, intermolecular interactions must also be taken into account because they usually have a large influence on the molecular organization. It is anyway apparent that long-range organization is not achieved, and the aims remain far distant from those that drove research toward molecular ferromagnets. Multilayer techniques have hardly been explored, but could, in future, provide materials with novel properties and interesting functionalities.

Physisorption requires in general the use of a UHV chamber to deposit the molecules, and this is sometimes problematic for SMMs, which are often unstable under such conditions. In this sense, Mn_{12} is an exemplary case, as the molecule was found to be surprisingly unstable when deposited. Matters improved by the use of electrospray techniques (UHV-ESD), which allows the deposition of intact Mn_{12}, but only with an irregular surface distribution and when placing an insulating layer below the molecules.

Simple molecules such as metal porphyrinate and metal Pc have also been physisorbed on gold surfaces. The molecules are stable and resist thermal evaporation under UHV. An important variable is the surface coverage, which may influence the molecular organization. A detailed study has been made on CuPc deposited on various surfaces, namely gold, ITO (indium tin oxide), and oxidized Si (Yoon *et al.*, 2012; Lüder *et al.*, 2014). For MPc monolayers, the molecules stand flat, while with multilayers the molecules orient perpendicularly. The driving force, of course, is the possibility of developing $\pi-\pi$ stacking interactions.

Chemisorption allows great variability by taking advantage of both the substrate network and of molecular appendages to create surface-ordered structures. In all cases, the surface must be strongly conducting and flat, favoring gold, silicon, HOPG, and BN. The chemical groups that are embedded in the target molecule have often used sulfur atoms as active centers in order to attach the molecule to the surface. This, of course, is based on the affinity of S for gold. A list of S-containing active groups for gold surfaces is shown below:

$CH_3(CH_2)_{n-1}SH$
$CH_3(O)C–S$
CN–S
Disulfide

The sulfur strategy can be followed in two different ways: either by prefunctionalizing the surface to make it suited to capture molecules, or by functionalizing the molecules to perform a direct deposition. The former prepares the deposition of the active molecule by reacting the surface with a bifunctional molecule A – B – C, where A is a group such as SH which binds on Au, C is a group that can bind to the target molecule M, and B is a spacer (an alkyl chain, a *para*-phenylene residue, etc.) used to electronically isolate the molecule from the delocalized states of the surface. The resulting structures are as follows:

$$\underset{\mathbf{1}}{\text{Au}} \quad \underset{\mathbf{2}}{\text{Au} - \text{A} - \text{B} - \text{C}} \quad \underset{\mathbf{3}}{\text{Au} - \text{A} - \text{B} - \text{C} - \text{M}}$$

where **1** is the virgin gold surface, **2** is the formed SAM of the linking molecules, and **3** is the final adduct containing also the magnetic systems. In principle, also **3** can be a SAM, but so far ordered states have not been achieved for SMMs on surfaces. An example is A = SH, B = $-(CH_2)_{15}-$ or $(CH_2)_{10}$–COOH. C is a Mn_{12} in which a carboxylate can be exchanged with C. A similar approach was used for attaching Mn_{12} to Si (Fleury *et al.*, 2005). Whether the Mn_{12} structure is preserved is currently not clear, and a final assessment will require additional experiments.

All these aspects are important, as they represent laudable attempts to gain control of the organization of the active moieties in order to optimize the properties of the system. The frame we have discussed so far is that of designing nanodevices that optimize the QIP storage and can be used for mass production of nanoassemblies. In all these stages, our present knowledge is at a very preliminary level, which needs many revolutionary developments, presently difficult to predict, to become possible. An aspect that is of fundamental relevance is whether a top-down or a bottom-up strategy must be pursued. The top-down strategy is reaching the limit, and devices with dimensions below 20 nm require highly sophisticated approaches and important investments. Methods such as microcontact printing

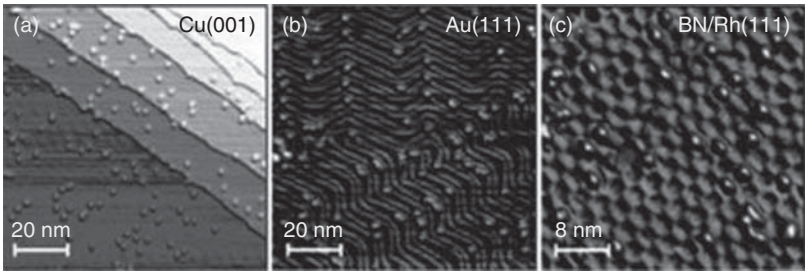

Figure 17.7 (a) Immobile molecules randomly distributed over the surface at 300 K. (b) On Au(111), molecules are found preferably at the elbow sites of the herringbone reconstruction ($T = 40$ K). (c) On the BN/Rh(111) surface, molecules adsorb in the depressions of the BN corrugation ($T = 1.5$ K). (Reproduced from Kahle, S. *et al.* (2012) with permission from The American Chemical Society.)

allow an inexpensive way of reaching the limit of 100 nm but do not seem to allow further reductions in size.

A lucid discussion of the possibilities associated with bottom-up approaches was reported by (Barth, Costantini, and Kern, 2005). The bottom-up scheme is based on growth phenomena, that is, putting together an assembly of molecules deposited on a substrate and the structures emerging by the operation of large number of molecular processes. Here we use an operative definition of molecules, calling a molecule about anything that can interact with other object, so that, under this definition, a "molecule" can be an atom, a cluster, a carbon nanoobject, a QD, or a true molecule.

Random interactions may give random results, but the nonequilibrium conditions may help kinetics to overcome thermodynamics. The whole process can be called *self-assembly* or *self-organized growth*. A beautiful picture is shown in Figure 17.7 (Kahle *et al.*, 2011).

In order for the growth to be successul, it is necessary to understand the game rules and to learn how to optimize the structures of the growing objects.

17.5 Is it Clean?

Once the molecule is placed on the surface, it is necessary to see them and to check the "purity" of the system. In this case, purity is not meant in the standard definition used by chemists, but in a more general way, meaning that the molecules retain the structural and chemical features of the bulk crystals, as opposed to systems that are fragmented, heavily distorted, reduced, or oxidized by the deposition process and the interaction with the substrate. In other words, it is necessary to perform structural and chemical characterization, at the very low concentrations typical of the surface-assembled systems. It must be recalled that surface chemistry has been developed for many years using techniques such as Fourier transform infrared (FTIR) and Raman spectroscopy, which have seen

use in the characterization of adducts with carbon nanomaterials and would perhaps deserve more attention in MM.

As everywhere in chemistry, mass spectrometry is a very powerful tool to characterize samples, and time-of-flight secondary-ion mass spectrometry (ToF-SIMS) has indeed the sufficient sensitivity to provide data on monolayers of molecules. The detection process occurs in two steps. The sample is bombarded by a beam of ions generating a second beam, which is monitored by a ToF (time-of-flight) detector. The technique can detect the upper layers to a depth of 1–2 nm. Without entering into the details of the mechanism, it can be stressed that it is possible to detect complex series of fragments that may be difficult to associate with species present on the surface.

X-ray based spectroscopies, such as XAS (X-ray absorption spectroscopy), are acquiring increasing importance due to the wealth of information they can produce. In fact, they can detect the presence of elements, their oxidation state, and their magnetic properties. The most commonly used X-ray spectroscopies are X-ray photoelectron spectroscopy (XPS), XAS, and X-ray magnetic circular dichroism (XMCD), all of which benefit from the availability of synchrotron radiation. XPS measures the absorption of monochromatic X-rays when they eject electrons from a surface. Owing to the frequency of the incoming radiation, the electrons involved in the process are the internal ones, such as 1s, and what is measured is the binding energy (BE). Different atoms are identified through the experimental BEs. Similar considerations hold for different oxidation states. It must be remembered that the depth of the sample observed by the experiment can be controlled by varying the angle of incidence of the X-ray beam on the sample surface (Mannini *et al.*, 2008).

The absorption of X-rays close to a given electronic state has a quasi-continuous plot, with sharp lines at the high-frequency edges. The frequency depends on the element, and its measurement provides information on the presence of a given element and on its chemical environment. The experiment can be performed on 1s levels, and the edge is called K, or at 2p and then $L_{2,3}$ edge, or 3d ($M_{3,4}$). In general, the K edge is used for light elements, L for 2p, K and L for 3d, and L and M for 4f and 5f. In many cases, the spectra are interpreted in a qualitative way, that is, to recognize the presence of given elements. Recently, transition metal L-edge X-ray absorptions were analysed using a combined DFT and restricted open-shell configuration interaction. The method includeds spin-orbit coupling, too. (Roemelt *et al.*, 2013).

17.6 X-Rays for Magnetism

The synchrotron provides a sensitive tool for measuring the magnetization of monolayers. XMCD is the magnetic circular dichroism at X-ray frequency. MCD measures the different absorption of right- and left-circularly polarized light by the sample, which is different from zero in the presence of optical activity or an

externally applied magnetic field. The addition of a magnetic field parallel to the direction of propagation of light induces an anisotropy in the medium, which leads to a different absorption of left- and right-polarized light, a phenomenon known for almost 200 years and discovered by Faraday. Something similar occurs at X-ray frequencies, but XMCD has many features in common with XAS in the sense that both are sensitive to the chemical nature of the samples.

The technique is more traditionally performed in the visible, UV, and IR ranges, where many applications have been reported. In particular, the simple CD experiments that show the presence of diastereoisomers have long been used in solution studies of organic molecules. In the last 15 years, the use of XMCD has been developing as an additional tool to the usual UV–vis spectroscopy. At the very beginning, this technique was applied to investigate thin films and metals, but now it is increasingly used in the study of transition-metal and lanthanide complexes. By means of XMCD, it is possible to make quantitative analysis on the distribution of spin and angular momenta as, differently from neutron diffraction, it is possible to separate the orbital and spin momenta.

The basic relation governing the absorption of circularly polarized rays propagating in the z-direction is

$$E_{cp} = E_0[\sin(\omega t - kz + \varphi_0)i \pm \cos(\omega t - kz + \varphi_0)j] \tag{17.1}$$

where $\omega = 2\pi\upsilon$ is the angular frequency, $k = 2\pi/\lambda$ is the wave number with λ wavelength, φ_0 is an arbitrary phase shift, and i and j are unit vectors along the x- and y-axis, respectively. For optics and chemistry literature, the positive and negative signs are valid for right and left polarization, respectively. In the physics literature, the reverse notation is commonly used, with the indication of "Feynman" notation. Practically the two notations are based on the observation of the polarized radiation from the point of view of the target or from the emitting source.

Experiments are based on the observation of the polarization dependence of the X-ray absorption edge of transitions such as the $3d^n \Rightarrow 2p^5 3d^{n+1}$ or $4f^n \Rightarrow 3d^9 4f^{n+1}$. Using the Russell–Sanders notation for the levels, including SOC (spin–orbit coupling), we assume that J is a good quantum number for the ground state multiplet and J′ for the excited ones. The dipole selection rule gives us $\Delta J = 0, \pm 1$ and, therefore, only transitions to $J' = J$, $J \pm 1$ are allowed. Right- and left-circularly polarized radiation produce excitation to different levels. The right-handed component ($\Delta M_J = +1$) can excite to those J′ levels that have $M' = -J + 1$ sublevels, while the left component ($\Delta M_J = -1$) induces transitions to $J' = J + 1$ levels as they contain $M' = -J - 1$ sublevels (Van Der Laan and Thole, 1990, 1991). At high temperatures, all the M sublevels are equally populated and no polarization dependence is observed: the dichroic effect increases on lowering T. In the final state configurations ($2p^5 3d^{n+1}$ or $3d^9 4f^{n+1}$), the levels with different total angular momentum J′ levels have an energy distribution due to the electrostatic interactions between the core-hole and valence electrons and the core-hole spin–orbit interactions. A direct consequence of these differences in energy is the differences in the spectra of left- and right-polarized radiation.

In the case of metallic samples or magnetic thin films, the most used model is based on a one-electron model with a two-step approach (Stohr and Wu, 1994). For a generic transition-metal or lanthanide ion, the experiments are performed using $L_{2,3}$ edges which generally are well separated even though some admixture is possible. One of the advantages in using these edges is the correspondence with transitions toward d, which are, in a magnetic compound, spin-polarized. This effect, together with SOC, strongly influences the cross section with the photon helicity.

The application of several sum rules allows the extraction of the average value $\langle L_z \rangle$ and $\langle S_z \rangle$ and hence the magnetic moment $M = -\mu_B \langle L_z + S_z \rangle$ on the absorbing atom (Carra *et al.*, 1993a,1993b). For instance, for the application to $L_{2,3}$ edges, it is possible to write for transition-metal ions (Arrio *et al.*, 1996)

$$\frac{I^+_{2,3} - I^-_{2,3}}{I^+_{2,3} + I^-_{2,3} + I^0_{2,3}} = -\frac{\langle \varphi_i | L_z | \varphi_i \rangle}{2(10-n)} \tag{17.2}$$

$$\frac{(I^+_3 - I^-_3) - 2(I^+_2 - I^-_2)}{I^+_{2,3} + I^-_{2,3} + I^0_{2,3}} = -\frac{2}{3(10-n)} \left[\langle \varphi_i | \mathcal{S}_z | \varphi_i \rangle + \frac{7}{2} \langle \varphi_i | \mathcal{T}_z | \varphi_i \rangle \right] \tag{17.3}$$

where n is the occupation number of the 3d orbital, $|\varphi_i\rangle$ the 3d ion ground state, $I_3{}^+$ the integral of the absorption cross section over the L_3 edge for left-polarized photons, and similar definitions for other I's and T_z the magnetic dipole operator. The +, −, 0 indices relate, respectively, to left, right, or linear polarization, and $I_{2,3}{}^+ = I_3{}^+ + I_2{}^+$. The component represents the magnetic dipole operator whose values average to zero in powder samples, or is usually considered to be zero in octahedral environments. The I values can be computed from the experimental data, so that direct determinations of $\langle S_z \rangle$ and $\langle L_z \rangle$ are possible.

17.7 Measuring Magnetism on Surfaces

An interesting application of this technique is the analysis of the behavior of Mn_{12} molecules when this kind of systems is deposited on surfaces. There are several researches focused on the effects of this operation on the structural and magnetic properties of the molecules after the dispersion: most studies showed redox instability of Mn_{12} complexes at gold surfaces, presumably accompanied by structural rearrangements that are difficult to reveal with other techniques such as XPS or STM (Mannini *et al.*, 2008). A detailed XMCD analysis on the Mn_{12} derivative deposited on a silicon surface has been performed in order to investigate whether SMM behavior was still present in the systems. The observed magnetic properties indicate that the deposition leads to the disappearance of SMM behavior even though the molecules seem to be structurally undamaged (Rogez *et al.*, 2009). Similarly, XMCD studies revealed the peculiar variation of the magnetic properties of a monolayer of copper–phthalocyanine on Ag(100) compared to bulk powder samples (Stepanow *et al.*, 2010). The analysis of XMCD spectra together

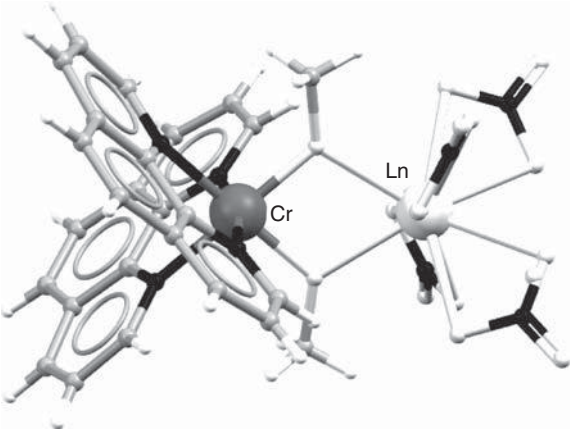

Figure 17.8 Ball-and-stick representation of $[Cr^{III}(phen)_2(\mu\text{-}MeO)_2Ln\text{-}(NO_3)_4]\cdot x$MeOH ($x = 2-2.73$).

with STM and X-ray natural linear dichroism showed that the observed magnetic susceptibility related to Cu^{2+} spin magnetic moment in a tetragonally distorted environment is about 9 times larger than the value observed on a powder sample. At the same time, a larger anisotropy in the in- and out-plane in the orbital moment was observed as a consequence of the deposition on a surface.

A powerful characteristic of XMCD is its elemental selectivity: it was fundamental, for instance, to discriminate the contribution from Ln (Ln = Gd, Dy, Lu) and Fe moment in the $[Fe_3Ln(\mu_3\text{-}O)_2(CCl_3COO)_8(H_2O)(THF)_3]$ "butterfly" molecule (Badía-Romano *et al.*, 2013). In this compound, the lanthanide ion is connected by bridging oxygen atoms to three Fe^{3+} ions, which occupy the vertices of a triangle. The lanthanide magnetization (M_{Ln}) dominates the total one, and both Gd and Dy are antiferromagnetically coupled to the cluster containing the iron atoms.

In the case of the Cr–Ln (Ln = Nd, Tb, Dy) dimers of generic formula $[Cr^{III}(phen)_2(\mu\text{-}MeO)_2Ln\text{–}(NO_3)_4]\cdot x$MeOH ($x = 2-2.73$) whose structure is shown in Figure 17.8 (Dreiser *et al.*, 2012), again the application of the XMCD allowed the independent measurement of the magnetization of Dy and Cr ions. These data were compared with the cluster magnetization measured by a classical SQUID apparatus. The possibility of analyzing the electronic states of single ions together with the magnetic structure of the dinuclear compounds led to the conclusion of the presence of an antiferromagnetic interaction of dipolar origin.

17.8
Transport through Single Radicals

One of the flagship activities of molecular spintronics is that of measuring the transport through a single molecule. A pictorial view is shown in Figure 17.9 (Kim *et al.*, 2011).

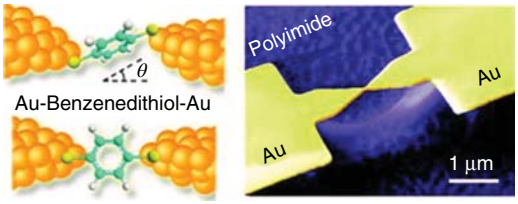

Figure 17.9 Illustrations of an Au-benzenedithiol-Au junction: top, the tilt angle (θ) of the benzene ring with respect to the current path; bottom the binding of sulfur (S) at the hollow site of Au atom sites (Left). Scanning electron microscopy image of the device (Right). (Reproduced from Lämmle, K. *et al.* (2010) with permission from The American Chemical Society.)

It is apparent that it is not a trivial experiment. If the strategy is that of exploiting surfaces, the first choice is that of deciding which material to use: conductor or semiconductor; reactive or inert; magnetic or nonmagnetic. An expertise was available on organizing SAMs on gold surfaces. The goal was that of monitoring supramolecular interactions. An obvious choice was using gold for not very reactive surfaces. The first experiments were performed using aromatic molecules in order to take advantage of the mobility of their π electrons. A sulfur donor was added to ensure good contact with the gold electrodes. Sometimes, two electrodes are obtained by digging a cavity in the metal using standard nanofabrication techniques. They, in turn were operated in such a way as to leave a gap of about 4 nm to host the molecule (Lämmle *et al.*, 2010).

As we have seen in Chapter 9, several organic radicals have been used either alone or in combination with TM and/or Ln ions to give MM. They have been explored for the possibility to organize them in layers. The investigated system contains verdazyl derivatives, whose formula is sketched in Scheme 17.1.

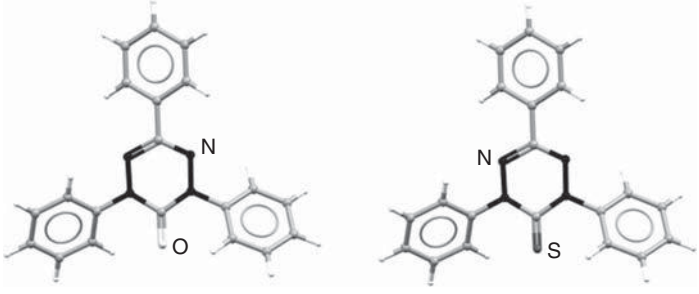

1,3,5,-Tripheny1-6-oxoverdazyl (TOV)

1,3,5,-Tripheny1-6-thioxoverdazyl (TTV)

Scheme 17.1

The archetypal radical was one of the first to be used for magnetic properties showing FM (ferromagnetic) coupling in organics. Many derivatives were investigated for several different properties, and one of the interesting features of

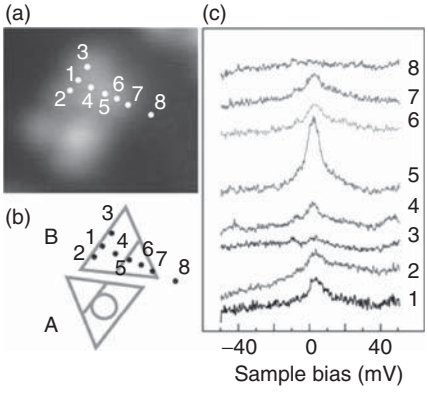

Figure 17.10 (a) STS detection positions on type B molecule in the A–B dimer. (b) Illustration of (a). (c) Changes of the Kondo resonance of the TOV molecule with the detection positions. Numbers for the positions in all panels are synchronized. (Reproduced from Liu, *J. et al.* (2013) with permission from The American Chemical Society.)

TOV was that it showed a Kondo resonance when investigated as layers deposited on gold (Liu *et al.*, 2013). The basic difference between the two is an oxygen atom for TOV which becomes a sulfur atom for TTV. TOV is completely flat, whereas in TTV the sulfur is bent out of the molecular plane. STM was used to monitor the organization of the molecules on the Au(111) surface. Several aggregates were evidenced. Two different types of molecules A and B were observed. The former had a protrusion which the latter did not have. STS spectra were recorded for several types of TOV molecules. The zero-bias peak was clearly observed for TOV molecules without the protrusion. No peak was observed for other TOV molecules or for TTV. The transition was attributed to a Kondo resonance which was associated with a high delocalization of the unpaired π electron (Figure 17.10).

Beyond providing an important step to a common language between molecules and QDs, systems like this can be used in STM to achieve submolecular spatial resolution and simultaneous characterization of both the adsorption configuration and the spin state. Nitronyl nitroxides have been investigated deposited on a gold(111) surface (Zhang *et al.*, 2013), taking advantage of the presence of thiolate groups on purpose to ease the formation of layers. An example of a used molecule is shown Scheme 17.2 and in Figure 17.11 (Mannini

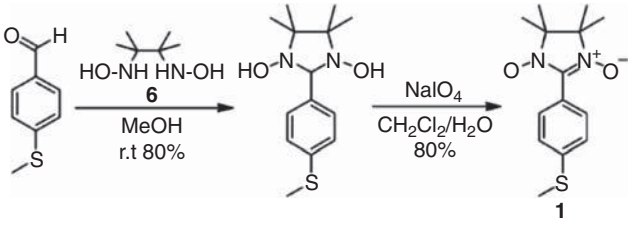

Scheme 17.2 Synthesis of the radical p-phenyl-S-methyl-nitronyl-nitroxide

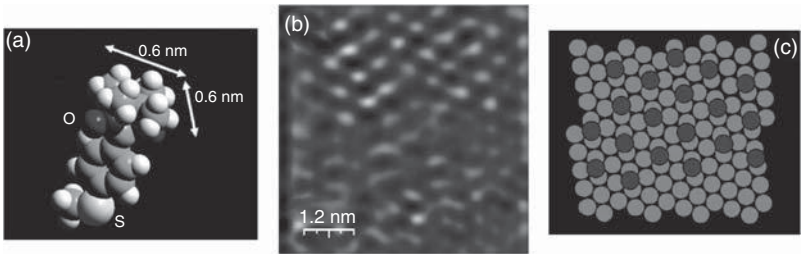

Figure 17.11 (a) Cartoon of the molecule. (b) Filtered SAM of the radical on gold surface. (c) Suggested model of the packing.

et al., 2007). ESR spectra of SAM were well resolved and showed the presence of interactions between neighboring molecules.

A more spintronic-oriented study was later reported using cyanophenyl NITR. The attachment of the radical to the surface was provided by the aromatic rings. The topography is more detailed, as shown in Figure 17.12 (Zhang *et al.*, 2013). The interaction with a magnetic field generates a splitting of the resonance peak resonance at the Fermi level in the differential conductance, which depends on the *g*-factor equal to 1.98. We recall that no such decrease from the value *g* of the radical was observed in the thiolate described previously. The origin of the zero-bias anomaly is in perfect agreement with the 50-year-old Anderson–Appelbaum theory of the Kondo effect (Anderson, 1966; Appelbaum, 1966).

17.9 Pc Family

Given the excitement produced by the discovery of SIM behavior in Pc derivatives of several Ln ions, it is certainly not unexpected that attempts were made to investigate the mechanism of charge transport in single molecules of Ln with Pc, in particular focusing on Kondo effects in these materials. We recall that Pc derivatives can be stable in two oxidation states, namely $Ln(Pc)_2^-$ and $Ln(Pc)_2$. Electron oxidation of $[LnPc_2]^-$ occurs at the ligand, resulting in the neutral $[LnPc_2]$ with an open shell π-electron system. The $TbPc_2$ molecule therefore has two spin systems, that is, an unpaired π electron on the Pc ligands and a Tb^{3+} ion with 4f electrons. The Kondo effect requires that $TbPc_2$ SIMs couple with magnetic impurities including Tb^{3+} ions and/or conducting electrons (Katoh *et al.* (2009).

An elegant approach was that of using organic field-effect transistors (OFETs), whose characteristics are modulated by an electrical field. They can be operated in both p-channel and n-channel modes. This unique characteristic simplifies the preparation processes when constructing complementary circuits. Currently, most ambipolar OFETs are composed of layered or mixed films of p-type and n-type semiconducting molecules.

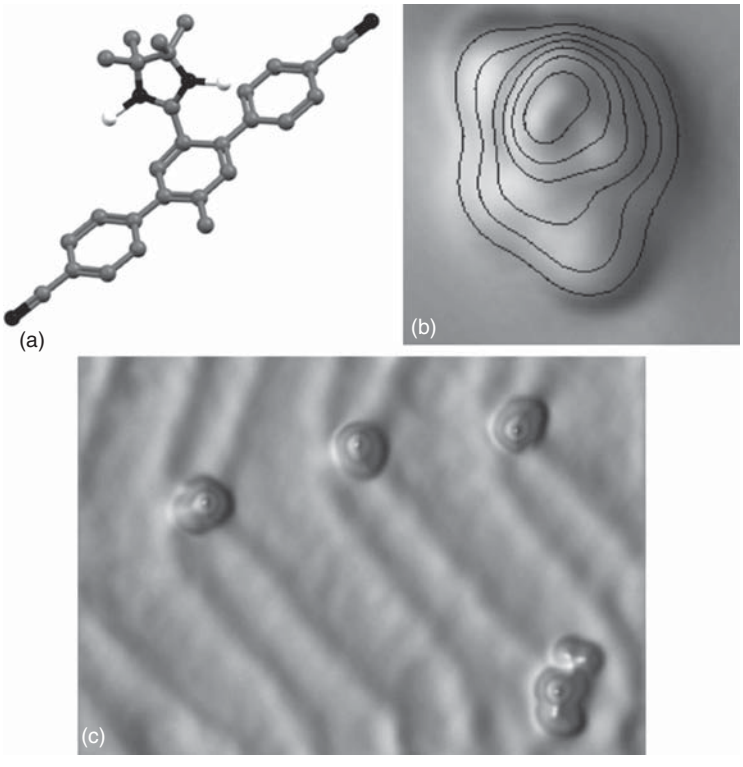

Figure 17.12 (a) The 2′-nitronylnitroxide-5′-methyl-[1,1′;4′,1″]terphenyl-4,4″-dicarbonitrile radical. (b) High-resolution topography of one organic radical molecule. Contour lines are at height intervals of 50 pm. (c) Topography of individual molecules on Au(111). The bottom right molecule is decorated by three neighboring dichloromethane molecules. (Reproduced from Zhang, Y-H. *et al.* (2013) with permission from Macmillan Publishers Limited.)

The delicate point is characterizing the data collected on the surfaces, where many points must rely on polite guesses. Several different techniques were used, but STM and STS had a major role. The STM images of the surface were used to characterize the molecules deposited on a Au(111) surface. On the Au(111) surface, after deposition of $TbPc_2$ molecules, two types of molecules were observed: the upper isolated molecule had four lobes, and the lower one had eight lobes. The analysis of the four-lobe molecule was made by comparing the measured height of ∼140 pm with the data of reported heights of isolated molecules of CoPc, FePc, and metal-free Pc, which have been observed at cryogenic temperatures. In addition, they showed a cross-like shape in the topographic image (Singh *et al.*, 2014). The MPc and Pc molecules might be formed by a cracking of the molecule MPc_2 in the sublimation process.

One of the key experiments was the dI/dV mapping of the four-lobed molecule. This technique was used to distinguish between MPc and Pc molecules. This type of dI/dV mapping, however, was obtained for approximately half of the isolated

molecules. The rest of the molecules showed no significant features in the dI/dV curves. The latter have been assigned to molecules missing the metal ion. A Kondo peak was observed only for TbPc. By fitting the STS signal, the energy width of the feature corresponded to a Kondo temperature (T_K) of ~250 K, which is similar to those for the 3d metal complexes CoPc and FePc. The Kondo effect was not observed with the fragments of DyPc and YPc.

A top-contact and bottom-contact thin-film OFETs device was made, which showed that the TbPc-based devices showed p-channel characteristics. On the other hand, DyPc-based devices exhibited both hole and electron transport properties (ambipolar channel characteristics). To the best of our knowledge, this was the first observation of electron transport properties in Ln^{3+}–Pc molecules, providing a good starting point for designing complexes with electron transport properties for OFETs. The use of the mixed MPc device makes it possible to study the processes associated with film formation and diffusion in two or three dimensions. The relationship between electronic transport properties and film/electronic structures is under investigation. Understanding and being able to measure the magnetic coupling/electronic transport properties of a single molecule of rare-earth metal^{III}–Pc_2 molecules is expected to play a key role in the design of spintronic devices. Currently, the understanding of the Kondo effect needs more thorough studies. We believe that the splitting energy of the sublevels of these molecules in a crystal field is critical for understanding the Kondo effect, and the relation between T_K and the blocking temperature (T_B) must be discussed further.

A beautiful example of the use of chemistry has been reported by Komeda *et al.* (2013). It could be described as double-faced molecules or the heteroleptic double-decker complex. The two faces can be different: for instance, Pc and naphthalocyanate (NPc). We call PcUp the molecule that is attached to the surface with the NPc face, and NPcUp the molecule with the Pc face attached (Figure 17.13).

Given the SIM nature of $Tb(Pc)_2$, it may be interesting to study the effect of transport of the molecule which has Pc attached to the electrode or the NPc. Of course, a tool is needed, and STM appears to be perfect for the job. Evidence was obtained that no long-range order was achieved in the film. Kondo resonance is observed for the two molecules as evidenced by the difference of signals for NPcUP and PcUp. In both cases, the Kondo peaks are associated with an unpaired electron in a π orbital, as confirmed by the spin-resolved DFT (density functional theory) technique.

An important parameter is the line width of the resonance. This can be converted to the Kondo temperature as

$$\Gamma(T) = 2((\pi k_B T)^2 + 2(k_B T_K)^2)^{\frac{1}{2}} \tag{17.4}$$

The calculated values are 32 and 48 K for Pc-up and NPc-up molecules, respectively.

We believe that the splitting energy of sublevels of these molecules in a crystal field is critical for understanding the Kondo effect.

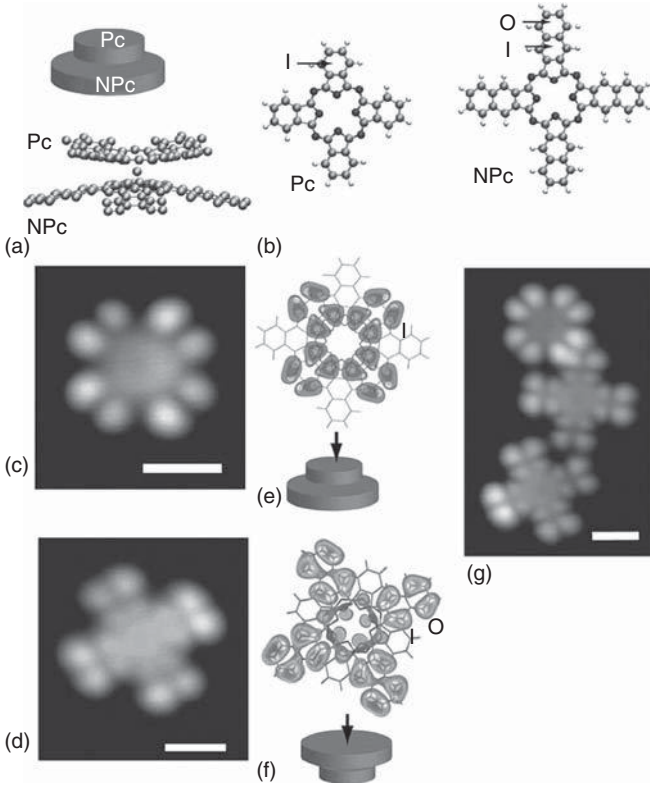

Figure 17.13 (a,b) Models of the TbN-PcPc double-decker molecules. "I" and "O" in (b) specify the position of the outer phenyl rings. (c–f) STM images and DFT simulated images of isolated PcUp and NPcUp molecules. (g) STM image of aggregates. White bars in (c), (d), and (g) are 1 nm. (Reproduced from Komeda, T. *et al.* (2013) with permission from The American Chemical Society.)

17.10 Mn_{12} Forever

As soon as the potential of molecules in spintronics was realized, the attention rather obviously fell on SMMs; and Mn_{12}, being an SMM superstar, was the first system to be investigated. Alas, Mn_{12} is far from being ideal if you try to use to organize it on surfaces. You may find appealing groups to generate tailored molecules for STM, but if you try to have confirmation from spectroscopic techniques, you immediately find that partial reduction has occurred. The best technique to this end has been XMCD, which in the accurate optimization operated by Sessoli *et al.* (Cornia *et al.*, 2011) has become a must to verify the structural properties of clusters organized on surfaces.

Taking into account these difficulties, Kern *et al.* used electrospray ion beam deposition as a gentle technique which was able to deposit Mn_{12} on several

supports, namely Cu(001), Au(111), and BN deposited on Rh(111) (Kahle *et al.*, 2011). The apparatus measures the chemical composition and the amount of deposited material, and the results seem to confirm that the surface molecules correspond indeed to Mn_{12}. But the key result must be the observation that the surface molecule has the same magnetic properties as those of the bulk. The magnetic properties were measured by inelastic spin-flip spectroscopy at 1.5 K. The technique used is STM, which measures the differential conductance of a two-probe device as the voltage sweeps across the excitation energy. The method can be used for different measurements, namely vibrational, electric, and magnetic (spin) properties. For the magnetic properties, the best results were obtained for molecules deposited on BN layers. The experiments were performed without an applied magnetic field and with 10 T orthogonal to the layer. The dI/dV versus V plots show several transitions. The one observed at lowest field is attributed to the $\Delta M = 1$ transitions between different M components of the $S = 10$ ground state. The ones at higher V correspond to transition involving the excited states $S = 9$. The agreement with experimental data is fair.

Dynamics is also taken into consideration. Using the line widths of the peaks, the lifetime of the peaks is estimated to be in the range 2–4 ps. From this, it is calculated that in order to do spin-pumping, currents of 100 nA would be needed, much too high for the fragile structure of Mn_{12} and possible only in bulk systems.

Using more stable and easily handled molecules can be more rewarding. Given the interesting double- and multiple-decker Ln compounds, which we have discussed for their bulk SMM properties in Chapter 13, it is exciting to see how they can be used in nanolayered structures.

17.11 Hybrid Organic and f Orbitals

One of the most promising perspectives for development is using multi-dot devices in a three-terminal scheme. It is based on letting a current flow through a nonmagnetic QD that is coupled to an SMM. An evocative image is that of a carbon nanotube (CNT) connecting SMM, and the coupling can be provided by different types of interactions such as dipolar, exchange, magneto-Coulomb, or flux. Beyond CNT, an interesting area to explore is that of graphene devices. Indeed, reports are available of magnetic coupling of porphyrin molecules through graphene. Devices of this kind are actively being investigated for measuring the single-molecule magnetic moment. A goal that is closer to be achieved after the implementation of nano-SQUID is a device that exploits SWCNTs to connect the superconducting rings.

An example of the opportunities provided by hybrid systems is the anchoring of an SMM such as $LnPc_2$ on a SWCNT. The first step was developing the chemistry needed to optimize the hybrid structure. The chosen target was TbPc-pyrene whose structure is sketched below. Pyrene is well known to be able to interact with SWCNT thanks to the $\pi-\pi$ stacking interactions. The process of producing clean objects is very delicate (Kyatskaya *et al.*, 1968).

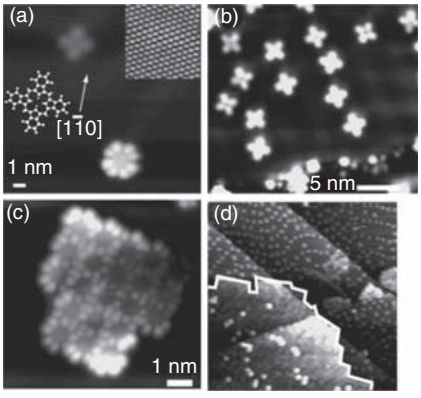

Figure 17.14 STM images of (a) single molecules of TbPc (upper) and $TbPc_2$ (lower). An atomic image of the Au(111) is shown in the inset. Schematic models of the Pc plane of the observed TbPc and $TbPc_2$ molecules are superimposed. (b) TbPc molecules on the terrace part of the Au(111) surface. (c) $TbPc_2$ film composed of 21 molecules. (d) Coexisting $TbPc_2$ islands and isolated TbPc molecules. (Reproduced from: "Direct Observation of Lanthanide(III)-Phthalocyanine Molecules on Au(111) by Using Scanning Tunneling Microscopy and Scanning Tunneling Spectroscopy and Thin-Film Field-Effect Transistor Properties of Tb(III)- and Dy(III)-Phthalocyanine Molecules", J. Am. Chem. Soc., **2009**, *131*, 9967 by Katoh, K. *et al.* with permission from The American Chemical Society.)

LnPc complexes can be deposited on a Au(111) surface using standard high-vacuum techniques. Using STM, a beautiful images were obtained, as shown in Figure 17.14. In order to understand what is seen, it is necessary to use computer modeling (Katoh *et al.*, 2009). An available package, the Vienna Ab initio Simulation Package (VASP), can be used for this purpose. It uses a model molecule, and the rest is shown in Figure 17.14b. The two Pc ligands in the Tb derivative are rotated by 45° and bent with respect with each other. The molecules on the surface are ordered, forming a square lattice. The neighboring molecules adopt different angles between planes, to minimize steric repulsion.

17.12
Magnetically Active Substrates

Using a magnetic substrate instead of the nonmagnetic one discussed so far, some interesting results can be obtained showing how an external magnetic field provided by ferromagnetic layers of Co and Ni can influence the possibilities of storing information. A suitable example is provided by octaethylporphyrin (OEP) iron chloride, which can form layers (Wende *et al.*, 2013). The flat nature of porphyrin and phthalocyanine has been mentioned several times, and shown to be well suited to organize on surfaces. Monolayer (ML) and submonolayer coverage of OEP Fe^{3+} chloride was achieved by *in situ* preparation of 5 ML Co/Cu(100) and 15 ML Ni/Cu(100). The nature of the species adsorbed was determined by X-ray techniques such as XAS, XMCD, and near-edge

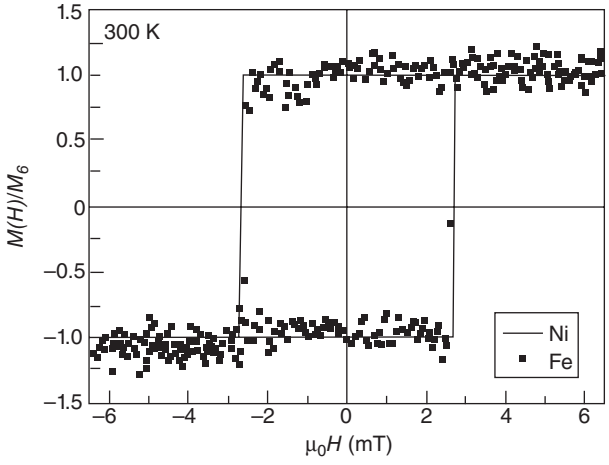

Figure 17.15 Hysteresis curves of the Fe atom (filled squares) and Ni (full line) obtained by the L_3 edge XMCD maxima of Fe OEP on Ni/Cu(100) at 300 K. (Reproduced from Wende, H. *et al.* (2013) with permission from Nature Publishing Group.)

X-ray absorption fine structure (NEXAFS). The evidence suggested a planar structure and the absence of the chloride, a result which is confirmed by calculations.

XMCD is a good technique for the characterization of the magnetic properties. The data show magnetic hysteresis at room temperature for Ni (remember that XMCD is element-sensitive). The exciting feature is that the same hysteresis is observed for Fe, as shown by Figure 17.15.

Now, Fe in the porphyrin environment is paramagnetic and should not show hysteresis. The qualitative explanation is that iron is coupled to Co and Ni. DFT calculations were performed on FeOEP with and without chloride, and the evidence pointed to reduced species. The surface structure was taken into account by including a fragment of face-centered cubic (fcc) Co. The analysis of the calculations showed a ferromagnetic coupling between Fe and Co, which must be due to superexchange through the nitrogen ion.

Emerging from the sea of theory, let us end up with a nice experiment that shows how grazing angle and orthogonal measurement provide the magnetization in-plane (Co) to out of plane (Ni) (Hermanns *et al.*, 2013). A possible role for elaborating magnetic interactions at a distance between magnetic molecules such as CoOEP is that of graphene. Graphene has many desirable properties for spintronic applications, such as high charge carrier mobility, low SOC, and hyperfine structure due to its p electrons. Another favorable characteristic is the planar nature of the electronic properties, which become metal-like. Therefore it has a huge functional anisotropy, and we are sure that the readers of this book now are easily convinced of the goodness of this property. The interaction of the graphene with molecules is of the van der Waals type, giving a weak coupling between the surface and the adsorbed molecule.

Repeating the experiments using CoOEP adsorbed on graphene-protected Ni by XMCD showed that there is an antiferromagnetic coupling between Co and Ni, which is transmitted via graphene. In fact, the sign of the XMCD of Co is opposite to that of Ni, a clear evidence of AFM coupling. A simple model is used to describe the temperature dependence of the magnetization of CoOEP and Ni. The Co data are described by a Brillouin function $B_J(\alpha)$as shown below:

$$M_{Co} = M_{Ni} B_J(\alpha) \tag{17.5}$$

where M are the magnetizations, J the spin, $\alpha = E_{ex}/(kT)$ with E_{ex} the exchange energy. The magnetization of nickel is appropriately that of a ferromagnet. The exchange energy is calculated as 1.8(5) meV. The coupling is not due to direct interaction between the two metal ions but rather by overlap of the p_z orbitals of graphene with the π orbitals of the porphyrin. The suggested mechanism is the following: the spin-minority Ni d orbitals hybridize with graphene p_z orbitals; p_z overlaps antiferromagnetically (AFM) with π of the porphyrin and this AFM with the z^2 orbital of Co. If no mistake has been made in developing the chain of interactions, the spin of the Ni is opposed to that of the Co. In moving along the chain, there is a narrow passage between graphene and porphyrin, which is responsible of the weak coupling.

These results are confirmed by DFT calculations, which are nowadays a must for working in MM. It is important to realize how hybrid systems such as metals, graphene, and magnetic molecules can coexist and work synergically to produce new magnetic systems.

17.13 Using Nuclei

Although electrons can play several important roles in spintronics, they have several drawbacks if the goal of their use is the development of quantum computing. In fact, all the possible schemes of operation of a quantum computer require long relaxation and long coherence times, and electrons can fulfill the requirements only with difficulty. The reason is simple: electrons are in the strong coupling regime, and in order to maintain stable entanglement, it is necessary to weaken the coupling, and this may not be obvious.

One of the possibilities to reduce the coupling is to change the spin. Nuclear spins can be used because they interact more weakly with the environment. This obvious observation was clear from the beginning, and the first examples of QC (quantum computing) were realized using NMR. Several different approaches were used to overcome the weak points of the nuclear strategy and to design tools to address and manipulate individual nuclear spins. A complex approach using a SMM together with STS has shown that it is possible to measure the reversal of the electronic magnetic moment and read the nuclear spin, together with the lifetime and temperature of a single nuclear spin.

A successful approach has been made to achieve electronic readout of a single $_{159}$Tb (100% natural isotope with $I = 3/2$) nucleus using the ubiquitous $TbPc_2$ (Komeda *et al.*, 2011). The properties of $TbPc_2$ have been described several times in the book: high stability; two-level system with a ground $S_{eff} = 1/2$; high uniaxial anisotropy; QTM quantum phase interference, spin state interference and coherent oscillations. In order to be successful, the experiment must minimize the interactions with the environment by measuring a single molecule. At the heart of the experiment is the use of STM on molecules that are organized in a transistor-like configuration using electromigrated junctions. Generally speaking, the electromigration is a technique in which a nanoscale gap in a narrow metallic wire situated on a gate insulator material is created by thermally assisted electromigration. The transistor is formed by the molecule $TbPc_2$ whose transport properties are controlled by the gate voltage V_g, and the voltage difference between the electrodes is controlled by the drain source voltage V_{ds}.

The system interacts with an applied magnetic field at temperatures below 1 K. The electron spin levels are split into four due to hyperfine interaction. There are two regimes depending on the strength of the magnetic field shown in Figure 17.16 for weak field, and there are 16 level crossings of which the level crossings between the $|+6\ M_I>$ and $|-6\ M_I>$, $M_I = 3/2, 1/2, -1/2, -3/2$ have a particular importance. Actually, because the ± 6 levels are coupled due to the transverse field induced by the LF (ligand field), the crossing is an avoided crossing and QTM is observed. The other crossings involve $|+6\ M_I>$ and $|-6\ M_I'>$, where M_I' is different from M_I (Vincent *et al.*, 2012).

At high field, a reversal of the magnetization can be observed which involves sizeable phonon coupling. This means that noncoherent tunneling is observed.

STS can be used to show that the electronic charge goes through the organic moiety and not through the metal ion. The Pc ligands can be considered as QDs, which interact with the Tb ion. This is the key to the use of the QD

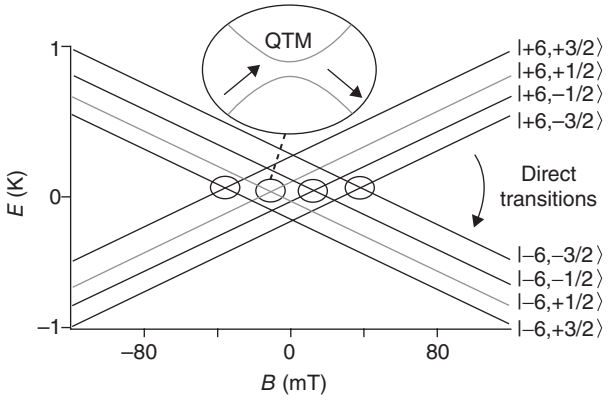

Figure 17.16 Energy of the two ground states, $J_z = \pm 6$, as a function of the magnetic field. (Reproduced from Vincent, R. *et al.* (2012) with permission from Macmillan Publishers Limited.)

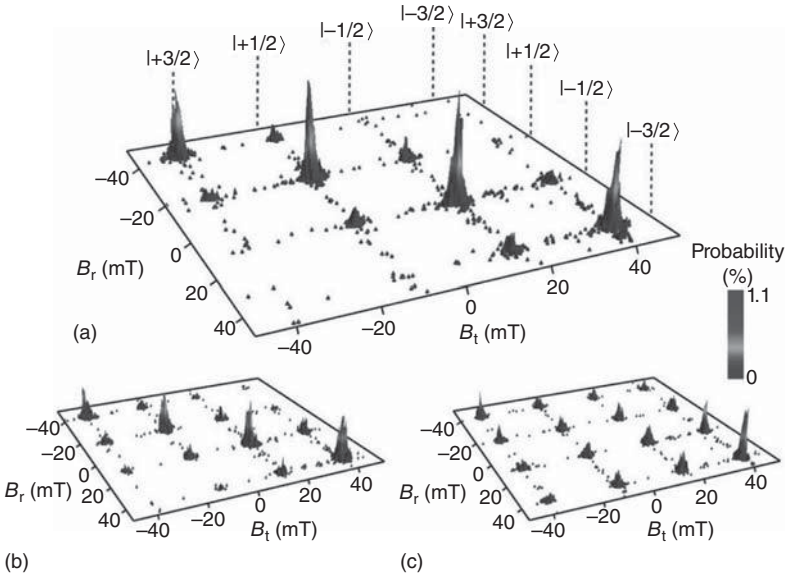

Figure 17.17 Transition matrix of the QTM events as a function of the waiting time. The switching fields of the Tb^{3+} magnetic moment of subsequent field sweeps are plotted in two-dimensional histograms for three waiting times t_w: (a) $t_w = 0$ s; (b) $t_w = 20$ s; and (c) $t_w = 50$ s. The two axes correspond to the trace and retrace field sweeps, Bt and Br, respectively. (Reproduced from Vincent, R. *et al.* (2012) with permission from Macmillan Publishers Limited.)

to obtain information on the metal ion. The experiment measures the differential conductance dI/dV, which evidenced a Kondo peak associated to an exchange interaction of 0.35 T between the spin of the ligand and the magnetic moment of Tb.

By varying V_g, it is possible to change the number of unpaired electrons on the molecule and shift between the Coulomb blockade and the Kondo regime. The magnetic field dependence is achieved as abrupt jumps of the differential conductance. There are four such jumps, which correspond to QTM of the four avoided crossings associated with the four hyperfine fields. The fields are in perfect agreement with those obtained from bulk measurements.

The last measurements report the dependence of the waiting time (t_w) between field sweeps. Figure 17.17 reports the two-dimensional histograms corresponding to 11 000 field sweeps. The axes of the diagram correspond to the trace and retrace field sweeps. The diagonals correspond to the data of nuclear spin states, while the off-diagonal data correspond to nuclear spin changed dMI = 1, 2, 3. The three diagrams refer to waiting times of 0, 20, and 50 s, respectively. The four peaks on the diagonal show a clear dominance of these transitions, which indicate a long lifetime of the nuclear spin states. Still after 20 s, the situation is not much changed. After 50 s, however, all the positions are essentially occupied, which means that numerous spin flips occur.

Finally, the last information so far obtained is the influence of transport on the spin-flip dynamics.

It is apparent that this is a promising perspective. The preliminary results indicate that there is the possibility of using molecular-size devices to read electronically the nuclear spin flips. Whether this is the first step for an exciting trip requires more experiments.

17.14 Some Device at Last

One of the possibilities open to implement a memory device is the spin valve, which we have briefly described in Section 17.1 in the scheme of metal multilayers. We recall that the spin valve is the heart of the GMR sensors which are present in modern hard disks. The idea of using SMM rather than metal layers suggested a modified design. An SMM should be laterally coupled to an SWCNT inserted in a circuit. The obvious choice for the SMM was a member of the family $Tb(Pc)_2$, which have almost ideal properties for the supramolecular opportunities provided by their structure and unique magnetic properties. The suggestion was that the huge magnetic anisotropy might influence the current passing through the SWCNT (Urdampilleta *et al.*, 2011).

In order to have control on the SMM–SWCNT interaction, a new asymmetric molecule was designed. One decker is standard, while the other carries a modified pyrene group with a six-hexyl chain (Figure 17.18).

The pyrene moiety has the function of an anchor, and also the hexyl groups yield efficient π-stacking interactions with the sp^2 carbons of SWCNT.

The spin valve device essentially consists in a source and a drain connected by a SWCNT. $Tb(Pc)_2$* molecules are randomly attached on the SWCNT, and

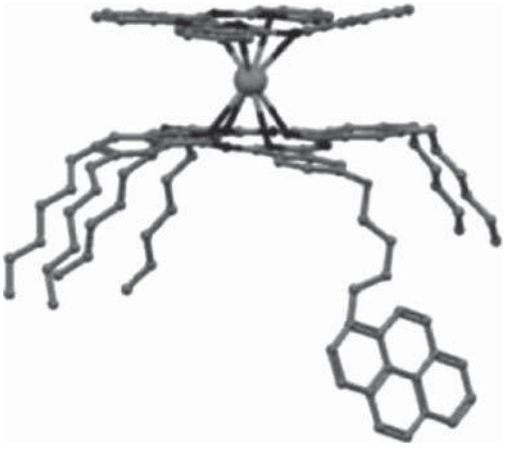

Figure 17.18 Sketch of the double-decker Tb^{3+} derivative. (Reproduced from Vincent, R. *et al.* (2012) with permission from Macmillan Publishers Limited.)

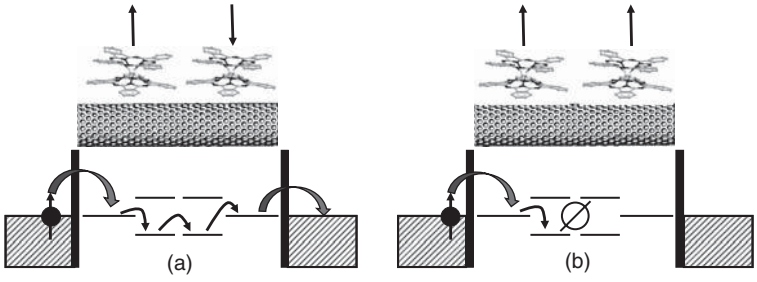

Figure 17.19 Scheme of the mechanism involving two TbPc2* molecules (a and b) grafted on a SWCNT. (Reproduced from Urdampilleta, M. *et al.* (2011) with permission from Macmillan Publishers Limited.)

the external magnetic field is applied in the plane of the sample. The ground state is a doublet ± 6 well separated from the excited states, which corresponds to a large magnetic anisotropy. Further the electron spin interacts with the $I = 3/2$ nuclear spin of Tb. This interactions splits the electronic structure in four hyperfine states. The sharp steps due to QT at the crossing levels are determined by ZFS and hyperfine interactions. The investigation of the magnetic properties of TbPc2 performed with a micro-SQUID at 0.04 K showed the presence of an hysteresis loop with four steps originated by the above mentioned hyperfine interaction.

The advantage of $Tb(Pc)_2^*$ over other SMMs is that it can switch at different fields according to the different mechanisms outlined above. Furthermore, it must be noticed that small differences are present in slightly different supramolecular positions, which combined with the versatility of physical properties may allow large differences between different molecules.

Interpreting the data within the spin valve scheme, we can imagine two molecules A and B and spin-degenerate conduction in the channel. Molecule A works as a spin polarizer and molecule B as the spin analyzer. Let us suppose that initially A and B are in parallel configuration and that at a given field A switches and the antiparallel order is achieved. This corresponds to lowest conductance (Figure 17.19a). In fact, the molecules induce localized states in the SWCNT via exchange interaction. The mismatch induced by the spin generates a tunnel barrier, hindering the charge flow. When B switches, a higher conductance occurs (Figure 17.19b). The coupling of the spin with the conduction electrons is justified by the presence of a radical delocalized on Pc.

References

Anderson, P.W. (1966) Localized magnetic states and fermi-surface anomalies in tunneling. *Phys. Rev. Lett.*, **17**, 95–97.

Appelbaum, J. (1966) "s-d" exchange model of zero-bias tunneling anomalies. *Phys. Rev. Lett.*, **17**, 91–95.

Arrio, M.A., Sainctavit, P., Cartier dit Moulin, C., Brouder, C., de Groot, F.M.F., Mallah, T., and Verdaguer, M. (1996) Measurement of magnetic moment at the atomic scale in a high TC molecular based magnet. *J. Phys. Chem.*, **100**, 4679–4684.

Badía-Romano, L., Bartolomé, F., Bartolomé, J., Luzón, J., Prodius, D., Turta, C., Mereacre, V., Wilhelm, F., and Rogalev, A. (2013) Field-induced internal Fe and Ln spin reorientation in butterfly [Fe_3LnO_2 (Ln = Dy and Gd) single-molecule magnets. *Phys. Rev. B*, **87**, 184403.

Baibich, M.N., Broto, J.M., Fert, A., Van Dau, F.N., Petroff, F., Etienne, P., Creuzet, G., Friederich, A., and Chazelas, J. (1988) Giant magnetoresistance of (001)Fe/(001)Cr magnetic superlattices. *Phys. Rev. Lett.*, **61**, 2472–2475.

Barth, J.V., Costantini, G., and Kern, K. (2005) Engineering atomic and molecular nanostructures at surfaces. *Nature*, **437**, 671–679.

Binasch, G., Grünberg, P., Saurenbach, F., and Zinn, W. (1989) Enhanced magnetoresistance in layered magnetic structures with antiferromagnetic interlayer exchange. *Phys. Rev. B*, **39**, 4828–4830.

Carra, P., König, H., Thole, B.T., and Altarelli, M. (1993a) Magnetic X-ray dichroism. General features of dipolar and quadrupolar spectra. *Phys. B: Phys. Condens. Matter*, **192**, 182–190.

Carra, P., Thole, B.T., Altarelli, M., and Wang, X. (1993b) X-ray circular dichroism and local magnetic fields. *Phys. Rev. Lett.*, **70**, 694–697.

Cornia, A., Mannini, M., Sainctavit, P., and Sessoli, R. (2011) Chemical strategies and characterization tools for the organization of single molecule magnets on surfaces. *Chem. Soc. Rev.*, **40**, 3076–3091.

Dreiser, J., Pedersen, K.S., Birk, T., Schau-Magnussen, M., Piamonteze, C., Rusponi, S., Weyhermüller, T., Brune, H., Nolting, F., and Bendix, J. (2012) X-ray magnetic circular dichroism (XMCD) study of a methoxide-bridged Dy III-Cr III cluster obtained by fluoride abstraction from *cis*-$[Cr^{III}F_2(phen)_2]^+$. *J. Phys. Chem. A*, **116**, 7842–7847.

Fleury, B., Catala, L., Huc, V., David, C., Zhong, W.Z., Jegou, P., Baraton, L., Palacin, S., Albouy, P.A., and Mallah, T. (2005) A new approach to grafting a monolayer of oriented Mn_{12} nanomagnets on silicon. *Chem. Commun.*, 2020–2022.

Hermanns, C.F., Tarafder, K., Bernien, M., Krüger, A., Chang, Y.-M., Oppeneer, P.M., and Kuch, W. (2013) Magnetic Coupling of Porphyrin Molecules Through Graphene, *Adv. Mater.*, **25**, 3473–3477.

Kahle, S., Deng, Z., Malinowski, N., Tonnoir, C., Forment-Aliaga, A., Thontasen, N., Rinke, G., Le, D., Turkowski, V., Rahman, T.S. *et al.* (2011) The quantum magnetism of individual manganese-12-acetate molecular magnets anchored at surfaces. *Nano Lett.*, **12**, 518–521.

Komeda, T., Isshiki, H., Liu, J., Zhang, Y.-F., Lorente, N., Katoh, K., Breedlove, B.K., and Yamashita, M. (2011) Observation and electric current control of a local spin in a single-molecule magnet, *Nat. Commun.*, **2**, 27.

Katoh, K., Yoshida, Y., Yamashita, M., Miyasaka, H., Breedlove, B.K., Kajiwara, T., Takaishi, S., Ishikawa, N., Isshiki, H., Zhang, Y.F., Komeda, T., Yamagishi, M., and Takeya, J. (2009) First observation of a Kondo resonance for a stable neutral pure organic radical, 1,3,5-triphenyl-6-oxoverdazyl, adsorbed on the Au(111) surface. *J. Am. Chem. Soc.*, **135**, 651–658.

Kim, Y., Pietsch, T., Erbe, A., Belzig, W., and Scheer, E. (2011) Benzenedithiol: A Broad-Range Single-Channel Molecular Conductor. *Nano Lett.*, **11**, 3734–3738.

Komeda, T., Isshiki, H., Liu, J., Katoh, K., Shirakata, M., Breedlove, B.K., and Yamashita, M. (2013) Variation of Kondo peak observed in the assembly of heteroleptic 2,3-naphthalocyaninato phthalocyaninato Tb(III) double-decker complex on Au(111). *ACS Nano*, **7**, 1092–1099.

Kondo, J. (1968) Effect of ordinary scattering on exchange scattering from magnetic impurity in metals. *Phys. Rev.*, **169**, 437–440.

Kyatskaya, S., Mascarós, J.R.G., Bogani, L., Hennrich, F., Kappes, M., Wernsdorfer, W., and Ruben, M. (2009) Anchoring of rare-earth-based single-molecule magnets on single-walled carbon nanotubes. *J. Am. Chem. Soc.*, **131**, 15143–15151.

Lämmle, K., Trevethan, T., Schwarz, A., Watkins, M., Shluger, A., and Wiesendanger, R. (2010) Unambiguous determination of the adsorption geometry of a metal–organic complex on a bulk insulator. *Nano Lett.*, **10**, 2965–2971.

Liang, W., Shores, M.P., Bockrath, M., Long, J.R., and Park, H. (2002) Kondo resonance in a single-molecule transistor. *Nature*, **417**, 725–729.

Lee, C.W., Kim, O.Y., and Lee, J.Y. (2014) Organic materials for organic electronic devices. *J. Ind. Eng. Chem.*, **20**, 1198–1208.

Liu, J., Isshiki, H., Katoh, K., Morita, T., Breedlove, B.K., Yamashita, M., and Komeda, T. (2013) First observation of a Kondo resonance for a stable neutral pure organic radical, 1,3,5-triphenyl-6-oxoverdazyl, adsorbed on the Au(111) surface. *J. Am. Chem. Soc.*, **135**, 651–658.

Lüder, J., Eriksson, O., Sanyal, B., and Brena, B. (2014) Revisiting the adsorption of copper-phthalocyanine on Au(111) including van der Waals corrections. *J. Chem. Phys.*, **140**, 124711.

Malavolti, L., Lanzilotto, V., Ninova, S., Poggini, L., Cimatti, I., Cortigiani, B., Margheriti, L., Chiappe, D., Otero, E., Sainctavit, P., Totti, F., Cornia, A., Mannini, M., and Sessoli (2015) Magnetic Bistability in a Submonolayer of Sublimated Fe_4 Single Molecule Magnets, *Nano Lett.*, DOI: 10.1021/nl503925h.

Mannini, M., Sainctavit, P., Sessoli, R., Cartier Dit Moulin, C., Pineider, F., Arrio, M.A., Cornia, A., and Gatteschi, D. (2008) XAS and XMCD investigation of Mn12 monolayers on gold. *Chem. Eur. J.*, **14**, 7530–7535.

Mannini, M., Sorace, L., Gorini, L., Piras, F.M., Caneschi, A., Magnani, A., Menichetti, S., and Gatteschi, D. (2007) Self-assembled organic radicals on Au(111) surfaces: a combined ToF-SIMS, STM, and ESR study. *Langmuir*, **23**, 2389–2397.

Park, J., Pasupathy, A.N., Goldsmith, J.I., Chang, C., Yaish, Y., Petta, J.R., Rinkoski, M., Sethna, J.P., Abruna, H.D., McEuen, P.L. *et al.* (2002) Coulomb blockade and the Kondo effect in single-atom transistors. *Nature*, **417**, 722–725.

Roemelt, M., Maganas, D., DeBeer, S., and Neese, F. (2013) A combined DFT and restricted open-shell configuration interaction method including spin-orbit coupling: Application to transition metal L-edge X-ray absorption spectroscopy. *J. Chem. Phys.*, **138**, 204101–204121.

Rogez, G., Donnio, B., Terazzi, E., Gallani, J.L., Kappler, J.P., Bucher, J.P., and Drillon, M. (2009) The quest for nanoscale magnets: the example of $[Mn_{12}]$ single molecule magnets. *Adv. Mater.*, **21**, 4323–4333.

Shores, M.P. and Long, J.R. (2002) Tetracyanide-bridged divanadium complexes: redox switching between strong antiferromagnetic and strong ferromagnetic coupling. *J. Am. Chem. Soc.*, **124**, 3512–3513.

Singh, S., Singh, A., Fitzsimmons, M.R., Samanta, S., Prajapat, C.L., Basu, S., and Aswal, D.K. (2014) Structural and magnetic depth profiling and their correlation in self-assembled Co and Fe based phthalocyanine thin films. *J. Phys. Chem. C*, **118**, 4072–4077.

Stepanow, S., Mugarza, A., Ceballos, G., Moras, P., Cezar, J.C., Carbone, C., and Gambardella, P. (2010) Giant spin and orbital moment anisotropies of a Cu-phthalocyanine monolayer. *Phys. Rev. B: Condens. Matter Mater. Phys.*, **82**, 014405.

Stohr, J. and Wu, Y. (1994) in *New Directions in Research with Third-Generation Soft X-Ray Synchrotron Radiation* (eds A.S. Schlachter and F.J. Wuilleumier), Kluwer Academic Press, p. 231.

Urdampilleta, M., Klyatskaya, S., Cleuziou, J.P., Ruben, M., and Wernsdorfer, W. (2011) Supramolecular spin valves. *Nat. Mater.*, **10**, 502–506.

Van Der Laan, G. and Thole, B.T. (1990) Magnetic dichroism in the x-ray-absorption branching ratio. *Phys. Rev. B*, **42**, 6670–6674.

Van Der Laan, G. and Thole, B.T. (1991) Strong magnetic x-ray dichroism in 2p absorption spectra of 3d transition-metal ions. *Phys. Rev. B*, **43**, 13401–13411.

Vincent, R., Klyatskaya, S., Ruben, M., Wernsdorfer, W., and Balestro, F. (2012) Electronic read-out of a single nuclear spin using a molecular spin transistor. *Nature*, **488**, 357–360.

Wende, H., Bernien, M., Luo, J., Sorg, C., Ponpandian, N., Kurde, J., Miguel, J., Piantek, M., Xu, X., Eckhold, Ph., Kuch, W., Baberschke, K., Panchmatia, P.M., Sanyal, B., Oppeneer, P.M., Eriksson, O. (2013) Substrate-induced magnetic

ordering and switching of iron porphyrin molecules. *Nat. Mater.*, **6**, 516–520.

Yoon, S.M., Lou, S.J., Loser, S., Smith, J., Chen, L.X., Facchetti, A., and Marks, T. (2012) Fluorinated Copper Phthalocyanine Nanowires for Enhancing Interfacial Electron Transport in Organic Solar Cells. *Nano Lett.*, **12**, 6315–6321.

Zhang, Y.-H., Kahle, S., Herden, T., Stroh, C., Mayor, M., Schlickum, U., Ternes, M., Wahl, P., and Kern, K. (2013) Temperature and magnetic field dependence of a Kondo system in the weak coupling regime. *Nat. Commun.*, **4**, 2110.

18
Hunting for Quantum Effects

18.1
From Classic to Quantum

The dramatic development of computing power has led to a great increase in the size and the complexity of the systems that can be addressed with computational techniques. We will not mention the impact of informatics in everyday life, which is apparent to everybody, but we will simply remind ourselves that our current era can be considered as the information age. The factors determining the revolution are multiple, but it is difficult to overestimate the importance of the miniaturization of memory storage devices. The smaller the size of memory units, the larger the number of elements or bits that can be assembled per unit area, with a resulting increase in the information density and complexity of circuits. The current size of memory units is of the order of tens of nanometers and the densities of the order of terabits for unit area. Although improvements have continuously taken place during the last 50 years, the process cannot continue forever: *sunt certi denique fines* (*the limits are well known*). There are essentially two types of limits: one is concerned with the increasing costs to be paid for implementing new and more effective fabrication plants that can scale the units to smaller sizes; another, even worse, is concerned with the fact that by reducing the size of the memories, the band structure breaks down and the description changes from classical to quantum mechanical. Below a certain size, it is therefore necessary to change the paradigms that control the fundamental working of devices, and substantial improvements are planned for the next generation of computers.

A revolutionary change can take place by taking advantage of the quantum properties of matter, and using them to develop a new way of storing and employing information. The idea was first suggested 25 years ago under the buzzword quantum computing (QC) (Deutsch and Jozsa, 1992). Nowadays, perhaps the most used expression is quantum information processing (QIP). The associated strategy is that of exploiting quantum effects in order to perform operations that are impossible with classical tools. In particular one can exploit quantum information (QI) to tackle encryption which cannot be violated or, in a less applications-oriented language, being able to map prime numbers. A general comment is in order here: the above-introduced operations are generally referred to by the people acting

Introduction to Molecular Magnetism: From Transition Metals to Lanthanides, First Edition.
Cristiano Benelli and Dante Gatteschi.
© 2015 Wiley-VCH Verlag GmbH & Co. KGaA. Published 2015 by Wiley-VCH Verlag GmbH & Co. KGaA.

in the field as *applied research themes*, which demand a parallel development of basic science (Stajic, 2013). Frankly speaking, in the authors' opinion, this is going to far. The applied issues are still essentially in the basic field although the first perspectives of something applicable start to appear (Hemmer and Wrachtrup, 2009).

The basic idea for QIP is to substitute bits, which exploit classic physics, with qubits, which exploit quantum mechanics. Several different systems have been suggested to be well suited for making qubits. We will not try to cover all the possibilities but will briefly report on the physical principles underlying the attempted routes to QIP. One of the early attempts involved the use of nuclear magnetic resonance (NMR), as it is a well-suited technique to detect quantum effects in macroscopic systems. A nucleus with a spin of 1/2, such as ^{1}H, is a simple two-level subsystem that can be used as a qubit. Further, a molecule containing nonequivalent (for an NMR experiment) ^{1}H nuclei can be considered as a base with more than 1 qubit. The best condition for this kind of experiments is the liquid state, as the presence of rapid molecular tumbling greatly simplifies analysis of the system. Intermolecular interactions are canceled out by tumbling, and a sample that contains many copies of each molecule can be treated as a single molecule in a mixed spin state (Jones, 2011). Initial results were interesting, new opportunities have been recently reported (Cooper *et al.*, 2014), and useful ways are being implemented to modify the scale (Magesan, Cooper, and Cappellaro, 2013). Indeed, the scalability is one of the conditions that must be met to implement a quantum computer. We will come back to this point in the following.

Another class of systems that show quantum effects in the bulk is that of superconductors, which indeed are actively investigated (Dicarlo *et al.*, 2009). The key feature for these systems is the Josephson junction, which is well known in the magnetism area as component of SQUID. Such systems are bistable and, when the state equations are expressed in terms of the flux basis, the flux states can be used to create a bidimensional Hilbert space where to perform quantum operations. It is very instructive, in this sense, to notice that the Hamiltonian governing the behavior of Cooper pair boxes can be mapped onto the spin Hamiltonian of Chapter 7 with both axial and transverse terms being present (Koch *et al.*, 2007). The main problem of such system has been the tunability of the device and the instability with respect to external driving. Both issues were largely overcome by the introduction of the transmon concept (transmon is a superconducting charge qubit (Schreier *et al.*, 2008) where a large inductance is used to strongly admix the flux states, so as to create a purely two-state system suitable for stable quantum operations (Devoret and Schoelkopf, 2013)). Such systems are particularly appealing because they can be coupled coherently to the photonic states of cavities, so as to create quantum operations among different scalable qubits. Semiconductor quantum dots, which we have introduced in Section 17.2, also seem to constitute a viable alternative route, but they still suffer from huge problems in scalability.

So far we focused on electrically conducting systems, but another category of properties that hold much promise are the optical ones. For instance, two polarized rays can define two different qubits if the polarization planes are orthogonal to each other. The starting point of this technique was the availability of single-photon sources, linear optical elements, and single-photon detectors (Knill, Laflamme, and Milburn, 2001). The development of QC by using the optical approach strongly depends on the improvement of high-efficiency sources of indistinguishable single photons, scalable optical circuits, high-efficiency single-photon detectors, and low-loss interfacing of these components (O'Brien, 2007).

Optics-based QC systems, which are akin to molecular magnets, comprise fullerene-based materials (qubit based on the electronic spin of atoms or molecules encased in fullerene structures). Among the most promising systems are nitrogen vacancy centers in diamond, which are under investigation for atom-sized magnetometers and have already been employed in quantum encryption systems already on the market. QCs based on inorganic crystals doped with rare-earth metal ions are also interesting (qubit realized by the internal electronic state of dopants in optical fibers).

We will try to highlight some promising results. But before proceeding, let us spend some time in defining some fundamental concepts. We will take the view point of QC, but the attention to quantum properties is more general.

18.2 Basic QIP

The basic concepts that are used in the QC field are the following:

- bit, qubit
- superposition of states
- quantum gating
- entanglement
- coherence and decoherence
- dephasing
- spin manipulation
- spin logic
- quantum communications
- fidelity.

A bit is a system that can be in one of two possible different states, called 0 and 1. There must be a corresponding value of a physical property, and it must be possible to switch from one state to the other.

A qubit is the quantum version of a bit. It is defined on a two-level system, where the levels are also labeled 0 and 1, but it exploits a different, less intuitive, physics. In particular, the qubit can simultaneously be in both the 0 and 1 states and does not necessarily have to be in just one of them. A qubit can be obtained using many different properties, but we will focus on magnetic properties, using the SH, as all

other systems can be mapped on it. We have already used several times the effective S = 1/2 to define a two-level system which is characterized by M = ±1/2 for spin up or spin down, respectively. As these are quantum states, the spin qubit can also be in a linear combination of 0 and 1, or in a superposition of states. Systems with these properties can be based on NMR, as in the first attempts to implement a quantum computer (Criger *et al.*, 2012). Recent attempts have focused on the electron spin levels, or on mixed electron–nuclear levels (hyperfine levels). These systems have long been investigated using quantum techniques, such as pulse techniques operating on electron and nuclear spins, which in principle can be extended to QC.

The starting point to move toward QC can be the general quantum state given by

$$|\Psi\rangle = \alpha|\uparrow\rangle + \beta|\downarrow\rangle \tag{18.1}$$

where $\alpha\alpha^* + \beta\beta^* = 1$. A useful formalism to describe a given quantum state is that of the so-called Bloch sphere, depicted in Figure 18.1. It depicts the surface of a sphere of unitary radius which hosts a polar reference frame. There is only need for a couple θ and φ to specify a bit on the surface of the sphere.

Any quantum operation is defined by a trajectory on the sphere described by the matrices of unitary transformations. The path connecting two points on the Bloch sphere is a quantum gate operation. A quantum gate corresponds to an operation defined within the Boolean algebra. Let us see some examples taking into account

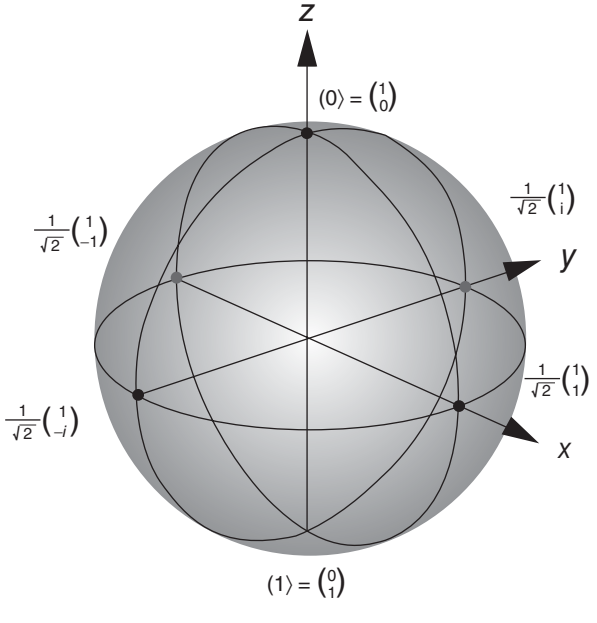

Figure 18.1 In the Bloch sphere each pair of antipodal points corresponds to mutually orthogonal state vectors.

that the matrix is defined using the Pauli matrices. The identity gate is represented by the identity matrix, while the NOT gate corresponds to inverting one qubit. For a spin, the NOT gate can be operated by flip techniques such as sending a proper microwave or radio waves pulse. Another common gate operation is the Hadamard transform, which converts the quantum state $|\uparrow\rangle$ into a superposition state $(|\uparrow\rangle + |\downarrow\rangle)/\sqrt{2}$. A superposition state is a quantum state where all the possible states coexist.

At this level, essentially everything can be a qubit, as long as the system retains the angular information (i.e., both θ and φ) over long times. There are infinite possibilities of choosing pairs of levels. We will soon show qubits made of single atoms, of single atoms embedded in fullerene molecules, or of organic radicals. But it is possible to use clusters of metal ions in the SIM and SMMs. It is apparent that clusters of more than two levels may be involved, and the Hilbert space will no longer be bidimensional. Therefore, we will have to work out models for multiple-level qubits, with the *caveat* that entanglement (as explained in the following) does not have a rigorous definition in such multidimensional spaces.

When the system is prepared, several factors of merit must be optimized in order to have an operable QC. Coherence of two waves gives the correlation between them. We recall that coherence in a tunneling process corresponds to a conservation of the phase. The phenomenon is different from relaxation. It may be defined also on the same wave, and it will be called self-coherence. It may be defined on very different types of waves. In a case relevant to QIP, coherence can be associated with a system of N electron spins described by a Hamiltonian that depends on the spin degree of freedom and on external control parameters. However, the interaction with environment tends to spoil the coherent character, leading to decoherence**.** The decay occurs with a characteristic time τ_d and the ratio between τ_d and the time of coherent manipulation τ_g is interpreted as a figure of merit. It is intuitively clear that the manipulation time must be as short as possible in order to perform many cycles per unit time and that τ_d must be as long as possible in order to use the device efficiently. If the ratio τ_d/τ_g is smaller than a threshold, typically 10^{-4}, the system is fault-tolerant. This is indeed one of the main criteria to test the qubit. Implicit in this is the temperature dependence. A system effective at room temperature is preferable to one operating below 4 K.

For two-bit systems, there are four basis states $|\uparrow\downarrow\rangle$, $|\downarrow\uparrow\rangle$, $|\uparrow\uparrow\rangle$, $|\downarrow\downarrow\rangle$, which require the introduction of the fascinating concept of entanglement. It is a typical quantum property that is often mentioned but not always properly. At least one of authors of this book, DG, has previously written an improper definition for it. Let us start from the accepted definition: two spins 1 and 2 are entangled if the two spin states $|\Psi\rangle$ can by no means be written as a product of the single spin states. This means that $|\Psi\rangle \neq |\varphi 1\rangle|\varphi 2\rangle$ for any pair of functions. The two-qubit system has four entangled Bell states:

$$|\Psi\pm\rangle = (|\uparrow\downarrow\rangle \pm |\downarrow\uparrow\rangle)/\sqrt{2} |\Phi\pm\rangle = (|\uparrow\uparrow\rangle \pm |\downarrow\downarrow\rangle)/\sqrt{2} \tag{18.2}$$

The important feature of the entangled state is that nothing is known about the state of their individual qubit. However, as soon one of the qubits is projected onto one of its eigenstates, the state of the other qubit is known with certainty. This property has opened perspectives to use entanglement it in quantum cryptography.

If the basis states are defined on spin, the four entangled states are the same as the singlet and triplet states. Remember that in the QC jargon combination is substituted by superposition.

The entangled state can be reached starting from an initial state say $|\uparrow\uparrow\rangle$ and applying the Hadamard transform to the first qubit yields $(|\uparrow\uparrow\rangle + |\downarrow\uparrow\rangle)/\sqrt{2}$. The following operation is a controlled NOT, CNOT, on the second qubit, yielding $(|\uparrow\uparrow\rangle + |\downarrow\downarrow\rangle)/\sqrt{2}$, with CNOT being a NOT operation working only if the first qubit is in state $|\uparrow\rangle$.

18.3 A Detour

Literally a bird's-eye-view allows us to enlarge the concept of quantum coherence and entanglement. In fact, it is well known that many animals sense the geomagnetic field for navigation. There are two suggested mechanisms, one based on magnetite, and the other based on radical pairs. We do not enter into a discussion of what has backed one hypothesis or the other, but we want to show how sophisticated quantum concepts such as entanglement can be used to justify common phenomena.

The radical pair model is based on the principle that the directionality of light entering the bird's eye is analyzed for photoselection effects (Pauls *et al.*, 2013). The effects are enhanced by coherence and entanglement, which develop even if initially they are not present. Therefore one of the routes followed to understand and enhance the avian navigation is that of entanglement. Recent suggestions concentrate on the duration of the entanglement, which is sensitive to the inclination of the radical pair with respect to the earth's magnetic field.

A quantitative model has been developed using a SH including the Zeeman interaction on the $S = 1/2$ and a hyperfine interaction. As for many other cases, anisotropy, which is here associated with hyperfine interactions, is needed for the system to be efficient. The dynamics was calculated using the Liouville equation, and the initial state was assumed to be in the singlet state. The decay rates of singlet and triplet are then calculated as a function of the weak earth's field (Lau, Rodgers, and Hore, 2012). In Figure 18.2, the triplet yields corresponding to different decay rates are shown. For rapid decay rates, the triplet yield varies very little in the field range of interest. Slow decay gives the opposite behavior, with rapid saturation in the field. So both fast and slow decay are inadequate to be employed in navigation. Matters are much more appealing for intermediate decays. The triplet yield in this case is very sensitive to small variations of the magnetic field. Summarizing entanglement decay rate is compatible for justifying

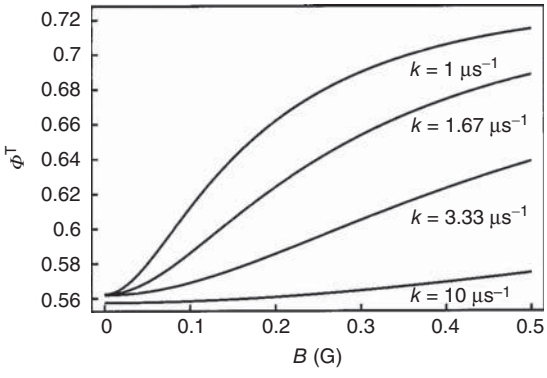

Figure 18.2 Triplet yields of three different decay rates as a function of magnitude of the external magnetic field. (Reproduced from Ritz,. T. *et al.*, (2000) with permission from Elsevier Science B.V.)

the radical pair mechanism. Anisotropy of the interaction is needed. It seems that the route outlined can be promising. Also, it is exciting that different scientific areas use the same language because synergic effects can thus be developed. Entanglement, for instance, was hardly used few years ago but now it is used in as different areas as animal navigation and quantum computing.

18.4 Endohedral Fullerenes

An interesting example of how to create entangled states was given by Mehring *et al.* using an endohedral fullerene with a P atom inside (Naydenov *et al.*, 2008). The system, P@C_{60}, is more complex than a simple two spin S = 1/2 systems, being based on electron spin S = 3/2 and P spin I = 1/2. This means that the energy matrix is an 8×8 one, including the electron and nuclear Zeeman, the hyperfine, and ZFS of the S = 3/2 spin due to low symmetry effects determined by the matrix in which the experiments were performed. The scheme of the energy levels is shown in Figure 18.3.

The electromagnetic pulses can be used to selectively excite transitions in a multilevel system. The pulses are described by the operators

$$P_x^{(nm)}(\beta, \varphi) = e^{-i\varphi S_z^{(nm)}} e^{-i\beta S_x^{(nm)}} e^{i\varphi S_z^{(nm)}} \tag{18.3}$$

where m and n tag the involved levels, β is the rotation angle, and φ is the phase. Using appropriate pulses, access is achieved to the entangled state and a signal is observed that oscillates according to

$$\langle S_z^{(13)} \rangle = \frac{1}{4}(1 - \cos(2\pi(\upsilon_S - \upsilon_I)\delta t)) \tag{18.4}$$

where υ_S and υ_I are the phase frequencies for electron and nuclear spin respectively. The signal for the entangled state oscillates with a frequency of $\upsilon_{ent} = \upsilon_S + \upsilon_I$ and in this case a frequency of 1.525 MHz was observed.

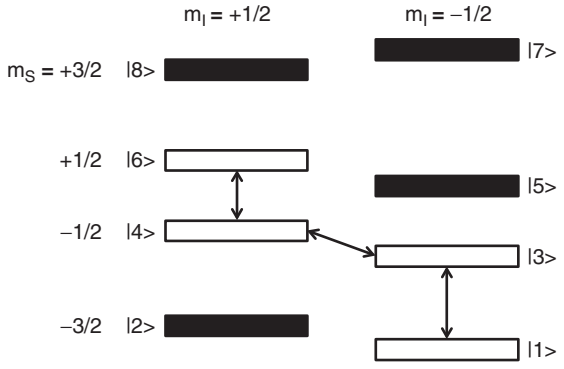

Figure 18.3 Energy level scheme of P@C_{60}. The white bars and arrows denote the chosen subsystem and the corresponding ESR and NMR transitions.

It is perhaps here the occasion to highlight some features of ESR, which make this technique appropriate to initialize and manipulate qubits (Morton *et al.*, 2005). One of the issues to discuss is that of the intrinsic error inherent to pulsed magnetic resonance experiments. In particular, while the decoherence time T_2 is generally quoted as the ultimate figure of merit for qubit implementations, understanding and minimizing the systematic errors inherent in qubit manipulations is equally important. There are two principal types of systematic error associated with a single-qubit rotation: rotation angle errors, and rotation axis errors. In magnetic resonance experiments, rotation angle errors arise from an uncertainty in the Rabi oscillation period, associated with errors in the magnitude and duration of the applied radio frequency (rf) pulse. On the other hand, rotation axis errors arise from uncertainty in direction of the rf magnetic field in the transverse plane of the rotating frame. In an ESR experiment, a qubit rotation is achieved by applying an on-resonance microwave pulse of controlled power and duration. With pulsed magnetic field strength B_1 and pulse duration t, the rotation angle is

$$\theta = g\mu_B B_1 t/\hbar \tag{18.5}$$

It is possible to neglect off-resonance effects when the ESR line width is much smaller than the excitation width of the rf pulses used in the experiments. As stressed earlier, the problem in using this technique is the error connected to the uncertainty δ of the measured rotation angle θ: the measured signal is proportional to $\cos(\delta)$. Actually, it is not very easy to determine the error with a reasonable accuracy. A different approach is based on a technique that involves the application of a long rf pulse and observing the Rabi oscillations over a number of periods. As an example, we report the results of an experiment on i-N@C_{60} which has been proposed as a qubit as it shows a multilevel structure which is more akin to the situation encountered in ion- and atom-quantum computers (Mehring, Scherer, and Weidinger, 2004). Another advantage derives from the fact that in this system a ^{15}N atom is inserted in the cavity of a C_{60} fullerene molecule.

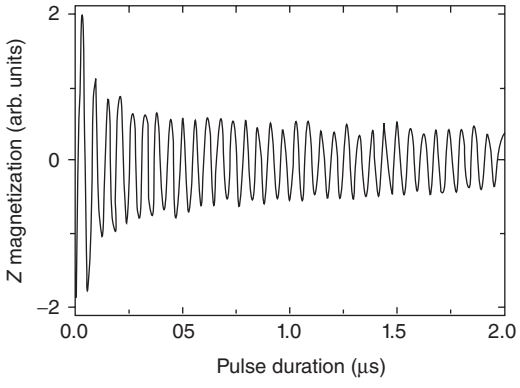

Figure 18.4 Rabi oscillations for i-N@C_{60} in CS_2 at 190 K. (Reproduced from Morton, J.J.L. *et al.* (2005) with permission from The American Physical Society.)

As a consequence, the almost spherical surrounding leads to very narrow lines, even in the solid state, which allows precise control of the quantum states. A second interesting feature of this system is the high degree of isolation of the spin system from the surrounding, which can show long decoherence time.

A typical spectrum, reported in Figure 18.4, shows Rabi oscillations whose amplitudes decay at long pulse durations over 80 oscillations.

This decay is caused by inhomogeneities in both the B_1 fields in the ESR cavity spins which are rotated with slightly different Rabi frequencies gradually losing coherence, and in the static B_0 field.

Very often, commercial ESR spectrometers do not have the precision required to perform experiments such as those described previously with the required accuracy. Typically, the error in the rotation angle can be of the order of 10% due to the inhomogeneity of the oscillatory magnetic field, while an error of about 0.3° is attributable to the management of the rotation axis.

A first improvement in the attempt to reduce errors in the rotation angles can be attained by using a sequence of pulses in place of a single pulse. Among the various sequences, it is possible to apply the technique of a pulse followed by a series of refocusing pulses. These methods are derived from NMR application, and some of them, such as the Carr–Purcell (CP) and the Carr–Purcell–Meiboom–Gill (CPMG) (Meiboom and Gill, 1958; Zielinski and Hürlimann, 2005). The rotation axis errors can be reduced by using a pulse sequence called sequence for phase error amplification (SPAM, Morton *et al.*, 2005), which works similar to the CP sequence to accumulate flip angle errors. The SPAM methodology provides a method of setting relative phases between channels with very high precision: rotation angle errors can be reduced to the order of 10^{-6}, which is two orders of magnitude below the limit often indicated for fault-tolerant quantum computation (Steane, 2003).

In the following, we will try to analyze some systems to check how they comply with the criteria for QIP.

18.5 Criteria for QIP

We will focus on molecular magnets as it was postulated, by examining the properties of Mn_{12} and Fe_8 clusters; this class of compounds could be interesting for quantum computing because they can be used to build dense and efficient memory devices and one single crystal can serve as a storage unit of a dynamic random access memory device (Leuenberger and Loss, 2001). From that fundamental paper, many systems have been investigated taking advantage of their versatility on the number and type of magnetic centers in mononuclear and polynuclear TM, and Ln derivatives. The spin is embedded in a molecular structure which can be used to optimize the magnetic properties, the interactions with the environment, the choice of the parameters of the environment, and so on. We will try to clarify these points in the following.

Dephasing indicates that a system is evolving from a pure quantum state, with well-defined θ and φ angles, to a statistical mixture. Excitation relaxation and dephasing decay exponentially and define the longitudinal and transverse relaxation times. This allows, as noticed by Affronte *et al.*, the decomposition of any unitary transformation into a discrete sequence of local transformations (Troiani and Affronte, 2011). One of the characteristics of employing nanomagnets is that of having larger size compared to single-electron devices. This, on one side, can be an advantage due to the opportunity to tune the properties but, on the other hand, it reduces the spatial resolution. The figures of merit for a molecular magnet largely depend on the strength of dipolar interactions and on the interactions with the nuclear moments because, in the high temperature limit (i.e., above the millikelvin region), the nuclear bath is not a pure state. The state of the molecular magnet then evolves toward a mixture.

A quantum computer is defined by the possibility of exploiting the quantum properties in the best possible way. The conditions for checking that a given system may be well suited for being employed for QC are defined by the so-called Di Vincenzo criteria (DiVincenzo, 2000), as explained in the following.

- *The definition of quantum states*
  The qubits must be well defined and they must be scalable, that is, there must be procedures for involving increasing numbers of spins. This is a good point for molecular systems. Work has already been done to organize SMMs in ordered arrays, as in the case, for instance, of SMM compounds formed by 3d–4f pairs coordinated by macrocycles which are arranged in one-dimensional networks by bridging the dimers with $[W(CN)_8]^{3-}$ anions (Dhers *et al.*, 2013).
- *Initialization procedure*
  It must be possible to initialize the qubits at $t = 0$ in a well-defined state. This may be bound to the application of a magnetic field at low temperature to condense the ensemble in the ground state. There is a good library

of magnetic molecules that can be explored (Halcrow, 2013; Hardy, 2013; Layfield, 2014).

- *Quantum gates*
  It must be possible to implement a universal set of quantum gates. We have seen previously a couple of examples of elementary gates which can be extended in efficiency and complication. Addressing and shifting the properties of the magnetic molecules must be performed at faster rates compared to decoherence time as discussed previously.
- *Low decoherence*
  This is one of the key issues that require a minimal interaction with the environment.
- *Readout method*
  Of course, reading information requires work. The first point requires the choice of the material to be used and the molecular states to be used for encoding quantum information. The second dictates the initialization of the process in order to have the system in a well-defined state at the start reference time.

Early attempts to use molecular magnets as qubits yielded phase coherence times up to 3 μs. Another favorable result has been obtained on $[V^{IV}_{15}As^{III}_{6}O_{42}(H_2O)]^{6-}$ using pulsed ESR techniques (Bertaina *et al.*, 2008) Section 18.8.

An alternative method takes advantage, instead, of local magnetic fields of electric fields in order to drive nuclear spin resonance. The method is based on a three-terminal nuclear spin qubit transistor. It is based on a $TbPc_2$ molecule coupled to the source gate and drain. The ground state of $TbPc_2$ is described by an effective spin $S = 1/2$ with $M = \pm 6$. The electron spin is coupled to the nuclear spin $I = 3/2$ of ^{159}Tb. The hyperfine interaction splits the doublet in to four levels, and the states can be labeled as $|M_S\ M_N>$ where $M_S = \pm 1/2$, $M_N = \pm 1/2 \pm 3/2$. These correspond to four different qubit states. By adding an external magnetic field, the avoided crossings (see Section 13.3) can be observed. The effect is of the order of microkelvin. QTM is generated by sweeping the magnetic field, and the position is nuclear spin-dependent. Therefore, it is possible to measure the state of the nuclear spin qubit (Dei and Gatteschi, 2011; Komeda *et al.*, 2011; Urdampilleta *et al.*, 2013).

A second stage uses exchange interaction of the electron spin with quantum dot to influence the conductance. The experiment was repeated 75 000 times, and showed four non-overlapping Gaussian -like ditributions corresponding to four nuclear spin states. The T_1 relaxation times are of the order of 17 – 34 s.

At least, a third stage should be that of implementing the electronic manipulation of a single nuclear spin taking advantage of the hyperfine Stark effect which monitors the change of the hyperfine constant as a function of an external electric field (Thiele *et al.*, 2014). The effect is well known and widely used for accurate measurements of time. The field effect is large, and a small periodic modulation can give rise to fields of 300 mT.

The single nuclear spin manipulation can be achieved focusing on the $|+3/2\rangle$, $|1/2\rangle$ manifold. The external field is swept until QTM is observed at the typical

field of $|+3/2\rangle$. The application of a microwave eventually yields Rabi oscillations. The evolution of the Rabi frequency for the three gate voltages was interpreted as indication of feasibility of all electric control of a single nuclear spin. An exciting opportunity indeed!

18.6 Starting from Inorganic

As done before for SIM, we start from an inorganic compound to describe the QC opportunities of Ln. A system that has been thoroughly investigated is Er^{III}-doped $CaWO_4$ (Bertaina *et al.*, 2009). The crystal has C_4 symmetry. The lanthanide enters the lattice by replacing Ca^{2+} ions, which are 8-coordinated. Charge compensation is managed by absorbing Na^+ ions. The choice has been made to introduce the Rabi oscillations which are a trademark of quantum behavior and is widely used in the QIP field.

Experimentally, the magnetic behavior of ^{167}Er isotope (natural abundance 22.94%), with $I = 7/2$ and hyperfine constant $A = -125$ MHz, and accounts for about 23% of the natural abundance, was analyzed. ESR spectra provided a reasonable fit with easy plane anisotropy with $g_{||} = 1.2$ and $g_{\perp} = 8.4$. To calculate the Rabi frequency, it is possible to use two different approaches. The use of a laboratory frame (LF) allows computing the amplitude of the probability of transition induced by the microwave field h_{Wv} perpendicular to the static field H. The splitting at avoided level crossing, which is equal to the Rabi frequency, is determined in the rotating frame (RF) approach.

The calculation is simpler for systems with lower anisotropy. In this situation, by using the LF method it is possible to derive the Rabi frequency by using

$$\Omega_R = g^{\alpha}\mu_B h^{\alpha}_{wv}/2\hbar \tag{18.6}$$

where Ω_R is the Rabi frequency, the effective g factor in the direction of the microwave field. In the case of more anisotropic systems, such as those where Ln are present, when the RF approach is used, Ω_R is given by

$$\Omega_R(\varphi) = \mu_B h_{wv}\frac{g_{\perp}g_{||}}{2\hbar g(\varphi)} \tag{18.7}$$

where φ is the angle of H with the c-axis and $g(\varphi) = \sqrt{g_{||}^2\cos^2\varphi + g_{\perp}^2\sin^2\varphi}$.

Rabi oscillations are found to change dramatically on varying the orientation of the static (H) or/and dynamical field away from the crystal axes. The coherence time at 2.5 K is about 50 µs, which is interesting.

Rather expectedly, POM-based systems have been used in the QC frame. In the series of compounds based on POM, a particularly original one, $[Gd(P_5W_{30}O_{110})]^{12-}$, GdW_{30}, which we have briefly introduced in Section 13.12, contains a pentagonal cavity which hosts a Ln. The interesting feature is that it is possible to measure the low-lying levels originating from the ZFS of the ground

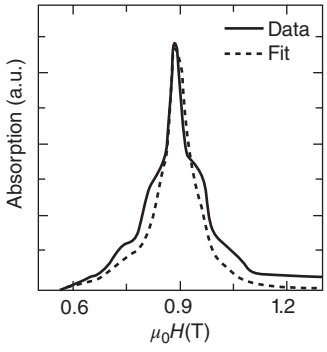

Figure 18.5 Powder ESR absorption spectra of GdW_{30} at $T = 10$ K and $\upsilon = 25$ GHz. The experimental data (solid lines) and the best fits (dotted lines) are reported. (Reproduced from Martínez-Pérez, M.J. *et al.* (2012) with permission from The American Physical Society.)

$^8S_{7/2}$ with great accuracy and with these data to discuss the possibility of using GdW_{30} as a qubit. Let us recall the required parameters for a good qubit.

The first is the energy gap Δ between the qubit levels. Since the imagined applications use rf techniques associated with resonance frequencies of superconductive microcavities, the usable window is 2–20 GHz. The first step is to decide the SH to be uses for the splitting of the ground level. Assuming C_{5v} symmetry, the terms to be introduced correspond to $n = 2$, $k = 0$; $n = 4$, $k = 0$; $n = 6$, $k = 0, 5$. Attempts to use this SH were unsuccessful to reproduce the ESR spectra. It was decided to use only the $n = 2$, $k = 0, 2$ terms for the sake of simplicity, and an acceptable fit was achieved as shown in Figure 18.5 (Martínez-Pérez *et al.*, 2012).

The best fit parameters are indicative of an easy plane anisotropy. Above $T = 200$ mK the relaxation follows an Arrhenius law with $U_{\text{eff}} = 2.2$ K to be compared with 2.15 K which is the calculated value using LF. Data were collected also on GdW_{10}, which shows a relaxation rate slower than that of GdW_{30}. These data show that the two Gd derivatives behave as SMM, in a different fashion compared to the other reported SMMs that depend on easy axis anisotropy. The mechanism therefore depends on the coordination of the Gd ion.

18.7 Molecular Rings

A few years ago there was great interest in studying the magnetic properties of ring-shaped molecules, which can in principle include n magnetic centers, n varying from 1 to ∞. It is apparent that a ring with infinite centers is equivalent to a chain. Therefore, rings can be considered models of 1D materials and, indeed, they have been used for extrapolating the properties of 1D materials (Bonner and Fisher, 1964; De Jongh and Miedema, 2001).

The SH suitable to describe the magnetic properties of a molecular ring can be written as

$$\mathcal{H} = J \sum_{i=1,n} \mathcal{J}_i \cdot \mathcal{J}_{i+1} + \sum_{i=1,n} \mathcal{J}_i \cdot \mathbf{D}_i \cdot \mathcal{J}_{i+1} + \sum_{i>j} \mathcal{J}_i \cdot \mathbf{D}_{ij} \cdot \mathcal{J}_j + \mu_B \sum_{i=1,n} g_i B \cdot \mathcal{J}_i \qquad (18.8)$$

where the first term represents the isotropic exchange interaction, the second and third terms account for the local anisotropic exchange and the intracluster spin–spin interaction, and the fourth one is the Zeeman interaction.

In the field of MM, there is a large variety of molecular wheels or rings exhibiting ferro- or antiferromagnetic interactions. Among them, the rings containing an odd number of identical magnetic centers are perfect examples of spin-frustrated systems if antiferromagnetic interactions are operative (Baker *et al.*, 2012). In recent times, magnetic wheels are attracting interest because they are considered good candidates that can provide opportunities for observing quantum coherence (Troiani *et al.*, 2005).

A molecular magnet that has been thoroughly investigated in the QIP frame is an eight-membered ring which can have eight chromium(III) ions or seven chromium(III) and one nickel(II) ions. The structures of the two rings are shown in Figure 18.6.

This class of compounds is for sure a good basis for the researches of people interested in developing new perspectives for QIP using molecular magnets. In this case, the work was not simply the theoretical one but some roads to really develop QC have been explored.

The coupling between next-neighbor atoms is antiferromagnetic, and the ground states are $S = 0$ for Cr_8 and $S = 1/2$ for Cr_7Ni. In order to have more information, also two analogous compounds were synthesized in which paramagnetic Ni was substituted by diamagnetic Cd and Zn, and, as expected, the ground states of the rings with Cd and Zn have $S = 3/2$. The interpretation of the experimental data was performed in the strong field frame. The series of compounds Cr_7M have been investigated at best through magnetic susceptibility, ESR, and inelastic neutron scattering (INS). ESR was interpreted using a numerical diagonalization technique which can be applied to the low-lying levels of the clusters (Piligkos *et al.*, 2009). The method was applied using SHs describing the isotropic and anisotropic exchange. The importance of the high quality of the ESR spectra may be fully appreciated by looking at the spectra shown in Figure 18.7.

It is a single-crystal K-band spectrum of Cr_7Ni at 10 K. The spectra were recorded with the field lying in the ring plane. The spectra at 5 K are dominated

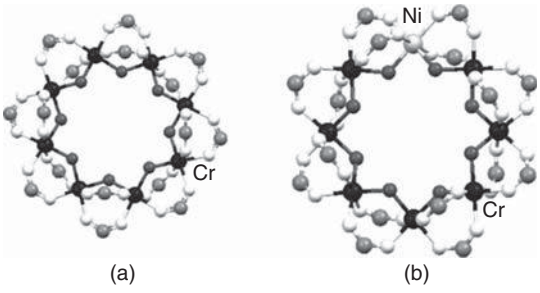

Figure 18.6 (a) Molecule of $[Cr_8F_8(Piv)_{16}]$ (HPiv = pivalic acid or trimethyl acetic acid) (van Slageren *et al.*, 2002). (b) Molecule of $[(Me_2NH_2)(Cr_7NiF_8(Piv)_{16})]$ (Larsen *et al.*, 2003). In both cases, solvent molecules and *t*-butyl groups are omitted for clarity.

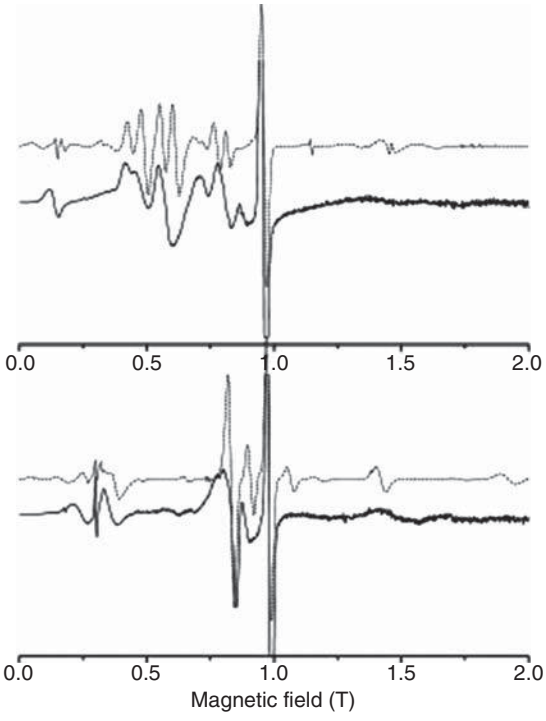

Figure 18.7 Experimental (—) and simulated (- - - -) K-band (23.92 GHz) single-crystal ESR spectra of Cr_7Ni recorded at 10 K with the external magnetic field in the plane defined by the metal centers (upper panel) or 6° to the normal to it (lower panel). (Reproduced from Piligkos, S., *et al.* (2009) with permission from WILEY-VCH Verlag GmbH & Co. KGaA.)

by the signal of the ground $S = 1/2$ state. The spectrum is anisotropic with $g_{xy} = 1.74$ and $g_z = 1.78$. The unusual g-values are due to the fact that the **g** tensor is the result of the projection of the individual **g** tensors on the total spin. Using standard techniques, it is found that

$$g_{\mathrm{CrNi}} = 5/4 g_{\mathrm{Cr}} - 1/4 g_{\mathrm{Ni}} \tag{18.9}$$

The negative coefficient is due to the AF coupling. The simulated spectra were computed using the relevant parameters in Table 18.1.

The analysis of the INS data showed that the first excited state is $S = 3/2$ and the second $S = 5/2$ for Cr_7Ni (Caciuffo *et al.*, 2005). They were reproduced by fixing the $J_{\mathrm{Cr-Cr}}$ coupling constant to the value derived by the analysis of the Cr_7Zn system ($J_{\mathrm{Cr-Cr}} = 11.53\,\mathrm{cm}^{-1}$) and the derived parameters were $J_{\mathrm{Cr-Ni}} = 13.63\,\mathrm{cm}^{-1}$, $D_{\mathrm{Ni}} = -4.84\,\mathrm{cm}^{-1}$, and $D_{\mathrm{Cr}} = -0.24\,\mathrm{cm}^{-1}$ There is some difference between the ESR and the INS fits, with the former arguably being more reliable owing to the higher resolution.

An important point to discuss is the validity of the giant spin model used so far. It is time to discuss the role of S mixing, which can be important in the QIP-oriented

Table 18.1 Spin Hamiltonian parameters used for the computation of the ESR spectra of Cr_7M^{2+} wheels (M^{2+} = Cd, Ni).

	Cr_7Cd	Cr_7Ni
g_{Cr}	1.96	1.96
$g_{M^{2+}}$	—	$g_{\perp} = 2.229$, $g_{\|\|} = 2.238(3)$
D_{Cr} (cm^{-1})	−0.134(8)	−0.134
$D_{M^{2+}}$ (cm^{-1})	—	−1.33(2)
J_{Cr-Cr} (cm^{-1})	11.54	11.54
$J_{Cr-M^{2+}}$ (cm^{-1})	—	17.32
D_{Cr-Cr} (cm^{-1})	−0.106(6)	−0.106
$D_{Cr-M^{2+}}$ (cm^{-1})	—	−0.075(9)

description of qubit behavior of TM compounds. This can be done by comparing the calculated average value $\langle S_z^2 \rangle$ with the eigenvalues obtained by the fit and the giant spin value S. The calculations showed that the deviations from the giant spin values are small, with a tendency to increased deviations for the higher energy multiplets.

The analysis of the anisotropy of the two lowest energy levels showed that the first excited $S = 3/2$ has a rhombic component $E/D = 0.12$. Since no calculation has been made including anisotropic exchange, the E/D ratio brings in both contributions.

The last step is to check the qubit nature of Cr_7Ni: it is necessary to measure the T_1 (intrinsic spin lattice) and T_2 (phase coherence) times. The advantage of Cr/Ni on other potential qubit is the spin $S = 1/2$, which simplifies the relaxation behavior. T_1 and T_2 were measured in frozen solution using standard techniques. Both T_1 and T_2 were found to increase on decreasing temperature, the former being more rapid. Experiments were performed also on perdeuterated samples, and T_2 was found to be a factor of 6 (T_2 deuterium) longer. The phase decoherence time reached 0.55 μs at 1.8 K and 3.8 μs for the perdeuterated sample. Assuming that τ_g is of the order of 10 ns, the figure of merit would be of the order of 10^2, which is a very exciting perspective indeed.

The treatment of the Cr_7M systems has been very accurate and has provided deep insight into the compound and the general strategy to be used in designing clusters with desired properties. Indeed, the following step associated with the development of two-qubit systems is a very elegant step forward. The idea is very simple: design a bridge connecting two Cr_7Ni moieties as schematized in Figure 18.8 (Affronte *et al.*, 2005).

The bridge can be chemically active and magnetically inactive, or chemically and magnetically active. The first reported attempts used 1,8-diaminooctane; therefore this can be considered as magnetically inactive because it is a diamagnetic bridge. Of course, it can transmit superexchange, and therefore it is not truly inactive. The idea is that of putting the two qubits in speaking terms with each other and see how and if they can be entangled.

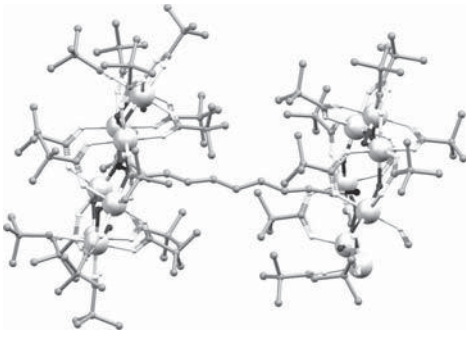

Figure 18.8 Structure of $[1,8\text{-daoH}_2][Cr_7NiF_8(Piv)_{16}]_2$ (1,8-dao = 1,8-diaminooctane) in the crystal. Hydrogen atoms are omitted for clarity.

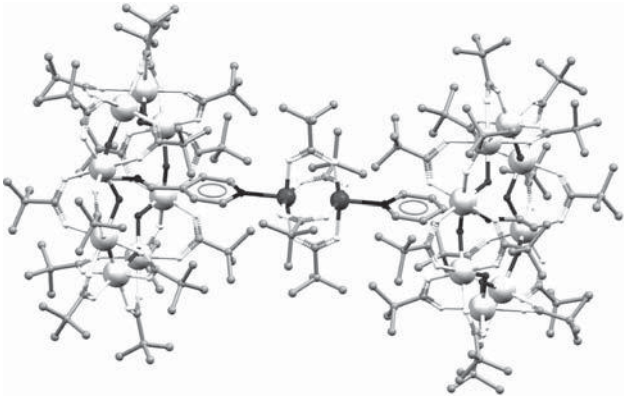

Figure 18.9 Structure of $[Cu_2(Piv)_4][(EtNH_2CH_2py)(Cr_7NiF_8(Piv)_{16})_2]$ in the crystal. Hydrogen atoms are omitted for clarity. Ni, Cr = light gray and Cu = dark gray.

The strategy consisted in using copper compounds as bridges, as depicted in Figure 18.9.

The extent of the interaction between the two moieties forming the dimer can be schematized as follows. First, the Cr_7Ni moieties, which we assume are little perturbed compared to the same isolated moieties; let us call them **1** and **1′.** The corresponding Hamiltonians are identical to each other, H_1. The bridge zone can have 0, 1, 2, and so on, metal centers interacting with **1** and **1′** in a symmetric mode. Let us see what happens when there is a single bridge. The starting point is three isolated doublets if we switch on only the intra-Cr_7Ni interactions. By switching on the other interactions, the data of the specific heat of magnetization and ESR are used to reconstruct the energy levels. Clear information comes from the specific heat, which shows an anomaly at $T < 1\,K$. This is evidence for weak coupling and is confirmed by the data of Cr_7Ni which does not show anomalies. ESR spectra at 5 K are completely different from the sum of the spectra of the components.

The picture that emerged from the analysis of the low-temperature data correspond to three weakly interacting Kramers doublets. The next problem is to check the possibility of entangling the three qubits. To this end, it is useful to refer to a well-established analysis previously reported.

18.8 V_{15}

This is an example of the possibility to use relatively large clusters to make qubits. V_{15} is a member of a series of polyhedral structures containing a variable number of vanadium ions which can be in oxidation state +4 and +5 (Müller *et al.*, 1988). V_{15} contains 15 vanadium(IV) ions, with spin $S = 1/2$. Vibronic coupling within the coordination environment of the $3d^1$ ion determines a strong interaction in the *z* direction individuated by the V=O bond direction. The 15 ions are arranged in three planes of 6, 3, and 6 ions, respectively. The coupling in the hexagonal planes is strong antiferromagnetic in such a way that the spins in the ring are nonmagnetic at relatively high temperature (Gatteschi *et al.*, 1991). The three ions in the triangle are weakly AFM coupled and give rise to spin frustration effects, which have been carefully investigated by Tsukerblatt *et al.* (Maslyuk *et al.*, 2013) (Figure 18.10). To make a long story short, the low-lying levels are two Kramers doublets separated by $0.22(2)\,cm^{-1}$ and a spin quartet $2.6\,cm^{-1}$ above the barycenter of the other two (Chaboussant *et al.*, 2004).

Like in the previous examples, Rabi oscillations were looked for and found at $\Omega_R = 18.5(2)$ MHz for the transitions within the $S = 3/2$ multiplets and 4.5(2) MHz for the transitions involving the $S = 1/2$ levels (Bertaina *et al.*, 2008). In addition, when the transition "1/2" is excited, a whole spectrum of Rabi oscillations is generated, which correspond to the avoided level crossing.

In general, the expectation was that, despite the fact that increasing the number of spins and the structural complexity should give short-lived coherence, V_{15} allowed the detection of long-lived Rabi oscillations. Further, it was possible to

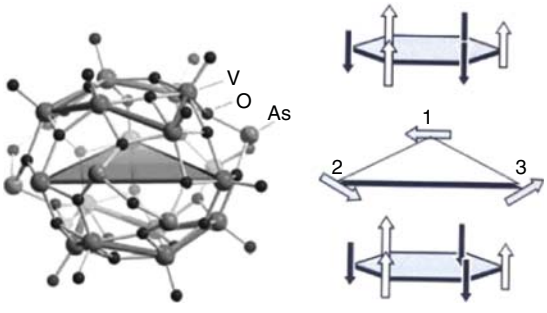

Figure 18.10 Structure of the anion $[V_{15}As_6O_{42}(H_2O)]^{6-}$ (left). (Reproduced from Maslyuk, V.V. *et al.* (2013) with permission from John Wiley & Sons, Inc.) Spin alignment in the three layers of the cluster (right). The spins in the middle triangle are frustrated.

make some guesses of the origin of the decoherence. A major source is the hyperfine interaction, which depends on ^{51}V, ^{75}As, and ^{1}H. In order to reduce the interaction between the clusters, a new V_{15} embedded in surfactant, which keeps the cluster pretty far from each other, was synthesized. The role of the surfactant must also be considered: a new hybrid material, based on the use of a cationic surfactant $[Me_2N[(CH_2)_{17}Me]_2]^+$ (DODA = dimethyldioctadecylammonium) as an embedding material for the anionic organic-inorganic hybrid polyoxometalates, conveys protons which perturb the coherence. Simple calculations suggest that, compared to that of the original V_{15}, the dipolar interaction is essentially negligible (Jia *et al.*, 2013).

18.9
Qubit Manipulation

The last topic we want to treat in this chapter is that of spin addressing and spin manipulation, a fundamental issue to understand whether QIP is a perspective, may be in a far future, or a fascinating dream. Perhaps, the proposed qubit which is closest to the molecular magnets is quantum dots. The latter have been tested with pulsed electric fields to demonstrate the possibility of manipulating the systems. The developed techniques were successfully improved for the one- and two-qubit quantum gates. The idea is that the quantum gate to implement is the so-called square root of swap, from which all other logical operations can be developed. The quantum dots are subject to a gate-voltage pulse that switches on the exchange interaction between the qubits. It is necessary to optimize the pulse and the time of application.

18.10
Some Philosophy

Let us take the opportunity to make some consideration of the changes in the philosophical aspects of science associated with the changes determined by the last scientific and technological results. The problem of quantum measurement is in the background of quantum computing. The approach now predicts that the Galilean concept of reproducibility of observations, which is fundamental to physics, does not hold and must be substituted by the reproducibility of statistical experiments, which is fundamentally different.

The measurement we conduct in our laboratories is controlled by the way in which the quantum object communicates with the surrounding environment. Hence, we retrieve the information conveyed by the quantum object to the environment, which is entangled with it. One of the key points is that environment-induced decoherence, where the environment itself acts as the observer and destroys superpositions, is essential. However, it should be stressed that this is only one possible way of conceiving how quantum information can

be transformed into classical information. The approach used so far in MM has many limitations once applied to single molecular objects. Indeed, this approach obeyed the concept of a science based on experiments, where in principle it is possible to know a value of a property of a discrete molecular system. Quantum phenomena are characterized by holism or inseparability, as entanglement shows. This feature distinguishes quantum physics from classical physics, and it determines two different cognitive approaches in reciprocal, open contrast. This concept is not new (it is intrinsic in the formulation of the Schrödinger equation) but, surprisingly, it has been ignored by most of the scientific community. Entanglement is synonymous with inseparability, and simply means in its essence that when two states are entangled it is not possible to separately determine the properties of the two constituent states. This feature is common in the microscopic world. Therefore, it is the key to the description of all the aspects of the interactions of the molecule as a quantum object with itself and with the environment, the measurement apparatus, and the observer. Accordingly, it rules the physical world we investigate and necessitates its adoption as an epistemic methodology. This is the important timely lesson we can learn from the future developments of MM.

The last chapter is a clear example of how much MM has changed in terms of the background knowledge needed to be able to design experiments and perform them. It is a revolution analogous to that of the 1950s, when the discovery of the new possibility provided by quantum mechanics allowed, for the first time, tackling difficult problems moving from magnetochemistry to MM. The present is a time where quantum mechanics is employed at a high level of sophistication demanding all the actors in the field to use a host of concepts, be they chemists, physicists, materials scientists.

This chapter is an attempt to provide some tools.

References

Affronte, M., Casson, I., Evangelisti, M., Candini, A., Carretta, S., Muryn, C.A., Teat, S.J., Timco, G.A., Wernsdorfer, W., and Winpenny, R.E.P. (2005) Linking rings through diamines and clusters: exploring synthetic methods for making magnetic quantum gates. *Angew. Chem. Int. Ed.*, **44**, 6496–6500.

Baker, M.L., Timco, G.A., Piligkos, S., Mathieson, J.S., Mutka, H., Tuna, F., Kozłowski, P., Antkowiak, M., Guidi, T., Gupta, T. *et al.* (2012) A classification of spin frustration in molecular magnets from a physical study of large odd-numbered-metal, odd electron rings. *Proc. Natl. Acad. Sci.*, **109**, 19113–19118.

Bertaina, S., Gambarelli, S., Mitra, T., Tsukerblat, B., Muller, A., and Barbara, B. (2008) Quantum oscillations in a molecular magnet. *Nature*, **453**, 203–206.

Bertaina, S., Shim, J.H., Gambarelli, S., Malkin, B.Z., and Barbara, B. (2009) Spin-orbit qubits of rare-earth-metal ions in axially symmetric crystal fields. *Phys. Rev. Lett.*, **103**, 226402.

Bonner, J.C. and Fisher, M.E. (1964) Linear magnetic chains with anisotropic coupling. *Phys. Rev.*, **135**, A640–A658.

Caciuffo, R., Guidi, T., Amoretti, G., Carretta, S., Liviotti, E., Santini, P., Mondelli, C., Timco, G., Muryn, C.A., and Winpenny, R.E.P. (2005) Spin dynamics of heterometallic Cr_7M wheels (M=Mn, Zn,

Ni) probed by inelastic neutron scattering. *Phys. Rev. B*, **71**, 174407.

Chaboussant, G., Ochsenbein, S.T., Sieber, A., Güdel, H.U., Mutka, H., Müller, A., and Barbara, B. (2004) Mechanism of ground-state selection in the frustrated molecular spin cluster V15. *Europhys. Lett.*, **66**, 423–429.

Cooper, A., Magesan, E., Yum, H.N., and Cappellaro, P. (2014) Time-resolved magnetic sensing with electronic spins in diamond. *Nat. Commun.*, **5**, 3141.

Criger, B., Passante, G., Park, D., and Laflamme, R. (2012) Recent advances in nuclear magnetic resonance quantum information processing. *Philos. Trans. R. Soc. London, Ser. A Math., Phys. Eng. Sci.*, **370**, 4620–4635.

De Jongh, L.J. and Miedema, A.R. (2001) Experiments on simple magnetic model systems. *Adv. Phys.*, **50**, 947–1170.

Dei, A. and Gatteschi, D. (2011) Molecular (nano) magnets as test grounds of quantum mechanics. *Angew. Chem. Int. Ed.*, **50**, 11852–11858.

Deutsch, D. and Jozsa, R. (1992) Rapid solution of problems by quantum computation. *Proc. R. Soc. Lond. A Math. Phys. Sci.*, **439**, 553–558.

Devoret, M.H. and Schoelkopf, R.J. (2013) Superconducting circuits for quantum information: an outlook. *Science*, **339**, 1169–1174.

Dhers, S., Feltham, H.L.C., Clérac, R., and Brooker, S. (2013) Design of one-dimensional coordination networks from a macrocyclic {3d-4f} single-molecule magnet precursor linked by $[W(CN)_8]^{3-}$ anions. *Inorg. Chem.*, **52**, 13685–13691.

Dicarlo, L., Chow, J.M., Gambetta, J.M., Bishop, L.S., Johnson, B.R., Schuster, D.I., Majer, J., Blais, A., Frunzio, L., Girvin, S.M. *et al.* (2009) Demonstration of two-qubit algorithms with a superconducting quantum processor. *Nature*, **460**, 240–244.

DiVincenzo, D.P. (2000) The physical implementation of quantum computation. *Fortschr. Phys.*, **48**, 771–783.

Gatteschi, D., Pardi, L., Barra, A.L., Muller, A., and Doring, J. (1991) Layered magnetic structure of a metal cluster ion. *Nature*, **354**, 463–465.

Halcrow, M.A. (2013) The foundation of modern spin-crossover. *Chem. Commun.*, **49**, 10890–10892.

Hardy, J.G. (2013) Metallosupramolecular grid complexes: towards nanostructured materials with high-tech applications. *Chem. Soc. Rev.*, **42**, 7881–7899.

Hemmer, P. and Wrachtrup, J. (2009) Where is my quantum computer? *Science*, **324**, 473–474.

Jia, Y., Tan, H.Q., Zhang, Z.M., and Wang, E.B. (2013) Thermotropic liquid crystals built from organic–inorganic hybrid polyoxometalates and a simple cationic surfactant. *J. Mater. Chem. C*, **1**, 3681–3685.

Jones, J.A. (2011) Quantum computing with NMR. *Prog. Nucl. Magn. Reson. Spectrosc.*, **59**, 91–120.

Knill, E., Laflamme, R., and Milburn, G.J. (2001) A scheme for efficient quantum computation with linear optics. *Nature*, **409**, 46–52.

Koch, J., Yu, T.M., Gambetta, J., Houck, A.A., Schuster, D.I., Majer, J., Blais, A., Devoret, M.H., Girvin, S.M., and Schoelkopf, R.J. (2007) Charge-insensitive qubit design derived from the Cooper pair box. *Phys. Rev. A*, **76**, 042319.

Komeda, T., Isshiki, H., Liu, J., Zhang, Y.-F., Lorente, N., Katoh, K., Breedlove, B.K., and Yamashita, M. (2011) Observation and electric current control of a local spin in a single-molecule magnet. *Nat. Commun.*, **2**, 217.

Larsen, F.K., McInnes, E.J.L., Mkami, H.E., Overgaard, J., Piligkos, S., Rajaraman, G., Rentschler, E., Smith, A.A., Smith, G.M., Boote, V. *et al.* (2003) Synthesis and characterization of heterometallic $\{Cr_7M\}$ wheels. *Angew. Chem. Int. Ed.*, **42**, 101–105.

Lau, J.C.S., Rodgers, C.T., and Hore, P.J. (2012) Compass magnetoreception in birds arising from photo-induced radical pairs in rotationally disordered cryptochromes. *J. R. Soc. Interface*, **9**, 3329–3337.

Layfield, R.A. (2014) Organometallic single-molecule magnets. *Organometallics*, **33**, 1084–1099.

Leuenberger, M.N. and Loss, D. (2001) Quantum computing in molecular magnets. *Nature*, **410**, 789–793.

Magesan, E., Cooper, A., and Cappellaro, P. (2013) Compressing measurements in quantum dynamic parameter estimation. *Phys. Rev. A: At. Mol. Opt. Phys.*, **88**, 062109.

Martínez-Pérez, M.J., Cardona-Serra, S., Schlegel, C., Moro, F., Alonso, P.J., Prima-García, H., Clemente-Juan, J.M., Evangelisti, M., Gaita-Ariño, A., Sesé, J. *et al.* (2012) Gd-based single-ion magnets with tunable magnetic anisotropy: molecular design of spin qubits. *Phys. Rev. Lett.*, **108**, 247213.

Maslyuk, V.V., Mertig, I., Farberovich, O.V., Tarantul, A., and Tsukerblat, B. (2013) Electronic and spin structures of polyoxometalate V15 from a first-principles non-collinear molecular-magnetism approach. *Eur. J. Inorg. Chem.*, **2013**, 1897–1902.

Mehring, M., Scherer, W., and Weidinger, A. (2004) Pseudoentanglement of spin states in the multilevel N15@C system. *Phys. Rev. Lett.*, **93**, 206603.

Meiboom, S. and Gill, D. (1958) Modified spin-echo method for measuring nuclear relaxation times. *Rev. Sci. Instrum.*, **29**, 688–691.

Morton, J., Tyryshkin, A., Ardavan, A., Porfyrakis, K., Lyon, S., and Briggs, G. (2005) Measuring errors in single-qubit rotations by pulsed electron paramagnetic resonance. *Phys. Rev. A*, **71**, 012332.

Müller, A., Penk, M., Krickemeyer, E., Bögge, H., and Walberg, H.-J. (1988) $[V_{19}O_{41}(OH)_9]^{8-}$, an ellipsoid-shaped cluster anion belonging to the unusual family of V(IV)/V(V) oxygen clusters. *Angew. Chem. Int. Ed. Engl.*, **27**, 1719–1721.

Naydenov, B., Mende, J., Harneit, W., and Mehring, M. (2008) Entanglement in P@C60 encapsulated in a solid state matrix. *Phys. Status Solidi B Basic Res.*, **245**, 2002–2005.

O'Brien, J.L. (2007) Optical quantum computing. *Science*, **318**, 1567–1570.

Pauls, J.A., Zhang, Y., Berman, G.P., and Kais, S. (2013) Quantum coherence and entanglement in the avian compass. *Phys. Rev. E*, **87**, 062704.

Piligkos, S., Weihe, H., Bill, E., Neese, F., El Mkami, H., Smith, G.M., Collison, D., Rajaraman, G., Timco, G.A., Winpenny, R.E.P. *et al.* (2009) EPR spectroscopy of a family of $Cr(III)_7Ni(II)$ (M=Cd, Zn, Mn, Ni) "wheels": studies of isostructural compounds with different spin ground states. *Chem. Eur. J.*, **15**, 3152–3167.

Schreier, J.A., Houck, A.A., Koch, J., Schuster, D.I., Johnson, B.R., Chow, J.M., Gambetta, J.M., Majer, J., Frunzio, L., Devoret, M.H. *et al.* (2008) Suppressing charge noise decoherence in superconducting charge qubits. *Phys. Rev. B: Condens. Matter Mater. Phys.*, **77**, 180502(R).

van Slageren, J., Sessoli, R., Gatteschi, D., Smith, A.A., Helliwell, M., Winpenny, R.E.P., Cornia, A., Barra, A.-L., Jansen, A.G.M., Rentschler, E. *et al.* (2002) Magnetic anisotropy of the antiferromagnetic ring $[Cr_8F_8Piv_{16}]$. *Chem. Eur. J.*, **8**, 277–285.

Stajic, J. (2013) The future of quantum information processing. *Science*, **339**, 1163.

Steane, A.M. (2003) Overhead and noise threshold of fault-tolerant quantum error correction. *Phys. Rev. A*, **68**, 042322.

Thiele, S., Balestro, F., Ballou, R., Klyatskaya, S., Ruben, M., and Wernsdorfer, W. (2014) Electrically driven nuclear spin resonance in single-molecule magnets. *Science*, **344**, 1135–1138.

Troiani, F. and Affronte, M. (2011) Molecular spins for quantum information technologies. *Chem. Soc. Rev.*, **40**, 3119–3129.

Troiani, F., Ghirri, A., Affronte, M., Carretta, S., Santini, P., Amoretti, G., Piligkos, S., Timco, G., and Winpenny, R.E.P. (2005) Molecular engineering of antiferromagnetic rings for quantum computation. *Phys. Rev. Lett.*, **94**, 207208.

Urdampilleta, M., Klyatskaya, S., Ruben, M., and Wernsdorfer, W. (2013) Landau-Zener tunneling of a single Tb3+ magnetic moment allowing the electronic read-out of a nuclear spin. *Phys. Rev. B: Condens. Matter Mater. Phys.*, **87**, 195412.

Zielinski, L.J. and Hürlimann, M.D. (2005) Probing short length scales with restricted diffusion in a static gradient using the CPMG sequence. *J. Mag. Res.*, **172**, 161–167.

19
Controlling the Growth

19.1
Introduction

From the previous presentation of the development of molecular magnetism, there surely emerged one common feature, namely that of controlling the growth of the assemblies of magnetic building blocks to obtain novel systems that give rise to new properties. The idea is to focus on complex phenomena that give rise to emerging properties by increasing the number of building blocks that can interact with each other. It is apparent that it is mandatory to learn how to control the growth mechanism, which may take different routes depending on the type of aggregate one has in one's mind. Systematic approaches have been attempted to describe classes of objects with different structures and topologies, and much progress is being made even though there are no attempts for a global approach. In this chapter, we cover in a rather random approach several approaches aiming to design and build finite and infinite objects. Here we will focus on the state of the art of systems in which there is control of the 3D structure as observed in the so-called metal–organic frameworks, MOFs, an example of which is shown in Figure 19.1.

Another class of compounds in which the growth mechanism is of fundamental importance is large clusters that are obtained with several different techniques. An example is $[Ln_{13}(H_2O)_6(phen)_{18}(ccnm)_6(CO_3)_{14}]^{5+}$ (phen = 1,10-phenanthroline, ccnm = carbamoylcyano-nitrosomethanide), a member of a series named "lanthaballs," the structure of one of which is shown in Figure 19.2 (Chesman *et al.*, 2009). The structure is based on a Ln ion which coordinates six carbonate groups, $[Ln(CO_3)]_6$. The carbonates bridge the core with 12 Ln ions, which define a distorted icosahedron. With variations to the synthetic procedure, a Ln_{14} configuration is obtained, which however has a much less regular structure and which is difficult to correlate to the structure of Ln_{13}.

A fundamental factor that requires control is the shape of the cluster. In Figure 19.3 is shown the structure of a cluster of 44 Cu, which shows a prolate structure.

Introduction to Molecular Magnetism: From Transition Metals to Lanthanides, First Edition.
Cristiano Benelli and Dante Gatteschi.
© 2015 Wiley-VCH Verlag GmbH & Co. KGaA. Published 2015 by Wiley-VCH Verlag GmbH & Co. KGaA.

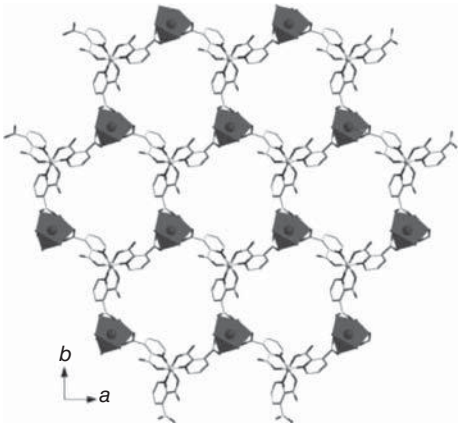

Figure 19.1 Honeycomb structure of $[GdCo(pyridine\text{-}2,3\text{-}dicarboxylic\ acid)_3(H_2O)_3]_n$. (Reproduced from Mahata P. *et al.* (2005) with permission from The Royal Society of Chemistry.)

Figure 19.2 Structure of the cationic ball $[Pr_{13}(H_2O)_6(phen)_{18}(ccnm)_6(CO_3)_{14}]^{5+}$.

Finally, we will briefly mention the beginning of a systematic effort to relate the structure and properties of 2D systems in the form of the so-called tessellation problem (Figure 19.3).

19.2 Metal–Organic Frameworks MOFs

The development of molecular magnetism has brought the attention of researchers on new classes of magnetic materials that often cover several disciplines. We have already described some of them, and now we want to treat two active areas that provide many opportunities for lanthanide-based systems.

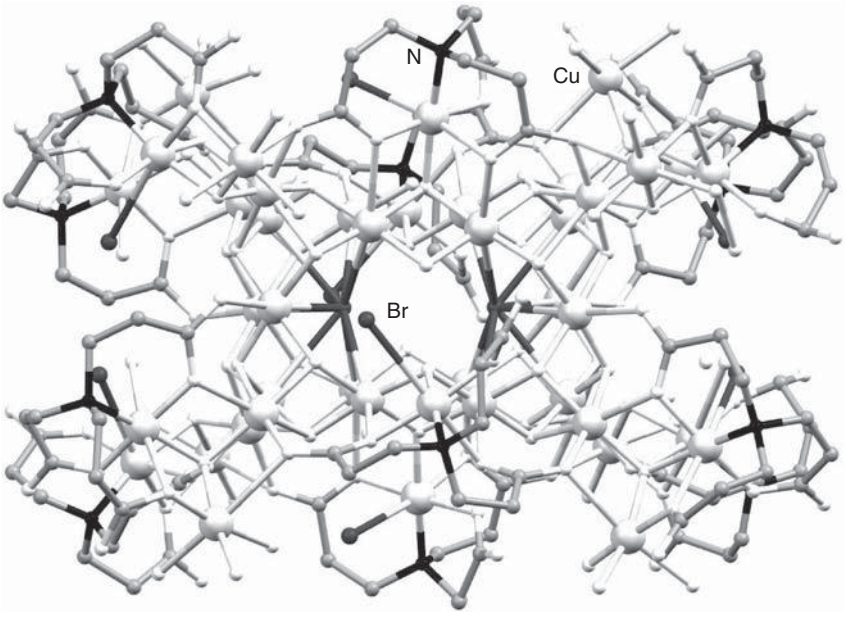

Figure 19.3 Structure of $[Cu_{44}(\mu_8\text{-}Br)_2\text{-}(\mu_3\text{-}OH)_{36}(\mu\text{-}OH)_4(N(CH_2CH_2CO_2)_3)12Br_8(OH_2)_{28}]$ $Br_2 \cdot 81H_2O$ (Murugesu *et al.*, 2004). Hydrogen atoms are omitted for clarity.

In the last few years, many classes of materials have been investigated for their 3D framework structure. As a result of the porosity of the structure, there is a major interest in this area for different applications: among them storing fuels and unwanted gases is of utmost importance (Murray, Dinc, and Long, 2009). Much work has been performed on systems where the structure provides unique opportunities for optimizing reactivity, catalysis, luminescence, and so on. A general name widely used for these materials is MOF. In order to show what must be understood for MOF, a perusal of Figure 19.4 should be enough (Lorusso *et al.*, 2013). It corresponds to a 3D array of gadolinium ions connected by formate anions. The size of the pores can be tuned using different carboxylate ligands.

Hybrid inorganic–organic framework materials are defined as compounds that contain both inorganic and organic moieties as integral parts of a network with infinite bonding connectivity in at least one dimension (Cheetham, Rao, and Feller, 2006). This definition excludes systems that are molecular or oligomeric. Most of the known hybrid frameworks may be divided into two categories. The coordination polymers or MOFs, as they are also known (especially when they are porous), can be defined as extended arrays composed of isolated metal atoms or clusters that are linked by multifunctional organic ligands L; these are based upon M–L–M connectivity. Second, there are systems that contain extended arrays of inorganic connectivity, referred to as *extended inorganic hybrids*. At present, the vast majority of known materials in this area are based on oxygen

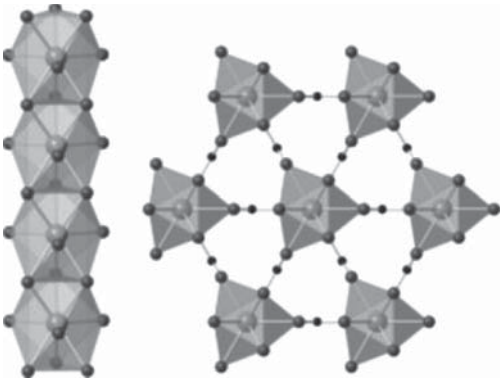

Figure 19.4 Views of the structure of $Gd(HCOO)_3$ parallel (a) and perpendicular (b) to the *c*-axis. (Reproduced from Lorusso G. *et al.* (2013) with permission from WILEY-VCH Verlag GmbH & Co. KGaA.)

bridges. These hybrid metal oxides, which contain infinite metal–oxygen–metal (M–O–M) arrays as a part of their structures, represent a subgroup of a larger class in which there is extended M–X–M bonding via other atoms such as Cl, N, or S. It is possible to find a classification in the literature (Furukawa *et al.*, 2014).

The interest in MOF is not originally magnetic; but the 3D structure can be appealing for magnetic properties, as we have repeatedly been saying (bulk magnetic properties are possible only in 3D systems), and indeed several magnetic studies are being reported. Magnetic MOF can be considered as a branch of coordination chemistry where metals are bound in a solid by coordination bonds to organic ligands.

From the structural point of view, there is a great interest in finding a logical way to develop a catalog, and thus in the development proposed by O'Keeffe *et al.* (2000), which consequently brings the notion of Yaghi's secondary building units (O'Keeffe *et al.*, 2008) where the atoms in a crystal are replaced by clusters and the organic connections between them make the bonds. Following this approach, many simple and basic crystal structures, for example NaCl, CsCl, $CdCl_2$, rutile, diamond, quartz, and so on (Han and Smith, 1999), were realized which happen to be the way magnetic materials were classified as the structure defines the exchange pathways (Blundell, 2001). Interestingly, as the inorganic nodes get bigger and the organic linkers longer, and of different geometry and multitopicity, a variety of highly stable lightweight materials has been synthesized (Férey, 2008). Some of these materials have spaces between the nodes containing solvents, which can be emptied and refilled without loss of the mosaicity of the crystals.

One-dimensional (1D) coordination polymers are relatively common in the early literature, even though they were not recognized at the time as part of a vast and remarkable family of materials (Rao, Cheetham, and Thirumurugan, 2008). Examples include porphyrin coordination polymers with interesting

magnetic properties, first discovered by Basolo and coworkers in the 1970s and characterized by X-ray diffraction at a later date (Anderson, Weschler, and Basolo, 1974; Goedken *et al.*, 1976). The complexes with tetracyanoethylene (TCNE) have been discussed in Section 9.4, stressing their interesting magnetic properties.

An example of magnetic MOF containing high-spin cobalt(II) which may be relevant to SMM and/or SCM as well will be worked out. An exhaustive review is available (Kurmoo, 2009). Two simple chain compounds of the formula $Co(PhCOO)_2$ have been reported. The benzene ring of the benzoate magnetically isolates the zigzag chains from each other. There are two forms: one crystallizes in the orthorhombic group (*Pcab*) (Gavrilenko *et al.*, 2005), while the other belongs to a monoclinic group (*C*2/*c*) (Gavrilenko *et al.*, 2008). In both the systems, the crystals are composed of alternating octahedral and tetrahedral cobalt centers bridged by one oxygen atom and one carboxylate (Figure 19.5).

The two derivatives show a different magnetic behavior: the orthorhombic modification is reported to be a long-range-ordered ferromagnet with a Curie temperature of 3.7 K. The monoclinic one behaves like a paramagnet to very low temperature and becomes an SCM below 0.6 K. Both compounds have highly anisotropic susceptibilities. For the former the easy axis is not parallel to the chain axis, but for the latter it is parallel.

Changing the carboxylate changes the magnetism. For Co(1,4-napdc) (1,4-napdc = napthalene-1,4-dicarboxylate) (Maji *et al.*, 2005) and Co_2(pm) (pm = 1,2,4,5-benzene-tetracarboxylate) (Kumagai, Kepert, and Kurmoo, 2002), the Curie–Weiss fit of the high-temperature data gave positive Weiss constants of +27 K and +16 K, respectively. On the other hand, that of $Co_2(dobdc)(H_2O)_2 \cdot 8H_2O$ (dobdc = 2,5-dioxyterephthalate) is negative (−6 K) (Huang *et al.*, 2000). These values suggest that the exchange within the chains

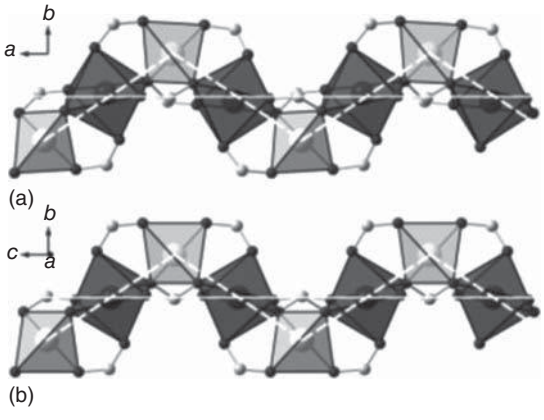

Figure 19.5 The chain structure of $Co(PhCOO)_2$. (a) Orthorhombic crystal. (b) Monoclinic crystal. (Reproduced from Gavrilenko S.K. *et al.* (2008) with permission from WILEY-VCH Verlag GmbH & Co. KGaA.)

in each of these compounds is ferromagnetic. The chains interact antiferromagnetically between them, and long-range antiferromagnetic order sets in at 5.5, 8, and 16 K, respectively. In each case, a field high enough to overcome the transverse coupling energy reverses all the moments to a ferromagnetic state and the compounds then exhibit hysteresis. This behavior is well known, and the system is a metamagnet. Applying a transverse field that is stronger than the coupling between chains the system leads to a field-induced transition. The critical metamagnetic fields are quite different from each other: 250 Oe for Co(1,4-napdc), 430 kOe for $Co_2(dobdc)(H_2O)_2 \cdot 8H_2O$, and 1400 Oe for Co_2(pm). The large variation in the critical field does not scale with the interchain distance as one might expect. Most unexpectedly, the AC susceptibility of Co(1,4-napdc) and Co_2(pm) shows the presence of both real and imaginary components. A spontaneous magnetization was confirmed for Co_2(pm) by zero-field-cooled (ZFC), and field-cooled (FC) measurements at a field of 1 Oe, which demonstrated the presence of a canted state at 13 K below the collinear Néel state at 16 K (Figure 19.6).

The ZFC–FC measurements are typical of ordering systems. The two curves are different in the range 2–12.8 K. The ZFC is about 0 at 2 K because of the rapid

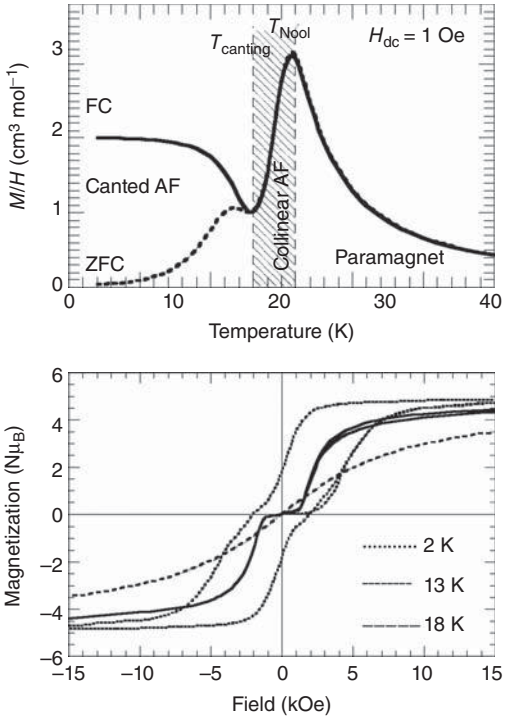

Figure 19.6 ZFC–FC magnetization of Co_2(pm) in 1 Oe taken after zero-field cooling to 2 K, showing the bifurcation point at 12.8 K. (Reproduced from Kurmoo, M. (2009) with permission from The Royal Society of Chemistry.)

cooling in zero field does not allow the orientation of the spin according to the canted antiferromagnet and the system behaves like a paramagnet. On increasing the temperature, the magnetization increases. A canted antiferromagnet is a system in which the magnetic moments are aligned in the usual antiferromagnetic manner but the spins are not exactly antiparallel. Their directions form an angle, giving a net small magnetization. In the FC, the magnetization of the system adjusts to the varying magnetic fields. If we look at the FC magnetization (M) at 2 K in a static field of 1 kOe, M is that of the canted ferromagnet, and on increasing temperature the magnetization decreases until at 12.8 K when the curve is equal to that of the ZFC. Above this temperature, the two curves are identical and the system is paramagnetic. Therefore, the ZFC–FC measurement provides information on the phase diagram of the compound.

The lack of such measurements for the other two compounds limits a full comparison. Heat capacity measurements for Co_2(pm) estimates that 60% of the entropy is found below the Néel temperature and the effective spin of the cobalt is 1/2. Unpublished neutron diffraction data of Co_2(pm) in zero field show that the moments are perpendicular to the chain, and the nearest-neighbor chains connected by O–C–O bridges point also in the same direction while those of adjacent layers are antiparallel (Green, M.A., Kumagai, H., and Kurmoo, M. unpublished results). However, in a field of 40 kOe all the moments are parallel to each other.

Rare-earth solids are good candidates to exhibit interesting photoluminescent properties (Maspoch, Ruiz-Molina, and Veciana, 2007). Therefore, much work has been devoted to optimizing these properties. Just to mention some results, Song and Mao reported a series of phosphonate-decorated lanthanide oxalates with open-framework structures exhibiting blue, red, and near-IR luminescence. Also, Férey and coworkers (Férey, 2008) obtained a porous material with very efficient red, green, and blue emission after doping the complex $Y_{12-x}Eu_x(C_9O_6H_3)$($x = 0.024$) with Eu, Tb, and Dy, respectively. Red fluorescence has been found in other lanthanide complexes, while emission of green light was observed in $[Tb(C_4H_4O_4)1.5(H_2O)] \cdot 0.5H_2O$. Another interesting feature of lanthanide polymers is observed in $Er(bpdc)1.5(H_2O) \cdot 0.5DMF$ (bpdc = 4,4'-biphenyldicarboxylic acid), which exhibits the characteristic emission of Er^{3+} around 1540 nm excited at 980 nm.

Interesting photoluminescence properties were reported in some lanthanide silicates with the composition $Na_{1.08}K_{0.5}Ln_{1.14}Si_3O_{8.5}1.78\ H_2O$ (where Ln is Eu, Tb, Sm, and Ce). These materials combine microporosity with interesting photoluminescence properties, and their structural flexibility allows fine-tuning of the luminescence properties by introducing a second type of lanthanide ion in the framework. Finally, it is worth mentioning that, in addition to fluorescence, another property that has been extensively studied for open-framework inorganic materials is that of nonlinear optics. In this case, a considerable variety of noncentrosymmetric inorganic materials have been shown to exhibit interesting second-harmonic generation, although in some cases third-order nonlinear open-framework coordination polymers have also been reported.

19.3
From Nano to Giant

In the quest for the Holy Grail of molecular system showing concurrently classical and quantum properties, the chemical approach is to try to increase the size of the molecules. One of the most promising areas in this field of research is the synthesis of giant clusters. The above definition is vague, because "giant" is a relative concept and what is gigantic now will be normal tomorrow. Indeed, the area is developing rapidly and the synthetic techniques are improving.

There is no doubt that one of the earliest investigators of giant clusters is Achim Müller who reported the synthesis of ever large clusters aimed at building the "hedgehog" molecule containing up to 368 Mo ions (Müller and Gouzerh, 2012). In his work, he suggested the similarity of giant clusters and proteins, with the possibility of observing self-assembly in inorganic systems. Also, the use of the term "*keplerate*" has been pushed in Bielefeld (Müller *et al.*, 1999a). We recall that keplerate is used to indicate a molecular structure that contains Platonic and Archimedean solids one inside another like Russian dolls. Of course, on increasing the size of clusters there is a dramatic increase in the difficulty to really understand the magnetic properties. As an example, we will use a series of polyoxomolybdates, which in our opinion have been efficiently characterized and provided a reasonable rationalization.

In this chapter, we just report a few examples of clusters with interesting molecular structures to elucidate the difficulties in examining the magnetic properties of this kind of compounds.

19.4
Molybdates

Perhaps the most important results in the magnetic properties of large clusters can be found in a series of polyoxomolybdates of the formula $[(Mo^{VI})(Mo^{VI})_5O_{21}L_6]_{12}(linker)_{30}$ where linker is an $(icosidodecahedral)_{30}$ cluster containing 30 metal ions (Müller *et al.*, 1999b). The structure of the Fe_{30} cluster is shown in Figure 19.7. The Mo_{72} cluster is diamagnetic, while the magnetic ions so far investigated are V^{4+}, Cr^{3+}, and Fe^{3+}. Ln^{3+} can be added to the reaction but only six lanthanides can be hosted (Kortz *et al.*, 2009).

The three TMs provide a good choice for exploiting the different nature of the spins. V^{4+} has $S = 1/2$ and corresponds to a quantum spin. Fe^{3+} has $S = 5/2$,

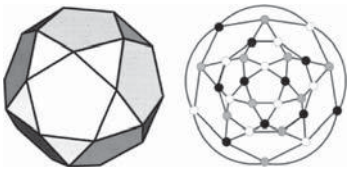

Figure 19.7 (a) The 30 non-Mo ions of the $Mo_{72}TM_{30}$ molecule located on the vertices of an icosidodecahedron. (b) Planar projection of the icosidodecahedron. All edges and vertices are identical to those shown in (a). (Reproduced from Axenovich, M. and Luban M. (2001) with permission of The American Physical Society.)

which can be approximated with a classical spin. Cr^{3+} (S = 3/2) has a spin state which is intermediate between the two other 3d ions. This situation offers the possibility to have a general idea on the approach needed to gain a good insight of the magnetism of large clusters. The HDVV model, which is useful to examine the properties of a system containing interacting quantum spins, provides a useful starting point to treat the magnetism of these molecules. However, there is a big problem related to the number of spins present in giant cluster. If we have N interacting paramagnetic ions with each spin equal to S, the analysis of thermodynamic problem of the system would require the diagonalization of square matrices defined on a Hilbert space of dimension $DIM = (2S + 1)^N$. In the present case for the $Mo_{72}(TM)_{30}$ derivatives, DIM varies from 2^{30} to 6^{30}: it means that we should work on systems containing from 1 073 741 824 levels up to a number which is around one-third of the Avogadro number! Therefore, for studying similar derivatives there are two choices: (i) a qualitative analysis, and (ii) a quantitative one, which requires some strategy to develop approximated methods tailored on some specific feature of the system under analysis. We will describe those used in the reported compounds and will give some more general hints at the end of the chapter.

Let us start with the magnetic measurements performed on the Fe_{30} derivative, which suggest the presence of antiferromagnetic coupling among the metal ions which could be operative in coupling nearest-neighbor Fe^{3+} ions. The expected coupling should be very weak, as testified by the room-temperature value of χT which corresponds to 30 uncoupled S = 5/2 ions. Starting from this hypothesis and considering the impossibility to deal with the classical approach involving the whole cluster, the magnetic susceptibility is calculated as

$$\chi = \lim_{H\to 0}\frac{M}{H} = \frac{30N_A g^2 \mu_B^2 S(S+1)}{3kT}\left(1 + \sum_{n=2}^{30}\langle s_1 \cdot s_n\rangle\right) \tag{19.1}$$

where N_A is the Avogadro number, k is the Boltzmann constant, and $\langle s_1 \cdot s_n\rangle$ is the general two-spin correlation function which depends on the temperature and coupling constant. With this approach, experimental data were nicely reproduced in the range 30–300 K with $g = 1.974$ and $J = 9.5\,cm^{-1}$ (Müller *et al.*, 2001). As the presence of an antiferromagnetic coupling is confirmed, below 30 K the spin arrangement requires a different approach. As shown in Figure 19.7a, the metal ions are arranged at the corners of three- and five-membered rings. We have discussed in Chapter 18 that molecules with triangular shapes exhibit spin frustration in the presence of AFM coupling when an odd number of interacting spins are present. Therefore, this cluster is a textbook example of spin frustration in a large cluster. The low-temperature magnetic properties have been discussed using techniques of analytical graph theory (Figure 19.7b). In the framework of classical Heisenberg approach for the interacting spins in presence of frustration, it was possible to reproduce the magnetic behavior of the cluster from room temperature down to 0.1 K and in external magnetic field up to 600 kOe, giving an idea on the relative spin orientation (Axenovich and Luban, 2001).

The temperature dependence of the χT values of the V^{4+} derivative is indicative of the presence of an antiferromagnetic coupling also for this cluster (Müller *et al.*, 2005). This system contains $S = 1/2$ spin in a slightly oblate cluster, which is not as symmetric as the iron and chromium derivatives. The best way to reproduce the magnetic susceptibility was the use of Quantum Monte Carlo (QMC) calculations employing a single exchange-coupling constant. It is useful to mention that this type of approach was applied to reproduce the magnetic susceptibility from room temperature down to 120 K: the QMC method is not fully reliable at low temperatures in a spin-frustrated system as a consequence of an antiferromagnetic coupling. Within this approximation, the fitting procedure yielded a very high value of the coupling constant with respect to the value observed in the Fe_{30} derivative as a result of an efficient spin coupling by electron delocalization.

Cr^{3+} with spin $S = 3/2$ is in between V^{4+} and Fe^{3+}. Even for this compound, which is isomorphous with the Fe^{3+} cluster, the magnetic data are consistent with a predominant antiferromagnetic interaction (Todea *et al.*, 2007). Because of the spin value of the Cr^{3+} ions, it was not possible to apply the classical approach, and the QMC calculations for data above 30 K confirmed the presence of an AF coupling mechanism with an intensity similar to the one observed in the Fe_{30} derivative.

19.5 To the Limit

Outside the polyoxomolybdate world, there are a number of large clusters with different magnetic properties but, following our track, we will mainly focus on systems that contain Ln. Just to start defining what we are talking of here is Figure 19.8. A Sino-American team reported an exciting series of clusters comprising Ln and Ni (Kong *et al.*, 2009b). A particularly appealing one is a cluster comprising 136 metal ions, $La_{60}Ni_{76}$.

This compound, formulated as $[La_{60}Ni_{76}(ida)_{68}(OH)_{158}(NO_3)_4(H_2O)_{44}](NO_3)_{34} \cdot 42H_2O$ (ida = iminodiacetate) based on crystallographic analysis, was obtained under hydrothermal conditions from a mixture of $Ni(NO_3)_2 \cdot 6H_2O$, $La(NO_3)_3 \cdot 6H_2O$, and iminodiacetic acid in deionized water, and its composition was verified by satisfactory microanalysis. The structure reported in Figure 19.8 is aesthetically appealing but it needs a guided tour to be understood. It is always exciting to compare molecular shapes with real objects, and the authors suggest that Russian nesting dolls can be used as the structure can be seen as a series of clusters of increasing sizes like which surround progressively the smaller ones. Indeed, so far the interest for the cluster has arisen mainly from the structure and in particular from the spontaneous organization of the different ions in different clusters. Let us check how the model works.

The inner shell is defined by a rectangular parallelepiped of eight Ni^{2+} ions (Figure 19.9). The distance between the two squares is 1.16 nm. This core is

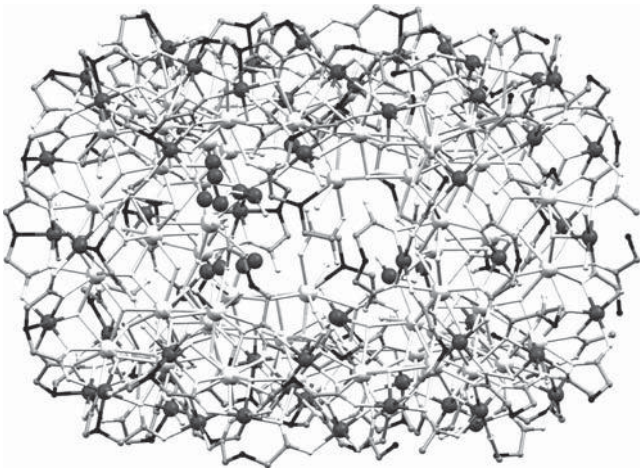

Figure 19.8 A ball-and-stick view of the cationic cluster: Ln = light gray; Ni = dark gray.

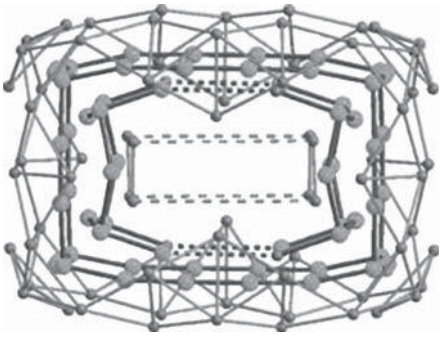

Figure 19.9 Four-shell presentation of the $La_{60}Ni_{76}$ framework. (Reproduced from Kong, X.-J. *et al.* (2009b) with permission from The Royal Society of Chemistry.)

surrounded by a second shell defined by 20 La atoms and 4 Ni atoms, which corresponds to a parallelepiped of 0.78 nm × 0.78 nm × 1.53 nm. The two opposed square faces contain eight La on the whole. A third shell contains 40 La and the outermost is formed by 64 Ni^{2+} ions. All the adjacent shells of metals are linked by triply bridging hydroxo groups.

The analysis of the magnetic properties of a system containing 76 potentially interacting metal centers is a hard job. In the presence of a complex topology of exchange patterns, often it is possible just to offer a very qualitative description. In this system, the temperature dependence of the magnetic susceptibility of the cluster was measured from 2 to 300 K in an applied magnetic field of 1000 Oe. The χT values suggested the probable presence of a weak ferromagnetic interaction between the Ni^{2+} ions and inter-cluster antiferromagnetic interactions.

With a similar synthetic strategy, a cluster with the general formula $[Gd_{54}Ni_{54}(ida)_{48}(OH)_{144}(CO_3)_6(H_2O)_{25}](NO_3)_{18} \cdot 140H_2O$ has been reported

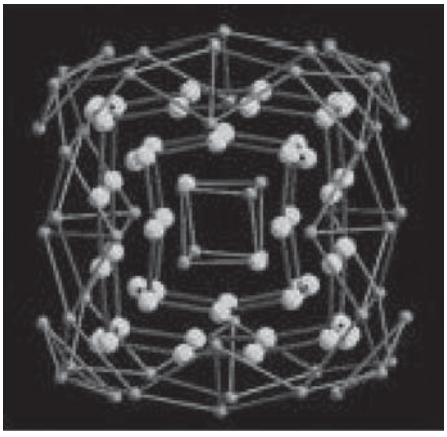

Figure 19.10 Four-shell presentation of the metal frameworks. (Reproduced from Kong, X.-J. *et al.* (2008) with permission from WILEY-VCH Verlag GmbH & Co. KGaA.)

(Kong *et al.*, 2008). The overall structure of the cluster resembles that of $La_{60}Ni_{76}$ with a similar four-shell nesting-doll-like arrangement of the metal ions, as shown in Figure 19.10.

The innermost shell contains six Ni^{2+} and two Gd^{3+} ions in a rather cubic structure. Around there is a first shell formed by 20 Gd^{3+} ions followed by another one with 32 Gd^{3+} ions. These three shells are included in a cage with 48 Ni^{2+} ions. The shells are bridged by water molecules and/or by triply bridging OH groups.

The magnetic susceptibilities were measured in an applied field of 1000 Oe over the temperature range 2–300 K. The room-temperature χT value is slightly smaller than the value calculated for 54 uncorrelated Ni^{2+} ions (53.97 emu K mol^{-1} for $S = 1, g = 2.00$) and 54 uncorrelated Gd^{3+} ions ($S = 7/2, g = 2$; 425.52 emu K mol^{-1}): the observed value is 463.0 emu K mol^{-1} and the expected one is 479.49 emu K mol^{-1}. On lowering the temperature, the χT values decrease gradually, reaching a value of 402.7 emu K mol^{-1} at 2 K. As previously observed, the number of paramagnetic ions in the cluster prevents a detailed analysis of its magnetic properties. It is only possible to suggest the presence of antiferromagnetic interactions.

A similar qualitative analysis has been performed for the Er^{3+} derivative with formula $[Er_{60}(\text{L-thre})_{34}(\mu_6\text{-}CO_3)_8(\mu_3\text{-}OH)_{96}(\mu_2\text{-}O)_2(H_2O)_{18}]Br_{12}(ClO_4)_{18}(H_2O)_{40}$ (L-thre = L-threonine) whose cluster core containing the 60 metal ions is reported in Figure 19.11 (Kong *et al.*, 2009a).

Even in this system, the fascinating structure of the cluster does not allow an equally fascinating definition of the exchange mechanism involving the 4f ions. The room-temperature χT value of 608.87 emu K mol^{-1} is smaller than the value of 688.80 emu K mol^{-1} calculated for 60 noninteracting Er^{3+} ions ($^4I_{15/2}$, $g = 6/5$). The temperature dependence of the magnetic susceptibility in the 20–300 K range can be fitted nicely to the Curie–Weiss law, yielding

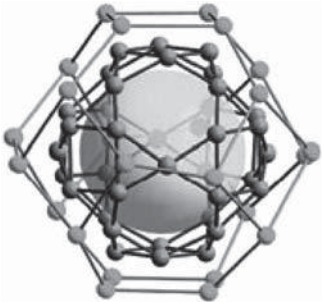

Figure 19.11 Cluster core structure with 60 metal atoms. The structure can be described as an outer truncated octahedral shell of 24 metal atoms enclosing an inner doubly truncated octahedral shell of 36 metal atoms. (Reproduced from Kong, X.-J. *et al.* (2009) with permission from The American Chemical Society.)

$C = 632.9\,\mathrm{emu\,K\,mol^{-1}}$ and $\Theta_{\mathrm{Weiss}} = -11.91\,\mathrm{K}$. These parameters are indicative of an antiferromagnetic interaction, but it was not possible to say anything more.

A common feature can be observed in the cluster reported in this chapter and more examples described in the literature (Kong *et al.*, 2010): they are characterized by shell-like structures. A comparative analysis of the methods required for their synthesis may be indicative of three different strategies for obtaining at least the core of such large molecules. There is the family of the polyoxometalates, the systems where metal–metal bonding is present, and the synthesis of which uses ligands whose ability to act as bridging moieties is well established. Their syntheses are obviously very sensitive to the reaction conditions so that changing the conditions may lead to clusters of different nuclearities and altered structures.

19.6 Controlling Anisotropy

As we have stressed while dealing with several systems in the previous chapter, anisotropy is an important feature in influencing the magnetic properties of molecular magnetic materials. For instance, the presence of a metal ion with highly anisotropy is often the necessary starting point in preparing SMM, SIM, and SCM as evidenced by the use of ions such as Dy^{3+}.

Therefore, it is possible to forecast that a large cluster containing an anisotropic ion such as Co^{2+} should be a good candidate for producing a system with the previously indicated magnetic properties. But chemistry is fascinating, as sometimes the final result is completely different from the expected one. For instance, by a solvothermal reaction of cobalt acetate with *p-tert*-butylthiacalix[4]arene (H_4TC4A), a compound of formula $[Co^{II}{}_{24}Co^{III}{}_{8}(\mu_3\text{-}O)_{24}\,(H_2O)_{24}(TC4A)_6]$ was synthesized (Bi *et al.*, 2009). The compound is a $[Co_{32}]$ cluster with a highly symmetric core, as shown in Figure 19.12.

As it is not easy to analyze the magnetic behavior of a system in which Co^{2+} ions are involved in exchange coupling, the magnetic behavior indicates that substantially antiferromagnetic interactions are operative in the Co_{24} shell and that no SMM behavior is operative above 2 K.

On the other side, in some other fields of application of magnetic materials, the absence of anisotropy is a fundamental feature to reach interesting results. The

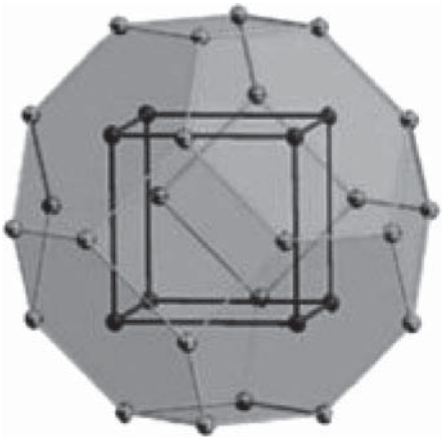

Figure 19.12 Co_{32} core formed by an inner cube of eight Co^{3+} ions surrounded by 24 Co^{2+} ions. (Reproduced from Bi, X. *et al.* (2009) with permission from The American Chemical Society.)

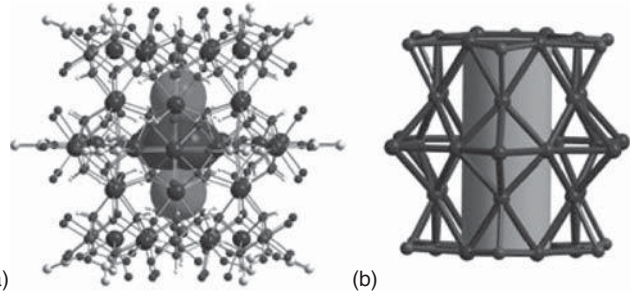

Figure 19.13 (a) Ball-and-stick view of the cluster cation along the *c*-axis. (b) Arrangement of the 48 metal ions. (Reproduced from Peng, J.-B. *et al.* (2011) with permission from WILEY-VCH Verlag GmbH & Co. KGaA.)

latest researches on magnetocaloric effects (MCEs) offered by molecular systems indicate that clusters with peculiar magnetic properties may present interesting features, as will be explained in Chapter 23. To exhibit a large MCE, a molecule should have a negligible magnetic anisotropy, low-lying excited spin states, and a large spin ground state which often requires dominant ferromagnetic exchange. We want to report here a couple of examples of these new compounds to show how a giant cluster, thanks to high number of paramagnetic centers, can be play a relevant role in this field even though antiferromagnetic interactions are operative.

As an isotropic ion, Gd^{3+} seems a good starting point because its ground state has a large S value and it is substantially isotropic. For these reasons, it is largely used in preparing clusters hoping to get some relevant MCE. For instance, a compound of formula $[Gd_{36}Ni_{12}(CH_3COO)_{18}(\mu_3\text{-}OH)_{84}(\mu_4\text{-}O)_6(H_2O)_{54}(NO_3)Cl_2]-(NO_3)_6Cl_9 \cdot 30H_2O$ has been reported, whose structure is shown in Figure 19.13 (Peng *et al.*, 2011).

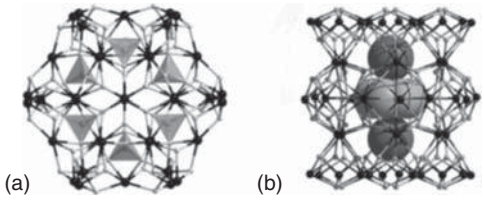

Figure 19.14 Ball-and-stick view of (a) Gd_{38} and (b) Gd_{48} clusters. (Reproduced from Guo, F.-S. *et al.* (2013) with permission from WILEY-VCH Verlag GmbH & Co. KGaA.)

The magnetization value at 2 K is large enough to make this compound a possible candidate for low-temperature magnetic cooling.

An interesting system containing Gd^{3+} ions and chloroacetic acid (CAA) has been reported by a Chinese team (Guo *et al.*, 2013). By using different anion templates, these researchers were able to extract selectively from a solution of CAA two different compounds of formula $[Gd_{38}(\mu\text{-}O)(\mu_8ClO_4)_6(\mu_3\text{-}OH)_{42}(CAA)_{37}(H_2O)_{36}(EtOH)_6](ClO_4)_{10}(OH)_{17} \cdot 14DMSO \cdot 13H_2O$ and $[Gd_{48}(\mu_4\text{-}O)_6(\mu_3\text{-}OH)_{84}(CAA)_{36}(NO_3)_6(H_2O)_{24}(EtOH)_{12}(NO_3)Cl_2]Cl_3 \cdot 6DMF \cdot 5EtOH \cdot 20H_2O$ (Figure 19.14). It is possible to dynamically convert the Gd_{38} derivative into the Gd_{48} one upon Cl^- and NO_3^- stimulus.

The magnetic behavior of Gd_{38} and Gd_{48} compounds does not differ very much from the other previously reported compounds of similar cluster. The room-temperature χT values are both close to the expected ones for 38 and 48 uncorrelated Gd^{3+} ions, respectively. On analyzing the temperature dependence of χT and the lowest temperature limits, it was possible to deduce the presence of dominant antiferromagnetic interaction. The interesting feature is that the magnetization values at 1.8 K are in any case very high, making both systems suitable for test in the search of compounds that present interesting MCE.

19.7
Cluster with Few Lanthanides

As outlined previously in the description of the two Gd clusters, a high magnetization can be useful in several applications. On this basis, the search for ferromagnetic interaction can be a useful tool in reaching this goal. Looking in the database of exchange mechanisms, 3d–4f systems are potential candidates, and several clusters containing Cu^{2+} and Ln^{3+} ions have been synthesized. For instance, the simple reaction of $Ln(NO_3)_3 \cdot xH_2O$ (Ln = Dy, Gd) and $Cu(OAc)_2 \cdot H_2O$ with TPA (TPA = tritylphosphonic acid) in 1 : 2 : 1 ratio in the presence of base leads to the formation of a 3d–4f heterometallic cluster with a $Cu_{24}Ln_6$ core, as shown in Figure 19.15 (Baskar *et al.*, 2010). It can be described as a cuboctahedron formed by 12 Cu^{2+} ions enclosed inside a cube formed by the 8 Ln^{3+} ions. The six faces of the cube are capped by six Cu^{2+} dimers.

It is very difficult to reach a well-defined result in the analysis of the magnetic properties of the cluster containing Dy^{3+} because it is not possible to discriminate

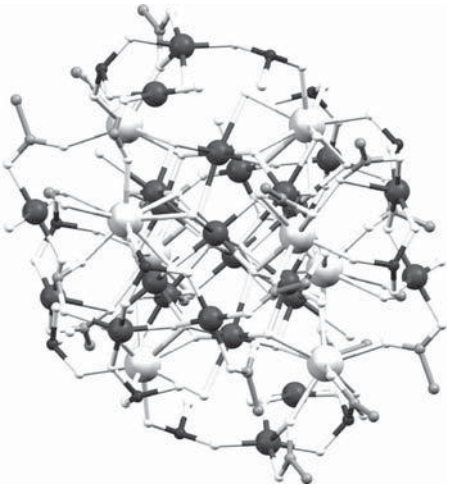

Figure 19.15 View of the metallic core of Dy_8Cu_{24}. Dy = light gray; Cu = dark gray.

between the contributions of magnetic exchange and crystal field effects due to the presence of this 4f ion. The low-temperature data suggest the presence of a large-spin ground state whose nature is not clear. More interesting are the properties of the Gd derivative. The magnetization studies are consistent with a ground state with S = 34 even though the curve does not follow the Brillouin's function. Some other spin levels close to the ground level seem populated even at 1.8 K. The spin state with S = 34 can be rationalized on the assumption that all the interactions within the central $[Cu^{II}_{12}Gd^{III}_{8}]$ core are ferromagnetic while the exchange between the six external Cu dimers is strongly antiferromagnetic. As for the potential SMM behavior, it was not observed for the magnetically isotropic Gd^{3+} derivative, while it was reported for the Dy^{3+} one even though the energy barrier is very small ($U_{\text{eff}} = 4.6\,\text{K}$, $\tau_0 = 2.1 \times 10^{-8}$ s).

19.8 Analyzing the Magnetic Properties

One of the crucial points in the analysis of the magnetic properties of a molecule starting from a simple dimer up to a giant cluster is the definition of the nature and intensity of the exchange coupling. The general strategy to reach this final goal is an overview of the molecular structure and, on this basis, a sketch of the potential exchange mechanisms with the relative coupling constants. This basis is necessary to choose an appropriate approach to reproduce the experimental magnetic data. Very often, the temperature dependence of the magnetic susceptibility is the only experiment to be used for some fitting procedure. It is useful to stress that this kind of data is just indicative of a depopulation mechanism driven by the temperature changes whereas the distribution in the energy space of the levels depends on several parameters such as the coupling mechanisms, CF effects, ZFS,

and so on. A second point to consider is that in presence of weak interactions, as in many Ln^{3+} derivatives, the high-temperature data are substantially noninformative on the nature and intensity of the coupling. All these conditions are useful to suggest a strategy for extracting reliable parameters from these experiments. It is basic to use a model with a reduced set of parameters. For instance, it is a good approximation to use the same coupling constant even in presence of small structural differences in the environment of the paramagnetic centers. When it is possible, it should be useful to extract information on the electronic structure of the ions present in the molecule from different sources. A more difficult strategy is the selective substitution of paramagnetic ion with diamagnetic ones taking advantage, in the case of lanthanides, of the isomorphism often offered by the derivatives of the 4f family.

Even while using all the precautions indicated previously, there is a huge problem when the system to analyze is a cluster of dimensions similar to those of the compounds described in this chapter. In the majority of the systems, the analysis of the magnetic properties ends with a generic indication of the overall behavior without any quantitative indication. A first hint of the problem was reported in the description of the TM_{30} clusters where the problem regarding the matrices required to describe the magnetic behavior of those clusters was clearly highlighted. There is the possibility of calculating the energy level distribution even when the number of interacting centers is relatively high by using an approach based on irreducible tensor operators (ITOs). The ITOs are equivalent to standard spin operators and are particularly well suited for calculations in the spin Hamiltonian formalism, because the total spin quantum numbers S correspond to the irreducible representations of the orthogonal rotation group. For this reason, their use allows considerable simplifications in the calculations, the principal one being that it is no longer necessary to write the functions explicitly but is sufficient to simply indicate the individual, intermediate, and total spin to calculate the matrix elements of the Hamiltonian matrix (Barra *et al.*, 1992). Just to give two numbers, it may be useful to consider a cluster containing six Mn^{2+} ions ($S = 5/2$). According to the usual expression, it is possible to calculate that the total dimension of the Hamiltonian matrix as $46\,656 \times 46\,656$. If the ITO approach is applied, the matrix can be block-factorized according to all the spin states from 0 to 15/2, as shown in Table 19.1.

Sometimes, this approach is not fully successful like in the case of Mn_{12}. In this case, the total spin states are of the order of 10^8. It is possible to obtain with the ITO technique spin S varying from zero to 22, and there are many of these sates (such as those with $S = 3, 4, 5$) involving more than 10^6 states. So it is not possible to perform a full calculation of the whole system. It was necessary to develop a specific strategy connected to the exchange pathway of these molecules (Gatteschi, 1999).

If the cluster possesses some symmetry, there are in the literature examples of the use of point group symmetry by symmetry permutations for different spin sites of the cluster, as the spin Hamiltonian is symmetric relative to the interchange of identical particles. In the case of the Fe_8 cluster, the total degeneracy due to the presence of eight $S = 5/2$ spins is 1 679 616. By grouping these states according to

Table 19.1 Total spin states for a cluster of six S = 5/2.

Spin	Number of spin states	Spin	Number of spin states
15	1	7	405
14	5	6	505
13	15	5	581
12	35	4	609
11	70	3	575
10	126	2	475
9	204	1	315
8	300	0	111

the quantum number S, which varies from 0 to 20, there are blocks with size higher than 15 000. The total symmetry of the cluster is very close to D_{2d} and, therefore, it is possible to group the spin states according to their S values and their symmetry. The final result is shown in Table 19.2 (Delfs *et al.*, 1993).

It is possible to notice that now the largest block has a dimension around 4000×4000 and it is easy to extract information on the level distribution in the energy space. The procedure is not as straightforward as in the case of ITO, and

Table 19.2 Symmetry classification of the total spin states for Fe_8 in the D_{2d} group.

S	*A*	B_1	B_2	B_3	Total degeneracy
20	1	—	—	—	1
19	2	1	2	2	7
18	10	6	6	6	28
17	22	18	22	22	84
16	60	50	50	50	210
15	118	108	118	118	462
14	243	225	224	224	916
13	419	401	420	420	1 160
12	717	696	686	686	2 779
11	1 088	1 061	1 092	1 092	4 333
10	1 614	1 578	1 568	1 568	6 328
9	2 174	2 138	2 184	2 184	8 680
8	2 841	2 799	2 780	2 780	11 200
7	3 401	3 359	3 420	3 420	13 600
6	3 927	3 885	3 854	3 854	15 520
5	4 139	4 097	4 170	4 170	16 576
4	4 155	4 122	4 076	4 076	16 429
3	3 704	3 671	3 750	3 750	14 875
2	3 019	3 001	2 940	2 940	11 900
1	1 899	1 881	1 960	1 960	7 700
0	703	703	630	630	2 666

this is obvious from the fact that starting from larger systems the final result is not as successful as in this case. There are, in any case, attempts useful to approach the magnetic properties in a semiquantitative fashion.

19.9
Two-Dimensional Structures

The systems we have discussed so far have been of the 0D, 1D, or 3D type. Let us check what can be done for 2D structures. Whether the bottom-up approach may be successful depends on the ability to optimize the boundary conditions. An elegant approach in this direction has been reported on the use of Ce directed molecular self-assembly of a five-vertex Archimedean surface.

A recently developed tool for manipulating 2D structures is scanning tunneling microscopy (STM), which allows the control of the organization of metal ions one at a time. Reichert *et al.* (Écija *et al.*, 2013) chose lanthanide ions in conjunction with the dicarbonitrile polyphenyl species, $NC-(Ph)_n-CN$, ($n = 3, 4$), to explore the opportunities of Ln-directed molecular self-assembly for organizing different

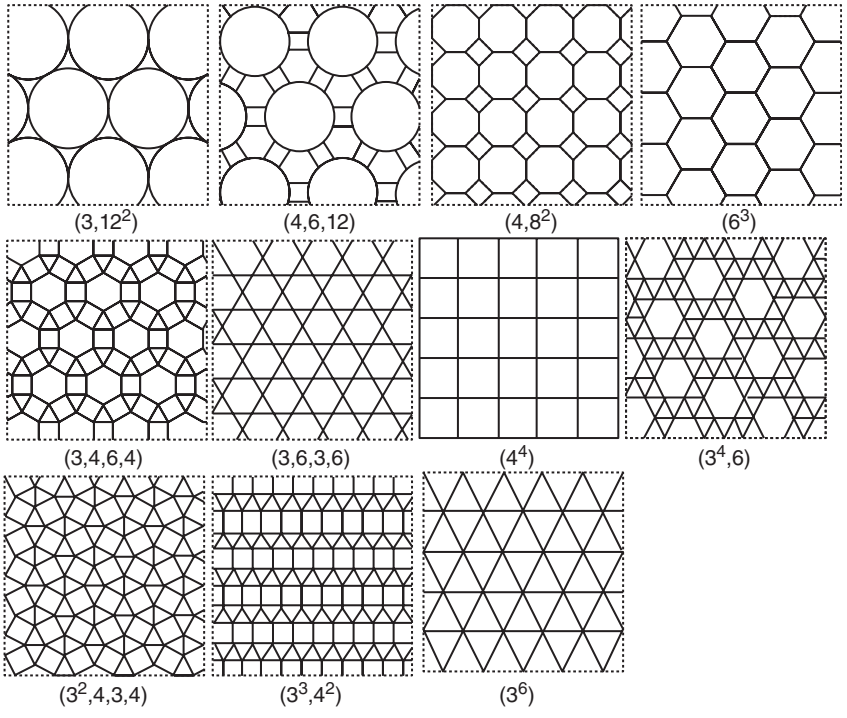

Figure 19.16 The 11 Archimedean lattices or uniform tilings, in which all polygons are regular and each vertex is surrounded by the same sequence of polygons. The notation (3^4, 6) for example means that every vertex is surrounded by four triangles and one hexagon.

tessellation schemes on Ag (111) surfaces. Indeed, they found with Ce that for L/Ce 5 : 1 pentameric units are formed.

Varying the ratio the system must obey the condition of tessellation. The definition is cumbersome but the content is relatively simple. It is the problem of tasseling a surface, which of course has to do with the way one can follow to properly pave a room. But it is a symmetry problem as well as an art problem. The first systematic approach was made by Kepler, which is at the basis of several important conditions such as the compatibility of different polygons in higher hierarchy objects.

An example of Archimedean tiling is shown in Figure 19.16.

When you know them, you observe and recognize them. For instance, they are present in supramolecular dendritic liquids, liquid crystals, and so on. On a less passive way, the theory helped in working out self-assembly protocols to a Kagome lattice. This is an archetypal frustrated lattice and the successful implementation of Kagome suggested the exploration of other frustrated systems. Among these, a key role is played by the planar five-vertex structures.

The investigated systems used the dicarbonitrile polyphenyl species whose chemistry is well known. The use of Ce relies on the catalytic properties associated with it to be able to expand the coordination number from 6 to 10. It is suggested that an interest for Ln will be that of helping in the synthesis of high-coordination-number systems on the surfaces.

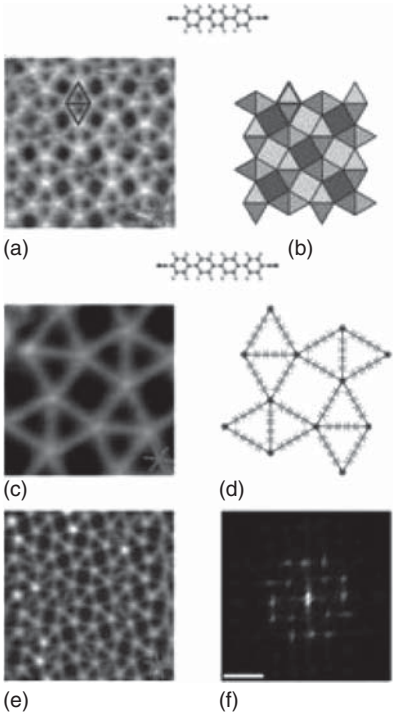

Figure 19.17 Supramolecular Archimedean snub tiling. (a) STM image of the lanthanide-directed assembly of a supramolecular snub square tessellation on Ag(111) for a NC–Ph_3–CN to Ce stoichiometry of 5 : 2. (b) Tessellation scheme of A with 3.3.4.3.4 sequence of triangular and square tiles. (c) High-resolution image of a snub square tiling motif constituted of NC–Ph_4–CN linkers and Ce centers. (d) Structure model of *C* showing the fivefold coordination of the Ce centers (depicted as solid circles). (e) STM image of a snub square tiling domain involving NC–Ph_4–CN linkers and Ce centers. (f) Fast Fourier transform of *E* revealing the spatial periodicity of the tiling pattern. (Reproduced from Ecija, D. *et al.* (2013) with permission from The National Academy of Science.)

The synthetic procedure is similar to the addition of molecular linkers. These are added together with Ce on the Ag(111) face (Écija *et al.*, 2013). Pentameric units are formed with angles smaller than the pentagonal angle (65(5)° vs 72°). By increasing the concentration with a linker/Ce ratio of 4 : 1, a regular network structure emerges. The observed motifs in various domains can be different, but they are regular and conform to the Archimedean indications. An example is shown in Figure 19.17.

References

Anderson, D.L., Weschler, C.J., and Basolo, F. (1974) Reversible reaction of simple ferrous porphyrins with molecular oxygen at low temperatures. *J. Am. Chem. Soc.*, **96**, 5599–5600.

Axenovich, M. and Luban, M. (2001) Exact ground state properties of the classical Heisenberg model for giant magnetic molecules. *Phys. Rev. B*, **63**, 100407.

Barra, A.L., Gatteschi, D., Pardi, L., Mueller, A., and Doering, J. (1992) Magnetic properties of high-nuclearity spin clusters. fourteen- and fifteen-oxovanadium(IV) clusters. *J. Am. Chem. Soc.*, **114**, 8509–8514.

Baskar, V., Gopal, K., Helliwell, M., Tuna, F., Wernsdorfer, W., and Winpenny, R.E.P. (2010) 3d-4f Clusters with large spin ground states and SMM behaviour. *Dalton Trans.*, **39**, 4747–4750.

Bi, Y., Wang, X.-T., Liao, W., Wang, X., Wang, X., Zhang, H., and Gao, S. (2009) A $[Co_{32}]$ nanosphere supported by p-tert-butylthiacalix[4]arene. *J. Am. Chem. Soc.*, **131**, 11650–11651.

Blundell, S.J. (2001) *Magnetism in Condensed Matter*, Oxford University Press, Oxford.

Cheetham, A.K., Rao, C.N.R., and Feller, R.K. (2006) Structural diversity and chemical trends in hybrid inorganic–organic framework materials. *Chem. Commun.*, 4780–4795.

Chesman, A.S.R., Turner, D.R., Moubaraki, B., Murray, K.S., Deacon, G.B., and Batten, S.R. (2009) Lanthaballs: chiral, structurally layered polycarbonate tridecanuclear lanthanoid clusters. *Chem. Eur. J.*, **15**, 5203–5207.

Delfs, C., Gatteschi, D., Pardi, L., Sessoli, R., Wieghardt, K., and Hanke, D. (1993) Magnetic properties of an octanuclear iron(III) cation. *Inorg. Chem.*, **32**, 3099–3103.

Écija, D., Urgel, J.I., Papageorgiou, A.C., Joshi, S., Auwärter, W., Seitsonen, A.P., Klyatskaya, S., Ruben, M., Fischer, S., Vijayaraghavan, S. *et al.* (2013) Five-vertex Archimedean surface tessellation by lanthanide-directed molecular self-assembly. *Proc. Natl. Acad. Sci. U.S.A.*, **110**, 6678–6681.

Férey, G. (2008) Hybrid porous solids: past, present, future. *Chem. Soc. Rev.*, **37**, 191–214.

Furukawa, S., Reboul, J., Diring, S., Sumida, K., and Kitagawa, S. (2014) Structuring of metal-organic frameworks at the mesoscopic/macroscopic scale. *Chem. Soc. Rev.*, **43** (16), 5700–5734.

Gatteschi, D. (1999) Quantum size effects in molecular magnets. *Philos. Trans. R. Soc. London, Ser. A*, **357**, 3079–3097.

Gavrilenko, K.S., Punin, S.V., Cador, O., Golhen, S., Ouahab, L., and Pavlishchuk, V.V. (2005) In situ generation of carboxylate: an efficient strategy for a one-pot synthesis of homo- and heterometallic polynuclear complexes. *J. Am. Chem. Soc.*, **127**, 12246–12253.

Gavrilenko, K.S., Cador, O., Bernot, K., Rosa, P., Sessoli, R., Golhen, S., Pavlishchuk, V.V., and Ouahab, L. (2008) Delicate crystal structure changes govern the magnetic properties of ID coordination polymers based on 3d metal carboxylates. *Chem. Eur. J.*, **14**, 2034–2043.

Goedken, V.L., Peng, S.M., Molin-Norris, J.A., and Park, Y.A. (1976) Carbon monoxide complexes of iron(II): synthesis and structural studies of five- and

six-coordinate complexes of the macrocyclic ligand, $C_{22}H_{22}N_4^{2-}$. *J. Am. Chem. Soc.*, **98**, 8391–8400.

Guo, F.-S., Chen, Y.-C., Mao, L.-L., Lin, W.-Q., Leng, J.-D., Tarasenko, R., Orendáč, M., Prokleška, J., Sechovský, V., and Tong, M.-L. (2013) Anion-templated assembly and magnetocaloric properties of a nanoscale $[Gd_{38}]$ cage versus a $[Gd_{48}]$ barrel. *Chemistry (Weinheim an der Bergstrasse, Germany)*, **19**, 14876–14885.

Han, S. and Smith, J.V. (1999) Enumeration of four-connected three-dimensional nets. I. Conversion of all edges of simple three-connected two-dimensional nets into crankshaft chains. *Acta Crystallogr., Sect A: Found. Crystallogr.*, **55**, 332–341.

Huang, Z.-L., Drillon, M., Masciocchi, N., Sironi, A., Zhao, J.-T., Rabu, P., and Panissod, P. (2000) Ab-Initio XRPD crystal structure and giant hysteretic effect (Hc = 5.9 T) of a new hybrid terephthalate-based cobalt(II) magnet†. *Chem. Mater.*, **12**, 2805–2812.

Kong, X.-J., Ren, Y.-P., Chen, W.-X., Long, L.-S., Zheng, Z., Huang, R.-B., and Zheng, L.-S. (2008) A four-shell, nesting doll-like 3d–4f cluster containing 108 metal ions. *Angew. Chem. Int. Ed.*, **47**, 2398–2401.

Kong, X.-J., Wu, Y., Long, L.-S., Zheng, L.-S., and Zheng, Z. (2009a) A Chiral 60-metal sodalite cage featuring 24 vertex-sharing $[Er_4(\mu_3\text{-}OH)_4]$ cubanes. *J. Am. Chem. Soc.*, **131**, 6918–6919.

Kong, X.J., Long, L.S., Huang, R.B., Zheng, L.S., Harris, T.D., and Zheng, Z. (2009b) A four-shell, 136-metal 3d-4f heterometallic cluster approximating a rectangular parallelepiped. *Chem. Commun.*, 4354–4356.

Kong, X.J., Long, L.S., Zheng, Z., Huang, R.B., and Zheng, L.S. (2010) Keeping the ball rolling: fullerene-like molecular clusters. *Acc. Chem. Res.*, **43**, 201–209.

Kortz, U., Müller, A., van Slageren, J., Schnack, J., Dalal, N.S., and Dressel, M. (2009) Polyoxometalates: fascinating structures, unique magnetic properties. *Coord. Chem. Rev.*, **253**, 2315–2327.

Kumagai, H., Kepert, C.J., and Kurmoo, M. (2002) Construction of hydrogen-bonded and coordination-bonded networks of cobalt(II) with pyromellitate: synthesis, structures, and magnetic properties. *Inorg. Chem.*, **41**, 3410–3422.

Kurmoo, M. (2009) Magnetic metal-organic frameworks. *Chem. Soc. Rev.*, **38**, 1353–1379.

Lorusso, G., Sharples, J.W., Palacios, E., Roubeau, O., Brechin, E.K., Sessoli, R., Rossin, A., Tuna, F., McInnes, E.J.L., Collison, D. *et al.* (2013) A dense metal–organic framework for enhanced magnetic refrigeration. *Adv. Mater.*, **25**, 4653–4656.

Mahata, P., Sankar, G., Madras, G., and Natarajan, S. (2005) A novel sheet 4f-3d mixed-metal pyridine dicarboxylate: synthesis, structure, photophysical properties and its transformation to a perovskite oxide. *Chem. Commun.*, 5787–5789.

Maji, T.K., Kaneko, W., Ohba, M., and Kitagawa, S. (2005) Diversity in magnetic properties of 3D isomorphous networks of Co(II) and Mn(II) constructed by napthalene-1,4-dicarboxylate. *Chem. Commun.*, 4613–4615.

Maspoch, D., Ruiz-Molina, D., and Veciana, J. (2007) Old materials with new tricks: multifunctional open-framework materials. *Chem. Soc. Rev.*, **36**, 770–818.

Müller, A. and Gouzerh, P. (2012) From linking of metal-oxide building blocks in a dynamic library to giant clusters with unique properties and towards adaptive chemistry. *Chem. Soc. Rev.*, **41**, 7431–7463.

Müller, A., Krickemeyer, E., Bögge, H., Schmidtmann, M., and Peters, F. (1999a) Organizational forms of matter: an inorganic super fullerene and keplerate based on molybdenum oxide. *Angew. Chem. Int. Ed.*, **37**, 3360–3363.

Müller, A., Sarkar, S., Shah, S.Q.N., Bögge, H., Schmidtmann, M., Sarkar, S., Kögerler, P., Hauptfleisch, B., Trautwein, A.X., and Schünemann, V. (1999b) Archimedean synthesis and magic numbers: "sizing" giant molybdenum-oxide-based molecular spheres of the keplerate type. *Angew. Chem. Int. Ed.*, **38**, 3238–3241.

Müller, A., Luban, M., Schröder, C., Modler, R., Kögerler, P., Axenovich, M., Schnack, J., Canfield, P., Bud'ko, S., and Harrison, N. (2001) Classical and quantum magnetism in giant keplerate magnetic molecules. *ChemPhysChem*, **2**, 517–521.

Müller, A., Todea, A.M., van Slageren, J., Dressel, M., Bögge, H., Schmidtmann, M., Luban, M., Engelhardt, L., and Rusu, M. (2005) Triangular geometrical and magnetic motifs uniquely linked on a spherical capsule surface. *Angew. Chem. Int. Ed.*, **44**, 3857–3861.

Murray, L.J., Dinc, M., and Long, J.R. (2009) Hydrogen storage in metal-organic frameworks. *Chem. Soc. Rev.*, **38**, 1294–1314.

Murugesu, M., Clérac, R., Anson, C.E., and Powell, A.K. (2004) Structure and magnetic properties of a giant $Cu(II)_{44}$ aggregate which packs with a zeotypic superstructure. *Inorg. Chem.*, **43**, 7269–7271.

O'Keeffe, M., Peskov, M.A., Ramsden, S.J., and Yaghi, O.M. (2008) The Reticular Chemistry Structure Resource (RCSR) database of, and symbols for, crystal nets. *Acc. Chem. Res.*, **41**, 1782–1789.

O'Keeffe, M., Eddaoudi, M., Li, H., Reineke, T., and Yaghi, O.M. (2000) Frameworks for extended solids: geometrical design principles. *J. Solid State Chem.*, **152**, 3–20.

Peng, J.-B., Zhang, Q.-C., Kong, X.-J., Ren, Y.-P., Long, L.-S., Huang, R.-B., Zheng, L.-S., and Zheng, Z. (2011) A 48-metal cluster exhibiting a large magnetocaloric effect. *Angew. Chem., Int. Ed. Engl.*, **50**, 10649–10652.

Rao, C.N.R., Cheetham, A.K., and Thirumurugan, A. (2008) Hybrid inorganic–organic materials: a new family in condensed matter physics. *J. Phys. Condens. Matter*, **20**, 083202.

Todea, A.M., Merca, A., Bögge, H., van Slageren, J., Dressel, M., Engelhardt, L., Luban, M., Glaser, T., Henry, M., and Müller, A. (2007) Extending the $[(Mo)(Mo)_5]_{12}M_{30}$ capsule keplerate sequence: a $[Cr_{30}]$ cluster of $S = 3/2$ metal centers with a $[Na(H_2O)_{12}]$ encapsulate. *Angew. Chem. Int. Ed.*, **46**, 6106–6110.

20
ESR

20.1
A Bird's Eye View of ESR of Ln

Essentially, all Ln ions are paramagnetic, so they are potentially suitable for electron spin resonance (ESR) investigations. In the practice, however, the resonances can be observed only at low T and high fields, if at all. If we look at Dy compounds, which we have so extensively treated in the previous chapters, we discover that only few examples of ESR spectra have been reported. We have already mentioned that the energy levels of molecular magnets often can be considered as a ladder of doublets, based on spin Hamiltonian functions $|J \pm M_J>$, where J originates from the LS coupling. The ground state of the Dy compounds of interest can be described by one Kramers doublet, which corresponds to a function where $J = 15/2$ and $M_J = \pm 15/2$. The transitions within the ground doublet are highly forbidden by the selection rule $\Delta M_J = \pm 1$. Interdoublet transitions involving excited states such as $M_J = \pm 13/2$ are expected at field

$$H_r = \pm(\Delta' - g_J \mu_B H_0) \tag{20.1}$$

where Δ' is the energy separation between the two Kramers doublets in zero field, taken as positive. H_0 is the resonance field for the free electron. If Δ' is of the order of 10 cm^{-1}, fields of 20 T may easily be needed. High fields and high frequencies are widespread now and, presumably, the number of reports on Ln will increase, perhaps bringing the same results the technique brought to TMs.

The approach for the energy levels is that of the spin Hamiltonian, so for an isolated magnetic center there will be operators associated with the Zeeman energy, usually limited to linear terms in the applied field. For $S > 1/2$, the ZFS terms will be included. We recall that the energies of the levels involved in ESR (this technique is alternatively electron paramagnetic resonance (EPR)) are expressed using operator equivalents, and the use of Stevens' operators is widespread in ESR spectroscopy. The main difference in these applications is the β_k factor, which is equal to 1 for the use in spectroscopy. The forms of the operator equivalents are easily found in the literature.

The new terms to be introduced for ESR spectra are those involving the magnetic nuclei which can be present. In general, the most relevant terms for ESR are

Introduction to Molecular Magnetism: From Transition Metals to Lanthanides, First Edition.
Cristiano Benelli and Dante Gatteschi.
© 2015 Wiley-VCH Verlag GmbH & Co. KGaA. Published 2015 by Wiley-VCH Verlag GmbH & Co. KGaA.

those describing the interaction between the nuclear and the electron spin, while the nuclear Zeeman and the nuclear quadrupole are neglected. For a system with one nuclear spin, the electron nuclear interaction is described by the so-called hyperfine term

$$\mathscr{H} = \mathscr{S} \cdot \mathbf{A} \cdot \mathscr{I} \tag{20.2}$$

The Hamiltonian related to Eq. (20.2) is discussed in Chapter 21.

When passing from one center to two centers, it is necessary to add the terms reported in Chapter 7.

20.2 Gd in Detail

The ESR spectra of RE are difficult to interpret because of the unquenched orbital moment. To avoid pitfalls, we start from Gd and from an example where accurate approaches were used for getting experimental information and theoretical interpretation. We have already introduced the system in Chapter 7 and now we will complete the treatment. The sample was Gd-doped $YBa_2Cu_3O_{6+x}$, the well-known YBCO high-T_c superconductor (Jánossy *et al.*, 1999). For small values of x, the system is an antiferromagnetic (AF) insulator characterized by planar arrangements. Doping with Gd^{3+} has been used to monitor the magnetic susceptibility and the domain structure. ESR spectra were measured on single crystals at 9, 75, 150, and 225 GHz, which correspond to resonant fields of 0.3, 2.7, 5.4, and 8.1 T for the free electron, respectively. The ground $^8S_{7/2}$ level is split by an applied magnetic field, and transitions occur with selection rule $\Delta M = \pm 1$. There are $2S$ degenerate transitions at $H_M = g_e H_0$, where H_0 is the resonance field for the transition $M \rightarrow M + 1$. The intrinsic intensity of the transition is proportional to $| < M + 1|S_+|M > |^2$. For $S = 7/2$, the ratios of the intensities are $7:12:15:16:15:12:7$. The actual intensity depends on the different populations of the two levels involved in the transition, which in turn depends on the temperature and the resonant field. However, in many cases the degeneracy of the multiplet is removed by crystal field (CF), which admixes excited states into the ground one. Since the separation of these levels is large, ZFS is small and can be treated parametrically using the same type of parameters used within the Steven or Wybourne formalism.

In presence of a tetragonal symmetry, it is necessary to use in a CF approach the Hamiltonian

$$\mathscr{H}_{\text{tetra}} = \frac{1}{3} b_2^0 \mathscr{O}_2^0 + \frac{1}{60} b_4^0 \mathscr{O}_4^0 + \frac{1}{60} b_4^4 \mathscr{O}_4^4 + \frac{1}{1260} b_6^0 \mathscr{O}_6^0 + \frac{1}{1260} b_6^4 \mathscr{O}_6^4 \tag{20.3}$$

where b_k^q are empirical CF parameters and O_k^q are spin operator equivalents. If an orthorhombic distortion along a principal axis is operative, the Hamiltonian becomes

$$\mathscr{H}_{\text{tetra}} = \frac{1}{3} b_2^2 \mathscr{O}_2^2 + \frac{1}{60} b_4^2 \mathscr{O}_4^2 + \frac{1}{1260} b_6^0 \mathscr{O}_6^0 + \frac{1}{1260} b_6^4 \mathscr{O}_6^4 \tag{20.4}$$

A simplified treatment uses only the second-order terms and the new parameters D and E, with $D = b_2{}^0$ and $E = b_2^2$. E is different from zero for symmetry lower than axial, and D is zero for symmetry higher than axial. The values of E/D are limited to the range $0-1/3$

The states originating from the $S = 7/2$ have energies depending on D as $E(M) = D[M^2 - 21/4]$, where $21/4$ corresponds to $S(S+1)/3$. For a magnetic field H parallel to the tetragonal axis, the energies of the levels are $E(M) = g\ M\mu_B H + (M^2 - 21/4)D$. The corresponding ESR transitions $M \rightarrow M+1$ are in resonance at

$$H_M = H_0 + (1 - 2M)D' \tag{20.5}$$

where D' is the ZFS parameter expressed in magnetic field units. The spectra that corresponded to one transition when $D = 0$ now becomes structured into $2S$ transitions, the so-called fine structure.

Single-crystal ESR spectra recorded at 2.5 K with the magnetic field parallel to the *c*-axis are shown Figure 20.1 while those recorded in the *ab* plane are reported in Figure 20.2. The spectra confirm some of these predictions: there are seven transitions, symmetric around a field corresponding to $g = 1.99$. This value has been observed also in other Gd^{3+} compounds. The shift from the value of the free electron value is small but significant. It has been attributed to the admixture in the ground state of an excited $^2P_{7/2}$ (Simon *et al.*, 1999). The separations of the observed lines are more complex than predicted using Eq. (20.5). In fact, if other terms of higher order are included, a good agreement is achieved.

The intense line labeled as 1 is the transition $|-7/2>$ to $|-5/2>$ of an isolated Gd^{3+} while all the near sites are occupied by Y.

Matters are different if one of the next neighbor (NN) sites, labeled as A, is occupied by Gd^{3+}. The two spins interact via isotropic exchange and dipolar field. When one of the two ions is excited from $|-7/2>$ to $|-5/2>$, the other one remains in the ground state. Therefore, the energies of the coupled states can be labeled as $S = S1 + S2$, $M = M1 + M2$, $|M = -7> \ -|M = -6>$, which can be calculated using Eq. (20.5). The main line 1 is now accompanied by a

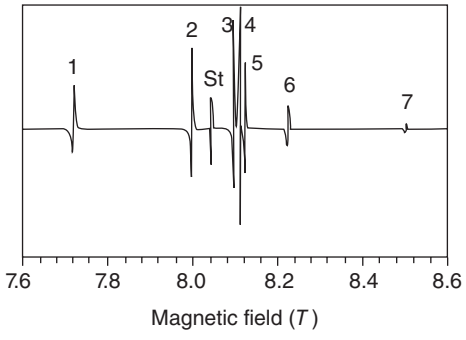

Figure 20.1 ESR spectrum at 225 GHz and 25 K of Gd:$YBa_2Cu_3O_{6+x}$ for a magnetic field oriented along the *c*-axis. Lines 1–7 are the fine-structure lines, and St denotes the internal reference. (Reproduced from Simon, F. *et al.* (1999) with permission from The American Physical Society.)

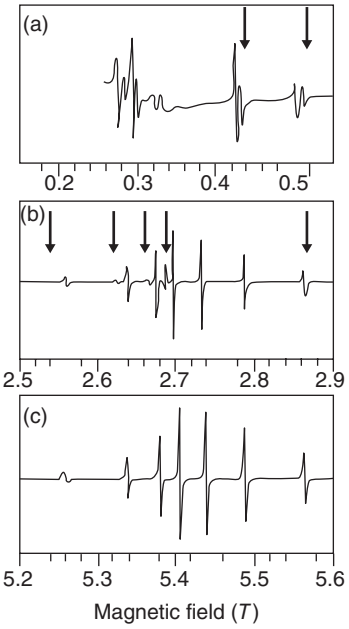

Figure 20.2 Gd:YBa_2Cu3O_{6+x} ESR spectra at 25 K for magnetic field along a principal axis in the *ab* plane. (a) 9 GHz, (b) 75 GHz, and (c) 150 GHz. (Reproduced from Simon, F. *et al.* (1999) with permission from The American Physical Society.)

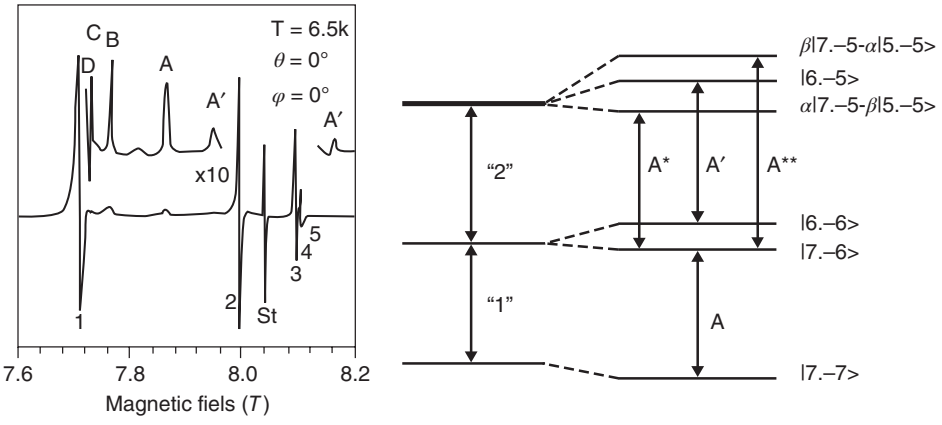

Figure 20.3 Gd-Gd pair satellites at higher temperatures. The transition *A** is used to measure the isotropic exchange interaction. The 1, 2, 3, 4, 5 transitions are the $|-7/2> \rightarrow |-5/2>$, $|-5/2> \rightarrow |-3/2>$ and other fine-structure lines of isolated Gd (left panel). Energy-level scheme of an interacting Gd-Gd pair. The transitions *A* and *A*′ are independent of *J*, while *A** and *A*** depend on *J* (right panel). (Reproduced from Simon, F. *et al.* (1999) with permission from The American Physical Society.)

satellite. For the NN, $D_{\text{dip}} = 43$ mK, corresponding to $g_{\text{Gd}} = 1.9871$ and a distance of 0.38586 nm. The general scheme of satellites and their dependence on the isotropic exchange are shown in Figure 20.3.

The calculated and experimental dipolar fields are in excellent agreement with each other. For instance, the calculated dipolar field for site A is 168.3 mT and the

shift of the satellite is 154.5 mT. A nice agreement of the calculated dipolar fields with the observed shift from transition "1" of Figure 20.3 has been reported even for next neighboring and near-next neighboring Gd^{3+} ions. The conclusive result is that the isotropic exchange is dominant, 156 mK, but the dipolar exchange is not much smaller.

20.3
Gd with Radicals

In Chapter 9, we have treated at some length compounds in which Gd and other Ln interact with SQ radicals. We reported an analysis that used several techniques including ESR. We show here more technical details. Gd is an interesting probe because the ESR spectra are relatively simple to interpret and should allow us to discuss in detail the observed properties.

Magnetic data suggest a moderate antiferromagnetic (AFM) coupling, which gives a ground S = 3 state. Let us show the X-band spectrum of GdDTBSQ (Figure 20.4) (Caneschi *et al.*, 2003).

Well, it is not of immediate interpretation, but some useful points emerge. The spectrum shows signals from 0 to 15 kOe. This suggests an upper limit to D of 2 kOe. Another important information is that there is a pair of levels at zero field which is separated by one quantum of microwaves; matters become much clearer by looking at the spectra recorded at 95, 190, and 295 GHz at 10 K shown in Figure 20.5.

The spectra are reported in a scale centered at H_0, the resonance field of the free electron at a given frequency. The field range is ±10 kOe. The appearance of the spectra is clearly determined by the fine structure due to the ZFS. In axial symmetry and a field parallel to the unique axis, one would expect six transitions separated by 2D. The pattern in perpendicular field should correspond to

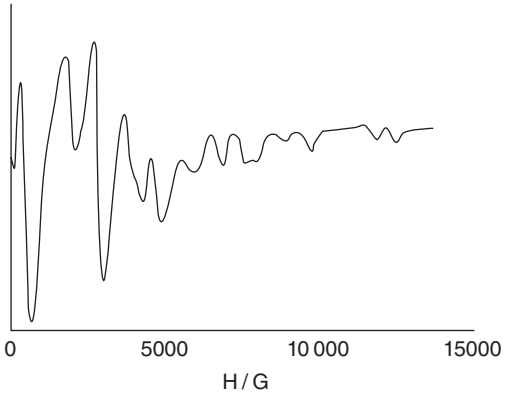

Figure 20.4 Experimental X-band ESR spectra of GdDTBSQ at 4 K.

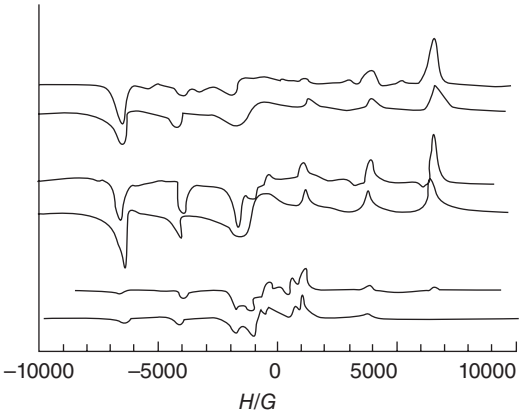

Figure 20.5 HF-ESR spectra of GdDTBSQ recorded at 95 GHz (lower), 190 GHz (middle), and 295 GHz (upper) at 10 K, normalized on a 20 000-G scale ($g = 2.00$ at $H = 0$ G). For each frequency, lower spectrum is the simulated one and the upper spectrum is the experimental one.

a separation D. However, in rhombic symmetry, which is evaluated by the E/D ratio, the corresponding perpendicular pattern should split in two: this is exactly what isoccuring here.

The spectra therefore clearly are indicative of an E/D ratio close to 1/3. The best fit was obtained for $D = 0.122(2)\ \text{cm}^{-1}$, $E/D = 0.287(1)$, $g_{x,y} = 1.998(2)$, $g_z = 1.992(2)$. The fit appears good, but we must remember that the D tensor has the contribution of the dipolar and the exchange terms. In order to obtain independent information, it would be useful to switch off the paramagnetic moment of the radical using a diamagnetic analogue. Here we use tropolonate instead of SQ. The former is diamagnetic, and the measurement on GdTrop should provide information on Gd.

The ESR spectra of GdTrop at variable frequency were satisfactorily fitted with $g_{xy} = g_z = g = 1.995(2)$; $D = -0.123(1)$, $E/D = 0.220(1)$ (Caneschi *et al.*, 2003). Standard projection techniques suggest that the ZFS tensor of the $S = 3$ total spin state $D_{S=3}$ is given by the sum of two terms, as

$$D_{S=3} = (-1/8)\, D_{\text{Gd}} + (5/4) D_{\text{GdR}} \tag{20.6}$$

where D_{Gd} is the D tensor of GdTrop and D_{GdR} is the dipolar tensor associated with GdDTBSQ. The analysis is made difficult by the lack of data that are required by Eq. (20.6). An attempt was made to calculate the dipolar tensor corresponding to D_{GdR}, but it was not an easy task. In fact, the dipolar interaction is relatively easy to calculate if the dipoles are localized on metal ions; in GdDTBSQ, one of the dipoles is delocalized on the radicals. Attempts were made to delocalize the spin on the radical in two different ways. In one approach, the assumption of a spherical spin density was used (1) while the other attempt a π distribution on the radical was assumed (2). The corresponding calculated tensors, as reported in Table 20.1, were rather different from each other.

Table 20.1 Principal values of the zero-field splitting tensors for GdDTBSQ and GdTrop – obtained from the simulations of the HF-ESR spectra ($D = 3/2\ D_{33}$; $E = [D_{11} - D_{22}]/2$).

GdDTBSQ (cm^{-1})	GdTrop (cm^{-1})	Dipolar (1) (cm^{-1})	Dipolar (2) (cm^{-1})
$D_{11} = -0.0055$	$D_{11} = +0.014$	$D_{xx} = -0.142$	$D_{xx} = -0.093$
$D_{22} = -0.0755$	$D_{22} = +0.068$	$D_{yy} = +0.003$	$D_{yy} = +0.016$
$D_{33} = +0.081$	$D_{33} = -0.082$	$D_{zz} = +0.139$	$D_{zz} = +0.077$

20.4 Including Orbit

Beyond Gd, the reported series includes Sm, Eu, Tb, Dy, Ho, Er, and Yb. The vast majority of systems are ESR-silent except DySQ and YbTrop. The former shows a zero-field transition. For Dy, a ground doublet is expected, and magnetic data suggest an average g_{eff} value of 10 for DyTrop. The observed zero-field transition might be due to the interaction with the radical spin.

More informative are the EPR spectra of YbTrop. It is typical of a Kramers doublet with $g_z = 5.45$, $g_x = 0.91$, $g_y = 1.01$. A hyperfine splitting of the low-field transition is attributed to ^{171}Yb, which has $I = 1/2$, $A_z = 0.146\ \text{cm}^{-1}$. The g-values are close to the axial value, suggesting that the best description of the coordination is square antiprism. In the following, we will work out in some detail the energy levels by taking advantage of the simplicity of the system. We believe that this is a useful exercise (Peijzel *et al.*, 2005).

The evidence of the ESR spectra is for quasi-tetragonal symmetry. The presence of fourfold symmetry is indicative of the fact that the operator to be used is $O_4^4 = 1/2\ (J_+^4 + J_-^4)$ which admixes states differing by 4 in the M_J value. As a consequence, the two pairs of levels that are admixed are given by

$$\cos\theta_1|\pm 7/2\rangle \ + \ \sin\theta_1|\mp 1/2\rangle \tag{20.7}$$

$$\cos\theta_2|\pm 5/2\rangle \ + \ \sin\theta_2|\mp 3/2\rangle \tag{20.8}$$

The corresponding g-values can be obtained by fitting the experimental data to the two sets of equations (20.9) and (20.10).

$$\begin{aligned} &For\ \theta_1 : \quad g_z = \ g_J(7\cos^2\theta - \ \sin^2\theta) \\ &g_{x,y} = \ g_J 2\sin^2\theta \left[(J + \ 1/2)^{1/2}(J + \ 1/2)^{1/2}\right] \end{aligned} \tag{20.9}$$

$$\begin{aligned} &For\ \theta_2 : \quad g_z = \ g_J(5\cos^2\theta - \ 3\sin^2\theta) \\ &g_{x,y} = \ g_J 2|\cos\theta\sin\theta|[(J + \ 5/2)(J - \ 3/2)]^{1/2} \end{aligned} \tag{20.10}$$

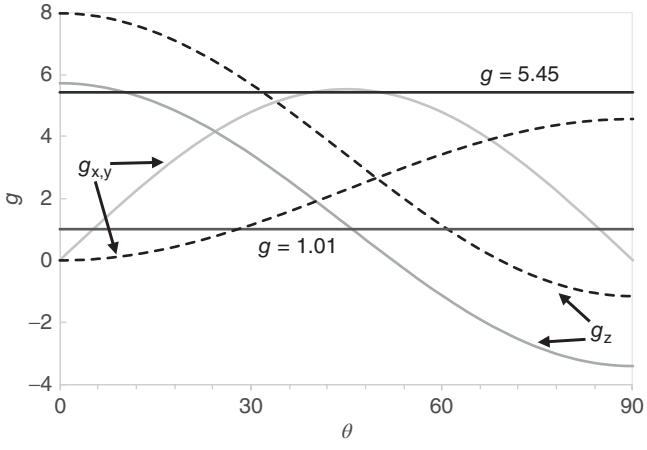

Figure 20.6 Dependence of the *g*-values on θ. Continuous lines represent Eq. (20.10) and dotted lines represent Eq. (20.9).

A simple way to check the strategy of the fit is to plot the calculated *g*-value as a function of θ. The results are shown in Figure 20.6.

It is apparent that acceptable fits can be obtained only for Eq. (20.10). This corresponds to a system very close to $M_J = \pm 5/2$ and to occupancy of 85% of $4f_d$ type orbitals.

Assuming D_{2d} symmetry, the four Kramers' doublets are expected to have the following parameters:

M_J	$g_{\|\|}$	$g_\perp$
±7/2	8	—
±5/2	40/7 = 5.5	—
±3/2	24/7 = 3.5	—
±1/2	8/7 = 1.1	8/7
Experimental	5.45	1.01

$g_\perp$ at this level of approximation is zero, but the admixture of the states via the $\mathcal{O}_4^4$ operator induces some changes, as shown before.

Notwithstanding the difficulties associated with the unquenched orbital moment, it is rewarding to use ESR for the ions that are not silent. A beautiful example is a Ho derivative of the polyoxometalate (POM) $[W_5O_{18}]^{6-}$. As described previously, POMs form a series of single ion magnets (SIMs) which have been intensively studied. The Ho derivative has been characterized for LF parameters using the fit of the magnetic data, yielding a splitting of the ground J = 8 to give a ground $M_J = \pm 4$ state (Ghosh *et al.*, 2012). The crystals

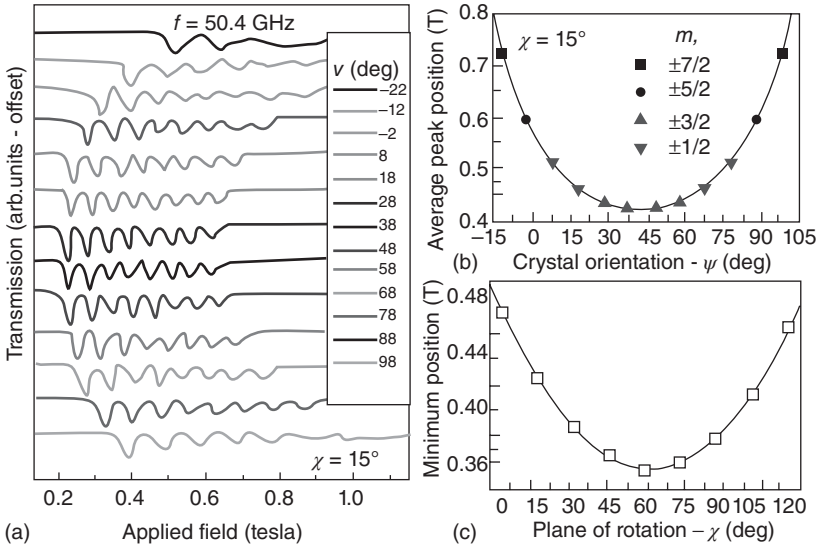

Figure 20.7 Single-crystal ESR spectra at 50.4 GHZ of $[Ho^{III}(W_5O_{18})_2]^{9-}$. (a) Representative set of spectra recorded at 2 K as a function of the crystal orientation ψ, for one particular plane of rotation ($\chi = 15°$). The eight peak positions from each spectrum in (a) were averaged in $\pm M_I$ pairs resulting in a single data point in (b) for each value of ψ. (c) Plot of the minimum position of the resonance fields for nine different planes of rotation. (Reproduced from Ghosh, S. *et al.* (2012) with permission from The Royal Society of Chemistry.)

are triclinic, but the symmetry around Ho is not far from D_{4d} and this symmetry was used to fit the magnetic data. Single-crystal ESR spectra were recorded at 50.4 GHz. Eight transitions were observed for every crystal orientation, as shown in Figure 20.7. They correspond to the hyperfine splitting determined by the value of $I = 7/2$ of ^{165}Ho. Let us have a look at what can be expected for the field parallel to z. in the high-field limit, the energies of the Zeeman levels are given by $E(M, M_J) = Mg_z\mu_B H_z + M_i A_z$, where M_J is the spin projection on the magnetic field. The ESR transition is forbidden because only states with $\Delta M_J = \pm 1$ can be involved in a standard configuration where the oscillating field is perpendicular to the static field. Matters are different for a configuration where the oscillating field is parallel to the static field. In this case $\Delta M_J = 0$.

The 50.4-GHz spectra yield eight signals with regular spacing between them. This is surprising because of the expectation discussed previously. The intensity of the spectra has not been measured, but the evidence is for weak signals. The spectra were recorded also at 9 GHz. The change in frequency changes the type of spectra which move from the (quasi) high-field limit of 50 GHz to the intermediate regime of the X band. This means that the energies of the states must be calculated by diagonalizing the $(17 \times 8)(17 \times 8)$ Hamiltonian matrix; the fit was good with the values shown in Table 20.2.

Table 20.2 Final parameters used in spectra simulation.

B_0^2	B_0^4	B_0^6	B_4^4	$A_\parallel$	$A_\perp$	$g_\parallel$	$g_\perp$
18.03 GHz	209 MHz	−1.53 MHz	94.3 MHz	830 MHz	Undeterm.	1.25	<0.7

20.5 Involving TM

In order to show the difficulties inherent to the interpretation of the ESR spectra of systems containing rare earth ions, we use present a system which has resisted the attacks using single crystals, leaving almost as many doubts as when the analysis started. Usually, one likes to show exemplary positive cases, but here we show a negative one – or at least controversial. Since we are the authors, it should not raise debates (Sorace *et al.*, 2009).

$[Ln(DMF)_4(H_2O)_3\,M(CN)_6]$, where DMF is *N*,*N*′-dimethylformamide Ln is a lanthanide ion and M is a TM ion (Fe^{3+}, Co^{3+}), is an interesting series of compounds which in principle can be used to monitor the interactions between lanthanides and low-spin iron(III) (Figuerola *et al.*, 2002). The presence of diamagnetic ions such as La and Co allows us to obtain the spin Hamiltonian parameters of Fe and, for instance, Ce by measuring the properties of LaFe derivative and CeCo one. The formula is simple, and it might suggest high symmetry, but unfortunately this is not the case. The three compounds crystallize in the monoclinic space group, and no symmetry is present in the dinuclear unit. The TM is octahedrally coordinated by six CN ions, one of which is bridging the RE ion. This is 8-coordinated by four oxygen atoms of DMF, three from water, and the nitrogen of the bridging cyanide. The coordination polyhedron can be described as a bicapped trigonal prism, as confirmed by polytopal analysis. With some good will, a symmetry plane can be imagined for the Ln, but it does not correspond to any symmetry element for the TM.

The first step for the analysis is measuring the polycrystalline powder spectra of CeCo, in order to have some direct information on the symmetry of Ce. The spectra are as expected for a completely anisotropic Kramers' doublet. They can be fitted with an anisotropic spin Hamiltonian for $S = 1/2$, yielding $g_1 = 0.98$, $g_2 = 1.77$, $g_3 = 2.82$. This should correspond to the ground Kramers' doublet. No evidence of the two other doublets of $J = 5/2$ is achieved. In order to get an idea of the nature of the doublet, it is useful to calculate the *g*-values of the $\pm M_J$ doublets. The values are shown in Table 20.3. The set of *g*-values which more resemble the experimental ones are those with $M_J = \pm 1/2$.

We assume that the ground Kramers doublet can be expressed as

$$\Phi_\pm = a|\pm 5/2> + b|\pm 1/2> + c|\mp 3/2> \tag{20.11}$$

Table 20.3 Expected *g*-values for Kramers doublets.

M	$g_{\parallel}$	$g_{\perp}$
1/2	g_J	$3\,g_J$
3/2	$3\,g_J$	0
5/2	$5\,g_J$	0

It is possible to fit the experimental *g*-values with two parameters θ and φ, which are related to *a*, *b*, and *c*:

$$a = \cos\theta;\ b = \sin\theta\cos\varphi;\ c = \sin\theta\sin\varphi \tag{20.12}$$

The best fit to the experimental values shown above is performed using the following equations:

$$\begin{aligned} g_x &= g_J(3a^2 + 2ac\sqrt{5} + 4bc\sqrt{2}) \\ g_y &= g_J(3a^2 + 2ac\sqrt{5} - 4bc\sqrt{2}) \\ g_z &= g_J(5a^2 + b^2 - 3c^2) \end{aligned} \tag{20.13}$$

Assigning g_1 to *x*, g_2 to *y*, and g_3 to *z*, the best fit is $g_1 = 0.91$, $g_2 = 1.75$, $g_3 = 2.77$, $\theta = 38°$, $\varphi = 162°$. In this formalism, the largest coefficients belong to $|\pm 5/2>$ and $|\pm 1/2>$. If the assignment is changed, for instance, $g_1 \rightarrow z$; $g_2 \rightarrow y$; $g_3 \rightarrow z$, the coefficients of the functions change to $\theta = 101°$, $\varphi = 128°$. In this case, the contribution of $|\pm 5/2>$ is almost negligible.

The *g*-values are compared with those reported for other Ce derivatives in Table 20.4.

The next important aspect is that of assigning the *g*-values to the principal directions in the molecule. Single-crystal measurements must be performed, but this

Table 20.4 Observed g values in Cerium(III) derivatives.

Sample	g_1	g_2	g_3	References
Ce^{3+} in $CaWO_4$	2.91	1.42	1.42	Misra, Chang, and Felsteiner (1997)
Ce^{3+} in $SrTiO_3$	3.01	1.12	1.12	Misra and Isber (1998)
Ce^{3+} in $Y(NO_3)_3{\cdot}6H_2O$	3.56	1.23	1.21	Misra and Isber (1998)
Ce^{3+} in $Y_2(SO_4)_3{\cdot}8H_2O$	3.45	1.29	1.21	Misra and Isber (1998)
Ce^{3+} in $YAlO_3$	3.162	0.402	0.395	Asatryan, Rosa, and Mareš (1997)
Ce^{3+} in $[Ln(C_5H_4NCO_2)_3(H_2O)_2]_2$	2.325	1.630	0.339	Baker *et al.* (1997)
$[Ce(DMF)_4(H_2O)_3Co(CN)_6]$	2.82	1.77	0.98	Figuerola, Tangoulis, and Sanakis, (2007a)

may not be sufficient. In fact, CeCo crystallizes in the monoclinic space group $P2_1/c$ with four molecules per unit cell. This means that there are two pairs, which are related by an inversion, that are structurally and magnetically equivalent, and they are related to the others by a screw axis. The ESR experiment on an oriented single crystal measures the resonance of the two nonequivalent molecules. CeCo is particularly simple because only transitions within the ground Kramers doublet are observed (Figuerola, Tangoulis, and Sanakis, 2007b). The spectra were recorded in three orthogonal planes defined by the laboratory axes X, Y, and Z. Y is parallel to the monoclinic b-axis, X is parallel to (1 0 1), and Z is orthogonal to both. The two molecules are equivalent in the XZ plane and one signal is observed for every orientation of the magnetic field in this plane, as shown in Figure 20.8. By rotating along X and Z, the two molecules are nonequivalent but related by a binary axis.

Therefore the spectra are symmetric. The spectra are fitted to curves of the type $g^2 = \cos^2\alpha g_{xx}^2 + \sin^2\alpha\ g_{yy}^2 + 2\ \sin\alpha\ \cos\alpha\ g_{xy}^2$. And here steps in a problem, namely, that of the junction of curves belonging to different rotations. The curves in the plane XY are two that merge for field parallel to X and Y. In the fitting procedure, we must associate other rotations. For instance the two curves X must be associated with the X of the rotation Y. Another problem occurs after the fit when we must decide how to assign the experimental curve. It is not mission impossible, but certainly not the adamant results one would expect from single crystals. There four different choices are reduced to one comparing the calculated g-values with those obtained from the analysis of powder spectra. The final choice is that which orients the g tensors in a predictable way in the molecule. The results are shown in Figure 20.9.

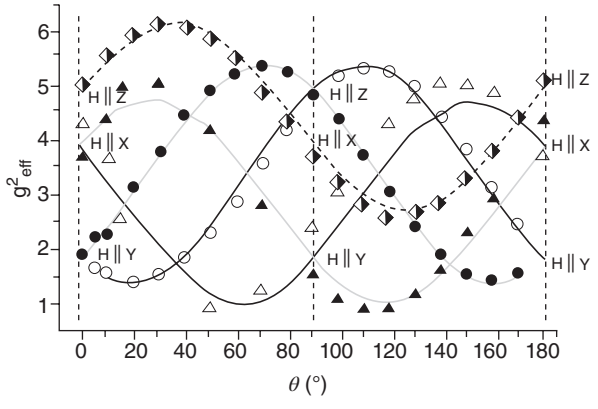

Figure 20.8 Angular dependence of the ESR resonance fields for single crystals of Ce-Co rotating in three orthogonal planes, and the best fit curves. Circles indicate rotations around *X*, diamonds around *Y*, and triangles around *Z*; the full and empty circles show the signals from the two magnetically nonequivalent individuals in the first and third rotations.

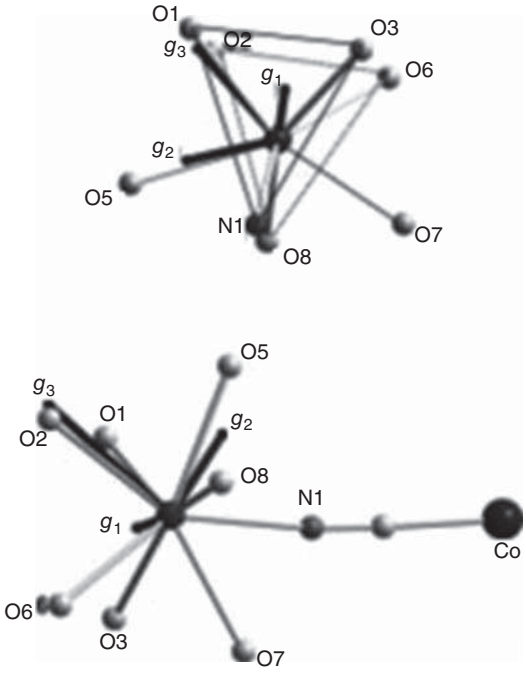

Figure 20.9 Orientation of the *g* tensor of Ce-Co (a) with respect to the bicapped trigonal prism of the coordination sphere of the Ce center and (b) with respect to the Co-C-N-Ce plane.

Analogous difficulties were met in the analysis of the data of LaFe. Even worse is the situation relative to CeFe. The spectra resemble those of a triplet, and this may be possible since CeCo and LaFe are two Kramers' doublets. The best results of the fit were obtained by using the Zeeman parameters of the isolated ions perturbed by the generalized bilinear Hamiltonian including isotropic, anisotropic, and antisymmetric interactions. For both sets, the dipolar interactions were calculated

Table 20.5 cosines of the principal axes *x*, *y*, and *z* of the experimentally determined **D** tensor and of the calculated dipolar tensor.[a) b)]

	D^{xx}_{tripl}	D^{yy}_{tripl}	D^{zz}_{tripl}	D^{xx}_{dip}	D^{yy}_{dip}	D^{zz}_{dip}	Ce-Fe direction
cos α	−0.1046	0.0	0.9945	0.4465	−0.2418	−0.8615	0.8340
cos β	0.0	1.0	0.0	0.8770	−0.0729	0.4750	0.5367
cos γ	0.9945	0.0	−0.1046	0.1776	0.9676	−0.1796	0.1277
Values	0.021	0.063	−0.084	0.0105	0.0037	−0.0142	

a) All the cosines are expressed in the *XYZ* laboratory frame (is the angle with *X*, β with *Y*, and *g* with *Z*).

b) In the last line, the corresponding values (in cm^{-1}) are listed for the sake of clarity.

and found to be comparable to the exchange contribution. The fit with all the parameters is shown in Table 20.5.

The main conclusions achieved are (i) LF can do the job, (ii) interactions involving Ln are difficult, and (iii) introducing antisymmetric exchange improves the understanding of the interaction. More data are needed.

20.6 Ln Nicotinates

Several different series of lanthanides with different ligands have been investigated by ESR. A pedagogical one is the series of the nicotinates. Lns form dinuclear species of the formula $[Ln(ND)_3(H_2O)_2]_2$ ($ND = C_5H_4NCOO^-$), which crystallize in the monoclinic space group $P2_1/c$. The dimers have no symmetry, and the Lns are 8-coordinate with the geometry of a distorted square antiprism. The two tetragonal planes are defined by four oxygen atoms of four bridging carboxylates, three water molecules, and one terminal nicotinate, respectively. The metal ions are separated by about 0.43 nm, and the Ln-Ln vector **r** makes an angle of about 9° with the S_8 pseudo-tetragonal axis (Malkin *et al.*, 1996).

The dinuclear structure, reported in Figure 20.10, allows us to measure the *g*-values of both mononuclear and dinuclear species, providing information on the extent and the nature of the interaction. The experiments were performed on single crystals of diamagnetic La doped with f mole fractions of paramagnetic ions. For $f = 0.001$, only the spectra of the individual ions will be observed, while for $f = 0.01$ satellites due to the dinuclear species will appear.

The crystals grow with well-developed (110) and $(1\bar{1}0)$ faces, and the rotations were performed along the [110], $[1\bar{1}0]$, and [100] directions. The angular dependence of the *g*-values of CeND yielded the principal values and principal directions, which are reported in Table 20.6.

The *g*-values reflect the complete anisotropy of the coordination environment. g_1 is close to the r and S_8 directions. Nd has a pseudo-*XY* symmetry with g_3, which is close to S_8, and smaller than g_1 and g_2 which are very close to each other. Ising symmetry, which requires that g_1 is close to or parallel to S_8, is observed in Er and Tb but not in Dy (Baker *et al.*, 1991b).

The investigation of the concentrated sample provides information on the extent of the interaction between the Ln ions, and in particular on the relative importance of the dipolar and exchange interactions. In a simple scheme, one must expect

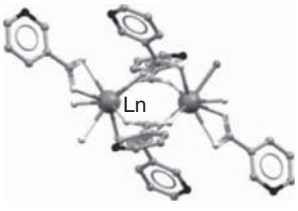

Figure 20.10 Ball-and-stick representation of $[Ln(ND)_3(H_2O)_2]_2$. Hydrogen atoms are omitted for clarity.

Table 20.6 Principal *g*-values and directions for Ce^{3+} ions in LaND containing 0.01 mole fraction of Ce^{3+}.

	g_1	g_2	g_3
	2.325	1.630	0.339
l	0.3794	0.3655	−0.8500
m	±0.5661	±0.6349	±0.5258
n	−0.7318	0.6807	−0.0340

that the line of the mononuclear species is split according to the magnetic field dependence of the energies of the ground levels for Kramers and non-Karmers ion (Baker *et al.*, 1991a).

The dimer can be represented by two S = 1/2 states which are weakly coupled. The four functions can be schematized as $|++>$, $|+->$, $|-+>$, $|-->$ and the interaction described as

$$\mathscr{H} = \mu_B B \cdot g \cdot (\mathscr{S}_1 + \mathscr{S}_2) + \mathscr{S}_1 \cdot \mathrm{J} \cdot \mathscr{S}_2 \tag{20.14}$$

This can be specialized as

$$\mathscr{H} = \mu_B B_z \cdot g_z \cdot (\mathscr{S}_{1z} + \mathscr{S}_{2z}) + \mathrm{J}\mathscr{S}_{1z}\mathscr{S}_{2z} \tag{20.15}$$

The Hamiltonian for the magnetic interaction can be written as

$$\mathscr{H} = (\mu_0 \mu_B^2 / 4\pi r^3) \left\{ \sum_{jk} \left[\sum_i g_{ij}^{(1)} g_{ik}^{(2)} - 3 \sum_i r_i g_{ij}^{(1)} \sum_m r_m g_{mk}^{(2)} \right] \mathscr{S}_j^{(1)} \mathscr{S}_k^{(2)} \right\} \tag{20.16}$$

Once the **g** tensors and the distances are known, the dipolar contribution can be calculated. An example is shown in (Table 20.7):

Table 20.7 Components K_{ij}/h (MHz) of the interaction matrix for nearest neighbor Nd^{3+} pairs.

Parameter	Measured	Dipolar
K_{aa}/h	−572(54)	−820
K_{ab}/h	−2368(60)	−1562
K_{ac}/h	−1326(62)	−767
K_{bb}/h	3168(78)	435
K_{bc}/h	2330(54)	−122
K_{cc}/h	−2598(80)	385
K_{11}/h	1384	−814
K_{12}/h	−3776	−1588
K_{13}/h	600	−638
K_{22}/h	1522	532
K_{23}/h	622	−316
K_{33}/h	−2906	282

The first six values are evaluated relatively to crystal axes. The other six are relative to principal axes of the **g** matrix.

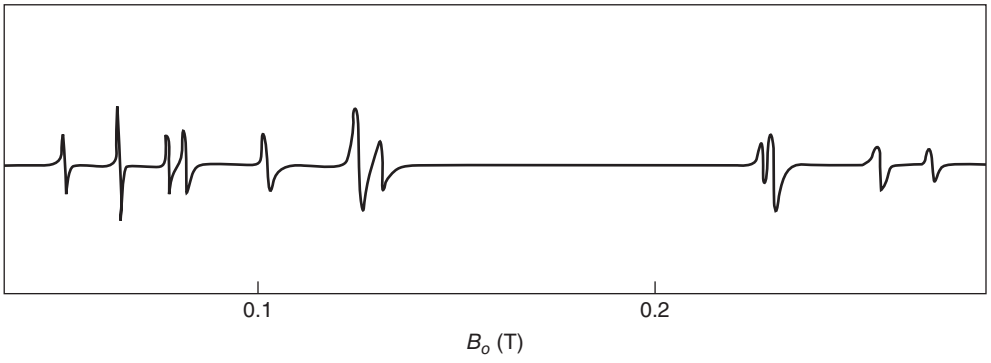

Figure 20.11 EPR spectrum of LaND (1% Tm) at a frequency near 17 GHz for B_0 parallel to the *a*-axis. (Reproduced from Baker, J.M. *et al.* (1986) with permission from The Royal Society.)

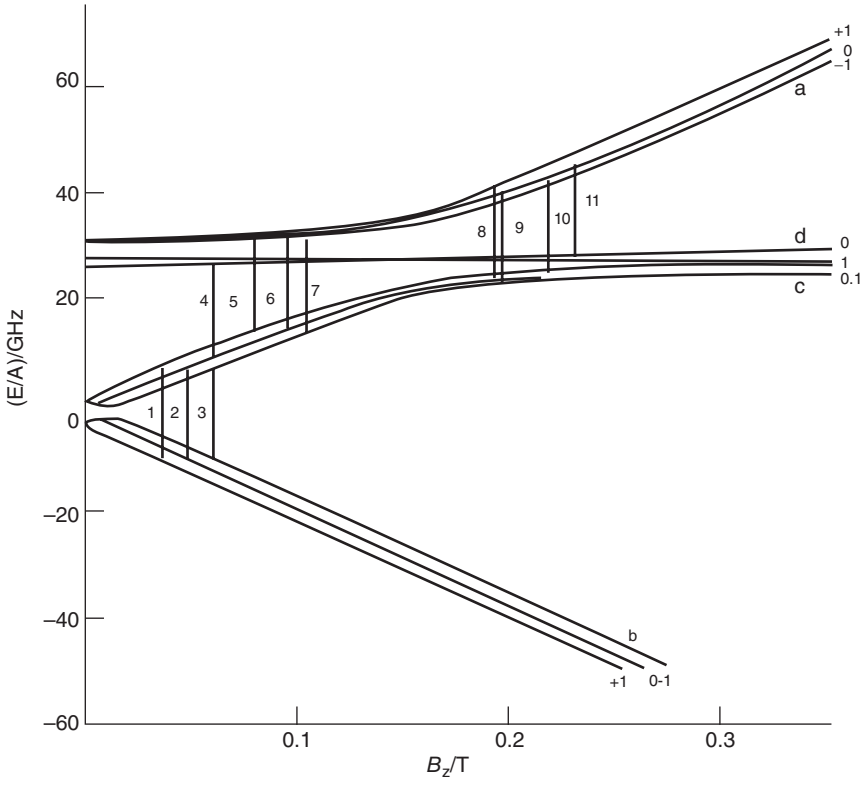

Figure 20.12 Energy level diagram for pairs of Tm^{3+} ions in LaND showing transitions observed near 17 GHz. (Reproduced from Baker, J.M. *et al.* (1986) with permission from The Royal Society.)

It is evident that the measured parameters are much different from the calculated ones for the dipolar interaction. Similar is the case for Ce, suggesting that for early Ln exchange interactions are important.

The spectra of diluted Tm reported in Figure 20.11 show a large number of bands (Baker *et al.*, 1986).

It is apparent that there is something more than a simple dipolar interaction (Figure 20.12). Using the spin Hamiltonian

$$\mathcal{H} = g_z \mu_B B_z (\mathcal{S}_{1z} + \mathcal{S}_{2z}) + \delta(\mathcal{S}_{1x} + \mathcal{S}_{2x}) + A(\mathcal{S}_{1z}\mathcal{I}_{1z} + \mathcal{S}_{2z}\mathcal{I}_{2z}) + J\mathcal{S}_{1z}\mathcal{S}_{2z} \tag{20.17}$$

the spectra have been assigned including dipolar interaction and hyperfine splitting involving ^{169}Tm. Qualitatively, the ground state is a doublet $| \pm 6 >$ treated as an effective spin S = 1/2. In the dinuclear cluster each transition is split into three lines, and the fit of the spectra has been done with the following parameters:

$$g_z = 13.2(3), \quad J/h = 26.9(3)\text{GHz} \quad A/h = 4.4(2)\text{GHz} \quad \delta/h = 9.46(14)\text{GHz}$$

20.7 Measuring Distances

The use of Gd in research regarding biological matters is increasingly used in the measurements of distances in proteins starting from the approach described in Section 7.4. It may be interesting to describe a new experiment based on a four-pulse double electron–electron resonance (DEER) sequence (Jeschke, 2002). The first requirement is the presence of two different spins located at a distance *r*. By exciting the two allowed transitions of spin 1 and the two allowed transitions of spin 2 by a selected pulse sequence, it is possible to measure a frequency (ω_{dd}), which is related to the dipolar interaction between the two unpaired electrons by

$$\omega_{dd} = \frac{2\pi g_1 g_2}{g_e^2} (3\cos^2\theta - 1)\frac{52.04}{r^3} \tag{20.18}$$

where g_1 and g_2 are the *g*-values of the two interacting centers, r is their distance, θ is the angle between **r** and the external magnetic field **B**, and ω_{dd} is expressed in megahertz if r is measured in nanometers. The method allows reliable measurements of distances in the range 1.5–8.0 nm and, therefore, it is possible to get structural information on biomolecules and proteins. To date, the most used spin carriers are stable organic radicals such as nitronyl nitroxides already described in the book. Recently, it has been suggested the use of Gd^{3+} ion as a potential spin label (Potapov *et al.*, 2010; Raitsimring *et al.*, 2007). This change of strategy improves the quality of the experiment, showing an enhancement in sensitivity at higher frequencies, for instance, in the W-band, 95 GHz. Further, at these frequencies the anisotropy effects associated with conformationally restrained nitroxide radicals are eliminated. If an appropriate Gd^{3+} complexes is bound in two different selected positions of a protein in a rigid

environment, accurate distance measurements in the 6-nm range can be performed. The reliability of this result was confirmed by comparing the measured distances with those modeled by the the 3D molecular structures of the same protein.

Writing about ESR and lanthanides involves a large number of systems, and it is a difficult task. We hope to have at least given a feeling of what can be done and what can be obtained.

References

Asatryan, H.R., Rosa, J., and Mareš, J.A. (1997) EPR studies of Er^{3+}, Nd^{3+} and Ce3+ in YAlO3 single crystals. *Solid State Commun.*, **104**, 5–9.

Baker, J.M., Cook, M.I., Hutchison, C.A., Leask, M.J.M., Robinson, M.G., Tronconi, A.L., and Weber, R.T. (1991a) Magnetic resonance, optical and magnetic studies of the nicotinate dihydrates of Dysprosium and Erbium. *Proc. R. Soc. London, Ser. A*, **434**, 695–706.

Baker, J.M., Cook, M.I., Hutchison, C.A., Martineau, P.M., Tronconi, A.L., and Weber, R.T. (1991b) Magnetic resonance studies of Dy^{3+} and Er^{3+} in lanthanum nicotinate dihydrate. *Proc. R. Soc. London, Ser. A*, **434**, 707–717.

Baker, J.M., Hutchison, J., Hutchison, C.A., and Martineau, P.M. (1986) Electron paramagnetic resonance of Tm(III) ions in lanthanide nicotinate dihydrates. *Proc. R. Soc. London, Ser. A*, **403**, 221–233.

Baker, J.M., Hutchison, C.A., Jenkins, A.A., and Tronconi, A.L. (1997) Magnetic resonance studies of Nd(III) and Ce(III) in lanthanum nicotinate dihydrate. *Proc. R. Soc. London, Ser. A*, **453**, 417–429.

Caneschi, A., Dei, A., Gatteschi, D., Massa, C.A., Pardi, L.A., Poussereau, S., and Sorace, L. (2003) Evaluating the magnetic anisotropy in molecular rare earth compounds. Gadolinium derivatives with semiquinone radical and diamagnetic analogues. *Chem. Phys. Lett.*, **371**, 694–699.

Caneschi, A., Dei, A., Gatteschi, D., Poussereau, S., and Sorace, L. (2004) Antiferromagnetic coupling between rare earth ions and semiquinones in a series of 1: 1 complexes. *Dalton Trans.*, 1048–1055.

Figuerola, A., Diaz, C., Ribas, J., Tangoulis, V., Granell, J., Lloret, F., Mahía, J., and Maestro, M. (2002) Synthesis and characterization of heterodinuclear Ln^{3+}–Fe^{3+} and Ln^{3+}–Co^{3+} complexes, bridged by cyanide ligand (Ln^{3+} = Lanthanide Ions). Nature of the magnetic interaction in the Ln^{3+}–Fe^{3+} complexes. *Inorg. Chem.*, **42**, 641–649.

Figuerola, A., Tangoulis, V., and Sanakis, Y. (2007a) Anisotropic exchange interactions in [LnFe] dinuclear systems: magnetometry, dual mode X-band electron paramagnetic resonance, and mössbauer spectroscopic studies. *Chem. Phys.*, **334**, 204–215.

Figuerola, A., Tangoulis, V., and Sanakis, Y. (2007b) Anisotropic exchange interactions in [LnFe] dinuclear systems: magnetometry, dual mode X-band electron paramagnetic resonance, and mössbauer spectroscopic studies. *Chem. Phys.*, **334**, 204–215.

Ghosh, S., Datta, S., Friend, L., Cardona-Serra, S., Gaita-Arino, A., Coronado, E., and Hill, S. (2012) Multi-frequency EPR studies of a mononuclear holmium single-molecule magnet based on the polyoxometalate $[Ho(III)(W_5O_{18})_2]^{9-}$. *Dalton Trans.*, **41**, 13697–13704.

Jánossy, A., Simon, F., Fehér, T., Rockenbauer, A., Korecz, L., Chen, C., Chowdhury, A.J.S., and Hodby, J.W. (1999) Antiferromagnetic domains in $YBa_2Cu_3O_{6+x}$ probed by Gd^{3+} ESR. *Phys. Rev. B: Condens. Matter*, **59**, 1176–1184.

Jeschke, G. (2002) Distance measurements in the nanometer range by pulse EPR. *ChemPhysChem*, **3**, 927–932.

Malkin, A.B.Z., Vinokurov, A.V., Baker, J.M., Leask, M.J.M., and Robinson, M.G. (1996)

The crystal field in the lanthanide nicotinates. *Proc. R. Soc. London, Ser. A*, **452**, 2509–2526.

Misra, S.K., Chang, Y., and Felsteiner, J. (1997) A calculation of effective g-tensor values for R^{3+} ions in $RBa_2Cu_3O_{7-\delta}$ and $RBa_2Cu_4O_8$ (R = rare earth): Low-temperature ordering of rare-earth moments. *J. Phys. Chem. Solid*, **58**, 1–11.

Misra, S.K. and Isber, S. (1998) EPR of the Kramers ions Er^{3+}, Nd^{3+}, Yb^{3+} and Ce^{3+} in $Y(NO_3)_3 \cdot 6H_2O$ and $Y_2(SO_4)_3 \cdot 8H_2O$ single crystals: study of hyperfine transitions. *Phys. Rev. B: Condens. Matter*, **253**, 111–122.

Peijzel, P.S., Meijerink, A., Wegh, R.T., Reid, M.F., and Burdick, G.W. (2005) A complete $4f^n$ energy level diagram for all trivalent lanthanide ions. *J. Solid State Chem.*, **178**, 448–453.

Potapov, A., Yagi, H., Huber, T., Jergic, S., Dixon, N.E., Otting, G., and Goldfarb, D. (2010) Nanometer-scale distance measurements in proteins using Gd^{3+} spin labeling. *J. Am. Chem. Soc.*, **132**, 9040–9048.

Raitsimring, A.M., Gunanathan, C., Potapov, A., Efremenko, I., Martin, J.M.L., Milstein, D., and Goldfarb, D. (2007) Gd^{3+} complexes as potential spin labels for high field pulsed epr distance measurements. *J. Am. Chem. Soc.*, **129**, 14138–14139.

Simon, F., Rockenbauer, A., Fehér, T., Jánossy, A., Chen, C., Chowdhury, A.J.S., and Hodby, J.W. (1999) Measurement of the Gd-Gd exchange and dipolar interactions in $Gd_{0.01}Y_{0.99}Ba_2Cu_3O_6$. *Phys. Rev. B: Condens. Matter*, **59**, 12072–12077.

Sorace, L., Sangregorio, C., Figuerola, A., Benelli, C., and Gatteschi, D. (2009) Magnetic interactions and magnetic anisotropy in exchange coupled 4f–3d systems: a case study of a heterodinuclear Ce^{3+}–Fe^{3+} cyanide-bridged complex. *Chem. Eur. J.*, **15**, 1377–1388.

21
NMR

The use of nuclear magnetic resonance (NMR) in the study of the magnetic properties of a wide range of different molecules and the results of these researches are reported in a large number of papers (Enders, 2011; Bertini, Luchinat, and Parigi, 2012). The aim of this chapter is just to elucidate the relevance of lanthanides in this technique. Rare earths have played an important role in the development and practical applications of NMR. Most 4f metals present nuclides active in this technique, as shown in Table 21.1, and their peculiar magnetic properties are widely used in several fields ranging from chemistry to medicine.

The potentialities of lanthanides in this field are summarized in three paragraphs: the applications of NMR spectroscopy of rare earths nuclides; the use of 4f ions as probes in determining the structure in solution of compounds from small molecules to proteins; and the utility of these ions in improving the quality of magnetic resonance imaging (MRI).

21.1
NMR of Rare Earth Nuclides

Although there is the possibility of a direct use of NMR in the study of an f-block element, as shown in Table 21.1, there are only a few examples of this type of analysis, and no evidence of any systematic study of some class of lanthanide derivatives exists. A probable reason of this lack of information is the difficulty of recording NMR spectra due to the general low sensitivity, the magnetic properties of the majority of these elements, and the presence of large quadrupole moments in many of the active nuclei.

21.2
NMR of Lanthanide Ions in Solution

Although solid-state NMR is no longer the *rara avis* of some years ago (Emsley and Bertini, 2013), there is no doubt that solution NMR are typically used for investigations. The presence of a lanthanide ion induces significant modifications of

Introduction to Molecular Magnetism: From Transition Metals to Lanthanides, First Edition.
Cristiano Benelli and Dante Gatteschi.
© 2015 Wiley-VCH Verlag GmbH & Co. KGaA. Published 2015 by Wiley-VCH Verlag GmbH & Co. KGaA.

Table 21.1 NMR properties of the main lanthanide isotopes.

Nuclide	Spin	Natural abundance (%)	Frequency factor[a)]	Gyromagnetic ratio[b)]	Quadrupole moment[c)]	Receptivity vs. ^{13}C
^{139}Ce	3/2		0.10862	2.906		
^{141}Pr	5/2	100	0.29025	7.765	−4.1	1.62×10^3
^{139}Nd	7/2	12.17	0.05510	−1.474	−0.56	2.43
^{143}Nd	7/2	8.3	0.3413	−0.913	−0.25	0.393
^{147}Pm	7/2		0.1351	3.613	0.67	
^{147}Sm	7/2	14.97	0.04158	−1.1124	−0.18	1.28
^{149}Sm	7/2	13.83	0.03430	−0.9175	0.056	0.665
^{151}Eu	5/2	47.82	0.24475	6.5477	1.14	4.64×10^2
^{153}Eu	5/2	52.18	0.10979	2.9371	2.9	45.7
^{155}Gd	3/2	14.73	0.03092	−0.8273	1.6	0.124
^{157}Gd	3/2	15.68	0.04034	−1.0792	1.92	0.292
^{159}Tb	3/2	100	0.24038	6.4306	1.34	3.94×10^2
^{161}Dy	5/2	18.88	0.03441	−0.9206	2.38	0.509
^{163}Dy	5/2	24.97	0.04766	1.275	2.51	1.79
^{165}Ho	7/2	100	0.21344	5.71	3.49	1.16×10^3
^{167}Er	7/2	22.94	0.02898	−0.7752	2.83	0.665
^{169}Tm	172	100	0.0799	−2.1376		2.89
^{171}Yb	1/2	14.31	0.17699	4.7348		4.50
^{173}Yb	5/2	16.08	0.04869	−1.3025	2.8	1.23
^{175}Lu	7/2	97.41	0.11434	3.0589	3.46	1.73×10^2

a) To find the resonant frequency of this nuclide on your system in an applied field of 1 T, multiply its ^1H frequency by the factor shown.
b) $\times 10^{-7}$ rad T^{-1} s^{-1}.
c) $\times 10^{28}$ m^2.

NMR spectra of different molecular species in solution. The relevant feature that makes 4f ions very useful in analyzing the structure of molecules in solution is their paramagnetism. This property is fundamental in enhancing the relaxation rates and inducing remarkable shifts of the nuclear resonance frequency. There are two different approaches to get this type of information: a direct one when the paramagnetic ion is introduced in the molecule, or when a well-suited molecule containing the lanthanide(III) ion is added to the solution containing the diamagnetic molecule to be analyzed. All the treatments analyzed in this paragraph strictly apply to the influence of 4f ions on the ^1H nucleus which is present in most of the analyzed NMR spectra.

In any case, these techniques are based on two relevant characteristics that are specific to 4f ions: they present very different electronic and magnetic properties along the group and, at the same time, very often they form complexes that, at least in first approximation, are almost isostructural. These peculiarities allow obtaining several pieces of information on the structure of the studied system by extracting information from experimental data of compounds that show different magnetic properties but similar geometrical organization.

As previously indicated, the binding of a paramagnetic lanthanide ion to a molecule results in two evident effects (Bertini and Luchinat, 1996a). On one side, the rate at which M_z, the z component of the nuclear magnetization vector, reaches thermodynamic equilibrium by interacting with the "lattice," namely its surroundings, becomes faster, in the presence of a Ln moiety. This phenomenon is observed by measuring the increase of the spin–lattice relaxation rate (T_1^{-1}). The second observable effect is a variation in the time required by the transverse component M_{xy} of the magnetization to return to zero by a complex mechanism which depends on the resonant nuclear spins in the surroundings of the observed one (spin–spin relaxation rate, T_2^{-1}). The total effect is generally named *lanthanide-induced relaxation* (LIR) (Babailov, 2008). The variations in relaxation rates generally depend on the distance r between the paramagnetic ion and the resonating nucleus, with a dependence of the type r^{-6}. The other observed effect is a shift in the resonance frequency of the nuclei of the molecule, referred to as the lanthanide-induced shift (LIS) (Piguet and Geraldes, 2003). Some components of LIS depend on geometrical factors, such as the distance of nuclei from the paramagnetic center and the polar angle of the Ln nucleus with respect to a reference frame. It is, therefore, useful to develop a strategy to extract this information, which is crucial for determining the structure of the molecule in solution. The first, and often difficult, step is to assign the resonance peaks to each nucleus. In the following, an analysis of LIS and LIR allows us to get the structural parameters: it is fundamental in this procedure to have spectra coming from isostructural compounds to extract all the parameters with a reasonable accuracy.

The key point of these researches is the analysis of the isotropic shift, that is, the contribution of the paramagnetic center to the shifts of resonant nuclei (δ^{obs}), which moves the resonance peak well apart from the diamagnetic position (Bertini and Luchinat, 1996b):

$$\delta^{\text{obs}} = \delta^{\text{dia}} + \delta^{\text{para}} \tag{21.1}$$

Under the assumption of similar molecular structures, δ^{dia} can be measured by recording the NMR spectra of the diamagnetic ions Y^{3+}, La^{3+}, or Lu^{3+}. The shift δ^{para} is originated by the effects of the electron magnetic moment directly on the nucleus and all over the space around it. To analyze a very complex system like this one, it is generally useful to separate the hyperfine contribution to δ^{para} due to overlapping of nuclear and electron wavefunctions from the "classical" dipole–dipole one. The former part of the hyperfine interaction is called *contact* or *Fermi contact interaction*, and the latter is called *dipolar* because it is through space and can be analyzed considering the dipolar interaction of two magnetic dipoles. Therefore, δ^{para} is the sum of two contributions called the *Fermi contact shift* (δ^{cont}) and *pseudocontact* shift (δ^{dpcs}).

The actual spectra depend on the tumbling rate of the molecules in solution. For small molecules, tumbling rate is fast in such a way that only the averages of the properties are obtained from experiment. Fermi contact is isotropic, while the

dipolar has contribution from spin and orbit. The former averages to zero. This, of course, in solution and solid state data are different.

A magnetic field induces in a material an electronic static total magnetic moment that can be expressed as the sum of different effective moments of each magnetic center. Any nucleus senses the sum of this external magnetic field and the field originated by the electron's static magnetic moments. The Fermi contact shift originates, in presence of an applied external magnetic static field $\boldsymbol{B}_0$, from an additional magnetic field generated at one nucleus by the electron magnetic moment located at that nucleus. The Hamiltonian to deal with the contact interaction is

$$\mathscr{H} = \mathscr{I} \cdot \mathbf{A} \cdot \mathscr{S} \tag{21.2}$$

where $\mathbf{A}$ is the contact coupling tensor, and I and S are the spin operators for nuclei and electrons, respectively. In the high-field approximation ($g_e \mu_B \; {}_0 \gg A$), the contact contribution to chemical shift for nucleus i is

$$\delta^{\text{cont}} = \frac{A_i}{\hbar} \frac{g_e \, \mu_B \, S(S+1)}{3\gamma_I kT} \tag{21.3}$$

where γ_I is the magnetogyric ratio of nucleus, S is the spin quantum number, μ_B is the Bohr magneton, T is the absolute temperature, $A_i/\hbar$ is the isotropic hyperfine constant in hertz, and k is the Boltzmann constant.

If the expectation value of S_z is evaluated by operating on each $|S, M_S>$ level considering the population, and summing up over all the levels, it is possible to obtain

$$\langle S \rangle_z = -\frac{g_e \, \mu_B \, S(S+1)}{3kT} B_0 \tag{21.4}$$

where B_0 is the external static magnetic field. Comparing this with Eq. (21.3), it is possible to derive

$$\delta^{\text{cont}} = -\frac{A_i}{\hbar \gamma_I B_0} \langle S_z \rangle \tag{21.5}$$

As in a magnetic field there is an excess of population in the $m_s = -1/2$ state, $<S_z>$ is negative for a free electron and therefore the shift contribution is positive. This contribution to the chemical shift is transmitted through covalent bonds and, as the radial extension of the 4f orbitals is small, the Fermi contact contribution to the observed shift can be neglected for nuclei distant more than 4–5 bonds from the paramagnetic center, unless extensive conjugation is present. The isotropic hyperfine coupling constant is related to the unpaired spin density at the nucleus by the relationship

$$A = \frac{\mu_0}{3S} \hbar \, \gamma_I \, g \, \mu_B \sum_i [|\Psi_i^-(0)|^2 - |\Psi_i^+(0)|^2] \tag{21.6}$$

where $|\Psi_i^-(0)|^2$ and $|\Psi_i^+(0)|^2$ are the negative and positive spin densities at the nucleus of the ith molecular orbital.

There is another effect on a nucleus due to the presence of a magnetic moment induced by the presence of B_0. This induced magnetic moment creates

a dipolar magnetic field which adds to the external one. A nucleus will sense this new magnetic field depending on its position within the field. As this kind of interaction is a through-space one, it is referred as *dipolar*. The molecular rotation in solution averages this interaction to zero. However, the electron magnetic moment is constituted by a spin and an orbital contribution. Whereas the former is isotropic, the latter is anisotropic. In the presence of sizeable orbital contributions to the electron magnetic moment, the induced magnetic moment changes in intensity upon molecular rotation in an external magnetic field and the magnetic susceptibility tensor associated with the molecule becomes anisotropic. Under these circumstances, the dipolar energy does not average to zero, and the average magnetic field that is added to the external magnetic field (expressed in terms of chemical shift) is

$$\delta^{\mathrm{dip}} = \frac{1}{4\pi r^3}\left[\chi_{\parallel}\cos^2\alpha\ \left(3\ \cos^2\theta - 1\right) + \ \chi_{\perp}\ \sin^2\alpha\ (3\ \sin^2\alpha\cos^2\Omega - 1) + \frac{3}{4}\ \left(\chi_{\parallel} + \ \chi_{\perp}\right)\ \sin 2\alpha\ \sin 2\theta\cos\Omega\right] \tag{21.7}$$

where α is the angle between the molecular z-axis and the external magnetic field, θ is the angle between the paramagnetic center-nucleus vector $\boldsymbol{r}$, and Ω is a polar angle related to the projection of $\boldsymbol{r}$ on the molecular xy plane.

By integration over all the molecular orientations, Eq. (21.7) becomes

$$\delta^{\mathrm{dip}} = \frac{1}{12\pi r^3}\ (\chi_{\parallel} + \ \chi_{\perp})(3\ \cos^2\theta - \ 1) = \ \delta^{\mathrm{psc}} \tag{21.8}$$

Looking at Eqs. (21.2)–(21.5), it is easy to realize that both terms are difficult to determine. Therefore, the separation of the δ^{cont} and δ^{psc} contributions to the total paramagnetic shift is not a simple task, but it is the starting point for a quantitative structural analysis. In presence of an isostructural series of Ln^{3+} complexes, it is possible to demonstrate that for a given 4f ion (j) the Fermi contact contribution on nucleus i contains the term

$$\delta_{ij}^{\mathrm{cont}} = \ F_i\langle S_z\rangle_{\mathrm{Ln}} \tag{21.9}$$

where F_i is a proportionality constant which depends on the nature of nucleus i and $<S_z>$ has been calculated for all the rare earths (see Table 21.2).

If the Ln^{3+} complex possesses at least a C_3 axis of symmetry, the pseudo-contact term can be expressed as a sum of two terms: one is given by the Eq. (21.10), and the second is a function of three parameters. Among these three

Table 21.2 Calculated $<S_z>$ and C_{Ln}[a)].

	Ce	Pr	Nd	Sm	Eu	Tb	Dy	Ho	Er	Tm	Yb
$<S_z>$	0.98	2.97	4.49	−0.06	−10.68	−31.82	−28.54	−22.63	−15.37	−8.21	−2.59
C_{Ln}	−6.48	−11.41	−4.46	0.52	4.00	−86.84	−100.0	−39.25	32.40	52.53	21.64

a) All data are scaled to −100 for Dy (Di Pietro, Piano, and Di Bari, 2011).

parameters, the first (G_i for a given nucleus i) is a geometric factor which, according to the expression of pseudocontact shift, has the following form at a given temperature T:

$$G_i = \frac{1}{T^2} \frac{3\ \cos^2\theta - 1}{r_i^3} \tag{21.10}$$

For the second term, it is necessary to introduce the crystal field (CF) effects and, for this purpose, one makes direct use of the B_2^0 Stevens parameter. The third term (C_{Ln} for a given lanthanide *j,* named Bleaney's factor) is a magnetic constant at a given temperature T which can be calculated as the second-order magnetic axial anisotropy of the paramagnetic lanthanide ion and scaled to −100 for Dy (Table 21.2).

Summarizing, the paramagnetic shift can be parameterized with two contributions that depend (i) on the lanthanide ion and (ii) on geometrical feature of the molecule:

$$\delta_{\mathrm{Ln}}^{\mathrm{para}}(i) = F_i \langle S_z \rangle_{\mathrm{Ln}} + C_{\mathrm{Ln}} \cdot B_2^0 \cdot G_i \tag{21.11}$$

Reilly suggested a method that starts by dividing the overall previous expression by $<S_z>$:

$$\frac{\delta_{\mathrm{Ln}}^{\mathrm{para}}(i)}{\langle S_z \rangle_{\mathrm{Ln}}} = F_i + \frac{C_{\mathrm{Ln}}}{\langle S_z \rangle_{\mathrm{Ln}}} B_2^0 \cdot G_i \tag{21.12}$$

When LIS is largely determined by the contact contribution it is preferable to proceed in the same way but with a different starting equation for the linear relationship:

$$\frac{\delta_{\mathrm{Ln}}^{\mathrm{para}}(i)}{C_{\mathrm{Ln}}} = \frac{F_i \langle S_z \rangle_{\mathrm{Ln}}}{C_{\mathrm{Ln}}} + B_2^0 \cdot G_i \tag{21.13}$$

As general strategy, under the assumption that the pseudocontact term is the dominating one, it is necessary to select among the Ln^{3+} derivatives in a series of similar derivatives, the so-called reference compound. It is preferable to choose a 4f ion with a large $C_{\mathrm{Ln}}/<S_z>_{\mathrm{Ln}}$ ratio and, according to the values reported in Table 21.2, Yb, Pr, and Ce are the best candidates. At this stage, it is necessary to characterize completely the NMR spectra of the chosen system and plot all the $\delta_{\mathrm{Ln}}^{\mathrm{para}}(i)$ versus $\delta_{\mathrm{ref}}^{\mathrm{para}}(i)$. Fitting the data would yield a straight line passing through the origin. If this experimental evidence does not show up, there are two possible explanations: the compounds are not isostructural, or the contact term is not negligible and, therefore, this strategy is not the right one. For a series of isostructural compounds, at a fixed temperature T, it is possible, using the reported $<S_z>_{\mathrm{Ln}}$ and C_{Ln} values, to extract with a simple procedure either F_i or G_i if the $<S_z>_{\mathrm{Ln}}$ and C_{Ln} values for the complexed lanthanide ion are similar to those observed in the free ion; F_i does not change on changing Ln, and the CF parameter B_2^0 is constant along the series. The first two conditions are reasonably fulfilled in most of the analyzed systems, while the third one is under discussion to date, as in some cases the deviation from linearity was attributed in change along the series in the geometrical

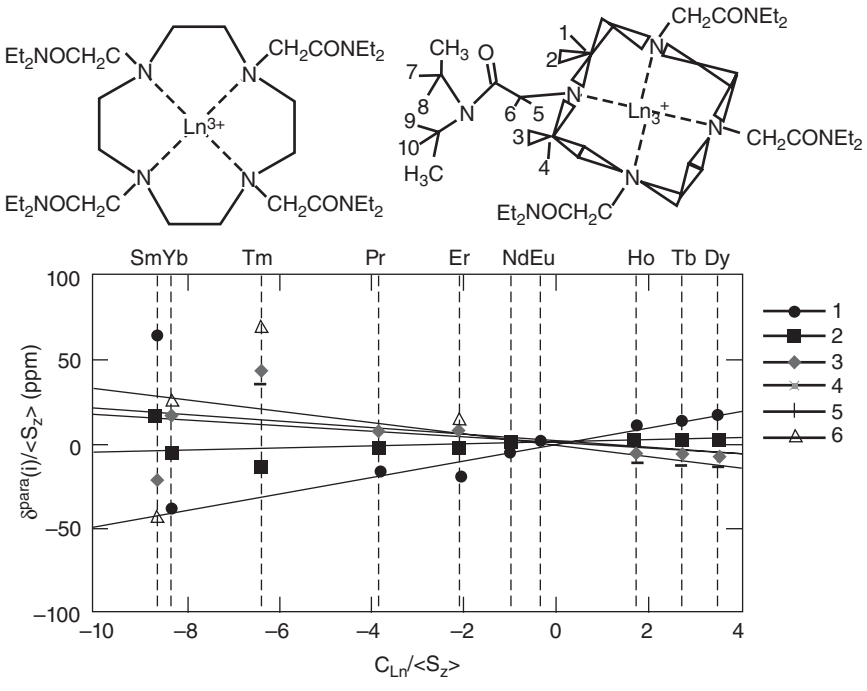

Figure 21.1 Reilley plots for a selection of protons in LnDOTAM (Reilley, Good, and Desreux, 1975). (Reproduced from Di Pietro, S. *et al.* (2011) with permission from The American Chemical Society.)

factor G_i. In other systems such as the macrocyclic and acyclic axial lanthanide complexes, the analysis of the experimental data showed significant variation of B_2^0 and/or F_i.

An improvement in the strategy to get the structural term from the LIS can be achieved by plotting separately the data for lanthanide ions from Ce to Eu with respect to those from Tb to Yb excluding Gd which is considered as a break point in this general behavior. A nice example of this kind of study is illustrated in Figures 21.1 and 21.2, where the data of the LnDOTAM series are reported (DOTAM = 1.4.7.10-tetrakis(*N*,*N*-diethylacetamido)-1,4,7,10-tetraazacyclododecane) (Di Pietro, Piano, and Di Bari, 2011).

Under the usual NMR experimental conditions, we already noticed that, in presence of a magnetic field, nuclei that possess a nonzero spin are partially polarized generating a nuclear magnetization. If the magnetization is stimulated toward a nonequilibrium state, the process that restores the equilibrium distribution is formed by several mechanisms, which are indicated with the general term "relaxation." The most common analysis is based on the observation of the spin nuclear relaxation of the component of the magnetization parallel (z-axis) and perpendicular to the direction of the external magnetic field $\mathbf{B_0}$. The mechanism that involves the relaxation of the z component of the magnetization, that is, the

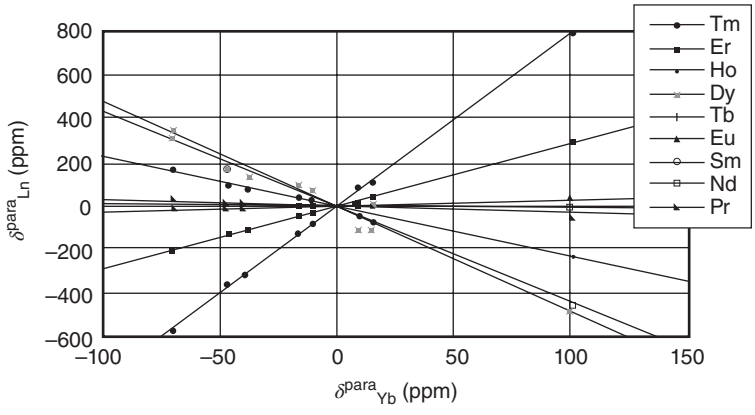

Figure 21.2 Plots of δ^{para}_{Ln} (*i*) versus δ^{para}_{ref} (*i*) for LnDOTAM. (Reproduced from Di Pietro, S. *et al.* (2011) with permission from The American Chemical Society.)

equilibrium recovery, is determined by the so-called spin–lattice or longitudinal relaxation time $T_{1.}$ On the other hand, the relaxation of the transverse nuclear magnetization M_{xy} is governed by the spin–spin relaxation time T_2, which reflects a nonequilibrium process. When the paramagnetic center is present, the overall mechanisms are influenced by the presence of unpaired electrons. If these electrons are introduced in the system by a lanthanide ion, the phenomenon is called LIR, which is determined by a contact and a dipolar contribution to the relaxation phenomena for the *i*th resonating nucleus at a distance r_i from the Ln ion (Solomon, 1955; Bloembergen and Morgan, 1961):

$$T^{-1}_{1\text{Contact}} = \frac{2J(J+1)(g_J-1)^2A^2}{3\hbar^2}\left(\frac{\tau_c}{1+\omega_s^2\,\tau_e^2}\right)$$

$$T^{-1}_{2\text{Contact}} = \frac{2J(J+1)(g_J-1)^2A^2}{3\hbar^2}\left(\tau_c+\frac{\tau_c}{1+\omega_s^2\,\tau_e^2}\right)$$

$$T^{-1}_{1\text{Dip}} = \frac{2J(J+1)\gamma_N^2 g_J^2\,\mu_B^2}{15\,r_i^6}\left(\frac{\mu_0^2}{4\pi^2}\right)\left(\frac{3\tau_c}{1+\omega_I^2\,\tau_c^2}+\frac{7\tau_c}{1+\omega_s^2\,\tau_c^2}\right)$$

$$T^{-1}_{2\text{Dip}} = \frac{2J(J+1)\gamma_N^2 g_J^2\,\mu_B^2}{15\,r_i^6}\left(\frac{\mu_0^2}{4\pi^2}\right)\left(4\tau_c+\frac{3\tau_c}{1+\omega_I^2\,\tau_c^2}+\frac{13\tau_c}{1+\omega_s^2\,\tau_c^2}\right) \qquad (21.14)$$

There is another relaxation mechanism that originates from the interaction of the nuclear spin with the thermal average of the electronic spin, named *Curie spin*. This contribution may be relevant in high magnetic fields, where Curie spin becomes large, and for molecules that rotate slowly such as as proteins. This relaxation mechanism is called *magnetic susceptibility relaxation* or *Curie spin relaxation* (Gueron, 1975; Vega and Fiat, 1976):

$$T^{-1}_{1\text{Curie}} = \frac{2\omega_I^2 g_J^4\,\mu_B^4\gamma_N^2 J^2(J+1)\,B_0^2}{5\,r_i^6(3kT)^2}\left(\frac{\mu_0^2}{4\pi^2}\right)\left(\frac{3\tau_R}{1+\omega_I^2\,\tau_R^2}\right) \qquad (21.15)$$

$$T_{2\text{Curie}}^{-1} = \frac{g_J^4\ \mu_B^4 \gamma_N^2 J^2(J+1) B_0^2}{5\ r_i^6 (3kT)^2} \left(\frac{\mu_0^2}{4\pi^2}\right) \left(4\tau_R\ +\ \frac{3\tau_R}{1+\omega_I^2\ \tau_R^2}\right) \tag{21.16}$$

where μ_0 is the permeability of free space, γ_N is the nuclear magnetogyric factor, k is the Boltzmann constant, ω_s and ω_I are the angular frequencies for electron and nuclear spin transitions, respectively, in the external applied magnetic field B_0. τ_c is the correlation time of the electronic of the paramagnetic ion, τ_R is the rotational correlation time of the molecule, and $\overline{\chi}$ is the mean value of the magnetic susceptibility.

As for LIS, the first step necessary to analyze the experimental data is the evaluation of the diamagnetic contribution to the relaxation phenomena.

$$\text{LIR} = T_{i\ \text{obs}}^{-1}\ - \text{T}^{-1}{}_{i\ \text{dia}} \tag{21.17}$$

where $\text{T}^{-1}{}_{\text{i obs}}$ is the observed relaxation rate and $\text{T}^{-1}{}_{\text{i dia}}$ is the relaxation rate of the same nucleus i in an isostructural diamagnetic derivative such as with La^{3+} or Lu^{3+}. If such compounds are not available or are not isostructural with the others in the series, a reference compound n of with a $\text{T}^{-1}{}_{\text{i dia}}$ value of 0.5_2 s^{-1} is a good approximation, as the observed relaxation rates are usually very large.

In most cases, the contact contribution to LIR ($T_{1\text{Contact}}^{-1}$ and $T_{2\text{Contact}}^{-1}$) is negligible compared to the other two (the Curie and the dipolar contributions). If the relaxation times are not known with a high accuracy, it is possible in any case to determine the ratio of the distances between the nuclei and the ion. For small molecules, all the four terms have the same relevance, while for large molecules such as proteins the dipolar and Curie terms have similar values in T_1 and the Curie contribution dominates as in T_2.

The dipolar terms are connected to the effects on a given nucleus of the magnetic field generated by unpaired electrons. With the exception of Gd^{3+}, whose electronic relaxation times are very long as expected for a $4f^7$ configuration, for the other paramagnetic ions in the group, from Ce^{3+} to Yb^{3+}, τ_c, the correlation time, which describes the random fluctuations of the electron–nuclear dipolar interactions, is very short and its order of magnitude is around 10^{-13} s. This has the consequence that $\omega_s^2\ \tau_c^2\ <<\ 1$ for most magnetic fields used in NMR spectroscopy. With this assumption, the above reported equations can be simplified as

$$T_{1\text{Dip}}^{-1} = T_{2\text{Dip}}^{-1} = \frac{4}{3} \left(\frac{\mu_0^2}{4\pi^2}\right) \frac{2J(J+1)\gamma_N^2 g_J^2\ \mu_B^2}{r_i^6}\ \tau_c \tag{21.18}$$

It is useful to note that the term $g_J^2\ \mu_B^2\ J(J+1)$ could be substituted by the experimental μ_{eff}^2 value. Concerning the Curie relaxations rates, it is possible to assume that in general $\omega_I^2\ \tau_R^2\ <<\ 1$ and therefore the two above-mentioned equations can be written as

$$T_{1\text{Curie}}^{-1} = \frac{6}{5} \frac{\omega_I^2 g_J^4\ \mu_B^4 \gamma_N^2 J^2(J+1)}{r_i^6 (3kT)^2} \left(\frac{\mu_0^2}{4\pi^2}\right) \tau_R \tag{21.19}$$

$$T_{2\text{Curie}}^{-1} = \frac{7}{5}\frac{g_J^4\ \mu_B^4\gamma_N^2 J^2(J+1)\omega_I^2}{r_i^6(3kT)^2}\left(\frac{\mu_0^2}{4\pi^2}\right)\tau_R \tag{21.20}$$

As the two Curie relaxation rates are not equivalent as the dipolar ones are, it is possible to utilize this feature for a further simplification:

$$T_{2\text{Obs}}^{-1} - T_{1\text{Obs}}^{-1} = T_{2\text{Curie}}^{-1} - T_{1\text{Curie}}^{-1} = \frac{1}{5}\frac{g_J^4\ \mu_B^4\gamma_N^2 J^2(J+1)\omega_I^2}{r_i^6(3kT)^2}\left(\frac{\mu_0^2}{4\pi^2}\right)\tau_R \tag{21.21}$$

This experimental result depends only on r_i^6 and τ_R. The rotational correlation time of the molecule can be derived by its determination in diamagnetic isostructural derivatives. Alternatively, with the assumption that in the Curie relaxation mechanism the molecular tumbling plays a determinant role, τ_R can be predicted through the Stokes equation

$$\tau_R = \frac{4\pi\eta a^3}{3kT}\ \frac{\eta M_R}{dN_A kT} \tag{21.22}$$

where η is the viscosity of the solution, a is the radius of the molecule (supposed spherical), M_R is the molecular weight, d is the density of the solute, and N_A is the Avogadro number.

Then the main problem in this strategy is the determination of T_2^{-1}, as the signal line width is affected by local B_0 inhomogeneity and unresolved scalar couplings. A simple approach to solve this problem is based on the observation of the signal of a nucleus sufficiently far from the paramagnetic center for which the contact contribution is zero. Working with this hypothesis, it is possible to estimate a relative distance of the Ln nucleus i using the equation

$$\frac{T_{1\text{ref}}^{\text{para}}}{T_{1i}^{\text{para}}} = \frac{r_i^6}{r_{\text{ref}}^6} \tag{21.23}$$

21.3 Lanthanide Shift Reagents (LSR)

If it is possible to attribute the chemical shifts, their relative intensity, and coupling constants to a resonating nucleus, the structural organization of an organic molecule can be deduced with a high degree of reliability. The most common problem in the analysis of the NMR spectra of diamagnetic molecules is the resolution of the signals of the resonating nuclei, especially in ^{1}H experiments, due to the intrinsic low sensitivity of this nuclear chemical shift to changes in chemical and structural surroundings,. There are two different strategies to tackle this problem. The first strategy is relatively simple: an increase of the external applied magnetic field produces a linear expansion of the NMR spectrum. The other approach substantially is based on the introduction in the system of paramagnetic centers which generate a secondary internal field. The additional advantage of this option is the possibility of changing the sequence of the observed signals. These

secondary fields are very often anisotropic and their magnitude and direction vary according to the primary external field. Furthermore, the influence of these paramagnetic ions is strongly dependent on the distance within the resonating nucleus and decreases rapidly with the distance (Aime *et al.*, 2006).

The starting point of this technique is the addition to the solution containing the diamagnetic molecule of an appropriate compound containing a paramagnetic Ln^{3+} ion. The presence of unpaired electrons induces a paramagnetic shift, which is due to the above-described interactions: a Fermi contact and a pseudocontact or dipolar interaction that follows the equations already reported. The first is the dominant one for paramagnetic centers with a substantially isotropic **g** tensor, and the dipolar shift is more relevant in presence of anisotropic **g** tensor. The Fermi contact shift is transmitted to the diamagnetic molecule either through σ and π bonds and its intensity decreases rapidly on increasing the strength of the σ bonds.

A relevant problem in lanthanide shift reagent (LSR) studies is generated by the influence of the paramagnetic ions on the relaxation mechanisms. Substantially, an enhancement of relaxation rates is observed with the negative consequence of changes in line width of some resonances. Again, the peculiar properties of Ln^{3+} are of fundamental relevance to deal with this type of problem. Compared to paramagnetic systems based on transition ions, the lanthanide series offers different magnetic properties of ions with similar molecular structure. In such a way, it is possible to derive structural information on the diamagnetic systems. A well-defined strategy is based on the observation that it is possible to use a shift reagent, called Ln^S, which contains a paramagnetic ion with a highly anisotropic **g** tensor: in this system, a large paramagnetic contact shift is expected with a short electronic spin relaxation time and, therefore, a limited line broadening. An additional advantage in using lanthanides is the possibility of generating shifts of the observed signals in opposite directions. For instance, this kind of effect has been observed in some series of isostructural salts where $\chi_{\parallel} > \chi_{\perp}$ for Ln^{3+} = Pr, Nd, Sm, Dy, and Ho, while $\chi_{\perp} > \chi_{\parallel}$ for Ln^{3+} = Er and Yb. At this stage, the Ln^{3+} ion can be substituted, without change in the structure, with a different one with a long relaxation time and an isotropic *g* tensor, called Ln^R, which allows the calculation of the paramagnetic relaxation rate. It was suggested to use the two LSRs at the same time and in such a way that the first paramagnetic center spreads the spectrum of the diamagnetic system which becomes of the first order, while the presence of the second ion allows the determination of the relaxation rates for each nucleus because the spread of signals due to the other Ln prevents signal overlapping. A classic example of this strategy is the use of the fod (1,1,1,2,2,3,3-heptafluoro-7,7-dimethyl-4,6-octanedionate) derivative of Gd^{3+} and Eu^{3+} ($Ln(fod)_3$). The electronic structure of the ground state of Gd^{3+} is responsible for the highly isotropic magnetic moment and the long electron spin relaxation time. Therefore, this ion is a perfect relaxation reagent. On the other side, Eu^{3+} exhibits a diamagnetic ground state ($^7F_0$) with an excited one ($^7F_1$) separated in energy by a few hundred wavenumbers. This paramagnetic state contributes to the dipolar shift, and the total

electronic structure produces an anomalously inefficient nuclear spin–lattice relaxation rate.

A fundamental point for using this technique is the formation of an aggregate between the diamagnetic molecule under analysis and the Ln^{3+} complex added to the solution. Namely, in the solution, there is an equilibrium of type

$$DM + LSR \Leftrightarrow DM - LSR \; K_{eq} = \frac{[DM - LSR]}{[DM][LSR]}$$

where DM is the diamagnetic molecule, LSR is the lanthanide shift reagents, DM-LSR is the adduct whose formation is fundamental to observing the variations in chemical shifts of the nuclei of DM, and K_{eq} the equilibrium constant of the reaction. In almost all systems, at least at room temperature, the equilibrium in solution is rapid on the NMR time scale. It is in any case necessary that in solution there is always some free DMs and that the two molecules form only one type of adduct whose stoichiometry can be experimentally estimated.

An expression can be derived to evaluate the Δ_{shift}, namely the difference of the resonant frequency of a given nucleus before and after the addition of LSR:

$$\Delta_{shift} = \frac{K_{eq} \; \delta_{DM\text{-}LSR}}{1 + K_{eq}} \tag{21.24}$$

where $\delta_{DM\text{-}LSR}$ is the LIS of the aggregate. For low concentration of the lanthanide complex, a linear dependence on the concentration of $\delta_{DM\text{-}LSR}$ is observed. As some experiments showed that the shift parameters derived by the previous expression could depend on the initial substrate concentration, an analysis of data can be exploited by using a more precise approach. It is possible to derive the following expression based on the initial concentration of the diamagnetic molecule to investigate $[DM]_0$:

$$\Delta_{shift} = \frac{[DM - LSR] \; \delta_{DM\text{-}LSR}}{[DM]_0} \tag{21.25}$$

Considering K_{eq} and $\delta_{DM\text{-}LSR}$, it is possible to define the relationship

$$[DM]_0 \left(1 - \frac{[LSR]_0 \; \delta_{DM\text{-}LSR}}{\Delta_{shift}}\right) = \frac{[LSR]_0 \; \Delta_{shift}}{\delta_{DM\text{-}LSR}} - \left(\frac{1}{K_{eq}} + [LSR]_0\right) \tag{21.26}$$

Under the assumption that $\delta_{DM\text{-}LSR}/\Delta_{shift}$ is negligible for low concentrations of LSR, the above reported expression simplifies to

$$[DM]_0 = \frac{[LSR]_0 \; \Delta_{shift}}{\delta_{DM\text{-}LSR}} - \left(\frac{1}{K_{eq}} + [LSR]_0\right) \tag{21.27}$$

If $[DM]_0$ values are plotted against $1/\delta_{DM\text{-}LSR}$, the values of $\delta_{DM\text{-}LSR}$ as slope and of $\delta_{DM\text{-}LSR}$ as intercept can be obtained.

In this chapter, we have completely shifted gear focusing on nuclei rather than electrons and in solution rather than solid. We had already touched upon these themes and now it is instructive to have a glance from the complementary point of view.

References

Bertini, I. and Luchinat, C. (1996a) *Coordination Chemistry Reviews*, Chapter 1, vol. **150**, pp. 1–28.

Bertini, I. and Luchinat, C. (1996b) *Coordination Chemistry Reviews*, Chapter 2, vol. **150**, pp. 29–75.

Aime, S., Crich, S.G., Gianolio, E., Giovenzana, G.B., Tei, L., and Terreno, E. (2006) High sensitivity lanthanide(III) based probes for MR-medical imaging. *Coord. Chem. Rev.*, **250**, 1562–1579.

Babailov, S.P. (2008) Lanthanide paramagnetic probes for NMR spectroscopic studies of molecular conformational dynamics in solution: applications to macrocyclic molecules. *Prog. Nucl. Magn. Reson. Spectrosc.*, **52**, 1–21.

Bertini, I., Luchinat, C., and Parigi, G. (2012) *NMR of Biomolecules: Towards Mechanistic Systems Biology*, Wiley-VCH Verlag GmbH & Co. KGaA, pp. 154–171.

Bloembergen, N. and Morgan, L.O. (1961) Proton relaxation times in paramagnetic solutions. Effects of electron spin relaxation. *J. Chem. Phys.*, **34**, 842–850.

Di Pietro, S., Piano, S.L., and Di Bari, L. (2011) Pseudocontact shifts in lanthanide complexes with variable crystal field parameters. *Coord. Chem. Rev.*, **255**, 2810–2820.

Emsley, L. and Bertini, I. (2013) Frontiers in solid-state NMR technology. *Acc. Chem. Res.*, **46**, 1912–1913.

Enders, M. (2011) in *Modeling of Molecular Properties* (ed. P. Comba), Wiley-VCH Verlag GmbH & Co. KGaA, pp. 49–63.

Gueron, M. (1975) Nuclear relaxation in macromolecules by paramagnetic ions: a novel mechanism. *J. Magn. Reson. (1969)*, **19**, 58–66.

Piguet, C. and Geraldes, C.F.G.C. (2003) in *Handbook on the Physics and Chemistry of Rare Earths* (eds K.A. Gschneidner Jr., J.-C.G. Bünzli, and V.K. Pecharsky), Elservier Science, Amsterdam, pp. 353–463.

Reilley, C.N., Good, B.W., and Desreux, J.F. (1975) Structure-independent method for dissecting contact and dipolar nuclear magnetic resonance shifts in lanthanide complexes and its use in structure determination. *Anal. Chem.*, **47**, 2110–2116.

Solomon, I. (1955) Relaxation processes in a system of two spins. *Phys. Rev.*, **99**, 559–565.

Vega, A.J. and Fiat, D. (1976) Nuclear relaxation processes of paramagnetic complexes the slow-motion case. *Mol. Phys.*, **31**, 347–355.

22
Magnetic Resonance Imaging

The diffusion of the magnetic resonance imaging (MRI) technique in biological and medical fields is the history of a great success, as it does not require invasive diagnostic procedures and offers great spatial resolution without the use of ionizing radiation as required by, for example, X-ray, positron emission tomography (PET), and computed tomography (CT) techniques. Even though the first report on a one-dimensional (1D) MRI image was reported in 1952 (Carr, 1952), the crucial event was the discovery that it was possible to distinguish *in vivo* tumors and normal tissues: the NMR proton signals coming from tumor samples were present for longer times than those from healthy tissues when the spectrometer was switched off (Damadian, 1971). The third fundamental contribution arrived in 1973 with the publication of the first 2D and 3D images collected by using NMR spectrometry (Lauterbur, 1973).

The theoretical background of MRI is relatively simple. It is based on the experimental observation that biological tissues can be discriminated by observing a difference in density and relaxation time of water hydrogen nuclei (protons). The relaxations times (T_1 and T_2 as defined in Chapter 22) of pure water are of the order of about 2 s at 298 K and are roughly independent of the external magnetic field B_0. If proteins are added to the solution, T_1 and T_2 become considerably shorter, and the degree of shortening depends on B_0.

As there are many articles and books dealing with this subject (Caravan *et al.*, 1999; Merbach, Helm, and Toth, 2013), we give in this section only some basic principles just to stress the potentiality of molecular magnetism in this field due to the different abilities of magnetic centers to affect the relaxation mechanisms.

It is useful to remember that a short T_1 generally yields great intensity to NMR signals while short T_2 values are not relevant in determining this intensity; but in general, a sizable increase in $1/T_2$ worsens the quality on the signal. This feature also suggested the use of paramagnetic and superparamagnetic systems that would be able to enter tissues under examination with the goal of decreasing T_1 and, in any case, T_2 too. Therefore, with the aim of improving the quality of MRI images, there is, in the daily practice, a continuous increase in the use of the so-called MRI contrast reagents. These systems are molecules that, beyond biocompatibility and low toxicity, are able to positively modify the $1/T_1$ ratio by at least of 50–100%, which is the lowest limit to have some evident improvement in

Introduction to Molecular Magnetism: From Transition Metals to Lanthanides, First Edition.
Cristiano Benelli and Dante Gatteschi.
© 2015 Wiley-VCH Verlag GmbH & Co. KGaA. Published 2015 by Wiley-VCH Verlag GmbH & Co. KGaA.

the quality of the signal. There are on the market two different classes of paramagnetic molecules identified on their ability to influence differently T_1 and/or T_2. *Positive* contrast agents generally are paramagnetic molecules that contain ions with large numbers of unpaired electrons, such as Mn^{2+} (five) and Gd^{3+} (seven), and the symmetric S ground states are ideal to have a long relaxation mechanism. The action of systems containing similar ions has a roughly equivalent effect on T_1 and T_2, but as T_1 is larger than T_2, the shortening of T_1 dominates the contrast of MR images. The tissues that take up the contrast agent give a brighter images, this being one a function of T_1. *Negative* contrast agents are generally based on superparamagnetic systems such iron oxide nanoparticles. Their presence increases the contrast of the images, obtained with T_2-weighted sequences, and the areas they reach are darker with respect to the surrounding.

In the presence of paramagnetic or superparamagnetic ions, the contrast efficiency is expressed in terms of the so-called nuclear longitudinal (related to T_1 shortening) or transverse (related to T_2 shortening) relaxivity: the higher its value, the better is the contrast in the images. The nuclear relaxation rates are expressed by two additive contributions related to diamagnetic and paramagnetic components:

$$\left(\frac{1}{T_j}\right)_{\text{obs}} = \left(\frac{1}{T_j}\right)_d + \left(\frac{1}{T_j}\right)_p \quad j = 1, 2 \tag{22.1}$$

where d and p refer to the diamagnetic host and the paramagnetic contribution, respectively. The paramagnetic contribution is dependent on the concentration of paramagnetic species. The enhancement of $(1/T_j)_p$ derives from two contributions, namely

$$\left(\frac{1}{T_j}\right)_p = \left(\frac{1}{T_j}\right)_{\text{inner-sphere}} + \left(\frac{1}{T_j}\right)_{\text{outer-sphere}} \quad j = 1, 2 \tag{22.2}$$

The inner-sphere contribution derives from the hyperfine field fluctuations produced on the (most often hydrogen) nuclei of the solvent molecules (in most cases water or part of blood, plasma, similar to water) by rotational Brownian motions, electronic spin fluctuations, and exchange between bound and bulk water, while the outer-sphere effect refers to relaxation enhancement of nuclei of solvent molecules coming from diffusion processes that alter the local hyperfine field fluctuations they feel. Rigorously, in Eq. (22.2) for some compounds one should introduce a second sphere coordination contribution, which we neglect here and in the following (Figure 22.1).

The factors influencing the inner-sphere relaxation mechanisms are expressed by the following formulas (Caravan *et al.*, 1999):

$$\frac{1}{T_1^{\text{InnSph}}} = \frac{qF_{\text{r}}}{T_{1\text{r}} + \tau_{\text{r}}} \tag{22.3}$$

$$\frac{1}{T_2^{\text{InnSph}}} = \frac{qF_r}{\tau_r}\left[\frac{T_{2\text{r}}^{-1}\left(\tau_{\text{r}}^{-1} + T_2^{-1}\right) + \Delta\omega_{\text{r}}^2}{(\tau_{\text{r}}^{-1} + T_{2\text{r}}^{-1})^2 + \Delta\omega_{\text{r}}^2}\right] \tag{22.4}$$

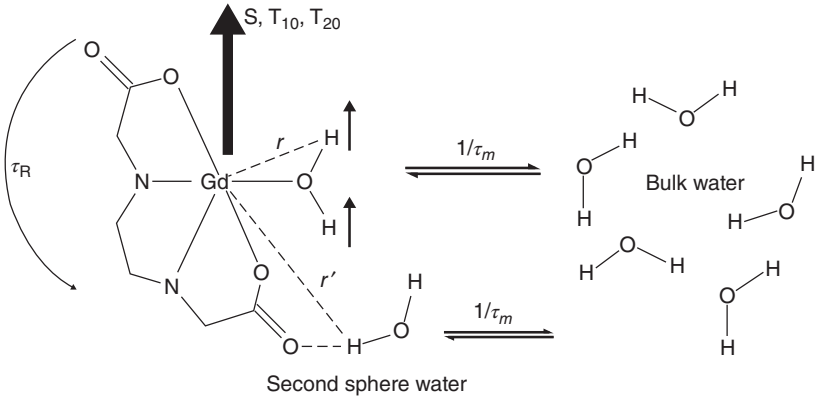

Figure 22.1 Solvent exchange involving the inner and outer sphere of coordination. (Reproduced from: "Strategies for increasing the sensitivity of gadolinium based MRI contrast agents", Chem. Soc. Rev., **2006**, *35*, 512 by Caravan, P. with permission from The Royal Society of Chemistry.)

$$\Delta\omega_{\text{obs}}^{\text{InnSph}} = qF_{\text{r}}\left[\frac{\Delta\omega_{\text{r}}}{\left(1+\tau_{\text{r}}T_{2\text{r}}^{-1}\right)^2+\tau_{\text{r}}^2\Delta\omega_{\text{r}}^2}\right] \tag{22.5}$$

The InnSph superscript refers to the behavior of molecules surrounding the magnetic center as an inner sphere, F_{r} is the mole fraction of bound solvent nuclei, q is the number of bound solvent nuclei per metal ion (generally called the *hydration number*), τ_{r} is the lifetime of the solvent molecule in the complex (i.e., the inverse of τ_{r} is the solvent exchange rate between the coordinated and the bulk solvent molecules), and the "r" subscript refers to the relaxation rate of the water (solvent) molecule coordinated to the compound. $\Delta\omega$ refers to the chemical shift difference between the paramagnetic complex and a diamagnetic reference. T_1 and T_2 are the nuclear relaxation times defined previously in the paragraph describing the lanthanide-induced relaxation (LIR) effects. At this stage it is useful to recall the Curie spin relaxation mechanism described in the previous chapter due to its relevance for some Ln ions. It was discovered that the molecular susceptibility may be involved in a nuclear relaxation mechanism (Gueron, 1975). Substantially, the Curie spin relaxation mechanism is directly proportional to the second power of the external field and to the square of the magnetic moment of the molecule. It easy to realize the relevance of this mechanism for systems containing Tb^{3+}, Dy^{3+}, and Ho^{3+} because of their magnetic moments and short electronic relaxation times. The Curie spin relaxation mechanism mainly affects T_2 and can become the dominant relaxation mechanism at high fields and/or when rotational correlation times are long. More detailed analyses are given in the literature (Caravan, Greenfield, and Bulte, 2001).

An additional contribution, very relevant in presence of Gd^{3+}, derives by the fluctuation of the zero-field splitting/ZFS), which originates, for example, by molecular vibrations or collision with solvent molecules which can produce changes in the Gd^{3+} environment. This phenomenon induces an electronic spin

relaxation expressed by the longitudinal and transverse terms:

$$\frac{1}{T_{1e}} = B\left[\frac{1}{1+\omega_s^2\tau_v^2} + \frac{4}{1+4\omega_s^2\tau_v^2}\right] \tag{22.6}$$

$$\frac{1}{T_{2e}} = \mathrm{B}\left[\frac{5}{1+\omega_s^2\tau_v^2} + \frac{2}{1+4\omega_s^2\tau_v^2} + 3\right] \tag{22.7}$$

$$B = \frac{1}{10\tau_{s0}} = \frac{\Delta^2}{50}[4S(S+1)-3]\tau_v \tag{22.8}$$

where τ_v is the correlation time of the modulation of the transient ZFS, τ_{s0} refers to the electronic relaxation time in a zero external magnetic field, and Δ is the trace of the ZFS tensor. It should be also remembered that the expressions of the total correlation times that influence the nuclear relaxation are

$$1/\tau_{cj} = 1/\tau_R + 1/T_{je} + 1/\tau_r \; j = 1, 2 \tag{22.9}$$

$$1/\tau_{ej} = 1/T_{je} + 1/\tau_r \; j = 1, 2 \tag{22.10}$$

where $1/T_{1e}$ and $1/T_{2e}$ are the electron spin relaxation time of the metal ion. This approach is a very simple one, as Eqs. (22.9) and (22.10) do not include explicitly all the relaxation mechanisms that can be found in the literature (Helm, 2006).

According to the reported expression, it is possible to observe that an increase in *q*, namely, the solvent molecules bound to the paramagnetic center, will increase the inner-sphere relaxivity. Another critical point is the mean distance between the solvent protons and the paramagnetic ion, as the dependence of relaxation from this parameter is based on r^{-6}: a decrease of 2 pm produces a 50% increase in relaxivity. The use of compounds that are able to generate coordination number around gadolinium of 6 or 7 will allow the entry in the inner sphere of two or three water molecules. Unfortunately, increasing the number of water-coordinated molecules results in a decrease in thermodynamic stability and an increase in toxicity.

If the coordination around the paramagnetic center is saturated by donor atoms, that is, no solvent molecule can bind a gadolinium ion, there is a mechanism that enhances relaxivity involving an outer sphere of solvation. This relaxivity depends on the electronic relaxation time of the metal ion, on the distance of closest approach of the solute and solvent *r,* on the solvent diffusion coefficient (*D*), and on a diffusional correlation time $\tau_d = r^2/D$.

As already indicated, Mn^{2+} and Gd^{3+} ions are the ideal candidates for the role of positive contrast agents for MRI. Actually, the first experiments were performed using some Mn^{2+} salts. It was immediately evident that there are enormous problems along this way. The salts are toxic and the ion may interfere with several biological mechanisms. The same happens for Gd^{3+}: it is toxic as most heavy metals, and its ionic radius is similar to that of calcium(II). These requirements can be satisfied by using ions included in some organic system that is able to insulate the metal ion with respect to the surroundings. These compounds, when considered

Table 22.1 Clinically relevant gadolinium(III) chelates (Idée *et al.*, 2009).

Chemical name	Generic name	Brand name	Log K_{therm} [a)]	Log K_{cond} [b)]
[Gd(DTPA-BMA)(H_2O)]	Gadodiamide	*Omniscan*	16.9	14.9
[Gd(DTPA)(H_2O)]$^{2-}$	Gadopentetate	*Magnevist*	22.1	18.1
[Gd(EOB-DTPA)(H_2O)]$^{2-}$	Gadoxetate	*Eovist*	23.5	18.7
[Gd(DO3A-butrol)(H_2O)]	Gadobutrol	*Gadovist*	21.8	
[Gd(DTPA-BMEA)(H_2O)]	Gadoversetamide	*OptiMARK*	16.6	15.0
[Gd(DOTA)(H_2O)]$^{-}$	Gadoterate	*Dotarem*	25.8	18.8
[Gd(BOPTA)(H_2O)]$^{2-}$	Gadobenate	*MultiHance*	22.6	18.4
[Gd(HP-DO3A)(H_2O)]	Gadoteridol	*ProHance*	23.8	17.1
[Gd(Ms-325)]	Gadofosveset	*Vasovist*	22.06	18.9

a) K_{therm} is defined as [ML]/[M] × [L].
b) K_{cond} takes into account the protonation constants of the ligand, and therefore describes the equilibrium between Gd^{3+} and its ligand at physiological pH. K_{cond} is measured at the physiological pH 7.4.

as contrast agents to be used in humans, must have water solubility, stability when dissolved in water (which can guarantee the chelation of the metal ion as long as the compound remains in the body), rapid excretion, and a low osmotic potential when in solution for clinical applications. An additional fundamental feature is the presence of at least one water molecule directly bound to the metal ion (Bottrill, Kwok, and Long, 2006).

Up to now, in the medical practice, only the derivatives based on gadolinium are employed. Researchers active in the field have proposed several different compounds but only a few of them have been approved for clinical use. They are reported in Table 22.1 and their molecular structures are outlined in Scheme 22.1.

As shown in the above scheme, in all Gd^{3+} derivatives the metal ion is 9-coordinated by eight donor atoms from the ligand and a solvent water molecule with the most probable coordination geometry close to a tricapped trigonal prism. It may be useful to remember that the presence of water directly bound to Gd^{3+} is a factor influencing the "inner-sphere" relaxation mechanism as represented by the q parameter in Eqs. (22.3)–(22.5). For this reason, there have been several attempts looking for new ligands where, on varying the number of donor atoms, it is possible to modulate q and to optimize the residence lifetime for the coordinated water molecules (Terreno *et al.*, 2010).

Recently, Mn^{2+} derivatives have been considered, again, as positive contrast agents for integrating the classical Gd^{3+} ones. Their action is slightly different from that of the previously described agents, as the Gd^{3+}-like action is difficult to obtain for this ion which shows a typical coordination number of six and stable derivatives with $q \neq 0$. For instance, the only complex approved for clinical use, MnDPDP, (DPDP = dipyridoxyl diphosphate, below), belongs to this category. In some tissues, it passes the cell membrane through Ca^{2+} channels and releases Mn^{2+} ions that can interact with some present species influencing the relaxation mechanism of surrounding protons (Scheme 22.2).

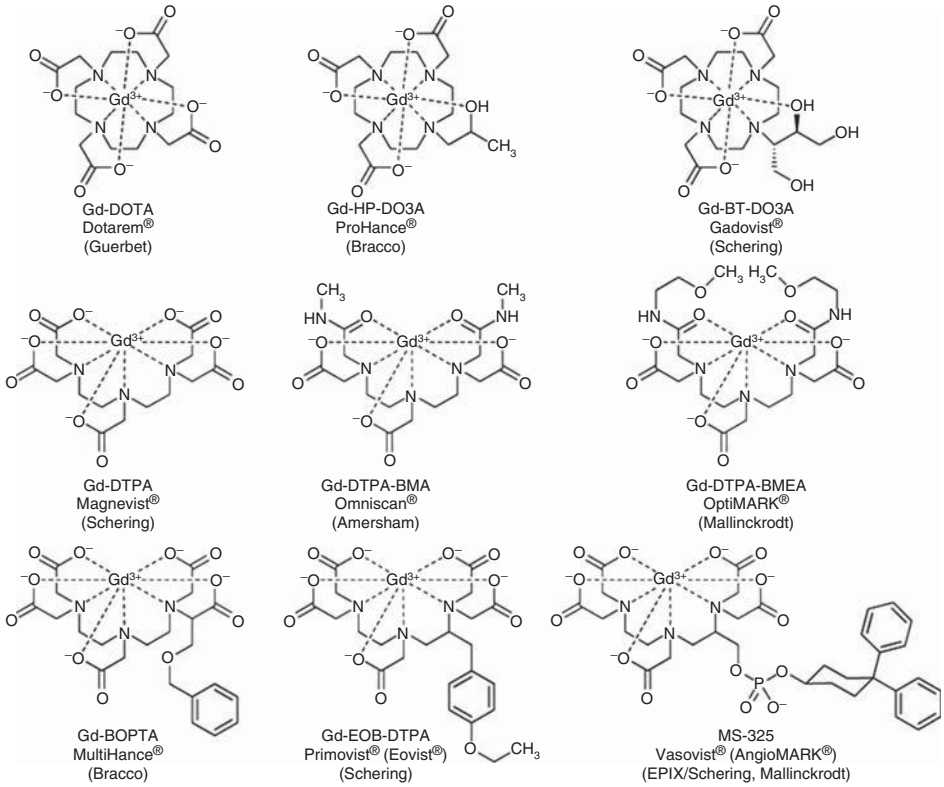

Scheme 22.1 Gd-containing parts of clinically used contrast agents. (Reproduced from Caravan, P. (1999) with permission from The American Chemical Society.)

Negative contrast agents are those that are able to effectively reduce T_2 substantially of water protons to an extent much larger than T_1. This effect is primarily induced by the ability of a particle possessing high magnetization to generate intense magnetic susceptibility on water molecules around the particle itself. An example of these systems is contrast agents composed of nanoparticles formed by a crystal core of magnetite (Fe_3O_4) and maghemite (γ-Fe_2O_3), in a generally uncontrolled percentage of mixing, coated with a chosen material. They are designated according to their size: SPIOs (super paramagnetic iron oxides, average hydrodynamic diameter >30 nm to several micronmeters) or USPIOs (ultrasmall super paramagnetic iron oxides, average hydrodynamic diameter <50 nm). The main issue for practical application is the possibility of producing the oxide particles with controlled dimensions and dispersion. The task is complicated by the colloidal nature of ferrites.

As a result of the progress in constructing magnets for MRI capable of generating high external fields, the necessity of finding contrast agent able to be effective in these condition has moved the research toward the use of chelates containing ions such as Dy^{3+} or Ho^{3+}. These ions are characterized by their highly anisotropic

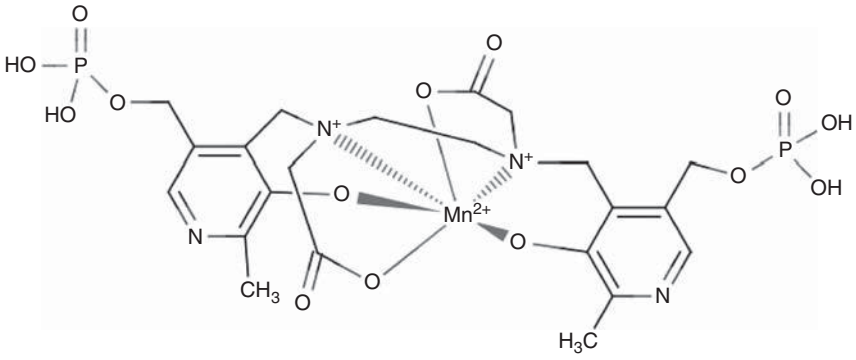

Scheme 22.2 MRI contrast agent containing Mn.

ground state and, accordingly, by very short electronic relaxation times. Therefore, they are efficient contrast agents at intermediate and high magnetic field strengths. An additional interesting feature for systems that can act as T_2-weighted MRI is the markedly different chemical shift between the water bound to the Ln^{3+} ion and the bulk water. The potential use of ions such as Dy^{3+} and Ho^{3+} is an interesting new field where it is possible to work on their high magnetic moments, the chemical shift, and the residence time (Norek and Peters, 2011).

22.1
Chemical Exchange Saturation Transfer (CEST)

Coordination compounds containing paramagnetic ions are widely used in MRI for clinical purposes and have been successful in that field. As explained previously, such contrast agents produce a signal enhancement allowing better differentiation between different tissues, as well as better visualization of different structures. However, these agents are not selective and get distributed uniformly throughout the extracellular space and, therefore, it is often necessary to use an alternative mechanism for generating image contrast to provide additional information to improve diagnosis by MRI.

One of the most effective solutions to this problem is the chemical exchange saturation transfer (CEST) technique. It belongs to the large group of NMR experiments in the field of saturation transfer (ST) techniques, as described by Overhauser, who discovered the possibility to use saturation of the electron line to modulate nuclar relaxation and magnetization (Overhauser, 1953). The CEST approach is based on the observation of the MRI signal in presence of a slowly exchanging molecular group that possesses a chemical shift distinct from that of water. This signal is selectively saturated and the saturation is transferred to the bulk water via chemical exchange. The advantage is the sensitivity of chemical exchange to the environment of a contrast agent. In such a way, it is possible to analyze important physiological parameters such as pH, temperature, enzymatic activity, and specific metabolic processes.

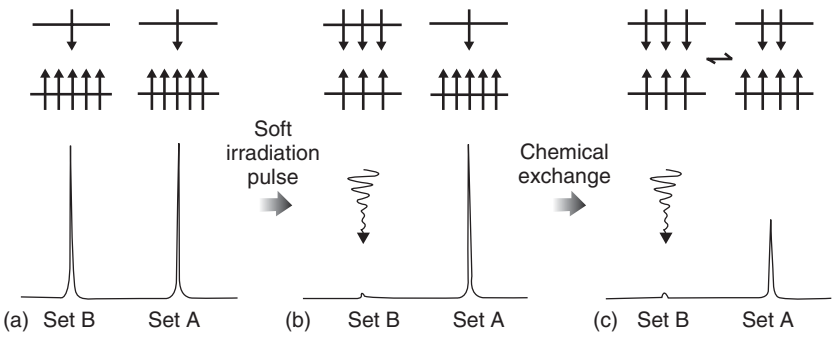

Figure 22.2 Schematic representations of the distribution of spins, aligned with and against the field (upper and lower energy levels, respectively) (*above*) and simulated NMR spectra (*below*) for two chemically distinct pools of nuclei (a), two spins after a saturation pulse has been applied to one pool (b), and for a system undergoing chemical exchange after a saturation pulse has been applied to one pool (c) (Sherry and Woods, 2008). (Reproduced from Sherry, A.D. and Woods, M. (2008) with permission from Annual Reviews.)

In order to observe CEST, the exchange process that occurs between two magnetically distinct environments must be slow on the NMR timescale (Aime *et al.*, 2006). That is, the rate of exchange (k_{ex}) must be not greater than the difference in frequency between the two chemical environments ($\Delta\omega$) : $\Delta\omega \geq k_{ex}$. Let us consider a system that meets this condition and presents two sets of protons resonating at different frequencies, such as those present in a ligand molecule (set A) and in the solvating water (set B) (Woods, Woessner, and Sherry, 2006). The process starts with a low-power pulse at the resonance frequency of nuclei in set B. If the pulse is strong enough, the number of spins aligned against the magnetic field is increased, and, as soon as it becomes equal to the number of spins aligned with the field, the system gets fully saturated, the magnetization becomes equal to zero, and no NMR signal is observed. The spins in set A are, initially, in their Boltzmann equilibrium, but the chemical exchange mechanism will modify this condition. Spins are transferred from one set to another, and vice versa. As a result, some spins aligned against the field are transferred from set B to set A, while spins aligned parallel to the magnetic field move from set A to set B. The net result is a decrease in the magnetization of set A with subsequent decrease in the intensity of NMR signal (Figure 22.2).

The results of a CEST analysis are, often, reported using the magnetization transfer asymmetry (MTR_{asym}) defined as

$$MTR_{asymm}(\Delta\omega) = MTR(\Delta\omega) - MTR(-\Delta\omega) \tag{22.11}$$

$$MTR(\Delta\omega) = 1 - \frac{I_{sat}}{I_0} \tag{22.12}$$

where I_{sat} is the intensity of saturated bulk water signal, and I_0 is the signal intensity without saturation. $MTR(\Delta\omega)$ and $MTR(-\Delta\omega)$ are the signal intensities

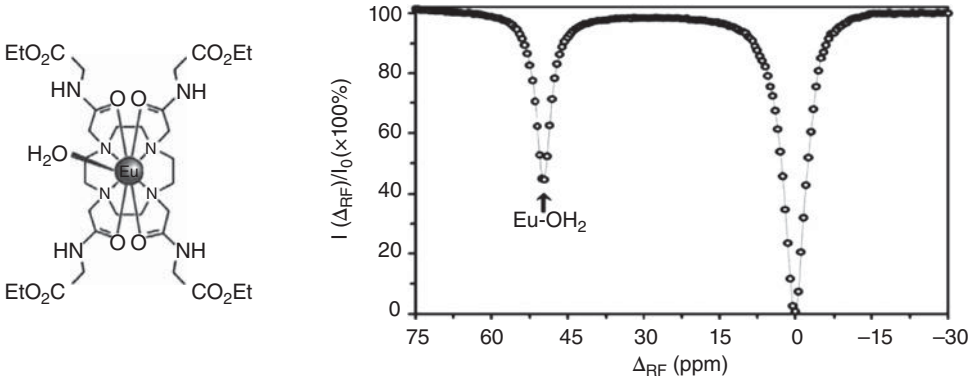

Figure 22.3 Z-spectrum of EuDOTA–4AmCE (Vinogradov, Sherry, and Lenkinski, 2013). (Reproduced from Vinogradov, E. *et al.*, M. (2013) with permission from Elsevier Inc.)

acquired with rotating frame (RF) irradiation applied on-resonance with the exchanging pool and at the frequency symmetric around water. Practically, the experiment is performed by presaturating selectively the sample in incremental steps over a range of frequencies and plotting the remaining bulk water signal, I_{sat}/I_0, versus the saturation frequency. The obtained spectrum is called the Z-spectrum and is referred to also as a CEST spectrum. In Figure 22.3, the Z-spectrum for EuDOTA–4AmCE (DOTA = 1,4,7,10-tetraazacyclododecane-1,4,7,10-tetraacetic acid) is shown. The peak at 0 ppm in the Z-spectrum represents direct saturation of bulk water, while the peak at approximately +50 reflects chemical exchange between the Eu^{3+}-bound water molecules in the complex. As the magnitude of percent saturation transfer (I_{sat}/I_0) is a measure of the efficiency of CEST agents, it is useful to analyze the factors influencing this ratio. Starting from the modified Bloch equations, in presence of a complete saturation of set B, it is possible to derive a steady-state solution of the form (Vinogradov, Sherry, and Lenkinski, 2013):

$$\frac{I_{sat}}{I_0} = \frac{1}{1 + \frac{cq}{55.5}\frac{T_{1A}}{\tau_{ex}}} \tag{22.13}$$

where c is the concentration of the CEST agent, q is the number of bound water molecules per CEST complex, T_{1A} is the spin–lattice relaxation time of bulk water, and $\tau_{ex} = 1/k_{ex}$.

According to Eq. (22.13), an improvement of the CEST effect can be achieved either by increasing the agent concentration whose limits are imposed by biological reasons, or by increasing the exchange rate between sets A and B.

When a CEST experiment is performed in an MRI apparatus, a usual spectrum is registered where the saturation transfer technique acts as a negative contrast agent due to its effect which decreases the water proton signal. A first advantage is due to the possibility to collect in the same instrument two different spectra with or without the CEST effect by just turning on or off the radio frequency (rf) saturation source.

In the simplest situation, it is possible to analyze spectra generated by endogenous species having a component capable of exchanging a proton with the solvent water. Otherwise, it is necessary to introduce molecules that can act as CEST agents. In the last few years there has been an impressive increase in this field of research including the investigation and realization of mechanisms than the simple proton exchange; in this respect, we suggest the reader to check the dedicated literature (van Zijl and Yadav, 2011). If the attention is focused on proton-exchanging CEST agents, it is necessary to consider classes of molecules that depend on the nature of the added molecules: diamagnetic (diaCEST) and paramagnetic chemical exchange saturation transfer (PARACEST) systems.

The diaCEST agents must present in the molecules specific types of proton exchange groups such as -NH, $-NH_2$, or -OH moieties (Ward, Aletras, and Balaban, 2000). As the basic condition to observe saturation effects in presence of a chemical exchange is that $\Delta\omega \geq k_{ex}$, the diaCEST effect is limited to those hydrogen atoms that belong to sites with an exchange rate $\approx 2 \times 10^3\ s^{-1}$ as highest limit. Furthermore, the chemical shift of these protons is generally within 5 ppm from water resonance, and this is a problem as the saturation of these groups may induce a partial saturation of the bulk water protons with a subsequent limitation in the amount of power that can be applied.

The use of PARACEST contrast agents is a fundamental step toward overcoming the problem connected with the chemical shift of the water proton. When the water molecule is coordinated to a paramagnetic ion, ^1H can vary from +500 to −720 ppm: a consequence of this large range of $\Delta\omega$ values is the proportional increment of the k_{ex} values allowable for observing CEST effect. The wide range of possible exchange rates opens several possibilities to modulate the overall mechanism. As in diaCEST contrast agents, the exchangeable protons belong either to O–H or N–H groups on a ligand or to water molecules coordinated to the metal ion and, following the previous statement, it is possible to work on coordinated metal ions and/or ligand molecules looking for the best contrast agent. For instance, the rate of water molecule exchange in the Gd^{3+} derivatives usually used as T_1-shortening MRI contrast agent is too fast for a CEST experiment ($1/k_{ex} << 1$ μs). It has been demonstrated that slight chemical modifications on the structure of ligand, as the well-known DOTA, may induce a significant variation in the rate of the water molecule dynamics (Aime *et al.*, 1999). Alternatively, it is possible to choose the more suitable metal ion considering that the used contrast agent must exhibit an exchange rate τ_M that meets the intermediate to slow exchange criteria, $\Delta\omega \cdot \tau_M \geq 1$ at various B_0 fields. On checking the data collected in Table 22.2, it is possible to predict which LnDOTA–4AmCE complexes should work as PARACEST agents. It is useful to remember that the most common clinical MR imaging field strengths are in the 1.5–3.0 T range.

PARACEST agents may be employed to sample the temperature and pH of the examined tissues just following the dependence of the rate of proton and water exchange on these parameters. Concerning the determination of temperature, it suffices to consider that the rate depends on the Arrhenius' law and this allows one to use the resonance experiment as a temperature probe. The influence of pH is

Table 22.2 ^{1}H chemical shifts and lifetimes (τ_M) of Ln^{3+}-bound water in the LnDOTA–4AmCE complexes (Zhang *et al.*, 2003).

			$\Delta\omega\cdot\tau_M$		
Complexes	τ_M^{298} **(μs)**	$\delta(^1H)$ **(ppm)**	**11.75 T**	**4.7 T**	**1.5 T**
Pr^{3+}	20	−60	3.8	1.5	0.5
Nd^{3+}	80	−32	8.0	3.2	1.0
Sm^{3+}	320	−4	4.0	1.6	0.5
Eu^{3+}	382	50	60.0	24.0	7.7
Tb^{3+}	31	−600	58.5	23.4	7.5
Dy^{3+}	17	−720	38.5	15.4	4.9
Ho^{3+}	19	−360	21.5	8.6	2.8
Er^{3+}	9	200	5.7	2.3	0.7
Tm^{3+}	3	500	4.7	1.9	0.6
Yb^{3+}	3	200	1.9	0.5	0.2

more complex to define in detail. For instance, the variation of pH over the physiological range does not affect the CEST effect induced by Eu(DOTA)-tetra-amide, while it is able to influence the result if the CEST agent is the isomorphous Yb^{3+} derivative of the same ligand. If an admixture of the two complexes is analyzed, it is possible to directly observe the variation of the resonance on pH by recording the CEST spectra saturating alternatively the Eu^{3+} and Yb^{3+} peaks (Aime *et al.*, 2002).

The possibility of playing with chemistry on the ligand structure opens the way to the use of PARACEST contrast agents based on mechanisms different from the simple proton or water exchange. There are several systems suitable for studying different biological mechanisms whose description is easily found in the specialized literature (Sherry and Woods, 2008; Siriwardena-Mahanama and Allen, 2013; Woods, Woessner, and Sherry, 2006).

References

Aime, S., Barge, A., Bruce, J.I., Botta, M., Howard, J.A.K., Moloney, J.M., Parker, D., de Sousa, A.S., and Woods, M. (1999) NMR, relaxometric, and structural studies of the hydration and exchange dynamics of cationic lanthanide complexes of macrocyclic tetraamide ligands. *J. Am. Chem. Soc.*, **121**, 5762–5771.

Aime, S., Barge, A., Castelli, D.D., Fedeli, F., Mortillaro, A., Nielsen, F.U., and Terreno, E. (2002) Paramagnetic lanthanide(III) complexes as pH-sensitive chemical exchange saturation transfer (CEST) contrast agents for MRI applications. *Magn. Reson. Med.*, **47**, 639–648.

Aime, S., Crich, S.G., Gianolio, E., Giovenzana, G.B., Tei, L., and Terreno, E. (2006) High sensitivity lanthanide(III) based probes for MR-medical imaging. *Coord. Chem. Rev.*, **250**, 1562–1579.

Bottrill, M., Kwok, L., and Long, N.J. (2006) Lanthanides in magnetic resonance imaging. *Chem. Soc. Rev.*, **35**, 557–571.

Caravan, P., Ellison, J.J., McMurry, T.J., and Lauffer, R.B. (1999) Gadolinium(III) chelates as MRI contrast agents: structure, dynamics, and applications. *Chem. Rev.*, **99**, 2293–2352.

Caravan, P., Greenfield, M.T., and Bulte, J.W.M. (2001) Molecular factors that

determine Curie spin relaxation in dysprosium complexes. *Magn. Reson. Med.*, **46**, 917–922.

Carr, H. (1952) *Free Precession Techniques in Nuclear Magnetic Resonance*, Harvard University, Cambridge, MA.

Damadian, R. (1971) Tumor detection by nuclear magnetic resonance. *Science*, **171**, 1151–1153.

Gueron, M. (1975) Nuclear relaxation in macromolecules by paramagnetic ions: a novel mechanism. *J. Magn. Reson.*, **19**, 58–66.

Helm, L. (2006) Relaxivity in paramagnetic systems: theory and mechanisms. *Prog. Nucl. Magn. Reson. Spectrosc.*, **49**, 45–64.

Idée, J.-M., Port, M., Robic, C., Medina, C., Sabatou, M., and Corot, C. (2009) Role of thermodynamic and kinetic parameters in gadolinium chelate stability. *J. Magn. Reson. Imaging*, **30**, 1249–1258.

Lauterbur, P.C. (1973) Image formation by induced local interactions: examples employing nuclear magnetic resonance. *Nature*, **242**, 190–191.

Merbach, A.S., Helm, L., and Toth, E. (2013) *The Chemistry of Contrast Agents in Medical Magnetic Resonance Imaging*, John Wiley & Sons, Inc., New York.

Norek, M. and Peters, J.A. (2011) MRI contrast agents based on dysprosium or holmium. *Prog. Nucl. Magn. Reson. Spectrosc.*, **59**, 64–82.

Overhauser, A.W. (1953) Polarization of nuclei in metals. *Phys. Rev.*, **92**, 411–415.

Sherry, A.D. and Woods, M. (2008) Chemical exchange saturation transfer contrast agents for magnetic resonance imaging. *Annu. Rev. Biomed. Eng.*, **10**, 391–411.

Siriwardena-Mahanama, B.N. and Allen, M.J. (2013) Strategies for optimizing water-exchange rates of lanthanide-based contrast agents for magnetic resonance imaging. *Molecules*, **18**, 9352–9381.

Terreno, E., Delli, C.D., Viale, A., and Aime, S. (2010) Challenges for molecular magnetic resonance imaging. *Chem. Rev. (Washington)*, **110**, 3019–3042.

Vinogradov, E., Sherry, A.D., and Lenkinski, R.E. (2013) CEST: from basic principles to applications, challenges and opportunities. *J. Magn. Reson.*, **229**, 155–172.

Ward, K.M., Aletras, A.H., and Balaban, R.S. (2000) A new class of contrast agents for mri based on proton Chemical Exchange Dependent Saturation Transfer (CEST). *J. Magn. Reson.*, **143**, 79–87.

Woods, M., Woessner, D.E., and Sherry, A.D. (2006) Paramagnetic lanthanide complexes as PARACEST agents for medical imaging. *Chem. Soc. Rev.*, **35**, 500–511.

Zhang, S., Merritt, M., Woessner, D.E., Lenkinski, R.E., and Sherry, A.D. (2003) PARACEST agents: modulating mri contrast via water proton exchange. *Acc. Chem. Res.*, **36**, 783–790.

van Zijl, P.C.M. and Yadav, N.N. (2011) Chemical exchange saturation transfer (CEST): what is in a name and what isn't? *Magn. Reson. Med.*, **65**, 927–948.

23
Some Applications of MM

23.1
Magnetocaloric Effect

The magnetocaloric effect (MCE) is the temperature variation of a material subjected to magnetic field variation. In a very rough description, this effect is generated when, for instance, in adiabatic condition a magnetic field is applied a ferromagnet forcing the transition to the ordered state. This transition induces the magnetic contribution to the total entropy to decrease. Because in an adiabatic process the total entropy must not change, the crystalline lattice entropy should increase. The overall effect is the heating of the material. The opposite effect on temperature is observed when the magnetic field is removed. As shown in Figure 23.1, the adiabatic transformation induced by switching on a magnetic field induces an increase of temperature (horizontal arrow) $T_1 - T_0$, which is often indicated as the magnetocaloric potential ΔT_{ad}. When the magnetic field is applied isothermally, the magnetic entropy change is observed (vertical arrow): $\Delta S_M = T_1 - S_0$. Please, note that in the following entropy is in italics (S).

At constant pressure, the entropy of a magnetic solid can be expressed as a function of the absolute temperature (T) and the applied magnetic field (H) with the formula

$$S(T,H) = S_M(T,H) + S_{Lat}(T,H) + S_{El}(T,H) \tag{23.1}$$

where S_M, S_{Lat}, and S_{El} are the magnetic, lattice, electronic contributions, respectively. Applying the Maxwell relationship between the magnetization (M), the magnetic field strength, and the heat capacity at constant pressure (C), it is possible to write at a certain absolute temperature T:

$$\left(\frac{\delta S(T,H)}{\delta H}\right)_T = \left(\frac{\delta M(T,H)}{\delta T}\right)_H \tag{23.2}$$

which, for an isothermal and isobaric process, becomes

$$\Delta S_M(T,\ \Delta H) = \int_{H_1}^{H_2} \left(\frac{\delta M(T,\ H)}{\delta T}\right)_H dH \tag{23.3}$$

It means that the magnetic entropy change is proportional to the derivative of magnetization with respect to temperature at constant field and to the magnetic

Introduction to Molecular Magnetism: From Transition Metals to Lanthanides, First Edition.
Cristiano Benelli and Dante Gatteschi.
© 2015 Wiley-VCH Verlag GmbH & Co. KGaA. Published 2015 by Wiley-VCH Verlag GmbH & Co. KGaA.

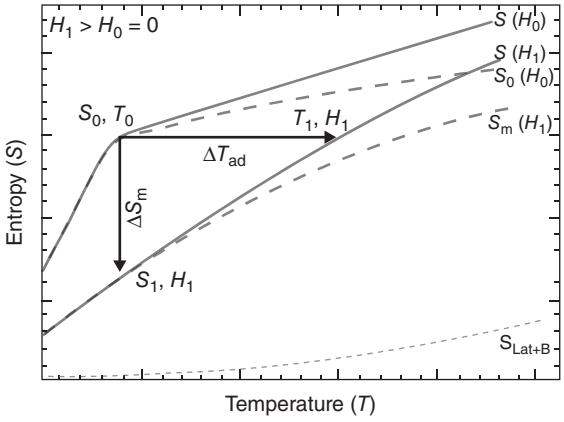

Figure 23.1 The $S-T$ diagram illustrating the existence of the magnetocaloric effect. The solid lines represent the total entropy in two different magnetic fields: $H_0 = 0$ and $H_1 > 0$. The horizontal arrow shows ΔT_{ad} and the vertical arrow shows ΔS_M when the magnetic field is changed from H_0 to H_1. The dotted line shows the combined lattice and electronic (nonmagnetic) entropy, and the dashed lines show the magnetic entropy in the two fields. S_0 and T_0 are zero-field entropy and temperature, S_1 and T_1 are entropy and temperature at the elevated magnetic field H_1 (Pecharsky and Gschneidner, 1999). (Reproduced from Pecharsky, V.H. *et al.* (1999) with permission from Elsevier Science B.V.)

field change. Similarly, it is possible to derive the magnetic potential

$$\Delta T_{ad}(T,\ \Delta H) = -\int_{H_1}^{H_2} \left(\frac{T}{C\,(T,\ H)}\right)_H \left(\frac{\delta M\,(T,H)}{\delta T}\right)_H dH \tag{23.4}$$

where H is the applied magnetic field and M and C are the field- and temperature-dependent magnetization and specific heat, respectively. It is evident that a strong temperature dependence of the magnetization is a basic requirement for observing a large MCE. As a consequence of this behavior, systems such as metals, which order ferromagnetically, show, in a constant magnetic field, a high value of $\Delta T_{ad}(T,\ \Delta H)$ at temperatures close to the critical temperature (T_c). For instance, a classic example of this behavior is gadolinium which has $T_c = 294$ K and, therefore, exhibits relevant MCEs close to room temperature. For the same reason, ferromagnetic materials with similar properties, such as lanthanide alloys and manganites, are widely used for cooling around room temperature. The thermal hysteresis present in magnetically ordered materials is a problem that makes complex the use of this type of systems as an alternative to classical refrigerants.

Things are different for paramagnetic materials. Since the first studies on $Gd_2(SO_4)_3 \cdot H_2O$ (Giauque and MacDougall, 1933), it was possible to observe a MCE also in a paramagnetic salt. According to the relationship between temperature and magnetization, the MCE becomes effective in this class of compounds only at very low temperatures. In any case, it is possible to apply paramagnetic demagnetization for cryogenic purposes at temperatures very close to absolute

zero with the limitation for common use as low-temperature refrigerants because of the required presence of relatively high fields to provide a significant cooling power.

This is the situation for a classical magnetic system. The impact of molecular magnetism (MM) in its more recent development is modifying the approach to MCE. At this stage, it is useful to stress that a system with a magnetic moment of spin S consists of $2S + 1$ magnetic levels. Therefore, at given temperature $T \neq 0\,\mathrm{K}$ the entropy per mole related to the magnetic degrees of freedom is

$$S_{\mathrm{m}} = R \ln(2S + 1) \tag{23.5}$$

where R is the gas constant and S represents the effective spin describing the multiplicity of the states taking part in the magnetic process (Evangelisti and Brechin, 2010). This relationship makes clear that a molecule should exhibit a large total spin S to be a good candidate for producing an efficient cooling. In the literature are reported spin values up to 83/2 (Ako *et al.*, 2006) but high spin value is a relevant point but it is not enough by itself to determine a significant MCE: a fundamental point is the absence of an anisotropy barrier. It is possible to demonstrate (Evangelisti and Brechin, 2010) that the presence of a negligible anisotropy is fundamental to producing high performance in a magnetic refrigerant, as in this condition it is possible to have a high density of the low-lying spin states and consequently a large entropy change. The first case of an SMM showing a high S value ($S \leq 25$) and a low anisotropy was reported for an Fe14 cluster (Shaw *et al.*, 2007). This case is useful even to demonstrate that the presence of spin frustration helps in improving MCE for reasons similar to those underlined previously (Schnack, Schmidt, and Richter, 2007).

Another feature to consider is the presence of a magnetic interaction between the spins of the cluster. First of all, it rather straightforward that ferromagnetic interaction can help in improving the magnetocaloric properties compared to antiferromagnetic ones. If a molecule contains n noninteracting spins s, Eq. (23.5) becomes

$$S_{\mathrm{m}} = nR \ln(2s + 1) \tag{23.6}$$

As soon as magnetic exchange becomes relevant, n spins s give a new spin state which derives from their coupling with $S_{\mathrm{tot}} = ns$, which must be included in the S_{m} expression giving a different value for $S_{\mathrm{m}}(S_{\mathrm{m}} = R \ln(2ns + 1))$, which is in any case lower than the value derived in Eq. (23.6). It is necessary, therefore, to consider the variation of S_{m} with temperature, which is different in the presence of magnetic interactions especially where these interactions become relevant. In these systems, it is, at least in principle, possible to observe large entropy variations even in presence of small changes in temperatures and/or external magnetic fields.

In the last few years, following an explosion of studies on SMM, several magnetic clusters have be studied on the side of MCE, reaching very promising results as reported in Table 23.1, where the entropy changes $-\Delta S_{\mathrm{m}}$ for a few magnetically isotropic molecular cluster are reported with some experimental conditions.

Table 23.1 Estimated specific entropy change upon application of a magnetic field $\mu_0 H$ and temperature T (Sessoli, 2012).

	$-\Delta S_m$ (J K^{-1} kg^{-1})	$\mu_0 H$ (T)	T_{max} (K)	References
Fe_{14}	17.6	7	6	Shaw *et al.* (2007)
Mn_{10}	13.0	7	2.2	Manoli *et al.* (2007)
Mn_{14}	25	7	3.8	Manoli *et al.* (2008)
Gd_7	23	7	3	Sharples *et al.* (2011)
Cu_5Gd_4	31	9	3	Langley *et al.* (2011)
Ni_6Gd_6	26.5	7	3	Zheng, Evangelisti, and Winpenny (2011)
Gd_2	41.6	7	1.8	Evangelisti *et al.* (2011)
$Gd_3Ga_5O_{12}$	27	5	5	McMichael, Ritter, and Shull (1993)

In the last row, the corresponding values for gadolinium gallium garnet, which is generally assumed as standard for low-temperature MCE commercial application, is reported.

As final comment, it is worth noting that the most recent developments in this technology suggest that magnetic refrigeration has some advantages over classical refrigeration systems based on the vapor-compression cycle. There are no harmful gases involved, and the cooling efficiency in magnetic refrigerators working with gadolinium has been shown to reach 60% of the theoretical limit, compared to only about 45% in the best gas-compression refrigerators (Gutfleisch *et al.*, 2011).

23.2 Luminescence

Luminescence is the spontaneous emission of radiation from an electronically excited species (or from a vibrationally excited species) not in thermal equilibrium with its environment. If the origin of the emission is a biological process, the correct definition is bioluminescence; if it is a chemical reaction, the name is chemiluminescence; and if the emission is an electromagnetic radiation in the visible region due to direct photoexcitation, the phenomenon is called photoluminescence, which is often identified as fluorescence, phosphorescence, and delayed fluorescence as described in Figure 23.2.

Just a glance at the above simple scheme is enough to realize that good candidates as luminescent probe must be substances very rich in electronic levels. From this point of view, trivalent lanthanides ions have without doubt an ideal electronic structure suitable for producing luminescence (Bunzli, 2006). As stressed in Chapter 1, they have the [Xe] $4f^n (n = 0-14)$ configurations, which can generate $14!/n!\,(14-n)!$ energy levels. It means, for instance, that ions such as Gd^{3+}, Eu^{3+}, and Tb^{3+} are characterized by more than 3000 levels, which are defined by the three quantum numbers S, L, and J, within the frame of the Russell–Saunders and spin–orbit coupling scheme.

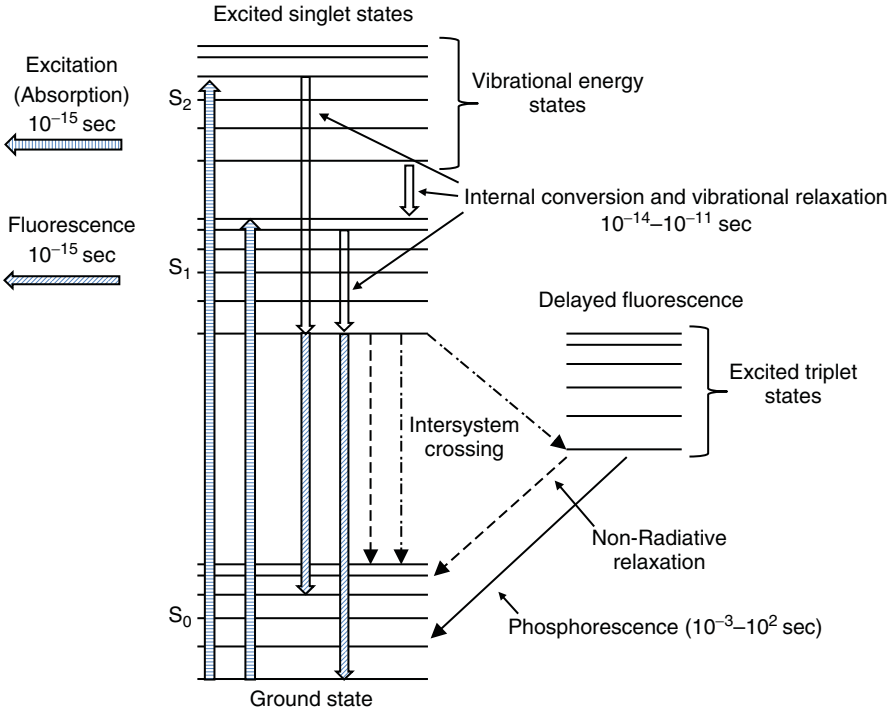

Figure 23.2 Some examples of absorption/emission processes.

The observed transitions within all these levels are of three different types: 4f–5d, charge-transfer transitions (CTTs) (ligand-to-metal, LMCT, or metal-to-ligand, MLCT), and intra-configurational 4f–4f (see Table 23.1) (Bunzli and Eliseeva, 2010). When an electron is excited to the 5d subshell, the observed transition, according to parity rules (Laporte selection rules), is an allowed one. In general, they are characterized by a very high energy that is outside the visible and near-infrared (NIR) region with some exception for Ce^{3+}, Pr^{3+}, and Tb^{3+}, It is worth mentioning a frequency dependence on the Ln^{3+} chemical environment due to the sensitivity of 5d orbitals to the coordination sphere. The CTTs are, again, very high in energy, and only in a few cases (Eu^{3+} or Yb^{3+}) are they observed in the visible region.

According to the above descriptions of the 4f–5d transitions and CTTs, only the 4f–4f transitions may be active in the visible–NIR region and, therefore, useful for practical applications. A first important feature is due to the evidence that the partially filled 5s5p subshells shield the 4f orbitals and, as a consequence, their energy patterns show a low sensitivity to the chemical environments. Therefore, the luminescence phenomenon gives optical bands characteristic of each metal. Historically, the identification of the various lanthanides was first of all a spectroscopic problem, and later a chemical one. Another characteristic of the emission process is the generation of sharp bands because the excitation of an electron to

a 4f orbital does not produce a large reorganization in the ligand structure of the molecule.

The light emission based on this processes can be analyzed by using two parameters: (i) the quantum yield (Q) and (ii) the lifetime of the excited states. Quantum yield can be defined according to equation

$$Q = \frac{\text{Number of emitted photons}}{\text{Number of absorbed photons}} \tag{23.7}$$

while the lifetime of the excited states (τ_{obs}) is equal to $1/k_{obs}$ where k_{obs} is the rate constant of the depopulation of the excited states measured in s^{-1}. For a 4f–4f transition

$$Q_{Ln}^{Ln} = \frac{k^{rad}}{k_{obs}} = \frac{\tau_{obs}}{\tau^{rad}} \tag{23.8}$$

Q_{Ln}^{Ln} is defined as the intrinsic quantum yield, which depends on k^{rad}, the radiative rate constant. If radiative deactivation processes are active, which is the most common situation, $k_{obs} > k^{rad}$: there are, in the literature, few examples of $Q > 90\%$. Therefore, one of the main issue in designing Ln^{3+} systems to be used in a luminescent device is the minimization of deactivation processes.

These transitions are intra-configurational and, according to electric dipole selection rules, they are forbidden transitions. There are, however, several mechanisms that can slightly modify this situation. One of these mechanisms is the modification of the symmetry around the Ln^{3+} ions due to vibrations, which temporarily influences the geometric molecular arrangement. The presence of vibronic couplings is relevant even in defining the nature and energy of the emitted radiation. As these characteristics are strongly related to the depopulation of the excited states, as shown in Figure 23.2, a relevant feature is the difference in energy between the lowest excited level and the highest level of the ground multiplet. If this difference is small, vibrational mechanism can produce nonradiative deactivation mechanisms. From this point of view, the best emitting ions are Eu^{3+}, Gd^{3+}, and Tb^{3+}, as shown in Table 23.2. Another possible pathway that allows the 4f–4f transitions is the J-mixing and the mixing with wave functions, as 5d orbitals, with an opposite parity. As these couplings of vibrational and electronic states with 4f orbitals depend on the strength of their interactions with the surroundings, which is in any case small as previously outlined, the oscillator strengths are small. As a consequence, the overall mechanism is not very efficient and the extinction coefficient (ε) for the trivalent cations is approximately of the order of $1-10\ M^{-1}\ cm^{-1}$.

Another important feature of these transitions is the S-value of the electronic spin state involved in transition. It is generally observed the transitions with $\Delta S = 0$ give rise to fluorescence while those with $\Delta S \neq 0$ produce phosphorescent transitions (see Table 23.2). Finally, it has been experimentally observed that some peculiar transitions which are electric dipolar in nature are extremely sensitive to modification of the coordination characteristic of the metal ion: they are called *hypersensitive* or *pseudo-quadrupolar* transitions because they tend to obey to electric quadrupole selection rules.

Table 23.2 Selected luminescent properties of Ln^{III} ions.[a)]

Ln	G	I	F	λ/μm or nm[b)]	Gap/cm^{-1}[b]	τ^{rad}/ms[b)]
Ce	$^2F_{5/2}$	5d	$^2F_{5/2}$	Tunable, 300–450	—	—
Pr	$^3H_4$	$^1D_2$	$^3F_4$, $^1G_4$, $^3H_4$, $^3H_5$	1.0, 1.44, 600, 690	6 940	(0.05[c)] –0.35)
		$^3P_0$	^3H_J ($J = 4 - 6$)	490, 545, 615	3 910	(0.003[c)] –0.02)
		$^3P_0$	^3F_J ($J = 2 - 4$)	640, 700, 725	—	—
Nd	$^4I_{9/2}$	$^4F_{3/2}$	^4I_J ($J = 9/2 - 13/2$)	900, 1.06, 1.35	5 400	0.42 (0.2–0.5)
Sm	$^6H_{5/2}$	$^4G_{5/2}$	^6H_J ($J = 5/2 - 13/2$)	560, 595, 640, 700, 775	7 400	6.26
		$^4G_{5/2}$	^6F_J ($J = 1/2 - 9/2$)	870, 887, 926, 1.01, 1.15	—	—
		$^4G_{5/2}$	$^6H_{13/2}$	877	—	—
Eu[d)]	$^7F_0$	$^5D_0$	^7F_J ($J = 0 - 6$)	580, 590, 615, 650, 720, 750, 820	12 300	9.7 (1–11)
Gd	$^8S_{7/2}$	$^6P_{7/2}$	$^8S_{7/2}$	315	32 100	10.9
Tb	$^7F_6$	$^5D_4$	^7F_J ($J = 6 - 0$)	490, 540, 580, 620	14 800	9.0 (1–9)
				650, 660, 675		
Dy	$^6H_{15/2}$	$^4F_{9/2}$	^6H_J ($J = 15/2 - 9/2$)	475, 570, 660, 750	7 850	1.85 (0.15–1.9)
		$^4F_{15/2}$	^6H_J ($J = 15/2 - 9/2$)	455, 540, 615, 695	1 000	3.22[b)]
Ho	$^5I_8$	$^5S_2$	^5I_J ($J = 8, 7$)	545, 750	3 000	0.37 (0.51[c)])
		$^5F_5$	$^5I_8$	650	2 200	0.8[c)]
		$^5F_5$	$^5I_7$	965	—	—
Er[e)]	$^4I_{15/2}$	$^4S_{3/2}$	^4I_J ($J = 15/2, 13/2$)	545, 850	3 000	0.7[c)]
		$^4F_{9/2}$	$^4I_{15/2}$	660	2 850	0.6[c)]
		$^4I_{9/2}$	$^4I_{15/2}$	810	2 150	4.5[c)]
		$^4I_{13/2}$	$^4I_{15/2}$	1.54	6 500	0.66 (0.7–12)
Tm	$^3H_6$	$^1D_2$	$^3F_4$, $^3H_4$, $^3F_3$, $^3F_2$	450, 650, 740, 775	6 650	0.09
		$^1G_4$	$^3H_6$, $^3F_4$, $^3H_5$	470, 650, 770	6 250	1.29
		$^3H_4$	$^3H_6$	800	4 300	3.6[c)]
Yb	$^2F_{7/2}$	$^2F_{5/2}$	$^2F_{7/2}$	980	10 250	2.0 (0.5–2.0)[f)]

a) G = ground state; I = main emissive state; F = final state; gap = energy difference between I and the highest SO level of F.
b) Values for the aqua ions, unless otherwise stated, and ranges of observed lifetimes in all media, if available, between parentheses.
c) Doped in Y_2O_3 or in $YLiF_4$ (Ho), or in $YAl_3(BO_3)_4$ (Dy).
d) Luminescence from $^5D_1$, $^5D_2$, and $^5D_3$ is sometimes observed as well.
e) Luminescence from four other states has also been observed: $^4D_{5/2}$, $^2P_{3/2}$, $^4G_{11/2}$, $^2H_{9/2}$.
f) Complexes with organic ligands: 0.5–1.3 ms; solid-state inorganic compounds: ≈2 ms.

Ln	Excited state[a)]	End state	Emission color	Luminescence type
Pr	$^1G_4$	^3H_J	NIR	Phosphoresce
	$^1D_2$	^3F_J	NIR	Phosphoresce
	$^3P_0$	^3H_J	Orange	Fluorescence
Nd	$^4F_{3/2}$	^4I_J	NIR	Fluorescence
Sm	$^4G_{5/2}$	^6H_J	Orange	Phosphoresce
Eu	$^5D_0$	^7F_J	Red	Phosphoresce
Gd	$^6P_{7/2}$	$^6S_{7/2}$	UV	Phosphoresce
Tb	$^5D_4$	^7F_J	Green	Phosphoresce
Dy	$^4F_{9/2}$	^6H_J	Yellow-Orange	Phosphoresce
Ho	$^5F_5$	^5I_J	NIR	Fluorescence
	$^5S_2$	^5I_J	Green	Fluorescence
Er	$^4S_{3/2}$	^4I_J	—	Fluorescence
	$^4I_{13/2}$	$^4I_{15/2}$	NIR	Fluorescence
Tm	$^1G_4$	^3H_J	Blue	Phosphoresce
Yb	$^2F_{5/2}$	$^2F_{7/2}$	NIR	Fluorescence

a) Most luminescent excited state.

To overcome the problem of low-efficiency of 4f–4f transitions, there is the possibility of sensitizing their luminescence in metal-organic systems by increasing the population of Ln^{3+} ion excited states by using a luminescence sensitization, alternatively named the *antenna effect*. Schematically, the energy transfer is generally described as the consequence of three steps (as described in Figure 23.3) that largely influence the efficiency of the total mechanism: (i) an initial energy contribution to populate the lowest lying singlet excited states of

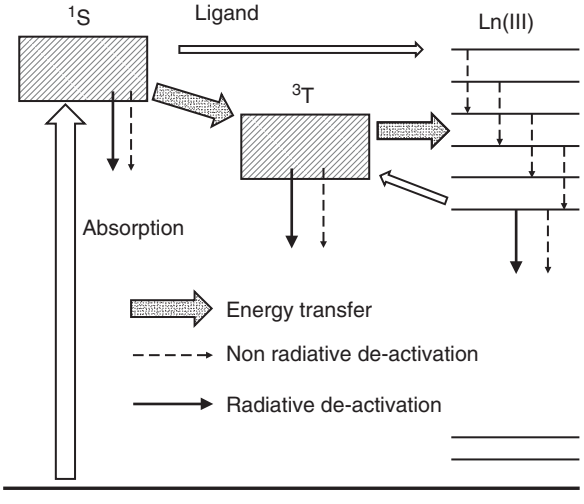

Figure 23.3 Antenna effect for the luminescence in Gd^{3+} and Eu^{3+}.

the organic ligand (for most organic chromophores $\varepsilon \approx 10^4 - 10^5\ M^{-1}\ cm^{-1}$); (ii) a subsequent intersystem crossing to its triplet state; and (iii) a final energy transfer to the excited level of lanthanide ion. The direct transfer of energy from the ligand singlet state to the metal ion is another possible mechanism. However, because of the short lifetime of the singlet state, this transfer is often not very efficient (Armelao *et al.*, 2010).

The three-step process is made complex by the various mechanisms of energy transfer involved in each passage. In any case, what is relevant for practical applications is the total efficiency of the process which is influenced by the efficiency of populating and depopulating the excited levels, thereby minimizing the effects of nonradiative pathways. To deal with the quantitative aspects of the luminescent feature of lanthanide ions, it is useful to consider the overall quantum yield of a metal-organic Ln^{3+} compounds:

$$Q_{Ln}^{L} = \eta_{sens} Q_{Ln}^{Ln} \tag{23.9}$$

where Q_{Ln}^{L} and Q_{Ln}^{Ln} are the quantum yields result from indirect and direct excitation, respectively, while η_{sens} represents the efficacy of the energy transfer from the surroundings to the metal ion. In a simplified model, it is possible to consider only the energy of the lowest triplet state and, therefore, the quantum yield becomes

$$Q_{Ln}^{L} = \eta_{isc} \eta_{et} Q_{Ln}^{Ln} \tag{23.10}$$

where η_{isc} represents the intersystem crossing efficiency, namely, the yield of the singlet–triplet transition, and η_{et} the efficiency of the triplet-to-metal energy transfer. The singlet-to-triplet transition induces some variation in the system geometry. The more relevant feature in luminescence phenomena is the variations of the ligand–metal ion mean distances. If there is a noticeable increase in distances, it is possible to observe energy transfers until all the triplet levels are populated: as soon as the lowest vibrational state is depopulated, the phosphorescence stops. On the other side, if a small expansion in ligand distances is observed, it is possible to get a very efficient luminescence ($\eta_{sens} \approx 1$) in the case of a transfer rate larger than the radiative and nonradiative deactivation of the triplet state.

Among the nonradiative processes, the vibrational mechanisms are the more relevant. The minimization of these kinds of mechanisms is one more important issue in sketching molecular structure. For instance, in biological application of luminescent phenomena, the luminescence is severely quenched by interaction with water molecules via OH vibrations. Therefore, the design of molecular systems is strictly connected to the number of water molecules required to complete the coordination sphere around the Ln^{3+} ion.

23.2.1
Electroluminescent Materials for OLED

The most updated technologies require, in many fields, the use of a flat screen. Most of them are liquid crystals displays (LCDs) but an increasing number of

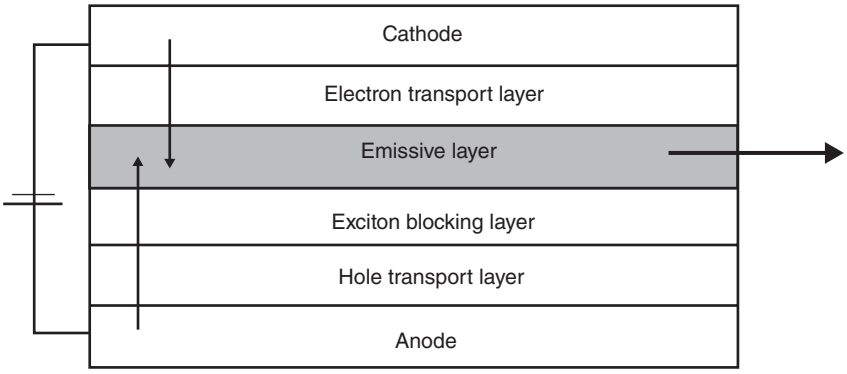

Figure 23.4 Typical OLED cell structure.

devices are based on the application of organic light-emitting diodes (OLEDs). The advantage of this technology is that the displays are self-luminescent and, therefore, thinner and lighter than LCDs as they do not require backlighting. In OLED displays, only the necessary pixels are active and not the entire panel, thereby reducing significantly the energy consumption. Furthermore, they are robust and may be deposited on flexible substrates, offering truer colors and wider angles of viewing (Kido and Okamoto, 2002).

The basic phenomenon that allows this kind of system to produce light and colors is electroluminescence. It means that the device must include a material that emits light in response to the passage of an electric current or to a strong electric field. A typical cell is shown in Figure 23.4. The core of the device is the emissive layer, which can be deposited directly as an active layer or, alternatively, in more recent production techniques by doping the electron transport layer, generally using tris(8-hydroxyquinolate)aluminum (Alq_3). All the layers, which are deposited by using the usual techniques from plasma to Langmuir–Blodgett depositions, should have a high transparency to the emitted radiation.

When an external electric field is applied, electrons move from the cathode (generally Mg-Ag or Li-Al alloys) and holes from the anode (indium tin oxide, ITO). The emissive layer is inserted between electron and transport layers plus an exciton blocking layer (in present devices very often it is 2,9 dimethyl-4,7 diphenyl-1,10-phenantroline). The electron transport mechanism uses the available lowest occupied molecular orbital (LUMO), while the HTL (hole transport layer) transports hole within the highest occupied molecular orbital (HOMO). This layer should have a low ionization potential to promote the injection of holes from the anode. The crucial moment is their presence in the same place where they form a bound neutral state, or exciton, whose mobility is confined to the right zone by the exciton blocking layer (EBL). The EBL should have a higher exciton energy level with respect the emissive layer because it helps to block the migration of excitons outside the emissive layer. Relaxation to the ground state of the electron–hole couple produces a release of energy which activates the fluorescence or phosphorescence phenomenon in the emissive layer.

These layers at very beginning of this technique were based on fluorescent organic materials. The organic substrates are in a spin-singlet state, while the excitons can exhibit either a triplet state or a singlet state. Because of the difference in the spin states, the triplet excitons relax substantially through thermal or vibrational mechanism without the emission of photons. If the hole–electron recombination is statistically driven, the internal quantum efficiency, which is related only to the singlet–singlet transition, will have an efficiency of approximately 25%. Coordination compounds have been attracting the attention of researchers, which have electronic structures and relaxation mechanisms more suitable for producing phosphorescence. The mechanisms of energy transfer that are active from host and the dopant molecules are of three different types: Förster, Dexter, and charge-trapping. The first mechanism involves a dipole–dipole coupling of the donor (D) and acceptor (A) states with a dependence on the donor–acceptor distance of the type d_{DA}^{-6}. To have an efficient transition, it is necessary that both D and A molecules are in the singlet state. However, even the ${}^3D^* + {}^1A \Leftrightarrow {}^1D + {}^1A^*$ is a rather efficient pathway as the slow rate of energy transfer could be balanced by the long lifetime of the triplet state if the donor molecule is an efficient phosphor. Dexter transfer mechanism is active for relatively short distances (~1 nm), the exciton transfer from D to A being mediated by intermolecular exchange: this mechanism loses efficiency rapidly on increasing the D–A distance. In this mechanism, the key point is the preservation of total spin, namely there are two allowed transitions:

$${}^1D^* + {}^1A \Leftrightarrow {}^1D + {}^1A^* \qquad {}^3D^* + {}^1A \Leftrightarrow {}^1D + {}^3A^*$$

In the third mechanism, a guest molecule traps the charge and produces an exciton by recombination with an opposite charge on a neighboring phosphorescent molecule.

The three mechanisms are, of course, competitive, and the efficiency of the actual process depends on the lifetime of excitons, their mobility within the emissive film, and the film thickness. In the case of the singlet–singlet transitions, all the three mechanisms are active with different roles, with the Förster one being the more effective one (Evans, Douglas, and Winscom, 2006).

For efficient phosphorescent materials, three parameters are essential in defining their possible use in OLEDs. They should offer the emissivity in the three fundamental colors (red, ~650–700 nm; green, ~500–550 nm; and blue, ~450–470 nm); to date, the challenge is of getting a good emitter in the blue region. Long lifetimes could produce problems of saturation because, if the molecule remains in the triplet state for a long time, there is a limiting factor in the conversion of the electrical to photon energy. Suitable lifetimes for the guest phosphorescent molecule are, at 298 K, in the 5–50 μs range. It is obvious that the best system should exhibit a quantum yield very close to unity: though in real devices the lowest limit for useful compounds is around 25%. For all the reason outlined above, metal-organic systems containing 3d ions have been largely used in preparing commercial OLEDs as the flexibility of their physical properties offers the possibility of several applications. The use of lanthanide ion has been

increasingly successful mainly due to two factors: their emission bands are extremely sharp, offering the possibility of highly brilliant colors with the advantage that the variations of the chemical environment do not substantially affect the emitted wavelength; and by modulating the antenna effect, it is possible to achieve very high quantum efficiency. The use of terbium(III) and europium(III) derivatives as green and red emitters is well established, while there have been several attempts on the application of samarium, dysprosium, and terbium compounds to develop, respectively, orange, yellow, and blue electroluminescent OLEDs. The main pathways to increase the emissive efficiency are the reduction of nonradiative deactivation processes by reducing the presence of O–H, N–H, and N–N oscillators in the coordination spheres and the production of rigid systems with high coordination numbers to avoid the presence of coordinated water molecules.

23.2.2
Biological Assays and Medical Imaging

The luminescence of several lanthanide derivatives can be used to obtain quantitative information on structural and kinetic parameters of biological systems. The interest on luminescent lanthanide bioprobes is based on the possibility of using Ln^{3+} coordination compounds as luminescent sensors in time-resolved luminescent (TRL) immunoassays. The development of this technology has generated several applications in many fields of biology, biotechnology, and medicine, including analyte sensing and tissue and cell imaging, as well as monitoring drug delivery. The Ln^{3+} compounds suitable for their use as bioprobes must possess a lot of specific properties. They should be water soluble, thermodynamically stable in biological fluids, and inert from a kinetic point of view. Further, they should have intense absorption above 330 nm to minimize destruction of live biological material, an efficient sensitization of the metal luminescence, the possibility of embedding the emitting ion into a rigid, protective cavity, thereby minimizing nonradiative deactivation, a long excited state lifetime, and high photostability (Bunzli, 2010).

References

Ako, A.M., Hewitt, I.J., Mereacre, V., Clérac, R., Wernsdorfer, W., Anson, C.E., and Powell, A.K. (2006) A ferromagnetically coupled Mn19 aggregate with a record S = 83/2 ground spin state. *Angew. Chem.*, **118**, 5048–5051.

Armelao, L., Quici, S., Barigelletti, F., Accorsi, G., Bottaro, G., Cavazzini, M., and Tondello, E. (2010) Design of luminescent lanthanide complexes: from molecules to highly efficient photo-emitting materials. *Coord. Chem. Rev.*, **254**, 487–505.

Bunzli, J.C.G. (2006) Benefiting from the unique properties of lanthanide ions. *Acc. Chem. Res.*, **39**, 53–61.

Bunzli, J.C.G. (2010) Lanthanide luminescence for biomedical analyses and imaging. *Chem. Rev.*, **110**, 2729–2755.

Bunzli, J.C.G. and Eliseeva, S.V. (2010) Lanthanide NIR luminescence for telecommunications, bioanalyses and solar energy conversion. *J. Rare Earths*, **28**, 824–842.

Evangelisti, M. and Brechin, E.K. (2010) Recipes for enhanced molecular cooling. *Dalton Trans.*, **39**, 4672–4676.

Evangelisti, M., Roubeau, O., Palacios, E., Camón, A., Hooper, T.N., Brechin, E.K., and Alonso, J.J. (2011) Cryogenic magnetocaloric effect in a ferromagnetic molecular dimer. *Angew. Chem. Int. Ed.*, **50**, 6606–6609.

Evans, R.C., Douglas, P., and Winscom, C.J. (2006) Coordination complexes exhibiting room-temperature phosphorescence: evaluation of their suitability as triplet emitters in organic light emitting diodes. *Coord. Chem. Rev.*, **250**, 2093–2126.

Giauque, W.F. and MacDougall, D.P. (1933) Attainment of temperatures below 1° absolute by demagnetization of $Gd_2(SO_4)_3 \cdot 8H_2O$. *Phys. Rev.*, **43**, 768–768.

Gutfleisch, O., Willard, M.A., Brück, E., Chen, C.H., Sankar, S.G., and Liu, J.P. (2011) Magnetic materials and devices for the 21st century: stronger, lighter, and more energy efficient. *Adv. Mater.*, **23**, 821–842.

Kido, J. and Okamoto, Y. (2002) Organo lanthanide metal complexes for electroluminescent materials. *Chem. Rev.*, **102**, 2357–2368.

Langley, S.K., Chilton, N.F., Moubaraki, B., Hooper, T., Brechin, E.K., Evangelisti, M., and Murray, K.S. (2011) Molecular coolers: the case for $[Cu(II)_5Gd(III)_4]$. *Chem. Sci.*, **2**, 1166–1169.

Manoli, M., Collins, A., Parsons, S., Candini, A., Evangelisti, M., and Brechin, E.K. (2008) Mixed-Valent Mn supertetrahedra and planar discs as enhanced magnetic coolers. *J. Am. Chem. Soc.*, **130**, 11129–11139.

Manoli, M., Johnstone, R.D.L., Parsons, S., Murrie, M., Affronte, M., Evangelisti, M., and Brechin, E.K. (2007) A ferromagnetic mixed-valent mn supertetrahedron: towards low-temperature magnetic refrigeration with molecular clusters. *Angew. Chem. Int. Ed.*, **46**, 4456–4460.

McMichael, R.D., Ritter, J.J., and Shull, R.D. (1993) Enhanced magnetocaloric effect in $Gd_3Ga_{(5-x)}Fe_xO_{12}$. *J. Appl. Phys.*, **73**, 6946–6948.

Pecharsky, V.K. and Gschneidner, K.A. Jr., (1999) Magnetocaloric effect and magnetic refrigeration. *J. Magn. Magn. Mater.*, **200**, 44–56.

Schnack, J., Schmidt, R., and Richter, J. (2007) Enhanced magnetocaloric effect in frustrated magnetic molecules with icosahedral symmetry. *Phys. Rev. B*, **76**, 054413.

Sessoli, R. (2012) Chilling with magnetic molecules. *Angew. Chem. Int. Ed.*, **51**, 43–45.

Sharples, J.W., Zheng, Y.-Z., Tuna, F., McInnes, E.J.L., and Collison, D. (2011) Lanthanide discs chill well and relax slowly. *Chem. Commun.*, **47**, 7650–7652.

Shaw, R., Laye, R.H., Jones, L.F., Low, D.M., Talbot-Eeckelaers, C., Wei, Q., Milios, C.J., Teat, S., Helliwell, M., Raftery, J. *et al.* (2007) 1,2,3-triazolate-bridged tetradecametallic transition metal clusters $[M_{14}(L)_6O_6(OMe)_{18}X_6]$ (M = Fe(III), Cr(III) and V(III/IV)] and related compounds: ground-state spins ranging from S = 0 to S = 25 and spin-enhanced magnetocaloric effect. *Inorg. Chem.*, **46**, 4968–4978.

Zheng, Y.-Z., Evangelisti, M., and Winpenny, R.E.P. (2011) Large magnetocaloric effect in a wells–dawson type $\{Ni_6Gd_6P_6\}$ cage. *Angew. Chem. Int. Ed.*, **50**, 3692–3695.

Appendix A

acac	pentane-2,4-dionate
AFM	Antiferromagnetic
AMFI	Atomic mean field integrals
ANO-RCC	Relativistic contracted atomic natural orbitals
B3LYP	Becke 3-parameter Lee-Yang-Parr
BMA	bis-methylamide
bpea	N,N-bis(2-pyridylmethyl)-ethylamine
CASPT2	Complete active space perturbation theory
CASSFC	Complete active space self-consistent field
CEST	chemical exchange saturation transfer
COT	Cyclooctatetraene
CP	Coordination polymers
DQC	double quantum coherence
DTPA	diethylene triamine pentaacetic acid
DTPA-BMA	5,8-Bis(carboxymethyl)-11-[2-(methylamino)-2-oxoethyl]-3-oxo-2,5,8,11-tetraazatridecan-13-oic acid
DTPA-BMEA	[8,11-biscarboxymethyl)-14-[2-[(2-methoxyethyl)amno]-2-oxoethyl]-6-oxo-2-oxa-5,8,11,14-tetraazahexadecan-16-oato]
FID	Free induction decay
FiM	Ferrimagnetic
FM	Ferromagnetic
GGA	Generalized gradient approximations
Hdbm	1,3-diphenyl-1,3-propanedione
Hdpm	dipivaloylmethane
HDVV	Heisenberg Dirac Van Vleck
IRMOF	Isoreticular metal-organic framework
LF	Ligand field
LIESST	Light-induced spin-state trapping
LUMO	Lowest Unoccupied Molecular Orbital
mal	malonate
MBPT	Many-body perturbation theory
MC	Magnetochemistry
MCE	Magnetocaloric effect

Introduction to Molecular Magnetism: From Transition Metals to Lanthanides, First Edition.
Cristiano Benelli and Dante Gatteschi.
© 2015 Wiley-VCH Verlag GmbH & Co. KGaA. Published 2015 by Wiley-VCH Verlag GmbH & Co. KGaA.

MM	Molecular magnetism
MMOF	Magnetic metal-organic framework
MO	Molecular orbital
MOF	Metal-organic framework
MRI	Magnetic resonance imaging
MST	Molecular spintronic
NN	Next neighbor
NNN	Next nearest neighbor
PARACEST	paramagnetic chemical exchange saturation transfer
Pc	Phthalocyanine
PCP	Porous coordination polymers
PELDOR	pulsed electron-electron double resonance
PMOF	Porous metal-organic framework
POM	Polyoxometallates
QDPT	QuasiDegenerate perturbation theory
QIP	Quantum information
RASSI-SO	Restricted Active Space State Interaction – Spin Orbit coupling
SCM	Single chain magnet
SCO	Spin crossover
SIM	Single ion magnet
SWCN	Single-walled carbon nanotube
SMM	Single molecular magnet
SOC	Spin – orbit coupling
SOMO	Single Occupied Molecular Orbital
terpy	2,2′:6′,2″-terpyridine
TM	Transition metal
TMMC	Tetramethylammonium Manganese Chain
ZFS	Zero-field splitting
ZIF	Zeolitic imidazole framework
VASP	Vienna *ab initio* simulation package
YBCO	Yttrium barium copper oxide

Appendix B

Quantity	Symbol	Gaussian and cgs emu[a)]	Conversion factor, C[b)]	SI and rationalized mks[c)]
Magnetic flux density, magnetic induction	B	gauss (G)[d)]	10^{-4}	tesla (T), $Wb\,m^{-2}$
Magnetic flux	Φ	maxwell (Mx), $G\,cm^2$	10^{-8}	weber (Wb), volt second (V·s)
Magnetic potential difference, magnetomotive force	U, F	gilbert (Gb)	$10/4\pi$	ampere (A)
Magnetic field strength, magnetizing force	H	oersted (Oe),[e] Gb/cm	$10^3/4\pi$	A/m[f]
(Volume) magnetization[g]	M	emu/cm^3[h]	103	A/m
(Volume) magnetization	$4\pi M$	G	$10^3/4\pi$	A/m
Magnetic polarization, intensity of magnetization	J, I	emu/cm^3	$4\pi \times 10^{-4}$	T, Wbm^{-2}[i]
(Mass) magnetization	σ, M	emu/g	1	$A{\cdot}m^2\,kg^{-1}$
			$4\pi \times 10^{-7}$	$Wb{\cdot}m\,kg^{-1}$
Magnetic moment	m	emu, erg/G	10^{-3}	$A{\cdot}m^2$, joule per tesla ($J\,T^{-1}$)
Magnetic dipole moment	j	emu, erg/G	$4\pi \times 10^{-10}$	$Wb{\cdot}m$[i]
(Volume) susceptibility	χ, κ	dimensionless, emu/cm^3	4π	dimensionless
			$(4\pi)^2 \times 10^{-7}$	henry per meter (H/m), Wb/(A·m)

Introduction to Molecular Magnetism: From Transition Metals to Lanthanides, First Edition.
Cristiano Benelli and Dante Gatteschi.
© 2015 Wiley-VCH Verlag GmbH & Co. KGaA. Published 2015 by Wiley-VCH Verlag GmbH & Co. KGaA.

Quantity	Symbol	Gaussian and cgs emu[a)]	Conversion factor, C[b)]	SI and rationalized mks[c)]
(Mass) susceptibility	χ_ρ, κ_ρ	cm^3/g, emu/g	$4\pi \times 10^{-3}$ $(4\pi)^2 \times 10^{-10}$	$m^3\ kg^{-1}$ $H{\cdot}m^2\ kg^{-1}$
(Molar) susceptibility	χ_m, κ_{mol}	cm^3/mol, emu/mol	$4\pi \times 10^{-6}$ $(4\pi)^2 \times 10^{-13}$	$m^3\ mol^{-1}$ $H{\cdot}m^2\ mol^{-1}$
Permeability	μ	dimensionless	$4\pi \times 10^{-7}$	H/m, Wb/(A·m)
Relative permeability [j]	μ_r	not defined	—	dimensionless
(Volume) energy density, energy product [k]	W	erg/cm^3	10^{-1}	$J\ m^{-3}$
Demagnetization factor	D, N	dimensionless	$1/4\pi$	Dimensionless

a) Gaussian units and cgs emu are the same for magnetic properties. The defining relation is $B = H + 4\pi M$.

b) Multiply a number in Gaussian units by C to convert it to SI (e.g., $1\ G \times 10^{-4}\ T/G = 10^{-4}\ T$).

c) SI (*Système International d'Unitès*) has been adopted by the National Bureau of Standards. Where to conversion factors are given, the upper one is recognized under, or consistent with, SI and is based on the definition $B = \mu_o(H + M)$, where $\mu_o = 4\pi \times 10^{-7}\ H/m$. The lower one is not recognized under SI and is based on the definition $B = \mu_o H + J$, where the symbol I is often used in place of J.

d) 1 gauss = 10^5 gamma (γ).

Index

a

angular overlap model (AOM)
– angular distortion 42
– f orbital energy 41
– parameters 41
– properties 41
– superposition model 41
aquo ions
– angular distortion 40
– best fit factors 39
– coordination geometry 38
– diagonal matrix 39
– ground multiplet 40
– non-diagonal matrix 39
– symmetry operations 39
atomic force microscopy (AFM) 298
atomic mean field integrals (AMFI) 86

b

ball and stick (BS) approach 173, 175
bidentate ligands 51
Brillouin equation 70
Brillouin function 81
broken symmetry approach (BS) 130

c

carboxylates 17, 62
chemical exchange saturation transfer (CEST) technique
– advantage 417
– diaCEST agents 418
– magnetization transfer asymmetry 416
– PARACEST agents 418
– proton exchange 417, 418
– saturation transfer technique 415
– spin distribution 415, 416
– Z-spectrum 417
chemisorption 306
colossal magnetoresistance (CMR) 297
configuration interaction (CI) method 85
copper acetate
– *ab initio* techniques 132
– anisotropic components 133
– covalency effects 133
– DDCI3 133
– dinuclear structure 132
– effective Hamiltonian theory 135, 136
– perturbation theory 133
– post-CASSCF method 134
– relative energy 135
– singlet triplet separation 132
– spin orbit contribution 134
– T dependence 132
– temperature dependent magnetic susceptibility 132
crystal field (CF)
– Dq parameter 38
– group theory 37
– non-vanishing parameters 37
– operator equivalent 35
– parameters 35
– qualitative agreement 35
– radial integrals 35
– Stevens/Wybourne approach 36
– symmetry requirements 36
– tetragonal environment 36
– transition metals 38
crystal field strength 80
Curie law 70
– Curie–Weiss law 71
– effective magnetic moment 70
– Ln(III) ions magnetic information 71
– transition metal ions, wave functions 72
Curie spin relaxation 402
Curie–Weiss law 71

Introduction to Molecular Magnetism: From Transition Metals to Lanthanides, First Edition.
Cristiano Benelli and Dante Gatteschi.
© 2015 Wiley-VCH Verlag GmbH & Co. KGaA. Published 2015 by Wiley-VCH Verlag GmbH & Co. KGaA.

cyclooctatetraene 17
cyclooctatetraene dianion (COT)
– chloride salt 55
– coordination sphere 55
– crystal structure 55
– cyclopentadienyl derivatives 55
– sodium salt 55
cyclopentadiene 17

d

d magnetic orbitals
– HS-LS transition 11
– octahedral environments 12
– SCO 10, 12
– SMM 13
d orbitals
– aufbau approach 163
– chirality
– – crystal structure 170
– – ECM 169
– – magnetic chirality 169
– – MChD 169, 170
– – non-enantiopure materials 169
– – non-zero contribution 170
– – refraction and absorption 170
– – space groups 170
– – properties 169
– – spin chirality 169
– 4*d* and 5*d* ions
– – exchange coupling constants 168
– – J coupling constants 165
– – Jahn Teller distortion 167
– – magnetic properties 165
– – NiM_2 adduct 168, 169
– – octahedral coordination 165
– – photomagnetism 165
– – pseudo-spin operator 167
– – six carbon donors 165
– – trigonal bipyramidal pentanuclear cluster 165
– 3*d* metal ions 164, 165
– DFT
– – Bn parameters 172
– – BS approach 173, 175
– – epochal paper 172
– – molecular structure 172
– dynamic Jahn-Teller 163
– f-d interactions 171
– Gd transition metals 176
– Ham effect 163
– high spin state 163
– low spin state 163
density functional theory (DFT)
– Coulomb repulsion 87
– *D* values 91, 92
– electron density 87
– electron kinetic energy 87
– electron nucleus interaction 87
– exchange correlation energy 87
– *in silico* approach 91
– Kohn Sham equations 87
– Koopmans theorem 87, 88
– octahedral environment 92
– polynuclear system 90
– quasi-routine technique 87
– wavefunction approach 87
– Xα method 87
diamagnetic (diaCEST) agents 418
diamagnetic susceptibility 69
dI/dV mapping 315
difference dedicated configuration interaction (DDCI) 135
diketonates 17, 58, 59
discrete Fourier transform (DFT)
– Bn parameters 172
– BS approach 173, 175
– epochal paper 172
– molecular structure 172
double decker Tb(III) derivative 324
double electron–electron resonance (DEER) sequence 391, 392
double quantum coherence (DQC) 159
Douglas–Krell–Hess (DKH) Hamiltonian 86
dressing ions
– ligand modes 33
– metal-ligand interaction 33
– paddlewheel motif 33
– transition metal ions 33
Dy-Pc based devices 316
dysprosium (Dy) 18
– AFM interaction 283
– angular dependence 279, 280
– archetypal Dy3 283
– axial symmetry 279
– binary symmetry 279
– bottom up approach 287
– chirality 282
– components 277
– dynamic properties 286
– Eu(III) ion 291
– exchange coupling constants 291
– 4*f* orbital 279
– features 277
– field dependence 280, 281
– Heisenberg cluster 283
– Ising spins 285
– Kramers doublets 280, 281
– local anisotropy axes 285

– magnetic properties 277, 278
– magnetic susceptibility 288
– magnetic tensor 279
– magnetization 283
– microstates 284
– monoclinic symmetry 278
– normalized magnetization 289
– Pauli matrices 284
– performing measurement 278
– perturbation 292, 293
– relaxation mechanism 289
– single-ion easy anisotropy axes 288
– spin chirality 286
– toroidal dipoles 282
– triangular cluster 284
– triangular moieties 288, 289
– triclinic crystals 289
– Zeeman splitting 285

e

effective magnetic moment 70
electron paramagnetic resonance (EPR)
– DEER sequence 391, 392
– dipolar fields 378
– fine structure 377
– GdDTBSQ
– – axial symmetry 379
– – fourfold symmetry 381
– – g values 381, 382
– – GdTrop 380
– – HF-EPR spectra 379
– – magnetic evidence 382
– – rhombic symmetry 380
– – X band spectrum 379
– – zero field splitting tensor 380, 381
– – zero field transition 381
– ground states 375
– hyperfine term 375
– intense lines 377
– intrinsic intensity 376
– Ln nicotinates
– – angular dependence 388
– – components 389
– – dinuclear structure 388
– – dipolar and exchange interaction 388, 389
– – hyperfine splitting 391
– – Ising symmetry 388
– – LaND 389
– – pseudo-XY symmetry 388
– orbit 382, 383
– tetragonal symmetry 376, 377
– transition metal
– – coordination polyhedron 384
– – experimental curves 386
– – polycrystalline powder 384, 385
– – principle 384
– – two not-equivalent molecules 385, 386
– – x, y and z axes 386, 387
– Zeeman energy 375
electron spin resonance (EPR), *see* electron paramagnetic resonance (EPR)
electron spin resonance (ESR) spectroscopy 153
electronic structures 16
electronic structures, free ions
– Aufbau configuration 25
– cation and electric dipoles 25
– 4f orbitals 26
– Fermi–Dirac statistics 27
– ground multiplets 27, 28
– magnetic field 31, 32
– Russell–Saunders coupling scheme 27
– spin orbit coupling
– – f orbitals 30
– – features 29
– – Hamiltonian energy 29
– – interelectronic repulsions 28
– – j–j coupling scheme 31
– – lanthanides 30
– – quantum number 29
– – Slater determinant 30
– – transition metal ions 28
– – tripositive lanthanide ions 29
enantiopure chiral magnets (ECM) 169
exchange and superexchange interaction 17
experimental susceptibility 69

f

f magnetic orbitals 13, 14
f orbital system 176, 177
ferromagnets 17
– anisotropy 117
– bricks, infinite array
– – icosidodecahedral structure 103
– – types 103
– – unpaired electrons 102
– – zero dimensional 102
– building blocks 99, 100
– dipolar interactions
– – coordinate system 112
– – D12 tensor 111
– – EPR spectroscopy 113
– – equivalent Hamiltonian 111
– – exchange interaction 113
– – g tensors 111
– – Gd(III) ions 110, 111, 112
– – slow decay 110

ferromagnets (*contd.*)
– – Y ions 111
– giant spin 114
– isotropic and anisotropic interaction 115
– magnetic interactions
– – Cr(III) free ion 104
– – Curie constant 106
– – Curie–Weiss law 106
– – dipolar 105
– – exchange interaction 105
– – group theory 108
– – HDVV Hamiltonian 104
– – Ising approach 108
– – Landé interval rule 105
– – magnetic ordering 108, 109
– – spin alignment 109
– – spin angular momentum 104
– – temperature dependence 106
– – Van Vleck equation 105
– Mn12 molecule 116, 117
– non collinearity 117
– one dimensional array 100
– orbital degeneracy
– – diamagnetic dilution 123
– – electronic ground states 119
– – exact diagonalization 120
– – isotropic and anisotropic terms 124
– – Kramers doublets 122
– – lanthanide derivatives 123
– – Lines model 120
– – Ln isolation 121
– – matrix elements 121
– – Pauli matrices 120
– – qualitative diagram 123
– – SH interaction 121
– – SOC 120
– – Zeeman term 122
– paramagnetic system 100
– single building block 115
– spin Hamiltonian approach 113, 114
– spin Hamiltonian parameters 116
– spin orientation 100
– three dimensional representation 101

g

generalized gradient approximations (GGAs) functionals 92
giant magnetoresistance (GMR) 296
Glauber model
– configurations 254
– dinuclear copper compound 255
– domain wall 256
– infinite array 255
– Orbach mechanism 254
– scaling function 256
– stochastic techniques 254
– temperature independent behavior 254
– time evolution 254

h

Hamiltonian approach 16
highly oriented pyrolitic graphite (HOPG) 306
hybrid organic magnetic molecules 318

i

intermediate coupling 299
intrinsic optical bistability (IOB) 113
ions magnetism
– Curie law, *see* Curie law
– diamagnetic susceptibility 69
– experimental susceptibility 69
– magnetic induction 69
– paramagnetic magnetization 70
– Van Vleck equation, *see* Van Vleck equation
irreducible tensor operators (ITO) 367

j

Jahn-Teller theorem 77, 136

k

Kondo effect 300, 301, 316

l

Landau–Zener–Stuckelberg (LZS) model 208
lanthanide induced relaxation (LIR) 397
lanthanide induced shift (LIS) 397
lanthanide shift reagents (LSR)
– diamagnetic molecules 406
– *g* tensor 405
– linear expansion 404
– secondary internal field 404
– shift reagent 405
light-induced spin-state trapping effect (LIESST) 12
Lines model 120
luminescence
– absorption/emission processes 425, 426
– antenna effect 429
– biological assays 432
– charge transfer transitions 425
– definition 424
– 4*f*-5*d* orbitals 424, 425
– forbidden transitions 426
– hypersensitive/pseudo quadrupolar transitions 426, 428
– light emission 426

– medical imaging 432
– non-radiative pathways 429
– OLED 429–432
– properties 426, 427

m
magnetic anisotropy
– 4*f* charge density 49
– *f* orbitals 48
– properties 47
– quadrupolar moment 48
– spin orbit coupling 47
– uniaxial anisotropy 47
magnetic circular dichroism (MCD) 169
magnetic coercitivity 296
magnetic resonance imaging (MRI)
– CEST
– – advantage 417
– – diaCEST agents 418
– – magnetization transfer asymmetry 416
– – PARACEST agents 418
– – proton exchange 417, 418
– – saturation transfer technique 415
– – spin distribution 415, 416
– – Z-spectrum 417
– chemical shift 414
– clinical applications 412
– contrast agents 413
– contrast reagents 409, 410
– coordinated water molecules 413
– coordination number 412
– Curie spin relaxation mechanism 411
– electronic relaxation time 412
– inner-sphere relaxation mechanism 410
– molecular structures 413
– nuclear longitudinal 410
– principles 409
– relaxation time 409
– residence time 414
– transverse relaxivity 410
– ZFS 411
magneto chiral effect (MChE) 169, 170
magnetocaloric effect (MCE)
– commercial application 423, 424
– constant pressure 421
– magnetic degrees of freedom 423
– magnetic entropy 421
– n-non-interacting spin 423
– paramagnetic demagnetization 422
– S-T diagram 421
– spin frustration 423
– thermal hysteresis 422
– vapor-compression cycle 424
magnetocrystalline anisotropy, *see* magnetic anisotropy
magnetogiric ratio 398
metal organic frameworks (MOFs) 18
– analysis 361
– anisotropy
– – applications 363
– – ball-and-stick view 364
– – magnetization value 364
– – symmetric core 363
– – temperature dependence 365
– cationic cluster 361
– cobalt(II) 355
– crystallographic analysis 360
– Cu-dimers 366
– 2D structure 369, 370
– 3D system 354
– definition 353
– depopulation mechanism 366
– development 352
– 3d–4f heterometallic cluster 365
– exchange mechanism 366
– features 363
– gadolinium 353
– giant clusters 358
– growth mechanism 351
– inner shell 360
– ITO 367
– magnetic susceptibility 362
– metal ions 362, 363
– metamagnet 355, 356
– M–L–M connectivity 353
– molybdates
– – antiferromagnetic coupling 359
– – Hilbert space 358, 359
– – isomorphous 360
– – structures 358
– – temperature dependence 359, 360
– monoclinic 355
– M–X–M bonding 354
– one-dimensional coordination polymers 354, 355
– orthorhombic modification 355
– photoluminescence properties 357
– point group symmetry 367
– quantitative indication 367
– red fluorescence 357
– spin states 367
– structures 352
– Yaghi's secondary-building-units 354
– ZFC-FC measurement 356
molecular magnetism (MM) 297
– complexity 7
– – *d* magnetic orbitals

molecular magnetism (MM) (*contd*.)
– – HS-LS transition 10
– – octahedral environments 12
– – SCO 10, 12
– – SMM 13
– diamagnets 2
– dipolar magnets 3
– exponential growth 15
– *f* magnetic orbitals 13, 14
– *f* orbital approach 1
– goals 14
– graphic outline 16
– lanthanides
– – heterogeneous catalysis 19
– – magnetocrystalline anisotropy 20
– – mischmetal/Auer metal 18
– – Nd, Dy, Eu, Tb, and Y 20
– – optical spectra 19
– – peculiar property 19
– – permanent magnet industry 20
– – $SmCo_5$ and $Nd_2Fe_{14}B$ 19, 20
– material description 2
– metallic and ionic lattices 4
– organic molecules 4
– origin 5
– *p* magnetic orbitals
– – dithiadiazolyl radical 9
– – EPR spectroscopy 8
– – inorganic radicals 9
– – intermolecular reactivity 9
– – nitroxide and tetracyanoethylene 8
– quantum mechanics 3, 4
– SI *vs.* emu 21
– tantalizing expression 1
– time and space 2
molecular orbital (MO) 17
– charge transfer processes 127, 128
– complexity
– – D tensors 88, 90
– – EPR spectra 89
– – g tensors 88
– – ground state 90
– – INDO methods 90
– – LF formalism 88
– – spin orbit coupling 89
– – ZFS parameters 89
– copper acetate
– – *ab initio* techniques 132
– – anisotropic components 133
– – covalency effects 133
– – DDCI3 133
– – dinuclear structure 132
– – effective Hamiltonian theory 135, 136
– – perturbation theory 133
– – post-CASSCF method 134
– – relative energy 135
– – singlet triplet separation 132
– – spin orbit contribution 134
– – T dependence 132
– – temperature dependent magnetic susceptibility 132
– correlation effects
– – 4f orbitals 86
– – ab initio techniques 84
– – AMFI 86
– – CASSCF/CASPT2 states 85
– – configuration interaction 84
– – Coulomb correlation 84
– – coupled cluster 84
– – Dirac approach 85
– – DKH Hamiltonian 86
– – electron correlation 84
– – g tensor 86
– – MBPT 84
– – SCF 84
– d orbitals, structural requirements 129
– degenerated states 136, 137
– DFT
– – Coulomb repulsion 87
– – *D* values 91, 92
– – electron density 87
– – electron kinetic energy 87
– – electron nucleus interaction 87
– – exchange correlation energy 87
– – *in silico* approach 91
– – Kohn Sham equations 87
– – Koopmans theorem 87, 88
– – octahedral environment 92
– – polynuclear system 90
– – quasi-routine technique 87
– – wavefunction approach 87
– – Xα method 87
– DOTA complexes
– – CASSCF-CASPT2/RASSI-SO method 94
– – Dy-Na interaction 94
– – experimental and calculated luminescence spectra 94
– – LnDOTAa 95
– – magnetic anisotropies and luminescence 93
– – $Na[Dy(DOTA)(H_2O)]\cdot 4H_2O$ compound 93
– – pseudo four-fold symmetry axis 95
– excited state 128
– *f* orbitals and orbital degeneracy
– – Cartesian components 139
– – HDVV 139

– – octahedral symmetry, splitting 138
– – techniques 138
– – wavefunctions 139
– – Yb ions 138
– ferromagnetic contribution 128
– ligand field model 83
– physical properties 127
– quantitative calculations 83
– schematic diagram 128
– SH parameters
– – broken symmetry approach 130
– – covalency effects 130, 131
– – eigenfunctions 130
– – error cancellation effects 131
– – exchange parameter 132
– – Heisenberg constant 130
– – maximum delocalization 130, 131
– valence bond theory 129
molecular spintronics
– CMR 297
– detection process 308
– detection schemes 303, 304
– GMR 296
– hybrid organic magnetic molecules 318
– magnetic field sensors 296
– magnetic multilayers 296
– magnetic substrate 319
– magnetism measurement 310
– Mn12 317
– molecular organization on surfaces 303
– molecules and mobile electrons
– – Coulomb blockade 300
– – Coulomb oscillations 302
– – electron beam lithography fabrication 301
– – HOMO/LUMO properties 299
– – hybridization effects 299
– – Kondo effect 300, 301
– – metal thiolates 301
– – MM 297
– – molecular electronics 298
– – molecule-electrode interaction 298
– – QD 297
– – Schottky barrier 299, 300
– – SMM 297
– – STM 298
– molecules and surfaces selection
– – bottom up approach 307
– – chemisorption 306
– – immobile molecules 307
– – MPc monolayers 305
– – multilayer techniques 305
– – physisorption 305
– – self-assembly/self-organized growth 307
– – sulfur strategy 306
– molecules purity 307
– nanostructured magnetic devices 295
– nuclei
– – electronic magnetic moment 321
– – ground states energy 322
– – non coherent tunneling 322
– – nuclear spins 321
– – pc ligands 322
– – spin flip dynamics 324
– – STS 322
– – ^{165}Tb nucleus 322
– – $TbPc_2$ properties 322
– – transition matrix, QTM 323
– – waiting time 323
– organizing and addressing molecules 302
– Pc family
– – dI/dV mapping 315
– – Dy-Pc based devices 316
– – four-lobe molecule analysis 315
– – Kondo effect 316
– – Kondo temperature 316
– – Ln molecules 314
– – Ln(III)-Pc molecules 316
– – OFETs 314, 316
– – $Tb(Pc)_2$, SIM nature 316
– – TbNPcPc double-decker molecules 317
– – $TbPc_2$ molecule 314
– single radical transport
– – archetypal radical 312
– – Co-Salen molecule 312
– – electrode with radical bridge 312
– – high-resolution topography 314, 315
– – 2′-nitronylnitroxide-5′-methyl-[1,1′; 4′,1″]terphenyl-4,4″-dicarbonitrile radical 315
– – nitronyl nitroxides 313
– – SAM 312
– – TOV 312
– – verdazyl derivatives 312
– spin valve device 324
– TMR 297
– VASP 319
– X-rays
– – absorption 308, 309
– – dipole selection rule 309
– – $L_{2,3}$ edges 310
– – one-electron model 310
– – XMCD 308
– XASs 308
molybdates
– antiferromagnetic coupling 359
– Hilbert space 358, 359
– isomorphous 360

molybdates (*contd.*)
– structures 358
– temperature dependence 359, 360
monodentate ligands 51

n

nanostructured magnetic devices 295
n-electron valence second-order perturbation theory (NEPTV2) method 135
nitronyl nitroxides (NITs) 17
– automatized method 146
– bidentate ligand 60
– computational analysis 159
– diamagnetic nitrone 156, 157
– DQC 158
– energy levels 156
– experimental evidence 62
– first principle bottom up 146, 147
– initial reagents 60
– J_{AB} values 147
– Kramers doublets 156
– lead dioxide 60
– metal ion/radical ratio 61
– molecular structure 158
– N–N distances 160
– parameters 156
– PELDOR 158
– β-phase crystals 146
– polymorphs 146
– sodium periodate 60
– spin–spin interaction 160
– structural instability 146
– χT product 155, 156
– temperature dependence 148
– Van Vleck equation 147
– X band spectrum 158
nuclear magnetic resonance (NMR)
– *f*-block element 395
– lanthanide ion
– – crystal field effects 400
– – Curie relaxations rates 403
– – Fermi contact 397, 398
– – induced magnetic moment 398
– – isostructural 396
– – isostructural series 399
– – isotropic hyperfine coupling constant 398
– – LIR 396, 397
– – LIS 396, 397
– – LnDOTAM series 401
– – non-zero spin 401
– – paramagnetic shift 400
– – paramagnetism 395
– – pseudocontact shift 399
– – reference compound 400
– – relaxation mechanism 402, 403
– – resonant nuclei 397
– – rotational correlation time 404
– – second-order magnetic axial anisotropy 400
– – signal linewidth 404
– LSR
– – diamagnetic molecules 406
– – *g* tensor 405
– – linear expansion 404
– – secondary internal field 404
– – shift reagent 405
– properties 396
– uses 395

o

orbital degeneracy 176, 177
organic field-effect transistors (OFETs) 314, 316
organic light-emitting diode (OLED)
– advantages 430
– cell structure 430
– Dexter transfer mechanism 431
– dipole–dipole coupling 431
– electrons transport mechanism 430
– guest phosphorescent molecules 431
– parameters 431, 432

p

p magnetic orbitals 17
– dithiadiazolyl radical 9
– EPR spectroscopy 8
– inorganic radicals 9
– intermolecular reactivity 9
– nitroxide and tetracyanoethylene 8
– organic ferromagnet 8
p magnetic orbitals system
– allyl radicals 145
– antiferro- and ferromagnetic interactions 144
– charge transfer mechanism 145
– ferrimagnetic approach 143
– metallorganics magnets
– – building blocks 149
– – *d* orbitals 149
– – *f* orbitals 149
– – TCNE 150
– – TCNQ 151
– nitronyl nitroxides
– – automatized method 146
– – computational analysis 159
– – diamagnetic nitrone 156, 157
– – DQC 158

– – energy levels 156
– – first principle bottom up 146, 147
– – J_{AB} values 147
– – Kramers doublets 156
– – molecular structure 158
– – N–N distances 160
– – parameters 156
– – PELDOR 158
– – β-phase crystals 146
– – polymorphs 146
– – spin–spin interaction 160
– – structural instability 146
– – χT product 155, 156
– – temperature dependence 148
– – Van Vleck equation 147
– – X band spectrum 158
– polycarbenes 144
– semiquinone radicals
– – A–B pair 153
– – A–D pair 153
– – AFM coupling 154
– – antiferromagnetic coupling 155
– – asymmetric unit 152
– – Brillouin function 152, 153
– – DTBSQ 153
– – EPR spectroscopy 153
– – exchange mechanism 152
– – magnetic measurement 153
– – static deformation density 154
– – structures 152
– – π-symmetry 155
– – valence tautomerism 152
– thioradicals 147
paramagnetic chemical exchange saturation transfer (PARACEST) agents 418
paramagnetic Weiss temperature 71
Pascal's approach 69
Pc family
– dI/dV mapping 315
– Dy-Pc based devices 316
– four-lobe molecule analysis 315
– Kondo effect 316
– Kondo temperature 316
– Ln molecules 314
– Ln(III)-Pc molecules 316
– OFETs 314, 316
– $Tb(Pc)_2$, SIM nature 316
– $TbPc_2$ molecule 314
photon scanning microscopy (PSTM) 298
phthalocyanines (Pc) 17, 223, 224
– aromatic rings 54
– chromatography 53, 54
– Ln(III)
– – cube dodecahedron and squared antiprism 43
– – energy splittings 44, 45
– – Jz operator 43
– – pyrrole nitrogen atom 42
– – SAP 43
– – structural parameters 43
– porphyrins (RP) 53
– sandwich compounds 54
physisorption 305
polyoxometalates (POMs) 17, 231, 234
– angle dependent energy 45
– characteristics 58
– eλ parameters 44
– gadolinium 46
– geometrical perturbation 45
– Ising features 44
– ligand field parameters 46
– magnetic ions 56, 57
– magnetic properties 44
– sodium molybdate 56
– spin localized mixed valence derivatives 57
– spin-delocalized mixed valence derivatives 57
– structures 57
– Wybourne notation 47
pulsed electron-electron double resonance (PELDOR) 159
pyrazolylborates 17
– trifluoromethanesulfonate 52
– trigonal prismatic geometry 52, 53
– trispyrazolylborate anion 52
pyrene moiety 324

q

quantitative model 334
quantum computing (QC)
– definition 329
– detour 334
– endohedral fullerenes 335
– optical approach 331
– philosophical aspects 347
– QIP, *see* quantum information processing (QIP)
– SQUID devices 330
– transmon 330
– 15 vanadium(IV) 346
quantum dots (QD) 297
quantum information processing (QIP)
– bit 331
– Bloch sphere 332
– coherence and decoherence 333
– definition 330
– dephasing 338

quantum information processing (QIP) (*contd.*)
– electron and nuclear spins 332
– entangled state 334
– entanglement 333
– inorganic compound 340
– molecular rings
– – anisotropy analysis 344
– – 7 chromium(III) and one nickel(II) 342
– – copper compounds 345
– – Cr_7Ni moieties 345
– – crystal K band spectrum 342
– – 1D materials 341
– – EPR and INS 343
– – ESR and INS 342
– – frozen solution 344
– – giant spin model 343
– – isotropic exchange interaction 342
– – spin-Hamiltonian parameters 344
– qubit 331, 333, 347

r

radical pair model 334
remnant magnetization 200

s

scanning tunneling microscopy (STM) 298
scanning tunneling potentiometry (STP) 298
Schiff bases 17
– 3*d*-4*f* exchange interactions 62
– homo and heterobinuclear compounds 64
– primary imine 62
Schottky barrier 299
self-assembled monolayers (SAM) 312
self-consistent field (SCF) 84
sequence for phase error amplification (SPAM) 337
single chain magnets (SCM)
– antiferromagnetic chain 251
– chain-to-chain interaction 251
– *d* and *p* orbital
– – anisotropic Heisenberg Hamiltonian 259
– – CoPhOMe 257
– – crystal structure 258
– – flipping energy 259
– – isolated chain 258
– – magnetic relaxation 258
– – nitronyl nitroxides 257
– – temperature dependence 258
– diamagnetic defect 252
– f orbitals, Dy
– – ac measurements 269
– – coordination environment 268
– – CoPhOMe 268
– – 1D system 271
– – g tensor 269
– – interchain dipolar interactions 267
– – metamagnetic transition 271
– – monomer and polynuclear systems 268
– – puzzling result 269, 270
– – reference frame 269
– – supramolecular interactions 267
– – versatility 269
– *f* orbitals, Gd
– – cell representation 262
– – design 262
– – Ising approach 264, 265
– – magnetic properties 262
– – NNN magnetic interactions 265
– – paramagnetic phase 266
– – pitch Q 265, 266
– – χ;T values 263, 265
– – temperature 263
– Glauber model
– – configurations 253
– – dinuclear copper compound 255
– – domain wall 256
– – infinite array 255
– – Orbach mechanism 254
– – scaling function 256
– – stochastic techniques 254
– – temperature independent behavior 254
– – time evolution 254
– magnetic properties 251
– non-collinear system 260–262
– spin correlation function 252
– spin dynamics 252
– spin glass 259, 260
– static and dynamic properties
– – anisotropic systems 272
– – 1D system 271
– – exponential divergence 272
– – *f*-*p* chains 273
– – magnetization 272
– – mixed metal chain 273
– – parameters 272
single ion magnet (SIM) 180
– anionic double decker 224, 225
– CF parameters 225, 226
– magnetic site-dilution measurement 233
– phthalocyanine 223, 224
– POM 231, 232
– resonant tunneling
– – dipolar interaction 221
– – features 221
– – hyperfine constant values 221
– – spectral resolution 219
– ring-shaped aromatic ligands 233

– slow magnetic relaxation, Ho(III)
– – effective spin 218
– – hysteresis signals 219
– – irreducible representations 218
– – magnetic properties 218
– – micro SQUID 219
– – zero field 218
– Tb and Dy molecules
– – didactic approach 227
– – distortion angle 228
– – electron-phonon interaction 228
– – matrix element 227
– – Orbach and Raman contributions 227
– – properties 227
– – relaxation times 228
– transverse components 222
– triple decker compounds 229, 230
single-molecule magnets (SMMs) 18
– ac susceptibility 243
– Arrhenius plot 242
– Arrhenius plot τ_0 207
– Berry phase effects 197
– blocking temperature 240
– dinuclear compounds 245
– energy quanta 196
– 4*f* orbital 245
– Fe4 structure
– – Arrhenius relaxation 205
– – H_3L ligands 202
– – helical pitch γ 203
– – Hilbert space 201
– – iron(III) clusters 201
– – isotropic and Zeeman components 204
– – local binary axes 204
– – low lying level 202
– – magnetic properties 203
– – Orbach model 203
– – quantum tunneling 205
– – robustness 205
– – trigonal symmetry 202
– Jahn-Teller elongation axis 242
– Kramers doublets 246
– Kramers ion 243
– magnetic dilution effects 210
– magnetic hysteresis 196
– metallacrown ligands 241
– Mn12Ac analysis 196, 197
– Orbach process 243
– ovph complex 246
– polynuclear system 245
– QTM 213
– quantum tunneling process 243
– radical bridge 247, 248
– spin topology 242
– μSQUID technique 245, 246
– structures 239
– superparamagnets
– – long range order 199
– – nanoparticles 200
– – Néel temperature 200
– – saturation value 200
– – short range order 199
– – superparamagnetism 201
– – thermal motion block 199
– systematic approach 241
– tunneling
– – equilibrium magnetization 208
– – low temperature relaxation 208
– – LZS model 208
– – Monte Carlo simulation 208
– – multispin model 209
– – propeller-like core 208
– – rhombic anisotropy 209
– two-well model 197
– uses 239
– Ueff, Δ, τ0, and blocking temperature 198
– valdien complexes 245
– wavelength dependence 196
– XMCD tool 211, 212
– Y/Dy ratio 245
– ZFS 195, 197, 198
single-walled carbon nanotube (SWCN) 318
SMM–SWCNT interaction 324
spin crossover systems (SCO) 10
spin dynamics 17
– angular frequency 189
– Cole–Cole plot 190
– density 179
– differential susceptibility 190
– external and internal fields
– – dipolar interaction 187, 188
– – hyperfine interaction 187, 188
– – orbit–lattice parameters 189
– in-phase susceptibility 190
– isomorphous series 180
– localized/delocalized ion 179
– magnetization 189
– measured susceptibility 190
– out-phase susceptibility 190
– phonons
– – continuum limit waves 182
– – Debye temperature 182
– – direct process 182, 183
– – frequency hν 186
– – $Ho(EtS)_3$ 183
– – Ho(EtS)3 184
– – Kramers and non-Kramers ion 182
– – linear dependence 184

spin dynamics (*contd.*)
– – Orbach process 186
– – orbit lattice coupling 183
– – power dependence 185
– – Raman process 185, 187
– – relaxation rate 184
– – relaxation time 186
– relaxation process 181
– SIM 180
– spin lattice relaxation time T_1, 181
– spin–spin relaxation time T_2, 181
– – dipole–dipole interaction 191, 192
– – Fermi's golden rule 192
– – Raman mechanism 192, 193
– – Suhl–Nakamura model 191
– τ distribution 190
– τ distribution 191
spin glass-like materials (SGL) 200
spin Hamiltonian (SH) approach 74
spin polarized scanning tunneling microscopy (SPSTM) 298
spintronics 18
state interaction (SI) matrix 134
strong coupling 299
superparamagnetism 200
superposition model 40

t

TbNPcPc double-decker molecules 317
TbPc molecules 319
TbPc2 molecules 319
TbPc-pyrene 318
temperature independent paramagnetism (TIP) 73
tetracyanoethylene (TCNE) 150
– 3d metal ions 165
tetracyanoquinodimethane (TCNQ) 151
– 3d metal ions 165
tetra-phenyl-porphyrine (TPP) 149
thioradicals 147
time-of-flight secondary ion mass spectrometry (ToF-SIMS) 308
time-resolved luminescent (TRL) immunoassays 432
tunnel magnetoresistance (TMR) 297

v

Van Vleck equation
– anisotropy
– – Bleaney scheme 81
– – Dy(III) ion 79
– – Ising type 74
– – Jahn Teller effect 77
– – lanthanide ion 79, 81
– – non-degenerate wave function 76
– – octahedral cobalt(II) complexes 78
– – orbital moment 77
– – spin orbit coupling 75
– – tetragonal distortion 78
– – unquenched orbital contribution 77
– – Zeeman effect 76, 77
– – zero-field splitting 76
– aquo ion of Ce(III) 73
– magnetic susceptibility 72
– octahedral Co(III) compounds 73
– spin Hamiltonian approach 74
– TIP 73
– Yb(III) energies and eigenfunctions 74
vibronic coupling 136
Vienna Ab initio Simulation Package (VASP) 319

w

weak coupling 299

x

X-ray absorption spectroscopy (XAS) 308
X-ray based spectroscopies (XASs) 308
X-ray magnetic circular dichroism (XMCD) 308, 310
X-ray photoelectron spectroscopy (XPS) 308

z

Zeeman effect 76, 77
Zeeman perturbation 73
Zero-field splitting (ZFS) 76, 89, 195, 411

WILEY END USER LICENSE AGREEMENT

Go to www.wiley.com/go/eula to access Wiley’s ebook EULA.